Research and
Technology 1994

Annual Report of the
Marshall Space Flight Center

NASA TM–108470

National Aeronautics and
Space Administration

George C. Marshall Space Flight Center
Marshall Space Flight Center, Alabama 35812

On July 16, 1969, the Saturn/Apollo Program
marked the ending of one era and the beginning of
another. The advancements that led to this
achievement were unprecedented, forever changing
the way we perceive the Universe.

Today the synergistic spirit responsible for the first
manned lunar landing is still present at Marshall
Space Flight Center. We work toward the common
goals of improving lives and increasing the
understanding of the world in which we live. While
25 years have passed since "the day the Earth
revolved around the Moon," the refusal to become
complacent guides us into new directions and into
new frontiers.

This report summarizes the technology transfer, advanced studies, and research and technology
programs efforts now in progress, attesting to our capability to accept the scientific and technological
challenges that await us in 1995 and into the 21st century.

G.P. Bridwell
Director

Acknowledgments

To assist the reader, the MSFC contact, office code, and telephone number are included at the beginning of each article. The sponsoring organization and university and industry involvement are given at the end of each article. An abbreviations and acronyms list, an alphabetical index of contacts, and an index of key words are presented at the end of this report.

Table of Contents

Technology Programs

Structures and Dynamics

Saturn/Apollo Program

Answered Challenge to the Nation

Earthrise.
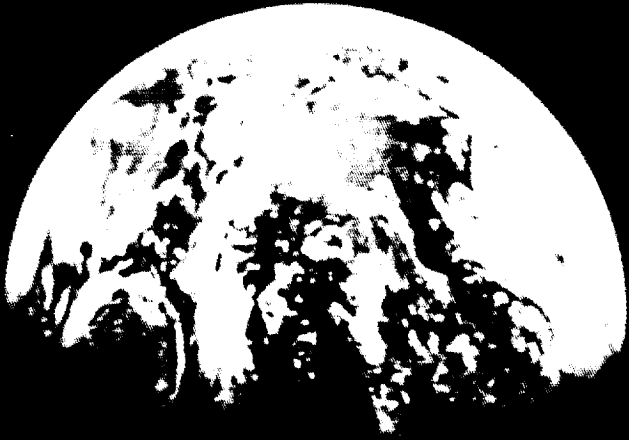
July 1994 marked the 25th anniversary of what President John F. Kennedy predicted to be "the greatest adventure on which man has ever embarked." For the first time, humankind walked on the lunar surface.
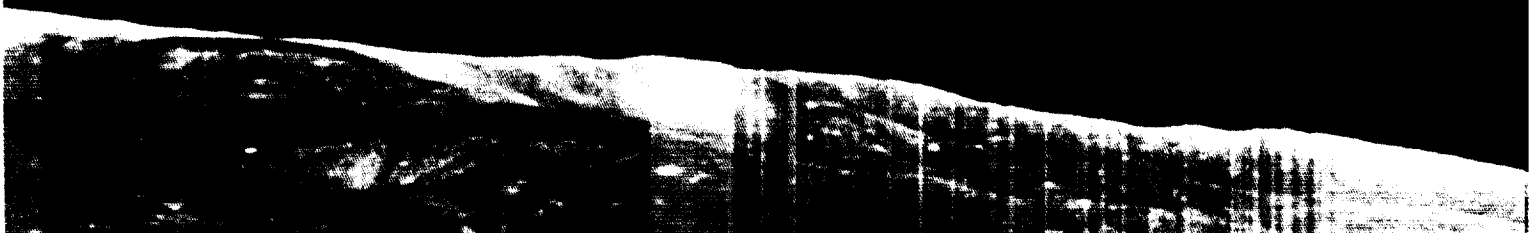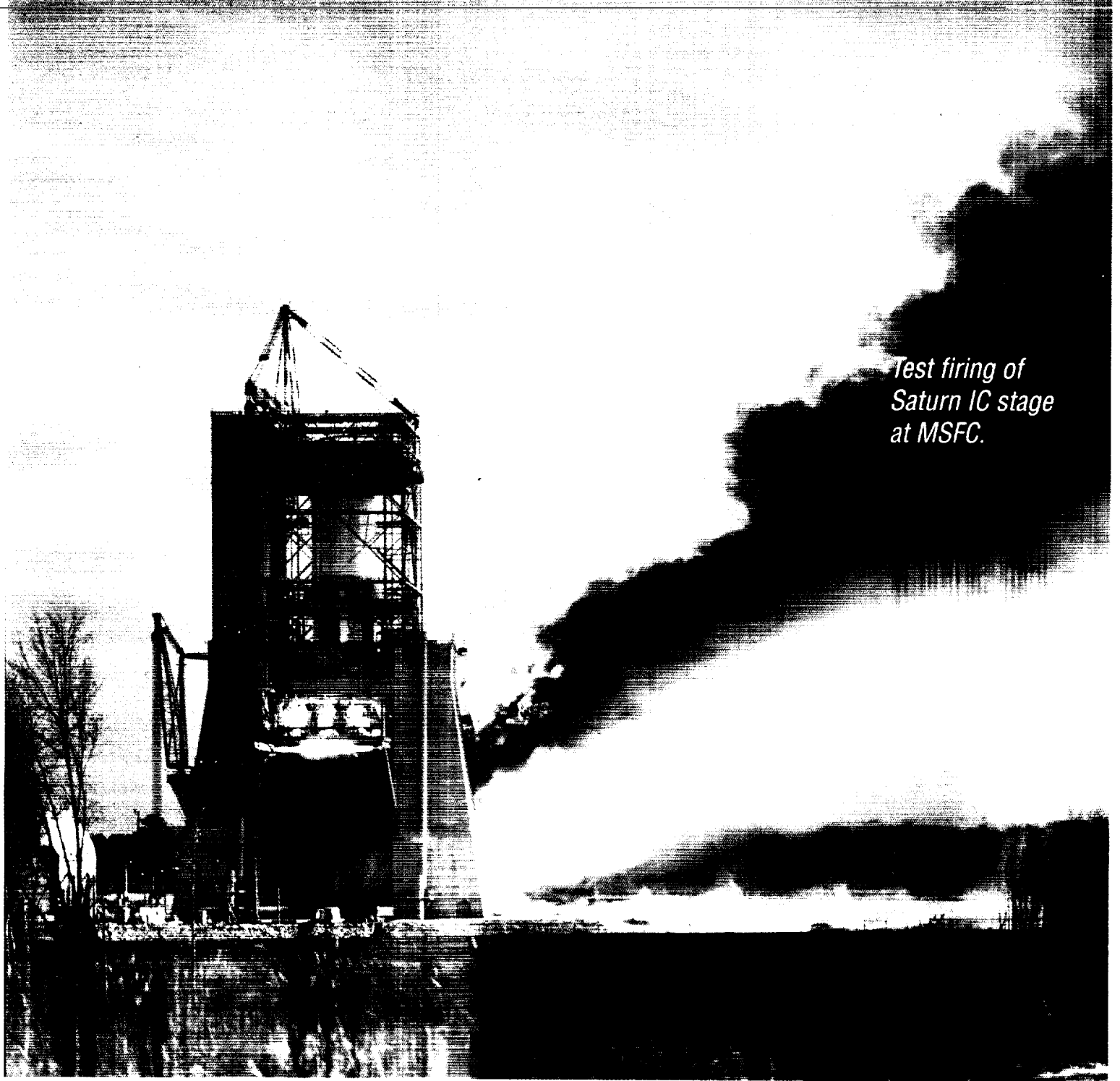
Test firing of Saturn IC stage at MSFC.

In a figurative sense, the journey started long before a Marshall Space Flight Center-developed Saturn V lifted the Apollo astronauts on their way to the lunar surface on July 16, 1969. In the same way, the journey did not end when the Apollo astronauts splashed down in the Pacific Ocean. The journey began in the minds of men like Wernher von Braun who, even as a young boy growing up in Germany, dreamed of space travel. The journey

continued in 1994 in the minds of employees and others associated with NASA and the Marshall Center.

Historians, who like to cite the origin of events in terms of place and time, usually note Kennedy's "Special Message to Congress on Urgent National Needs" on May 25, 1961: "I believe this Nation should commit itself to achieving the goal, before

this decade is out, of landing a man on the Moon and returning him safely to the Earth."

To prepare for that speech, the President had sought advice from Vice President Lyndon Johnson on the Nation's space options. One of the experts who provided Johnson with advice was Von Braun, the first Director of MSFC. Von Braun wrote Johnson a letter dated April 29, 1961. "This is an attempt to answer some of the questions about our national space program raised by the President in his memorandum to you dated April 20, 1961." One question that Von Braun addressed concerned the possibility of a manned lunar landing. "We have an excellent chance of beating the Soviets to the first landing of a crew on the Moon (including return capability, of course)," he told Johnson. The amount of influence that Von Braun's letter may have had on the Administration is open to debate. Nevertheless, Kennedy's call for a manned lunar landing directly impacted the future of the Marshall Center. As a result, the Center was directed to proceed with development of the Saturn V launch vehicle. Based on the F-1 rocket engine and the hydrogen-fueled J-2 engine, the Saturn V would be larger than any vehicle ever built. It would build upon MSFC's experience with the Saturn I and Saturn IB launch vehicles. More powerful than the Saturn I or Saturn IB, the Saturn V would provide the capability for lunar and planetary expeditions. Its design called for three stages and an instrument unit to manage guidance and control.

Kennedy had said that the manned lunar landing program would challenge the Nation. Speaking at Rice University in Texas on September 12, 1962, he said, "We choose to go to the Moon in this decade and do the other things, not because they are easy, but because they are hard, because that goal will serve to organize and measure the best of our energies and skills..." Developing the Saturn V meant just that for MSFC. More than 3 million pieces, making up 700,000 parts, were contained in a single Saturn V. At the height of the Saturn program, as many as 20,000 contractor companies were involved. Their involvement ranged from manufacturing the smallest components to static testing complete vehicle stages.

In Huntsville, the thunder rolled and the ground shook when engineers test-fired the mighty first stage of the Saturn V. Von Braun was at the helm, directing all aspects of Saturn V development. His commitment and dedication were unparalleled. To

anyone who might have thought of turning back or who might have felt weak in the knees after grasping the enormous proportions of the challenge, Von Braun portrayed confidence. "We have thrown our hat across the river," he wrote in 1964. The pace of the Center was fast and it grew faster. One employee recalled a visit to his work site by Von Braun: "You couldn't keep up with him as he walked down the hall."

Quality, however, was never sacrificed to urgency. Components were tested and retested and then tested again. Reliability became the hallmark of the Center. "The confidence factor derived from conservative design, extensive testing, and stringent quality control all based on meticulous attention to detail," an MSFC report stated.

Saturn changed the landscape. Old facilities were renovated and new facilities were constructed. Existing test stands were remodeled and a new test area was developed for propulsion and structural dynamic testing. Thousands of new workers joined the Marshall team, working either in Huntsville or at other sites. On July 15, 1960, when the Marshall Center came into existence, permanent civil service and contractor strength, both in Huntsville and at other locations, stood at 5,843. By Fiscal Year 1964, it had risen to 54,835. The 1960 Huntsville

Apollo 11 liftoff July 16, 1969.
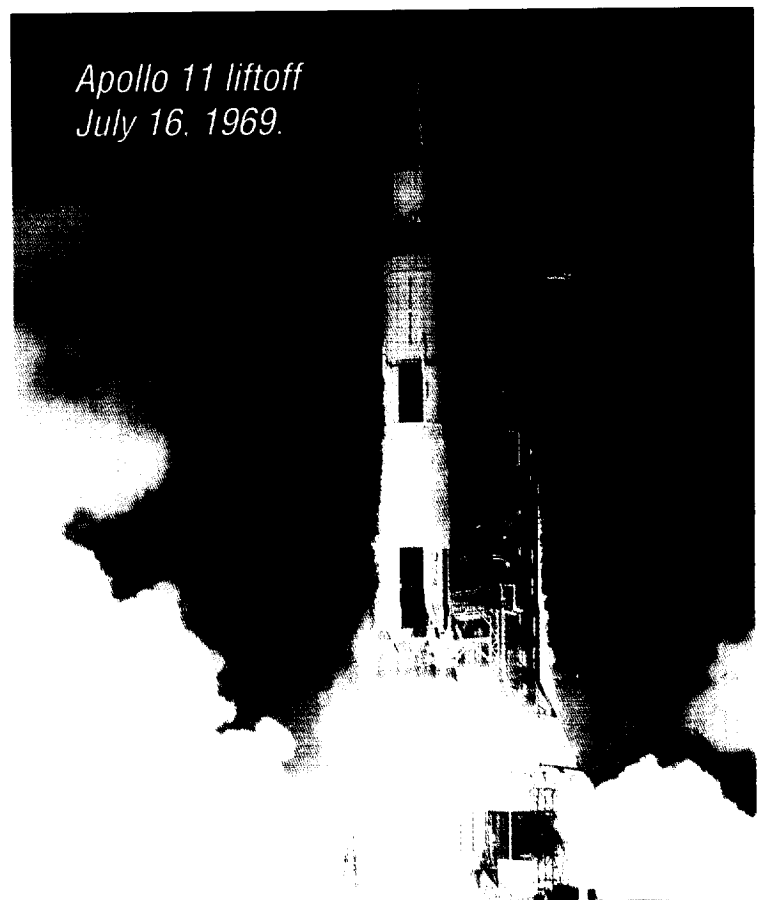
census put the city's population at 72,000. By 1964 that number had risen to 123,000.

Saturn development and testing continued. As a prelude to Apollo 11, NASA launched two unmanned and three manned Saturn V vehicles. All of that experience came together on July 16, 1969, when the giant launch vehicle lifted the Apollo 11 astronauts on their journey to the lunar surface.

The Apollo 11 astronauts spent a total of 21 hours and 36 minutes on the lunar surface. In addition to leaving behind several ceremonial articles, the astronauts returned 46 pounds of lunar samples to Earth.

After the Apollo astronauts completed their mission, Marshall Center employees and others in Huntsville danced in the streets. At one such celebration, Von Braun told those present, "Because of the beginning we have made here, the planets and stars may belong to mankind."

By 1974, the fifth anniversary of the first lunar landing, NASA had depended on the Saturn V launch vehicle to launch six more Apollo missions as well as the *Skylab* space station. The anniversary was an opportunity for Von Braun to reflect on the Apollo program and on the development of the Saturn V. His recollections were candid. When the decision was made to begin the Apollo program, "there wasn't a single discipline in which all the answers were available to support a manned flight to the Moon..." It was a "process of asking these various disciplines impossible questions and hoping they would come up with impossible answers to these impossible questions. This I believe had a tremendous catalytic effect on all these sciences and technologies. If you are told 'unless you come up with a meaningful answer we can't do it' that is a strong incentive..."

A tour through the Marshall Center test area or a glimpse inside its laboratories would have substantiated Von Braun's claim by revealing hundreds of engineers and scientists at work on a myriad of technical challenges. For example, the propulsion system for the first stage of the Saturn V depended on a cluster of five F-1 engines, each

producing 1.5 million pounds of thrust. In utilizing this cluster concept, first developed by the Von Braun team, engineers faced challenge after challenge. This system and others in the Saturn V required unique pumping, ducting, and venting schemes to obtain uniform propellant flow. The upper stages of the vehicle were fueled by liquid hydrogen. As a result, the whole field of cryogenics changed. Engineers not only learned more about using this highly explosive supercooled liquid as

rocket fuel, they learned more about transporting it and storing it in massive quantities.

Historian Roger Bilstein has traced the history of MSFC's development of the gigantic Saturn rockets throughout the 1960's. "In dealing with the technology of the Saturns in general, the most consistent factor seemed to be the enormous size of the vehicles," Bilstein wrote. The Saturn V stood 363 feet tall and weighed more than 6 million
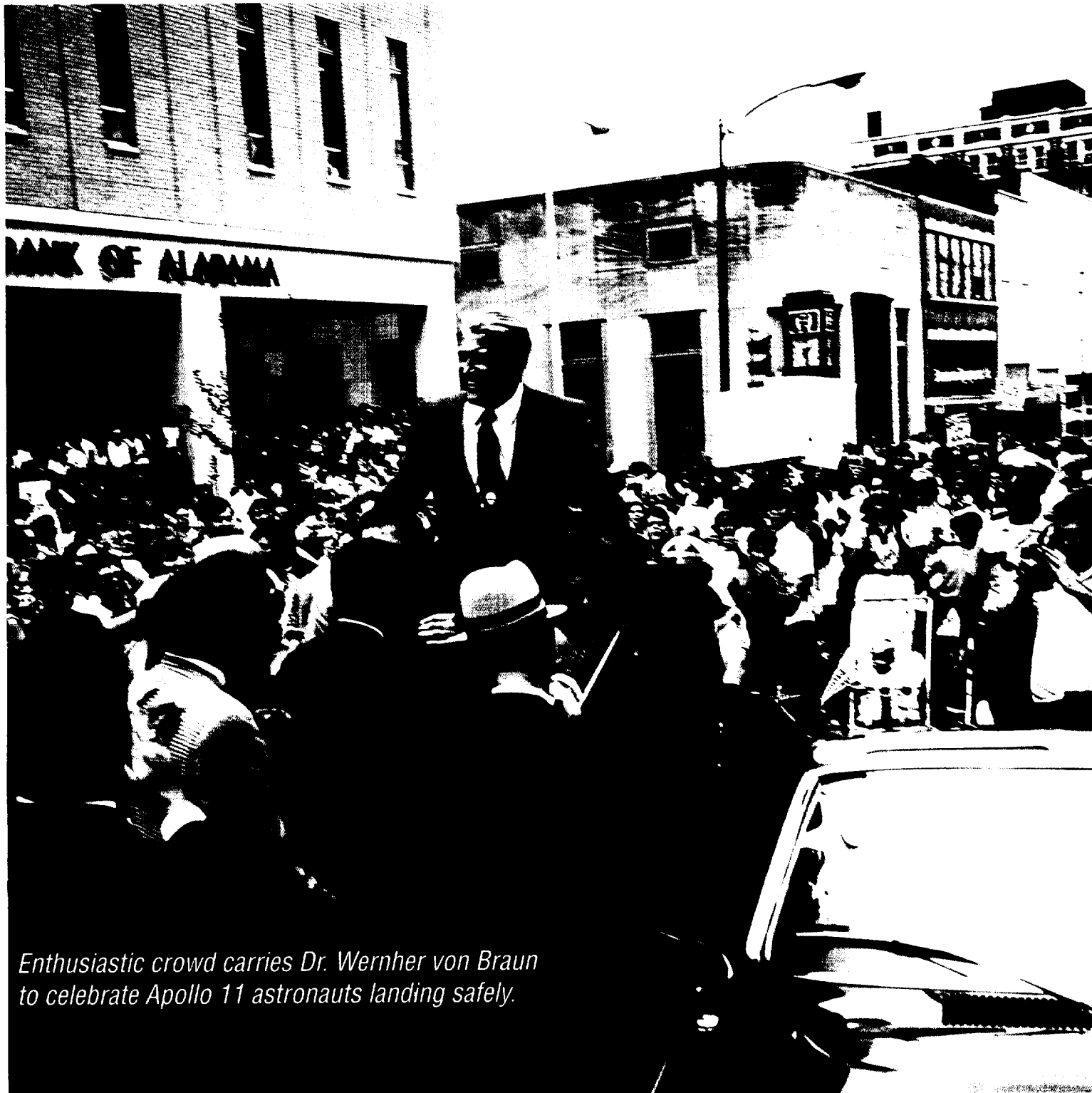
Enthusiastic crowd carries Dr. Wernher von Braun to celebrate Apollo 11 astronauts landing safely.

pounds when fully fueled. Even though the prototypes of some components existed, they were not as large as the new vehicle required. This meant that engineers at the Marshall Center and at other sites across the Nation had to develop special fabrication techniques. Gigantic tooling was required to form structures. In addition to basic advances in rocketry and propulsion, the work demanded advances in metallurgy, welding, insulation, materials science, static testing, and hundreds of other fields.

The Saturn V was also a study in contrasts. Engineers called it "the beast." Yet the design also called for the development of super-lightweight durable materials, microminiature components, and advances in the design of logic devices, computers, and other electronic components. A successful ground testing program was absolutely critical. MSFC laboratories developed new techniques for simulating harsh launch and space-flight conditions. Electronic simulators were developed to determine how the vehicle and its components would react to extreme pressures, temperatures, and dynamics. Special instrumentation was created to gather exacting analytical data on engine and component performance.

After visiting the Marshall Center during the 1960's, Gene Bylinsky, a writer for *Fortune Magazine*, reported that each stage of the Saturn V vehicle contained approximately 77 miles of wiring and that the fuel tanks were cavernous as cathedrals. The technological advances the project required were equally impressive. But the Saturn/ Apollo Program provided more than a harvest of scientific and engineering advances. It answered Kennedy's challenge to "make this effort, to solve these mysteries, to solve them for the good of all men, and to become the world's leading space-faring nation." This is the legacy of the Saturn/ Apollo Program that continued at the Marshall Space Flight Center in 1994.

Michael D. Wright/CN22
MSFC Historian
205–544–6840

"Houston...Tranquility Base here. The Eagle has landed."
– Neil Armstrong, July 20, 1969.
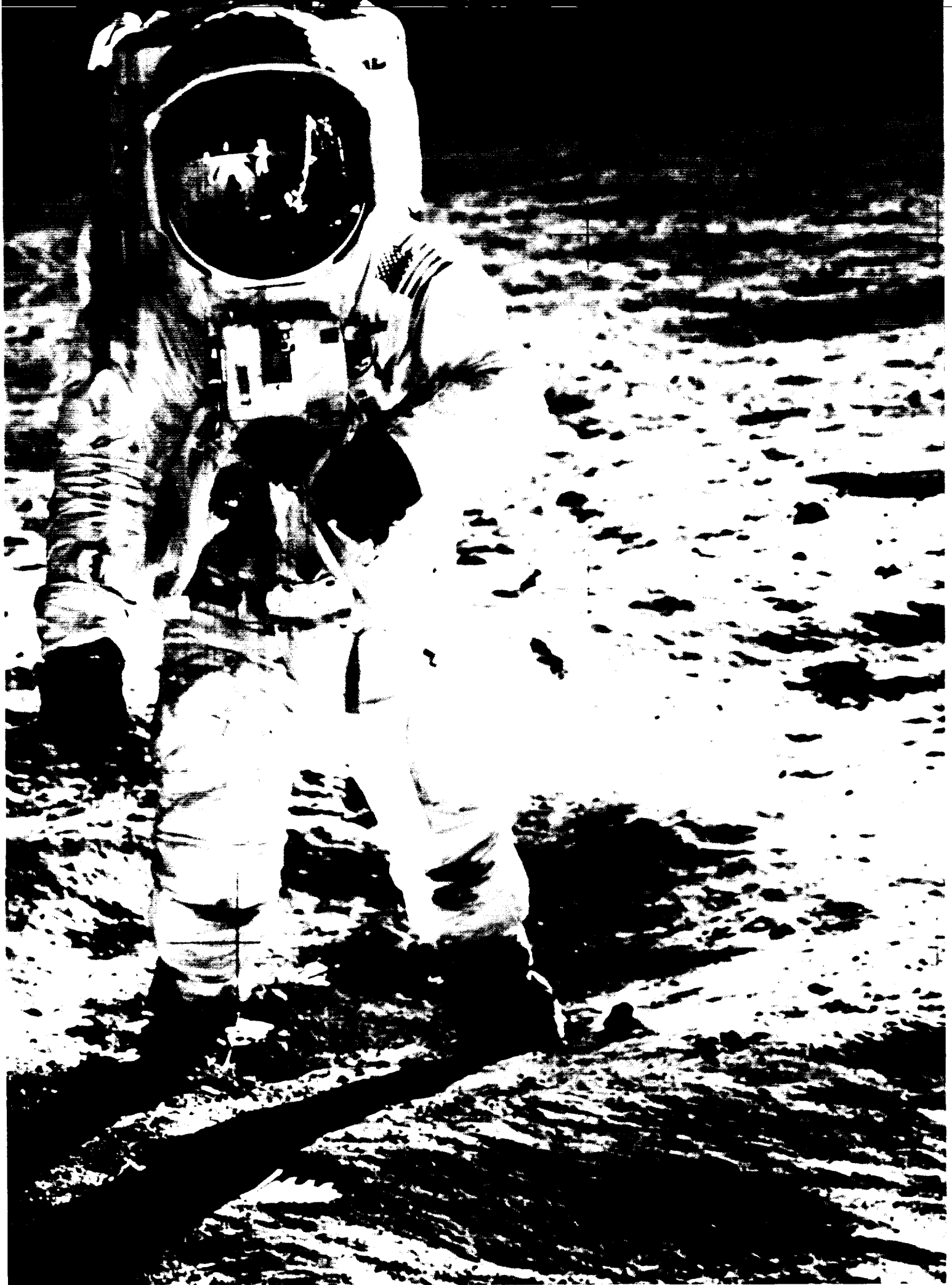
Technology Transfer

"American technology must move in a new direction to build economic strength and spur economic growth."

"Our most important measure of success will be our ability to make a difference in the lives of the American people, to harness technology so that it improves the quality of their lives and the economic strength of our Nation."
President Bill Clinton
February 22, 1993

NASA-developed technology and space-related experiments in general are an immensely valuable commodity that can rapidly lead to new processes and products at internationally competitive prices. MSFC, in response to directives to support technology transfer and commercialization from the White House and Congress, has been developing an aggressive Technology Transfer Program for some years. The effort at MSFC has been picking up momentum and is clearly leading toward the most efficient and expeditious methods to move space-related technology into the private sector. The goal is to have MSFC scientists and engineers maintain their historical excellence in space endeavors while also striving to work in partnerships with U.S. industry, academia, and other governmental organizations. The purpose is to make U.S. companies more competitive through the application of new technologies and processes.

The following material describes a few of the mechanisms initiated to make NASA/ MSFC technology and expertise more readily available to companies and reflects the technology transfer and commercialization partnership procedures being initiated by an enthusiastic and participative Center.

Harry G. Craft, Jr.
Manager
Technology Transfer Office

Technology Utilization Regional Alliances and Outreach

Through a strong outreach program, which includes Memoranda of Understanding with seven nearby states, hundreds of requests for technical assistance are received at the Marshall Center each year. The Technical Assistance Agreement is a simple, one-page form. It is designed for industry mainly, but forms are accepted from individual entrepreneurs, the academic community, and other research-type organizations. The program is dynamic. It moves technology quickly and with the least amount of effort to large and small businesses. The requests are reviewed by a Technology Applications Board, and action is taken on each one. In its first 5 years, the board has received and initiated action on about 2,000 requests.

The office considers requests for help with industrial or technical problems, information in a specific technical field, or proposals for cooperative research projects. Call 1–800–USA–NASA (1–800–872–6272), toll free.

Joint-Cooperative and Dual-Use Partnerships

A full range of joint agreements between NASA and industry, academic communities, and other organizations are available at the Marshall Center. Government and
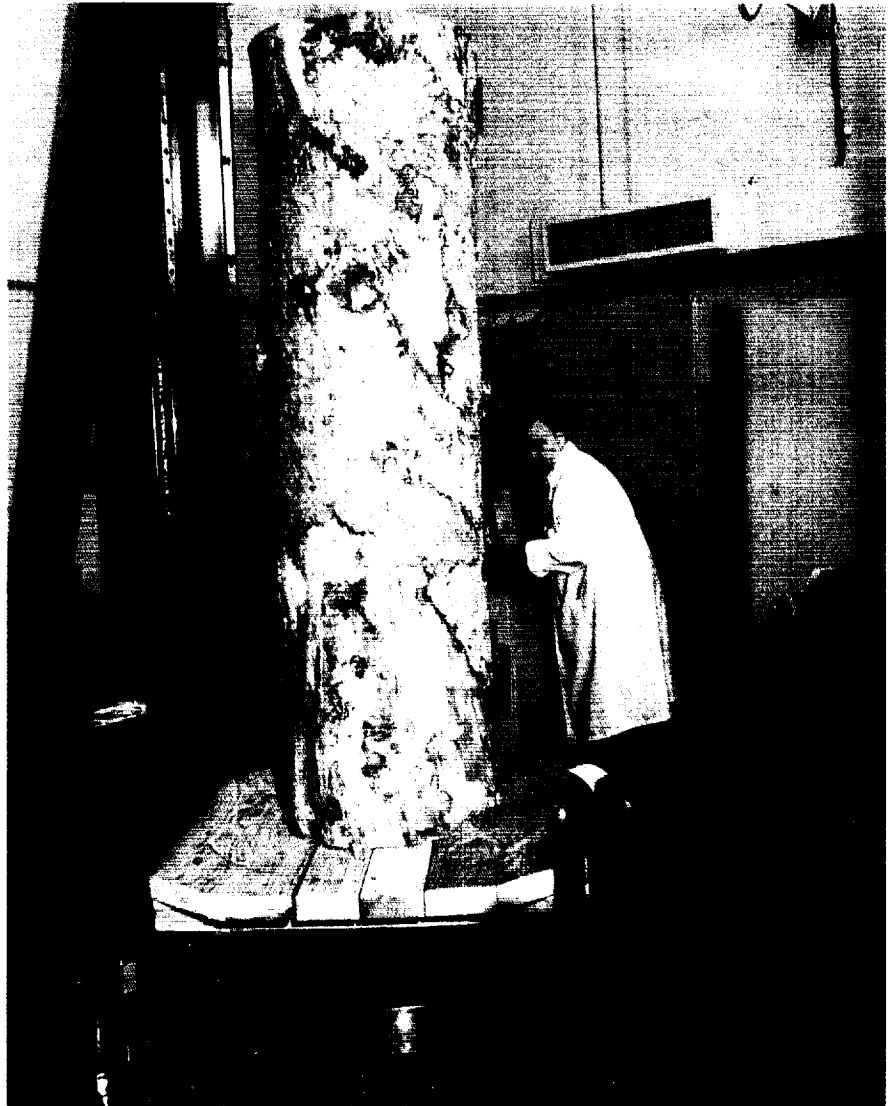
FIGURE 1.—The Advanced Computed Tomography Inspection System (ACTIS) has been used many times by private-sector and other government agency researchers. It is one of the only facilities of its kind available to the private sector to test the efficiency of large-scale industrial scanning. Use of the system can be arranged by the Technology Transfer Office.

private-sector engineers and scientists, working side-by-side, can pursue scientific and engineering

technologies needed both in industry and government (figs. 1, 2, and 3).

Figure 2.—Large electric actuators, developed to possibly replace the hydraulic actuators that gimbal the main engines of the space shuttle, have found a use in the private sector. This system moves and shakes the cabin of a flight simulator for science museums and recreational attractions. Research and technology by NASA and its contractors are useful in the private sector.

Usually, the end product or process is considered to be dual-use in nature— important to the Agency and to industry. These agreements can range from simple letter agreements involving small amounts of manpower or low-level utilization of unique test and laboratory equipment to more complicated agreements involving resources and longer lead times.

The Technology Transfer Office will accept proposals and negotiate with prospective partners on such questions as the resources to be contributed by each party, patent and licensing, and proprietary information. Interested firms or individuals are urged to contact the office.

Technology Reinvestment Project

Federal efforts to develop "dual-use" technologies with both military and commercial applications are also supported by the Technology Reinvestment Project (TRP). These type projects are increasingly available, and managing the Marshall Center involvement in this effort is one of the major functions of the Technology Transfer Office. The Technology Reinvestment Project is a key program sponsored by the Department of Defense in federal efforts to help defense firms convert from military to commercial markets.

The Marshall Center has the lead role in several Technology Reinvestment Projects and a supporting role in others.

A newer program, similarly designed, is the Aerospace Industry Technology Program (AITP), which is funded by NASA. NASA hopes to strengthen U.S. industry by advancing high-
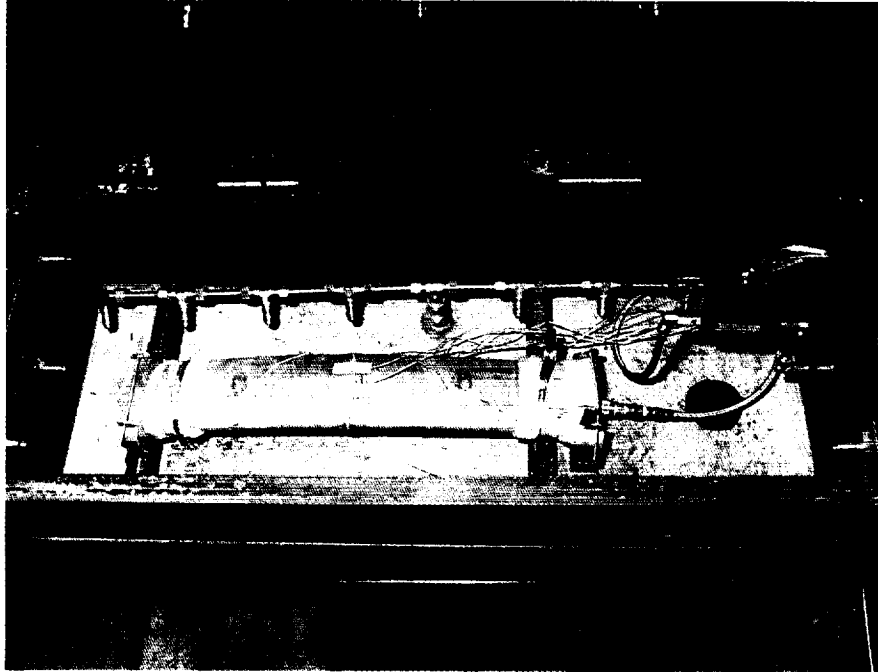
FIGURE 3.—A small business firm, unable to locate test facilities in the private sector, approached the Marshall Center, which agreed to set up a test procedure to simulate takeoff, landing, and altitude effects on a new design of environmental ducts for large aircraft. Test results enabled the firm to market its product.

National Network for Technology Transfer

The Technology Transfer Office has at its disposal, and is continually increasing its cooperation with, a nationwide network of organizations dedicated to technology transfer. NASA has sponsored the establishment of a National Technology Transfer Center and a series of regional centers spread across the Nation. The national center, located in Wheeling, West Virginia, can be contacted, toll-free, at 1–800–678–6882. There are six Regional Technology Transfer Centers covering all 50 states. Information about the nearest center can be obtained from the toll-free number. MSFC is also a member of the Federal Laboratory Consortium, an organization of government research laboratories pledged to cooperate in technology transfer. In addition to close cooperation with the other NASA Centers, the Marshall Center makes use of all the above organizations to better serve the American public.

payoff technologies that will lead to commercial products or processes that may support future NASA space missions.

Funding is periodically available for these advanced technology projects, designed to stimulate economic growth in American industry through the development of high-risk technologies.

Science Payloads in Space

Commercial development of experiments that need the low-Earth orbit space environment can be arranged in the Technology Transfer Office. The Marshall Center is dedicated to working technical and business arrangements with industry partners for space-flight projects. The Center pioneered the Joint Endeavor Agreement process to enable partnership experimentation in the space shuttle, Spacelab, and space station. Potential customers are provided facility descriptions, science consultation, experiment definition, payload definition and design systems engineering services, and other programmatic advice.

Examples of Successful Technology Transfer

• Several requests have been received for information concerning the new aluminum-lithium alloy proposed for use on the space shuttle external tank. It is estimated that 7,300 pounds can be saved and added to the payload. The new lighter, stronger metal has potential for many uses in private industry— ships, buses, trailers, wheelchairs, bicycles, auto parts, etc. It is

FIGURE 4.—Welding is important to NASA's space programs. For instance, there is more than a mile of welds, which must be perfect, in the space shuttle's large external tank. Several private-sector firms have received the benefit of Marshall's welding expertise. Welding problem statements are accepted by the Technology Transfer Office.

expected to be commercially available in about 1998.

• A small Tennessee firm submitted a problem statement describing a problem in a welding process while recycling 55-gallon industrial drums. The Marshall Center demonstrated a workable system that could be automated. The company has since estimated annual savings of 240,000 dollars in two plants (fig. 4).

• Environmental concerns bring many requests to the Marshall Center. Numerous ones for chlorofluorocarbon (CFC) substitutes led to the compilation of a critical area response (CAR) package which is periodically

updated and available free upon request.

- The Marshall Center Technology Utilization Office manages a team to design practical and low-cost devices available to amputees, primarily below-the-elbow amputees. The devices are attached by a quick-disconnect feature. The team includes, in addition to NASA engineers, a certified prosthetist-orthotist and several amputees who test the devices in real-life situations. One amputee in particular, a woman who lost her left arm to a crocodile in Africa, has been the focus of national media attention (fig. 5).

- In response to a problem statement submitted by a rehabilitation official, the Technology Utilization Office asked Marshall Center engineers to solve a problem involving a water-ski frame designed for use by wheelchair-confined persons, and mounted on a special ski. The new design has proven successful and is expected to be copied and used worldwide by handicapped water-skiers (fig. 6).

- A problem statement submitted by a prosthetics firm resulted in a revamping of its process for producing master molds used in the formation of prosthetic devices. A foam developed for space shuttle insulation was substituted for a plaster-of-paris type material. The new foam is lighter, more easily repaired, and less brittle.

FIGURE 5.—Ms. Sandra Rossi, St. Charles, Missouri, tests a prosthetic device designed by a team at the Marshall Center which specializes in such assistance. Ms. Rossi lost her lower arm to a crocodile while working in Zaire, Africa. The Marshall team, sponsored by the Technology Transfer Office, provided her with a range of artificial "helping hands," including a grasping clamp, spatula, a bowl gripper, and a carving fork.

FIGURE 6.—Marshall Center engineers and scientists volunteer time to assist handicapped persons pursue routine activities. In one case, a "ski seat" was designed to soften the ride of wheelchair-confined persons using a specially designed water ski. The design is expected to be copied throughout the world.

Advanced Studies

Twenty-five years ago, a human being first set foot upon the Moon. This tremendous achievement was built on many others in this century in which man first learned to fly. Since those exciting years of high adventure and discovery, many missions have been flown to expand our understanding of the final frontier of space. These missions have investigated the Sun, stellar and galactic astronomy, comets, cosmic rays, isotopic abundances in the magnetosphere, neutron fluxes, ultraviolet air glow in the Earth's atmosphere, the environment at large, and microgravity effects on materials and biological specimens.

In each case, old questions have been answered and new questions raised. As each technological challenge has been met and overcome, new spin-off technologies— including significant advances in communications, navigation, computers, and electronics—have been developed, directly benefiting mankind.

All of these missions, including the one to the Moon, began as a single thought—a good idea which was then studied and nurtured by people with extraordinary vision. Today's embryo missions range from lunar-based telescopes imaging the sky in the ultraviolet, to imaging the Sun in hard x rays and gamma rays with Fourier telescopes, to sweeping out the sky with infrared telescopes in Sun-synchronous orbit. Missions with near-Earth science objectives include understanding the global composition and dynamics of the Earth's magnetosphere, investigating the upper atmosphere with laser sounders, and developing satellite-supported emergency warning networks. Technologies supporting such missions include adaptive optics, tether applications, and passive thermal cooling.

In order for many of these and other missions not yet conceived to be realized, low-cost, reliable access to space is mandatory. NASA is currently defining and studying cost-effective launch vehicle concepts, along with their supporting technologies, to satisfy future national needs. These concepts include, but are not necessarily limited to, fully reusable vehicles that incorporate the most advanced structural, electrical, propulsive, and material technologies that research can offer. These vehicles emphasize high reliability, low recurring cost, and the ability to launch on schedule.

Through such activities, MSFC is carrying forward the efforts that began 25 years ago to ensure that the benefits of space are fully realized for all humankind.

James M. McMillion
Director
Program Development

SPACE
SCIENCE

Lunar Telescopes: Technology Requirements

Max E. Nein/PS02
205–544–0619

John D. Hilchey/PS02
205–544–0620

MSFC studies of the Lunar Ultraviolet Telescope Experiment (LUTE), which is a typical representative science experiment for future lunar missions, have provided an insight into future telescope technology requirements. Technology availability will be a dominant factor in the development of lunar science experiments. Inclusion of the appropriate technologies could be critical to assure the required scientific performance, simplify fabrication, enhance schedules, and significantly reduce costs. The telescope was described in *Research and Technology 1993*. This report very briefly summarizes some of the key technology requirements that were identified during the Lunar Ultraviolet Telescope Experiment studies.

Some noncritical development needs can be met with design solutions based on current technologies, materials, and hardware. An example in the telescope arena is the pointing and alignment system. Current technologies are adequate in most cases. However, because the Moon rotates at a very slow 0.5 arcsec/sec rate, actuators and drives are operating in the friction regime, normally not encountered in Earth-based systems. However, these requirements can probably be met with carefully designed pointing mechanisms based on contemporary technologies and hardware. Likewise, the

communications and data handling system could be derived from hardware now available, such as omnidirectional and small parabolic high-gain antennas, data compression systems, and standard electronics.

In contrast, a number of emerging technologies will be crucial in evolving the capabilities required of the Lunar Ultraviolet Telescope Experiment (fig. 7) and other telescopes if their performance is to measure up to the system requirements imposed by scientific needs and the aspects of the lunar environment that will be faced in long-term operations on the Moon's surface.

Optical System Technology

Although many unmanned and six manned spacecraft have landed and explored the harsh lunar environment, attaining and maintaining the desired optical performance of high-resolution telescopes during many lunar day/night cycles remains a major problem in the design of

these systems. It is therefore imperative to concentrate research tasks on some of the critical systems engineering problems that are anticipated but lack acceptable solutions.

Mirror Materials

The optical system of the Lunar Ultraviolet Telescope Experiment, with its passive thermal control, has to withstand large temperature swings in the range of 90 to 300 Kelvin (K). The optical performance of various mirror materials and their degradation during thermal cycling is of primary importance to the feasibility of high-resolution lunar telescopes. Historically, space optical systems
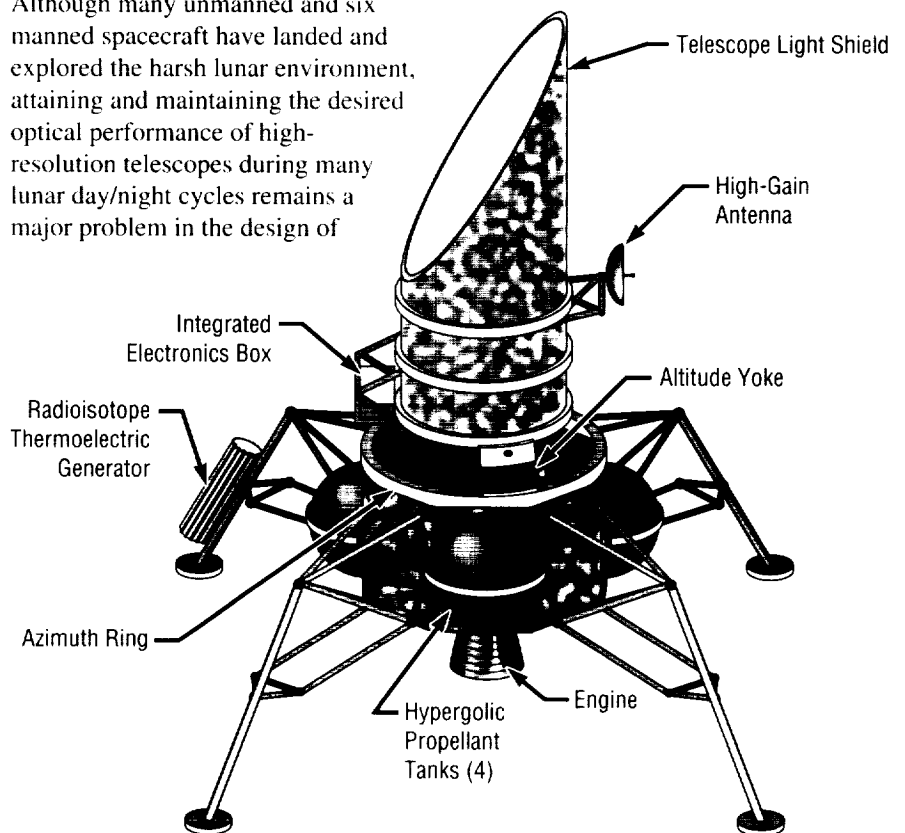
Figure 7.—Lunar Ultraviolet Telescope Experiment.

have been operated at the manufacturing temperature or at a constant temperature for which the optical prescription has been biased during manufacturing. In the case of the Lunar Ultraviolet Telescope Experiment, this is not possible because of the continuously changing temperatures during the lunar cycle (primarily in the daytime portion). Therefore, suitable mirror materials that combine the requirements for lightweight thermal stability and optical performance over a wide range of temperature variations must be assessed and evaluated.

Candidate materials such as beryllium, silicon carbide, and ultra-low expansion (ULE) glass exhibit desirable characteristics. However, many questions remain regarding their performance under the extreme temperature cycles to be encountered on the Moon. Such areas as thermo-structurally optimized design shapes, nonlinearity of material properties, and adhesion of substrate coatings and optical coatings must be investigated and verified to enable the selection of the right combination for Lunar Ultraviolet Telescope Experiment design.

Adaptive Optics

While a 1-meter aperture telescope may not require an adaptive optics system, larger telescopes—which will eventually be emplaced on the Moon—must have the ability to adjust the distortions caused by temperature gradients in the mirrors. Telescopes with apertures larger than approximately 3 meters must be assembled or deployed on the Moon from segments or folded flight configurations and thus will depend on adaptive optical systems.

It is therefore imperative that the technologies for active and adaptive optics currently under development for Earth- and space-based systems be extended for the thermal and structural requirements imposed by the lunar environment. Typical requirements in this arena include an actuated, deformable primary mirror that will maintain an optical surface figure within 100 angstroms (Å) in a lunar thermal environment; a lightweight secondary mirror actuation system that does not increase the obscuration ratio of the telescope; and active metering structures to accommodate large thermal gradients.

During the design process, it will also be essential to have an advanced, integrated, multibody dynamics analysis program. It should have the capability of dynamically modeling the thermal loads on an interconnected set of structures using temperature-dependent material properties, and it should interface with software for control system development and optical analysis.

Optical Coatings

In order to assure acceptable performance for extended periods of time in the lunar environment, one must investigate the durability and optical performance of high-reflectance coatings for the 1,000- to 3,000-angstrom band, both freshly applied ("new") and after exposure to a simulated lunar environment of temperature, vacuum, dust, potential contaminates, and galactic and solar proton radiation.

Detector Technology

The focal plane detectors currently envisioned for lunar telescopes are based on charge-coupled device

(CCD) mosaic arrays. Typical pixel sizes range currently from 7 to 17 micrometers (μm). However, for fast focal ratio (f#) systems with high resolution, they should be reduced to 5 micrometers if feasible.

Although tremendous advances in detector technology have been made in recent years, there is a continuous requirement to explore the capability to produce large-area charge-coupled device detectors with 5-micrometer pixels, or smaller, for scientific applications. These detectors must be either fabricated directly on a spherical substrate or must be sufficiently thinned so that they could be "stretched" to conform to a spherical surface to allow matching the detector to any image field curvature in the planned telescopes. Technology developments of this type are very expensive, and the drivers for such developments do not exist in the commercial fields. As a result, advances in many key technologies have depended on defense objectives. Because of the decline of these demands, advanced development of detectors for scientific instrumentation has become one of the critical enabling technologies.

Thermal Control Technology

The extreme temperature variations of a lunar day/night cycle, coupled with the absence of electrical power during the lunar night as dictated when using a solar array power system, require avionics components and systems to operate well beyond the qualification limits. The development of such avionic systems creates unknown engineering risks. To understand and quantify these risks, an applied technology and development program is needed to explore techniques for the

design, packaging, and thermal control of electrical and electronic avionics systems.

A technology effort is needed to investigate a common and integrated packaging concept that will integrate all thermal-sensitive circuits and components with a passive thermal control technique. The ultimate goal is to manage and store the waste operational heat of the avionics system during lunar day operation and utilize this stored heat to maintain an acceptable storage temperature during lunar night when the avionics are not operating.

Electrical Power System Technology
Historically, electrical power for space-based orbiting telescopes has been provided by photovoltaic arrays. During the short, up-to-90-minute "nighttime" of the orbital path, sufficient electrical energy can be stored in batteries which are recharged during the sunlit portion of the orbit. However, lunar-based experiments requiring electrical power cannot depend on photovoltaic arrays and batteries if they must operate during the night portion of the lunar cycle. While the 14-Earth-day-long lunar day is ideal for deriving power from solar arrays (except in the shadow of deep craters or regions near the poles), the mass and volume of electrical batteries to store the energy for nighttime operation is prohibitive. Therefore, the only reasonable energy source for nighttime operation is a radioisotope thermoelectric generator (RTG). The large amount of thermal energy produced by such a generator as a by-product of the radioactive decay process can be utilized to maintain operating temperatures of components and systems.

However, there are also problems associated with the use of radioisotope thermoelectric generators, not the least of which is the potential radiation effects on sensitive detectors. The use of the generators requires thermal control from the time the generator is installed. Thermal waste heat is continuously produced, and thus the location of the generator on the telescope must be carefully selected and cannot easily be changed during the development phase of the telescope because of the complex thermal interactions with the optical system. Thermal modeling and the means of transmitting thermal energy to components and subsystems where the thermal load can be of benefit must be assessed. Technology efforts are needed to assess and verify detector performance in the presence of a radioisotope thermoelectric generator.

Summary
The mission, engineering, and system studies accomplished since mid-1991 show that lunar telescopes are feasible scientific payloads to design and develop, and that they can be operated effectively on the lunar surface. Some of the required technologies and design approaches are available to initiate the definition and preliminary design phase of such a project. Other technology areas require immediate and intensive effort to assure they are ready to enable lunar telescope final design, development, and fabrication.

Sponsor: Office of Space Science

University Involvement: University of New Mexico; New Mexico State University

· · · · ·

The Magnetosphere Imager Mission

C. Les Johnson/PS02
205–544–0614

Carmine E. DeSanctis/PS01
205–544–0618

MSFC is responsible for defining future space science missions—one of which is the proposed Magnetosphere Imager (MI) mission, a natural extension of NASA's search for answers to questions about our planet and its workings. The Magnetosphere Imager mission complements NASA's Mission to Planet Earth, a series of experiments studying the relationships between the land, ocean, and atmosphere; how they interact with one another; and how external influences—such as the Sun and Earth's magnetic field—interact with them.

One of the most important discoveries of the space age was that of the Van Allen radiation belts around the Earth. This showed us that our planet is surrounded by vast clouds of intense radiation caused by Earth and its rotating magnetic field being impacted by the supersonically expanding atmosphere of the Sun. We know from 30 years of spacecraft flights through this region that these radiation clouds contain electrical storms and disturbances that play an important role in Earth's atmospheric processes, at times causing power failures and communication blackouts on Earth.

Technology has advanced such that pictures of this magnetospheric cloud can be made, similar to the satellite photos of ordinary clouds commonly

used for weather reports. Thus, researchers are poised to explore and expose this violent and variable region that surrounds the planet with entirely new types of pictures to be taken by the instruments flown on the Magnetosphere Imager.

The magnetosphere, a plasma region dominated by Earth's geomagnetic field, is considered to begin at an altitude of about 100 kilometers and to extend outward to a distant boundary that marks the beginning of interplanetary space. In this region of near-Earth space, material from our planet's atmosphere and its geomagnetic field are the dominant media within which "space weather" occurs.

For three decades, magnetospheric field and plasma measurements have been made by diverse instruments flown on spacecraft in many different orbits, widely separated in both space and time, and under various solar and magnetospheric conditions. Scientists have used this information to piece together an intricate, yet incomplete, view of the magnetosphere. A simultaneous global view, using various light wavelengths and energetic neutral atoms, could reveal exciting new data and help explain complex magnetospheric processes, thus providing a clearer picture of this region of space.

To provide these measurements, NASA initiated a science definition team (SDT) to develop the scientific rationale for a magnetospheric imaging mission, the Magnetosphere Imager. Concurrent with the formation of this team, MSFC was given responsibility for defining the mission and subsequently initiating an engineering team to perform concept studies.

In order to better understand this environment, the mission will pose the following questions:

• What does the global magnetosphere look like in quiet and disturbed conditions?

• How do the principal magnetospheric regions globally change in response to internal and external influences?

• How are the principal magnetospheric regions interconnected?

• What are the remote global signatures of the important astrophysical processes occurring in the magnetosphere?

The Magnetosphere Imager was originally conceived to be a part of the Space Physics Division's intermediate class of missions with a cost ceiling of 300 million dollars. The engineering studies performed at MSFC indicated that a spinning spacecraft with a despun platform, similar to General Electric's (now Martin Marietta's) Polar and Hughes' HS–376 spacecraft, launched aboard a Delta could easily accommodate the strawman science instruments defined by the imager's scientific team.

TABLE 1—*Evolution of the Magnetosphere Imager mission*

	Intermediate Class Mission	Sun-Earth Connections Mission
Cost Ceiling ($)	300M	100M
Launch Vehicle	Delta	Conestoga, Taurus, or Lockheed Launch Vehicle
Orbital Parameters	4,800 km x 44,500 km; 90°	4,800 km x 44,600 km; 90°
Instruments	Hot Plasma Imager Plasmasphere Imager (He⁺ 304) Geocoronal Imager Auroral Imager Proton Aurora Imager Plasmasphere Imager (O⁺ 834) Electron Precipitation Imager	Hot Plasma Imager Plasmasphere Imager (He⁺ 304) FUV Imager (combines functions of the Geocoronal, Auroral, and Proton Aurora Imagers)
Total Spacecraft Weight (kg)	1,300	300
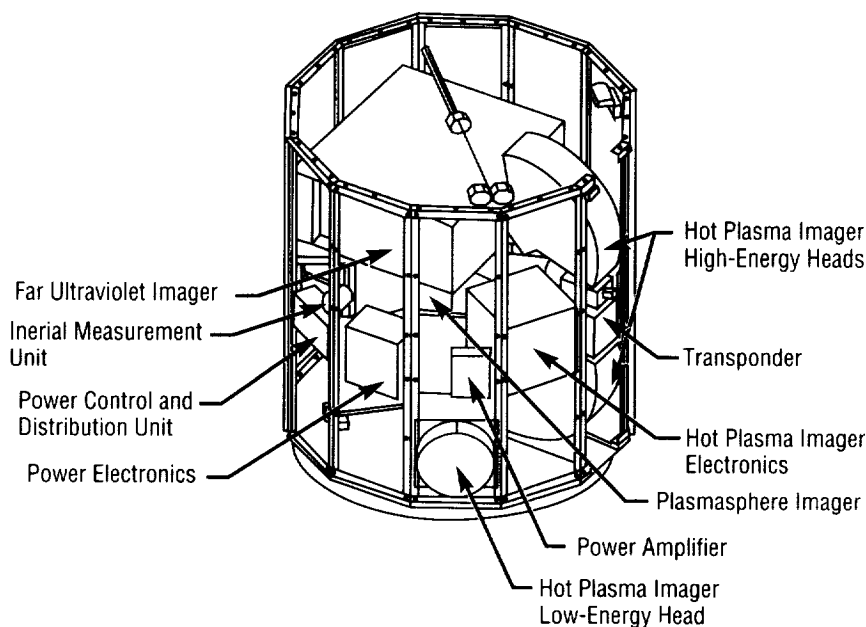
Figure 8.—The Magnetosphere Imager Sun-Earth connections spacecraft concept.

In early 1994, the science definition team and an MSFC engineering team were directed by the Space Physics Division to redefine the Magnetosphere Imager mission to fit within a new program, Sun-Earth Connections. This type of mission has a cost cap of 100 million dollars and must fly on a launch vehicle smaller than a Delta. The definition team met with MSFC and developed a new strawman instrument complement suitable for a smaller spacecraft still capable of meeting core scientific objectives. A summary of the two spacecraft concepts and their instrument complements can be seen in table 1.

The spin-stabilized imager spacecraft will use NASA's deep-space network to communicate the (orbital) average 40-kilobit-per-second data rate to the ground for distribution to the scientific team. Body-mounted gallium-arsenide solar cells will provide power to the spacecraft, and a passive attitude control system will maintain its 10-revolution-per-minute spin rate and attitude with respect to the orbit plane. A configuration drawing of the spacecraft concept is provided in figure 8.

MSFC is working closely with NASA's Office of Advanced Concepts and Technology in the development of the technology required for the Magnetosphere Imager instrument suite. To support these activities, several grants and contracts were awarded in 1994 through a NASA Research Announcement entitled, "Techniques and Technologies for Magnetospheric Imaging." The recipients are listed in table 2.

Sponsor: Office of Space Science, Space Physics Division

• • • • •

Table 2.—MSFC-funded research for advanced technology Magnetosphere Imager instrumentation

Institution	Research Title
Boston University	Development and Evaluation of Multilayer Coatings for O^+ Imagers
Lockheed Palo Alto Research Laboratory	Surface Conversion Techniques for Low-Energy Neutral Atom Imagers
Lockheed Palo Alto Research Laboratory	Measurement of Precipitation-Induced FUV Emission and Geocoronal Lyman Alpha from the MI Mission
Los Alamos National Laboratory	UV Rejection for Low-Energy Neutral Atom Imaging
University of Iowa	Simulation of Radio Sounding in the Plasmasphere
University of Massachusetts at Lowell	Instrument Definition of a Radio Sounder for Global Magnetospheric Imaging

Passively Cooled Reconnaissance of the Interstellar Medium

Jonathan W. Campbell/PS02
205–544–7076

From the beginning, this mission's goals have been to gain highly meaningful scientific information for minimal dollars—its impetus to be faster, cheaper, better.

The interstellar medium has never before been directly investigated. By taking advantage of a satellite in Sun-synchronous orbit around the Earth and the Earth's orbit around the Sun, a spectrometer pointed outward could, in principle, sweep out the entire sky in just 6 months. Cheaper, gravity-gradient stabilization would be employed, and the satellite could be launched via a low-cost Pegasus-class bus.

The Passively Cooled Reconnaissance of the Interstellar Medium (PRISM) will survey the galaxy at selected wavelengths, providing valuable data on the characteristics of the interstellar medium. Densities, velocities, and temperatures as a function of position will allow tremendous insight into where new stars are forming and in the evolutionary processes at work in our galaxy. Ordinary telescopes operating in the visible cannot see the center of the galaxy because of intervening clouds, but this mission will enable scientists to see beyond the clouds to study the mysteries at the center.

In addition, a substantial technological benefit may be realized in the areas of passive cooling of satellites. Present technology uses large, heavy, bulky dewars to cool the temperature of the telescope down to acceptable cryogenic temperatures. These dewars are inherently expensive and costly. This program would employ an alternate approach in which a system of nested, conical Sun shields would provide the necessary cooling passively. Indeed, MSFC could become the center of expertise for passive cooling.

Sponsor: Advanced Systems and Payloads Office

· · · · ·

High-Energy Solar Imager

Jonathan W. Campbell/PS02
205–544–7076

The High-Energy Solar Imager (HESI) mission deals with imaging the Sun in hard x rays and gamma rays. Solar flares occurring in the solar corona are highly transient events involving the release of tremendous amounts of energy. This energy takes many forms, including radiation across the electromagnetic spectrum, as well as high-energy protons and electrons. Hard x rays and gamma rays are part of this release and may be thought of as simply different colors of light invisible to the eye. Those high-energy photons do not reach the Earth since they are absorbed by the atmosphere. Imaging solar flares in these colors of photons should provide additional insight into the energy release and perhaps answer long-standing questions about the role of the Sun's magnetic field in storing energy. Since solar flares can be potential threats to men working in orbit and can disrupt vital communications and navigation networks here on Earth, having a better understanding of them may allow the eventual prediction of these events.

Hard x rays and gamma rays cannot be imaged as easily as the visible colors of light. The high-energy photons simply zip straight through conventional lenses and mirrors. For several years, MSFC has worked in developing new technology in the area of Fourier telescopes that employ fine grids and powerful computers to measure the Fourier components associated with hard x-ray and

gamma-ray radiation. In addition, MSFC is a leader in the area of stabilized booms for space-based applications. Both of these technologies are critical to achieving an optimum, low-cost mission concept.

The hard x rays produced by the Sun are the same color as the x rays used by a dentist in looking at teeth. One potential spin-off benefit from this mission to the man on the street is in the area of nonintrusive medical imaging. This technology offers the capability of producing extremely high-resolution snapshots of the interior of the human body.

Sponsor: Office of Space Science

• • • • •

QUICKSAT Missions

William T. Roberts/PS02
205–544–0621

Over the past 2 years, NASA has begun placing greater emphasis on the development of missions that are smaller, faster, and cheaper. This emphasis is motivated, in part, by the fact that NASA will be faced with budgets that will not be greatly increased for the next several years (and may, in fact, be reduced). Also, in the areas of space science and Earth science, there are major ("Flagship") missions requiring most of the available development funding, so that the wedge for the initiation of new missions will be very limited.

In mid-1993, MSFC began the development of a concept to build and fly small, inexpensive spacecraft missions, taking less than 2 years from design to launch. These missions will each be tailored to support limited and well-focused science objectives to be accomplished with a limited instrument complement in a limited (nominally 1 year) mission time. The types of missions being considered include small instruments for plasma, atmosphere, or solar imaging; missions to investigate ionospheric, magnetospheric, and auroral plasma and fields characteristics; solar wind monitoring missions; etc. MSFC will be working with industry, universities, research institutes, other government agencies, and the international community to develop and expand concept options.

For the initial QUICKSAT mission, MSFC has been working with the

Southwest Research Institute in San Antonio, Texas, on a no-exchange-of-funds agreement to define a dual spacecraft mission to investigate the spatial and temporal characteristics of auroral dynamic phenomena. This mission, named the Twin Auroral Plasma Probes (TAPP), will include state-of-the-art science instruments to measure the energy spectra and pitch-angle distributions of the auroral ions and electrons. The spacecraft will also include magnetometers to measure the magnetic field properties. The plan is to build two small (~28 inches in diameter) identical composite spacecraft which will be launched into a 500-kilometer polar orbit. A part of the mission will involve the use of the attitude control system to control the "aerodynamic drag profile" of the spacecraft, which will, in turn, provide control of the orbital velocity. Hopefully, this technique will enable the control of the separation and closing velocities between the two spacecraft. The subsystems to be used in the spacecraft are (for the most part) already developed, and the plan is to use a combination of parts screening and selective testing to assure mission success. The Southwest Research Institute is using internal funds to support their portion of this definition activity. An artist's conception of the Twin Auroral Plasma Probes is shown in figure 9.

Since the use of composite materials in the construction of small spacecraft is a fairly new technique, researchers are in the process of purchasing a copy of the spacecraft structure for a test and verification program (fig. 10), to include materials and environmental tests to assure a more accurate understanding of the consequences of using this type of spacecraft structure.
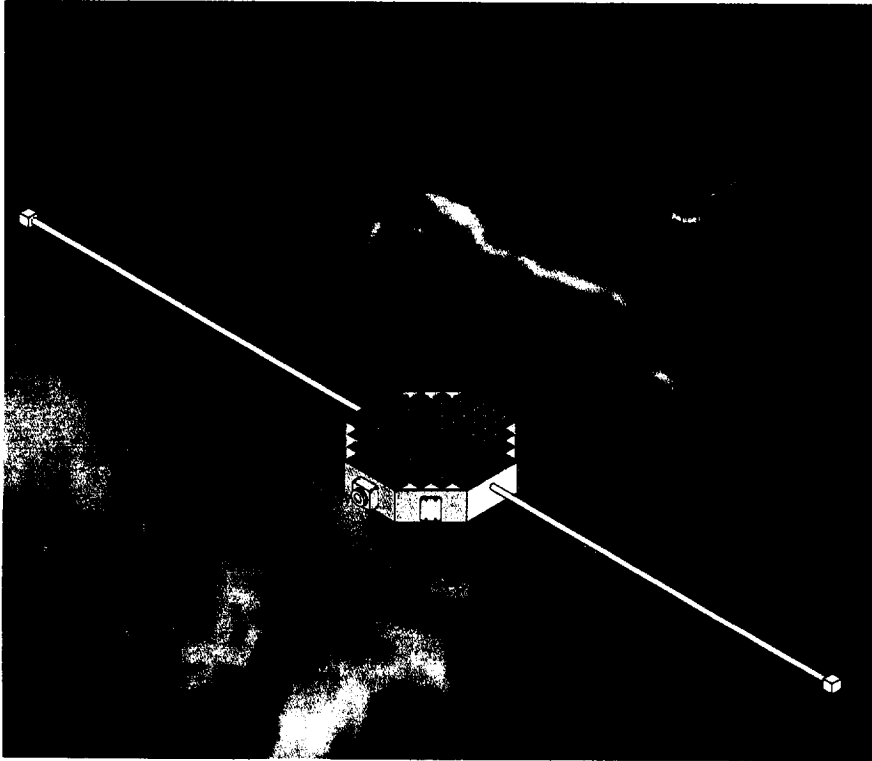
FIGURE 9.—Twin Auroral Plasma Probes.

FIGURE 10.—Spacecraft structure for verification test program.

The test program is scheduled to begin in the late summer or early fall of 1994.

The use of the spacecraft attitude control system for the command and control of the "differential drag" is being analyzed in some depth. If this technique can be demonstrated to operate in a satisfactory manner, there are potential applications to a number of future missions that involve spacecraft "clusters." For these future missions, the requirements to have multiple spacecraft fly in some specified and variable formations is fundamental to the successful accomplishment of the mission objectives. The benefits of being able to accommodate such requirements without the use of an onboard propulsion system are obvious, especially in cost and complexity. In May 1994, the Universities Space Research Association issued an Announcement of Opportunity, soliciting small, inexpensive missions to be launched by early 1997. The Southwest Research Institute/MSFC team is now preparing a proposal to respond to this announcement. MSFC researchers will propose to enter into a "joint-endeavor-type" agreement to build, test, and fly the Twin Auroral Plasma Probes within 2 1/2 years, and expect that more similar opportunities will be forthcoming.

The QUICKSAT concept is designed to provide the capability to maintain a viable space research program in a time when development resources are scarce. It is, however, also designed to provide a means of rapidly responding to science and applications missions needs. MSFC envisions that such a concept will find applications in other government agencies, and will be a means of further science and applications collaborations with the international community.

Sponsor: Office of Space Science

• • • • •

17

SPACE
SYSTEMS

National Adaptive Optics Mission Initiative

Edward E. Montgomery/PS04
205–544–1767

The National Adaptive Optics Mission Initiative (NAOMI) will establish a facility for testing advanced adaptive optics technologies (e.g., segmented mirrors, advanced control algorithms, and laser power beaming). In preparation for the initiative, MSFC led two precursor projects this year. One project was the integration of a Phased-Array Mirror, Extendible Large Aperture (PAMELA) telescope; the second was the Beam Transmission Optical System (BTOS) structure. A primary objective of structure prototyping efforts for both projects is to resolve control dynamics and other key technology issues associated with large aperture, adaptive primary optical telescopes or beam directors.

The Phased-Array Mirror, Extendible Large Aperture (fig. 11)—a 36-segment, $1/2$-meter aperture mirror—was developed initially by the Strategic Defense Initiative Organization (SDIO). MSFC integrated the telescope to produce an algorithm test-bed for adaptive optics control systems. This test-bed provides the capability to compare a variety of control algorithms to optimize response time and assess scalability to larger segmented mirrors.

Future large adaptive telescopes based on this design concept will require rigid support structures that can dampen vibrations in order to minimize the work of the control
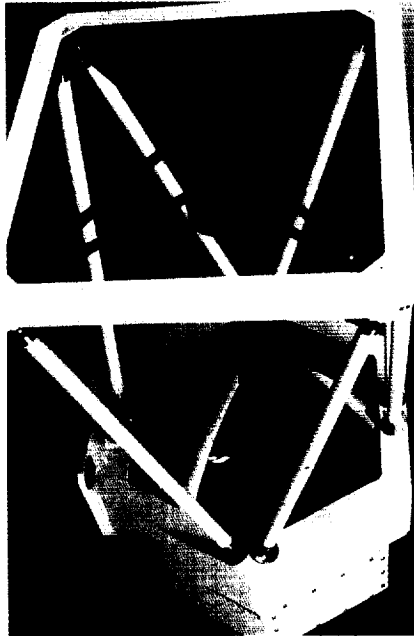
FIGURE 11.—Phased-Array Mirror, Extendible Large Aperture.

system. In a cooperative effort with the Jet Propulsion Laboratory (JPL), MSFC has developed a truss structure design based on composite materials. Since computer models cannot accurately predict dynamic characteristics over the full frequency range of interest, MSFC has procured struts and nodes for producing a prototype structure. Presently, MSFC is analyzing the stress test results conducted on these prototypes.

Plans for this year include the construction of the Beam Transmission Optical System structure for modal testing, and the completion of the Phased-Array Mirror, Extendible Large Aperture control algorithm test-bed. These activities will provide the foundation for the development of a 12-meter, adaptive optics telescope in the late 1990's. In a

concurrent program, the U.S. Navy Air-Warfare Center (USNAWC), in China Lake, California, has initiated site evaluation for the National Adaptive Optics Mission Initiative.

Segmented optics and composite truss structures enable the development of large ground-based telescopes with the capability to compensate for atmospheric disturbances. Future space-based telescopes could also benefit from segmented mirror technology. Additionally, large adaptive optics systems provide the steering and transmission systems for laser power beaming. The benefits of a laser power beaming system include life extension of existing geostationary satellites by reducing battery discharge. Studies by Comsat, Inc., indicate a potential 20-percent extension in the total life of a satellite.[1] Potentially, power beaming could increase the commercial communications satellite industry revenue by 500 million dollars per year.

[1]Meulenberg, A. July 1992. Application of Laser Power Beaming to Commercial Communication Satellites. Proceedings of the Space Laser Energy (SELENE) Advocacy Briefing and Progress Review, NASA/MSFC, AL.

• • • • •

Tether Applications in Space

Charles C. Rupp/PS04
205-544-0627

Successful flight of the second Small Expendable Deployer System (SEDS-2) on a Delta II launch vehicle in March 1994 demonstrated use of a closed-loop control law to deploy a tether to a stable local vertical orientation. This mission provided further insight into tether deployment friction and allowed improved understanding of the fundamentals of tether dynamics in space, leading to better analytical models. Knowledge from both Small Expendable Deployer System missions will be utilized on a third flight to deploy a student-developed satellite known as the Students for the Exploration and Development of Space Satellite (SEDSAT). This mission will be the first flight of the system on the shuttle.

Potential applications for tethers in the near future include the use of tethers to raise the orbit of payloads, to deorbit and recover commercial payloads, and to suspend payloads downward for atmospheric research. Other foreseen uses for tethers in the future include deorbiting orbital debris (such as spent rocket stages) or waste from the space station. Momentum exchange between the space station and departing vehicles could provide a reboost for the station.

Several commercial entities and universities have expressed interest in flying Small Expendable Deployer System hardware, either for continuation of research or to do work leading towards commercial applications. MSFC is providing consultation and limited planning support to some of these and may provide other functions as plans and concepts mature.

Sponsor: Office of Space Systems Development

• • • • •

Global Emergency Observation Warning and Relief Network

Angelia P. Bukley/PS02
205-544-0054

John A. Mulqueen/PD32
205-544-0534

The Global Emergency Observation Warning and Relief Network (GEOWARN) concept originated as a student design project at the 1993 International Space University summer session. The student design team, composed of 38 students from 16 countries, formulated a proposed system design that optimizes the use of existing remote-sensing resources augmented by the acquisition of a modicum of additional sensor platforms linked together via a computer network hosting an extensive geographical information system to perform the task of providing global disaster warning and relief support. The study was motivated primarily by the United Nations proclamation of the 1990's as the International Decade for Natural Disaster Reduction (IDNDR). During the first 4 years of this effort, some progress has been made in mitigating the problem of providing prompt and effective warning and relief for natural disasters on a global scale. However, a plethora of situations are documented that accentuate the need for improved post-disaster communications and information distribution and for the provision of adequate warning in the face of impending disasters. The Global Observation Warning and Relief Network is proposed as a system that can potentially fill the

existing gaps in the current disaster management regime by providing timely information both before and after an event has occurred, complementing the activities of existing international, national, and private relief and meteorological agencies.

A review of the proposed system as put forth by the student design team has revealed that a great potential exists for the realization of the concept. In an unfunded concept feasibility study that began in November 1993, MSFC's Program Development Office examined in detail the work done during the International Space University 1993 summer session. A team of 15 engineers and scientists dissected the proposed design and evaluated the merit of the concept. The goals of the feasibility study were: (1) assessment of the technical, programmatic, and implementation aspects of the system; (2) identification of remote sensing, communication, and data processing requirements; and (3) identification of space-based, airborne, and ground-based elements. The primary focus of the feasibility study was on the technical issues associated with actual implementation of a global warning and relief system. A significant conclusion of the evaluation is that there are absolutely no technical impediments to realizing a system that could attain the goals of the proposed concept.

Indeed, a host of potential system elements have been identified during the course of the study that meet the operational requirements. These elements include remote sensing satellites, ground receiving stations, data processing centers, satellite

communications systems, simulations and models of weather and other natural phenomena, detailed geographical information systems, and user interfaces designed specifically for emergency management officials. Figure 12 schematically depicts these major elements and identifies the four major system functions. Data will be obtained from the remote sensing elements, processed and provided as usable information to disaster managers. Communications functions will also be supported where appropriate. Agencies throughout the United States and the world are aggressively pursuing individual projects and programs which could be integrated into the system.

The concept as presented by the International Space University is technically feasible, with only minor modifications to the proposed architecture. Prior to specifying the details of a final system configuration, an in-depth technical requirements study is necessary to ensure that all

critical parameters are addressed by the system. Such a study was not possible in the limited time available to the university team. A detailed requirements study is planned to commence in FY 1995 at the Marshall Center. The MSFC study team further acknowledges that development of the Global Emergency Observation Warning and Relief Network concept and its eventual realization will require significant interagency and international cooperation. It is also realized that the technical solution is only part of the total solution. There are an enormous number of social, political, and legal issues which must be addressed, or the concept will fail. The team requires and actively seeks the advice and cooperation of all relevant organizations to achieve the goal of providing global warning and relief for natural disasters.

Sponsor: Office of Mission to Planet Earth

• • • • •

Functions
– Data Gathering
– Data Processing
– Information Distribution
– Communication Support
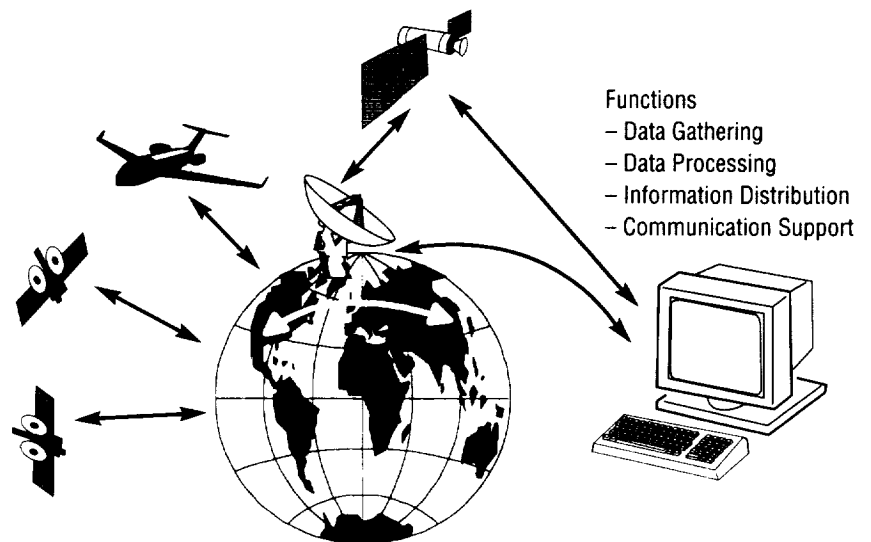
FIGURE 12.—Schematic depiction of the Global Emergency Observation Warning and Relief Network.

Direct Tropospheric Wind Measurements From Space—Wind Sounder Instrument and System Considerations

Vernon W. Keller/PS02
205-544-2470

The need for additional wind information in the lowest 15 kilometers of the Earth's atmosphere has been eloquently stated many times by various U.S. and international agencies. The Laser Atmospheric Wind Sounder (LAWS) was selected as an Earth Observing System (EOS) facility instrument to satisfy this need by providing accurate global wind measurements using a coherent Doppler lidar having 1-kilometer vertical resolution from ground to approximately 15 kilometers in altitude. The ability to make wind measurements from space with such an instrument is dependent upon the transmitted laser energy, the amount of natural aerosols (strength of the backscatter signal), and the ability to detect and process the return signal. The Laser Atmospheric Wind Sounder instrument required a large laser (~20 joules (J)) and a large telescope aperture (~1.5-meter diameter) to make measurements in those areas of the atmosphere where the backscatter is naturally low. Due to its size and complexity, the cost of such an instrument exceeded the budget constraints of the restructured Earth Observing System program, and so the wind instrument was "deselected" earlier this year. Since the natural aerosol backscatter varies by several orders of magnitude from one region

of the atmosphere to another, a less ambitious wind measurement system that provides high-accuracy wind data, but from only selected portions of the atmosphere, is feasible at substantially less cost than the Laser Atmospheric Wind Sounder instrument. Such an instrument is addressed by Kavaya and Johnson elsewhere in this document. The scientific benefits from such an instrument are currently being addressed by the Committee on Earth Studies, National Research Council.

Preliminary studies conducted this year have identified the launch vehicle and spacecraft characteristics required

to accommodate various instrument configurations. The instrument configuration that has recently attracted the most attention is a coherent Doppler lidar with a 0.5-meter-diameter telescope and a 0.5-joule laser. This instrument can be accommodated on a Taurus-class launch vehicle (fig. 13). A more detailed study of this instrument option and the spacecraft system required to accommodate it is in progress.

Sponsor: Office of Mission to Planet Earth

•••••
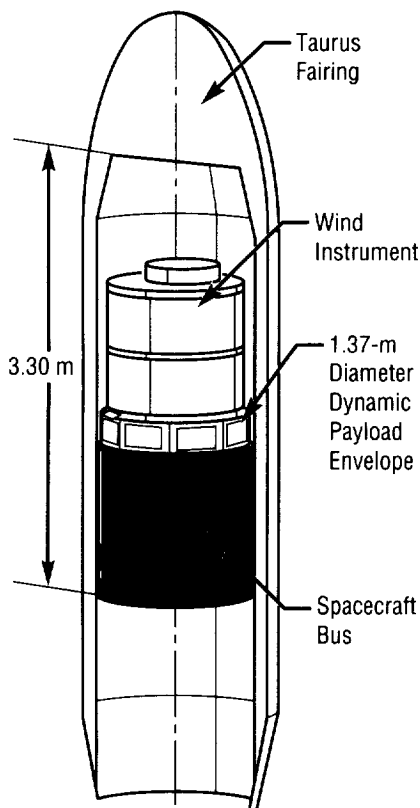
FIGURE 13.—Wind mission accommodation on Taurus.

SPACE TRANSPORTATION

Advanced Space Transportation Systems

Gary W. Johnson/PT51
205–544–0636

In January 1994, NASA completed a detailed study to assess alternate approaches for accessing space through the year 2030. Advanced space transportation systems investigated included an upgraded space shuttle, with the existing expendable fleet; new expendables, with transition from the shuttle and current expendables in 2005; and new, fully reusable vehicles employing advanced technologies, with transition from existing vehicles in 2008. Making significant reductions in space transportation costs, increasing flight-crew safety, and improving mission reliability were major goals of the study. Researchers concluded that it was indeed possible to achieve program objectives with an architecture that featured a new, advanced technology, single-stage-to-orbit (SSTO) pure rocket launch vehicle that promised significant reduction in both life-cycle and annual operating costs. Vehicle development would explore important new technologies with dual uses in industry (such as composite structures for cars and airplanes), placing the U.S. in an extremely advantageous position with respect to international competition and propelling the country into a next-generation launch capability.

As a result of the study team's recommendation, NASA began, in early 1994, a major activity to further develop enabling technologies and demonstrate the reusable launch vehicle (RLV) for the next generation.

This will ultimately lead to a large-scale, advanced technology demonstration vehicle, with transition to a new fleet in the next century. Vehicle concept definition, technology development, and early vehicle demonstration will be complementary activities. The focus of the vehicle concept definition activity is to establish targets for discipline technologies, encompassing three single-stage-to-orbit concepts: a winged configuration, which launches vertically and lands horizontally; a vertical-takeoff, vertical-landing vehicle; and a lifting body vehicle that launches vertically and lands horizontally (fig. 14). Associated technology development areas include reusable cryogenic tank systems, graphite-composite primary structures, advanced thermal protection systems, and advanced propulsion systems. An early demonstration program will utilize the Delta Clipper Experimental (DC-X) vehicle already built by McDonnell Douglas, incorporating some of the newer technologies now being developed.

The vehicle concept portion of the effort—a multiple concept maturity activity—focuses on three types of single-stage-to-orbit launch vehicles and their associated expendable upper-stage concepts for orbit transfer. Near-term goals are aimed at developing the three concepts into a common design definition and conducting system trade studies to better understand vehicle sensitivities to various parameters. The study will determine specific targets—categorized into cost, operations, and performance—that will be applied to the technology development activity.

Technology development consists of four multiyear efforts to define and demonstrate new technologies in the areas of reusable cryogenic tanks; a graphite-composite primary structure; lightweight, durable thermal protections systems; and advanced propulsion systems. All activities are joint government/industry partnerships, with the common objective of cultivating technologies toward full-scale development.

• The reusable cryogenic tank technology represents advances over current expendable aluminum tanks by the use of lighter, stronger materials. Materials under consideration include aluminum-lithium alloys for the oxidizer tanks

Winged Body
Vertical Takeoff—Horizontal Landing

Vertical Takeoff—Vertical Landing

Lifting Body
Vertical Takeoff—Horizontal Landing
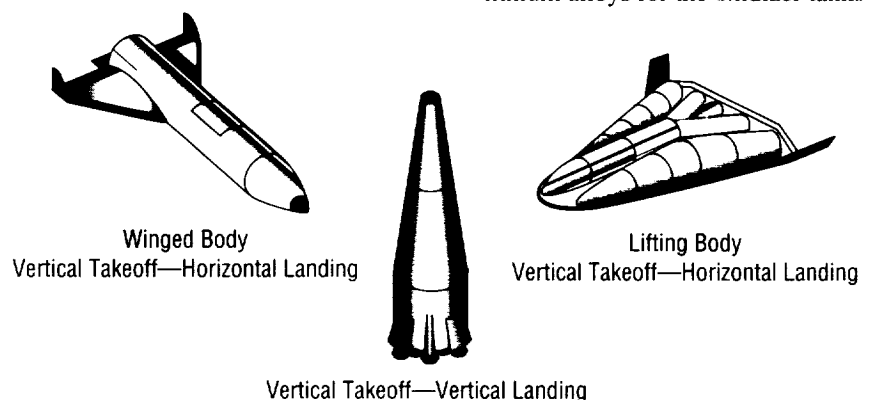
Figure 14.—Reusable launch vehicle concepts.

and graphite-composite for the fuel tanks. Both internal and external tank insulation is being investigated. One of the challenges in producing reusable tanks is that the tank must maintain structural integrity through many cycles over a broad temperature range, from the cryogenic cold to the intense heat experienced during atmospheric entry. Demonstration of the tank system life cycle is planned.

• Use of a graphite-composite primary structure has the potential of lighter weight and greater strength over current systems. In addition to the intertank structure, applications include the thrust structure, wing, and ceramic-matrix composite control surfaces.

• Advanced thermal protection systems offer the advantages of long life, light weight, and low maintenance to decrease the operational costs of reusable vehicles. Areas of investigation include flexible and rigid thermal protection system (TPS) development and validation, low-cost waterproofing techniques, ceramic-matrix composites, and metallic protection systems.

• The propulsion tasks are intended to advance the state of the art in single-stage-to-orbit development and initially focus on tripropellant (liquid oxygen/kerosene/liquid hydrogen) engine development. Tasks include tripropellant injector development and testing, subscale propulsion demonstrator system and modular thrust chamber development, and various Russian-developed technologies and systems.

NRA Products	DC–XA Planned Upgrades	ATD Potential Upgrades

• Reusable cryogenic tank
  – Metallic tank structures ➡
  – Graphic-composite tank structures ➡
  – Cryogenic insulation systems ➡
  – Integrated tank system life-cycle demonstration
	• Reusable cryogenic tank
	  – Metallic tank structures (LO_2)
	  – Graphite-composite tank (LH_2)
	  – Cryogenic insulation systems
		• Reusable cryogenic tank
		  – Metallic tank structures (LO_2)
		  – Graphite-composite tank (LH_2)
		  – Cryogenic insulation systems

• Graphite-composite primary structures
  – Intertank ➡
  – Thrust structure
  – Wing/aerosurfaces
  – Life-cycle demonstration
	• Graphite-composite primary structures
	  – Intertank
		• Graphite-composite primary structures
		  – Intertank
		  – Thrust structure
		  – Wing/aerosurfaces

• Lightweight, durable TPS
  – Flexible TPS validation ➡
  – Rigid TPS validation
  – Low-cost waterproofing techniques
  – Ceramic-matrix composites
  – Metallic TPS
	• Lightweight, durable TPS
	  – Selected TPS (thermal/acoustic)
		• Lightweight, durable TPS
		  – Flexible TPS validation
		  – Rigid TPS validation
		  – Low-cost waterproofing techniques
		  – Ceramic-matrix composites
		  – Metallic TPS

• Advanced propulsion
  – Tripropellant injector
  – Subscale propulsion demonstrator systems ➡
  – Modular thrust chamber
  – Russian-developed technologies and systems
	• Advanced propulsion
	
	  – Auxiliary propulsion unit
		• Advanced propulsion
		
		  – Subscale propulsion demonstrator systems
		  – Modular thrust chamber

• Space booster technology demonstrator (SBTD) potential		

FIGURE 15.—Technology program evolution and applications.

Many of the technologies are candidates for near-term ground and flight testing using the Delta Clipper Experimental vehicle, which is being obtained by NASA from the Air Force for use as a technology test-bed. An upgraded version (DC-XA) is planned to include aluminum-lithium alloy tanks for the oxidizer, graphite-composite hydrogen tanks, and cryogenic insulation systems developed under the reusable cryogenic tank technology efforts. A graphite-composite intertank structure is also planned, and selected thermal and acoustic protection systems will be incorporated. Propulsion technology upgrades include the auxiliary propulsion units.

Vehicle concept design and technology maturation and demonstration will determine future decisions on reusable vehicles for the national space transportation system. The major areas in the technology evolutionary program which will culminate in large-scale flight demonstration are illustrated in figure 15. This advanced technology demonstrator vehicle development activity is expected to result in a first flight prior to the year 2000, with the test program continuing for several years beyond. The decision date for full-scale development is currently planned before 2000, allowing for transition to the reusable launch vehicle fleet in the first decade of the next century.

Sponsor: Office of Space Systems Development

• • • • •

MagLifter

Joe T. Howell/PS05
205-544-8491

Achieving an affordable and reliable launch infrastructure is one of the enduring challenges of the space age. In a marketplace dominated by expendable launch vehicles (ELV's) grounded in the technology base of the 1950's and 1960's, diverse innovative approaches have been conceived since 1970 for reducing the cost per pound for transport to low-Earth orbit (LEO). For example, the space shuttle—a largely reusable vehicle—was developed in the 1970's with the goal of revolutionizing Earth-to-Orbit (ETO) transportation. Although the shuttle has provided many important new capabilities, it has not significantly lowered space launch costs. During the same period, a variety of other launch requirements (e.g., for vehicle research and development and microgravity experiments) has been met by relatively expensive, typically rocket-based solutions (e.g., rocket sleds and sounding rockets).

There are several basic strategies for cost reduction, including: (1) reducing the cost of hardware expended in launcher systems per pound of payload, (2) increasing the reusability per flight of highly reusable vehicles (HRV's), and (3) reducing the cost of launch operations for both of these. A variety of space launch concepts are still under study in this context, ranging from single-stage-to-orbit (SSTO) vehicles to "big, dumb boosters," and from air-breathing hypersonic Earth-to-Orbit vehicles like the National Aerospace Plane

(NASP) to advanced rocket concepts such as space nuclear thermal propulsion (SNTP). Some exotic concepts involving "gun-type" systems have also been studied.

However, past analyses of launch systems involving electric propulsion have been largely limited to electromagnetic versions of "cannons" such as rail guns and coil guns. Despite significant theoretical advantages, these electromagnetic systems have had both technical and programmatic difficulties in maturing beyond research and development and prototype-level demonstrations.

A new approach, involving the use of superconducting magnetically levitated (maglev) vehicles has been developed. This concept, the MagLifter (fig. 16), combines the technology base of maglev systems proposed for terrestrial applications with the best planned improvements in expendable launch and reusable vehicle systems. Together, the result suggests that dramatic improvements in Earth-to-Orbit costs may be possible. The MagLifter draws on a heritage of electromagnetic launch concepts and technical literature, but embodies several new technical characteristics that have not been thoroughly considered to date.

Sponsor: Office of Advanced Concepts and Technology

• • • • •

Payload Release Point

Gas Membrane (Design Option)

LAUNCH

Engine Start for Prerelease
Checkout (Design Option)

45° (55° Design Option)

10,000 feet
(Approximately)

Power System
(e.g., SMES Option)

2.5 miles

ACV Decelerator
Guideway

Total Ascent:
Approximately
6,500 feet

Staging
Facility

Vehicle
Fueling
and Final
Checkout

0.5–1.0 mile

3,500 feet
(Approximately)

Accelerator Guideway

Other Facilities Not Shown
(e.g., Mission Operations,
Propellant Storage, etc.)

System Cross Section

Tunnel (Design Option)

Periodic
Power
Storage
Units

Maglev Guideway

Example Payload: Highly
Reusable Vehicle (HRV)

Maglev Accelerator-
Carrier Vehicle

Structural Supports
(Distribution of Loads
on Payload Vehicle)

FIGURE 16.—The MagLifter Earth-to-Orbit concept.

Engine Diagnostics Using Cognitive Computing Techniques

Jonnathan H. Kim/PD14
205–544–5387

Ralph R. Kissel/EB24
205–544–3510

Thomas F. Zoladz/ED33
205–544–1552

Cognitive Computing Techniques (CCT) are numerical computation methods motivated by, or based on, biological, psychological, and physiological environment. Examples include artificial neural networks, genetic algorithms, and fuzzy logic. One important aspect of cognitive computing techniques is that they can bridge gaps between human knowledge and computer knowledge (data bases). Another importance comes from their ability to generalize, or to learn, without explicit instructions. These unique characteristics enable them to automate tasks that may have before been considered too difficult to automate. One such task under evaluation involves the dynamic bearing signature of the space shuttle main engine (SSME) high-pressure oxygen turbopump (HPOTP).

Main engine turbopump bearings fail primarily due to uneven ball wear. Bearing cage frequencies appear at the bearing cage rotational speed and subsequent harmonics in the high-frequency data. Using externally mounted accelerometers and strain
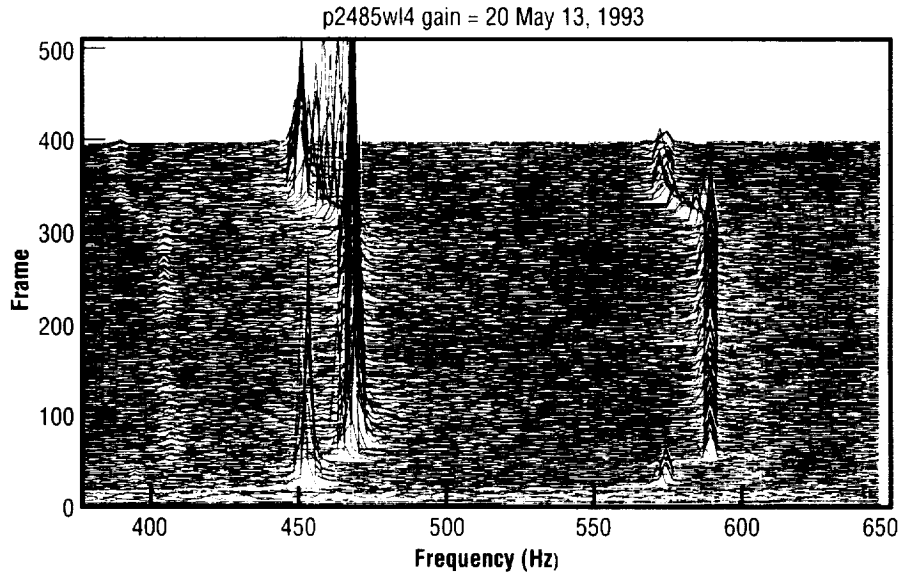
FIGURE 17.—Anomalous case.
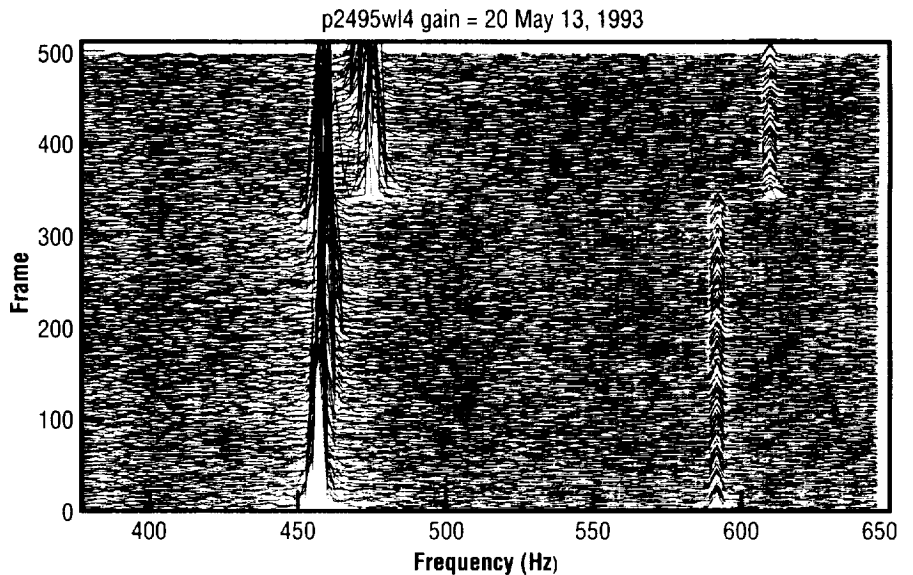
FIGURE 18.—Nominal case.

26

gauges, the vibration data are recorded. Spectral analysis is then performed by trained analysts; however, this is a very time- and labor-intensive task. Furthermore, the decision can often be very subjective, depending heavily on an analyst's training and expertise. Figure 17 illustrates a case in which the second harmonic cage (2C) frequency is prominently displayed at or about 400 hertz (Hz). Figure 18 depicts a data set with nominal engine vibration data. These two cases are extremes, and, in many instances, discrimination of anomalous peaks are not nearly so obvious. Under an MSFC Director's Discretionary Fund (CDDF), research has been conducted to see if a cognitive computing technique could be applied to reduce operations costs.

An artificial neural network with 13 input neurons and one output neuron was trained with an anomalous case and a nominal case with a frequency resolution of 1.25 hertz. This network was trained with the back propagation. A network with no hidden nodes seemed to work best. To test the network, researchers

Frame #1 Frame #2   Frame #9 Frame #10

FIGURE 19.—Peak detector.

determined the synchronous frequency (rotor speed) based on the engine thrust level. Twenty-one frequency bins centered at the expected second harmonic cage frequency were extracted. These data points were propagated, 13 points at a time, through the trained network to compile the results (in terms of number of hits) until all 21 points were used. Table 3 delineates the findings. The number of hits seems to correlate with the analyst's rating, where "0" represents nominal condition and "5" indicates a highly recognizable anomaly.

Also, a 30-input neural network was trained using 2.5-hertz data. The 30 input points consisted of 10 sets of three points. Each set was a consecutive time slice (frame), and each data point within a frame represented a 2.5-hertz bin (fig. 19).

This data set was designed to include the time dependency of the cage frequency data. Each frequency, in turn, was processed using the three-point range until the full spectrum had been processed. Results, in terms of hits, provided in table 4, seem to reveal all recognizable series of peaks. For case 2495, however, a high-pressure fuel pump was mistakenly identified as a possible anomaly.

Upon analysis, the linear model of cage frequencies, which is a function of the thrust level, did not work well in many cases. In order to fully automate the anomaly detection, a better model was needed. Based on a thrust-level schedule, a linear model of the synchronous frequency was constructed. This model was then compared (correlated) with the synchronous frequency found by detecting the largest peak in each time

TABLE 3.—Shift and propagate results

Test	ANN hit	Experts
1595	23	2
1675	34	2
2485	78	5
2495	12	0
449	23	4

TABLE 4.—Peak detector results

Test	2C	# Hits	3C	# Hits	Expert
1595	420	30	None		2
1675	400 (398)	77 (48)	None		2
2473	418 (420)	63 (121)	625	58	4
2485	403	110	None		4
2495	None		593	167	0
446	393	32	588	40	3

Raw SF (maxima found)

Expected SF of 2495ht13 & VIN9309

Newer and Better SF
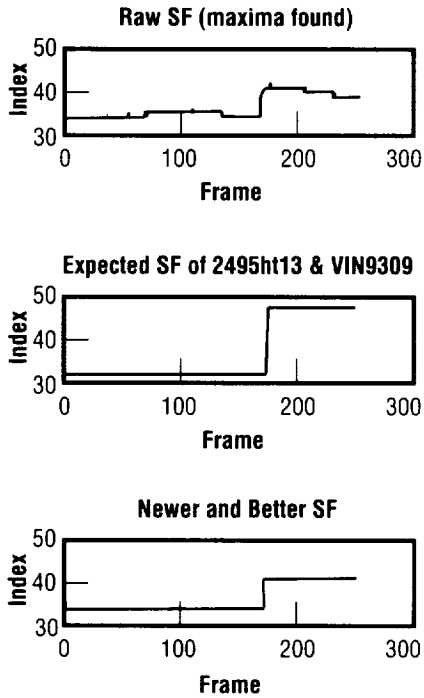
FIGURE 20.—Construction of synchronous frequency.

FIGURE 21.—Rotate and propagate.

TABLE 5.—*Rotate and propagate results*

Test	2C Hits	3C Hits	Expert
1595	21	37	2
1675	34	34	2
2495	19	148	0
446	26	123	3

frame. From this correlation, a new synchronous frequency was constructed, as shown in figure 20.

Based on the new synchronous frequency, approximate locations of cage frequencies were found. Then another neural network with 13 input neurons, 8 hidden neurons, and one output neuron was trained using one anomalous case and one nominal case. Figure 21 illustrates how the data were rotated through the input. The results are compiled in table 5. As in the case of the three-point peak detector, the neural network mistakenly identified a high-pressure fuel pump as a possible anomaly.

Further improvement can be made to discriminate anomalous cage peaks feed-through from other turbopumps (e.g., the high-pressure fuel turbopump). Also, more tests are required to establish a statistically meaningful threshold at which a decision can be made on the health of the bearing. Researchers feel, though, that cognitive computing techniques can play an important role in the automation of many tasks which might otherwise be too difficult to quantify.

While the tool will not replace trained analysts, it can be used to minimize laborious and time-intensive tasks.

● ● ● ● ●

RESEARCH

MSFC Small Business Innovation Research

Helen C. Stinson/PS05
205–544–7239

Small Business Innovation Research (SBIR) program objectives established by law include stimulating technological innovation in the private sector, strengthening the role of small business concerns in meeting federal research and development needs, increasing the commercial application of federally supported research results, and fostering and encouraging participation by socially and economically disadvantaged persons and women-owned small businesses in technological innovation.

There are three phases in the Small Business Innovation Research program: phase I, phase II, and phase III. The purpose of phase I is to determine the technical feasibility of the proposed innovation and the quality of the performance of the small business concern with a relatively small NASA investment before consideration of further federal support in phase II. The performance period is 6 months, with funding up to 70,000 dollars. To be eligible for phase I selection, a proposal must be based on an innovation having high technical or scientific merit that is responsive to a NASA need.

The objective of phase II is to continue development of selected innovations shown feasible in phase I that have the highest potential value to

NASA and to the U.S. economy. Phase II awards may not necessarily complete the research and development required to satisfy commercial or federal needs beyond the Small Business Innovation Research program, but completion of the research and development as well as commercializing the results should be pursued in phase III. Phase II lasts 2 years, with funding up to 600,000 dollars.

Phase III is pursuit by Small Business Innovation Research contractors of commercial applications of their project results, using private sector funds. This is in support of the Government's policy to stimulate technological innovation and provide for return on investment from Government-funded research/research and development that is in aid of the national economy. Phase III may also be follow-on, non-SBIR-funded contracts with the Government for SBIR-derived products or processes for use by the Federal Government.

Contact the MSFC Small Business Innovation Research program manager for more information about a particular program. A representation of completed MSFC Small Business Innovation Research contracts with the phase II results and commercialization of the end products/processes is provided as follows:

Company name: SatCon Technology
Contract number: NAS8–38944
Project title: Integrated Power and Attitude Control System for the Space Station and Other Applications

The phase II end-product of this effort is a 2-kilowatt-hour (kWh) carbon

fiber flywheel capable of delivering 2 kilowatts of power over a speed range of 20,000 to 40,000 revolutions per minute. The round-trip efficiency of the energy storage wheel, including power conditioning electronics, is expected to exceed 85 percent. The flywheel is supported on magnetic bearings which reduce the parasitic losses of the system. The flywheel is aimed toward a combined energy storage and an attitude control system for spacecraft.

SatCon is committed to developing flywheel products for automotive, industrial, utility, and aerospace applications. SatCon is currently in discussions with potential customers in all of these markets to develop products for their specific needs. Vehicle and transportation uses for energy systems offer enormous market potential. Commercialization opportunities with major automotive companies is being explored worldwide. SatCon is an active participant in the Northeast Alternative Vehicle Consortium (NAVC) for promoting alternative fuel vehicles. The company expects flywheels to significantly contribute to improving the efficiency of electric vehicles and hybrid-electric vehicles of the future.

The technology developed under this contract is directly applicable to the Flywheel Energy Storage Program SatCon currently has with Chrysler Corporation. Chrysler's PATRIOT project, a high-performance, hybrid-electric race vehicle, is a multimillion-dollar program that uses flywheel energy storage to improve the efficiency by load-leveling a turbine alternator. SatCon is also developing

components of the drive train, namely the turbo-alternator, the power conditioning unit, and the traction motor.

In addition to the program with Chrysler, SatCon is actively pursuing venues such as public utilities for commercialization of this technology as a load-leveling intermediate energy storage device and for uninterruptible power supplies (UPS).

Company name: AZ Technology, Inc.
Contract number: NAS8–38970
Project title: Portable Spectroreflectometer

This phase II effort developed and proved an instrument that provides in-space capability to optically measure the condition of external surfaces of operational spacecraft. Laboratory prototypes of two versions of the space-portable spectroreflectometer (SPSR)—a hand-held instrument for use by an astronaut on extravehicular activity and a remotely controlled version that is operated using a remote manipulator system (RMS)—were developed and tested.

The space-portable spectroreflector is a highly specialized instrument designed for in-space inspection of the optical and thermal properties of external materials used in the space environment.

These instruments will find application on space missions where there are maintenance and repair requirements or a need to assess the optical properties of materials. This is true for most long-term missions with lifetimes greater than 5 years (such as the space station, Hubble Space Telescope, and so forth). The

spectroreflectometer instruments are ideal standard utility instruments for use on these long-term missions, whether human-tended or robotically maintained. The hand-held tool will find additional applications inside orbital laboratories and at lunar or Martian bases.

Company name: Seca, Inc.
Contract number: NAS8–38961
Project title: Heat Transfer in Rocket Engine Combustion Chambers and Regeneratively Cooled Nozzles

The phase II deliverable of this effort was a computer code for analyzing conjugate heat transfer and fluid dynamics using real fluid properties in rocket engine systems. The real fluid properties model developed under the contract is currently being used to analyze fluid flow and combustion in a hybrid rocket motor for Martin Marietta Corporation and AMROC, Inc. The heat transfer analysis will probably follow this effort.

The conjugate heat transfer code can be utilized by any rocket engine manufacturer, government agency, or subcontractor to analyze engine fluid flow and heat transfer. It is particularly useful in studying the heat transfer to cryogenic fluids, such as liquid oxygen in engine injector systems, so that fluid quality and spray characteristics can be evaluated.

Company name: Foster-Miller, Inc.
Contract number: NAS8–38947
Project title: Tailored Composite Bumpers for Protection Against Orbital Debris

The phase II end-product of this endeavor was an innovative and effective z-direction bumper

configuration for protecting spacecraft against the effects of orbital debris traveling at hypervelocities in space. The key to this successful configuration was the technology for producing a graphite-reinforced, organic composite material having high loadings of metallic pins through the thickness.

The technology developed in the program is based on the z-fiber process on which Foster-Miller now holds the application patents. This program has resulted in a major contribution to the z-fiber technological base by supporting two new z-fiber thrusts: introduction of metallic pins into a laminate and use of high-volume fractions (≥ 2 to 3 percent) of z-fibers.

Interest in z-fiber composites for protection from hazards in space was high at Martin-Denver until recent Strategic Defense Initiative (SDI) program cutbacks; interest also remains at Comsat, and they will be reviewing final test data. An area of far greater near-term commercial potential exists and is being exploited by Foster-Miller. This involves the ability of the automated metallic pin insertion technology developed in this program to facilitate greatly enhanced resistance to impact damage in other types of aerospace structures. A major aerospace company is now in the process of qualifying a z-fiber application using metallic pins for a significant commercial aircraft application.

An alternate capability of commercial significance demonstrated on this program was the ability to place the pins in closer proximity than ever before without destroying laminate

properties. While the need for very close spacing was originally envisioned as the most effective means for fragmenting dangerous debris particles, researchers are now finding it to be of great potential use in thermal management for such applications as high-density electronics packaging, satellite battery power systems, and aircraft infrared signature control. Foster-Miller has demonstrated that high z-fiber volume fractions can triple the through-thickness thermal conductivity of graphite composites. The fiber insertion techniques advanced during this program have resulted in Foster-Miller receiving additional commercial and government support to further develop the technology for these applications.

Company name: Huntsville Sciences Corporation
Contract number: NAS8–38957
Project title: Finite Element and Adaptive-Grid Thermal Analyzer With Enhanced Graphics Capability

The project's phase II end-product was a thermal analysis software package including both two-dimensional and three-dimensional finite element conduction solvers and their supporting codes for surface modeling, grid generation, and results plotting.

During the second year of the phase II contact, Huntsville Sciences Corporation developed a marketing plan supported with company overhead monies to commercially sell the software product developed in phase II. The main focus of the marketing plan is to introduce the thermal software product to potential companies who specialize in

commercial software sales. Huntsville Sciences has contacted several companies and has given demonstrations of the software product. Through these efforts, two companies (Network Analysis Associates and Intergraph Corporation) have been identified who have expressed interest in commercially marketing the software.

Company name: Mayflower Communications Company
Contract number: NAS8–38479
Project title: Autonomous, Integrated Global Positioning System(GPS)/ Intertial Navigation System Navigation Experiment for Orbital Maneuvering Vehicles and Space Transfer Vehicles

The phase II end-product of this effort was a fully developed and tested Global Positioning System-based navigation and attitude algorithm and software which is reconfigurable in real-time, in response to mission contingencies, i.e., sensor health and status. The deliverable product was the navigation and attitude software implemented in Ada programming language.

Mayflower has made a business commitment to be a leading supplier of Global Positioning System-based navigation and attitude software and hardware products as a result of successful completion of contract NAS8–38479. The company is currently implementing the software, developed for NASA, on an Air Force-sponsored positioning system attitude receiver hardware platform. Mayflower has had ongoing discussions and informal negotiations with Motorola, Rockwell, and Fairchild to license the attitude

determination software for commercial application.

Mayflower recently has negotiated a teaming agreement with Fairchild Space and Defense Corporation of Germantown, Maryland, to evaluate and space-qualify the Mayflower Global Positioning System attitude receiver and then jointly market the product to both government and commercial customers. Commercial applications include attitude determination of low-Earth orbit mobile communication satellites being developed by TRW, Motorola, Loral, and others to provide wireless voice and data communications capability around the world.

Sponsor: Office of Advanced Concepts and Technology; Small Business Innovation Research

• • • • •

Research Programs

Since MSFC's inception, an active theoretical and experimental scientific research effort has been a key element of the Center's vitality and progress. The research has concentrated on several specific areas of science, all of which today fall within two of the five NASA Strategic Enterprises: Mission to Planet Earth and Scientific Research. Marshall's research projects have employed virtually every available means to reach the near-Earth space environment. These products have been used as a tool for exploring basic physical processes, and have been used to provide an unobstructed vantage point from which to look both outward and back at the Earth. Parallel laboratory studies and instrument development support and enable the flight experiments.

In the area of Earth system science, research has involved theoretical studies and computer modeling, instrument development, and experimental measurements. Topics include modeling of the global climate, the global hydrologic cycle, and the influence of clouds on climate; lidar, microwave, and optical instruments and experiments to measure wind, aerosols, precipitation, and lightning; and measurements of atmospheric and surface hydrology, both remotely and in situ.

Space physics activities have involved measurement, simulation, and modeling of ion and plasma processes in the ionosphere and the magnetosphere, and the development of laboratory and flight instruments. Analytical and experimental solar physics research concentrates on understanding the role of magnetic fields in solar processes. Ground measurements are made with solar vector magnetographs; and a flight instrument, the Solar X-Ray Imager, is in development. The astrophysics program includes development of two advanced x-ray detectors and a promising x-ray optical technique—a cosmic-ray scintillating optical fiber ionization calorimeter. The program also includes a new infrared array camera, as well as analysis of several exciting, unusual observations by the Burst and Transient Source Experiment on the Compton Gamma-Ray Observatory.

Microgravity science and applications studies concentrate on electronic and photonic materials and certain biophysical topics—especially protein crystal growth and analysis— and on improved techniques for materials fabrication and analysis in microgravity. Improved semi-conductor single-crystal growth methods are being developed, including a directional solidification furnace for the Second U.S. Microgravity Payload (USMP–2) mission. An advanced hand-held protein crystal growth apparatus will greatly simplify the reliable processing of multiple samples on manned missions.

Gregory S. Wilson
Director
Space Sciences Laboratory

EARTH SYSTEM SCIENCE

Numerical Modeling of Nonlinear Baroclinic Fluid Systems

Timothy L. Miller/ES42
205–544–1641

In developing a comprehension of the processes that affect global change on Earth, a component that presents one of the greatest challenges is that of the fluid system composed of the atmosphere and oceans. Clearly, a broader understanding of this system is important, since the atmosphere is the fluid system in which we live—the system that supplies the land with fresh water and shields life from harmful solar radiation. The oceans interact with the atmosphere through exchanges of heat, water, and momentum and provide a very large "thermal mass" for the system. Due to the complex nature of this system and the difficulty in obtaining sufficient observational data on it, accurately predicting its behavior for all but very short time periods remains an elusive goal. The aim of this research is to develop a clearer understanding of the Earth system through the use of various computer models to allow the study of the atmosphere, as well as the complicated behavior of a rather simple fluid system driven by horizontal temperature gradients and influenced by rotation.

One means of investigating the behavior of Earth's atmosphere and oceans is to conduct laboratory experiments in cylindrical and spherical containers where a fluid such as water is differentially heated and

rotated. Depending upon the strength of the differential heating and the rate of rotation, the flow may be very simple—steady in time and axisymmetric in structure. For other values of heating and rotation, the flow may be made of steady, regular waves, or it may be quite irregular and chaotic. Such experiments have been conducted in laboratories, both at MSFC and elsewhere, resulting in a numerical model developed at MSFC that tests our ability to predict flow types and to assist in comprehending such processes as heat and momentum transport. Additionally, studies are being performed to help design future space-flight experiments using the geophysical fluid-flow cell apparatus.

The GEOphysical fluid-flow SIMulator (GEOSIM) enables scientists to experiment with both spherical or cylindrical flows. Flow analysis proceeds in several steps: calculation of axisymmetric flow (that which would be seen if no variations in longitude were allowed); calculation of the linear stability of that flow to three-dimensional wave perturbations; calculation of the wave amplitude where interaction between the wave and the longitudinal mean flow is allowed; and the calculation of the fully nonlinear flow with full interaction between all components of the flow. The extent to which each of these steps can be directly applied to the actual flows depends upon the nonlinearity of the flow, which, in turn, depends upon the experimental parameters. For highly nonlinear flows, a time series of images of the predicted flow is produced; the images are shown in computer animations to illustrate the interactions between various types of structures in the flow.

Recent work has placed emphasis on vacillatory flow in the baroclinic annulus experiments. The flow occurring in the gap between two concentric, co-rotating cylinders that are differentially heated is computed with high resolution and for (typically) several tens of rotational periods. For certain combinations of rotation rates and temperature differences, the resulting flow is three-dimensional and undergoes a periodic oscillation in the amplitude of the "wave" part of the structure. Agreement between the computer simulations and previous laboratory experiments is very good. The computer calculations allow the investigation of more cases than has been done experimentally. This work has resulted in the demonstration that a numerical model can be used to identify deterministically predictable regions in parameter space, as opposed to regions in which the result is highly sensitive to numerical and physical parameters. An investigation into the mechanics of the various flow regimes is continuing.

Lu, H.-I., and Miller, T.L. 1994. Characteristics of Annulus Baroclinic Wave Structure During Amplitude Vacillation. Submitted to *Tellus*.

Lu, H.-I.; Miller, T.L.; and Butler, K.A. 1993. A Numerical Study of Wavenumber Selection in the Baroclinic Annulus Flow System. Accepted in *Geophysical Astrophysical Fluid Dynamics*.

Miller, T.L.; Lu, H.-I.; and Butler, K.A. 1992. A Fully Nonlinear, Mixed Spectral, and Finite Difference Model for Thermally

Driven, Rotating Flows. *Journal of Computational Physics* 101:265–75.

Miller, T.L., and Leslie, F.W. 1994. Numerical Modeling of Experiments in Rotating Buoyant Convection in a Hemispherical Shell With Latitudinal Thermal Gradients. Submitted to *Geophysical Astrophysical Fluid Dynamics*.

Sponsor: Office of Mission to Planet Earth

University Involvement: Institute for Global Change Research and Education

• • • • •

A Modeling Study of Marine Boundary-Layer Clouds

Daniel E. Fitzjarrald/ES42
205–544–1651

Marine boundary-layer clouds are important regulators of the Earth's climate because of their significant impact on the surface energy budget. Thus, general circulation models should realistically simulate the global and temporal variations of these clouds. Currently in the third year of a boundary-layer cloud effort, present research is aimed at development and improvement of the parameterization of marine boundary-layer clouds, as well as understanding the physical processes that regulate cloud structure.

Researchers have implemented a new prognostic scheme to define cloud cover and mean liquid water in the boundary-layer model following Tiedtke's unified approach method to predict any type of cloud. In this approach, mass-flux detrainment from convective updrafts is the basic source of the mean cloud variables. Scientists have used the one-dimensional version of the model to simulate the climactic downstream variation of boundary-layer clouds from the eastern North Pacific to the central Pacific Oceans. Also completed is a simulation of a Lagrangian experiment performed during the Atlantic Stratocumulus Transition Experiment (ASTEX), June 1992. The results of both simulations are in agreement with observations. The climate simulation predicted the

decrease of cloud cover and liquid water path from stratocumulus to trade-wind cumulus regions. This decrease is clearly associated with decoupling between cloud and subcloud layers and the development of vertical gradients of the boundary-layer structure. With the prognostic scheme of clouds, researchers not only obtain liquid water content, a crucial parameter for radiation calculation, but also are able to study the hydrological cycle associated with these clouds through a budget analysis of cloud variables.

Researchers have also used a regional version of the boundary-layer model to simulate the boundary-layer structure during the Atlantic Stratocumulus Transition Experiment. The diurnal variation (resulting from the decoupling between cloud and subcloud layers causing solar warming inside the clouds) of boundary-layer clouds is well-simulated compared with that from satellite data. During daytime, solar warming inside the clouds stabilizes the boundary layer so that a weak stable layer forms at the base of the cloud layer. Thus, the mass flux at the cloud base from the model is significantly reduced, and, consequently, the detrainment of mass from updrafts decreases during the day. The source term of the predictive equations of mean liquid water and cloud cover becomes very weak, leading to a reduction in these cloud variables. During night, solar warming disappears and the longwave radiative cooling at the cloud top is strong enough to maintain a well-mixed structure. Thus, the mass flux at the cloud base and the detrainment in the cloud layer and in the inversion are significantly larger than those in the

daytime, which gives more clouds. Figure 22 offers an example of the simulated diurnal variation. These simulations demonstrate that the mass-flux parameterization with a Tiedtke's cloud prognostic scheme provides a physically based parameterization for a general circulation.

Parameterization of a clear, convective boundary layer is also a weak area for a general circulation model (GCM), because the local gradient transport theory no longer applies. Scientists, however, have derived a parameterization from the traditional mass-flux convection scheme with the closure that negative entrainment flux at the top of a convective boundary layer (CBL) is proportional to the positive buoyancy flux (a classic assumption). This formulation gives updraft vertical velocity, thermodynamic profiles, and fractional area. One of the advantages of this scheme is that it can be used as a subcloud layer parameterization, and it can provide cloud-base, mass-flux updraft properties for cloud convection scheme. (Actually, it was initially intended to be a subcloud layer representation for a cumulus convection scheme.) The model gives a realistic behavior, although it seems that the scheme produces too much drying in the convective boundary layer. An example of the convective boundary-layer simulation is shown in figure 23.

Presently, researchers are testing a parameterization that uses the buoyancy-sorting mass-flux scheme—which is more physically based than the traditional entraining plume model—and Tiedtke's scheme to study the ability of these types of models in simulating boundary-layer clouds. Also ongoing is the one-dimensional and regional boundary-layer model simulations mentioned previously (climatic and Atlantic Stratocumulus Transition Experiment simulations) and the preparation of a manuscript for this study.
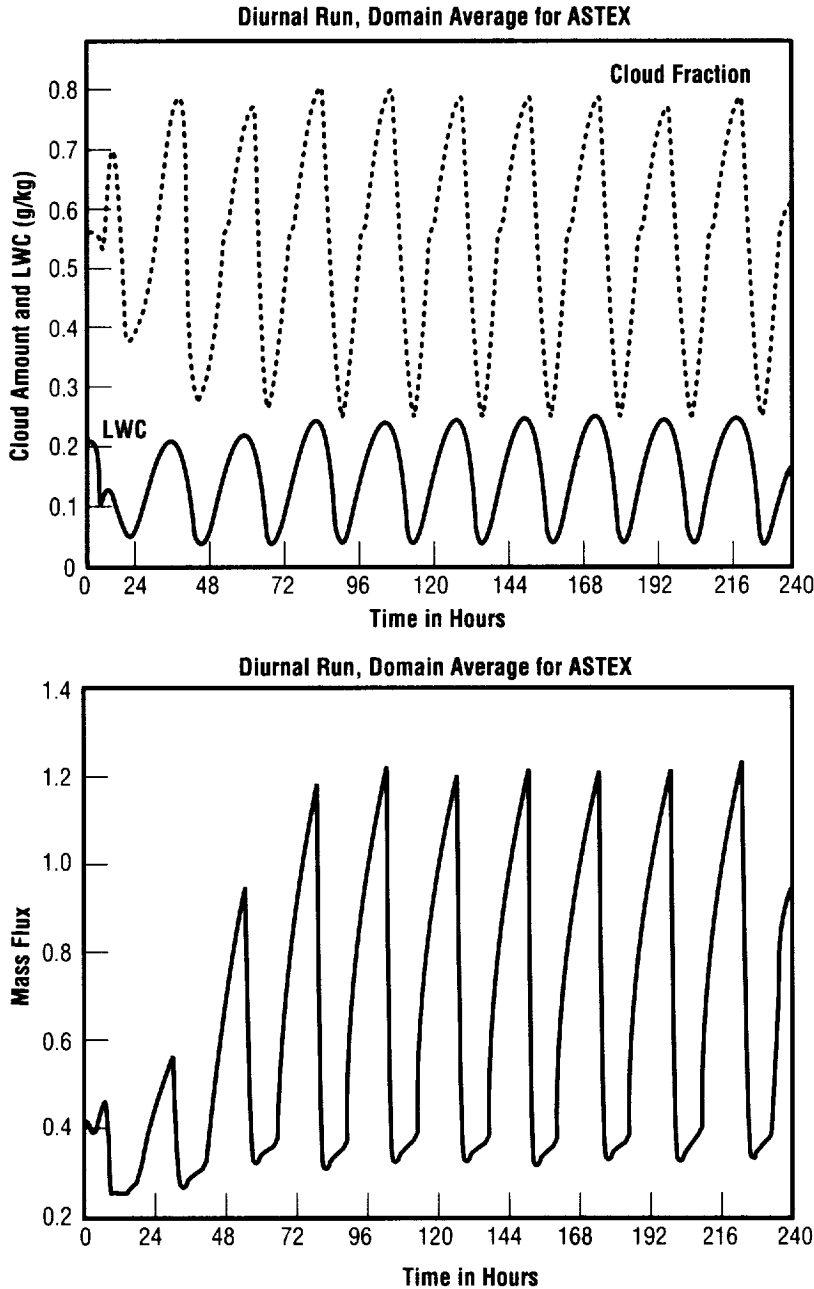
FIGURE 22.—The simulated diurnal variation of marine boundary-layer clouds.

Daytime Variation of CBL, August 15 FIFE

Height (m)

Water Vapor Mixing Ratio (g/kg)

Height (m)

Potential Temperature (K)
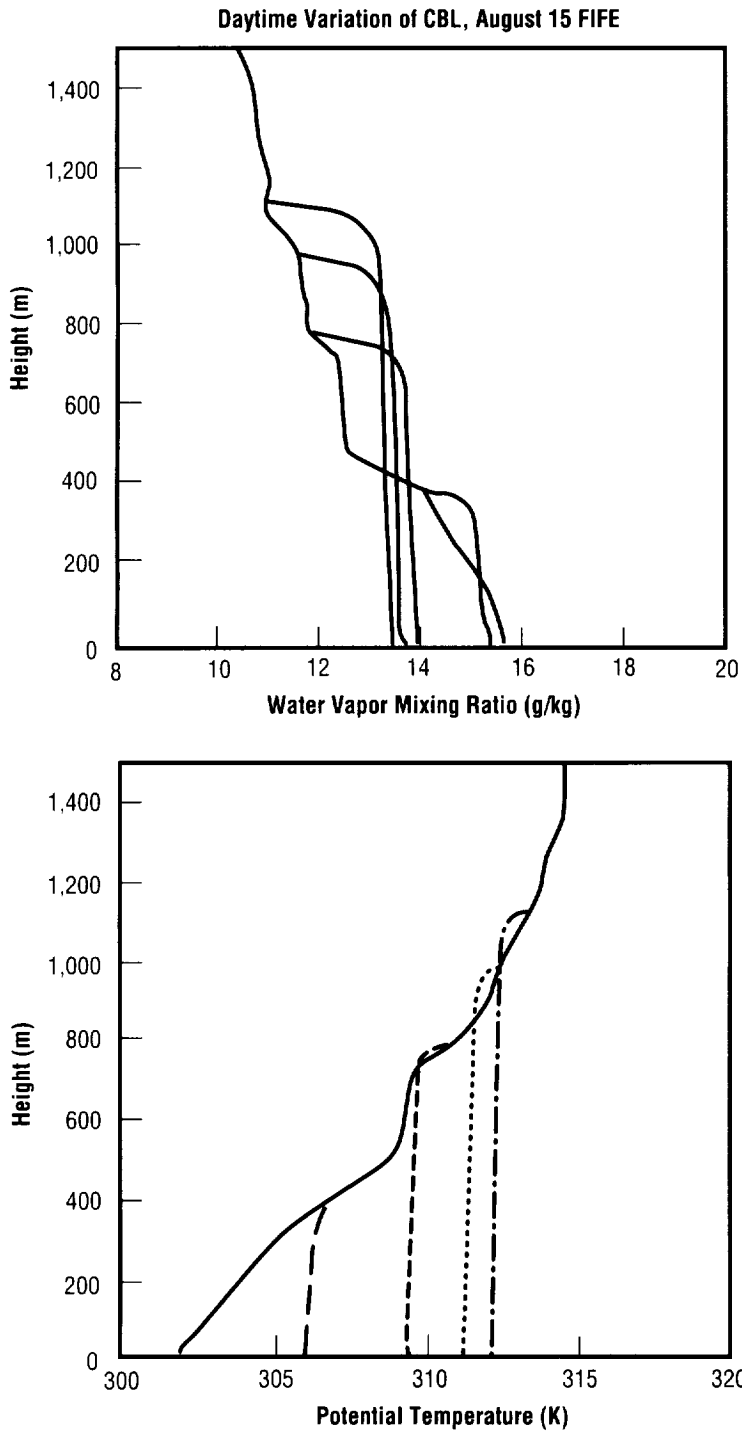
FIGURE 23.—The simulated convective boundary-layer structure, with the modified mass-flux scheme. (The numbers represent the local time.)

The submission of a proposal to continue the research of the current project is imminent. The focus of the new proposal will be to formulate a buoyancy-sorting, mass-flux scheme coupled with Tiedtke's prognostic cloud scheme.

Wang, S. August 23–27, 1994. A Mass-Flux Parameterization of Stratocumulus-Topped Boundary Layers. Workshop on Modeling Boundary-Layer Clouds. Boulder (accepted).

Wang, S. 1994. Application of Tiedtke's Prognostic Scheme of Clouds in a Simple Boundary-Layer Model.

Wang, S. 1994. Simulating Clear Convective Boundary Layers During FIFE Using a Mass-Flux Updraft-Downdraft Scheme.

Wang, S., and Minnis, P. September 22–27, 1994. Deriving the Boundary-Layer Structure During ASTEX Using a Satellite-Constrained Model. Second International Conference on Air-Sea Interaction and On Meteorology and Oceanography of Coast Zone. Lisbon, Portugal (accepted).

Wang, S., and Wang, Q. 1994. Roles of Drizzle in a One-Dimensional, Third-Order Turbulence Closure Model of the Nocturnal Stratus-Topped Marine Boundary Layer. *Journal of Atmospheric Science* 51:1559–76.

Global Atmospheric Modeling

Daniel E. Fitzjarrald/ES42
205-544-1651

During the past year, scientists at MSFC have continued their work on the development of analysis techniques and validation procedures for global models of the Earth's climate system. The ultimate goal of these efforts is to develop improved global climate models that can be used by policymakers and technicians involved in mitigating the effects of human interaction with our environment, such as global warming due to carbon dioxide emissions.

Climate models are derivatives of weather forecast models that are run at lower resolution, so much longer runs can be made. A typical climate simulation might be for a decade, in contrast to a forecast of a week for an operational global weather model. An important difference between the climate model and its progenitor is that the climate model must operate on its own, without being corrected every 12 hours with new data from the global network of observing stations. For this reason, it is more important to correctly simulate the interactions of the dynamical model with its boundaries. One of the most important of the interactions, and possibly the most difficult to correctly ascertain, is the interaction of the atmosphere with water in its various forms. This interaction, the global water cycle, is the subject of this effort's simulations. During the past year, these simulations have included studies of surface hydrology and boundary-layer cloud formulations.

The surface and its moisture act to the atmosphere as a memory device. Cloud formation is increased over areas that are moist because of recent rains. Surface temperatures are decreased because of shading from these clouds, evaporation from the wet surface, and transpiration of plants supplied with abundant moisture from below. The opposite sense of feedback can occur when there has been a deficit of precipitation, leading to the hot, dry April and May of 1988, for example. Of course, there may be other factors, such as variations of tropical sea-surface temperature. The aim of the modeler is to get all the various processes correct, more or less, so that their relative importance can be ascertained.

An example of the surface interaction is shown in figure 24, which depicts the April wetness of a subsurface layer (10 to 20 centimeters below the surface), the May transpiration of moisture by plants, and the correlation of these two quantities. The average of 10 April's of wetness was correlated with the average of 10 May's of transpiration. The simulation was calculated with the observed sea-surface temperatures from 1979 to 1988 as the only real data, which allowed the model to generate its own "climate." It can be seen that over much of North America there is positive correlation. It is through analyses of correlations such as these that the complicated interaction of the model atmosphere with its surface can be understood and the simulation improved.

Boundary-layer stratocumulus and trade-wind cumulus clouds are important regulators of the Earth's atmospheric climate. They are most commonly associated with large-scale subsidence and cover extensive areas over oceans to form a persistent feature of the climate. These clouds drastically reduce the amount of solar radiation absorbed by the Earth, but have little effect on the emitted infrared radiation to space. For these reasons, it is important that general circulation models used for climate studies realistically simulate the global distribution of boundary-layer clouds.

While the importance of these clouds is well recognized, their representation in climate models remains an unsolved problem. In the past year, researcher efforts in this area have been to evaluate the performance of simulations of boundary-layer clouds by a climate model and test various formulations of these clouds. Findings have indicated, in general, that the model simulates the right locations of maximum and minimum boundary-layer cloud cover over the globe. By comparing the model-simulated cloud cover and the International Satellite Cloud Climatology Project's (ISCCP's) low-level cloud cover (fig. 25), it is clear that the model gives maximum boundary-layer cloud cover over several major areas of these clouds compared with the climatology project's data. However, the model gives poor representation of seasonal variations of the cloud cover over some subtropical areas. The seasonal variation of stratus cloud cover observed from ground observations is poorly simulated by the climate model in two subtropical regions (fig. 25c).

AMIP 10-Year Average

April Wetness
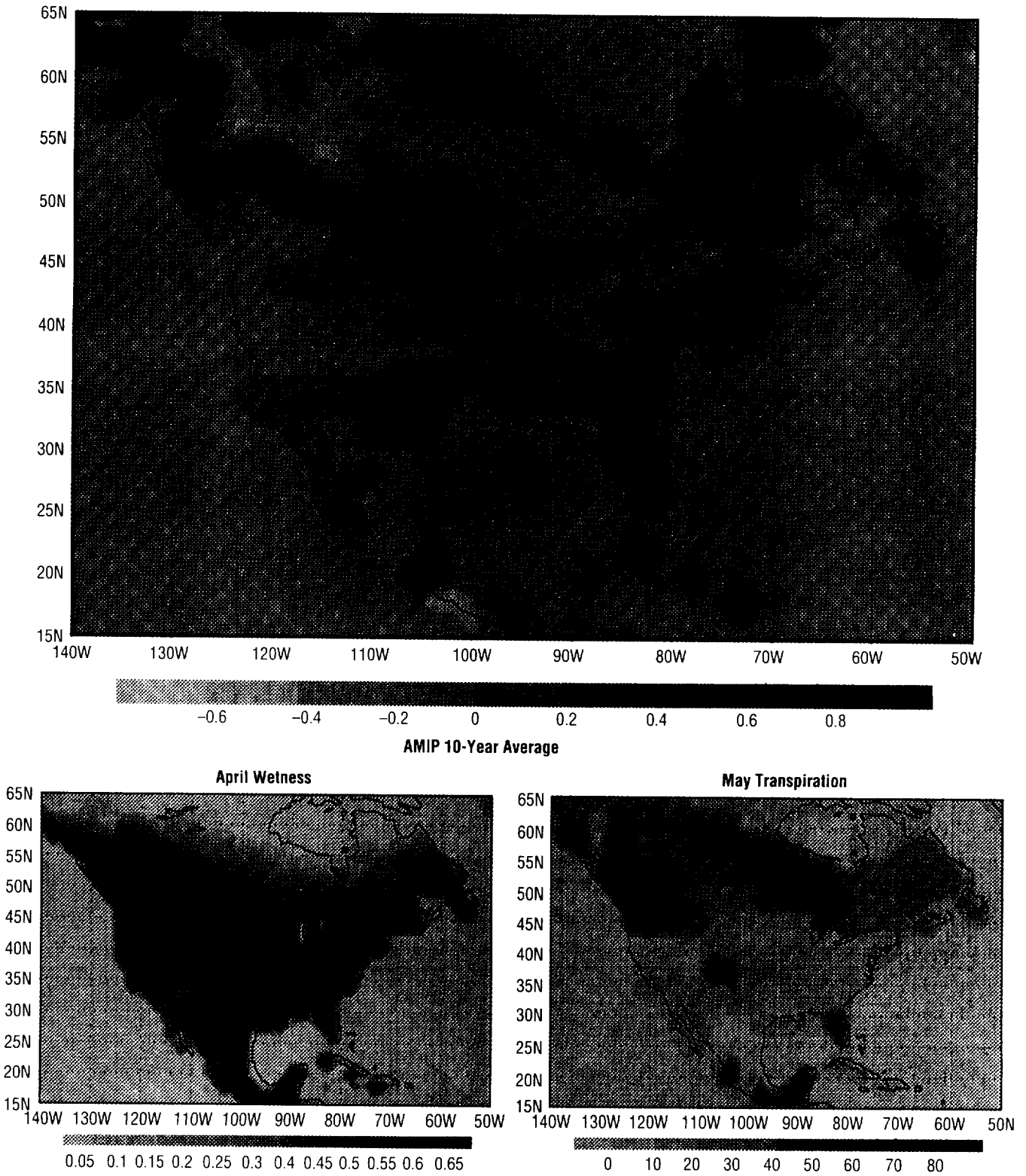
May Transpiration

FIGURE 24.—April wetness of a subsurface layer versus May transpiration of moisture by plants.
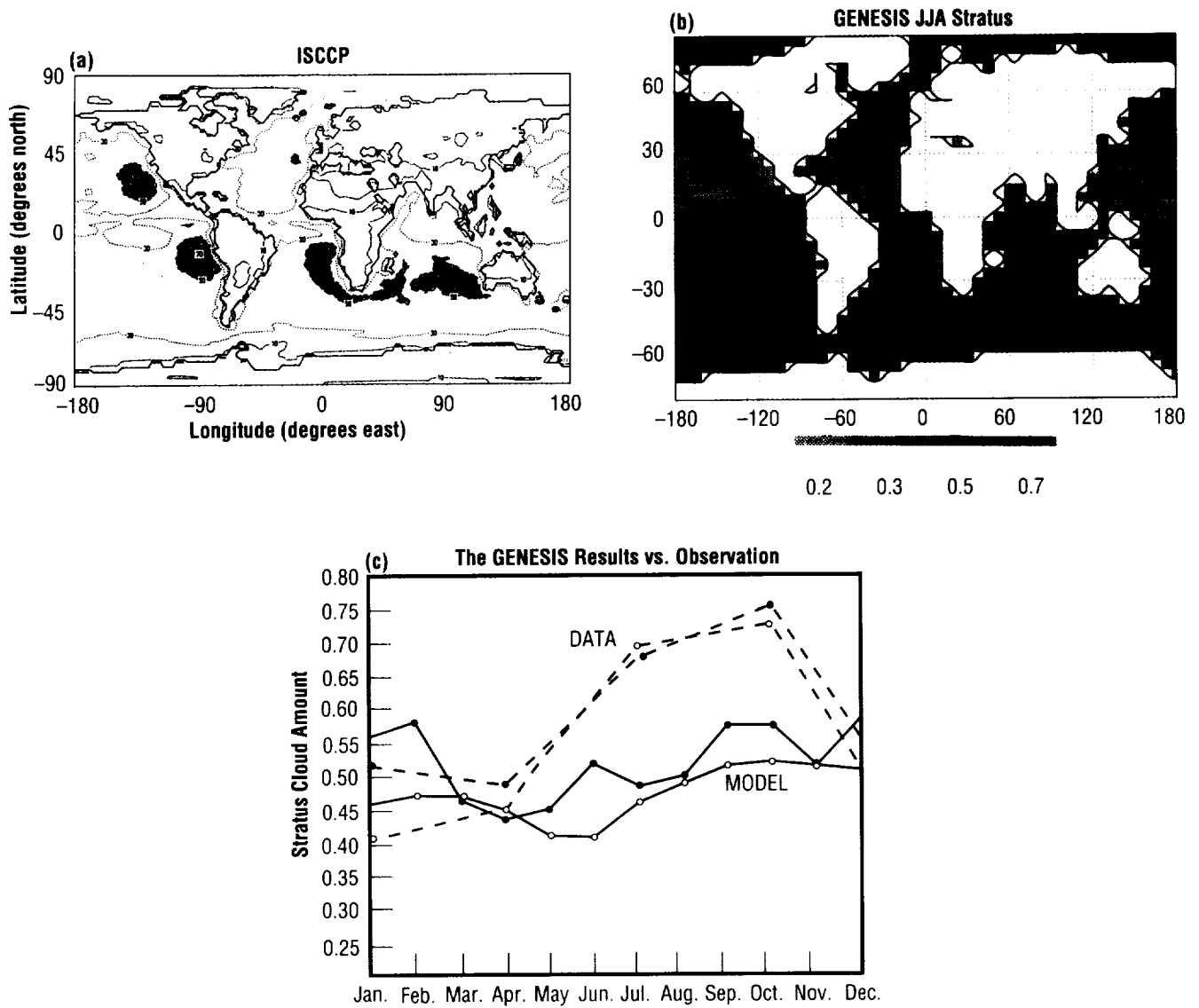
Figure 25.—The simulation of boundary-layer clouds with the GENESIS climate model: (a) low-level cloud cover from International Satellite Cloud Climatology Project data (the shaded areas represent cloud cover above 50 percent); (b) the low-level cloud cover from GENESIS; (c) seasonal variations of stratus cloud cover over the areas to the west coast of Peru (open circle) and of South Africa (solid circle). Dashed lines represent observations, and solid lines denote the modeled.

Ultimate goals of this research are to provide a physically based and computationally simple parameterization of boundary-layer clouds to general circulation's models. The past year's efforts represent the first step toward that goal.

• • • • •

Global Mass Circulations Induced by Cloud-Radiative Forcing

William M. Lapenta/ES42
205-544-1667

The general circulation of the atmosphere is usually considered to consist of the totality of motions, which characterizes the global-scale atmospheric flow. In particular, the study of the general circulation is concerned with the temporally and/or spatially averaged structures of winds, temperatures, and other climatic elements. An atmospheric constituent vital to the dynamics of the Earth's general circulation is water, which exists in all three phases. Clouds in particular can significantly affect and modulate the dynamics of the general circulation through their interaction with incoming and outgoing radiation. The thrust of this research program centers upon understanding the radiative implications of clouds on the mass transport associated with the general circulation, which helps determine the character of climate on different time and space scales. The approach used carries an emphasis on merging remotely sensed data from space with conventional gridded analyses of atmospheric state variables (e.g., wind, temperature, and moisture) and a numerical radiation model.

Parameters not easily obtainable from direct satellite measurements of the atmosphere are the three-dimensional radiative heating/cooling profiles. Estimates of these profiles may be obtained from numerical models of the global climate system, which serve as research tools to understand interactions between various physical and dynamical processes. However, because of the crude radiation parameterizations in the numerical models, care must be taken when scientifically interpreting their results. Therefore, this research uses satellite-derived geophysical parameters in conjunction with a more detailed and accurate numerical radiation model to obtain dynamically and physically consistent radiative heating/cooling budgets of the global atmosphere.

Input to the radiation model includes humidity and temperature profiles from the European Center for Medium-range Weather Forecasting (ECMWF) analyses and surface temperatures from the International Satellite Cloud Climatology Project (ISCCP). Also used are moisture data from the Special Sensor Microwave/Imager (SSM/I) and temperature data from the microwave sounding unit (MSU). Sohn shows that global averages computed for the summer of 1988 and winter of 1988-89 for the model-derived, top-of-atmosphere, clear-sky fluxes from adjusted moisture and temperature profiles are in very good agreement with results from the Earth Radiation Budget Experiment (ERBE).[1]

Ongoing research involves the diagnosis of mass circulations induced by the model-derived, three-dimensional heating profiles. These circulations will then be compared with "total" atmospheric circulations forced by all physical processes in the Earth system, which will be diagnosed independently from European Center analyses. Intercomparisons of these circulations will help quantify the importance of clouds in forcing global-scale atmospheric motions responsible for climate variability.

[1] Sohn, B.J. 1994. ECMWF Clear-sky Longwave Flux Estimation Constrained by SSM/I Precipitable Water and MSU Brightness Temperature: The Impact of Uncertainties in ECMWF Analyses. Submitted to the *Journal of Applied Meteorology*.

Sponsor: Office of Mission to Planet Earth

• • • • •

Infrared Spectroscopy of the Earth's Upper Atmosphere and Planetary Atmospheres

Mian M. Abbas/ES42
205-544-7680

Most atmospheric constituents exhibit vibrational-rotational transitions in the infrared spectral region (10 to 400 cm^{-1}), which may be observed in emission or absorption with high-sensitivity and high-spectral-resolution spectrometers. The observed spectrum of the Earth's atmosphere, for example, includes spectral features of the trace gases O_3, CO_2, H_2O, HO_2, H_2O_2, OH, N_2O, NO. NO_2, HNO_3, N_2O_5, ClO, $ClONO_2$, HF, Freons, HCl, and HCN. An understanding of the photochemical and dynamical process involving these gases is necessary for resolving some basic atmospheric issues such as the questions relating to the depletion of stratospheric ozone. The infrared thermal emission spectra of the planetary atmospheres observed from ground-based as well as from space missions also show spectral features of most of their major and minor constituents. The spectrum of Saturn's atmosphere observed by *Voyager*, for example, shows the spectral features of its major constituent, H_2, as well as such trace gases as CH_4, NH_3, PH_3, C_2H_2, and C_2H_6. The observed spectrum of the atmosphere of Titan, Saturn's largest satellite, exhibits a broad, pressure-induced continuum absorption of its major constituent, N_2, as well as the spectral features of some complex hydrocarbons (C_2H_2, C_2H_4, C_2H_6, C_3H_4, etc.) and nitriles (HCN, HC_3N, C_2N_2, etc.). Comprehensive studies of the chemical composition and the thermal structure of planetary atmospheres is crucial to an understanding of the origin and evolution of atmospheres.

A detailed analysis of the observed infrared spectra provides a wealth of information about the physical and chemical processes in atmospheres. A primary requirement for interpretation of the observed data is the availability of radiative transfer models capable of calculating the observed radiation for realistic atmospheric and observational conditions and analytical inversion programs for retrieval of vertical temperature and gas concentration profiles. This research program at MSFC focuses on the development and applications of infrared radiative transfer models and inversion methods for interpretation of data obtained from various NASA missions for studies of the physics and chemistry of Earth and other planets' atmospheres.

The inversion programs for retrieval of pressure-temperature (P-T) profiles from infrared solar absorption spectra obtained from orbiting space shuttle platforms have been developed and tested for synthetic data. These programs are currently being evaluated for retrieval of pressure-temperature profiles from observations made by the Atmospheric Trace Molecules Observed by Spectroscopy (ATMOS) experiment on the Atmospheric Laboratory for Applications and Science (ATLAS 1-2) shuttle missions carried out in 1992 and 1993. Infrared radiative transfer models and rapid inversion techniques are also being developed for interpretation of observations to be made with the composite infrared spectrometer (CIRS) from the Cassini Orbiter to be launched for studies of Saturn and its satellites. Preliminary studies for an analysis of the expected data from observations of Saturn and Titan are being carried out at the present time.

The infrared radiative transfer models for planetary atmospheres are also being employed in a program focusing on the development of photometric standards for observations of astronomical sources from the Infrared Space Observatory (ISO). An observational program—employing the Kuiper Airborne Observatory (KAO) for photometric flux measurements of the planets Uranus, Neptune, Mars, and the asteroids Ceres and Pallas— has been in progress for the last 2 years (principal investigator, Charles Telesco, ES84). Comparisons of model flux calculations with the observations are carried out to improve the models and develop photometric standards for inflight astronomical observations.

Sponsor: Office of Space Science

• • • • •

Diagnostics of the Global Hydrologic Cycle

Franklin R. Robertson/ES42
205-544-1655

Virtually all of the interesting processes that distinguish the Earth's climate from that of our planetary neighbors can be traced to the prominent role that moisture plays in the Earth's heat and water balance. Water, and its mobility through the oceans and the atmosphere, ensures a complex energy cycle for the planet. In gaseous form, water provides for absorption and downward reradiation of terrestrial radiation—the greenhouse effect. In liquid or solid form, water acts to provide a slight net-cooling to the Earth-atmosphere system, though not in a straightforward manner. Clouds have been found to actually provide a net-heating effect to the atmosphere, again by absorbing and reradiating downward radiation upwelling from the surface. However, cloud shading acts to reduce insolation and cool the Earth's surface. Latent heat release associated with rainfall production also acts as a heat source to the atmosphere. Collectively, these moist processes provide a thermodynamic forcing to global temperature characterized by several offsetting or counteracting effects. As a result, climate forcing and the response of the planetary wind field have much variability associated with them.

The Earth Systems Dynamics Group at MSFC has been involved for several years in using an array of data sets to quantify net cloud and water vapor impacts on atmospheric heating distributions and the perturbation response of global and regional wind

fields. One aspect of these studies has been to develop a diagnostic model to provide a unified description of vapor and condensate distributions and their relationship to large-scale vertical motion fields. Researchers have combined column-integrated, atmospheric water vapor from the spaceborne Special Sensor Microwave/Imager (SSM/I) with kinematic constraints from global-gridded analyses (e.g., those produced by the European Center for Medium-range Weather Forecasting (ECMWF)) as a means of reconstituting vapor, cloud, and precipitation in three dimensions and in time. This basic formalism is what is termed as a "semiprognostic assimilation procedure" since the methodology predicts only the evolution of the

moisture fields. Horizontal wind fields and vertical motions from the European Center's gridded analyses have been used to drive conservation equations for vapor, liquid, and ice. These equations, which also use bulk parameterizations of cloud microphysics (e.g., condensation, autoconversion, collection, precipitation evaporation, and fallout), are updated or constrained in such a way that where Special Sensor Microwave/Imager observations are available in space and time, the evolving model vapor is "nudged" to those values. Recently, this methodology has been used to diagnose the cloudiness over the Western Pacific for the Tropical Oceans Global Atmosphere Coupled Ocean Atmosphere Response
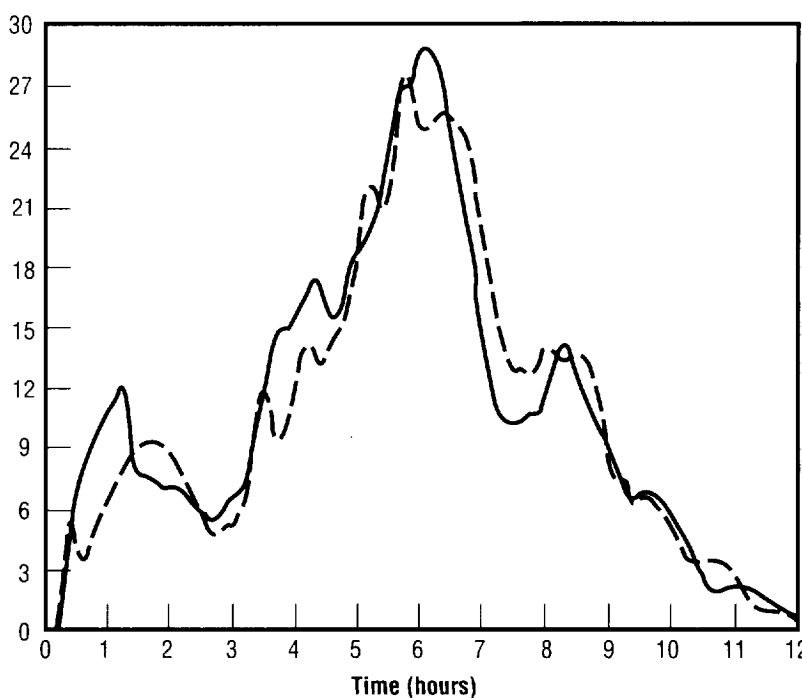

FIGURE 26.—Precipitating cloud ice, 10^4 kg m^{-1} (dashed line), and cloud net upward vertical motion, 10^7 kg s^{-1} (solid line), from cloud model simulation.

Experiment (TOGA COARE) held during 1993. The cloud, precipitation, and vapor analysis produced by researchers' methodology will be used to study how atmospheric convection interacts with warm sea-surface anomalies to anchor widespread, deep convection to this region of the tropics.

To achieve an independent estimate of the strength of the thunderstorm complexes, investigators have been analyzing the degree to which ice, snow, and other frozen condensates observed by the microwave/imager can be related to the vertical mass fluxes above the atmospheric freezing level—typically about 6 kilometers high. Using a numerical cloud model, scientists have examined budgets of ice production and the "memory" of the cloud vertical motion profile that is implicit in the ice. There is a definite relationship between a trace over 12 hours time of a simulated convective complex and the tendency for the ice present within the cloud to scale with, or track, the mean strength of vertical motion above the freezing level (fig. 26). This relationship will enable calibration of global maps of Special Sensor Microwave/Imager brightness temperatures in terms of mesoscale convective updraft strength. In turn, the vertical motion analyses from the European Center for Medium-range Weather Forecasting that scientists have used in diagnosing the cloud, rain, and water-vapor fields can be critiqued for their accuracy and representativeness.

Sponsor: Office of Mission to Planet Earth

. . . . .

Multicenter Airborne Coherent Atmospheric Wind Sensor

Jeffry Rothermel/ES43
205-544-1685

In spring 1995, the Multicenter Airborne Coherent Atmospheric Wind Sensor (MACAWS) will be put into operation for the first time. The instrument is an airborne-scanning, pulsed carbon dioxide (CO_2), Doppler lidar capable of multidimensional wind and calibrated aerosol backscatter measurement from the NASA DCC-8 research aircraft.

Since spring 1992, the sensor has been under joint development by the lidar remote sensing groups of MSFC, the National Oceanic and Atmospheric Administration (NOAA) Wave Propagation Laboratory, and the Jet Propulsion Laboratory. MSFC has lead responsibility for overall coordination, science definition, and mission planning. To minimize costs, each organization is sharing major hardware components and subsystems which, in nearly all instances, have been used in previous round-based or airborne applications.

The principal of operation is similar to that successfully employed by MSFC in previous airborne lidar experiments. A pulsed lidar beam is generated and precisely directed anywhere within a 60° solid angle using a scanning device mounted on the interior left side of the aircraft. The backscattered, Doppler-shifted radiation is measured to infer the line-of-sight wind velocity, assuming the aerosol scattering particles act as passive wind tracers. By scanning the lidar beam slightly forward and aft (coplanar scanning), a field of two-dimensional, ground-relative wind estimates is obtained
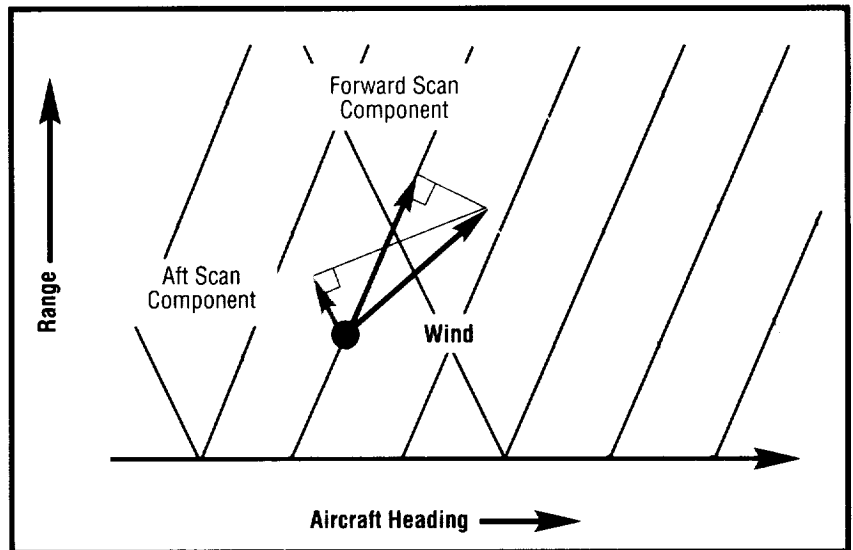

FIGURE 27.—Coplanar scanning method used to derive two-dimensional wind measurements using line-of-sight velocity.

within the scan plane (fig. 27). Multiple scan planes, revealing the three-dimensional structure of the velocity and aerosol backscatter, are obtained by appropriately varying the scanner settings during flight (fig. 28).

Following aircraft integration and check flights, the wind sensor will make an initial series of flights over the Eastern Pacific and Western U.S. using NASA Ames Research Center as a base of operations. The first objective is to improve understanding of atmospheric dynamic processes over critical scales of motion within the boundary layer and free troposphere, which are not routinely accessible with existing instrumentation. The goal is to apply these measurements toward improving parameterization schemes for subgrid scale processes represented within climate and general circulation numerical models. At the same time, observations will contribute toward improved understanding of specific mesoscale, or subgrid scale, processes and features such as marine and continental boundary-layer exchange, flow over complex terrain, and organized large eddies such as mesoscale cellular convection.

The second research objective is to investigate issues related to the performance of proposed, small-satellite Doppler lidar for measuring global tropospheric wind fields. Observations in this regard relate to design and performance simulation studies already underway at MSFC and affiliated organizations. The wind sensor will be used to duplicate the perspective from space, thereby providing unique information not present in ground-based lidar observations. For example, satellite
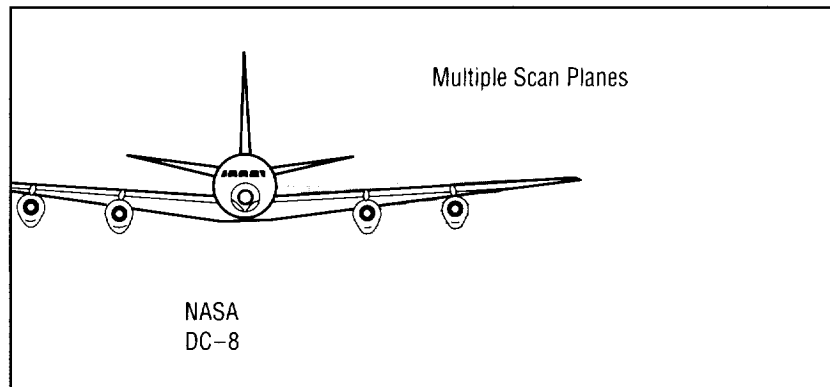
FIGURE 28.—Method for achieving three-dimensional coverage of wind measurements by generating multiple scan planes.

Doppler lidar data will contain a surface return signal applicable to calibration, atmospheric extinction estimation, and "ground-truth" velocity estimates. This information can be used to minimize velocity biases. Airborne studies will also provide guidance for improving signal processing algorithms. Other satellite Doppler lidar performance issues that will be addressed include impact of spatial variability on velocity and backscatter sampling, detailed cloud properties, Doppler estimation near aerosol gradients, and long-term monitoring of natural surfaces that may serve as potential calibration targets for backscatter estimation, as well as for monitoring instrument health. The Multicenter Airborne Coherent Atmospheric Wind Sensor may also serve to validate postlaunch performance of satellite Doppler wind lidar as well. Participation is planned in multiagency field programs addressing the understanding of the global energy and water cycle. Additional flights will be made to validate satellite sensors planned for operation in 1996 and beyond.

Rothermel, J.; Hardesty, R.M.; and Menzies, R.T. January 15–20, 1995. Characterizing Subgrid Scale Processes and Assessing Satellite Doppler Wind Lidar With MACAWS. Submitted to Sixth Symposium on Global Change Studies, Dallas, Texas.

Rothermel, J.; Hardesty, R.M.; and Menzies, R.T. March 8–12, 1993. Multicenter Airborne Coherent Atmospheric Wind Sensor. Preprints, Topical Meeting on Optical Remote Sensing of the Atmosphere, Salt Lake City, Utah.

Sponsor: Office of Mission to Planet Earth

• • • • •

45

Aircraft Investigations of Lightning and Thunderstorms

Richard J. Blakeslee/ES43
205–544–1652

In recent years, observations from the NASA ER–2 and DC–8 aircraft have been used to investigate relationships between lightning and storm electrification and a number of underlying and interrelated phenomena including the structure, dynamics, and evolution of thunderstorms and thunderstorm systems, precipitation distribution and amounts, atmospheric chemistry processes, and the global electric circuit. This research is motivated by the desire to develop an understanding needed for the effective utilization and interpretation of data from new-generation, satellite-based lightning detectors. These will include the MSFC-developed Optical Transient Detector (OTD) scheduled for launch in late 1994 followed by the Lightning Imaging Sensor (LIS) in 1997.

There is a particular emphasis in this program to "quantify" the lightning relationships that have been suggested by earlier observations. It is hoped that as a result of these kinds of investigations, lightning data alone and/or in conjunction with other remote sensing techniques will provide quantitative information about such storm characteristics as the occurrence and location of embedded convection, the strengths of updrafts and downdrafts, thermodynamic and electrical energy budgets, precipitation amounts and distributions, and atmospheric chemistry processes.

Lightning rates, distribution, and characteristics (i.e., number of strokes per flash, ratio of intracloud to cloud-to-ground lightning, discharge energy, etc.) are all factors that may prove useful in devising quantitative algorithms.

Lightning instruments have been integrated into the NASA ER–2 and DC–8 aircraft. This lightning instrumentation detects total storm lightning and differentiates between intracloud and cloud-to-ground discharges. The lightning instruments are also flown with other sensor systems (e.g., infrared, passive microwave, Doppler radar, etc.) to provide new understandings of thunderstorms and precipitation and support detailed satellite simulations of storm measurements through the acquisition and analysis of multiparameter data sets. By developing and maintaining the capability to monitor lightning and thunderstorms with these aircraft, NASA will also be able to provide important ground-truth verifications and calibrations when the Optical Transient Detector, Lightning Imaging Sensor, and other lightning detectors begin operation.

In January and February 1993, science flights were conducted during the international Tropical Ocean Global Atmosphere Coupled Ocean Atmosphere Response Experiment (TOGA COARE) to investigate electrical processes of tropical maritime convection and support multisensor precipitation algorithm development. The initial analysis of the data identified 117 overflights of electrified storms during 11 missions. Lightning was observed in only 23 of the storm overpasses (i.e., 19 percent).

Generally, the storms overflown showed weak electrical development, with the more intense storms having flash rates of only 1 to 2 discharges per minute. Whenever electric fields were observed, depressed brightness temperatures in the 85-gigahertz (GHz) channel of the Advanced Microwave Precipitation Radiometer (AMPR) indicated the presence of ice particles in the storm. However, small brightness temperature depressions in the 37-gigahertz channel are consistent with the weak electric fields and low lightning rates observed.

Sponsor: Office of Mission to Planet Earth

The Advanced Microwave Precipitation Radiometer

Robbie E. Hood/ES43
205–544–5407

The Advanced Microwave Precipitation Radiometer (AMPR) and its accompanying data acquisition system fly aboard a NASA ER–2 high-altitude aircraft to collect passive microwave upwelling emissions from the Earth's surface and atmosphere. The instrument is a cross-track scanning, total-power radiometer with four channels centered at 10.7, 19.35, 37.1, and 85.5 gigahertz (GHz). These frequencies are well-suited to the study of rain cloud systems, but are also useful for studies of various ocean and land surface processes. Advanced Microwave Precipitation Radiometer information may also be used for satellite simulations of the current Defense Meteorological Satellite Program Special Sensor Microwave/Imager (DMSP SSM/I), the Tropical Rainfall Measuring Mission (TRMM) Microwave Imager (TMI) scheduled for launch in 1997, and the Multifrequency Imaging Microwave Radiometer (MIMR) planned to fly aboard the Earth Observation System (EOS) PM–1 platform.

The Advanced Microwave Precipitation Radiometer was deployed during January and February 1993 as part of the Tropical Ocean Global Atmosphere Coupled Ocean Atmosphere Response Experiment (TOGA COARE) conducted in the western Pacific Ocean. The radiometer was also deployed during September 1993 to study precipitation over the Atlantic Ocean as part of the Convection and Moisture Experiment (CAMEX), which was based in Wallops Island, Virginia. Data collected during these two field missions have been quality-controlled and documented. Information from both experiments will be archived on the NASA/MSFC Distributed Active Archive Center (DAAC), while the Tropical Ocean Global Atmosphere Coupled Ocean Atmosphere Response Experiment data sets will also be archived on the NASA/Goddard Space Flight Center (GSFC) Distributed Active Archive Center.

The passive microwave information collected by the Advanced Microwave Precipitation Radiometer offers a rich and varied data set useful to the general scientific community for satellite simulation studies of rainfall. The high spatial resolution of the radiometer imagery provides new insight into the vertical hydrometeor profile of rain systems, which has not been previously obtained by satellite observations with coarser spatial resolutions. Examples of 19.35-gigahertz signal saturation for rain rates greater than 15 millimeters per hour are commonly observed in the Advanced Microwave Precipitation Radiometer observations. These saturation effects are never observed in corresponding satellite data due to the averaging of rain and non-rain scenes inherent in larger satellite footprints. Satellite rain retrievals may tend to underestimate rain rates due to this footprint averaging effect. However, preliminary analysis of Advanced Microwave Precipitation Radiometer data suggest the utility of the 10.7-gigahertz frequency to compensate for the 19.35-gigahertz saturation effects, since 10.7-gigahertz observations do not saturate as readily and can provide rainfall information at lower altitudes in the rain system.

Smith, E.A.; Xiang, X.; Mugnai, A.; Hood, R.E.; and Spencer, R.W. 1994. Behavior of an Inversion-Based Precipitation Retrieval Algorithm With High-Resolution AMPR Measurements Including a Low-Frequency, 10.7-GHz Channel. *Journal of Atmospheric and Oceanic Technology* 2:4:858–73.

Spencer, R.W.; Hood, R.E.; LaFontaine, F.J.; and Smith, E.A. 1994. High-Resolution Imaging of Rain Systems With the Advanced Microwave Precipitation Radiometer. *Journal of Atmospheric and Oceanic Technology* 2:4:849–57.

Sponsor: Office of Mission to Planet Earth

Hydrologic Studies Using Geostationary Operational Environmental Satellite 8

Gary J. Jedlovec/ES43
205-544-5695

Ronnie J. Suggs/ES43
205-544-7797

The Geostationary Operational Environmental Satellite (GOES) 8, launched April 13, 1994, is the first in a new series of operational geostationary satellites to provide continuous spatial and temporal multispectral observations of the Earth's system for the purpose of weather forecasting and global change research. This new series will provide improved observation capabilities, especially for moisture sensing, over the Visible Infrared Spin-Scan Radiometer (VISSR) Atmospheric Sounder (VAS) on the Geostationary Operational Environmental Satellite 7. Also, the new series will be the only new U.S. geostationary platform used for global change for the next 10 to 15 years.

The purpose of this current research effort at MSFC is to develop and evaluate the utility of the Geostationary Operational Environmental Satellite 8 products for hydrologic studies aimed at improving knowledge of the role of water vapor and its variability in global meteorology, as well as hydrological and climatological processes. These studies include the NASA research initiative Global Energy and Water Cycle Experiment (GEWEX) Water Vapor Project (GVaP) and the GEWEX Continental International Project (GCIP), which is a major experiment to understand the hydrological cycle over the continental United States.

In order to develop and evaluate the utility of Geostationary Operational Environmental Satellite 8 products for hydrological studies, four major research objectives have been established: (1) understanding features in water vapor imagery and their relationship to horizontal and vertical humidity distributions and various kinematic and dynamical processes; (2) quantifying the accuracy, representativeness, and informational content of imagery and derived products, including various measures of water vapor content and water vapor tracked winds; (3) developing new procedures for examining atmospheric water vapor that take advantage of the enhanced capabilities over those now available; and (4) as a result of the above, further the goal of improving understanding of the importance of atmospheric water vapor in the hydrologic cycle.

Over the past year, previous to the launch of Geostationary Operational Environment Satellite 8, MSFC research focused on total integrated water content (IWC) retrieval algorithm refinements and retrieval performance with simulated imager and sounder data. Most significant is the improvement in quality of integrated water content retrievals seen in the simulated results stemming from high radiometric quality and increased resolution over that of Geostationary Operational Environment Satellite 7. Specifically, the findings for simulated Satellite 8 imager and sounder data based on prelaunch noise estimates indicated that retrieved values of integrated water content should be significantly more accurate. Also, an increase in the spatial density of the integrated water content should result from a tradeoff between resolution and accuracy (i.e., finer spacing should be possible with integrated water content retrievals). For noise-free data simulated from a regional case study investigation, results showed that, for the daytime retrievals, the imager split-window channels perform as well as those of the sounder, and both perform as well or better than Satellite 7. At night, results illustrated that the accuracy of integrated water content retrievals with the sounder were significantly better than those from the imager.

Post-launch research currently underway is focusing on verifying the results obtained from simulated data with that obtained from actual observed data. Special data sets will be acquired through cooperation with the National Oceanic and Atmospheric Administration (NOAA)/National Environmental Satellite Data Information Service (NESDIS) in order to obtain specific data for case study investigations. The investigation will also focus on the optimal channel combinations from the imager and sounder for the retrieval of integrated water content. With the availability of actual Geostationary Operational Environmental Satellite 8 data, improvements in water vapor wind calculations will also be addressed as a result of the new capabilities.

Jedlovec, G.J., and Carlson, G.S. 1994. Guess Dependence of the Physical Split-Window Technique for the Retrieval of Integrated Water

Content. *Preprints, Seventh Conference of Satellite Meteorology and Oceanography.* Monterey, American Meteorology Society. In press.

Jedlovec, G.J.; Guillory, A.R.; and Carlson, G.S. 1994. The Retrieval of Integrated Water Content From GOES I. *Preprints, Seventh Conference of Satellite Meteorology and Oceanography.* Monterey, American Meteorology Society. In press.

Sponsor: Office of Mission to Planet Earth

University Involvement: Florida State University

• • • • •

Global Aerosol Backscatter Experiment

Maurice A. Jarzembski/ES43
205–544–0240

An atmospheric, global-scale aerosol backscatter model is being developed under NASA's GLObal Backscatter Experiment (GLOBE). The purpose of this model is to provide information for assessing the performance of any space-based lidar that will be designed at a given wavelength to measure tropospheric winds. In cloud-free conditions, the accuracy of wind measurements depends on the magnitude of backscattered signals from atmospheric aerosols. This model will be versatile enough that for many atmospheric conditions, with use of appropriate conversion functions, it will be possible to predict the magnitude of aerosol backscatter coefficients at several different wavelengths, depending on the choice of the space-based lidar. Various universities, other NASA centers, and U.S. government and international agencies have participated and provided data under the program, with scientific direction provided by MSFC.

Intensive characterization of the MSFC continuous-wave (CW) Doppler lidars has been performed in the Aerosol Optical Properties Laboratory (AOPL), greatly improving data quality and sensitivity. The continuous-wave lidar data sets are extremely important as they provide direct validation of any ` wavelength-dependent backscatter modeling using in-situ aerosol

microphysics measurements. Good agreement was obtained between the aerosol microphysics data and the continuous-wave lidar data sets at flight level. An example time-series comparison of measured MSFC continuous-wave lidar data and modeled aerosol backscatter coefficients from the GLObal Backscatter Experiment II Hawaii-to-American-Samoa transit flight on May 20, 1990, is shown in figure 29.

Modeled values were calculated at the 9.1-micrometer (μm) wavelength from Mie theory, using flight-level aerosol size distribution measurements from the University of Hawaii's Laser Optical Particle Counter (LOLC) and from NASA/Ames Research Center's Forward-Scattering Spectrometer Probe (FSSP); aerosol refractive index estimates were obtained from the Laser Optical Particle Counter data. Pulsed lidar data sets close to the aircraft (averaging 1 to 2 kilometers above and below the aircraft) showed fair agreement with modeled backscatter from the microphysics data when the aerosol loading in the atmosphere was fairly homogeneous near the aircraft level (fig. 30). The horizontal dashed line in figures 29 and 30 represents the lidar sensitivity level. Various flight case studies showed similar backscatter variations in all data sets corresponding to seasonal- and synoptic-scale meteorological features in the middle and upper troposphere. Clean tropical and subtropical conditions with generally low humidity and predominantly small-sized, freshly produced sulfuric acid aerosols gave low backscatter, while the quite humid InterTropical Convergence Zone (ITCZ) gave high and variable backscatter characteristic of the
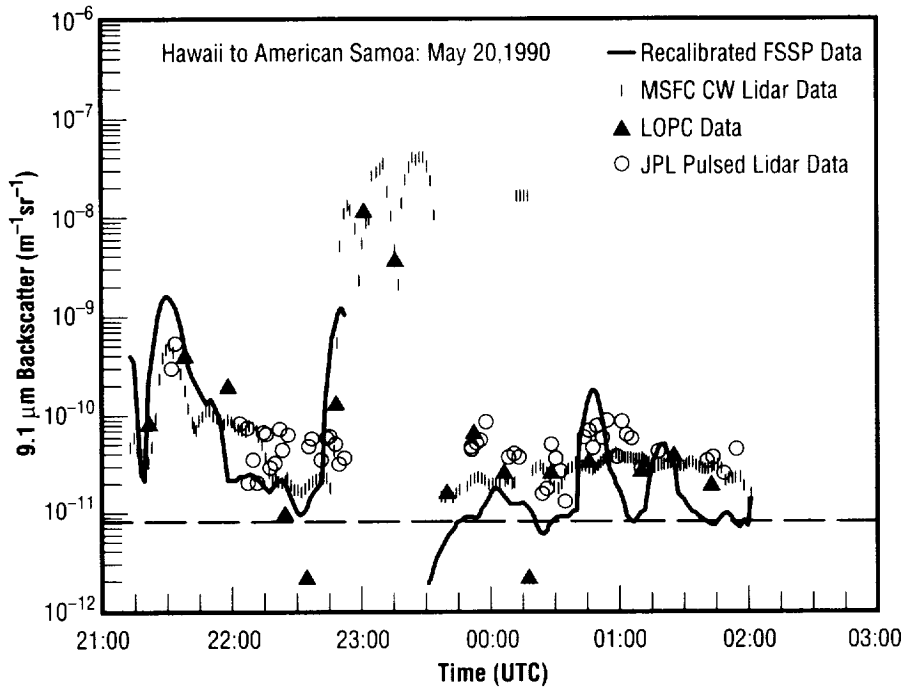
FIGURE 29.—GLObal Backscatter Experiment II (Flight 6), 9.1-micrometer backscatter.
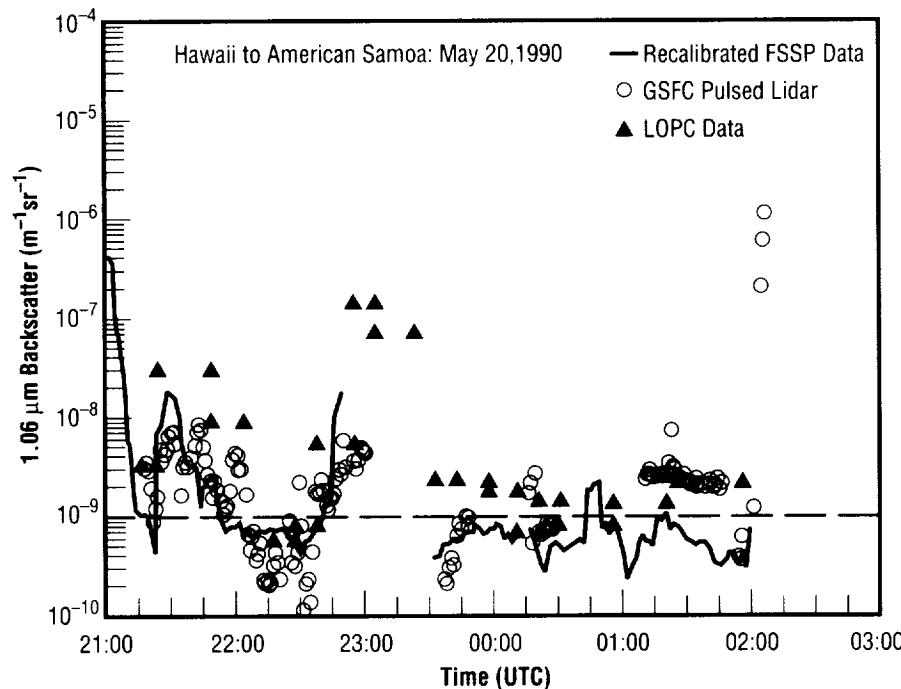
FIGURE 30.—GLObal Backscatter Experiment II (Flight 6), 1.06-micrometer backscatter.

convective activity associated with that zone. Moderately high to very high backscatter was observed in the planetary boundary layer (PBL) and in air masses with continental-type aerosols such as dust plumes or haze layers. Compositional changes in the aerosol measured by the Laser Optical Particle Counter were modeled in different mixture models to study their effect on aerosol backscatter at various wavelengths. Lognormal size distributions with comparable input parameters were used to model aerosol microphysics to predict the wavelength dependence of backscatter. Conversion functions were derived using both measured and modeled microphysics to convert backscatter measured at certain wavelengths during GLObal Backscatter Experiment II to other wavelengths where no measurements are yet available.

A preliminary global-scale model for aerosol backscatter at 9.1 and 2.1 micrometers has been developed and used for performance studies for the prospective space-based lidar. Many first drafts of papers covering the results obtained have already been written, and future plans are to concentrate on finishing these papers.

Sponsor: Office of Mission to Planet Earth

University Involvement: Institute for Global Change Research and Education

• • • • •

Regional-Scale Atmospheric Moisture Variability

Anthony R. Guillory/ES43
205–544–6462

Atmospheric water vapor plays the principal role in interconnecting various aspects of the hydrologic cycle. As a part of the Global Energy and Water Cycle Experiment (GEWEX), NASA has proposed a new research initiative called the GVaP, or GEWEX Water Vapor Project. The overall goal of the project is to improve understanding of the role of water vapor in meteorological, hydrological, and climatological processes through improved knowledge of water vapor and its variability on all scales. A better understanding of its role will require long-term observations of both small- and large-scale water vapor features, a major goal of NASA's Mission to Planet Earth (MTPE) program.

Defining moisture variability on varying scales (temporal and spatial) is beneficial to several disciplines. Detailed water vapor observations are essential to improved analysis and prediction of convective storms. For example, thunderstorms have been observed to develop in regions of rapidly evolving moisture gradients. Vertically integrated moisture (or integrated water content (IWC), also called precipitable water) is another essential in the objective prediction of clouds and precipitation. High-resolution moisture data are also needed in studies of atmospheric radiation and electromagnetic wave propagation, but such data are not available from conventional sources.

Remote sensing of the atmosphere from satellites has the potential to fill this data void. Geostationary satellites, in particular, provide excellent temporal and spatial resolution. Research being undertaken at MSFC focuses on using data from the National Oceanic and Atmospheric Administration's (NOAA) Geosynchronous Operational Environmental Satellites (GOES) in the physical split-window (PSW) algorithm, which is a physically based, split-window integrated water content technique.

Split-window techniques attempt to exploit differential absorption of water vapor in two adjacent spectral bands to produce an integrated water content estimate. One such technique requires infrared data at 11 and 12 micrometers. The 11-micrometer channel lies in a relatively transparent part of the spectrum; therefore, most of its observed emission is from the surface. The 12-micrometer channel is in a spectral region where upwelling radiance from the surface is primarily subject to absorption and emission by water vapor, but it also includes other constituents (e.g., carbon dioxide (CO_2)). Thus, by comparing spectral emissions of one location in both channels, estimates of the integrated water content at that location can be made.

High-resolution temporal and spatial data sets from the Geosynchronous Operational Environmental Satellites will be used to quantify the observed water vapor variability over the continental United States for a period of several months. The MSFC goals are to: (1) quantify the magnitude of moisture variability and define achievable accuracy of water content from satellite platforms; (2) investigate the temporal and spatial moisture variability on continental and finer scales to explore interconnections between scales of variability, clouds, and other atmospheric features; and (3) show the importance of local sources of moisture and their impact on regional hydrologic processes.

Guillory, A.R.; Jedlovec, G.J.; and Fuelberg, H.E. 1993. A Technique for Deriving Column-Integrated Water Content Using VAS Split-Window Data. *Journal of Applied Meteorology* 32:1226–41.

Star, D.O'C. and Melfi, S.H. (eds.). 1991. The Role of Water Vapor in Climate. A Strategic Research Plan for the Proposed Global Energy and Water Cycle Experiment (GEWEX) Water Vapor Project (GVaP).

• • • • •

Cloud Morphology as Inferred From Polarimetric Radar, Passive Microwave, and Lightning Observations

Steven J. Goodman/ES44
205-544-1683

An understanding of the relationships among the processes that lead to the electrification of clouds and the subsequent production of lightning is necessary in order to better interpret global cloud measurements from such future space missions as the Tropical Rainfall Measuring Mission (TRMM), scheduled for launch in 1997. As yet, few detailed case studies have examined the morphology of the coevolving microphysical, electrical, and kinematic properties of clouds. In this work, researchers extend the data base of multisensor observations using case studies obtained from the Convection and Precipitation/ Electrification (CaPE) experiment conducted in the vicinity of Cape Canaveral, Florida, in 1991.

This experiment presented an opportunity to acquire surrogate Tropical Rainfall Measuring Mission measurements using ground-based sensors, satellites, and instrumented airplanes. The remote sensor suite (rain radar, passive microwave radiometer, visible/infrared imager, and lightning optical detector) can be approximated by the following surrogate multisensor measurements: the National Center for Atmospheric

Research (NCAR) CP2 dual-frequency polarimetric radar; ground-based lightning and electric field networks; the NASA ER2 airplane instrumented with an Advanced Microwave Precipitation Radiometer (AMPR), multispectral imager, and lightning/field-mill sensors; and geostationary and polar-orbiting imagers and radiometers (Defense Meteorological Satellite Program Special Sensor Microwave/Imager (SSM/I) radiometer). The Advanced Microwave Precipitation Radiometer is a four-frequency (10.7-, 19.35-, 37.1-, and 85.5-gigahertz (GHz)) radiometer with frequencies similar to the Special Sensor Microwave/Imager passive microwave sensor and the Tropical Rainfall Measuring Mission microwave imager. The lightning/field-mill instruments provide a measure of intracloud and cloud-to-ground lightning activity that would be observed by the Lightning Imaging Sensor (LIS) being provided by MSFC. Of particular interest is the

relationship between the development of the mixed-phase region of the cloud and its correlation with changes of passive microwave brightness temperatures (at 37 and 85 gigahertz) and lightning flash rates. In this initial study, the lightning, radiometer, and radar data are used to examine the morphology of a multicellular storm observed northwest of Cape Canaveral on August 12, 1991. Three ER2 overflights of the storm were made at 22:09, 22:18, and 22:27 universal time coordinated (UTC) during the mature and redevelopment phase of the thunderstorm complex. Five CP2 volume scans of this storm were collected during a 22-minute period at 22:05, 22:09, 22:13, 22:18, and 22:27 universal time coordinated.

This study shows (fig. 31) the evolution of the cloud-to-ground lightning activity (KSC CG) as detected from the Kennedy Space Center ground strike network from 22:05 to 22:31 universal time
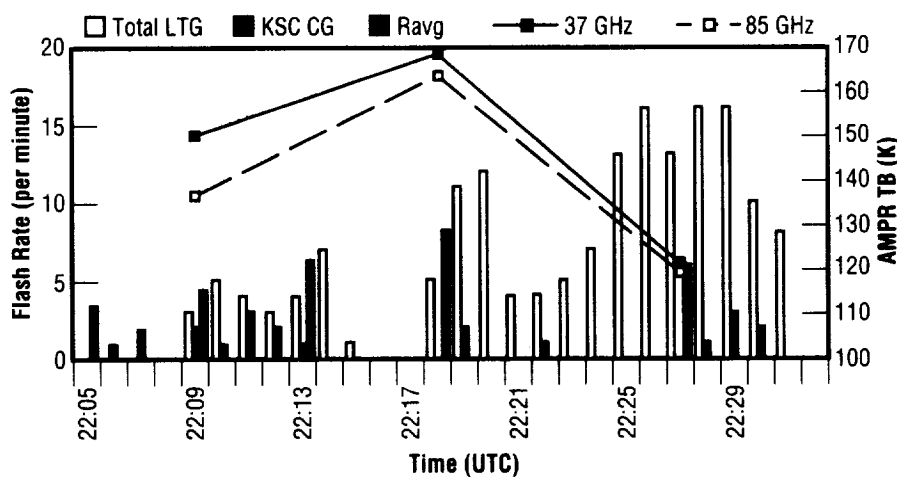

FIGURE 31.—Time series of lightning (flashes per minute), rain rate (mm h⁻¹), and microwave brightness temperatures at 37 and 85.5 gigahertz.

coordinated, storm average radar-derived rain rate (Z = 300 R$^{1.6}$) for each of the five scans (Ravg); the total lightning (in-cloud and ground discharges) detected after 22:09 from the ER2 field-mill sensors (total LTG); and minimum Advanced Microwave Precipitation Radiometer brightness temperatures (TB in Kelvin (K)), at 37 and 85 gigahertz during the three successive ER2 overpasses of the storm complex. The intracloud-to-ground-strike ratio is approximately 7:1, on average, for the 22-minute time series. However, no ground strikes are observed at all during the onset of the final surge in lightning activity from 22:23 to 22:28, which is associated with a large decrease in the minimum TB's.

The first surge in lightning rates accompanies an already-mature cell. The subsequent decrease of lightning activity and increasing (warming) TB's are both qualitatively consistent indications of a weakening storm. The peaks of the weighting functions at 37 and 85 gigahertz occur within and near the top of the mixed-phase region, approximately at 7- to 10- and 10- to 12-kilometer height intervals. The strong, nearly equal brightness depression during the third overpass in both the 37- and 85-gigahertz frequencies indicates the likely presence of both a larger ice volume and large hail.

This relationship is further illustrated (fig. 32) by an air-mass storm observed near Huntsville, Alabama, in 1986 with the National Center for Atmospheric Research CP2 radar. This storm produced 110 in-cloud flashes and only six ground discharges. Note that the total lightning rates are in

phase with the vertical development of the radar echo and, hence, the minimum brightness temperatures at 37 and 85 gigahertz (which are strongly depressed by the presence of precipitation-sized ice and graupel/hail particles). The peak rain rate follows the collapse of the storm, indicated by decreasing flash rates, warmer brightness temperatures, and the arrival of small hail at the ground. Thus, the ice playing an important role in the charging of the cloud is also responsible for scattering at these microwave frequencies.

This study represents the first in a series of studies planned to investigate

the relationships among lightning activity, microwave brightness temperatures, and storm structure and morphology. The total lightning activity and microwave brightness temperatures both show dependence on the development of the mixed-phase region. The increase of total flash rates with storm mass above the freezing level supports the earlier studies of storms in Alabama, Florida, New Mexico, and elsewhere. These continental storm observations suggest that brightness temperature and lightning flash-rate variations are indicators of the path-integrated ice scattering that is dominated by the changes in ice volume (integrated
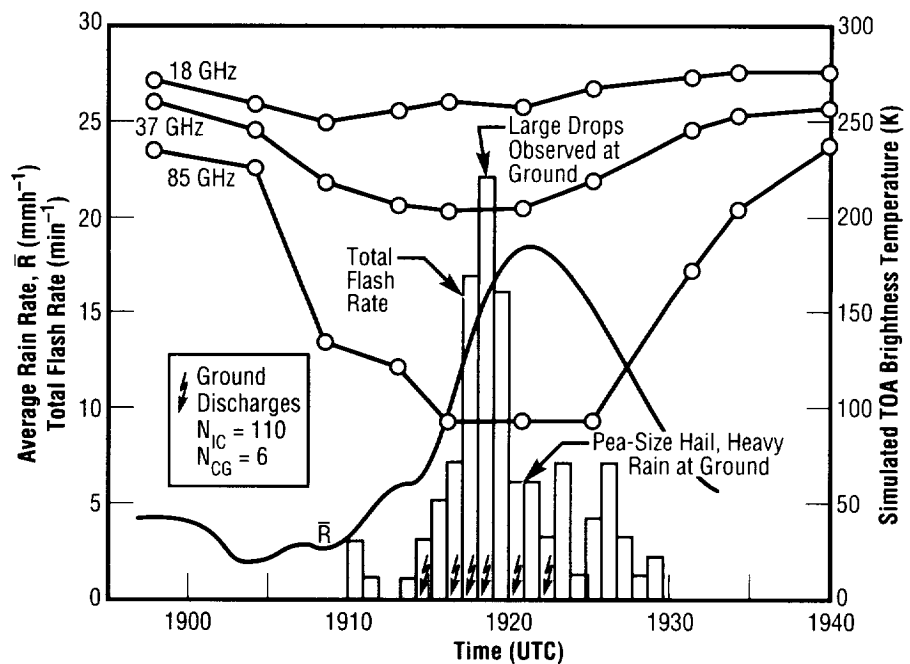

FIGURE 32.—Total lightning, radar-derived storm average rainfall, and simulated top-of-atmosphere (TOA) brightness temperature time history of the July 20, 1986, Cooperative Huntsville Meteorological Experiment (COHMEX) storm.

mass flux) and/or hail size within the mixed-phase region. Future studies in the tropics are planned for November to December 1995.

Goodman, S.J., and Raghavan, R. May 24–28, 1993. Investigating the Relationships Between Precipitation and Lightning Using Polarimetric Radar Observations. *Preprints, 26th Conference on Radar Meteorology,* Norman, Oklahoma. American Meteorology Society, Boston, Massachusetts, 793–95.

Sponsor: Office of Mission to Planet Earth

University Involvement: Institute for Global Change Research and Education

• • • • •

Mesoscale Study of Surface Heat Fluxes and Boundary-Layer Processes in a Desert Region

Dale A. Quattrochi/ES44
205–544–8104

A critical factor in understanding the response of natural arid ecosystems to global climate change is the relationship between soil moisture availability, surface energy partitioning, and plant growth. This particular project is designed to improve scientific understanding of energy and water-cycling (hydrometeorology) in natural arid ecosystems. Little information is available on continuous evapotranspiration by such naturally occurring arid vegetation as cheatgrass, greasewood, or sagebrush.

Desert vegetation has evolved by noticeably different methods of conserving water than those used by more commonly studied agricultural crops. The processes employed vary with the severity of drought stress placed on vegetation. Hence, arid landscapes are fundamentally different from agricultural and forest ecosystems in the processes that govern the energy and water balance of the surface. This investigation seeks to elucidate and quantify the processes that control surface evaporation and the partitioning available energy in an arid landscape.

Within this purview, the objectives for this research are fourfold:

• To improve scientific understanding of the processes and states that govern the local energy and water fluxes in a Great Basin ecosystem within the Western United States;

• To test and validate the tools necessary to scale local energy and water balance measurements made at intensive study sites to provide regional (i.e., valley-wide) estimates of fluxes and energy exchanges;

• To develop the relationships between soil, location, and seasonal variations in soil moisture and salinity required to support measurement and analysis of energy and water-cycling processes;

• To develop and validate the necessary remote sensing data analysis algorithms to permit observation and measurement of energy processes within desert ecosystems from the plant (i.e., leaf) to regional scales.

The study site for the project (ongoing since mid-1992) is a high-elevation desert valley, the Steptoe or Goshute Valley, located approximately 40 kilometers west of Wendover, Nevada, near the Nevada-Utah state line. The valley is about 50 kilometers long and 35 kilometers wide and is surrounded by mountains with elevations reaching greater than 2,700 meters. Vegetation in the valley is representative of that which exists throughout similar valleys in the Basin and Range region of the Western United States, consisting primarily of
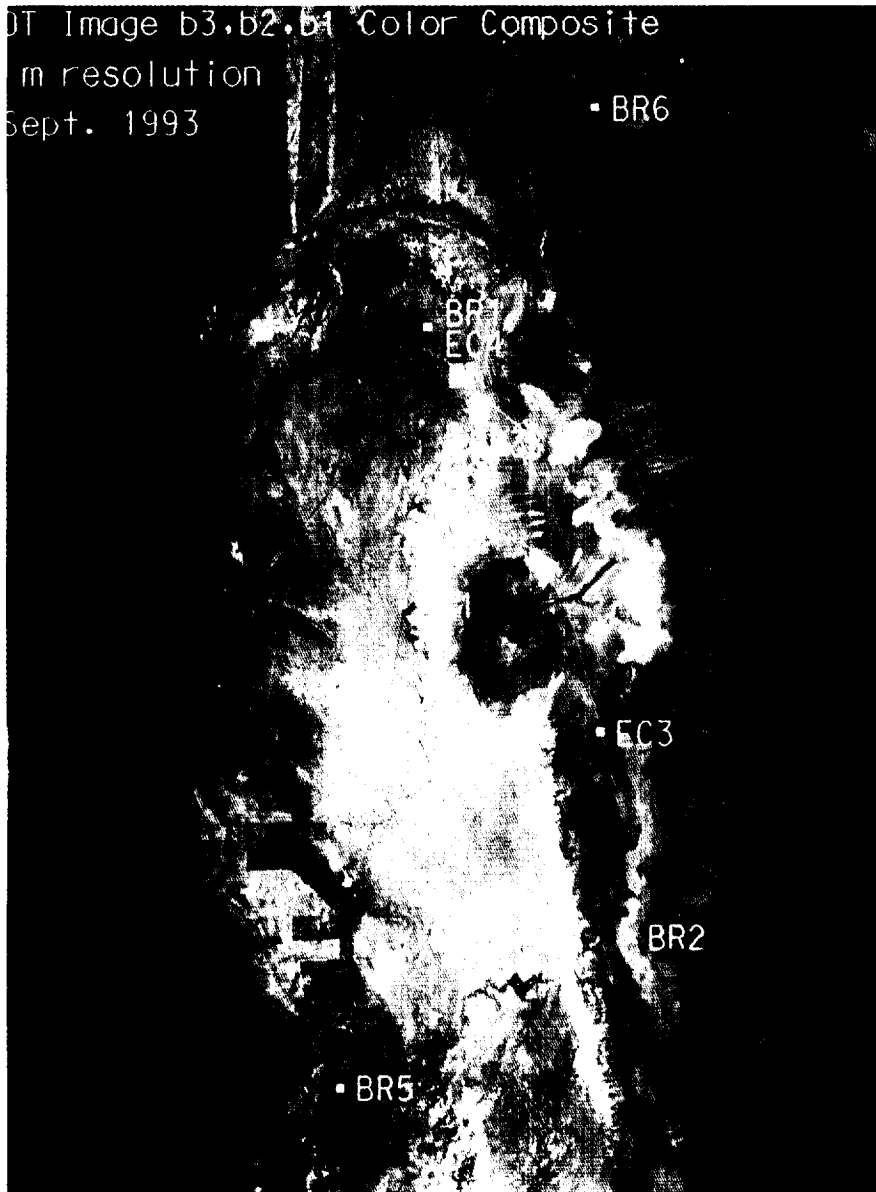
FIGURE 33.—Goshute Valley, Nevada.

meteorological stations (known as Bowen ratio (BR) stations) have been permanently established throughout the Goshute Valley for the 3-year duration of this investigation. These stations measure such important meteorological characteristics as wind speed, humidity, incoming solar radiation, and soil moisture, and are strategically located in specific vegetation zones within the valley. During intensive measurement periods throughout the growing season, other instruments—known as eddy-flux correlation stations (ER) that measure near-ground meteorological and vegetation parameters—are placed in the field to support the measurements obtained by the Bowen ratio stations. The information provided by these ground-based instruments will be important to analyzing landscape characteristics and vegetation as identified on seasonal satellite remote-sensing data over the study site.

Accomplishments to date have focused on data collection and initial analysis of the satellite and ground-based meteorological station data obtained from April through October 1993. Three intensive measurement periods were conducted in 1993, with significant energy balance, soil moisture, and vegetation data collected. Another field data collection campaign will be conducted during the late spring and summer of 1994 for comparison with those data obtained during 1993.

greasewood (*Sarcobatus vermiculites*), sagebrush (*Artemisia tridentata*), and cheatgrass (*Bromus tectorium* L).
Figure 33 is a remote sensing image of the Goshute Valley obtained on

September 9, 1993, by the French SPOT satellite.

To accomplish the stated goals for the project, six ground-based

The information derived from this research will be important to developing a better scientific comprehension of the biophysical processes and responses that affect

local and regional climates over desert mountain terrain. In this regard, the research is important in furthering the objectives of the NASA Mission to Planet Earth program by examining the interrelationships between vegetation, soils, and regional energy balances to assist in developing better models of land-atmosphere interactions.

Sponsor: Office of Mission to Planet Earth

University Involvement: Department of Plants, Soils, and Biometeorology, and the Department of Biological and Irrigation Engineering at Utah State University.

Other Government Involvement: U.S. Army, Dugway Proving Ground, Meteorological Division

Surface Hydrologic Modeling at Regional Scales

Steven J. Goodman/ES44
205–544–1683

One of the current focuses of the Integrated Hydrologic Processes Group in MSFC's Earth System Science Division is surface hydrology and the interactions between the surface and atmosphere. The CaPE Hydrometeorology Project (CHymP) arose from involvement in the Convection and Precipitation/ Electrification (CaPE) experiment held in central Florida during the period of July 8 to August 18, 1991. Project efforts seek to establish and apply methodologies for the diagnosis of land surface and atmospheric water budget components for the Convection and Precipitation Electrification region (~25,000 square kilometers). The underlying philosophy guiding this study is that these techniques can be tested and applied in conjunction with GCIP (GEWEX [Global Energy and Water Cycle Experiment] Continental-Scale International Project) activities over regional scales and ultimately applied over the Mississippi basin.[1]

In support of the Convection and Precipitation/Electrification experiment, numerous measurement systems were in place, including more than 200 precipitation gauges, four weather radars, streamflow gauges, groundwater level monitors, portable automated mesonet (PAM) stations measuring surface radiation and meteorological parameters, Kennedy Space Center wind towers, and a set of seven stations deployed to measure

surface energy and radiation fluxes. The many disparate data sets collected have been integrated and preprocessed in a geographic information system (GIS) and used in diagnostic studies of the surface and atmospheric water budgets. The components being examined are surface runoff, groundwater storage, and surface evapotranspiration and precipitation. Surface runoff and groundwater storage have been estimated based on streamflow and groundwater data collected over the study domain. Evapotranspiration was measured at a few point sites within the study domain, but can be estimated accurately over the entire area only by using a surface flux model. To this end, researchers have modified and enhanced existing models, resulting in the Simulator for Hydrology and Energy Exchange at the Land Surface (SHEELS).[2] Using this tool, sensitivities of surface hydrologic processes to potential changes in surface conditions such as deforestation and urbanization may be examined.

Precipitation has been estimated in various ways on a daily basis for the convection and precipitation/ electrification domain based on a combination of radars and rain gauges. As a first step, the team applied conventional reflectivity-rain rate (Z-R) relationships to regional composite weather radar imagery. The relationship applied was $Z = 300 \, R^{1.4}$, referred to as the Florida Area Cumulus Experiment (FACE) Z-R that was developed for convective rainfall conditions. This relationship is the current default algorithm for deriving rainfall from the National Weather Service WSR–88D Doppler radar systems. However, researchers found

24-Hour Rainfall (mm)
Ending 1200 UTC
August 1, 1994

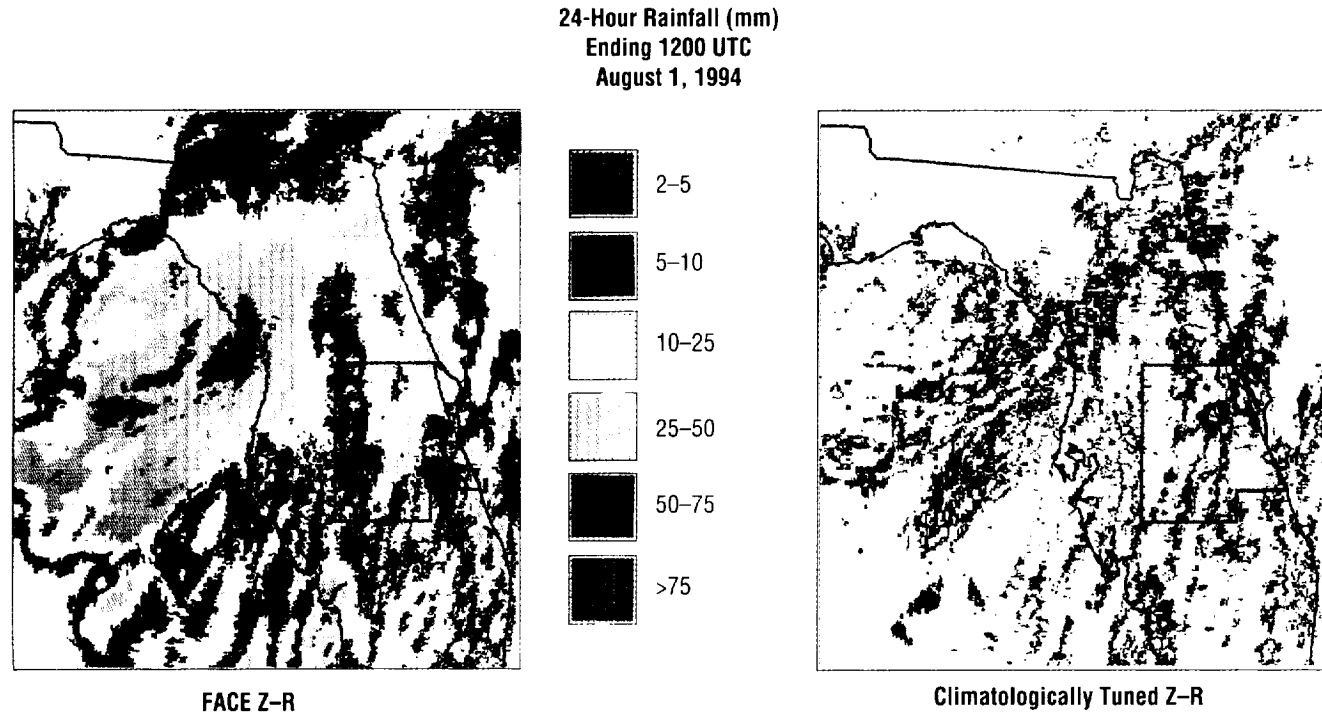FACE Z-R   Climatologically Tuned Z-R

FIGURE 34.—Florida Area Cumulus Experiment and climatological Z-R comparisons of daily rainfall.

daily rainfall derived from the Florida Area Cumulus Experiment Z-R for the study area to be approximately 70 percent higher on average than the corresponding rain-gauge estimates. This led to the development of a "climatologically tuned" Z-R relation based on the probability matching method (PMM). This technique uses rain-gauge observations to develop a Z-R relationship to reproduce the probability distribution of rain rates, thus producing rainfall estimates that are unbiased with respect to gauge amounts.

A comparison of daily rainfall from the Florida Area Cumulus Experiment and climatological Z-R for a regional area encompassing the convection and precipitation/electrification area is

shown in figure 34. It is clear that there are very large differences in rainfall depending on the choice of a Z-R relation. The advantage of applying a climatologically tuned relationship is that it gives a more accurate rainfall estimate when integrated over space and time, providing useful input into regional-scale hydrologic studies.

[1]Goodman, S.J.; Crosson, W.L.; Laymon, C.A.; and Duchon, C.A. 1992. Surface Energy and Land-Atmosphere Water Budgets During the CaPE Hydrometeorology Project, Abstr. *EOS, Transactions of the American Geophysical Union* 73:183.

[2]Laymon, C.A.; Crosson, W.L.; and Goodman, S.J. 1994. Simulator for Hydrology and Energy Exchange at the Land Surface and its Development Through the CaPE Hydrometeorology Project, Abstr. *EOS, Transactions of the American Geophysical Union* 75:173.

Sponsor: Office of Mission to Planet Earth

University Involvement: University of Oklahoma; Columbia (TN) State Community College

• • • • •

SPACE PHYSICS

Ionospheric Plasma Heating by Auroral Winds

Craig J. Pollock/ES83
205–544–7638

On February 23, 1991, NASA's Argon Release for Controlled Studies (ARCS IV) sounding rocket was launched into high altitude over an intense post-breakup aurora. Experiments on the rocket were designed to diagnose the low-energy plasma, both in its natural state and as it was perturbed by an onboard ion accelerator. During the flight, researchers studied the natural heating of the ambient ion plasma (hydrogen ion, H$^+$; oxygen ion, O$^+$) within regions of a strong electric field directly over a visible auroral arc. These observations were made using the MSFC-developed super thermal ion composition spectrometer (STICS) and the Cornell University DC electric-field instrument (DCE). Confirmation of spatial proximity to auroral field lines was documented through measurement of kiloelectron-volt-precipitating electrons by charged-particle spectrometers provided by the University of New Hampshire.

Figure 35 shows plots of the measured temperature (parallel and perpendicular to B, the local geomagnetic field) of the hydrogen ion (fig. 35a) and oxygen ion (fig. 35b) species as functions of time throughout the flight. These temperatures have been derived as integral moments over the three-dimensional species distribution functions measured by the super thermal spectrometer. For such
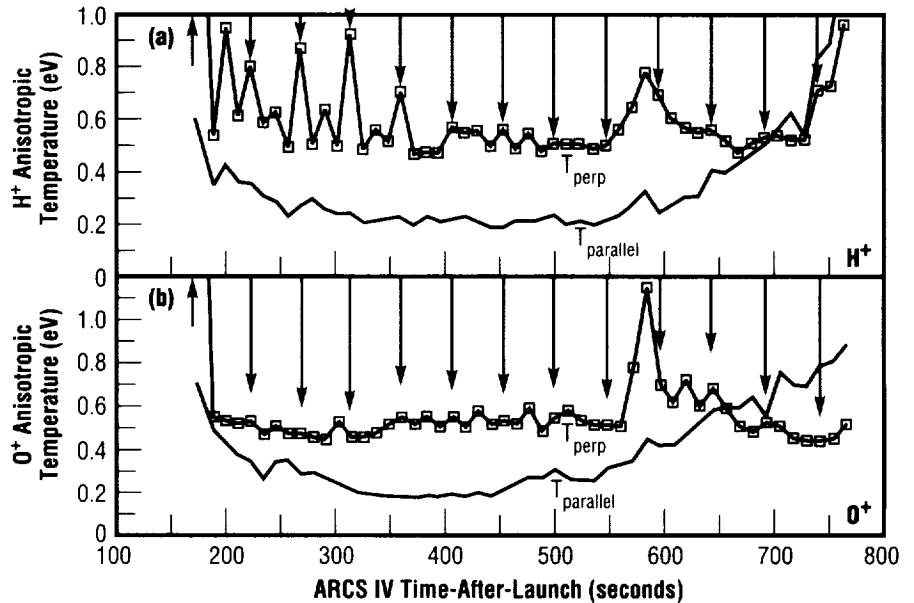
Figure 35.—Argon Release for Controlled Studies (ARCS IV) ion temperatures.

moments, the spectrometer's time resolution was limited to about 10 seconds. Temperature enhancements, particularly in the hydrogen ions, prior to 400 seconds time after launch (TAL), are due to

operation of an onboard argon ion (AR$^+$) accelerator which operated at the times indicated by arrows, and have been reported previously. The feature of interest in this report is the large temperature enhancement in both

Figure 36.—Argon Release for Controlled Studies IV time after launch.

species just before 600 seconds after launch. Comparison of perpendicular and parallel temperatures in figure 35 shows the heating to be largely in the direction p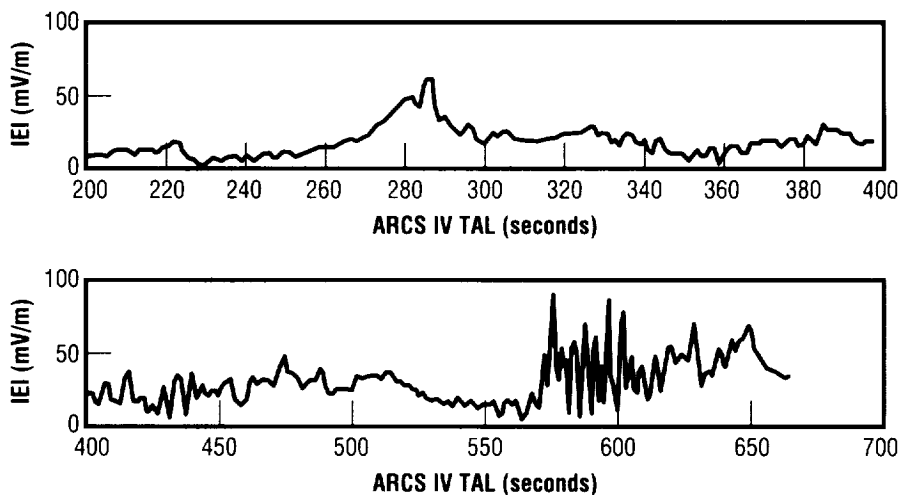erpendicular to the ambient geomagnetic field. This indicates a heating mechanism involving electric fields, since these are typically directed perpendicular to B in a magnetized plasma, such as that found in the Earth's ionosphere.

Figure 36 shows the DC electric field as measured throughout the flight with the Cornell DC electric-field instrument and indicates a large amplitude (nearly 100 millivolts per meter (mV/m)) and variability of the measured field during the interval (just prior to 600 seconds after launch) when the super thermal spectrometer was observing enhanced ion temperatures. Findings are unclear as to whether the large field amplitudes themselves or the steep field gradients associated with the variability were responsible for the ion heating. Each could, in principle, have produced the heating. Electric fields cause the plasma to drift perpendicular to B. Collisional coupling to the ambient neutral species (which is not subject to electric-field drift) has been predicted to cause the ion plasma to form a torus, or ring, in velocity space, with the major and minor toroidal radii corresponding to the ion drift velocity and pre-interaction temperature, respectively. In this scenario, the toroidal ion distribution would be unstable to the growth of plasma waves and give up free energy to parallel electron heating, leading to a filling in of the hole in the ion torus and an enhanced perpendicular ion temperature. On the other hand, shears in the DC electric field have also been

predicted to contribute to the destabilization of electrostatic plasma waves in the frequency range between the ion gyro frequency and the local lower hybrid frequency, possibly leading to the perpendicular ion heating by these waves. The large amplitude and variable electric fields shown in figure 36 may contribute, via one or both mechanisms, to the ion heating shown in figure 35. The three-dimensional spectrometer oxygen ion data indicate a toroidal velocity distribution, although the data are not conclusive.

Energetic electron spectrometers flown on the same rocket by the University of New Hampshire confirm that intense energetic electron precipitation was occurring on the same magnetic field lines on which the ion heating and large electric fields were seen. This has led researchers to the conclusion that they were observing the source region and initial heating mechanism for ion outflows commonly observed by orbital spacecraft flying over the terrestrial auroral zones.

In January 1995, the same group of investigators will participate in the Sounding of the Cleft Ion Fountain Energization Region (SCIFER) sounding rocket mission. This mission is designed to investigate the heating of ions at high (1,000 to 1,400 kilometers) altitude in the vicinity of the dayside magnetospheric cleft, from which the most prodigious ion outflows emanate. Previous research from orbital platforms has shown that strong DC electric fields and spatial electric field gradients are closely associated with these dayside outflows.

Ganguli, G.; Keskinen, M.J.; Romero, H.; Heelis, R.; Moore, T.; and Pollock, C. 1994. Coupling of Micro- and Macro-Processes Due to Velocity Shear: An Application to the Low-Altitude Ionosphere. *Journal of Geophysical Research* 99:8873.

Observations
of Downward-Moving
Oxygen Ions
in the Polar
Ionosphere

Michael O. Chandler/ES83
205–544–7645

The polar ionosphere and magnetosphere have long been thought of as regions of ion outflow—primarily as a result of the polar wind effect which, under steady-state conditions, results in hydrogen ions (H⁺) and helium ions (He⁺) flowing upward through stationary oxygen ions (O⁺). In the more complex, time-dependent state, periods of oxygen ion flow will occur as a result of changes in the underlying ionosphere. For example, variations in the solar illumination result in pressure variations that disturb the balance along the flux tube and induce flow. A relatively rapid decrease in the ionospheric pressure can result in the downward flow of oxygen ions, as observed in the nightside, mid-latitude ionosphere. A similar effect can be achieved as a convecting flux tube passes through a stationary region of ion heating. In this case, the sudden increase in pressure followed by a similarly sudden decrease can induce upward and then downward flow of oxygen ions.

Ions which have escaped the collisional region of the topside ionosphere will travel along complicated trajectories under the influence of gravity, the convection electric field, and any acceleration and/or energization processes present.

These ions—when present within flux tubes that convect into the polar cap—may be gravitational-bound and appear as downward-flowing ions. While the light ions (hydrogen and helium) are observed to escape the ionosphere, heavier ions, such as oxygen ions, can either escape or fall back into the polar ionosphere, depending on whether or not they receive sufficient energy to reach

escape velocity. The ratio of escaping to infalling oxygen ions should be a function of both the initial acceleration mechanism and the length of the subsequent transport path. For example, in the absence of horizontal convection, an ion with an energy less than the escape energy would reenter the local ionosphere. Conversely, in the presence of convection, the same ion can reenter the ionosphere at a
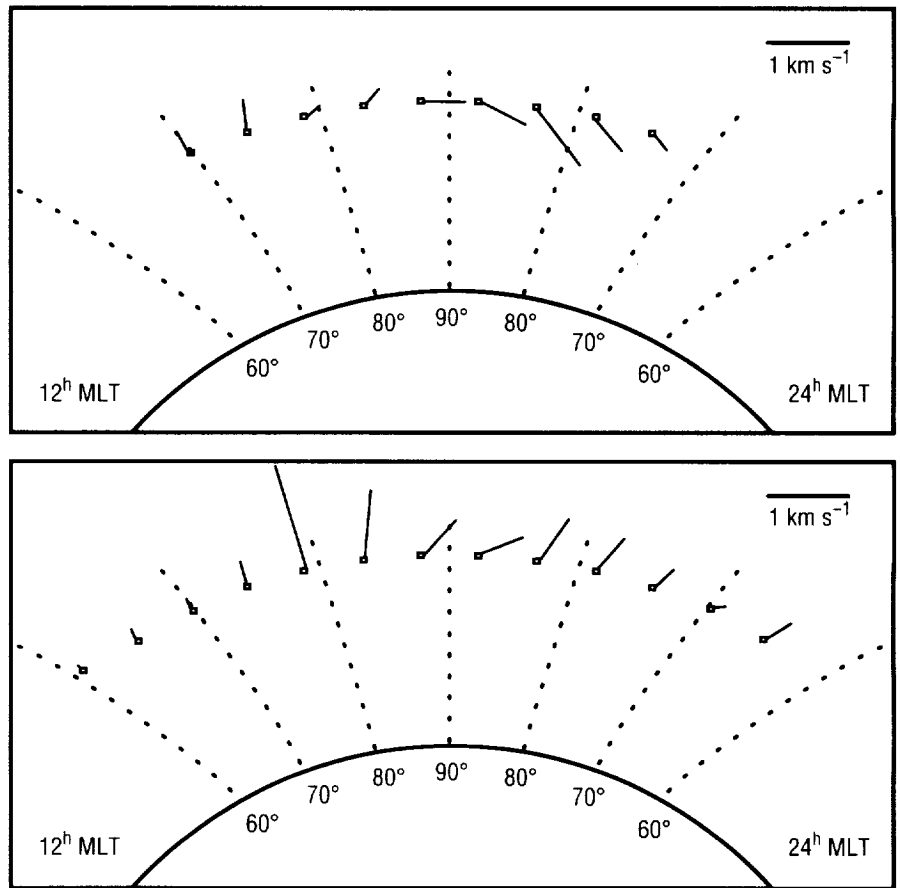

FIGURE 37.—Two-dimensional oxygen ion velocity vectors along a path from 12ʰ to 24ʰ magnetic local time (MLT) using all data between 2,000 and 4,000 kilometers, with southward and northward interplanetary magnetic fields.

different location within the polar cap or be transported to the auroral zone at sufficient altitudes to be reenergized and rerouted back into the magnetosphere. Thus, at times, oxygen ions of polar ionospheric origin should be observable moving both upward and downward along polar cap field lines.

The results from observations of oxygen ion velocities at high latitudes show both upward and downward flow. The upflows occur primarily in the auroral zone and associated regions, while both upflow and downflow occur in the polar cap. The direction of the ion flow in the polar cap is highly correlated with the direction of the interplanetary magnetic field (IMF), which is the magnetic field embedded in the solar wind. The magnetic field clearly separates the ion flows, revealing average downward velocities during periods of southward interplanetary magnetic field and average upward velocities during periods of northward interplanetary magnetic field.

The two-dimensional nature of the oxygen ion motion has been obtained by combining observed field-aligned velocities with model-derived, cross-field velocities. The resultant velocities were projected onto a polar cap anti-sunward (noon-to-midnight) path and averaged (fig. 37). The results clearly illustrate the different flow patterns associated with southward and northward interplanetary magnetic fields. For northward fields, the flow is strongly upward at dayside auroral latitudes and decreasing (but still upward) on the nightside. For southward fields, the pattern changes such that, for

latitudes between 80° on the dayside and 75° on the nightside, the flow is downward. These two-dimensional velocity vectors are consistent with the trajectories for gravitationally trapped ions. Such ions follow ballistic trajectories with their "impact" locations determined by the speed of cross-field convection. The observations show that the downward speed is highest on the nightside of the polar cap, which corresponds to the region most distant (in terms of convection path) from the outflow regions—consistent with the idea that these ions reached a higher apex and, thus, have been accelerated longer by gravity. Therefore, the downward flows represent the return flow of accelerated auroral zone ions into the polar cap ionosphere.

Sponsor: Office of Space Science

• • • • •

Inner Magnetosphere Circulation of Thermal Ions

Barbara L. Giles/ES83
205-544-7637

Exploration of what is now known as the magnetosphere began in 1957 with the discovery of the Van Allen radiation belts by the first U.S. orbiting satellites. The initial exploratory phase has evolved into one of quantitative studies in which scientists seek information on such problems as the origin of the various types of particles making up the magnetospheric plasma, or on the evolution of particle distributions during their transport through various magnetospheric regions. From a statistical study of the occurrence of magnetospheric low-energy ion particles, using measurements from the retarding ion mass spectrometer (RIMS) onboard the Dynamics Explorer 1 satellite, distinction is made between different ion angular distributions that indicate the particle flow characteristics. Occurrence frequencies determined as a function of spatial location were used to produce a "map" of the magnetosphere's low-energy ion components. Figure 38 shows outlines of the spatial areas for which distinct equatorial ion distribution types occur in the statistical results (but do not denote areas of exclusive distribution type). The intention is to indicate, in a general sense, the spatial areas where different distribution categories occur.
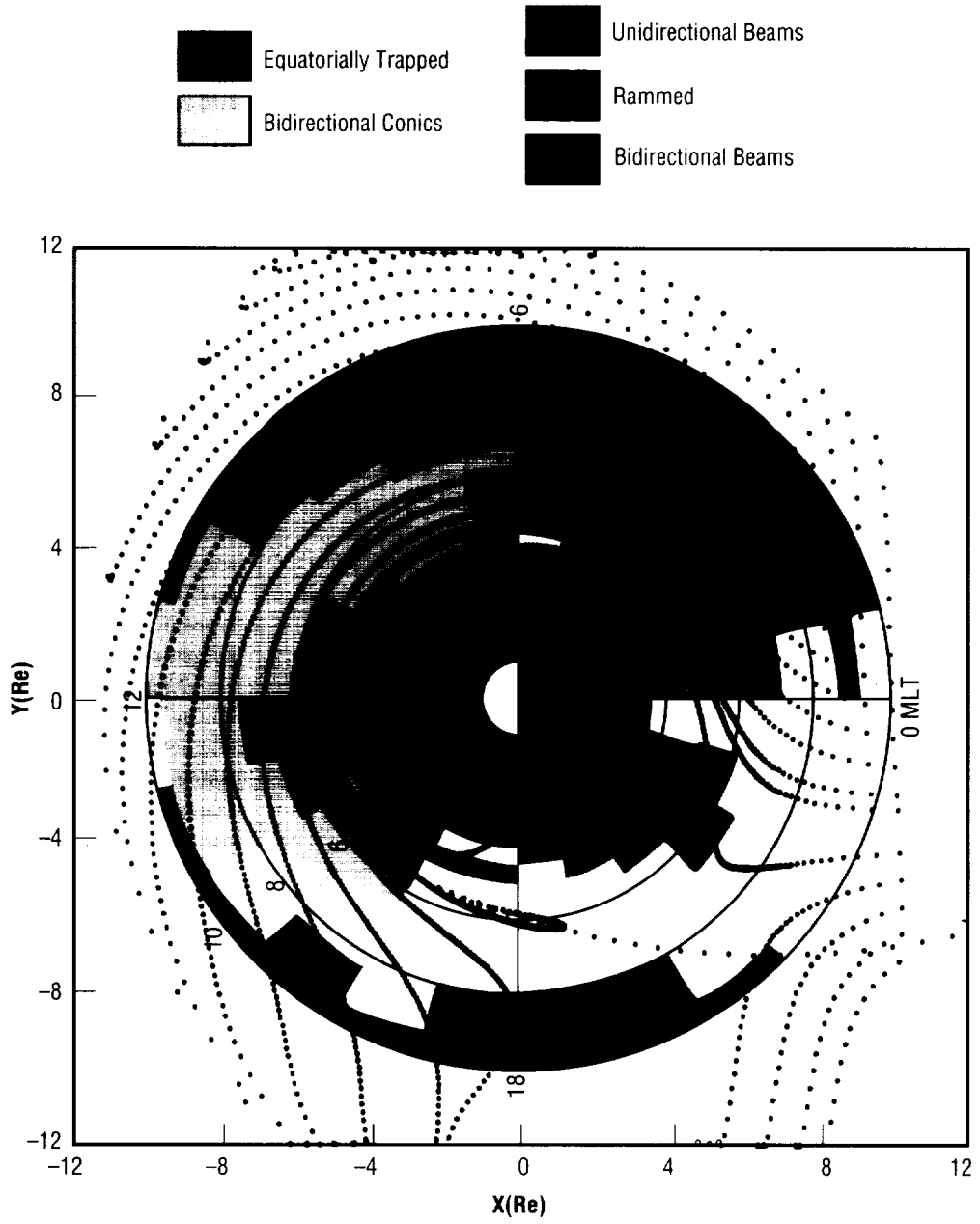
FIGURE 38.—Equatorial ion distribution.

Unidirectional field-aligned beam distributions correspond to ion distributions that have not undergone magnetic mirroring and are supplied from the auroral zone ionosphere and the dayside polar cusp region. The data analysis shows that the majority of these auroral beams flow along high-latitude magnetic field lines that are either open to the magnetotail and plasma sheet region or closed in a highly elongated fashion such that bouncing occurs over long time periods and is disrupted by nonadiabatic processes. The high-latitude outflows originating at somewhat lower L-shells have shorter bounce times and evolve into bidirectional field-aligned distributions during sunward convection. Bidirectional conic distributions in the dayside trough region are believed to be evidence of loss cones developing from bidirectional field-aligned distributions during sunward convection. After several bounce periods, the bidirectional field-aligned distributions experience loss-cone formation through charge exchange in the dayside upper atmosphere.

Characteristic particle drift times have been calculated for quiet magnetospheric conditions for zero-energy protons and are indicated in figure 38 by black dots along particle trajectory paths. (The time interval between dots is 300 seconds.) The trajectories fall into four general categories. First are those beginning at 22.0, 22.2, 22.4, and 22.6 magnetic local time (MLT). These follow sunward and westward drift paths to enter the duskside magnetopause at ~15 R_E; drift times range from 71 to 210 minutes. Second are trajectories beginning at 22.8, 23.1, and 23.2 magnetic local times. Protons drifting sunward in this time range are increasingly affected by curvature drift, increase in pitch angle, and either precipitate to the ionosphere or begin mirroring during convection. Third are the 23.4- to 0.8-magnetic-local-time trajectories that generally follow the convection electric field eastward past dawn and then westward across the dayside before entering the dusk magnetopause. Convection drift times to the magnetopause range from 21 hours for a proton starting at a local time of 23.4 to 6 hours for a proton starting at 0.8 local time. Last are the trajectories for protons beginning at 1 magnetic local time or greater. These flow eastward to the dayside or dawnside magnetopause with drift times decreasing from about 5 hours to less than 2 hours.

While it is unrealistic to expect a close correlation between trajectories calculated for a quiet magnetic field configuration and statistical results that average over a range of magnetic activity conditions, there are general trends that agree. The rammed distributions of the inner plasmasphere correspond to the corotation region interior to—and inaccessible to—the sunward-drifting proton trajectories. The bidirectional field-aligned distributions align generally with convection paths of drift times in comparison to the mirroring period. In a global eastward drift, these ions are driven into the dayside through the effect of the large-scale, dawn-dusk convection electric field. Unidirectional distributions occur on paths sufficiently short so that the flux tubes are emptied before mirroring can occur.

Spatial distribution of the statistical results and the equatorial drift-path calculations indicate that thermal ionospheric ions originating at the equatorward portion of the midnight auroral zone (those not lost to the plasma sheet region) become mirroring, bidirectional distributions during sunward convection. Those originating at somewhat lower L-shells also evolve into bidirectional field-aligned distributions during sunward convection; then, through the combined action of mirroring, convection, and recombination, evolve further into bidirectional conic distributions by pitch-angle diffusion after several bounce periods with loss-cone formation by the dayside upper atmosphere.

Giles, B.L.; Chappell, C.R.; Moore, T.E.; Comfort, R.H.; and Waite, J.H., Jr. 1994. Statistical Survey of Pitch-Angle Distributions in Core (0–50 eV) Ions from Dynamics Explorer 1: Outflow in the Auroral Zone, Polar Cap, and Cusp. *Journal of Geophysical Research*. In press.

Giles, B.L.; Moore, T.E.; and Comfort, R.H. 1994. Statistical Survey of Pitch-Angle Distributions in Core (0–50 eV) Ions From Dynamics Explorer 1: Map of the Earth's Low-Energy Plasma Component. Submitted to *Journal of Geophysical Research*.

Sponsor: Office of Space Science

• • • • •

Beam Imaging Diagnostics

Victoria N. Coffey/ES83
205–544–7635

During a recent test of the Thermal Ion Dynamics Experiment (TIDE) flight instrument in the Low-Energy Ion Facility (LEIF), researchers noticed that the beam of particles from the ion source was bending due to the Earth's magnetic field. To shield the particles from this field, a drift tube of mu metal was placed directly below the ion source and above the instrument aperture. After this change, beam diagnostics were conducted by an imaging sensor so that the source could be characterized for its flux uniformity at different particle energies. Following is a brief overview of the Low-Energy Ion Facility Laboratory and the imaging sensor, as well as a description of the procedure used for the ion source characterization and some results from this test.

The Low-Energy Ion Facility is a laboratory system designed around a vacuum chamber for testing and calibration of low-energy particle detectors over a range of particle energy, mass flux, and angular acceptance. In conjunction with detailed numerical ray-tracing studies, this facility provides the basis for the iterative design of space plasma instrumentation. It features a large vacuum chamber, an ion source designed to produce low-energy ion beams with large area, beam-imaging diagnostics; a motor-driven fixture for positioning the instrument relative to the ion beam; and data acquisition and analysis capability. The flight

instrument can be placed on a turntable fixture so that the instrument can be tilted ±90° and rotated ±180° relative to the ion source. Ions are produced in an electron bombardment source with an adjustable range of 1 to 150 electron volts (eV) and an effective circular aperture of 8.0 centimeters in diameter. A tandem electrostatic mirror, plus magnetic mirror configuration within the ion source, optimizes the use of the ionizing electrons, decreasing the nonthermal electron throughput to the instrument chamber while improving the flux uniformity. The automation of the motion controller, the ion source, and some of the common laboratory instruments using National Instrument's LabView™ has been written about in MSFC's *Research and Technology 1991* and *Research and Technology 1993*.

The imaging system from Surface Science Laboratories consists of the sensor mounted in the vacuum chamber, a position computer, a preamp, and computer software. Electron multipliers or microchannel plates in the sensor amplifies the incident particle flux so that each incoming particle provides a pulse of

charge on a resistive anode. This charge is divided among the four corners of the resistive anode in proportion to the position of incidence. The four output signals are amplified and shaped by the preamp and then sent to the position computer. Using the sums and ratios of voltage from the preamps, the position computer makes an analog computation of the incident positions in the x and y axes and provides output voltages corresponding to each. An analog-to-digital converter provides the image of the incoming flux to an Intel/80286 computer and the imaging software.

A Macintosh™ IIfx and the PC/286 were used for the testing procedure. The Macintosh™, with its LabView™ software, had the functions of tuning the ion source for the desired beam energy, commanding the motion control in the vacuum chamber, and monitoring the beam current. The PC/286 accumulated each image with the MCA2D™ program that was used to collect, display, or analyze the two-dimensional image.

A procedure, or virtual instrument (VI), was written that implemented a two-dimensional loop. After some

```
open file using file name of Macintosh date and time
write beam energy to file
bring in faraday cup under the ion source and measure current
do i = -20,20,10 azimuth angle sweep
  do j = -20,20,10 polar angle sweep
    notify user that movement has been completed and start accumulation
    if j = j*5 then bring in faraday cup to analyze beam energy
    write time, beam current, azimuth angle, and polar angle to file
  enddo
enddo
```

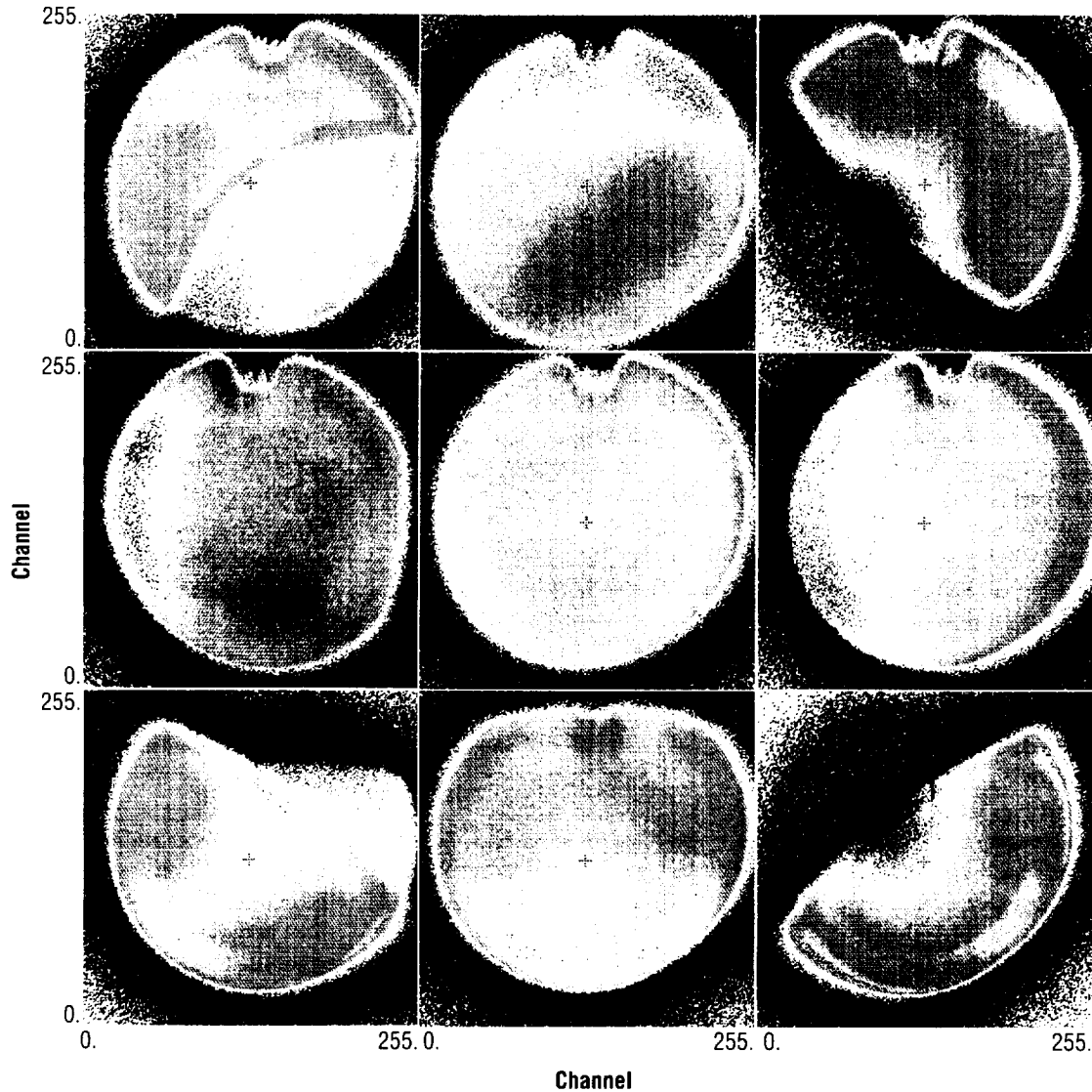FIGURE 39.—Macintosh LabView procedure.

FIGURE 40.—Imaged accumulations from a particle beam of 25 electron volts.

initialization steps, the instrument's outer loop commanded the motion controller, moving the imager to the first azimuth angle of the sweep. The process then continued to the inner loop, moving the imager to the first polar angle. After completion of this command, the LabView™ software sent a dialog box to the operator to take an accumulation (fig. 39). On the PC/286, an image would be accumulated over 60 seconds, typically receiving a maximum count rate of 300 hertz (Hz). The procedure would then continue until the completion of the polar sweeps in the inner loop. At the end of the procedure, an array of 25 images had been accumulated.

Figure 40 illustrates the imaged accumulations from a particle beam of 25 electron volts. The figure depicts nine accumulations from the range of azimuth and polar angle of −10°, 10°, to azimuth and a polar angle of −10°, 10°, with 10° increments in both dimensions.

Sponsor: Office of Space Science

• • • • •

65

Chromatic Display of Multidimensional Information

Thomas E. Moore/ES83
205–544–7633

Space plasma observations and simulations tend to generate multidimensional information that can be very challenging to display in a concise manner. In pursuit of higher density displays, researchers have developed a new method for using color to add a "depth" dimension to flat paper displays. The displays can be thought of as a hybrid between gray-scale and conventional color displays of data.

Because human color perception is based on the presence of three different types of light-sensitive cells on the retina of the eye, color has the potential to represent three quantities at once, i.e., the intensity of the red, green, and blue components of a particular color (RGB color description). A gray-scale image encodes data values on a color table that contains equal but varying red, green, and blue intensities. Another popular choice for color encoding is a "rainbow" color table, in which data values are encoded along a constant intensity scale extending from blue to red, with the intervening colors ordered spectrally by wavelength. Other scales have been developed that, for example, produce a monotonic gray scale when photocopied.

Using a spectrometer of sufficient resolution, it is possible to determine the atomic structure of a material from the "color" of its emitted light. Even

with the relatively meager resolving power of the human eye, the natural world takes on a fantastic variety of shades and hues that ultimately originate with the atomic structure of materials. Thought of in terms of the physical meaning of light, a specific color can be interpreted in terms of the gross shape of the frequency spectrum of its emitted light. In practice, the three-point resolution of the eye means that only a coarse spectral representation is possible. Table 6 summarizes the physical interpretation of color in terms of the frequency (v) spectrum of the light.

TABLE 6.—*Physical color interpretation*

Color	Interpretation
Gray	No Dependance on v (Flat)
Red	Strongly Peaked at Low v
Green	Strongly Peaked at Midscale in v
Blue	Strongly Peaked at High v
Pale Yellow	Weakly Peaked Toward Low v
Pale Blue	Weakly Peaked Toward High v
Magenta	Peaked at High and Low v

By direct analogy with this physical interpretation of color, a single pixel of color can represent the coarse dependence of any dependent variable upon an independent variable. When a multidimensional data set depends only coarsely on a variable, or when coarse knowledge of that dependence is sufficient, color can be effectively used to visualize that dependence. In combination with raster imaging of the remaining, more highly resolved dimensions of the data array, this type

of encoding multiplies the amount of data that is usefully displayed in a color graphic display by a factor of three.

A chromogram is a graphical representation of a function (designated as f) of three independent variables. The dependence on one of the three variables (designated as z) is encoded as color, while the dependences upon the remaining two variables (designated as x and y) are displayed as a raster image of colored pixels. The range of the encoded variable (z) is divided into three subranges that are associated with red, green, and blue light, respectively. The average value of the dependent variable in each of these ranges is used to scale the red, green, and blue components of the encoded color (fig. 41). The hue of the resulting color corresponds to the centroid of the dependence on z; the saturation corresponds inversely to the width of the dependence; and the brightness corresponds to the average value of the dependent variable (f) over all three ranges of z. (Note that z can be either linear or cyclic/angular.)
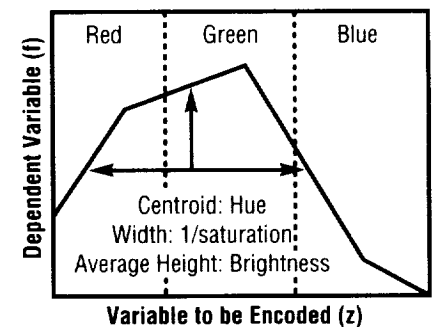

098b

FIGURE 41.—Schematic of the calculation of color values from the dependence of f (z).

The procedure for creating a chromogram begins with the definition of a color table that provides access to the full range of red, green, and blue intensity in any possible combination. The largest number of intensities that can be used with an 8-bit color system is six per color dimension, leading to $2^3 = 216$ possible color combinations. This limits the gray-scale resolution to only six values, which is barely adequate, but workable.

One dimension of a three-dimensional array must be chosen as the z axis for color encoding. Clearly the array must have an extent of at least three elements in the chosen dimension, but in general will have more. The coordinate corresponding to the z axis is then divided into three subranges, and average data values are computed for each color subrange, at each (x, y) in the array. These average values, which may be linear or logarithmic, are then scaled to the range of the individual color ranges (generally 0 to 255) and then translated into color lookup table entries for purposes of generating the image. As an aid to visual discrimination between brightness and hue, contours of brightness are superposed on the color raster image.

Quantitative documentation of a chromogram is accomplished by means of a "color wheel" and "brightness bar." Tic marks and labels placed around the perimeter of the wheel provide the accurate numerical correspondence between hue and the centroid position of the distribution. Contours of constant brightness, corresponding to the tic marks and labels along the brightness bar, provide for accurate quantitative

interpretation of the brightness as an average of the data over the range of the z variable.

Chromograms may be published, reproduced, or displayed on a video display screen without perspective calculations. However, it is not possible to produce an equivalent monochrome version of a chromogram. It is not necessary to view a chromogram from various perspectives to fully appreciate its three-dimensional structure. Chromograms have been produced successfully using a color table of 216 colors, but would benefit from the use of a larger color repertoire. The algorithms for interactive generation of chromograms are in the public domain as IDL procedures and may be obtained by anonymous file transfer protocol (ftp) from cyclops.msfc.nasa.gov in the /pub/ chromogram directory. A procedure-call version is being prepared.

Fok, M.-C.; Moore, T.E.; Kozyra, J.U.; Ho, G.C.; and Hamilton, D.C. 1994. A Three-Dimensional Ring Current Decay Model. *Journal of Geophysical Research.* Submitted.

Tufte, E.R. 1983. *The Visual Display of Quantitative Information.* Graphics Press: Cheshire, Connecticut, 153.

Sponsor: Office of Space Science

• • • • •

Simulated Space Storm Images for Magnetosphere Imager Mission Design

Thomas E. Moore/ES83
205-544-7633

One of the primary space weather phenomena to be studied by the Magnetosphere Imager (MI), a mission in phase B study at MSFC, is the terrestrial ring current produced by space plasma storms. This is a ring of energetic plasma encircling the Earth, similar in some ways to the Van Allen radiation belts, but lower in average energy, larger in number flux and mean radius, and more dynamic in terms of variability. It is called a "current" because the plasma particles carry millions of amperes of electrical current around the Earth, modifying the geomagnetic field.

The ring current is routinely monitored most often by means of ground-based magnetometers that record a reduction of the equatorial geomagnetic field, referred to as the "storm-time depression" and symbolized as "D_{st}." The largest storms produce a maximum depression approaching 1 percent of the mean value of the surface magnetic field. Nevertheless, this is sufficient to produce substantial induced currents and potentials in long conductors such as transcontinental power grids and intercontinental communications lines. Typically, the largest D_{st} changes are produced in a storm main phase lasting some 2 to 4 hours, which derives energy from a disturbance of the solar wind. The

D_{st} subsequently decays away over a characteristic time scale of a few to several days.

The energetic particles that carry the ring current have been monitored in space by numerous spacecraft over the past 30 years, but in very few cases have simultaneous measurements been obtained from as many as two or three spacecraft. Moreover, the local plasma of low-energy particles has rarely been observed in conjunction with the energetic particle populations. Consequently, researchers still understand neither the main-phase processes that create and transport the energetic plasma particles responsible for the ring current, nor the recovery processes that dissipate the energy stored temporarily in the ring current region. By obtaining hot plasma images in conjunction with cold plasma images, the Magnetosphere Imager mission aims to correct both deficiencies of past measurements. This will permit significant progress toward the development of a predictive capability for anticipating plasma storms.

Recent work at MSFC has produced three-dimensional simulations of the recovery-phase decay of the ring current, suitable for anticipating the nature of image sequences to be expected from the Magnetosphere Imager mission. These simulations are based upon models of the magnetic and electric fields in the magnetosphere, as a function of time during the recovery phase. The initial plasma distribution is obtained, with some extrapolation, from published space observations. The subsequent transport and loss of energetic particles is tracked using a Vlasov kinetic equation approach, accounting

for collisions with both atmospheric atoms and ionospheric ions. Energetic particles are assumed to move in fields that vary insignificantly over distances comparable to the radius of gyration in the local magnetic field, or over times comparable to the period of the gyration. These are robust assumptions during the recovery phase of plasma storms.

The results of these simulations include predictions of the flux of ions as a function of velocity (energy and

direction of motion), position in the magnetosphere (radius, local time, geomagnetic latitude), mass species (hydrogen ions, oxygen ions, helium ions, etc.), and time. These multidimensional results contain numerous features—the visualization of which benefits from sophisticated modern computer graphics techniques.

The specific visualization technique of interest here is imaging of the flux of fast neutral atoms emitted from the hot plasma region as the energetic ions
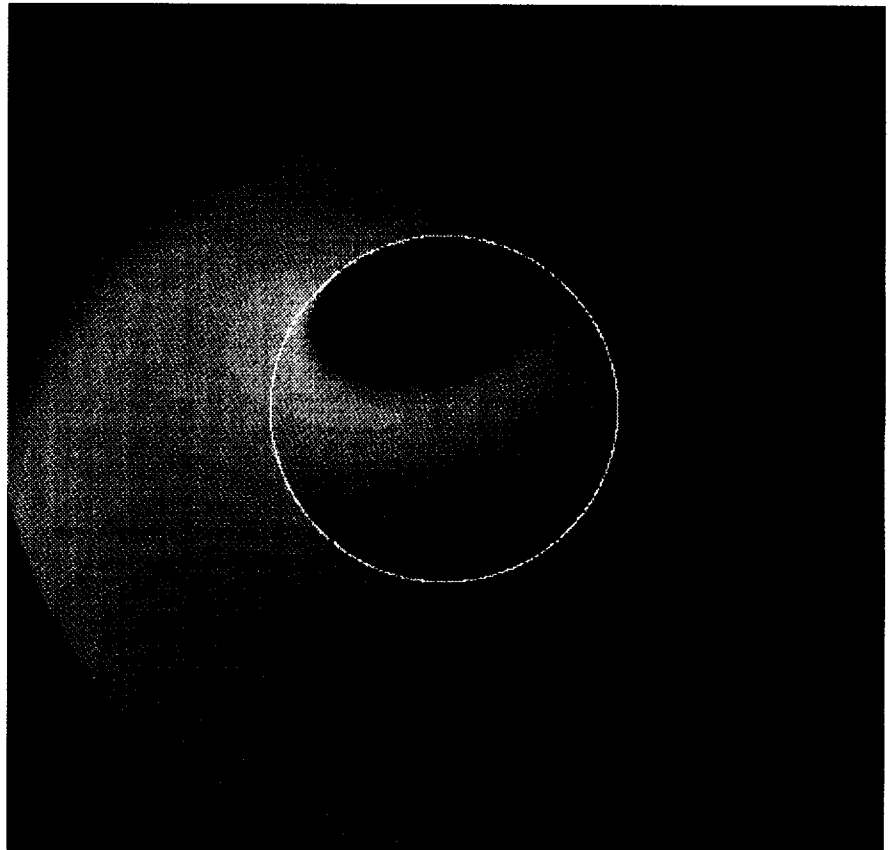

Figure 42.—An energetic neutral atom image of the terrestrial ring current in 1-kiloelectron-volt hydrogen atoms, seen from a position in the dawn meridian at +60 geomagnetic latitude.

undergo charge exchange interactions with the Earth's geocorona of hydrogen atoms. The fast neutral atoms travel from their point of origin in nearly straight lines and at high velocities, thus providing a signal that can be used to remotely sense sufficiently emissive parts of the magnetosphere from a single appropriate vantage point, using a suitable fast neutral atom camera.

Each pixel of the images so obtained will represent a line-of-sight integration through the emissive volume, which is structured in three dimensions and is optically thin. The kernel of the integration is a product of the flux of energetic ions, the number density of the geocoronal hydrogen, and the relevant cross section. An image generated from the model results described above (fig. 42) is useful in observing large-scale features of the hot plasma, notably the minimum of ion flux in the afternoon sector. This striking feature is basically a "shadow" of the Earth in the sunward circulation of plasma inside the magnetosphere, but is very energy dependent in nature.

A video sequence of such images has also been prepared that illustrates how well dynamical variations can clearly be seen in a time series of images spanning the development of magnetospheric storm events. For example, the minimum feature so evident in figure 42 is characteristic of one range of particle energies and has a position that varies with the strength of convection during the course of the simulated storm.

The procedure for computing an image from a specified distribution of hot plasma is straightforward. However, the quantitative hot plasma ion flux can only be obtained from such an image by a deconvolution from the hydrogen atom density. Development of such deconvolution techniques is still at a rudimentary stage, and it may be that "forward modeling" to fit the images could be the method of choice. If so, this effort will contribute to the planning of instruments for, and the eventual interpretation of, Magnetosphere Imager imagery.

Fok, M.-C.; Moore, T.E.; Kozyra, J.U.; Ho, G.C.; and Hamilton, D.C. 1994. A Three-Dimensional Ring Current Decay Model. *Journal of Geophysical Research.* Submitted.

Fok, M.-C.; Moore, T.E.; Chase, C.J.; and Roelof, E.C. 1994. ENA Images During the Recovery Phase of a Magnetic Storm. *EOS, Transactions of the American Geophysical Union* FS16:258.

Sponsor: Office of Space Science

University Involvement: National Research Council

• • • • •

Discovery of Centrifugal Acceleration of the Polar Wind

Thomas E. Moore/ES83
205-544-7633

As the solar wind blows past the Earth's magnetosphere, momentum transfer across the magnetopause causes magnetospheric plasma to accelerate in the downstream direction. The most efficient coupling occurs in the polar regions where geomagnetic field lines cross the magnetopause and link into the solar wind magnetic field. Magnetic field lines efficiently transmit plasma shear stress for very long distances along their length, in this case all the way down to the ionosphere itself. Owing to this action, all the plasma along a field line is required to move in the same direction and with a speed that maintains the identity of the field line as a coupled "flux tube" of plasma and magnetic field. In the polar cap region, these flux tubes evolve from a shape that is curved toward the Sun to one that becomes curved away from the Sun as they convect from dayside to nightside under the influence of the solar wind. Because of the shape of the magnetic field, plasma that flows antisunward finds itself in an accelerating (noninertial) frame of reference in which fictitious forces appear, similar to the centrifugal or coriolis forces in rotating frames of reference.

In work recently begun in a collaboration between MSFC and the University of Alabama in Huntsville,[1]

these forces have been found to substantially alter the hydrostatic force balance in the topside ionosphere, causing heavy ion constituents to join in the well-known light ion outflow of the ionosphere, called the polar wind. This centrifugal acceleration of heavy atmospheric components is superposed upon the "vacuum cleaner" effect of the very low plasma pressure in interplanetary space and the expansion effect of heat dissipated in the low ionosphere, both of which enhance the pressure gradient tending to force the ionosphere upward against gravity. These latter effects have been important components of basic polar wind theory since it was developed in the late 1960's. That ionospheric outflow is profoundly affected by convection through centrifugal forces is a fundamental elaboration of that theory. It appears that the solar wind interaction, in addition to vacuuming and boiling terrestrial matter off the Earth, can also fling it off the planet.

A simple calculation can illustrate the effect of convection on the escape of atmospheric gases in ionized form. The magnitude of the escape speed goes as:

$$\left(\frac{v_e}{v_{eo}}\right)^2 = \left(\frac{r}{r_o}\right)^{-1}$$

where v_e is the escape speed, r is geocentric radius, and the subscript "o" refers to values at the ionosphere. Ionospheric convection speed, v, increases as a function of radius as:

$$\left(\frac{v_c}{v_{co}}\right)^2 = \left(\frac{r}{r_o}\right)^3$$

Equating the convection speed to the escape speed, it is found that the convection speed exceeds the escape

speed above a "critical radius" that depends inversely on the strength of ionospheric convection:

$$\frac{r}{r_o} = \left(\frac{v_{eo}}{v_{co}}\right)^{1/2}$$

With a surface escape speed of 7.9 kilometers per second (km/s) and a brisk ionospheric convection speed of 1 kilometer per second, this yields a critical radius of only 2.8 R_E. This is the radius above which the net force on each particle is outward, and any ionospheric plasma at or above this critical altitude escapes freely, filling the nightside magnetosphere with terrestrial material.

A more rigorous model of the topside ionosphere adds the centrifugal effects to the well-established effects of electron and ion heating, with resulting expansion of the plasma into a vacuum (fig. 43). It can be seen that the heavy oxygen ion (O^+) has an escape flux that increases dramatically for increasing ionospheric convection speeds for cool ionospheric conditions. In a warmer ionosphere, the oxygen ion behaves more like the hydrogen ion (H^+), which is not gravitationally bound and escapes freely regardless of the centrifugal acceleration. In the case of gravitationally free ions, the additional acceleration causes outflow at a larger
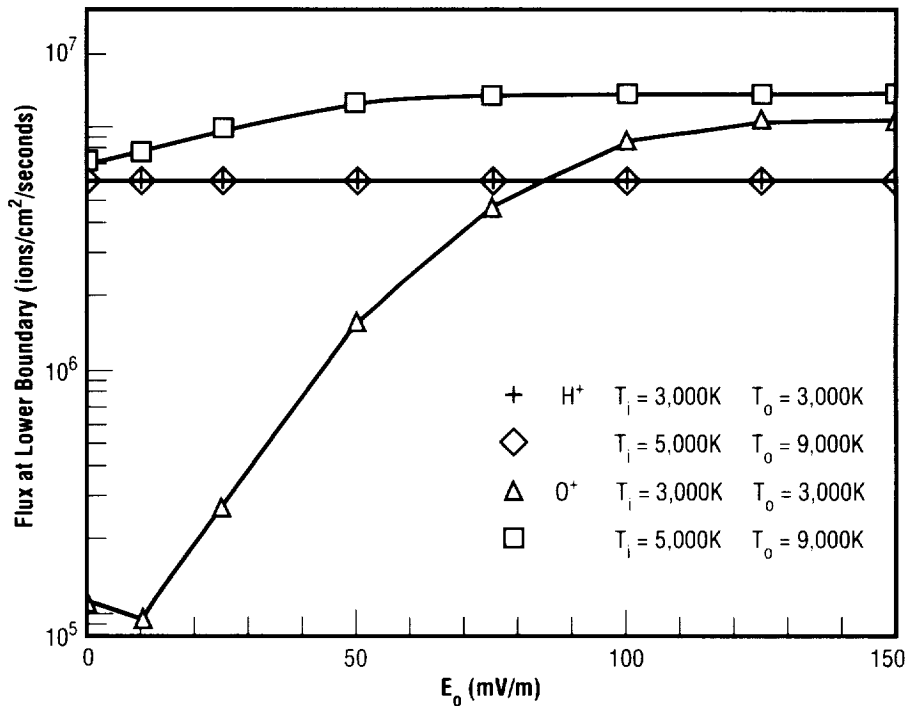

FIGURE 43.—Steady-state net upgoing ion fluxes at the ionosphere versus ionospheric electric field (convection speed) for hydrogen and oxygen with cool and warm ionospheric conditions.

speed and lower density (conserving flux).

Accumulating observations of polar ion outflows indicate that: (1) the polar oxygen ion has a significantly slower density fall-off with altitude than that expected in regions of cold ionosphere;[2] and (2) oxygen ions flow outward at high altitude with velocities significantly larger than expected for cold outflows.[3] These high-speed outflows have traditionally been attributed to ion heating in the ionosphere upstream of the observation point, but the present results suggest that strong convection-driven centrifugal acceleration may contribute strongly to these outflows as well. Preliminary comparisons of our modeled, steady-state velocity profiles with those observed indicate a much closer agreement than was otherwise obtainable. Further comparisons are being sought at present.

In addition to enhancing the mass flux of ionospheric plasma escape, the centrifugal force strongly accelerates more massive ions parallel to the magnetic field into the lobes and toward the plasma sheet, where they will gain much more energy and become part of the magnetospheric hot plasma and energetic particle population. In order to determine the relative roles of plasma heating and centrifugal acceleration of the entire topside ionosphere, it will be necessary to develop a more realistic two-dimensional (or more) description of a flux tube of plasma as it passes through the auroral zones and across the polar cap.

[1]Horwitz, J.L.; Ho, C.W.; Scarbro, H.D.; Wilson, G.R.; and Moore, T.E. 1994. Centrifugal Acceleration of the Polar Wind. *Journal of Geophysical Research* 99. In press.

[2]Chandler, M.O.; Waite, J.H., Jr.; and Moore, T.E. 1991. Observations of Polar Ion Outflows. *Journal of Geophysical Research* 96:1421.

[3]Ho, C.W.; Horwitz, J.L.; and Moore, T.E. 1994. Characterization of O+ Density, Flow Velocity and Temperature in the 3–5 R_E Polar Cap. *Journal of Geophysical Research* 99. In press.

Sponsor: Office of Space Science

University Involvement: University of Alabama in Huntsville

- - - - -

Space Plasma Weather and the Plasma Source Instrument

Thomas E. Moore/ES83
205-544-7633

During early 1994, a single plasma storm in the magnetosphere profoundly affected the operations of three commercial communications satellites: Intelsat-K suffered an anomaly in its operations; Anik-E1 was out of operation for 8 hours; and Anik-E2 was permanently disabled by damage to its attitude control systems. Post-failure analysis of available data on the state of the plasma in the magnetosphere shows that a space plasma (geomagnetic) storm was in progress at the time that the spacecraft damage occurred.

There are currently over 200 active or planned geosynchronous spacecraft, representing a worldwide investment of over 40 billion dollars. Annual revenues from the commercial segment of this investment is in the vicinity of 4 billion dollars. Commercial space activity continues to be a growth industry with a launch rate of around three per year. These facts make it clear that natural threats to space activities have serious economic impacts.

The most common effects of space environments on satellites result in "phantom commands," causing the spacecraft or specific subsystems to enter modes of operation that were not requested by ground operators. Because hazardous commands can be executed at random, they represent a

serious threat. The most frequent and serious phantom command is the turning "on" of a thruster without any corresponding "off" command. A recent case in point is the near-loss of *Clementine* to this very problem.

Two basic mechanisms are believed to account for most of the spacecraft anomalies and damage. Surface charging occurs when a spacecraft is immersed in a hot plasma environment—the well-known plasma sheath phenomenon. When some spacecraft exterior elements are electrically insulated from others, differential charging can cause repeated high-voltage discharges (up to ~20 kilovolts (kV)) to occur between these isolated components. The second mechanism is deep dielectric charging of insulating materials in spacecraft, caused by penetration of very high energy electrons and ions (from hundreds of kiloelectron volts (keV) to several million electron volts (MeV)) that are produced in large quantities during space plasma storms. The result is discharges within the dielectrics that release energy in ways that can be damaging to nearby semiconductor circuits.

Study of the early 1994 events has shown that the high-energy electron event that probably damaged the Anik spacecrafts could have been predicted 1 day in advance by a neural net model of the space storm, given real-time monitoring of the solar wind and the operation of a "space weather service."[1] The value of such predictions is clear, but is at best a fledgling capability built upon the past 30 years of space research and more recent global simulation efforts.

Research on the charging of spacecraft has long been an important aspect of MSFC space plasma physics activities. Competent observation of the low-energy plasma from spacecraft requires knowledge and, preferably, control of the spacecraft electrostatic environment. As part of the Thermal Ion Dynamics Experiment developed for the Potentials of Large Spacecraft in Auroral Regions (POLAR) spacecraft of the NASA Global

Geospace Study (GGS), MSFC has developed a spacecraft neutralization device known as the plasma source instrument, or PSI. The instrument's plasma source is shown in figure 44. The function of the plasma source instrument is to produce a low temperature (< 1 electron volt (eV) $\sim 10^4$ Kelvin (K)) plasma at the spacecraft, sufficiently dense to provide a supply of ions that is much larger than the rate at which electrons

FIGURE 44.—Photograph of the plasma source instrument to be flown on the Global Geospace Study (GGS) POLAR spacecraft as part of the thermal ion dynamics experiment.

are either collected from the ambient plasma medium onto spacecraft surfaces, or emitted from the spacecraft into the ambient medium by solar extreme ultraviolet (EUV) photoelectric production. The presence of such a local plasma is sufficient to limit the spacecraft floating potential to small values comparable with the plasma source instrument plasma temperature, i.e., ~1 volt (V).

The space station will also be equipped with a device similar to the plasma source instrument, with the objective of limiting the charging of the space station structure that would otherwise result from operations of the high-voltage (~150 volts) solar array with negative chassis grounding. Because of the large area of the space station and its solar array, the current capability of its plasma source will have to be considerably larger than that of the source instrument.

There are essentially three ways to address space weather hazards:
(1) monitor conditions and predict the occurrence of hazards so that evasive action may be taken; (2) analyze the occurrence of anomalies and failures resulting from space hazards and develop means of avoiding them; and (3) revise the design of spacecraft so as to minimize their susceptibility to space weather damage. Experience gained from operation of these neutralization devices, and further developments deriving from them, should lead to better understanding of spacecraft charging hazards, better prescriptions for the design of spacecraft, and perhaps a commercially viable means of mitigating such hazards in cases where they cannot be otherwise prevented.

[1]Freeman, J.W. 1994. The Effects of Storms in Space. *EOS, Transactions of the American Geophysical Union* 75, 16:314.

Moore, T.E.; Chappell, C.R.; Chandler, M.O.; Fields, S.A.; C.J. Pollock; Reasoner, D.L.; Young, D.T.; Burch, J.L.; Eaker, N.; Waite, J.H., Jr.; McComas, D.J.; Nordholt, J.E.; Thomsen, M.F.; Berthelier, J.J.; and Robson, R. 1994. The Thermal Ion Dynamics Experiment and Plasma Source Instrument. *Space Science Reviews.* In press.

Sponsor: Office of Space Science

Industry Involvement: Southwest Research Institute; Hughes Research Laboratories

• • • • •

Global Visualization of Magnetospheric Plasma

Dennis L. Gallagher/ES83
205-544-7587

The flight of the Magnetosphere Imager (MI) mission will bring new insight to our understanding of global magnetospheric processes, as well as new challenges in interpreting the images that the mission will return. In particular, the mission will obtain the first global pictures of the ring current and the plasmasphere, both optically thin plasma systems. The brightness at each position in the field-of-view results from the summation of all source luminosity along the line of sight. The collapse of information in depth in the Magnetosphere Imager field of view complicates the interpretation of the images, which leads to a dependence on the ability to model imaging plasma systems that will be observed.

The ring current and plasmasphere are important components of the Earth's magnetosphere. The magnetosphere is defined by the interaction between the solar wind and the Earth's magnetic field. Energy from the Sun and the Earth's rotation interact through magnetospheric current systems and particle transport to carry energy to the ionosphere and upper atmosphere, and to carry plasma from the ionosphere out into the magnetosphere.

For 35 years, since the Explorer I mission, magnetospheric observations have relied on the measurement of field and particle conditions in the

environment local to orbiting spacecraft. These measurements have provided direct insight into small-scale physical processes connecting particles to electric and magnetic fields. Current understanding of large-scale global processes, however, has depended upon our synthesis of many in-situ satellite observations separated in both space and time. The Magnetosphere Imager mission will provide the first direct measurement of global plasma systems in the magnetosphere, enabling us to view the dynamics and interrelationships of these plasma systems.

An effort is now underway in the Space Plasma Physics Branch to visualize global models of the plasmasphere. Global plasmaspheric visualization can be used to simulate Magnetosphere Imager images and to develop our ability to interpret them. The use of various models of global electric fields in time-dependent plasmaspheric modeling will result in different plasma structures. Density structures may vary in latitude, local time, and radial distance. Figure 45 shows a sample of a global image of the plasmasphere, as viewed from a perspective at high latitude over the northern magnetic hemisphere. Evident in the image is a large-scale wave structure on the plasmapause, a long tear or tail of plasma torn from the plasmasphere on the dayside, and the Earth's shadow where the luminosity in reflected solar light at 30.4-nanometer wavelength goes to zero. Through the simulation of typical Magnetosphere Imager viewing geometries, this visualization project will identify observable

features that can be used to recognize three-dimensional plasmaspheric density structures and to distinguish between electric field and plasmaspheric filling models that contribute to the formation of these structures.

ACTIVE PLASMASPHERE

He$^+$ 304Å image from:
R= 5 R$_E$
MLAT = 60 deg
MLT = 2,100 h

E–Field Convection Signatures:

Plasmaspheric "Tail"

Plasmapause "Ripples"

0.20R

Inner Plasmaphere

Earth Shadow

0.02R
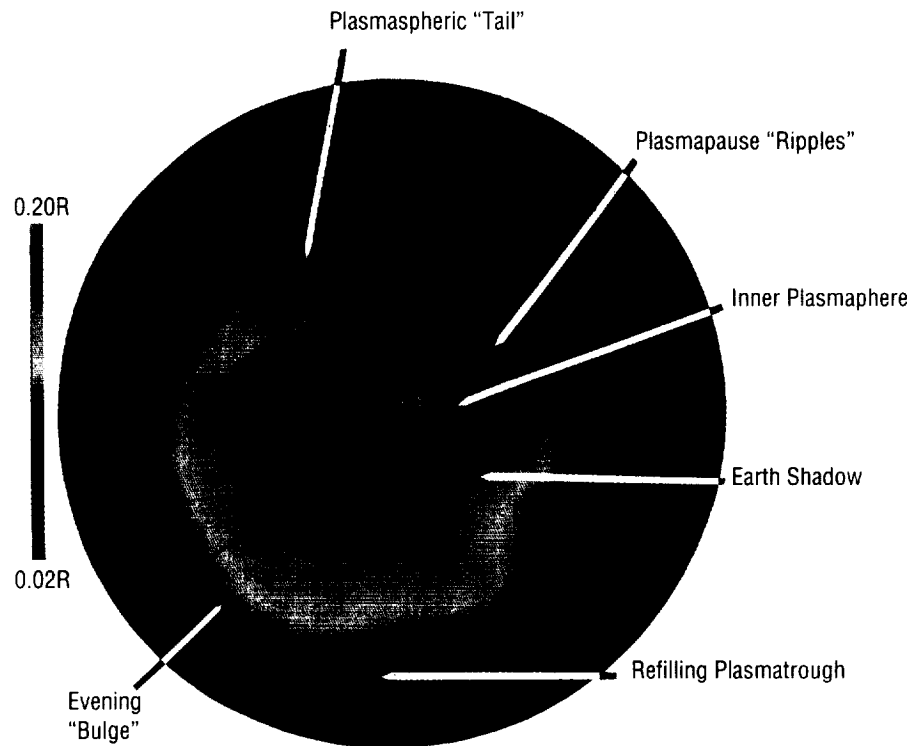
Refilling Plasmatrough

Evening "Bulge"

FIGURE 45.—Modeled response of plasmasphere to hypothesized, time-varying electric fields. (Image courtesy of E.C. Roel, Applied Physics Laboratory, Johns Hopkins University.)

Time-Dependent Modeling of the Plasmasphere

Paul D. Craven/ES83
205-544-7639

Driven by the Sun and the Earth's rotation, the Earth's magnetosphere is a dynamic system of electric currents, plasma energization, and trapped and precipitating particles. Although the magnetosphere is continually changing, this global system of particles and fields sometimes undergoes sudden, large-scale changes in shape and morphology during times of magnetic storms. Space weather can be responsible for the disruption of ground power grids, damage to commercial satellites, and the degradation of radio navigational and communication systems. In the same way that land, water, and air are components of the atmospheric system influencing weather on the ground, the plasmasphere is one of the components of the magnetospheric system involved in space weather.

The plasmasphere is a relatively dense region of ionized gases with a toroidal shape encircling the Earth at the magnetic equator. The plasmasphere extends from the ionosphere out to distances that range from about three Earth radii to more than six Earth radii. The plasmaspheric size, shape, and motion are all strongly influenced by space weather. Our understanding of space weather and ability to predict its effects depend upon our understanding of its components. The Space Plasma Physics Branch has a long history of measurement and study of the plasmasphere and is now involved in developing a time-dependent model of this system.

The plasmasphere is formed by the outflow of ionospheric plasma along magnetic field lines and by the action of electric and magnetic fields in the magnetosphere. Magnetospheric electric fields result from the rotation of the Earth and from the streaming of solar wind particles through the Earth's magnetic field. The addition of these electric fields leads to the motion of plasma across magnetic fields on trajectories, which either encircle the Earth or lead from the magnetotail to the dayside magnetopause.

Recent study has lead to the development of an empirical model of the plasmasphere that reflects conditions of steady or slowly changing geophysical conditions. This steady-state model can be used to constrain the description of global electric fields, which can then be used to simulate the motion of the plasmasphere during changing conditions.

A model often used to describe plasma motion in the equatorial plane uses an electric field that is uniform from dawn to dusk across the magnetosphere. This is added to the electric field resulting from the Earth's rotation. The total electric potential is given by:

$$p_1 = -c_1/r + c_2\, r \sin (\text{local time})$$

where c_1 and c_2 are constants, r is the geocentric distance of the plasma in the equatorial plane, and local time is measured from midnight to the east. The trajectories of the low-energy plasma, i.e., streamlines, in the equatorial plane separate into closed and open paths. Plasma on the open paths convect from the nighttime tail to the dayside magnetopause. Plasma on the closed paths convect around the Earth. The separatrix between the open and closed paths in the equatorial plane is often referred to as the plasmapause. The classical teardrop shape of the plasmapause in the equatorial plane is the separatrix formed from a uniform cross-tail electric field and a dipole magnetic field (p_1). A recently derived empirical model for steady geomagnetic activity, based on data from satellite measurements, results in a plasmapause that is similar in shape to the teardrop, but differs from it in ways that are significant to the form of the equatorial electric field. The empirically derived separatrix cannot be formed with a uniform cross-tail field. Researchers have found an expression of the electric potential, p_2, that, when added to the corotational field, does reproduce the empirical separatrix for low geomagnetic activity and which has four adjustable parameters to give the best fit to the data. By using the separatrix to derive an electric field, scientists can define potentials for different levels of geomagnetic activity and then use these electric fields to simulate the time-dependent motion of the plasma. Figure 46 shows the separatrix resulting from the expression for p_2 as the thick solid line. For comparison, streamlines for a constant cross-tail field are shown as thin lines. The corotational electric potential is also included in both cases.

Experts agree that the boundary of the plasmasphere is characterized by a sharp drop in plasma density; by the appearance of low-density structures within the plasmasphere; and by the
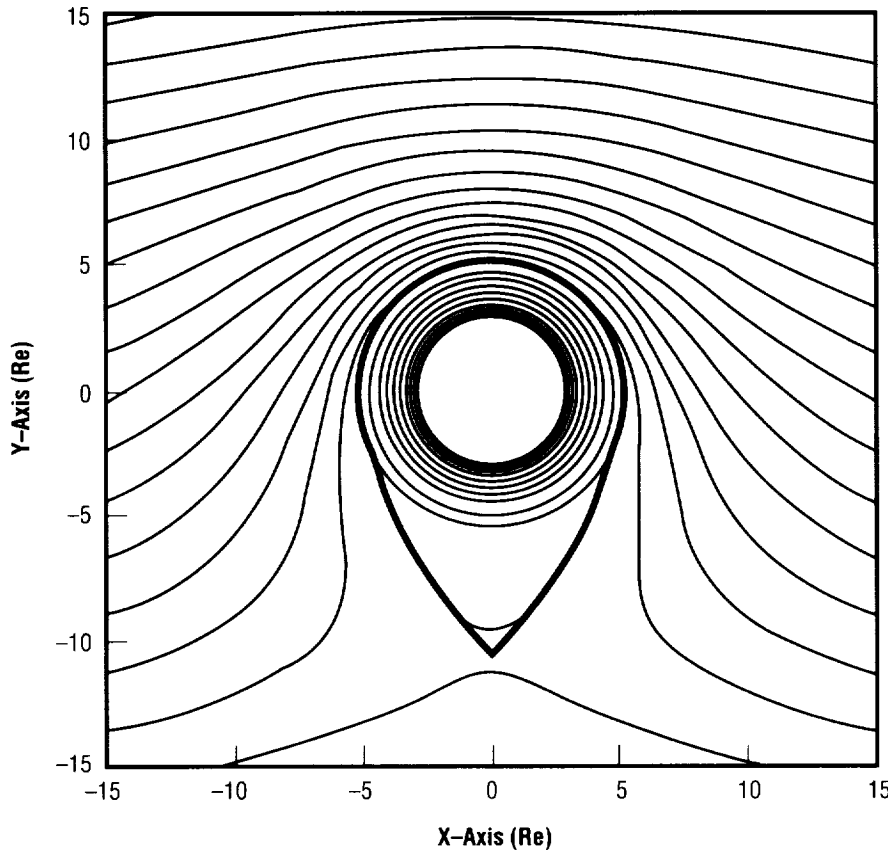
FiGURE 46.—Comparison of p_2 and constant cross-tail streamlines.

Vacuum Ultraviolet Spectrophotometric System

James F. Spann/ES83
205-544-5339

The need for spectrophotometric measurements of reflectance and transmittance in the vacuum ultraviolet (VUV) region of the spectrum, from 0.2 to 200 nanometers, has become more important in recent years with the development of all-dielectric, narrow-band filters in the far ultraviolet (FUV, from 100 to 200 nanometers) and the extreme ultraviolet (EUV, from 30 to 100 nanometers) and multilayer normal incidence mirrors in the x-ray ultraviolet (XUV, from 0.2 to 30 nanometers). The characterizations of optical materials and measurements of spectral performance of optical components have been essential ingredients in these recent developments. Since most spectrophotometric systems or spectrophotometers are used typically for in-air measurements, many of the optical components in these systems render them impractical for the vacuum ultraviolet region.

Recently, however, a spectrophotometric system useful in this region of the spectrum has been developed at MSFC. Optical components of various sizes and shapes can be measured over the 30- to 500-nanometer wavelength range. Multiple angles of incidence can be used in measurements of reflectance or transmittance. The

appearance of high-density, plasmaspheric-like structures outside the plasmasphere. However, the global morphology of these density structures and their part in the transport of matter through the magnetospheric system is not yet understood. Through the development of time-dependent simulations of the plasmasphere, it will be possible to test our understanding of the physics of space weather near the Earth. The comparison of simulations to localized satellite observations, when successful, will both validate the viability of the modeled physical

processes and reveal the global morphology of plasmaspheric structures, which have previously been unknown due to the inherently limited sampling of the plasmasphere by orbiting spacecraft.

Sponsor: Office of Space Science

University Involvement: University of Alabama in Huntsville

• • • • •

system has been used for various activities including the characterization of optical properties of thin films [1,2] and space-flight hardware for the Ultraviolet Imager (UVI) of the Global Geospace Study (GGS) Potentials for Large Spacecraft in Auroral Regions (POLAR) spacecraft.[3]

The system is composed of a light source (deuterium lamp or glow discharge lamp), a monochromator, optional collimating optics, a filter wheel, and a detector. Samples are cycled in and out of the reference beam from the monochromator to make the spectrophotometric measurements. Various detectors are used depending on the wavelength. To minimize the problem of contamination, the system is housed in a cryogenically pumped, hydrocarbon-free vacuum system. Housing in a class 10,000 clean room provides a safe environment for flight hardware or other contamination-sensitive samples being measured. Absolute measurements are made to less than 3 percent.

[1]Keffer, C.E.; Torr, M.R.; Zukic, M.; Spann, J.F.; Torr, D.G.; and Kim, J. Radiation Damage Effects in Far Ultraviolet Filters, Thin Films, and Substrates. *Applied Optics*. In press.

[2]Zukic, M.; Torr, D.G.; Spann, J.F.; and Torr, M.R. 1990. Vacuum Ultraviolet Thin Films. 1: Optical Constants of BaF_2, CaF_2, LaF_3, MgF_2, Al_2O_3, HfO_2, and SiO_2 Thin Films. *Applied Optics* 29:4284–92.

[3]Zukic, M.; Torr, D.G.; Kim, J.; Spann, J.F.; and Torr, M.R. 1993. Filters for the International Solar Terrestrial Physics Mission Far-Ultraviolet Imager. *Optical Engineering* 32:3069–74.

Sponsor: Office of Space Science

University Involvement: University of Alabama in Huntsville

• • • • •

SOLAR PHYSICS

Solar Magnetic Fields

Mona J. Hagyard/ES82
205-544-7612

The interaction of magnetic fields and plasmas is the root cause of the dynamic, high-energy phenomena of flares, mass ejections, and eruptive filaments observed on the Sun. In current solar research, therefore, extensive observational studies are carried out to develop an understanding of just how the solar magnetic field plays this key role in solar activity. MSFC has a unique instrument for observing the Sun's magnetic field, the MSFC Solar Vector Magnetograph, and the information derived from observations with this instrument has made significant contributions to an understanding of solar activity. In particular, this instrument permits observations of the transverse component of magnetic fields from which calculations of important solar parameters, such as electric currents and magnetic shear, can be made. Such parameters cannot be obtained from conventional solar magnetographs. Research at MSFC has shown significant correlations of these solar parameters with the occurrence of major solar flares. Thus, MSFC research shows promise in developing techniques to predict major flares, which will prove invaluable as NASA enters the era of space station, lunar bases, and planetary exploration—when people in space will be susceptible to the harmful effects of energetic particles and radiation produced by solar flares.

Over the past year, research in this program has been concentrated in

three main areas: the observational programs, data analysis and modeling, and the Experimental Vector Magnetograph (EXVM).

Solar observing programs were carried out in coordination with the Compton Gamma-Ray Observatory, the U.S.-Japanese Yohkoh solar satellite, and the MAX'91 program. These joint observations have resulted in a number of collaborations with scientists at other institutions, including: F. Drago and R. Falciani, Italy; P. Demoulin and B. Schmieder, France; L. Belkora, California Institute of Technology; A. Silva, Berkeley; C.C. Cheng, Naval Research Laboratory; and M. Machado and M. Rovira, Argentina.

Data analysis and modeling studies were carried out on the relationship between parasitic polarities and subflares followed by surging. Two events have been analyzed to date, and the results were reported at the spring American Geophysical Union (AGU) meeting in Baltimore, Maryland. Researchers continued the study of nonpotential fields associated with flares with emphasis on C-class flares and on the flares of June 1991—some of the largest flares of this solar cycle. Several new parameters—including the magnetic shear index and fractal dimensions—were developed to describe their nonpotentiality. Also, several papers have been written on the results of the June 1991 observations.

Other work has included the calculation of nonlinear, force-free fields using vector magnetograms as boundary conditions; a study of the properties of electric currents in active regions; a study of magnetic flux imbalance in active regions; the extrapolation of potential fields for a

finite field of view; and enhanced heating seen in Yohkoh images in areas of nonpotential magnetic fields.

Two new analysis techniques were developed to improve the interpretation of observational data from the MSFC vector magnetograph. These include a new method to calibrate data more accurately and a new method to resolve the 180° ambiguity in the azimuth of the transverse field.

The Experimental Vector Magnetograph represents a state-of-the-art vector magnetograph that will permit measurements of the solar magnetic field with the highest accuracy that modern technology allows. During the past year, all of its components—except the correlation tracker—were assembled, and the Experimental Vector Magnetograph was mounted on a horizontal bench where it was fed by a heliostat mirror. Extensive tests were carried out and adjustments made to the optics to achieve the desired optical performance. In March 1994, the first vector magnetograms were obtained. These were compared with vector magnetograms from the present MSFC vector magnetograph to show that the Experimental Vector Magnetograph produced the same results. Experimental data modes to reduce effects of solar oscillations were developed and will be tested when the correlation tracker is installed.

Adams, M.; Solanki, S.; and Hagyard, M.J. 1993. A Search for Sunspot Canopies Using a Vector Magnetograph. *Solar Physics* 148:201.

Ambastha, A.; Hagyard, M.J.; and West, E.A. 1993. Evolutionary and Flare-Associated Magnetic Shear Variations Observed in a Complex Flare-Productive Active Region. *Solar Physics* 148:277.

Cauzzi, G.; Falchi, A.; Falciani, R.; Smaldone, L.A.; Schwartz, R.A.; and Hagyard, M.J. 1994. Coordinated Studies of Solar Activity Phenomena. Submitted to *Astronomy and Astrophysics*.

Schmieder, B.; Hagyard, M.J.; Ai, G.; Zhang, H.; Kalman, B.; Gyori, L.; Rompolt, B.; Demoulin, P.; and Machado, M.E. 1993. Relationship Between Magnetic Field Evolution and Flaring Sites in AR 6659 in June 1991. *Solar Physics* 150:199.

Silva, A.V.R.; de Pater, I.; Lin, R.P.; McTiernan, J.M.; White, S.M.; Kundu, M.R.; Gary, D.E.; Hudson, H.S.; Hagyard, M.J.; and Doyle, J.G. 1994. Comprehensive Multi-Wavelength Observations of the 1992 January 7 Solar Flare. In Preparation.

Sponsor: Office of Space Science

• • • • •

Fractal Dimensions: Tools for Sunspot Magnetic Field Analysis

Mitzi Adams/ES82
205–544–3026

MSFC's solar group has traditionally examined data from the magnetic inversion line between opposite polarity sunspots to determine the likelihood of a solar flare. This type of analysis assumes that the energy to drive a solar flare is stored within the twisted magnetic field of the active region. The field has two components: one along the line of sight and one transverse to it. When the transverse component is aligned parallel to the magnetic inversion line, the field is said to be "sheared"—a highly stressed configuration that is the most probable state for the magnetic field just prior to a solar flare. One expects that as the flare occurs and energy is removed from the magnetic field of the active region, the amount of shear should decrease—the direction of the transverse component of the field should rotate from nearly parallel to the neutral line to more perpendicular—and its magnitude should decrease. However, the magnetic field associated with sunspots is not restricted to the area close to the neutral line. There may be other signposts in the field related to the flare event not detected by this analysis, but which may be detected with techniques of fractal statistics.

In the late 1970's, Benoit Mandelbrot created the term "fractal" to describe objects which are complex on their boundaries and have self-similar

subsections. These objects became a source of interest for the entertainment medium and, as such, have carried a stigma in the scientific community, where their validity for describing the physical world has not been understood. Recently, solar scientists from MSFC have joined with scientists from the University of Alabama in Huntsville (UAH) to develop a new tool for data characterization that uses fractal analysis statistics to look for changes in sunspot magnetic fields before, during, and after a solar flare.

Fractal objects may be characterized by their fractional (or fractal) dimension. While the concept of topological dimension is relatively familiar (a point has a dimension of zero, a line has a dimension of one, and a plane a dimension of two), the concept of fractal dimension may not be intuitively obvious. A collection of points and a jagged line provide excellent examples: the dimension of the collection of points is neither zero nor one, but somewhere in between; similarly, the jagged line's dimension would be between one and two. There are, however, many different methods of calculating fractal dimensions (table 7) that result in either an entropic or a morphological measurement. In general, a morphological fractal dimension describes the magnitude of the departure of data from a straight line, while the entropic method describes how much the data differs from white noise.

Although fractal analysis computer techniques have been developed only recently, the mathematical tools have been around for over 100 years. In 1890, David Hilbert described a very

TABLE 7.—*Methods of calculating the fractal dimension*

Compass Dimension	Divider Dimension
Box Counting	Grid
Column Counting	Mass
Length-Area	Percolation
Holder Exponent	Artificial Insymmetration Pattern
Phase-Space Morphing	Phase-Space Reconstruction
Liapunov Exponent	Radius of Gyration Exponent
Correlation Dimension	Maximum Entropy Method
R/S Analysis	ROSETA
Fixed-Point Hurst Coefficient	K Auto-Bin
Morphological Covering	FFT Fractal
Distribution Similarity	Spatial Hurst Coefficient

special type of curve which, given a patch of plane, meets every point in that patch. The idea of visiting every point in a plane may be extended to the analysis of image type data so that spatial correlation between pixels may be retained when converting a two-dimensional data set to one dimension, a necessary process for fractal analysis. After the data have been resequenced by the Hilbert method, H.E. Hurst's method of calculating the fractal dimension, range over standard (R/S) deviation, may be applied to study trends in the data. This type of analysis yields a global fractal dimension for the entire data set. For many applications, however, a local fractal dimension is desired. In this case, one applies a modified form of range over standard deviation analysis known as range over standard deviation experimental trend analysis (ROSETA). This algorithm divides the data set into partitions—sizes of which may be selected by the user—and determines a fractal dimension for each partition, thus producing a spectrum of fractal dimensions for the data set (fig. 47).

For the fractal analysis, MSFC/ University of Alabama in Huntsville researchers have calibrated data of a flaring active region obtained with a vector magnetograph on June 10, 1991. Over the course of the observing day, data were taken at 5-minute intervals, thus creating a unique record of the magnetic field. Figure 47 shows a

**Hurst Coefficient AR 6659
June 10, 1991**

FIGURE 47.—Hurst coefficients for 20 subsets of data.

spectrum of Hurst coefficients (related to the fractal dimension by $H = 2-F_D$) as calculated for the transverse component of the magnetic field for 20 partitions of the data. Note that from bin 0 to bin 6, there is very little change in the Hurst coefficient, which corresponds to little change in the transverse component of the sunspot's magnetic field. Between bins 6 and 17, however, the Hurst coefficient shows some variation and reaches a minimum value in bin 13. A Hurst coefficient that approaches 0.5 is an indication of purely uncorrelated data, white noise, or chaotic behavior. This bin containing the minimum Hurst coefficient corresponds to the location of the solar flare on the image. MSFC and UAH scientists are studying the relative changes of this feature with time to answer the questions: Is there a value of the Hurst coefficient that is correlated with the amount of energy released in the solar flare? Is there a relationship between the value of the Hurst coefficient and the probability of the occurrence of a solar flare? To answer these and other questions, this new fractal analysis tool will be applied to many other data sets, leading to a better understanding of sunspot magnetic fields and solar flares.

Sponsor: Office of Space Science

University Involvement: University of Alabama in Huntsville

• • • • •

Space Weather, Solar X-Ray Imaging, and Advanced Detector Development

John M. Davis/ES82
205-544-7600

Although space is commonly thought of as being empty, it is, in reality, filled with charged particles and magnetic fields that are mostly of solar origin. Both the particles and fields are capable of producing serious and damaging effects upon spacecraft and on man's activities on Earth. The study of these phenomena, with particular emphasis on predicting their occurrence and magnitude, is gaining in importance as space programs extend operations and as scientists better understand how the space environment can impact terrestrially based systems.

"Space weather" has its origin on the Sun. Solar flares (dramatic releases of energy in the solar atmosphere) can produce large fluxes of very energetic particles lasting for several days, giving rise to a radiation hazard for unprotected astronauts in high-latitude orbits or in interplanetary space, as well as radiation damage to spacecraft electronics. High-speed solar wind streams, originating from open magnetic field regions on the Sun, produce geomagnetic storms that generate large currents in the ionosphere. To close this circuit, return currents flow below or along the Earth's surface. These return currents can create havoc with electric power transmission grids and can increase corrosion in oil and gas pipelines. The

ionospheric currents frequently interfere with radio communications and can produce errors in satellite-based navigation systems.

The phenomena that lead to geomagnetic storms, solar flares, and coronal holes have signatures that can be observed in the solar corona, the outer layer of the Sun's atmosphere. The corona is a high-temperature, 2- to 3-million-Kelvin (K) plasma that radiates in the soft x-ray region of the electromagnetic spectrum. The soft x-ray emission can be imaged using space-borne telescopes, and the resulting images can be used to detect and locate the different types of phenomena. This information can then be used to provide an estimate of when their effects may arrive at the Earth. An instrument to make these observations, the Solar X-Ray Imager (SXI), is being developed for the National Oceanic and Atmospheric Administration (NOAA) to fly on one of the current series of geostationary operational environmental satellites (GOES).

The telescope consists of a grazing incidence mirror; a 12-position broadband filter wheel that selects various wavebands in the 6- to 60-angstrom (Å) region; a focal plane assembly consisting of a passively cooled, intensified, charge-coupled device (CCD) camera; and a high-accuracy Sun sensor for image navigation. These components are supported by, and enclosed within, a graphite/cyanate ester structure.

Since the phenomena the telescope is required to image cover the complete range of intensity of solar features, from the brightest (solar flares) to the dimmest (the quiet corona surrounding

coronal holes), special attention has been paid to maximizing the sensitivity at the long-wavelength end of the instrument bandpass where the dimmest features emit most strongly. This requirement affects the choice of the mirror coating and, more importantly, the detector, which should have a high quantum efficiency (QE) at the longer wavelengths of the bandpass. The quantum efficiency wavelength variation of the two candidate detectors, microchannel plates (MCP) and charge-coupled devices, are very different. Charge-coupled devices have very high quantum efficiencies (~1.0) at wavelengths shorter than 20 angstrom. As the wavelength increases, the efficiency falls off exponentially, approaching 0 at 40 angstrom and above. In contrast, microchannel plates have low efficiencies (< 0.1) at the shorter wavelengths. However, their quantum efficiency rises steadily with increasing wavelength, reaching a plateau at 0.2 for wavelengths greater than 20 angstrom. Because the geostationary operational environmental satellite spacecraft places strict limits on the image exposure time, the microchannel plate approach, although more complicated (requiring high voltages and a vacuum enclosure to operate), was selected because of its increased sensitivity to the cool, dim coronal features.

The complete focal plane detector consists of the microchannel plate, which is optically coupled through a fiber-optic taper to a 512 by 512 array charge-coupled device used as a readout device. The optical taper is also used to expand the image to match the plate scale in the focal plane to the scale of the coupled device's pixel. The charge-coupled device is

passively cooled using an external radiator to suppress thermal noise during the longer exposures.

Once the basic elements of the optical train are selected, it is possible to perform a sensitivity analysis. Researchers are developing software to implement this analysis with the goal of determining exposure times for the various coronal features so that these can be checked against the spacecraft performance. The calculations require both a knowledge of how the solar output, as a function wavelength, varies with the temperature and density of the emitting structures, and how the instrument responds to these spectra. The sensitivity can be formulated as follows:

$$E_i = \frac{A}{4\pi\delta^2} \int_\ell \int_\lambda Ne^2(\ell)$$

$$P(\lambda, T(\ell))\, \varepsilon_i(\lambda)\, d\lambda\, d\ell$$

where E_i is the energy detected per pixel per second from a particular solar feature. The constant outside the integral is a geometric factor describing the collecting area of the mirror that feeds each pixel. The double integral represents the integration both along the line of sight (the solar corona is optically thin) and over all wavelengths. The three terms inside the integrals represent the emission measure, $Ne^2(\ell)$; the emitted power, $P(\lambda, T(\ell))$; and the instrument response, $\varepsilon_i(\lambda)$. The first two terms rely upon knowledge of solar and atomic physics and are derived using theoretical models. The instrument response is the product at each wavelength of the mirror-collecting area, the prefilter and filter transmissions, and the detector

quantum efficiency. Estimated and theoretical values of the instrument parameters have been used for the initial calculation. The results of these calculations indicate that the exposure times are consistent with the solar pointing environment provided by the geostationary operational environmental satellite spacecraft.

The proposed detector satisfies the requirements established for the Solar X-Ray Imager for both spatial resolution (5 arcsec pixel) and sensitivity. However, it falls short of the performance that would ideally be required for scientific observations. If the observations are to be useful for scientific research, they need improved spatial resolution, and, in fact, this is likely to become a requirement for the next-generation instruments. In this case, future Solar X-Ray Imagers could be used, in addition to their operational modes, to provide context observations for dedicated solar missions such as the High-Energy Solar Imager (HESI), which is part of NASA's Space Physics Division's Solar Connections Program.

Consequently, scientists are continuing efforts to upgrade and develop new detectors to meet these requirements, including both x-ray sensitive and intensified charge-coupled devices. For the former, concentration is on thinned, back-illuminated devices for improved long-wavelength response in large arrays (1k by 1k, as a minimum) with a pixel dimension of 15 microns, providing a combination of low-noise and full-well depth to give a dynamic range of 2,000. For the hybrid-intensified charge-coupled devices, researchers are seeking microchannel

plates with smaller pore sizes to improve spatial resolution but still retain adequate dynamic range.

The most suitable candidates are being configured for flight testing as components of a sounding rocket payload. The payload can support two detector camera combinations that can be inserted into the focal plane of a grazing incidence telescope during flight. Flight opportunities occur approximately every 12 months.

∙ ∙ ∙ ∙ ∙

Solar Convection Zone Dynamics

David H. Hathaway/ES82
205-544-7610

The solar convection zone comprises the outer 30 percent of the Sun. The energy generated by nuclear fusion within the Sun's core is carried outward by convective fluid motions within this zone. How convection transports this energy is important for understanding the structure of stars and their evolution. For the Sun, at least, the convection does much more than just transport energy. Convective motions can also transport angular momentum and magnetic fields. Both of these processes are thought to play an important role in generating the Sun's magnetic field and in driving the 11-year cycle of solar activity.

Solar activity influences the Earth and near-Earth environments in many ways. Over the course of the last 11-year cycle, the total energy output of the Sun has varied by about one-tenth of 1 percent. At the same time, the ultraviolet output has varied by 3 to 4 percent, and emissions at higher energies have had even larger variations. Although the small change in the total output should not alter the Earth's climate by any appreciable amount, evidence suggests that variations might have been larger and more influential in the past. There is also evidence that other stars similar to the Sun exhibit even larger variations during their cycles. For certain, changes in the ultraviolet output of the Sun influence the formation of ozone in the stratosphere:

the more energetic emissions initiate major changes in the density of the Earth's uppermost atmosphere at spacecraft altitudes. During periods of solar maximum, the Sun flares and produces coronal mass ejections that can impact the Earth and produce a variety of harmful effects. Understanding and predicting solar activity is thus a major concern for both solar scientists and those concerned with the Sun's influence on Earth. Determining the nature of the fluid motions in the convection zone is thought to be the key for gaining that understanding.

Within the last two decades, several important discoveries about the Sun give great hope for ultimately understanding convection zone dynamics. Over 30 years ago, researchers found that the Sun's surface is in constant motion. Patches of the surface oscillate up and down within periods of about 5 minutes. In the early 1970's, scientists realized that these oscillations are actually sound waves produced by noisy convective motions trapped within the Sun by the structure of the Sun itself. These waves provide information about the inside of the Sun just like seismic waves in the Earth provide information about the inside of the Earth. Oscillation observations from Earth-based telescopes offer insight into the depth of the convection zone, its chemical composition, and about how the rotation rate changes from place to place within the convection zone. Analysis reveals that the convective motions redistribute angular momentum within the Sun so that the equatorial regions rotate more rapidly than the mid-latitude and polar regions.

More detailed observations are planned. Beginning this fall, the Global Oscillations Network Group (GONG) will start installing a network of six telescopes at widely dispersed positions around the Earth so that oscillations can be observed continuously. Next summer, NASA and the European Space Agency (ESA) will launch the Solar and Heliospheric Observatory (SOHO), which will carry several instruments to observe the oscillations from above the Earth's atmosphere. In the meantime, analysis techniques are under development for extracting new information about the Sun from these data.

Over the last several years, an analysis technique has been developed at MSFC for extracting information about the different types of flows on the surface of the Sun. Recently this technique has been applied to data obtained with a prototype Global Oscillations Network Group instrument at the National Solar Observatory in Tucson, Arizona.

Results indicate the presence of several interesting phenomena. The rotation of the surface layers is nonuniform and varies with time. The analysis confirms the solid body rotation and the differential rotation of the Sun while illustrating that the southern hemisphere rotated faster than the northern hemisphere in 1992. This asymmetry switched in 1993-1994, so that the northern hemisphere is now rotating more rapidly. Findings also reveal small, jet-like flows that may be associated with sunspots and other magnetic features.

The study further reveals the presence of a meridional circulation—a flow that carries fluid from the equator toward the poles in each hemisphere—and indications of changes over the 2-year period. In 1992, there was a secondary flow in which the surface flows converged at about 30° latitude. This flow disappeared in 1993 and now appears to have reversed so that the flows diverge in the mid-latitudes. Continuing observations should provide more detail about these flows and how they influence the Sun's magnetic field.

Current theories suggest that very large convective eddies, called giant cells, would be influenced by the Sun's rotation to produce the rapidly rotating equator and the Sun's magnetic field itself. Unfortunately, scientists have never been able to observe these giant cells, but one of the processes in this analysis program is designed to extract information on the spectrum of convective flows to determine the strength of the different sizes of convection cells. This spectrum is shown in figure 48.

The convection spectrum has a broad peak at wavenumbers of about 150, representing cells with diameters of about 30,000 kilometers that match the characteristics of the supergranulation cells discovered in 1961. These cells push the Sun's magnetic field elements to their borders, where the Sun's chromospheric network of hot emissions is formed. These cells are not believed, however, to produce the Sun's differential rotation or magnetic activity cycle—there is little or no

**Convection Spectrum
May 18, 1993–June 28, 1993**
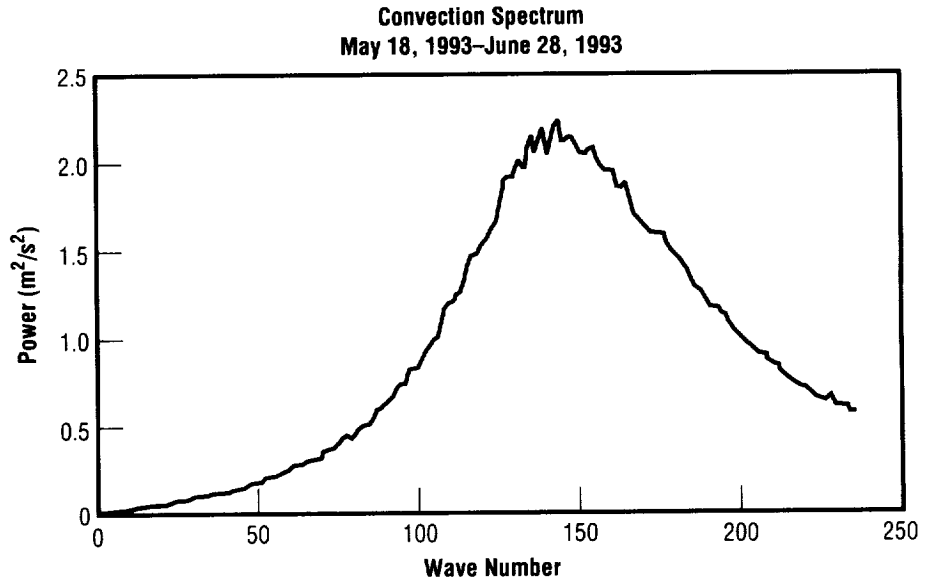
FIGURE 48.—Convection spectrum.

power in the larger cells as evidenced by the small signal at small wavenumbers. By reconstructing images of the large cells from the spectral information, findings suggest that even this signal cannot be due to giant cells. One must conclude that if giant cells exist, the flows they produce on the surface must be weaker than about 5 meters per second, as compared to the 300-meters-per-second flows in the supergranule cells.

Further work is planned with this analysis technique and with data from both the Global Oscillations Network Group and Solar and Heliospheric Observatory instruments. Although surface flows due to giant cells must be very weak, any discovery of a signal resulting from these cells provides important information on the

nature of the Sun's convection zone dynamics.

Hathaway, D.H. 1992. Spherical Harmonic Analysis of Steady Photospheric Flows, II. *Solar Physics* 137:15–32.

Sponsor: Office of Space Science

Industry Involvement: Global Oscillation Network Group of the National Solar Observatory

• • • • •

Solar Flares

Ronald L. Moore/ES82
205–544–7613

A solar flare is an explosion in the
solar atmosphere—an outburst of bulk
mass motion, plasma particle
energization, and radiation. The
greatest of these explosions sweep to
the far reaches of the solar system,
blasting out through the solar wind
and disrupting the magnetospheres
and ionospheres of planets.

All flares occur in regions of closed
magnetic field, straddling one or more
polarity inversion lines in the
magnetic flux on the Sun's surface.
Flares show a strong preference for
markedly nonpotential magnetic
fields, i.e., for fields that obviously
contain stored magnetic energy
because they are greatly deformed
from their minimum-energy, potential-
field configurations. Moreover, the
greatest flares occur in the largest
agglomerations of the strongest, most
highly nonpotential magnetic fields
found on the Sun—those rooted in the
large, impacted, opposite-polarity
sunspots exhibiting stark nonpotential
deformity. From these characteristics
of the magnetic field at flare sites, it is
widely held that a flare is an explosive
release of nonpotential magnetic
energy from the preflare magnetic
field. While there is little doubt that
the flare energy comes from the
magnetic field, the flare mechanism—
the physical process (or sequence of
processes) that works the explosive
conversion of magnetic energy into
mass motion, hot plasma, and

energetic particles—remains largely
unsettled. In other words, this
catastrophic conversion is the crux of
the flare problem.

During the past year, MSFC solar
scientists have found a promising new
candidate for the flare process by
which magnetic energy is dissipated
into plasma particle energy.
Researchers have come to this new
view of plasma energization in flares
by focusing on a particular
morphological class of flares known
as "two-ribbon, eruptive" flares. The
largest and most powerful flares are
usually of this type.

For two-ribbon, eruptive flares, there
is now a generally accepted picture for
the overall three-dimensional
magnetic field during the flare
(fig. 49)—a picture that has been
derived in part from previous flare
research with the MSFC vector
magnetograph. In this scheme, the
flare energy release is driven by the
eruption of a magnetic flux rope from
the sheared core of a closed bipolar
field. By its eruption and expansion,
the core flux rope works on the
surrounding envelope field of the
bipole, pushing up the top and
stretching the legs of this field arcade.
As the erupting flux rope vacates its
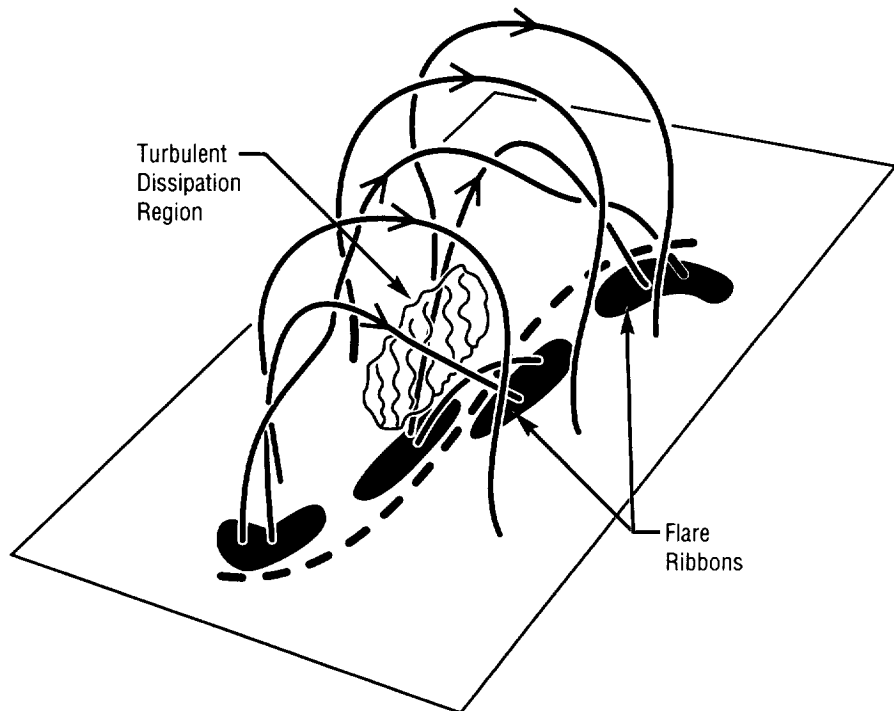
FIGURE 49.—Sketch of the erupting magnetic field and the turbulent
dissipation wall within it in the explosive phase of a
two-ribbon, eruptive solar flare.

preflare space in the core, the two stretched legs of the envelope cram together in this space and force reconnection at their interface. While it is generally accepted that this reconnection somehow yields the plasma particle energization in two-ribbon eruptive flares, there is no well-accepted model for this process. The main difficulty is that electrons with energies greater than or equal to 25 kiloelectron volts (KeV) must be produced at a very large rate ($\sim 10^{36}s^{-1}$) in order to provide the observed hard (≥ 25 kiloelectron volts) x-ray emission in the peak-power explosive phase of large flares. This is the well-established electron-bulk energization problem.

From the magnetic field and its reconnection in two-ribbon, eruptive flares, MSFC solar scientists have been led to the view that the reconnection region should be a thick sheet or curtain of magnetohydrodynamic (MHD) turbulence and that the explosive-phase electron bulk energization is accomplished in this turbulent wall. From this insight, a model for the production of the ≥ 25-kiloelectron-volt, explosive-phase electrons has been developed. Its main features are as follows:

• The dissipation region (fig. 49) is the interface between two crowds of oppositely directed, elementary flux tubes (each roughly 10^8 centimeters in diameter) that implode into each other in the vacancy left by the erupting core and then are strongly forced to reconnect.

• Magnetic energy of the reconnecting field is converted mostly into the bulk kinetic energy of the outflows from the reconnection sites because

the reconnection is strongly driven. For the same reason, the outflow is Alfvenic, and hence becomes magnetohydrodynamic-turbulent through shear-flow instability.

• The largest eddies of the turbulence have diameters of the order of the diameters of the reconnecting flux tubes ($\sim 10^8$ centimeters). The magnetohydrodynamic turbulence dissipates by cascading to small scales in one large-eddy turnover time (≤ 1 second).

• The magnetohydrodynamic turbulence dissipates at small scales ($\sim 10^5$ centimeters) by driving Fermi acceleration of the ambient electrons. The resulting bulk energization of the electrons to ~ 25 kiloelectron volts in each cascading large eddy produces an energy-release fragment of $\sim 10^{26}$ erg in ~ 0.3 seconds. These energy-release fragments match the observed subsecond spikey structure in the explosive-phase, hard x-ray burst. In the explosive phase of a large flare, the turbulent dissipation wall contains several hundred reconnection sites at each instant, enough to account for the $\sim 10^{29}$ erg/second power of the ~ 25-kiloelectron-volt electrons required to produce the observed flux of ~ 25-kiloelectron-volt hard x rays.

LaRosa, T.N., and Moore, R.L. 1993. A Mechanism for Bulk Energization in the Impulsive Phase of Solar Flares: MHD Turbulent Cascade. *Astrophysical Journal* 418:912.

LaRosa, T.N.; Moore, R.L.; and Shore, S.N. 1994. A New Path for the Electron Bulk Energization in Solar Flares: Fermi Acceleration by Magnetohydrodynamic Turbulence in Reconnection Outflows. *Astrophysical Journal* 425:856.

Moore, R.L., and Roumeliotis, G. 1992. Triggering of Eruptive Flares: Destabilization of the Preflare Magnetic Field Configuration. *Eruptive Solar Flares*, 69 (Svestka, Z.; Jackon, B.V.; Machado, M.E., editors), Springer-Verlag, Berlin.

Sponsor: Office of Space Science

A ROSAT Search for Coronal X-Ray Emission From Cool Magnetic White Dwarfs

Jason G. Porter/ES82
205-544-7607

White dwarfs have been known to be sources of x-ray emission since the detection of soft x rays from Sirius B, a hydrogen-rich (DA) white dwarf, in 1975. Since then, the Einstein, EXOSAT, and ROSAT observatories have found that quite a few single, hot DA stars are x-ray sources. In all of these cases, the best explanation for the origin of the x rays is not a hot corona surrounding the star (as in the Sun). Rather, the observed x-ray emission is produced in the hot layers just below the photosphere (the surface of the star in visible light). This mechanism works for DA stars with effective temperatures greater than 25,000 Kelvin (K) because the optical depth for soft x rays is much less than unity through the photospheres of such stars, so that thermal x rays of subphotospheric origin can freely escape into space.

However, theories of convection and wave generation in stars indicate that, for cooler DA stars with magnetic fields, hot coronae may be generated. The mechanism suggested is similar to the one believed responsible for the coronae surrounding cool, main sequence stars like the Sun. The x-ray emissions observed from nonbinary, nondegenerate cool stars are believed to be caused by the dissipation of nonradiative energy. A detailed explanation of how this energy is supplied to the atmosphere remains one of the long-standing puzzles of stellar astrophysics, but all of the suggested mechanisms have in common an interplay between convective motions and the magnetic field of the stars. Energy may be transported from the convection zone within the star to the stellar surface and then further to the outer atmosphere by magnetohydrodynamic (MHD) waves, or slow distortions of the surface fields by the movement of the field-line "footpoints" due to convective flows may lead to energy storage and transient release and, consequently, heating in the outer atmosphere. Observations of late-type stars show that if convection is not present, because the effective temperature is too high, then x rays are not detectable. A well-known example of this effect occurs in the A stars: the hotter members of the class (through about A5) show no evidence of x-ray emission, while the cooler A stars do. The data also demonstrate that the level of coronal activity is strongly correlated with the stellar rotation rate—higher x-ray fluxes are associated with higher rotation rates. This suggests that both convection and rotation are prerequisites for generating the coronal x rays observed from late-type stars. In current models of coronal activity, researchers assume that the coupling of rotation and convection can lead to a magnetic dynamo action. The resulting magnetic fields rise to the stellar surface through magnetic buoyancy and then interact with the fluid motions at the top of the convection zone by one or both of the mechanisms suggested above; as a result, coronal heating occurs.

One can, therefore, surmise that DA stars having both surface magnetic fields and convective zones should be sources of coronal x rays. The magnetohydrodynamic wave mechanism is the one suggested for DA stars—essentially, magnetohydrodynamic waves are generated by convective flows "jiggling" the magnetic field lines. The scenario for white dwarfs is like that for the main sequence stars, except that the observed magnetic fields of white dwarfs and those of late-type, main sequence stars are believed to have quite different origins. Researchers are fairly certain that any fields observed in white dwarfs are relics from the earlier stages in the life of these stars, rather than products of ongoing dynamo action. In general, no dynamo action in white dwarfs should be expected because observations show that they are very slowly rotating (often virtually static) stars.

Most DA stars with temperatures greater than 18,000 Kelvin have convective zones. (Furthermore, in such cool stars, one cannot expect to see any subphotospheric contributions to the soft x-ray flux, so any observed x rays must be coronal in origin). The additional requirement for generating coronae is for the white dwarfs to have surface magnetic fields. The practical field strength limit for detection by measurements of circular polarization is approximately 10^6 Gauss. There are only about 30 presently known white dwarfs (2 to 3 percent of the total population) with measured magnetic field strengths at or above this threshold, but most of these are DA stars.

Simple order-of-magnitude estimates of the magnetohydrodynamic wave energy fluxes generated in the convective zones of these stars can be obtained from the theory of wave generation in strong magnetic fields. With the assumption that a given fraction of the generated wave energy is converted into x rays (the rest is either transferred into heat lower in the atmosphere or escapes into space), the resulting coronal x-ray luminosities can be found by integrating the wave energy fluxes over the stellar surfaces. A conservative estimate based on the coronae of active, late-type dwarfs places this fraction at about 10 percent. The x-ray luminosities obtained in this way are of the order 10^{27-28} ergs s^{-1} for DA stars with temperatures of 8,000 to 13,000 Kelvin. With the currently operating ROSAT observatory, x-ray emission of this order should be detectable for some nearby white dwarfs.

Previous satellite observations have been limited to (1) comparatively short-duration survey observations incapable of detecting faint sources and (2) a few longer-duration observations of a select group of stars, predominantly hot objects. In view of this, researchers proposed several years ago to begin a long-exposure search for x-ray emission from some nearby cool magnetic white dwarfs using the ROSAT observatory. This program of observations has now been completed. Observed stars include the nearby cool magnetic DA stars GD 90, GD 356, and KUV 2316+123. Despite the theoretical predictions, and although deep exposures were obtained, no significant x-ray fluxes were detected at the locations of these objects. Bayesian statistics (appropriate for the case of few source counts in a non-negligible background) were used to set upper limits to the x-ray fluxes. These upper limits will provide significant constraints to the required revisions of theories of magnetohydrodynamic wave generation and dissipation in stellar atmospheres, as scientists continue to try to explain these processes.

Sponsor: Office of Space Science

University Involvement: University of Alabama in Huntsville

• • • • •

ASTROPHYSICS

X-Ray Astronomy Research

Brian D. Ramsey/ES84
205-544-7743

Martin C. Weisskopf/ES01
205-544-7740

Development work continues on detectors for x-ray astronomy. Three balloon flight instruments are currently being built, each incorporating new techniques developed in-house and each based on gas-filled proportional counters.

The first of these, the Marshall Imaging X-Ray Experiment (MIXE) detector, utilizes special gas mixtures and construction materials to give improved energy resolution and extra-low backgrounds. In addition, it incorporates a novel microstrip electrode array, fabricated using integrated circuit photolithographic processes that greatly improve the detector performance over conventional (discrete-wire) proportional counters. An inhouse development program, coupled with facilities provided by outside vendors, has led to the production of very large area devices (30 by 30 centimeters) for the flight program. A proving flight is scheduled for spring 1995 from Alice Springs, Australia.

The second instrument is a hard x-ray imaging polarimeter that utilizes an intensified charge-coupled device (CCD) camera to image the photoelectron tracks produced by x-ray interactions. It makes use of a special kind of gas counter, an optical avalanche chamber, that produces extremely large quantities of light photons (> 10^7) under x-ray irradiation. Analysis of the initial ejection direction of the photoelectron permits a measure of the polarization of the incident x-ray photon. After extensive initial tests, a preliminary design of the flight instrument has been completed, and many of the components are either on order or in-house. The instrument is scheduled to be completed by late 1995.

The third instrument, a hybrid detector, couples the optical avalanche chamber to a sodium iodide/cesium iodide phoswich detector. The addition of the gas detector provides enhanced response at low energies, as the chamber emits thousands of times more light than the scintillators. At high energies, the gas becomes transparent and the x-ray photons are registered in the crystal (as with a conventional phoswich detector). Both sections of the hybrid are read out with a common set of photomultiplier tubes under the crystals. The net result is a broadband instrument with high sensitivity. A half-scale model is currently being used to optimize the design and determine performance characteristics.

To date, flight experiments have been flown on a gondola in collaboration with the Harvard College Observatory, but work is underway to develop an MSFC gondola. This will incorporate a novel pointing system, the heart of which is an attitude determination technique based on the Global Positioning System. By determining the relative x, y, and z positions of several antennae around the gondola, the true orientation of the gondola can be ascertained and folded into the control loop to give pointing accuracy at the few-arc-minute level. The in-house gondola is scheduled for completion in mid-1995.

Various research projects support—or have spun off of—the balloon flight programs. Typical of these is the development of extensive software tools to model all aspects of photon (and subsequent charged particle) interactions within the detectors. These programs have recently shown the importance of modeling photoelectron tracks in gas detectors if true response matrices are to be developed for instrument calibration. A second example is the development of a liquid xenon proportional counter using techniques developed for gaseous detectors. Liquid xenon is very attractive as an absorption medium as it is 500 times more dense than the gas, and hence offers much greater absorption capabilities. This large increase in density also has the potential of resulting in much-improved spatial resolution and enhanced energy resolution. A small prototype chamber and associated gas liquification/purification system has recently been constructed and tests are underway.

The second observing run on a Sunyaev-Zel'dovich experiment is scheduled for mid-June at the Owens Valley interferometric telescope array. The Sunyaev-Zel'dovich effect, a spectral distortion of the primordial background radiation, offers a powerful probe of the cosmic distance scale and provides a measure of the size and age of the Universe. The novel instrument, developed mostly in-house, combines recent advances in microwave technology with existing

interferometers to provide a new approach to an exceptionally difficult measurement.

As a complement to the above experimental program, there is an active theoretical effort within the group that includes the calculation of high-resolution x-ray spectra from galaxy clusters through models for galaxy-cluster atmospheres. The goal of this research is to identify promising spectral diagnostics for cluster spectroscopy from such x-ray observatories as Advanced Satellite for Cosmology and Astrophysics (ASCA), Advanced X-Ray Astrophysics Facility (AXAF), and ASTRO-E. These diagnostics will help determine the basic properties of the cluster plasma, including temperature, density, and elemental abundances. Another goal of this research is to determine whether effects such as multiphase plasma flows, radioactive cooling, or plasma shocks by cluster merging possess unique quantitative spectral signatures.

A large body of software has been developed in support of the Advanced X-Ray Astrophysics Facility program that has widespread application, e.g., in the design of x-ray optics or the design and evaluation of imaging systems. One typical current application is the design of novel, continuously graded multilayers for broadband x-ray optics in the hard x-ray region. These multilayers are currently being developed for MSFC under the Small Business Innovation Research (SBIR) program and would be of use not only in astronomy, but in medical physics and x-ray photolithography.

Also in support of the Advanced X-Ray Astrophysics Facility program, a technique has been developed for in-situ monitoring of surface contamination of x-ray telescopes. This utilizes radioactive sources to measure the reflectivity at several wavelengths and offers many benefits over the traditional technique of witness samples.

Sponsor: Office of Space Science

• • • • •

Discovery of a Peculiar X-Ray Nova in Ophiuchus With the Burst and Transient Source Experiment

Alan Harmon/ES84
205–544–4924

In September 1993, a bright x-ray nova was discovered in the constellation of Ophiuchus (X-Ray Nova Ophiuchi 1993, GRO J1719–24 or GRS 1716–249) using the Burst and Transient Source Experiment (BATSE) on the Compton Observatory (figs. 50 and 51). The object was simultaneously detected by the Russian spacecraft GRANAT with the French SIGMA instrument. This object was visible for several months as a bright source whose intensity could be measured using the Earth occultation technique (see *Research and Technology 1992*) to relatively high energy (500 kiloelectron volts (keV)). It also exhibited a characteristic fast variability (1 to 10 seconds) that is thought to be associated with thermal or viscous instabilities in the accretion disk surrounding a black hole.

In *Research and Technology 1993*, researchers reported observations of another x-ray nova (X-Ray Nova Persei 1992, GRO J0422+32) which has a light curve typically resembling that of classical novae: a fast rise in brightness over a few days, followed by an exponentially decreasing intensity with a time constant (τ_{decay}) on the order of a month. Frequently, there is a brief recovery in brightness (called a secondary maximum), which

Source	τ_{rise} (days)	τ_{decay} (days)	τ_{1-2} (days)
4U 1543–47	2	2.5	70
GRS 1009–45	3	5	25
GRS 1124–68	<8	~10	140
GRO J0422+32	6	40	125
GRO J1719–24	5	~300	?

Time (Days)
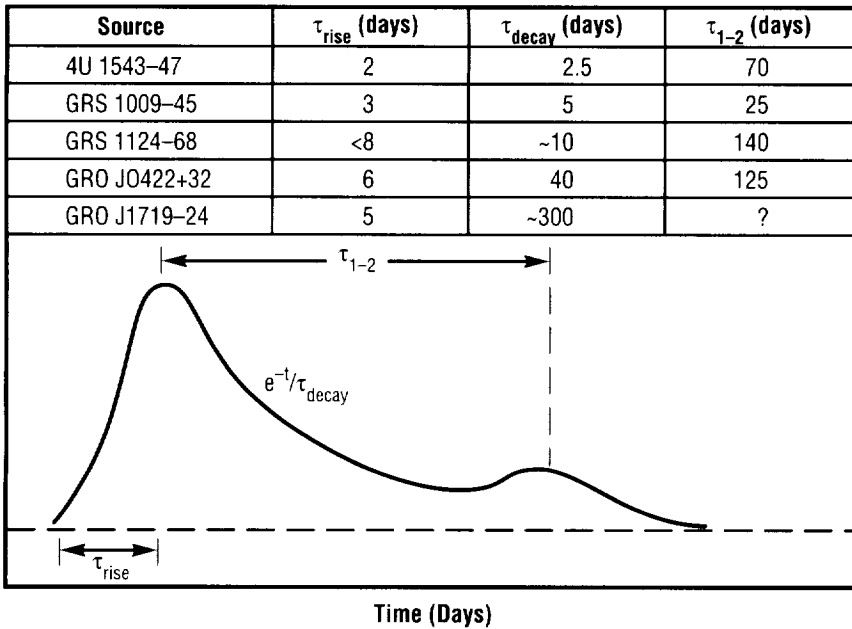
FIGURE 50.—The rise time (τ_{rise}), decay constant (τ_{decay}), and the time between first and secondary maxima (τ_{1-2}) for x-ray novae detected by the Burst and Transient Source Experiment. τ_{decay} was in excess of 300 days for GRO J1719–24, and no secondary maximum has been observed. The plot shows how these quantities are related to the light curve.
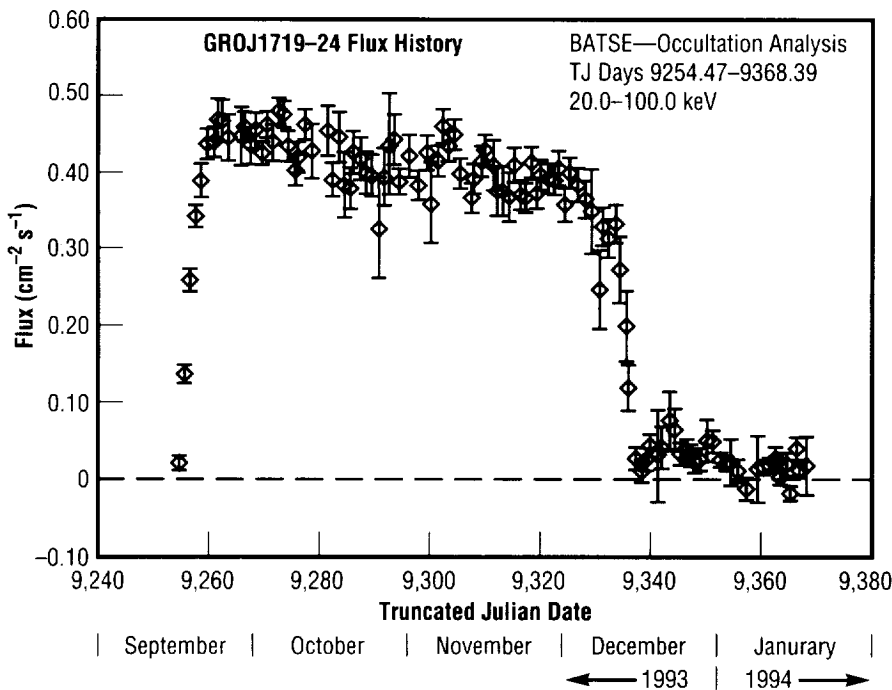
FIGURE 51.—The 20- to 100-kiloelectron-volt Burst and Transient Source Experiment light curve for GRO J1719–24 (X-Ray Nova Ophiuchus 1993).

is not well understood. The secondary maximum is followed again by a gradual decay. The object eventually returns to a quiescent state until another outburst occurs—anywhere from 1 to about 50 years. Very few x-ray novae have ever been seen to recur.

Because of its light curve, GRO J1719–24 is a very peculiar x-ray nova in comparison to others of its type. It had the typical rise time (τ_{rise}) of a few days; however, after a few weeks of observation, it was found that the intensity of the object was declining at a very slow rate of about 0.5 percent per day relative to its peak brightness. This corresponds to a τ_{decay} (assuming an approximately exponential decay) exceeding 300 days. Most other x-ray novae, particularly those observed at soft x-ray energies (1 to 10 kiloelectron volts), have decay constants averaging about 30 days, not showing much variation from one object to another. For x-ray novae detected by the Burst and Transient Source Experiment in the 20- to 2,000-kiloelectron-volt range, the decay constants for higher energy radiation vary greatly, ranging from 3 to 300 days, with GRO J1719–24 having the largest value.

The value of τ_{decay} is thought to be related to the size, mass, and geometry of the accretion disk as well as the rate of mass flow into the disk. The sudden increase in brightness of these objects is, in fact, thought to be caused by a large increase in mass accreting onto the black hole. Once matter reaches the accretion disk, viscous forces cause the matter to slowly spiral down into the black hole. The inner region

of the disk heats up, emitting x rays. The decrease in intensity of the x rays will reflect a gradual return to a normal quiescent state for the accretion disk. What makes GRO J1719–24 the most peculiar of all the x-ray novae detected by the Burst and Transient Source Experiment is the sudden drop in intensity in December 1993, over a period of about 1 week. No other x-ray nova has shown this behavior in the roughly 30-year history of high-energy astronomy. It is thought that the emission region, possibly in the innermost part of the disk, may have changed its character from being transparent to hard x rays and gamma rays, to becoming relatively opaque, even though less energetic radiation could still be present for months longer. Our understanding of these phenomena, and why GRO J1719–24 is so unusual, will require improvements of physical models of black hole accretion disks. The growing data base provided by the Burst and Transient Source Experiment all-sky monitoring should advance efforts to model such objects.

Sponsor: Office of Space Science

•••••

Gamma-Ray Flashes of Atmospheric Origin

Gerald J. Fishman/ES81
205–544–7691

The Compton Observatory was launched in April 1991 to perform observations of celestial gamma-ray sources. The Burst and Transient Source Experiment (BATSE) is one of four experiments on the observatory. It serves as an all-sky monitor and has detected over 1,000 cosmic gamma-ray bursts, several hard x-ray transients, numerous persistent and pulsed hard x-ray sources, and several thousand solar flares. In addition to these celestial sources, gamma-ray flashes from the Earth's atmosphere have been seen on rare occasions.

In order to be observable by orbiting detectors, the flashes had to originate at altitudes of at least 30 kilometers. At least a dozen events have been detected over the past 2 years. Several of the events seem to come from the direction of large weather systems, although concurrent weather imagery is not available in most cases. The energy spectra from the events are consistent with bremsstrahlung from energetic (MeV) electrons. The most likely origin of these high-energy electrons, while speculative at this time, is a rare type of high-altitude electrical discharge above thunderstorm regions.

Two unique features of these events are their extremely hard spectra and their short duration. These features are very distinct from other events that have triggered the Burst and Transient

Source Experiment detectors, such as gamma-ray bursts, solar flares, fluctuations of other known hard x-ray and gamma-ray sources, and bremsstrahlung from precipitating magnetospheric electrons. Furthermore, these events are located by the detectors as emanating from below the local horizon. Approximately half of the events consist of two closely spaced pulses, and one event has at least five distinct pulses of similar shape but variable spacing. Other independent detectors on another experiment on the Compton Observatory confirm these gamma-ray observations. The events are relatively rare, occurring less than once every 2 months. It is likely that other, weaker events of similar origin go undetected due to the trigger criteria implemented by the experiment. Sources of the flashes are located by comparing the relative responses of the eight Burst and Transient Source Experiment detectors which view different directions.

It is believed that prior instrumentation and experiments were incapable of detecting the phenomenon reported here for various reasons, or these events were overlooked as being spurious. Most detectors used in high-energy astronomy are collimated and would likely have missed these rare events. Typical temporal resolution of most experiments would not have been able to respond to these very brief incidents and/or would have had poor signal-to-noise when sampled with coarser time resolution. The observed counting rate ratios of the detectors are consistent with the source of these events originating from a large distance relative to the spacecraft dimensions. The time profiles of four of these
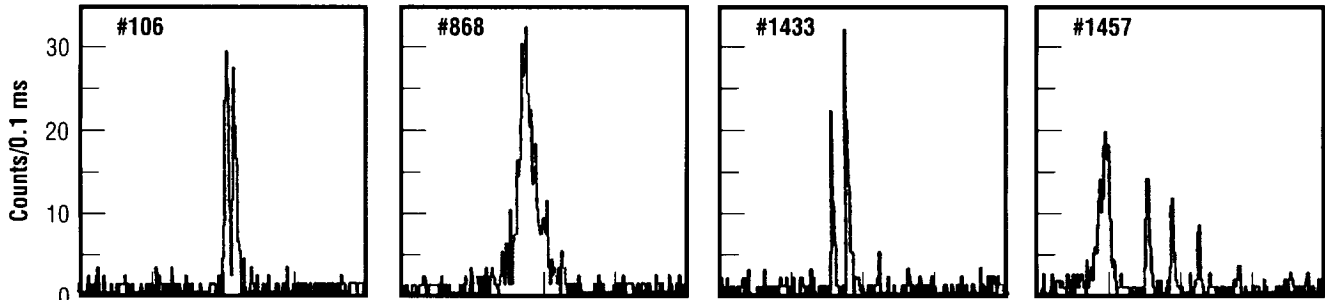
FIGURE 52.—Time profiles of four of the gamma-ray flashes. The time resolution of the plots is 0.1 millisecond per bin.

events are shown in figure 52. See also figure 53.

These gamma-ray events may be related to recently recorded optical discharge phenomena above thunderstorms and to other cloud-to-

stratosphere discharges that have been reported in the past. Numerous reports by aircraft pilots of upward discharges to the stratosphere have, in general, not been treated in the scientific literature. The possibility of runaway discharges above thunderstorms was

first discussed almost 70 years ago, as it was recognized that ionization from a lightning discharge could create a conducting channel for further current flow and lead to a "runaway" discharge to perhaps very high altitudes.

No prior references to gamma radiation from atmospheric electrical discharges or from electrons in the magnetosphere have been found in the literature. Because of the new and unique nature of these events, the lack of correlated observations in other spectral regions, and the paucity of concurrent weather data, determining the exact cause of the phenomenon requires further study.

Sponsor: Office of Space Science

• • • • •
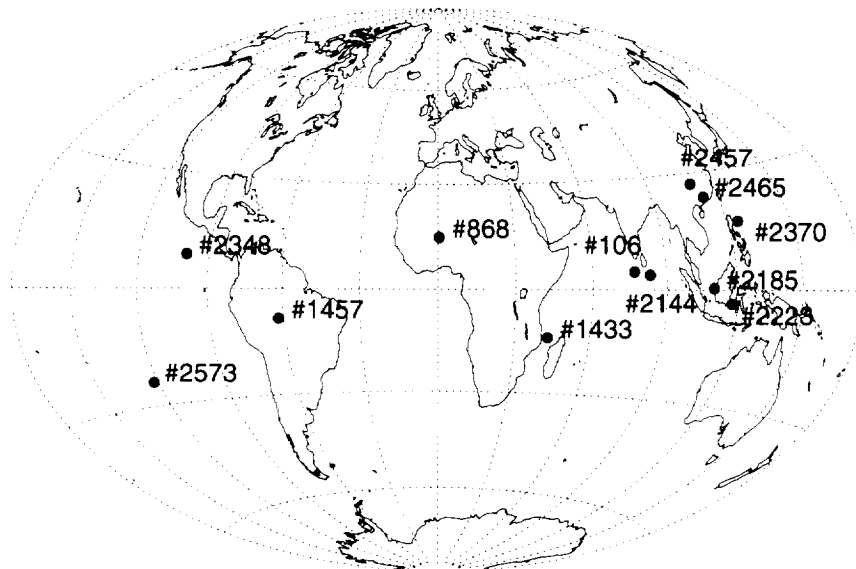
FIGURE 53.—The location of the events over the Earth appear to correlate with the location of enhanced thunderstorm regions. The spacecraft location is confined by its orbital inclination to latitudes below 28.5°.

Torque Studies of Her X-1

Robert B. Wilson/ES84
205-544-7695

The low mass x-ray binary system Her X-1, discovered using the UHURU spacecraft in 1972, has since been observed with some regularity by many additional spacecraft. The system exhibits 1.24-second pulses, due to the rotation of the neutron star (NS) in the system. It is in orbit (nearly circular) around an optically identified companion, a main-sequence B star. The orbital period of the system is 1.7 days. This places the companion so close to the neutron star that matter at its surface is not bound to it and spills across into a disk surrounding the neutron star. Material from the inner edge of this accretion disk joins the neutron star's magnetosphere and, following magnetic field lines, falls onto the neutron star's surface near the poles, releasing large amounts of energy due to the neutron star's very small (~10 kilometer) radius. This localized emission causes the pulses, similar to the pulses from the rotation of a lighthouse beacon.

The pulsed signal is interrupted every 1.7 days when the x-ray source is occulted by the companion. In addition, there is a modulation of the pulsed intensity that occurs within periods of approximately 35 days. Most models attribute this modulation envelope to obscuration by a tilted, precessing accretion disk. The start of the cycle is not a good "clock," with changes in the onset time of up to 2 days commonly observed. In spite of numerous observations prior to the
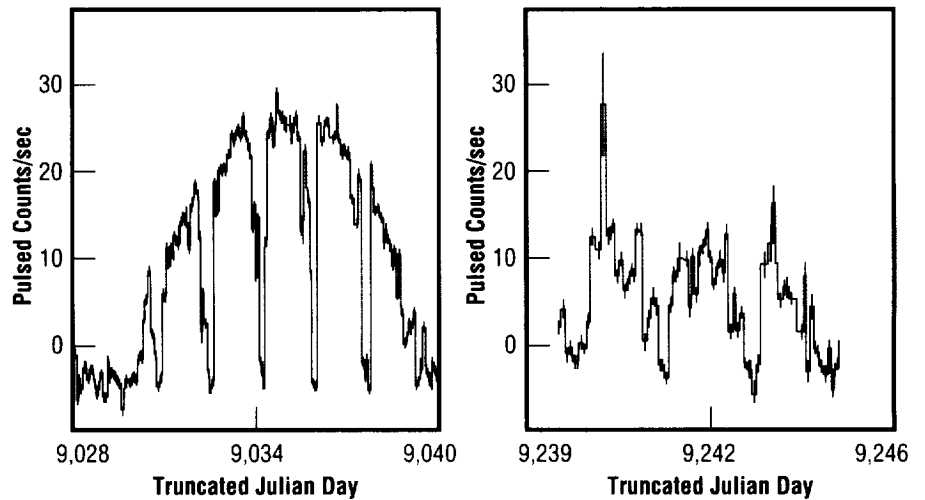
FIGURE 54.—Pulsed intensity of Her X-1 from the main-on portion of two different 35-day cycles, normalized to the same detector geometry. The eclipse of the x-ray source at 1.7-day intervals is evident. The measured source intensity at the peak differs by more than a factor of 2 between these examples.
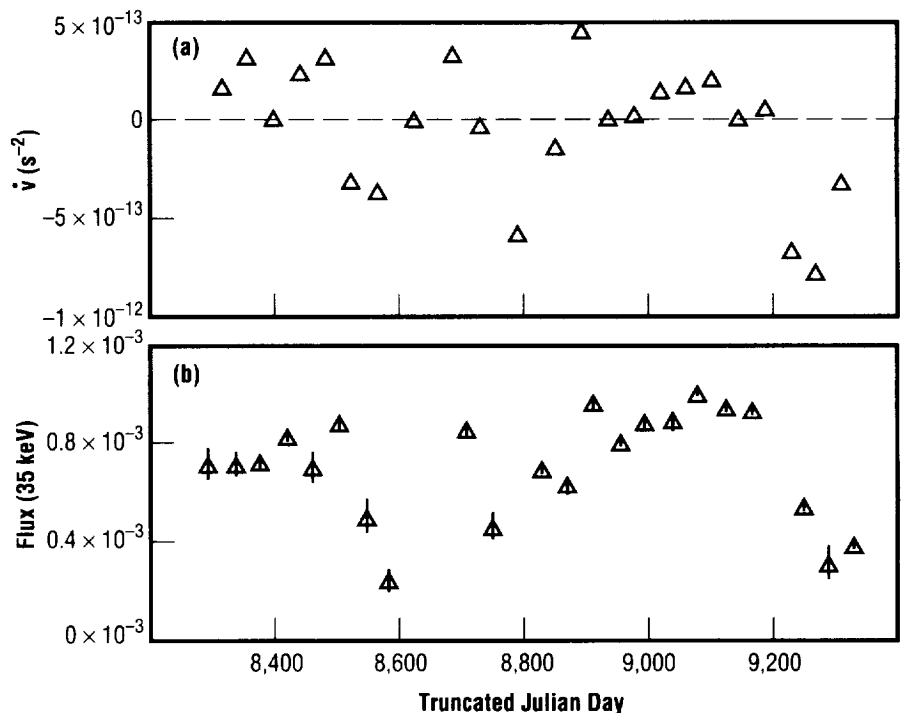
FIGURE 55.—(a) Frequency derivative history of Her X-1: an interval of 800 days is shown and three episodes of spin-down (frequency decreasing) are evident; (b) flux history of Her X-1: the observed source intensity at 35 kiloelectron volts is shown. (Note the similarity to the frequency history in (a)).

launch of the Compton Gamma-Ray Observatory (CGRO), the lack of continuity of observations has limited understanding of this long-term behavior.

The Burst and Transient Source Experiment (BATSE) instrument on the Compton Gamma-Ray Observatory has collected data for approximately 34 of these cycles, representing the longest duration coverage ever obtained by a single instrument and enabling a study of the relationship between source intensity and variations in pulsar rotation frequency induced by angular momentum transfer to the neutron star.

Figure 54 is a plot of pulsed intensity histories for two "main-on" portions of the 35-day cycle (emission is only detected by the Burst and Transient Source Experiment in the 20- to 100-kiloelectron-volt (keV) energy range during this portion of the cycle, lasting between 5 and 12 days). Characteristic of the source behavior in about 75 percent of the cycles observed, the intensity profile consists of a smooth envelope punctuated by eclipse intervals every 1.7 days. The intensity during the middle of the outburst appears to be somewhat flat-topped. If the tilted disk is the sole modulator of the pulsed intensity, the obscuration must be much different during the cycle portion (fig. 55).

Having used the arrival phases of the 1.24-second pulses to better determine the binary orbital parameters of this system, the average pulsar rotation frequency has been determined separately for each main-on interval. The rate of frequency change, proportional to the torque acting on the pulsar due to the mass accreting on
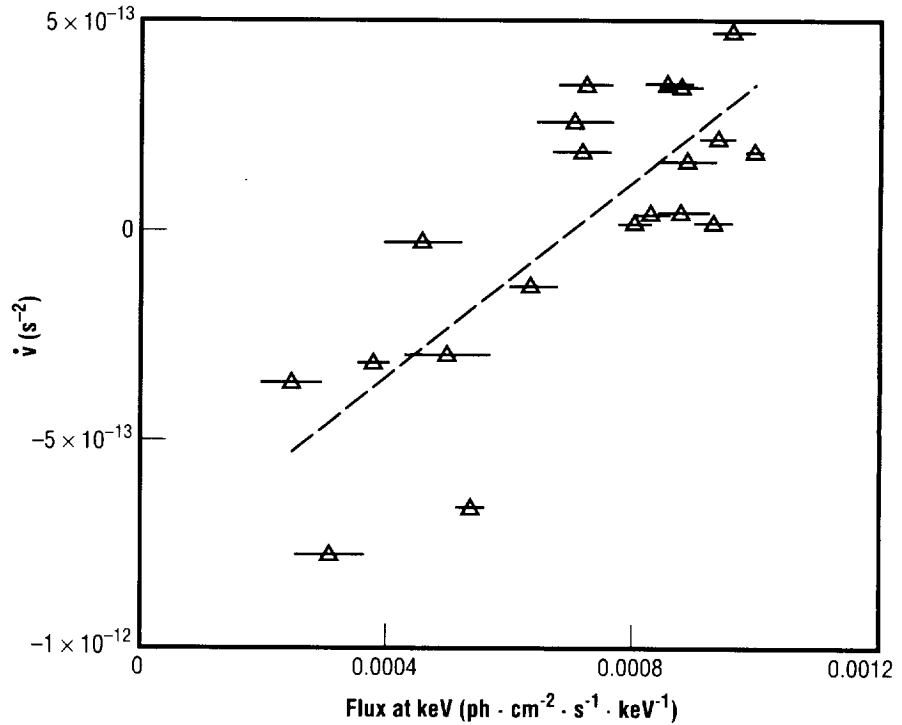
FIGURE 56.—Correlation plot of main-on source intensity versus the spin frequency derivative.

the system from the inner edge of the accretion disk, has been simply computed as the difference in observed frequency divided by the time difference between cycles. Figure 55(a) is a history of this spin derivative through the first 800 days of the mission. The source is ordinarily undergoing spin-up (increasing pulse frequency), with several episodes (near day numbers 8,600, 8,800, and 9,170) of spin-down.

Fluxes at the peak of each main-on outburst were determined by fitting an optically thin thermal bremsstrahlung spectral model. Figure 55(b) is a time history of the observed flux. Comparison with the frequency derivative history in figure 55(a)

shows that the source parameters are correlated; figure 56 shows this more directly.

If these changes in source brightness were due solely to disk obscuration effects, not actual source luminosity differences, no correlation would be expected between these parameters. This strongly implies that at the peak of each main-on, the hard x-ray luminosity is proportional to the rate of deposition of angular momentum onto the neutron star, and thus the mass accretion rate.

Sponsor: Office of Space Science

• • • • •

95

Scintillating Optical Fiber Ionization Calorimeter

Mark J. Christl/ES84
205-544-9496

The Scintillating Optical Fiber Ionization Calorimeter (SOFIC) is a novel detector for measuring the energy of high-energy cosmic-ray nuclei. This detector, developed by the Cosmic-Ray Group at MSFC over the past few years, will be flown on a high-altitude balloon in the spring of 1995 for a 1-day test flight.

The detector is well-suited for energy measurements of the cosmic-ray spectra from 10^{11} to 10^{13} electron volts (eV), a particularly important range because a change in the proton (hydrogen nucleus) spectral index has been reported in that range by several experimental groups. Questions remain as to the precise point at which this change occurs, because various measurements report it from 2×10^{12} to 40×10^{12} electron volts. A measurement of the change in the proton spectrum by this new and independent method will provide invaluable input into the theoretical models governing the source,
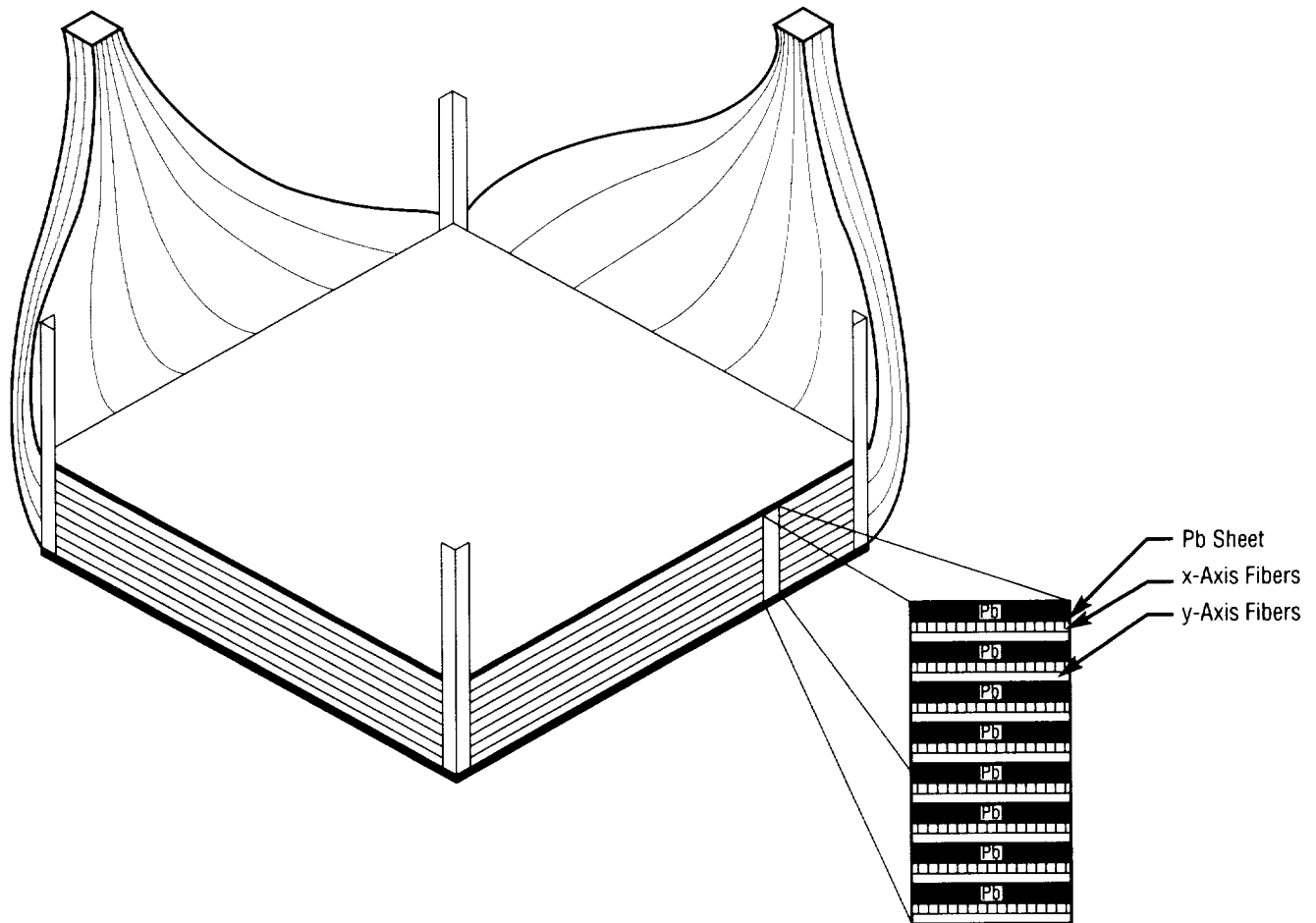
FIGURE 57.— A schematic of the Scintillating Optical Fiber Ionization Calorimeter detector design. The inset shows the configuration of lead sheets and two orthogonal layers (x, y) of scintillating optical fibers. The fibers from each axis are grouped together in a bundle where they are to be coupled to the image-intensified charge-coupled device camera system.

acceleration, and propagation of the galactic cosmic rays.

The detector (fig. 57) is made of 10 layers of lead plates and plastic scintillating optical fibers (SOF) stacked in alternating planes so that a stereoscopic view of the event can be retrieved. Four millimeters thick, the lead plates have an area of 50 by 50 centimeters. Two orthogonal layers of scintillating optical fibers, each containing 1,000 fibers laid side-by-side, are interleaved with the lead plates. The optical fibers—typically 1-meter long with a 0.5-millimeter-square cross section—are composed of a flexible plastic base and are doped with wave-shifting dyes to lower the self-absorption of the scintillation light. The outer surface is covered by a thin cladding (0.05 millimeters) with a slightly lower index of refraction. A significant fraction of the scintillation light is trapped in the fiber by total internal reflection at this boundary. When a charged particle traverses the fiber, a small amount of its ionization energy loss is converted to scintillation light by the doped fiber. This light is then piped along the axis to the end of the fiber where it is collected and recorded by an optical imaging system consisting of image intensifiers and charge-coupled device (CCD) cameras.

This scintillating optical fiber calorimeter is only one of the components that will be flown on the test flight. Two other detectors will be on the flight unit: a passive nuclear emulsion chamber and an electronic counter (for triggering on relativistic cosmic-ray events) that consists of a Teflon Cherenkov radiator viewed by six photomultiplier tubes. The nuclear emulsion chamber will provide a cross-check on the primary particle's charge and energy.

When high-energy cosmic rays collide with a target nucleus in the detector, a number of secondary particles (mostly charged and neutral pions) are produced. The neutral pions decay into two high-energy photons (gamma rays) that travel in the same direction as the original particle. As these photons pass through the lead material in the detector, they convert into energetic electron-positron pairs. These pairs will lose some of their energy by radiating additional photons (bremsstrahlung) as they traverse the downstream lead plates, and this new generation of photons will subsequently produce more electron-positron pairs, resulting in a concentrated, detectable shower of charged particles. This cycle of pair production and photon emission will continue to divide the energy of the original photons among all of the showering particles. When the kinetic energy of the shower particles nears a critical value, the shower will begin to diminish because energy loss processes other than the pair-photon cycle will have begun to dominate below this critical energy. All of these particles constitute what is termed an "electromagnetic cascade" or "shower." The arrangement of the lead plates and scintillating optical fibers in the calorimeter will provide a three-dimensional representation of the cascade for each cosmic ray that interacts in the detector. The amount and distribution of light recorded by the imaging system represents a sample of the cascade. This recorded data can later be used to reconstruct each of the individual events detected during the flight.

The energy of a cosmic ray is estimated from the "size" of the cascade. The size is determined by comparing the measured data (i.e., light intensity versus depth in the calorimeter) with a set of "transition" curves that represent the average behavior of a cascade for a specific set of parameters: primary charge and energy, trajectory, detector configuration, etc. The transition curves used for the comparison are compiled from a large number of computer simulations of the cascade process (fig. 58). These simulations include all of the physical processes necessary to reliably determine how the cascade will develop in the detector. After assigning an energy to each cascade and identifying the corresponding charge of the cosmic ray with data from the other detectors (Cherenkov counter, etc.), the energy spectra can be determined. The energy scale of the measured cosmic-ray spectra is based on the energy assigned to each electromagnetic cascade, which is only a fraction of the total energy of the interacting cosmic ray. However, the slope of this measured energy spectra correctly represents the slope of the incident cosmic-ray energy spectra, and therefore only a shift of the energy scale is needed to obtain the true cosmic-ray energy spectra. The amount of the energy shift is obtained by using computer simulations to estimate, on average, the fraction of the incident energy released into the electromagnetic cascades for various classes of interactions in the detector. Other correction factors will account for both the detection efficiency, as well as correcting for interactions that have occurred in the residual atmosphere above the balloon (~3 to 5 grams/(centimeter)^2).

Number of Events: 10
Incident Particle: Proton
E = 10.0 TeV Theta = 0 Degrees

O   Total
+   0.20 MeV
☆   0.50 MeV
◇   1.00 MeV
△   2.00 MeV
□   5.00 MeV
X   10.00 MeV

(Graph: Energy Dep (MeV) vs Depth (c.u.))

Number of Events: 10
Incident Particle: Proton
E = 0.5 TeV Theta = 0 Degrees

O   Total
+   0.20 MeV
☆   0.50 MeV
◇   1.00 MeV
△   2.00 MeV
□   5.00 MeV
X   10.00 MeV

(Graph: Energy Dep (MeV) vs Depth (c.u.))

FIGURE 58.—Simulation results for energy deposition in the Scintillating Optical Fiber Ionization Calorimeter for two different primary energies. The upper curve in each graph shows the total energy deposition in each layer of fibers, while the lower curves assume both a minimum (threshold) and maximum (saturation) detectable energy signal (Emax = 100 × Emin).

The development of the new detector has been possible because of the advances made in developing small scintillating optical fibers with good mechanical properties and larger optical attenuation lengths of more than 1 meter. An engineering flight on a high-altitude balloon should validate the design concept and its application to high-energy cosmic-ray studies. A detector based on the Scintillating Optical Fiber Ionization Calorimeter design may be utilized for future measurements in space with prolonged exposures to high-energy cosmic-ray particles.

Sponsor: Center Director's Discretionary Fund; Office of Space Science

University Involvement: University of Alabama in Huntsville

Industry Involvement: Bicron Corporation

• • • • •

Infrared Space Astronomy and Space Research

Charles M. Telesco/ES84
205–544–7723

In 1994, infrared (IR) astronomy at MSFC has focused on two research areas: (1) scientific and technical participation in the Infrared Space Observatory (ISO) program; and (2) the development of a new advanced infrared camera for astronomical and shuttle-related observations.

MSFC infrared astronomy efforts have continued to contribute to the development of the Infrared Space Observatory's spectrophotometer (ISOPHOT), a tool that will be one of the four infrared instruments to be flown aboard the European Space Agency's (ESA's) Infrared Space Observatory scheduled for launch in 1995—the next major infrared space experiment and the only one to be launched this decade. In 1994, negotiations were completed between NASA and the European agency to make NASA a full partner in the Infrared Space Observatory. MSFC responsibilities have included the definition and coordination of a broad range of astronomical observations to be carried out by the international team of scientists during their guaranteed observing time. Those planned observations include the search for the illusive substellar brown dwarfs and the determination of the energy output of some of the most distant galaxies in the Universe.

A major MSFC task is to establish the set of celestial objects that will serve as far-infrared photometric standards during the mission. To accomplish this task, MSFC astronomers carried out, in 1994, an extensive program of airborne and ground-based infrared observations using the NASA Infrared Telescope Facility (IRTF) in Mauna Kea, Hawaii, and the NASA Kuiper Airborne Observatory (KAO) to determine the spectral energy distributions of potential candidates. Extensive theoretical analysis and modeling of the data indicate, for the first time, that selected asteroids will be suitable photometric standards for the Space Observatory.

The MSFC mid-infrared camera, with 20 extremely sensitive bolometer detectors, has been operational since 1985. This camera has permitted a broad range of astronomical observations at major observatories. In 1994, this camera was used primarily to support the establishment of the in-orbit calibration sequence by obtaining ground-based infrared photometry of asteroids.

Development of an advanced, high-speed mid-infrared camera and spectrometer is nearing completion. This cryogenically cooled detector system—which will be an extremely versatile instrument using a state-of-the-art, arsenic-doped silicon detector array containing 10,000 pixels—will permit rapid imaging with very high spatial resolution as well as multi-resolution spectroscopy. In addition to its use for astronomical observations, this new camera will provide ground-based imaging of the orbiting shuttle so that we may better understand the environment of the shuttle during its

missions. The first field operation is scheduled at the Infrared Telescope Facility in the fall of 1994.

Telesco, C.M. 1993. Strong Limits on the 20-micrometer (μm) Emission From the High-Redshift Galaxy Infrared Astronomy Satellite (IRAS) 10214+4724. *Monthly Notice of the Royal Astronomical Society* 263:L37–39.

Telesco, C.; Schulz, B.; Campins, H.; and Osip, D. 1993. (2060) Chiron. International Astronomical Union (IAU) Circular 5898.

●●●●●

MICROGRAVITY SCIENCE AND APPLICATIONS

Kinetics of Diffusional Droplet Growth in a Liquid/Liquid Two-Phase System

Donald O. Frazier/ES01
205-544-7825

The objective of this work is to improve the understanding of diffusion-based droplet coarsening during phase separation and evolution of microstructure in two-phase systems. Experimental studies support the development of models that predict the evolution of structure. A transparent metal model system, succinonitrile/water (SCN/H_2O), allows direct observation of the events of interest. The succinonitrile/water system has an isopycnic point (the temperature where the densities of the two fluid phases are equal) near 42 °C and offers the opportunity to perform experiments on the ground, where gravity-driven sedimentation/buoyancy can be greatly reduced. However, even at the isopycnic point, gravity still influences mass transfer. As droplets grow and shrink, concentration gradients (and thus density gradients) form, which can lead to gravity-driven convective flows.

Experiments performed using two droplets will demonstrate gravitational influences. Varying the density difference between the two phases or changing the relative positions of the two droplets alters the effect of gravity on the rate of mass transfer. The magnitude of gravitational effects on droplet growth will be assessed first by performing experiments at different temperatures to vary the density differences. These experiments will also allow direct examination of the effects of curvature on droplet solubility for comparison with predictions from the Gibbs Kelvin equation. Information from these ground tests will be useful in the design of a flight experiment to study diffusional growth in microgravity.

Additional efforts include continued measurements of droplet size histories from quench experiments and refinements to the computer model that predicts droplet size distributions.

Glicksman, M.E.; Fradkov, V.E.; Mani, S.; Rogers, J.R.; Downey, J.P.; Witherow, W.K.; Facemire, B.R.; and Frazier, D.O. Coarsening of Three-Dimensional Droplets by Two-Dimensional Diffusion, Part II—Theory. Submitted to *Journal of Electronic Materials*.

Rogers, J.R.; Downey, J.P.; Witherow, W.K.; Facemire, B.R.; Frazier, D.O.; Fradkov, V.E.; Mani, S.; and Glicksman, M.E. Coarsening of Three-Dimensional Droplets by Two-Dimensional Diffusion, Part I—Experiment. Submitted to *Journal of Electronic Materials*.

Sponsor: Office of Life and Microgravity Sciences and Applications

University Involvement: Renasselaer Polytechnic Institute; National Research Council

• • • • •

Polydiacetylenes for Nonlinear Optical Applications

Donald O. Frazier/ES01
205-544-7825

One very promising class of organic compounds for nonlinear optical (NLO) applications is polydiacetylenes, which are novel in that they are highly conjugated polymers that can also be crystalline.[1] Polydiacetylenes offer several advantages over other organic materials: (1) because of their highly conjugated electronic structures, they are capable of possessing large optical nonlinearities with fast response times; (2) because they are crystalline, they can be highly ordered, which is essential for optimizing their nonlinear optical properties; and (3) because they are polymeric, they can be formed as thin films, which is useful for device fabrication. Researchers have actively been carrying out ground-based research on several compounds of interest.

The team has also been investigating a polydiacetylene derivative of 2-methyl-4-nitraniline (MNA), a well-known nonlinear optical material, for both second- and third-order nonlinear optical applications. Computations performed on this compound indicated that it should have large optical nonlinearities. Researchers have synthesized the compound and prepared thin crystalline films using vapor deposition techniques that exhibit good second harmonic generation. Because epitaxial growth

is often not possible for diacetylenes,[2] the effects of ordered polymer substrates—such as Teflon™ on the orientation and nonlinear optical properties of these films—is being investigated.[3] Indeed, the team has found that films grown onto oriented Teflon™ exhibit greater ordering and greater second harmonic generation (SHG) than those grown onto quartz glass under identical conditions.[4]

Most recently, researchers have developed a novel technique for preparing thin amorphous polydiacetylene films onto transparent substrates using photodeposition from monomer solutions.[5] Such films exhibit excellent third-order nonlinear optical behavior, degenerate four-wave mixing at 532 and 604 nanometers (nm), and give large χ^3 values on the order of 10^{8} to 10^{7} electrostatic units. This result is very exciting, as it demonstrates the tremendous potential of polydiacetylenes as nonlinear optical materials. Researchers intend to develop this method further and attempt to use techniques such as electric-field poling and substrate modification to induce orientation into the films (patent applications are pending).

It is well-known that gravitational effects, primarily buoyancy-driven convection and sedimentation, can be detrimental to both crystallization and polymerization processes. In the polydiacetylene films grown by photodeposition from solution on Earth, small (micron-sized) particles formed by sedimentation of precipitated polymer from the bulk solution become embedded in the films due to convection. These particles act as scattering centers and

lower the optical quality of the films. In the diffusion-controlled regime of microgravity, because of the very low diffusion coefficients of polymers, the rate of formation and size of these particles would be greatly lessened, thereby improving the optical quality of the films. Researchers are scheduled to fly an experiment on CONCAP IV–03 in May 1995 to investigate this process. Additionally, experimental results on physical vapor transport of phthalocyanines, another organic nonlinear optical material, have demonstrated that microgravity growth yields films with improved ordering and different crystal morphologies than films grown in one-gravity.[6] The team expects similar results for polydiacetylene thin-film growth and intends to conduct both ground-based and flight experiments in this area.

[1]Chemla, D.W., and Zyss, J. (eds.) 1987. *Nonlinear Optical Properties of Organic Molecules and Crystals,* *Vol. 2.* Academic Press: Orlando, FL.

[2]Thakur, M., and Meyler, S. 1985. *Macromolecules* 18:2341.

[3]Wittman, J.C., and Smith, P. 1991. *Nature* 352:414.

[4]Paley, M.S.; Frazier, D.O.; McManus, S.P.; Zutaut, S.E.; and Sangahadasa, M. 1993. *Chemistry of Materials* 5:1641.

[5]Paley, M.S.; Frazier, D.O.; Abdeldeyem, H.; and McManus, S.P. *Chemistry of Materials.* Submitted.

[6]Debe, M.K.; Poirier, R.J.; Erikson, D.D.; Tommet, T.N.; Field, D.R.; and White, K.M. 1990. *Thin Solid Films* 186:257.

Sponsor: Office of Life and Microgravity Sciences and Applications

Other Involvement: University of Alabama in Huntsville; Universities Space Research Association

• • • • •

Electromagnetic Field Effects in Semiconductor Crystal Growth

Martin P. Volz/ES75
205-544-5078

Convective flows in all Earth-based solidification experiments are usually unavoidable. In single species liquids, convection is the result of thermal buoyancy; in multiple species, liquid convection can result from either thermal buoyancy or solutal buoyancy. In general, the potential for convective flows scales with the well-known Rayleigh number

(1)

$$N_{Ra} = \frac{\beta_T g\,(\Delta T)\,L^3}{D_T \nu}$$

where β_T is the coefficient of thermal expansion, g is the gravitational force, ΔT is the characteristic temperature difference in the system, L is a characteristic length in the system, D_T is the thermal diffusivity, and ν is the kinematic viscosity. One way to raise the critical Rayleigh number is by applying an external magnetic field. The ability of external magnetic fields to dampen convective flows has been demonstrated for a number of different semiconductor systems. Another way of influencing fluid flows in a semiconductor growth system is to use a combination of both electric and magnetic fields. Indeed, it should be possible to combine electric and magnetic forces in such a way as to induce forced convection in the melt, replace unsteady natural convection, and provide for a more uniform

thermal and solutal layer in front of the solid-liquid interface. The specific objectives of this work are to investigate the effects that combined electric and magnetic fields have on gravitationally driven, fluid-flow processes during the bulk growth of selected semiconductor alloys and to examine the criteria for the onset of thermal instability as a function of electric, magnetic, and gravitational field strength in electrically conducting liquids.

A rectangular growth cell has been built and is shown schematically in figure 59. The two sides of the cell are made from graphite, and electric current passes between them through the melt. The growth cell is placed inside a four-zone Bridgman-Stockbarger furnace. Both the cell and furnace sit inside a transverse electromagnet with a maximum field strength of 0.5 Tesla. The applied magnetic and electric fields are perpendicular to the gravity vector.

In-situ temperature measurements have been made in indium antimonide (InSb). A thermocouple was placed inside a quartz sheath and then placed inside the molten semiconductor. One result is that when the cell is in a destabilizing thermal environment (hotter on the bottom and colder on the top), a magnetic field of approximately 0.04 Tesla is sufficient to suppress the time-dependent convection flows. Experiments have also been carried out with both magnetic and electric fields applied. In this situation, forced convection is observed, and the flows are, in general, time-independent. The forced convection may result from asymmetries in either the applied electric or magnetic fields.
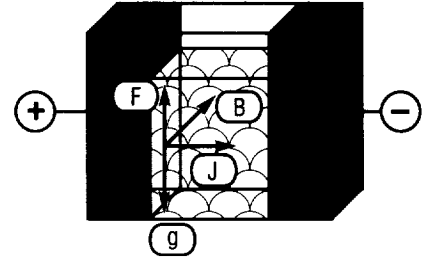
FIGURE 59.— Schematic diagram of the growth cell. Electric current passes from left to right through the melt. The direction of the magnetic field is into the paper, and the resultant electromagnetic force is up, in the opposite direction as gravity.

Temperature transients in the melt have been measured. If the magnetic field is already on, the application of current through the melt causes a sudden change in temperature at the thermocouple position. If hotter fluid flows toward the thermocouple, the temperature rises, and if colder fluid flows toward the thermocouple, the temperature drops. Using this method, an approximate map of the fluid flow has been made. At the beginning of a transient (fig. 60), the slope is expected to be linear and follow the relation:

(2)

$$\frac{dT}{dt} \sim k\frac{E}{B}\left(1 - e^{-\frac{\sigma}{\rho}B^2 t}\right),$$

where k is the initial thermal gradient at the thermocouple position, E and B
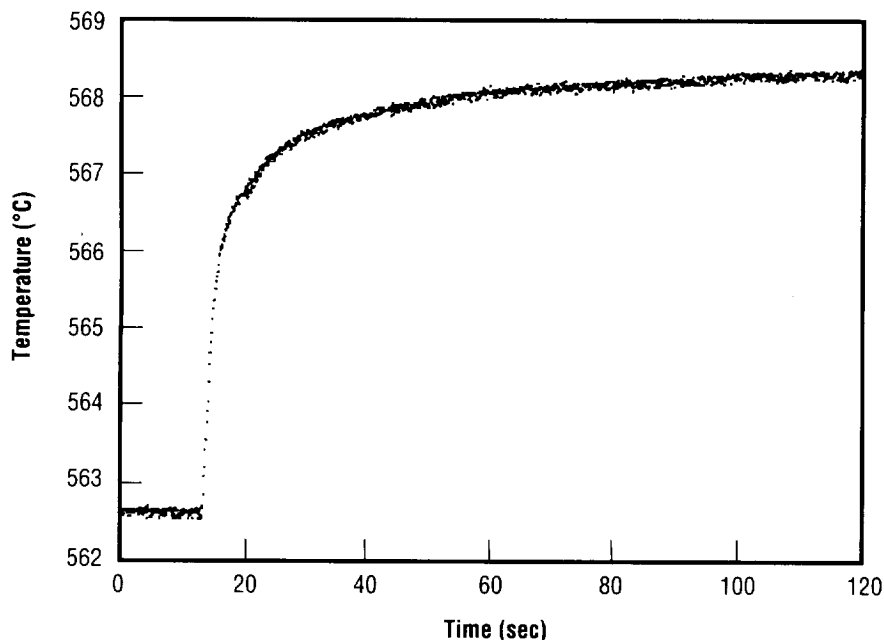
FIGURE 60.—Typical temperature transient induced by electromagnetic fields.

Prediction of Nonlinear Optical Properties of Organic Materials

Craig E. Moore/ES75
205–544–7585

To allow screening of potential nonlinear optical (NLO) organic compounds, researchers have developed a procedure to predict second- and third-order polarizabilities of organic materials that, within families of compounds, is accurate within 25 percent of the experimental values. This will facilitate nonlinear optical research by limited synthesis of new compounds to those most likely to exhibit appropriate properties. The procedure is as follows:

(a) Using a semiempirical Hamiltonian (AM1), the polarization of the molecule is calculated in the presence of 252 static fields. AM1 has been chosen because it has a more realistic treatment of the nitro groups in aromatic molecules than other semiempirical Hamiltonians, such as MNDO. The MOPAC program has been modified to perform these calculations.

(b) The polarization versus static-field information is processed by the HYPER program, developed in-house to generate all required tensor elements using polynomial fits. The polynomial fits are performed from orders 4 to 18, and the numerical uncertainty of the values obtained is used as measure of the error on the

are the magnitudes of the electric and magnetic field, σ is the electrical conductivity, and ρ is the density of the melt. At longer times, the melt achieves thermal equilibrium and the temperature at a given position reaches a steady-state value.

Work is now under way to better quantify the relationship between the effective magnetic viscosity and the applied electromagnetic fields. Future plans also include growing a selected number of semiconducting alloys by both the Bridgman-Stockbarger method and the traveling heater method (THM). The effect that applied electromagnetic fields have on the diffusion boundary layer, the rate of solid phase accrual, the slope of the solid/liquid interface, and the resultant morphology of the grown crystals will be assessed.

Sponsor: Center Director's Discretionary Fund

• • • • •

prediction. The advantages of the HYPER program over the procedure implemented in MOPAC are twofold: it estimates the effect of numerical instabilities in the data and calculates terms related through Kleinman symmetry independently, so that adherence to this property may be evaluated.

(c) For third-order polarizabilities, a term approximating core effects is added, based on the number and type of atoms present. These core corrections were obtained from empirical fits using published experimental values.

(d) In order to allow comparison of predictions with experimental values, adjustments are made to dynamic fields. In the case of second-order polarizabilities, a "correction equation" has been developed based on p-nitroaniline published measurements. In the case of third-order polarizabilities, the correction used is based on the two-level approximation (ground and one excited state).

(e) Finally, the values are adjusted to account for intermolecular effects—solvent effects, in particular. For second-order polarizabilities, scientists obtained two empirical corrections as a function of the refractive index and the dielectric constant of the solvent based on p-nitroanaline data. For third-order polarizabilities, researchers have used empirical data on benzene.

Although the procedure, as it is, has been proven useful for materials scientists, from a scientific point of

view, parts d and e (i.e., accounting for dispersion and intermolecular effects) need further work. Researchers are currently working on developing a correction for dynamic fields based on the two-level approximation.

Cardelino, B.; Moore, C.; and Zutaut, S.; 1994. Prediction of Nonlinear Optical Properties of Organic Materials. NASA Conference Publication 3250:153.

Cardelino, B.; Moore, C.; Penn, B.; Tan, L.; Martinez, A.; Romero, E.; Clark, R.D.; Ballard, J.; and Sanghadasa, M. 1993. Molecular Design of the Nonlinear Optical Properties and Synthesis of Organic Molecules. Proceedings of the Science and Technology Alliance Materials Conference, Greensboro, North Carolina.

Frazier, D.O.; Moore, C.E.; and Cardelino, B.H. (eds.) April 1993. Microgravity Studies of Organic and Polymeric Materials. Proceedings of a workshop held in Huntsville, Alabama. NASA Conference Publication 3250.

Moore, C.E.; Cardelino, B.H.; Penn, B.; Sanghadasa, M.; Barr, T.A., Jr.; Frazier, D.O.; and Clark, R.D. Prediction of the Static Second-Order Polarizabilities of (2,4)-Dinitro-Substituted Benzenes. Submitted to Chemistry of Materials (American Chemical Society).

Sponsor: Office of Life and Microgravity Sciences and Applications

• • • • •

Growth of Solid Solution Single Crystals

Sandor L. Lehoczky/ES75
205–544–7758

Donald C. Gillies/ES75
205–544–9302

Frank R. Szofran/ES75
205–544–7777

Dale A. Watring/ES75
205–544–7032

Ching-Hua Su/ES75
205–544–7776

The objective of this study is to establish the effects of processing semiconducting, solid-solution single crystals in a microgravity environment on the metallurgical, compositional, electrical, and optical characteristics of the crystals. The alloy system being investigated is the solid-solution semiconductor mercury $(Hg)_{1-x}$ cadmium $(Cd)_x$ tellurium (Te), with x values appropriate for infrared detector applications in the 8- to 14-micrometer (μm) wavelength region (fig. 61). The study consists of an extensive ground-based experimental and theoretical research effort supplemented by flight experimentation where appropriate. The objectives of the ground-based research effort are to: (1) obtain the experimental data and perform the analysis required to define the optimum growth parameters for the flight samples; (2) quantitatively establish the characteristics of the alloy crystals grown in a one-gravity environment as a basis for subsequent comparative evaluations of the alloy
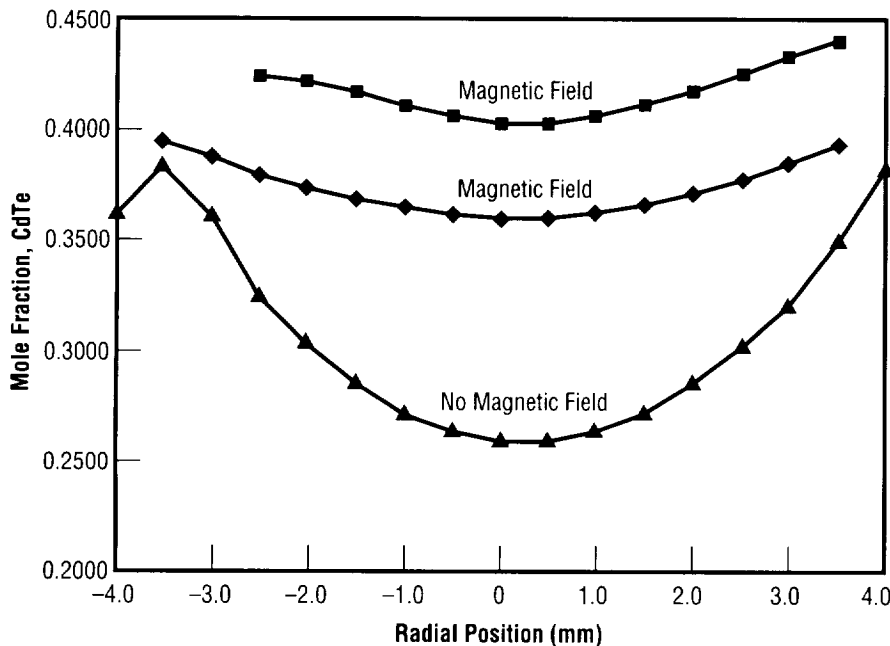
Figure 61.—Radial compositional profile for HgCdTe grown in the absence and presence of a stabilizing magnetic field.

crystals grown in microgravity; and (3) develop theoretical and analytical methods required for such evaluations. The ground-based portion of the investigation includes the evaluation of the relative effectiveness of stabilizing techniques, such as applied magnetic fields, for suppressing convective flow during the melt growth of the crystals.

The difficulty of growing bulk crystals, with both radial and axial homogeneity, of significant lengths in Earth's gravity is well documented. Because the mercury-tellurium-rich component rejected during solidification is more dense, the vertical Bridgman-Stockbarger growth process would appear to be both gravitationally and thermally stable against convection, but this is not generally true. Due to the relationships between the thermal conductivities of the melt, solid, and ampoule, it is practically impossible to avoid radial

temperature gradients in the growth region. In general, the presence of radial temperature gradients near the growth region causes a curvature in the solid-liquid interface which needs be neither an isothermal nor an isoconcentrational surface. Furthermore, the growth of high-quality crystals requires a slightly convex growth interface as viewed from the melt. Under the influence of stable growth conditions, such interface geometries readily lead to lateral alloy segregation because of the tendency of the more dense mercury-tellurium-rich liquid to settle at the portions of the surface having the lowest gravitational potential. Because the alloy solidus temperature decreases with increased mercury-tellurium content, the interface temperature will be lowered in this region, causing the interface curvature to increase. Although lateral diffusion will tend to drive the interfacial melt

compositions to some equilibrium values, most ground-based, melt-growth experiments show large radial compositional variations that are probably a direct consequence of such an interfacial fluid-flow phenomenon.

In low gravity, one expects that the highly desired, slightly convex growth surfaces will be easier to maintain because of the reduced tendency for stratification of the denser fluid component. At the same time, the near-elimination of radial temperature gradient-driven convection is expected to provide for better control of the lateral compositional distribution in the melts. It is thus expected that by growing under the influence of low-gravity conditions ($g \leq 10^{-6}g_0$), crystals with significantly improved crystallinity and compositional homogeneity can be prepared as compared to the best crystals that can be produced on Earth. It is also reasonable to expect that careful characterization of both the space- and ground-grown materials will lead to better insights into the peculiarities of the various growth mechanisms that will permit improvements in Earth-based processing of $Hg_{1-x}Cd_xTe$ and other compound semiconductor alloy systems.

It is generally believed that CdTe, $Hg_{1-x}Cd_xTe$, etc., probably possess extremely small yield strengths near their growth temperatures. If this is the case, the high dislocation density ($\sim 10^5$ centimeters^{-2}) usually seen in these crystals could be due, at least in part, to stresses induced by the sample's own weight, i.e., self-induced stresses. Therefore, a second goal of these experiments is to assess the validity of this hypothesis.

Over the past several years, a detailed evaluation has been performed on the effects of growth parameters on the axial and radial compositional uniformity, defect density, and optical properties in directionally solidified $Hg_{1-x}Cd_xTe$ and other similar compounds and pseudobinary alloys. A series of $Hg_{1-x}Cd_xTe$ alloy ingots ($0 < x \leq 0.6$) has been grown from pseudobinary melts by a vertical Bridgman-Stockbarger method using a wide range of growth rates and thermal conditions. Several of the experiments were performed in transverse and axial magnetic fields of up to 5 Tesla. Precision measurements were performed on the ingots to establish compositional distributions and defect density distributions for the ingots. Correlation between growth rates and thermal conditions and growth interface shapes has been established for the alloy system. To assist in the interpretation of the results and the selection of optimum in-flight growth parameters, the pseudobinary phase diagram ($0 \leq x \leq 1$), liquid and thermal diffusivities ($0 \leq x \leq 0.3$), melt viscosity, and the specific volumes as a function of temperature ($0 \leq x \leq 0.15$) have been measured. From these measurements and other available data, the heat capacity, enthalpy of mixing, and thermal conductivity of pseudobinary melts have been calculated using a regular associated solution model for the liquid phase. A one-dimensional diffusion model that treats the variation of the interface temperature, interface segregation coefficient, and growth velocity has been used to establish effective diffusion constants for the alloy system. Theoretical models have been developed for the temperature distribution and the axial and radial compositional redistribution during

directional solidification of the alloys. These were used along with the experimental results to select the parameters for the first flight experiment flown on the Second United States Microgravity Payload (USMP-2) mission. A microscopic model for the calculation of point-defect energies, charge-carrier concentrations, Fermi energy, and conduction-electron mobility as functions of x, temperature, and both ionized and neutral defect densities has been developed.

For selected samples, measurements were performed of electron concentration and mobility from 10 to 300K. The experimental data were in reasonably good agreement with theory and were successfully analyzed to obtain donor and acceptor concentrations for various processing conditions.

A five-zone Bridgman-Stockbarger-type Advanced Automated Directional Solidification Furnace (AADSF) has been designed and developed for the flight portion of the investigation. The furnace was successfully flown on the Second U.S. Microgravity Payload mission in March 1994, during which a 15-centimeter-long and 0.8-centimeter-diameter $Hg_{0.8}Cd_{0.2}Te$ alloy crystal was grown under precisely controlled residual acceleration conditions over a period of approximately 11 days. Preliminary x-radiographs of the crystal indicate that the growth was successful. Characterization of the crystal is in progress.

Sponsor: Office of Life and Microgravity Sciences and Applications

• • • • •

Test of Magnetic Damping of Convective Flows in Microgravity

Frank R. Szofran/ES75
205-544-7777

The fundamental objectives of this flight experiment are: (1) to experimentally test the validity of the modeling predictions applicable to the magnetic damping of convective flows in conductive melts as this applies to the directional solidification of metallic and semiconductor materials in the reduced gravity levels available in low-Earth orbit; and (2) to assess the effectiveness of magnetic fields in reducing the fluid flows occurring in these materials during space processing that result from density gradients (driven by the residual steady-state acceleration, or g-jitter) or surface tension gradients (Maragoni flow).

A 30-millimeter bore diameter furnace has been added to the facility that emulates the Crystal Growth Furnace. The control systems for both the new furnace and the existing 22-millimeter bore furnace have been improved to reduce the noise level in the system to improve thermal stability.

Experimentally, work has been carried out on several material systems including gallium (Ga)-doped germanium (Ge), $Ge_{0.95}$ silicon $(Si)_{0.05}$, copper $(Cu)_{0.95}$ nickel $(Ni)_{0.05}$, mercury $(Hg)_{0.84}$ zinc $(Zn)_{0.16}$ tellurium (Te), $Hg_{0.8}$ cadmium $(Cd)_{0.2}Te$, and $Cd_{0.9}Zn_{0.1}Te$. The last material was grown in collaboration with the Kristallographisches Institut of the

University at Freiburg, Germany, under an agreement signed during the past year. Several ingots of gallium-doped germanium have been grown at zero field and at 5 Tesla. The results, to date, show that diffusion-controlled growth can be obtained in 8-millimeter-diameter samples grown at 8 micrometers (μm) per second. One ingot of $Ge_{0.95}Si_{0.05}$ has been grown in the improved system in zero field, but has not been analyzed at this time.

An associated modeling effort has been focused on two fundamental issues: (1) the influence of residual gravity parallel to the growth interface in space on convection in the melt; and (2) characterization of convective intensity (on Earth, in space, with and without magnetic fields) in pseudobinary systems characterized by rejection of the more dense material at the growth front. Results indicated that for lightly doped systems the convective intensity in typical semiconductor melts is about 50 to 100 times more sensitive to gravity parallel to the growth interface than to the normal component of the gravity vector. In the second area, researchers continue to work on improving the numerical techniques for more accurate and efficient simulation of thermosolutal convection and have focused attention on improving understanding of convection in systems experiencing stabilizing solutal gradients on Earth. Scientists have shown that convection in these systems is not eliminated by solutal gradients and that a residual convection persists. This residual convection is not benign and results in higher radial compositional variations than would be expected to be present under diffusion-controlled growth. It

does not, however, alter the axial concentration profile from the diffusion-controlled case.

A significant activity planned for the near-term is to begin the determination of the role of g-jitter (in Earth's gravity) on the compositional distribution of grown crystals. Ultimately, of course, this investigation was selected for flight definition, and flight experimentation is the goal.

The near-future plans in the modeling area include: (1) investigation of the sensitivity of systems experiencing solutal forces to gravity parallel to the growth surface; (2) continuation of work on modeling of magnetic and microgravity effects on thermosolutal convection; and (3) detailed simulation of magnetic experiments of Ga:Ge and Ge-Si now in progress.

Sponsor: Office of Life and Microgravity Sciences and Applications

Industry Involvement: CAPE, Inc., Dr. Shariar Motakef

• • • • •

Structural Characterization of Organic Nonlinear Optical Materials— Diacetylenes and Polydiacetylenes

Marcus Vlasse/ES76
205–544–7781

Diacetylenes and polydiacetylenes ($R - C \equiv C - C \equiv C - R'$) are important technological organic materials that have shown promise as third-order nonlinear optical matrices for such applications as optical switching, four-wave mixing, and logic circuits.

The unique feature of these compounds is the solid-state polymerization (topotactic reaction) under the influences of an energetic radiation (e.g., ultraviolet rays, gamma rays, and x rays). The search for macroscopic single crystals of polymers which can be useful in the study of solid-state properties and possible applications to technological needs has been conducted for a number of years. These efforts have been mainly unsuccessful, except for the topochemical polymerization of certain conjugated compounds. Several classes of organic compounds can undergo polymerization when exposed to high-energy radiation. Such reactions provide a means of direct synthesis of highly crystalline polymers and macromolecular systems. A direct correlation has been established between the geometry and stereochemistry of the molecules in the crystal and the crystalline molecular structure of the polymer. One of the reactions is the topochemical polymerization of

monomer diacetylenes with conjugated triple bonds. This reaction is known to proceed as a 1,4-addition to the conjugated triple bonds. Single crystals of a number of these monomers and polymers have been studied by x-ray and neutron diffraction and Raman spectroscopy, and their stereochemistry has been established. However, not all diacetylenes polymerize readily, and some do not polymerize at all. At present, no detailed approach exists to predict which diacetylenes will polymerize to any specific extent.

Baughman advanced a phenomenological model, based on crystallographic studies and the principle of least motion, in which he specifies the stereochemical criteria governing the disposition of the molecules in the monomer crystal required in order to bring about polymerization. In such a model, the polymerization reaction is described as a rotational motion of the structural units with a specific spacing of the reactive diacetylene chains along the growth direction (some lattice vector $\vec{a}$) having a period d_1 and making an angle γ_1 with vector $\vec{a}$ (fig. 62). According to this theory, ideal parameters d_2 and γ_2 have values of 5.0 angstrom (Å) and 13 angular degrees, respectively. The reactivity of a monomer crystal would depend, therefore, on how close d_1 and γ_1 are to d_2 and γ_2. However, a number of other factors influence reactivity, and it is not possible to make quantitative predictions about specific compounds.

At the same time, computer modeling has been used as a means of screening potentially interesting polymerizable diacetylenes. These computer

Monomer   **Polymer**
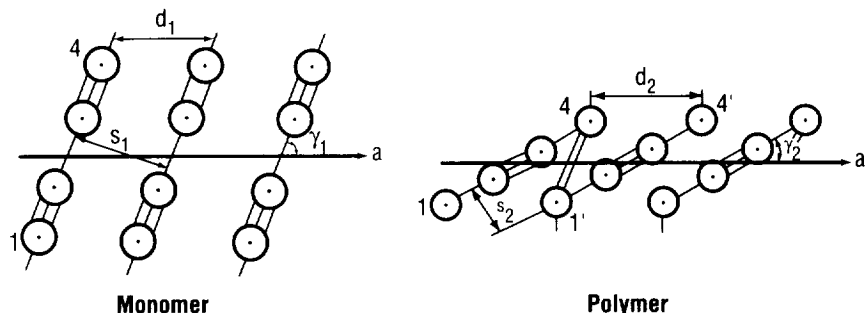
FIGURE 62.—An idealized picture of the solid-state polymerization of diacetylenes.

modeling methods make use of such semiempirical molecular orbital calculations as MNDO and ASM1. These models attempt to predict how a particular diacetylene monomer will pack in the crystal—a critical element to its ability to polymerize readily or not. In addition, these computations provide highest occupied molecular orbital/lowest unoccupied molecular orbital (HOMO-LUMO) bandgaps, which are of importance in predicting

some of the physical and optical properties of the diacetylenes. Again, these predictions are rather qualitative in nature and cannot take into account the specific arrangement that the monomer will adopt in the crystalline state.

The accurate crystal structure determination of a greater number of representative diacetylenes will go a long way toward the establishment of
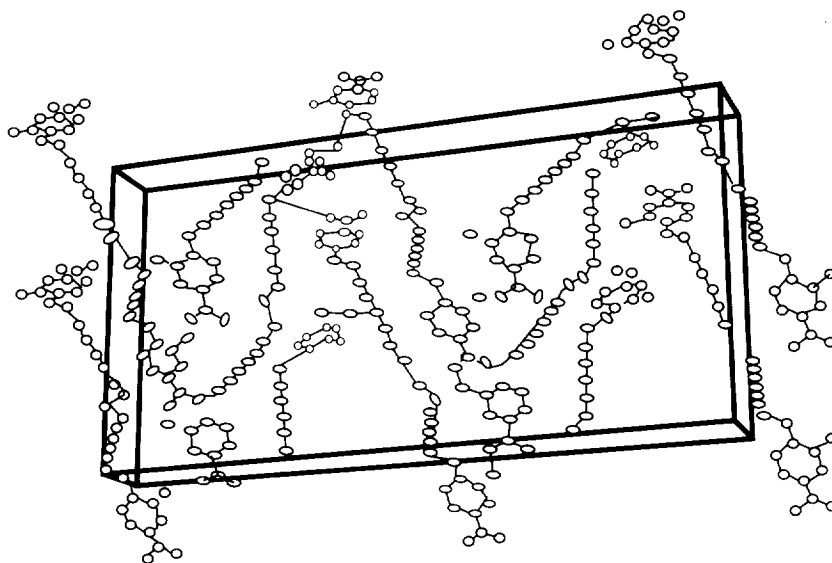
FIGURE 63.—Molecular arrangement of the diacetylenes chains in the crystal.

a more accurate model for predicting diacetylene reactivity based on the nature and shape of the functional R, R* groups attached to the diacetylene backbone.

The structures of several diacetylenes have been determined by accurate x-ray diffraction analysis. The detailed analysis of the structural information obtained from the last two studies (1, 2) indicates, in both cases, the period (d) and the orientational angle (γ) do not have the necessary values to allow significant polymerization to take place (fig. 63). In fact, these two diacetylenes are not active and do not polymerize to a significant degree. The phenomenological model established by Baughman seems to be operative for these two compounds.

Nevertheless, many more of these diacetylenes need to be accurately investigated by x-ray diffraction in order for a clearer picture to evolve—a picture that will allow researchers to establish predictive behavior for both polymerization reactions and the second- and third-order nonlinear optical properties.

Vlasse, M., and Koetzle, T.F. 1986. *Makromolecular Chemistry and Physics* 182:2241.

Vlasse, M., and Paley, M.S. 1994. *Makromolecular Chemistry and Physics* 195. To appear.

Sponsor: Office of Life and Microgravity Sciences and Applications

•••••

Atomic Structure of Glutathione S-Transferase/ HIV Fusion Protein

Daniel C. Carter/ES76
205-544-5492

As recombinant technology continues to make advancements, the number of important structural problems faced by structural biologists will expand tremendously, placing an increasing emphasis on the crystallization of important proteins, such as those derived from the viral genome of the human immunodeficiency virus (HIV). Crystallization of the latter has proven particularly difficult; to date, structures of only two of the 20 protein components of HIV–1 have been reported. Additionally, smaller peptide structures—from 8 to 20 amino acids in length—have historically been difficult to crystallize. Strategies employed to favorably effect the solubilities of such peptides or proteins for crystallization have included the formation of antigen/Fab complexes, the addition of such other substances as detergents to the crystallization milieu, or the chemical modification of the protein.[1] The formation of fusion proteins containing the desired peptide or protein of interest represents an alternative approach—one that is convenient within the confines of producing the recombinant protein of interest. The application of this structural approach has been successfully applied to the solution of a hexapeptide fragment of gp41 of HIV–1, representing a conservative

epitope recognized by the neutralizing human monoclonal antibody 2F5.[2]

Proteins or peptides of interest can be fused with glutathione S-transferase (GST) and expressed in a plasmid vector for rapid synthesis in *Escherichia coli*.[3] Fusion proteins, thus created, can be purified by affinity chromatography on immobilized glutathione. The system utilizes glutathione S-transferase from *Schistosoma japonicum* (*Sj*GST), a 26kD protein which functions as a dimer catalyzing nucleophilic addition of the reduced sulphydryl to a variety of electrophiles.[4] These reactions are important in the metabolism of potentially harmful alkylating agents. Because of the rapidity and purity with which the fusion products could be prepared, researchers undertook a series of co-crystallization experiments with the 2F5 antibody, utilizing a portion of the epitope fused to *Sj*GST as part of an ongoing effort to further elucidate HIV antigen/ antibody complexes.[5] Crystallization attempts of the antibody/antigen complex were unsuccessful; however, high-quality crystals of the *Sj*GST fusion protein were obtained. The crystals grow in the $P4_32_12$ space group with $a = b = 94.7$ angstrom (Å), $c = 58.1$ angstrom from solutions of polyethylene glycol (PEG) 3350 MW. The structure has been solved by the molecular replacement method using coordinates derived from glutathione S-transferase of the *u* gene class derived from rat liver (uGST)[6], representing the first example of an invertebrate glutathione S-transferase. *Sj*GST shows 42-percent sequence identity with uGST. The structure is refined including data to 2.5-angstrom

resolution and is notable among glutathione S-transferase structures in that it contains a monomer in the asymmetric unit and an ordered glutathione in the active site, providing further insight into glutathione S-transferase chemistry.

Electron density consistent with the hexapeptide fusion product, Glu-Leu-Asp-Lys-Trp-Ala (fig. 64), has been observed and incorporated into the refined structure. The conformation of the antigenic peptide is stabilized by crystal packing interactions with symmetry-related molecules (fig. 65). Although it is possible that the observed conformation of such a small peptide fragment might not be assuming its normal secondary structure within gp41, the tremendous potential of the method is clearly demonstrated. Because of the exact symmetry possessed by the *Sj*GST dimer in this crystal structure, the utilization of the fusion product with *Sj*GST may allow for a potentially expeditious route to the structure of the fusion product. Larger fusion products, representing more difficult phasing problems, could be overcome by the development of novel iodine or other modified, glutathione-based substrates (suggested by the protein complex) or by genetically engineering heavy atom sites within the *Sj*GST structure. An example is the case of the structure determination of uGST[7], which can then be utilized for complimentary phasing by isomorphous replacement methods.

Additional importance of *Sj*GST relates to its *Schistosoma* origin. Schistosomiasis, a major parasitic disease, second only to malaria, is estimated to infect over 250 million
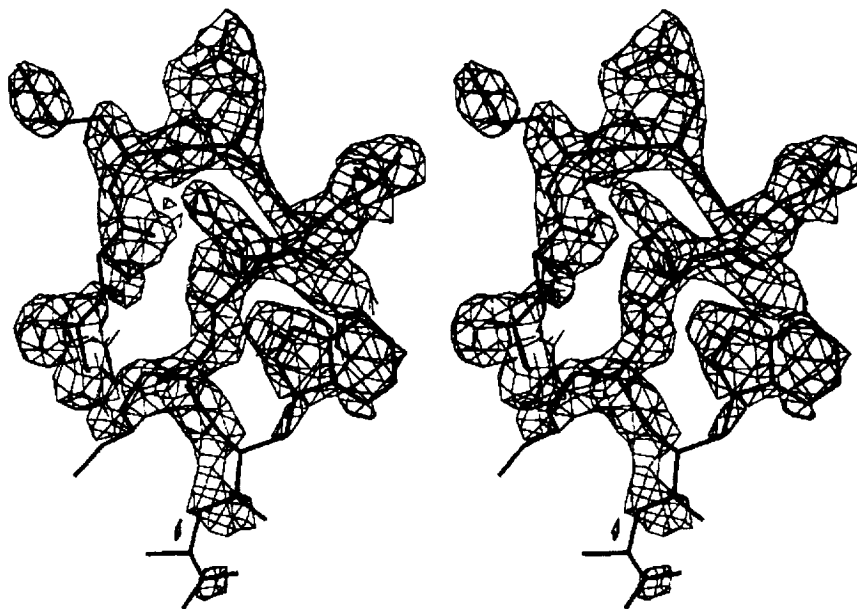
FIGURE 64.—Electron density of the HIV fusion hexapeptide Glu-Leu-Asp-Lys-Trp-Ala produced from a F_{obs}-F_{calc} Difference Fourier.
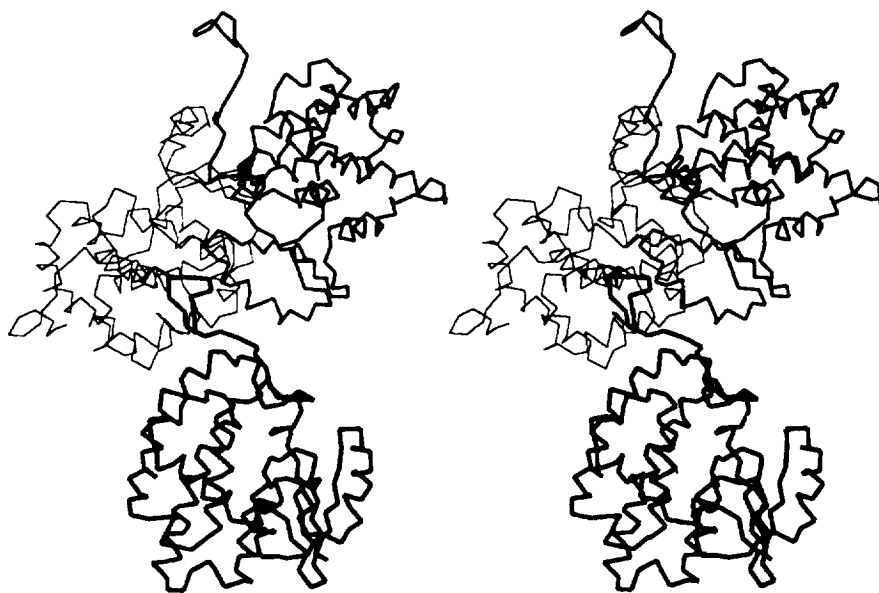
FIGURE 65.—A view of the crystal packing arrangement, illustrating the interaction of the fusion peptide with adjacent glutathione S-transferase molecules.

110

people worldwide. Since it has been suggested that the specific inhibition of glutathione S-transferase could offer the possibility of combining chemotherapy and immunotherapy to combat this disease,[8] the determination of other members of this parasitic family may be an attractive approach for developing a multispecies, cross-reactive vaccine against the transmission of schistosomiasis.

Detailed comparisons of the structure with other members of the glutathione S-transferase family will be published.[9] Coordinates of SjGST are available from the authors and have been deposited with the Brookhaven Protein Data Bank.

[1]Rayment, I., et al. 1993. *Science* 261:50–8

[2]Muster, T.; Steindl, F.; Purtscher, M.; Trkola, A.; Klima, A.; Himmler, G.; Rüker, F.; and Katinger, H. 1993. *J. Virol.* 67:6642–47.

[3]Smith, D.B., and Johnson, K.S. 1988. *Gene* 67:31–40.

[4]Rushmore, T.H., and Pickett, C.B. 1993. *J. Biol. Chem.* 268:11475–78.

[5]He, X.M.; Rücker, F.; Casale, E.; and Carter, D.C. 1992. *Proc. Natl. Acad. Sci. USA* 89:7154–58.

[6]Ji, X.; Zhang, P.; Armstrong, R.N.; and Gilliland, G.L. 1992. *Biochemistry* 31:10169–84.

[7]Sher, A.; James, S.L.; Correa-Oliveira, R.; Hieny, S.; and Pearce, E. 1989. *Parasitol* 98:S61–68.

[8]Hughes, A.L. 1993. Schistosoma. *Mol. Biochem. Parasitol.* 58:43–42.

[9]Lim, K.; Ho, J.X.; Keeling, K.; Gilliland, G.L.; Ji, X.; Rüker, F.; and Carter, D.C. Submitted to *Protein Science*.

Sponsor: Office of Life and Microgravity Sciences and Applications

• • • • •

Demonstration Flight of New Hand-Held Protein Crystal Growth Hardware

Daniel C. Carter/ES76
205-544-5492

The overall goal of this experiment was to demonstrate a new avenue for the large-scale production of protein crystals for scientific purposes. To accomplish this, new hardware must simplify access to the microgravity environment, as well as simplify preflight loading and postflight distribution and markedly increase the number of sample chambers available to each investigator while maintaining scientific standards. This has been demonstrated by the development of the hand-held version of the Protein Crystallization in Microgravity (HH-PCAM) hardware. Four such units (figs. 66 and 67) were flown in a mid-deck locker on flight STS–62. Each device contains a disposable plastic commercial tray that contains 24 chambers. Together with other special adaptations for microgravity, the hand-held hardware provides a mechanism to simultaneously activate and deactivate the 24 chambers in each tray. Major goals of this flight experiment were to assess the performance of the device in such areas as preflight loading and postflight distribution, stability of the samples in two gravity vector orientations on launch and landing, droplet stability based on a variety of differing crystal growth conditions and volumes, and documentation of performance of the device in microgravity via growth of a number of selected protein crystals.
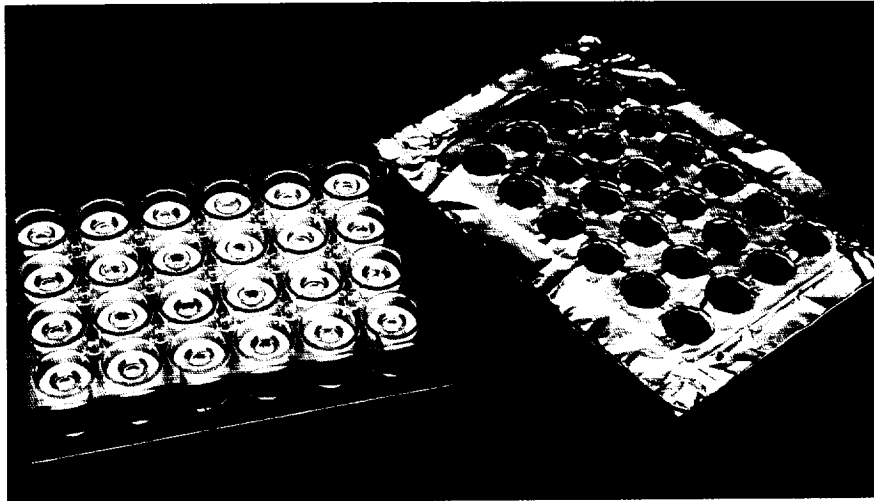
FIGURE 66.—Commercial tray (Cryschem™) illustrating the modifications for use in microgravity.
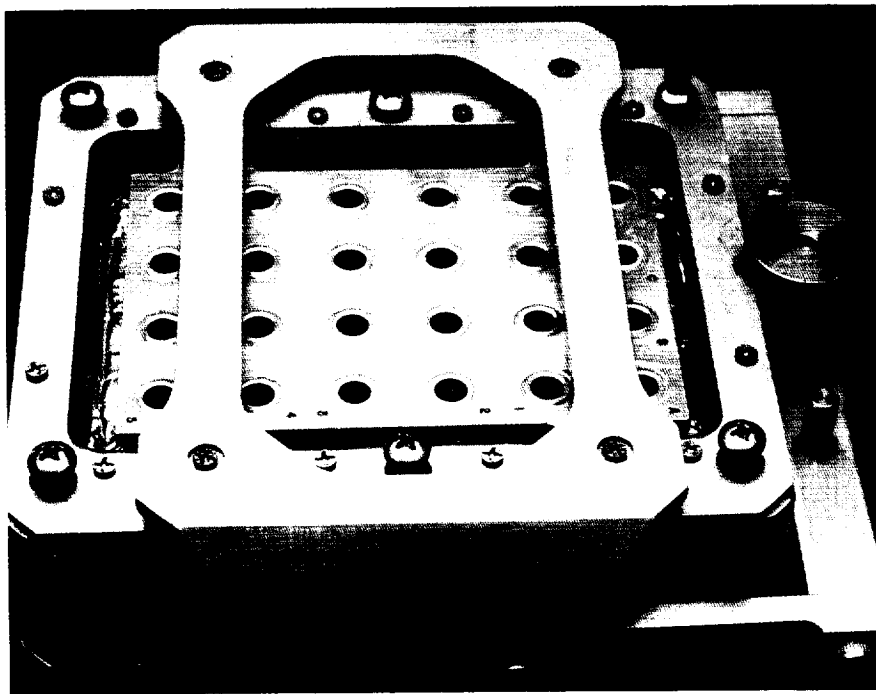
FIGURE 67.—Hand-held version of the Protein Crystallization in Microgravity (HH-PCAM) hardware.

Experiment activation and deactivation proceeded without anomaly. Improvised in-flight photography by mission specialist Pierre Thuot provided important confirmation that the droplets survived launch, as well as proof that crystals of all four proteins grew as expected. Some of the in-flight crystal photographs are the most spectacular to date.

Postflight retrieval and analysis of the hardware were also performed with ease and without anomaly. The experiment was recovered and brought to Birmingham, Alabama, within 6 hours after landing. The HH-PCAM's were returned to Marshall for evaluation, inspection, and analysis of the crystals. Removal of the samples for distribution took approximately 5 minutes for each of the 24 chamber trays and approximately another 30 minutes for complete photographic documentation. Because there was no temperature control during the demonstration, the analysis and application of the crystals produced was a secondary goal. However, serious analysis of x-ray diffraction data is currently in progress and results, so far, are encouraging.

In summary, the capabilities of the hardware were fully demonstrated during this flight demonstration. No improvements to the device or concept have been suggested by the experiment. Additionally, some of the crystals grown appear to be significantly better in diffraction resolution than any Earth-grown counterparts previously grown in an MSFC laboratory (fig. 68). Complete analysis of the control experiments are in progress. Based on this successful
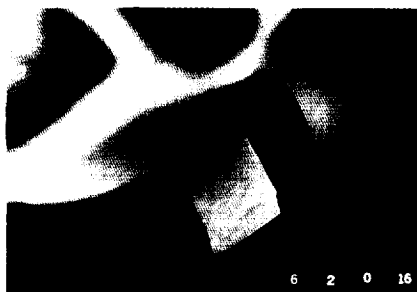
FIGURE 68.—One of several photographs showing beautiful single crystals of hen egg-white lysozyme, which were produced on flight STS-62.

demonstration, facility hardware is now under construction and will be manifested on STS-67, scheduled for launch in January 1995. This hardware will be maintained in a temperature-controlled environment (STES) in a single mid-deck locker and will house 378 individual experiments. The second generation PCAM hardware allows for an unprecedented number of protein crystal growth experiments to be conducted on each flight, thus allowing for greater accessibility of the microgravity environment for the production of protein crystals for scientific purposes. If further successful, this new hardware is expected to fill a requirement for protein and small molecule vapor-diffusion solution crystal growth through the early years of space station.

Sponsor: Office of Life and Microgravity Sciences and Applications

• • • • •

Atomic Structure of Cytochrome C5 From Azotobacter Vinlandii at 1.6 Angstroms

Daniel C. Carter/ES76
205-544-5492

The three-dimensional structure of cytochrome C5 from Azotobacter vinlandii has been refined to high resolution, including the incorporation of the ordered water structure. This is an 86 amino acid residue cytochrome which presumably participates in the single-electron transfer to cytochrome oxidase. The electron is delocalized on a protoporphorin ring that contains iron (fig. 69). X-ray diffraction data were collected on a Rigaku imaging plate area detector system utilizing a rotating anode source. Current R-factor to 1.6 angstroms (Å) is 17.2 percent. This represents the highest resolution cytochrome

Figure 69.—Electron localized on a protoporphorin ring that contains iron.

structure reported to date. Future studies include the continuation of the high-resolution refinement of both oxidized and reduced forms of the protein, as well as crystallization studies in microgravity. Complete atomic coordinates are available and have been deposited in the Brookhaven Protein Data Bank.

Carter, D.C.; Melis, K.A.; O'Donnell, S.E.; Burgess, B.K.; Furey, W.F., Jr.; Wang, B.C.; and Stout, C.D. 1985. Crystal Structure of Azotobacter Cytochrome C5, *Journal of Molecular Biology* 184:279-95.

Reynolds, R.; Ho, J.X.; Stout, C.D.; and Carter, D.C. Atomic Structure of Cytochrome C5 From Azotobacter Vinlandii at 1.6 Angstroms. Manuscript in preparation.

Sponsor: Office of Life and Microgravity Sciences and Applications

• • • • •

113

Surface Modification of Agarose for Liquid-Liquid Partition Chromatography

Raymond J. Cronise/ES76
205-544-5493

Liquid-liquid partition chromatography (LLPC) has been in use for over 50 years and has been commonly used to isolate a wide range of naturally occurring biopolymers. Although some attempts have been made to extend the chromatography to the separation of cells and subcellular particles, no such attempts have been completely successful. The only bottleneck seems to be finding a suitable support material that will selectively trap the stationary liquid phase, while allowing cells and particles to pass freely in the mobile liquid phase.

Martin and Synge presented a new model for simple description of the chromatographic process and a method for characterization of its efficiency.[1] In their chromatographic separation scheme, two immiscible liquids were used. One liquid was selectively "trapped" by a solid column support matrix, while the second liquid flowed freely through the column. This allowed molecules to selectively partition between the two liquids, thereby affecting the relative time a molecule takes to pass through the column.

A polyagarose-based gel filtration medium (sepharose) is commercially available with three different agarose contents: 2, 4, and 6 percent. By increasing the agarose concentration,

the matrix porosity is decreased, altering the fractionation range for the gel. Sepharose (sepharose 6MB) is available in a relatively monodispersive size (250 to 350 micrometers (µm)) for use with cell affinity chromatography. This size provides the necessary packing and interstitial space to allow free passage of cells. Additionally, sepharose 4B (45 to 165 micrometers) is available for separation of proteins and other macromolecule molecules. Both of these gel chromatography supports are also available with activated surfaces for coupling chemistry. The current effort has concentrated on coupling dextran to the surface for use as a stationary phase-support material for liquid-liquid partition chromatography.

CNBr-activated sepharose is produced by reaction with cyanogen bromide and probably produces the imidocarbonate and cyanate ester reactive groups. This reactive surface can be treated with a

functional tethering sublayer, such as ethylene diamine. By carrying out this reaction under mildly alkaline conditions (pH 8-9), an isourea linkage is formed (fig. 70) with a reactive primary amine for coupling dextran. The dextran can be reacted through the available carbonyl group on the reducing end of the polysaccharide. After nucleophilic addition to the carbonyl group, sodium cyanoborohydide is used to reduce the resulting schiff-base linkage.

[1]Martin, A.J.P. and Synge, R.L.M. 1941. A New Form of Chromatogram Employing Two Liquid Phases, *Journal of Biochemistry* 35:1358–68.

• • • • •

FIGURE 70.—Reaction scheme for coupling polysaccharides to activated sepharose surfaces.

Biophysics of Gravity Sensing

David A. Noever/ES76
205-544-7783

Gravity has a pronounced effect on biological cellular function, including cell proliferation, biosynthesis of cell-specific products, consumption of nutrients in the medium,[1] and kinetics of cell differentiation.[2] Despite the long history of interest in the mechanism and effects of gravity on biological function, research on cell mobility and orientation with respect to gravity is still an active field. Recent work[3] on the protozoa *Tetrahymena*, in particular, has called into question the traditional mechanisms for geotaxis (or gravitaxis) in upwardly oriented swimming.

Scientists, therefore, presently consider the effects of gravity sensing on single biological cell orientation and quantify directional swimming changes using variable gravity simulations. No air gaps or oxygen gradients will be present, so gravity alone will act to determine cell orientation. The research seeks to actively change the gravity level, to photographically monitor the angular orientation of biological cells, and to relate the geometric character of swimming trajectories to the gravitational biology of the organisms themselves.

To investigate gravitational effects on the orientation of single cells, movements of protozoa (*Tetrahymena*) and alga (*Euglena* and *Polytomella*) were recorded in a vertical cross section. Results showed that random

swimming dominates low-gravity phases, while upward-directed orientation dominates high-gravity phases. The experimental determination of average cell swimming direction in variable gravity has been accomplished. In airplane experiments, repeated application of changing gravity can isolate biological effects of acceleration and begin to quantify their importance relative to the competing influences of aerodynamic forces, light, chemicals, hydrostatic pressure, oxygen, and other physiological gradients. Two significant protists are shown to swim preferentially upward in a gravity field. The appealing aspect of the protist experiments for gravity sensing is the rapidity of cell reorientation; organisms are seen to randomize their statistical swimming direction within 20 seconds in low gravity.

To summarize current study findings:

• Gravity preferentially directs cell swimming upward (negative geotaxis) in *Tetrahymena* suspensions with a statistically definable preference for gravity orientation centered on 90 degrees (vertical).

• Vertical migration patterns of organisms in various gravity levels can be characterized by their lack of directional correlation (randomization), their rapid decay time (less than 20 seconds) for upward orientation, and their rapid recovery of oriented swimming when normal gravity returns.

• Vertical orientation does not require oxygen gradients since all experiments have been conducted in

sealed chambers without bubbles or air gaps.

Vertical migration patterns of single cells are a critical feature of their life cycle.[4] For plankton, understanding the link between gravity and vertical migration may shed light on interesting models of ocean-atmospheric exchange of gases and related issues of ocean ecology[5] and climate modeling.[6]

[1]Montgomery, P.; Cook, J.E.; Reynolds, R.C.; Paul, J.S.; Hayflick, L.; Stock, D.; Schulz, W.W.; Kimsey, S.; Thirolf, R.G.; Rogers, T.; and Campbell, D. 1978. The Response of Single Human Cells to Zero Gravity. *In Vitro* 14:165–73.

[2]Gmunder, F.K., and Gogli, A. 1988. Cultivation of Single cells in Spade, *Applied Microgravity Technology* 1:115–22.

[3]Shvirst, E.M.; Krinskii, V.I.; and Ivanitskii, G.R. 1984. Oxytaxis in Tetrahymena Pyriformis. *Biofiz.* 29:649–54. (transl: *Biophys.* 29:710–15).

[4]Noever, D.A. 1991. Evolution of Bioconvection Patterns in Variable Gravity. *Phys. Rev. A* 44:4491–4501.

[5]Ryther, J.H. 1969. The Role of Phytoplankton in Ocean Ecology. *Science* 166:72.

[6]Winet, H. 1975. Does Bioconvection Affect Algal Ecology? *J. Protozool* 22:19A.

Multicolor Holographic Interferometry

William K. Witherow/ES76
205-544-7811

Multicolor holographic interferometry advanced technology development is a technique that can be used in both ground-based and flight-fluid experiments. In a fluid experiment, gradients can be caused by temperature changes and/or concentration changes. Both types of gradients can cause the refractive index of the fluid to change. Standard optical techniques cannot separate the two gradients if both types occur simultaneously in an experiment. Multicolor holographic interferometry is a technique that can separate the two effects. The basis of the technique is to use more than one wavelength. By using two or more wavelengths, additional information is obtained so that measurements of simultaneously occurring temperature and concentration gradients can be made.

A breadboard system has been built utilizing the two wavelengths 632.8 nanometers (nm) from a helium-neon (He-Ne) laser and 441.6 nanometers from a helium-cadmium (He-Cd) laser. Experiments are being performed to determine the accuracy of the technique. In the experiments, gradients have been created with various concentrations of sugar water, and temperature gradients have also been added to the test cell. Currently, gels are being investigated to determine if they are transparent enough to use in the system. If gels can be used, then a variety of new experiments can be done in the ground-based system, since the gels solidify before use and have a low diffusion rate. An exponential gradient concentration maker is also available that can create an exponential gradient in the test cell. An exponential gradient will help determine the resolution of gradient that the system can detect.

Phase-shifting interferometry (PSI), used with the multicolor holographic interferometry technique, improves sensitivity and accuracy. In a standard interferogram, a set of fixed fringes are created by refractive index changes in the experiment test cell. The fringes from a standard interferogram are measured by determining where the maxima and minima lie. A photodetector is used to find the point at which the darkest part of the fringes lie, the minima. Typically, this type of measurement yields an accuracy of one-twentieth to one-fiftieth of a wavelength. The error in measurement results from the fact fringes are usually not sharply defined. Fringes typically have a finite width with a symmetrical increase in intensity. In addition, the fringes are spatially fixed so that the actual measured values only represent small regions of the total field of view. Thus, the refractive index in the test cell is only known at the fringes. Refractive index values between the fringes are interpolated.

In phase-shifting interferometry, a phase-shifting element is added to the object beam of the interferometer (fig. 71). Known discrete phase shifts, introduced into the system by the phase-shifter, causes the fringes in the output image to move to different locations (fig. 72). Translating the fringes in this fashion allows additional information to be measured from the image. In other words, by moving the fringes with the phase-shifter, the spaces that lie between the original spatially fixed fringes are now also measured.

A breadboard system that can fly on the KC-135 has also been built. This system will allow investigators to fly experiments using the multicolor holographic interferometry technique to determine its effectiveness in providing the data that the investigators want.

Papers that have resulted from this effort include:

Trolinger, J.D.; Lal, R.; Vikram, C.S.; and Witherow, W.K. 1991. Compact Space Flight Solution Crystal Growth System. Proceedings Society of Photo-optical Engineers (SPIE), 1557:250-8.

Vikram, C.S.; Witherow, W.K.; and Trolinger, J.D. 1991. Refractive Properties of TGS Aqueous Solution for Two-Color Interferometry. Proceedings SPIE, 1557:197-201.

Vikram, C.S., and Witherow, W.K. 1992. Critical Needs of Fringe Order Accuracies in Two-Color Holographic Interferometry. *Experimental Mechanics* 32:74-77.

Vikram, C.S.; Witherow, W.K.; and Trolinger, J.D. December 1, 1992. Determination of Refractive Properties of Fluids for Dual-Wavelength Interferometry. *Applied Optics* 31:7249-52.
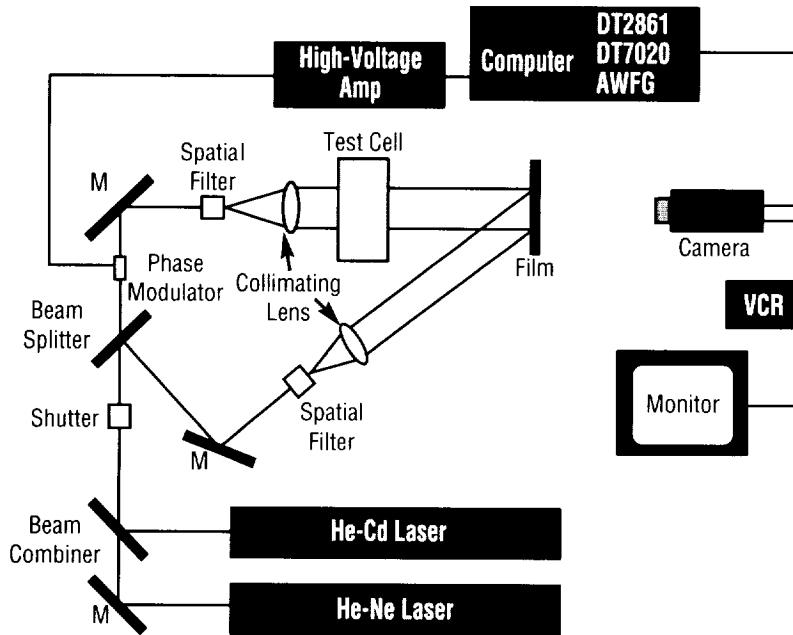
FIGURE 71.—Multicolor holographic analysis system.

Hologram 8B00   ΔT 3.4 C/cm
He-Ne 633 nm   ΔC 3.1 g/liter

FIGURE 72.—Phase shifting.

Vikram, C.S.; Witherow, W.K.; and Trolinger, J.D. September 1993. Special Beam Intensity Ratio Needs in Multicolor Holography. *Journal of Modern Optics* 40:1387–93.

Vikram, C.S.; Witherow, W.K.; Trolinger, J.D. November 1, 1993. Algorithm for Phase-Difference Measurement in Phase-Shifting Interferometry. *Applied Optics* 32:6250–52.

Vikram, C.S.; Witherow, W.K.; and Trolinger, J.D. Fringe Contrast and Phase Effects in Multicolor Holography. Accepted for publication in *Journal of Modern Optics*.

Witherow, W.K.; Rogers, J.R.; Facemire, B.R.; Armstrong, S.D.; Trolinger, J.D.; Webber, D.; and Vikram, C.S. February 28, 1994. Methods to Detect and Measure Gradients in Fluids and Materials Processing. Sixth International symposium on Experimental Methods for Microgravity Materials Science, San Francisco, CA. To be published in the proceedings.

Witherow, W.K.; Trolinger, J.D.; and Vikram, C.S. May 24, 1994. Multicolor Holographic Interferometry Advanced Technology Development. Microgravity Materials Science Conference. Poster session, Huntsville, AL.

Sponsor: Office of Life and Microgravity Sciences and Applications

• • • • •

Automated Statistical Crystallography Software

Raymond J. Cronise/ES76
205-544-5493

The proposed research aims to develop an automated image analysis system capable of determining fundamental geometric relationships in random cellular patterns. Random networks of cellular patterns abound in nature.[1,2,3] Examples include polycrystalline boundaries, magnetic bubble domains, acidic monolayers, and biological membranes. A striking universality among these networks has been identified; its basis derives not so much from any specific material property, but more broadly from mathematical restrictions on completely filling n-dimensional space. These space-filling restrictions are statistical in character, typically arising in network domains numbering in the hundreds or thousands. Their detailed analysis reveals much about phenomena which, prior to fast-imaging systems, proved realistically unsolvable and unapproachable. The analysis of sizes and shapes for several hundred thousand cellular patterns is required for reliable statistics. Previously, this analysis was too tedious to undertake on any significant scale. However, within the last 5 years, computer analysis of images has advanced dramatically. Now random patterns rival ordered crystals (randomness) for both structural richness and quantitative information about their energetics.

Algorithms have been developed to recognize and quantify random polygonal patterns. Two approaches are used to quantitate the geometric pattern statistics depending on the
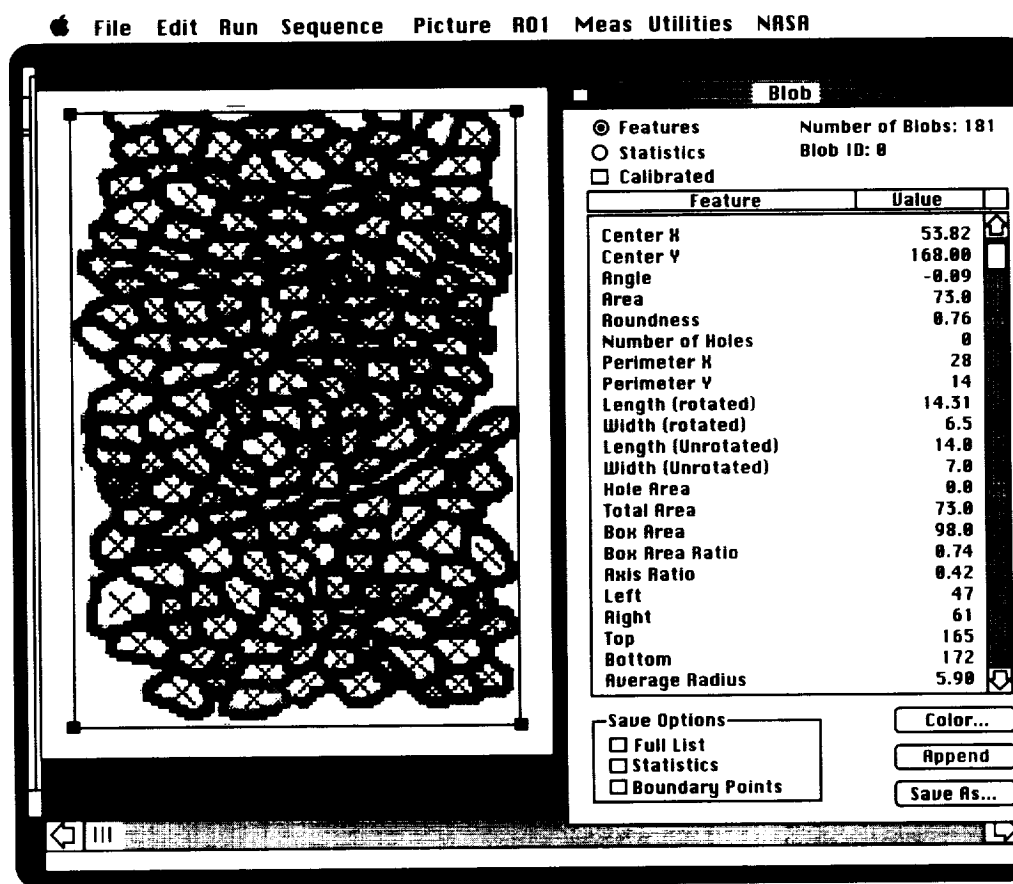
FIGURE 73.—Automated statistical crystallography software on the Macintosh platform.

nature of the polygon boundaries. When cell boundaries are found by connectivity analysis, the Hough transform method is used. If the cells are not closed objects or are represented by separate point objects, the method of Voroni is used. Connectivity analysis is used to identify the individual polygons and to provide the perimeter list of each cell. The Hough statistical transform uses the perimeter list to identify and then to count the straight line segments. These segments approximate the perimeter list of each polygon.

In the second method, connectivity analysis is used to identify the centroids of individual polygons. The method of Voroni is used to calculate the perpendicular bisectors between each object and its neighbors. These bisectors will intersect to form a closed polygon surrounding the object centroid. The number of sides, neighbors, perimeter, and area are then calculated. The results are tabulated and returned to a standard tab delimited text file. This package was written in McRail™ and runs under Image Analyst on the Macintosh™ platform (fig. 73).

[1]Weaire, D., and Rivier, N. 1984. *Journal of Contemporary Physics* 25:59–99.

[2]Glazier, J.A.; Gross, S.P.; and Stavans, J. 1987. *Physical Review A.* 36:306.

[3]Rivier, N. 1985. *Philos. Mag.* B52:795.

• • • • •

Preparative Electrophoresis for Space

Percy H. Rhodes/ES76
205–544–7807

Continuous-flow electrophoresis (CFE) remains the major technique which can factionate viable unmodified biological cells in excess of 10^8 cells per hour.

Although the electrophoresis separation process is simple in concept, flows local to the sample filament produced by the applied electric field have not been considered. These electrohydro-dynamical flows, similar to those formulated by G.I. Taylor[1] in 1965 for drops suspended in various liquids, distort the sample stream and limit separation. The flows[2] are proportional to the square of the imposed electric field and result from differences in the electric conductivity and dielectric constant between the sample and carrier buffer. These distortions are shown (fig. 74) for various ratios (R) of sample-to-buffer conductivity. This figure illustrates the chamber walls and sample streams as viewed in the chamber cross section.

On Earth the distortions due to electric conductivity variations are easily observed. However, distortion caused by dielectric constant changes are difficult to detect. This is because the dielectric constant is directly proportional to the sample concentration. High sample concentrations are not permissible on Earth due to sedimentation problems; thus experiments will be conducted on
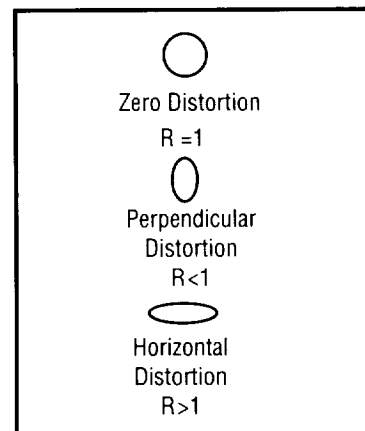
FIGURE 74.—Sample stream distortion for different electric conductivity ratios R.

International Microgravity Laboratory 2 (IML–2) using the French RAMSES continuous-flow electrophoresis chamber. The results of these experiments will be used to design continuous-flow electrophoresis chambers especially suited for operation in space, taking advantage of the unique environment of space to produce better separations of biological materials.

[1]Taylor, G.I. 1966. Studies in Electrohydrodynamics. *Proceedings of the Royal Society of London* 291:159–66.

[2]Rhodes, P.H.; Synder, R.S.; and Roberts, G.O. 1989. Electrodynamic Distortion of Sample Streams in Continuous-Flow Electrophoresis. *Journal of Colloid and Interface Science* 129:78–90.

• • • • •

Technology Programs

The wings that first carried us to the Moon were wings supported by dreams, skill, perseverance, and technological excellence. When the commitment was made, we didn't have the tools to succeed—yet by dreaming, learning, building, and overcoming our failures, disappointments, and complacency, we built a technological base that allowed the "one small step for man..."

We will never fully understand the positive impact the Apollo Moon Program had on our civilization; slowly but surely, however, the technology of Moon travel has filtered into our everyday lives in transportation, medicine, and other fields. It has changed forever how we tackle and solve engineering and science problems and helped fuel the birth of the "computer generation." The goal of putting a few thousand pounds of metal and plastic and a few hundred pounds of humanity on another celestial body fired the imaginations and focused the efforts of a generation. Traveling away from our planet allowed us to look back and view it as a fragile sphere of life.

Improvements in technology are some of the most effective engines to drive our country and all of humanity forward. Improved medical technology offers freedom from disease and suffering; better transportation technology offers freedom of movement, a broadening of perspectives, and improved understanding of our fellow travelers on this planet; advances in food technology offer freedom from starvation and hunger. In all cases, properly utilized technological advances ease our burdens and allow us to look outward to other people and to our planet and its health.

Our country is on the verge of another "small step for man" with the flight of the international space station. We do not know what benefits will accrue from the technological advances needed to implement this endeavor. We need only look at history, however, to understand that there will be benefits, and the whole of humanity will be the beneficiaries. Whether it is improved medicines, materials, avionics for Earth-bound transportation, or simply the ability to shrug off the shackles of complacency, the technologies of the next 25 years of space travel will impact us all.

For this reason, Marshall is dedicated to lead the development of those technologies and to assure that the first "small step for man" is followed by another, and another, and...

George F. McDonough
Director
Science and Engineering Office

Avionics

A Distributed Autonomous Coordination Architecture for Functionally Redundant Intelligent Systems

Bryan K. Walls/EB72
205–544–3311

Systems that perform the same tasks are functionally redundant. Examples include applications that are replicated across networked computers and programs that solve the same problem using alternative techniques. Functional redundancy can be exploited to increase resource availability, enhance the quality of problem solutions, and improve reliability. Group-based control models transparently decompose complex tasks, dispatch subtasks to redundant servers, collect results, and prepare coherent responses for client users or programs.

MSFC, working with Symbiotics, Inc., in a Small Business Innovation Research (SBIR) effort, is currently developing generalized group models for coordinating functionally redundant systems. The phase I effort of this project reviewed research on process groups and distributed artificial intelligence (AI) to establish comprehensive functional requirements; designed intelligent coordination models that satisfy these requirements; and validated these designs through rapid prototyping.

The phase II objectives include refining the phase I design models, implementing those models using distributed computing tools developed previously by Symbiotics, and applying the resultant control models to construct a demonstration prototype that coordinates intelligent systems for operations support of the international space station.

Phase II will result in advanced tools and techniques for developing complex distributed systems across heterogeneous computing environments. The innovative phase II group-based products will facilitate the development of advanced, one-to-many distributed client-server applications. Commercial applications include intelligent operations support for complex systems, concurrent engineering, office automation, groupware, and distributed data analysis and decision support.

Sponsor: Office of Advanced Concepts and Technology; Small Business Innovation Research

Industry Involvement: Symbiotics, Inc.

• • • • •

Abductive Power System Control and Diagnosis

Kurt E. McCall/EB72
205–961–4501

The objective of this phase I Small Business Innovation Research (SBIR) project is to demonstrate a superior prototype diagnostic system and controller for spacecraft electrical power systems based on AbTech Corporation's abductive polynomial network technology. For this effort, abduction can be defined simply as reasoning with numerical functions, rather than symbolic rules or decision tables. Using AbTech's abductive technology, designers can semiautomatically model the complex and dynamic behavior of aerospace power systems using polynomial equations (abductive polynomial networks). Abductive models strengthen fault detection and isolation capabilities, verify sensor readings, isolate sensor failures, and enhance system control for a variety of normal and failure conditions. This effort will attempt to demonstrate diagnostic and control techniques to decrease costs and increase efficiency and sophistication of spacecraft power system real-time operation.

In many cases, the operation of spacecraft is a very human-intensive task. Teams of highly trained and highly paid individuals operate consoles around the clock to monitor spacecraft telemetry for anomalies, resolving any that might occur. Because of the large quantity of telemetry that must be monitored,

operators can often do little more than make a cursory scan for out-of-limit values. In light of these limitations, the need for automated diagnostics and control is obvious.

Because of the gradual degradation of electrical power system (EPS) components during flight, and in view of the range of operating conditions during flight, the analytical modeling of an electrical power system is a difficult task. An alternative is the use of numerical models constructed from actual power system data. These data would be gathered from a hardware test-bed and simulations or generated by a human expert. If a comprehensive data base of examples is available, abductive techniques can be used to construct models that compactly describe complex relationships between system variables, whereas analytical methods might require thousands of symbolic rules or decision table entries to describe these relationships. The models can then be used to perform a variety of control and diagnostic tasks.

AbTech is presently interviewing domain experts at various NASA centers to find a particular spacecraft or hardware test-bed for which a comprehensive data base is available, so that the enhancements provided by abductive modeling technologies can be demonstrated. Abductive polynomial networks are not suitable for modeling every domain—for example, domains where the variables of interest are discrete or discontinuous. Since power systems have both discrete and continuous variables, AbTech will identify both the benefits and limitations of its technology in this area.

The specific type of analysis performed by the abductive models is also under consideration. AbTech does not intend to duplicate any type of analysis currently performed well by operators or existing monitoring systems. Operators at the Johnson Space Center (JSC) have suggested real-time fault detection and trend analysis as possible candidates for abductive modeling. Once the target system and type of analysis have been selected, AbTech will develop and deliver a prototype software demonstration to MSFC for evaluation.

AbTech's technology has the potential to increase the efficiency and sophistication of diagnostics and control of spacecraft power systems, performing in real-time certain types of analysis impractical for human operators. The automation of monitoring functions will result in decreased operational costs to NASA, requiring fewer personnel. There are a multitude of potential commercial applications of abductive polynomial techniques in the area of power systems, including aerospace, manufacturing, automotive, and medical power systems.

Sponsor: Office of Advanced Concepts and Technology; Small Business and Innovation Research

Industry Involvement: AbTech Corporation

• • • • •

An Intelligent Load Controller

Norma R. Dugal-Whitehead/EB72
205-544-3304

The design of the intelligent load controller (ILC) is the product of a Small Business Innovation Research (SBIR) phase II contract. This project investigated intelligent power source protection for space power applications. Work focused primarily on the use of distributed intelligence in the Space Station Module Power Management and Distribution (SSM/PMAD) system at the lowest levels of operation, including the power switchgear. The intelligent load controller resulting from the effort replaced the switchgear's generic card (GC) and remote power controller (RPC), providing enhanced protection capability, lowering power consumption, and decreasing the weight and size of the switchgear altogether. All of which have potentially contributed to a more efficient space-station-type power system.

Research efforts were divided into two major areas. The first dealt with the characterization of arcing on direct current (dc) power systems. Laboratory experiments were set up to simulate fault situations that could occur within the power distribution system. Findings indicated that conditions were such that arcing could go undetected by conventional protection techniques. For example, a loose power connector or a break in the power conductor could result in arcing that lasted for several seconds without being registered by standard

overcurrent or undervoltage protection devices. Such situations held the potential for severe shock hazards, noxious fumes, and fire aboard a space vehicle. An arc detection algorithm to detect arcing on direct current power distribution systems has been developed and implemented in the load controller. Recent testing has shown that the algorithm is reliable, but testing is ongoing.

The second area of research involved the actual design of the load controller itself. State-of-the-art metal oxide semiconductor field-effect transistors (MOSFET's) provided current limiting and load protection, replacing the present power-hungry design of the generic card and the remote power controller. Fewer components and fewer interconnections have reduced the total number of devices system-wide, thus improving the reliability of the entire power management system. In addition to its unique arc and ground fault detection capabilities, the intelligent load controller also offers the surge-current, I²t, undervoltage, and over-temperature protection, as well as the fast-trip (trip after being current-limited for 15 milliseconds) and current limiting features already provided by the remote power controller and generic card.

Sponsor: Office of Advanced Concepts and Technology; Small Business Innovation Research

Industry Involvement: MICON Engineering

•••••

Model-Based Electrical Power Distribution Controller

Norma R. Dugal-Whitehead/EB72
205–544–3304

The overall goal of this research effort has been the development of a software system to automate the monitoring and controlling of power distribution in electrical power systems. The resulting software system—the intelligent power controller (IPC)—successfully performs all facets of fault detection, isolation, and recovery (FDIR). This includes continuous monitoring of the power flow from a source to a set of loads; fast detection of anomalous behavior indicating the presence of a fault in or around power system components; generation of the

anomalous behavior diagnosis (explanation); isolation of the faulty object from the remainder of the system; and maintenance of power flow to critical loads and systems (e.g., life support, fire protection) despite fault conditions.

The intelligent power controller system has evolved from the Knowledge-based Autonomous Test Engineer (KATE), a diagnostic software shell developed at Kennedy Space Center (KSC). The Knowledge-based Autonomous Test Engineer consists of a set of software tools for developing and applying structure and behavior models to fault detection, isolation, and recovery applications, employing a technique called "model-based reasoning" in its diagnostic artificial intelligence (AI) system. The major impetus behind the development of the intelligent power controller has been the desire to test the hypothesis that model-based
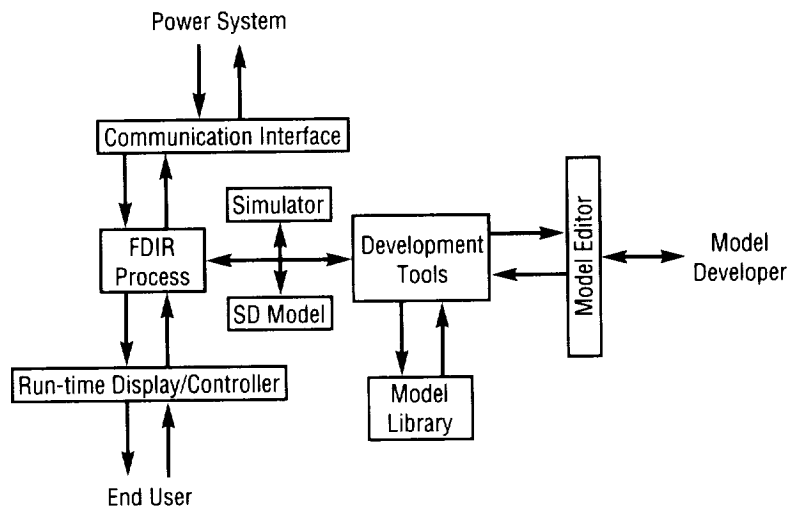
FIGURE 75.—Intelligent power controller architecture.

reasoning can be successfully applied to power distribution system fault detection, isolation, and recovery. By developing a commercially viable controller for use in utility as well as industrial power systems, the significance of this effort therefore has been the confirmation that indeed model-based reasoning can be successfully applied in this domain.

Developing the power controller required extensive testing in a real-time environment. To meet this requirement, researchers utilized the Space Station Module/Power Management and Distribution (SSM/PMAD) system breadboard, a system based on one of the early space station baseline configurations built to develop and test automation software for potential use on the space station. Both remote and local testing were performed. Remote testing consisted of the Internet transfer of data and commands between the breadboard, located in Huntsville, Alabama, and development sites, located at the University of Central Florida in Orlando, Florida, and the Florida Institute of Technology in Melbourne, Florida. Initially, the remote testing was simply a matter of expediency, but it soon became clear that the Internet delay was an important factor in evaluating the power controller in that it simulated a scenario representative of the intelligent power controller functioning as a ground-based controller of an in-flight spacecraft. Local testing, on the other hand, simulated conditions in which the controller would function as an onboard controller.

Figure 75 depicts the architecture of the system, including the fault

detection, isolation, and recovery process; communication interface; system design model; and run-time display controller elements tested at MSFC. All of these were found to operate successfully. The development tools, model library, and model editor—elements necessary to build a model off-line—are considered necessary for commercialization and will be the subject of the continuing research.

Sponsor: Office of Space Flight

University Involvement: University of Central Florida; Florida Institute of Technology

• • • • •

Load-Side Power Management

Douglas J. Willowby/EB74
205-544-3334

The demand diversion load-side power management breadboard will demonstrate a distributed power system that allows the direct matching of a spacecraft's solar array output to its battery and loads with no further regulation of the main power bus. This will deliver a lighter, more reliable spacecraft power system.

Over the lifetime of a mission, the solar array electrical output weakens due to radiation, micrometeoroid and debris impact, thermal cycling, and ultraviolet darkening—resulting in a greater beginning-of-life (BOL) output than at end-of-life (EOL). Since the solar array is normally sized to meet ending power requirements, there is a surplus in power during most of the mission; thus the solar array utilization factor is low at beginning-of-life and approaches 100 percent at end-of-life. The demand diversion system will enable 100-percent utilization of the solar array over the full life of the mission using a microcomputer to monitor all power system parameters and divert all available solar array power not required to recharge the batteries to the communication transponders and the experiments. This approach also eliminates the need for additional, conventional battery charge-control system hardware.

Researchers are currently experimenting with load-side power management to validate its practicality and to determine how it can be applied

to future spacecraft. This work consists of building a command data system breadboard and test-bed and simulating a spacecraft mission. Breadboards are being built by the University of Alabama in Huntsville (UAH) Students for the Exploration and Development of Space (SEDS), and the test-bed is located in MSFC's Building 4475. The SEDS Satellite (SEDSAT), which will use a load-side power management with a distributed power architecture, has been slated as the mission to be simulated. The actual simulation will demonstrate the power system prior to flight and establish test-bed data to be compared with actual flight data when the Students for the Exploration and Development of Space Satellite-1 is launched in 1996.

The test-bed microcomputer will monitor voltages, currents, and temperatures of the batteries and other system components to perform its demand diversion function. The microcomputer determines the battery's need and diverts excess power to simulated variable transponder loads. If power demand exceeds available power, then the power to the simulated variable transponder loads will be reduced. The microcomputer will also be able to turn off various noncritical loads if the satellite runs into a critical power situation. The use of variable power transponders converts excess energy radiation to radio frequency energy at the efficiency of the transponder, which has the added benefit of increasing the link margin of the space-to-ground radio link throughout much of the satellite's orbit. The electrical power system also provides state-of-the-art, high-efficiency direct current/direct current (dc/dc)

converters at the loads, eliminating the need for central power supplies to preregulate power. In addition, each converter provides integral power filtering and short-circuit protection.

Weight, cost, and reliability are major factors in the selection of any spacecraft subsystem. The demand diversion test-bed will contribute to the understanding of power system architectures and operations to enhance those factors.

Sponsor: Center Director's Discretionary Fund

University Involvement: University of Alabama in Huntsville

• • • • •

Metal Hydride Battery Developmental Study for Application to Future Space Power System Designs

John E. Lowery/EB74
205-544-0080

MSFC is currently working to characterize nickel-metal hydride (Ni-MH) and silver-metal hydride (Ag-MH) cell design, performance, and operation in terms of their applicability to future space programs. Because the Occupational Safety and Health Administration (OSHA) is taking steps to significantly lower the limits of cadmium exposure in the workplace, the future of nickel-cadmium (Ni-Cd) batteries is uncertain. Restrictions imposed will directly affect the production of nickel-cadmium batteries, so the NASA battery steering committee has begun to initiate moves to limit specifications for them in future missions. Nickel-metal hydride batteries—expected to be a direct replacement for nickel-cadmium batteries—potentially have a higher energy density, a lower cost, and are environmentally safer. Silver-metal hydride cells potentially have an energy density even higher than that of nickel-metal hydride and could possibly be used as a replacement for silver-zinc (Ag-Zn) batteries, given that silver-metal hydride batteries are expected to have a lower associated cost and will be more environmentally safe.

The approach adopted to investigate power system needs and requirements for future space programs has been to:

- Evaluate cell vendors offering nickel-metal hydride and silver-metal hydride cell technology

- Obtain representative cells from qualified aerospace battery vendors

- Assemble a test-bed with adjustable operational parameters

- Test cell groups against proposed needs and requirements

- Analyze performance of the cells and establish a data base for comparison to nickel-cadmium, nickel hydrogen (NiH$_2$), and silver-zinc cells.

Delivery of nickel-metal hydride cells occurred in May 1993. Cells were placed into a test-bed, with characterization beginning in June 1993. Parametric testing and characterization is scheduled to continue into FY95. MSFC is currently testing nickel-metal hydride cells in three areas: life-cycling in low-Earth orbit (LEO), storage testing, and parametric testing. Parametric evaluation includes charge retention, high-rate pulse ability, thermal effects, and so forth. This work is being carried out in the Energy Sources Branch of the Astrionics Laboratory, with funding from the Center Director's Discretionary Fund (CDDF).

A flight demonstration of the nickel-metal hydride technology is scheduled for the spring of 1996, when a 16-cell battery will be launched aboard the shuttle in the Students for the Exploration and Development of Space Satellite (SEDSAT), developed at the University of Alabama in

Huntsville (UAH). MSFC assistance to the students has included development of their power system, design review, and operational suggestions. This satellite will hopefully provide an excellent opportunity to demonstrate and evaluate the performance of nickel-metal hydride cells on a low-Earth orbit satellite. A test-bed—with a 16-cell battery currently cycling in it—has been established to study the applicability of the nickel-metal hydride cells to the student satellite mission.

Representative 20-ampere-hour silver-metal hydride cells have been ordered from Eagle-Picher. These cells have become an item of interest as knowledge of nickel-metal hydride has increased. Parametric testing is planned with comparison to the characteristics of silver-zinc cells for possible substitution.

Planned future work includes continued testing of cell groups against proposed needs and power requirements with adjustments as indicated by program evolution and maturation. Cell performance will be analyzed and used to establish a data base for comparison to nickel-cadmium, nickel-hydrogen, and silver-zinc. This data base will be useful in producing trade studies for selection of energy-source candidates on future programs. A NASA technical memorandum and an Intersociety Energy Conversion and Engineering Conference (IECEC) paper are anticipated to characterize performance of the nickel-metal hydride cells in terms of their applicability to future programs.

Sponsor: Center Director's Discretionary Fund

University Involvement: University of Alabama in Huntsville

• • • • •

Advanced X-Ray Astrophysics Facility—Imaging (AXAF-I) Performance Modeling

David E. Zissa/EB52
205–544–3486

The four pairs of cylindrical mirrors for the Advanced X-Ray Astrophysics Facility—Imaging (AXAF–I) program are now being fabricated by Hughes Danbury Optical Systems (HDOS). Image modeling software developed at MSFC for the completed Verification Engineering Test Article I (VETA–I) x-ray test of the largest mirror pair (1.2 meters in diameter) is now being further developed to support image modeling of the Advanced X-Ray Astrophysics Facility—Imaging mirror system. The software will be used to predict the image for the ground test and orbital environment. Predictions will be based on mirror surface metrology, thermal-structural model results, alignment measurements, and the x-ray test or on-orbit environment. A comparison of predictions and measurements from the x-ray ground test system will be used to predict the on-orbit image. The results of this model will be crosschecked with performance predictions from the Smithsonian Astrophysical Observatory (SAO) and from the contractor team of TRW, Kodak, and Hughes.

With their highly annular entrance apertures and cylindrically shaped mirrors, commercial optical design and analysis programs are not tailored for grazing-incidence mirror systems. The GRAZTRACE™ model being developed includes the effects of x-ray source position, x-ray source size, mirror figure errors, mirror surface roughness, mirror reflectivity, alignment, and detector shape. There are links to mirror surface metrology data and the mirror distortion predictions of standard structural analysis programs. Mirror figure errors are incorporated into the ray-trace model by interpolating the metrology data and structural model results onto a finely spaced grid. Individual surface terms such as curvature and slope errors can also be applied.

With the CONVOLVE™ program, ray-trace results can be convolved with the x-ray scattering distribution predicted—using the EEGRAZ™ program written by Paul Glenn of Bauer Associates—from the roughness of the mirror surfaces. Ray-trace results can also be convolved with the detector aperture shape and the x-ray source size. An interactive interface is being developed to use the collection of programs involved. The output of the program includes image plots as well as parameters such as x-ray collecting error, root-mean-square (rms) image size, and image-encircled energy distribution. This model, which is also applicable to other grazing incidence x-ray optical systems, is being developed at MSFC as part of the Advanced X-Ray Astrophysics Facility—Imaging program with assistance from the University of Alabama in Huntsville (UAH).

Zissa, D.E. 1992. Comparison of Ring-Focus Image Profile with Predictions for the AXAF VETA–I Test. Proceedings of the Society of Photo-optical Instrumentation Engineers (SPIE), 1742:91–103.

Glenn, P.; Reid, P.; Slomba, A.; and Van Speybroeck, L. 1988. Performance Prediction of the AXAF Technology Mirror Assembly Using Measured Mirror Surface Errors. *Applied Optics* 27:1539.

•••••

Shuttle Landing Wind Profiling

Steve C. Johnson/EB54
205–544–3478

Michael J. Kavaya/EB54
205–544–8453

Two demonstrations of new wind profiling technology for shuttle landing were conducted at the Shuttle Landing Facility at Kennedy Space Center (KSC). The wind profilers demonstrated were capable of providing more real-time and/or local winds than the currently used Rawinsonde. The Rawinsonde is a radio-tracked balloon that rises slowly, sometimes drifting far from the area where the wind measurement is desired. As a consequence, the correlation between the actual winds encountered by the shuttle and those measured by the balloon is often reduced. The new sensors' performances were evaluated through wind measurement comparisons with the Rawinsonde and other existing profilers at the Kennedy Center as well as with winds derived from the shuttle flight data. Other evaluation factors included technological maturity, operational capability, and cost.

An Air Force holmium, thulium: yttrium aluminum garnet (Ho, Tm: YAG) lidar, or laser radar, operating at a wavelength of 2.09 micrometers (μm); a National Oceanic and Atmospheric Administration (NOAA) carbon dioxide (CO_2) lidar operating at 10.59 micrometers; and a Radian Corporation 915-megahertz (MHz)

boundary-layer radar were demonstrated, concurrent with the landings of STS–54 and/or STS–56. The lidars selected were the leading, eye-safe lidar wind profiling technologies. The boundary-layer radar was a recently commercialized instrument based on technology developed at the National Oceanic and Atmospheric Administration's Aeronomy and Wave Propagation Laboratory. The lidars used mirror scanners to direct the beam anywhere within a hemisphere. The lidars measured the range-gated, radial component of the velocity of entrained aerosols—accurate tracers of wind— in the atmosphere along the scan line of sight. A constant elevation, variable azimuth scan was typically used to produce a wind profile in a few minutes. A fixed-angle scan, parallel to the shuttle glideslope, was also used to instantaneously measure the in-plane winds (winds in the plane of the runway and glidescope) during shuttle landing. The radar measured the range-gated, radial component of the velocity of atmospheric refractive index variations—also accurate tracers of wind—along three fixed scan directions. Velocities along a vertical beam and along two beams orthogonal in azimuth at 21° from vertical were combined to produce wind profiles after an hour of averaging. A single, phased-array antenna was used to sequentially and repetitively point the beam in each of the three directions.

None of the systems demonstrated was all-weather, in that the lidar signals were blocked by clouds and the radar signals were corrupted by rain. However, the shuttle must land in conditions with good visibility, so

none of the systems was precluded. The lidars both required operators, but the radar operated autonomously. Wind profiles from all three sensors demonstrated compared more favorably than wind profiles from the Rawinsonde to the winds derived from the shuttle flight performance. Despite the more rapid update rate and flexible scanning of the lidars, the radar was selected for the shuttle landing wind profiling application because of its autonomous capability and relatively low cost. Several of the radars are being purchased by the Air Force for placement around the runway at Kennedy Space Center.

The lidars and radar demonstrated have the potential to enhance shuttle safety through more real-time and/or local wind measurements than the currently used Rawinsonde. The same systems can be used to enhance the safety of commercial air travel. Ground-based or airborne lidars, in particular, could be used to remotely and instantaneously sense dangerous wind shear during aircraft takeoff and landing.

Sponsor: Office of Space Flight

• • • • •

Direct Tropospheric Wind Measurements From Space— Coherent Lidar Design and Performance Prediction

Michael J. Kavaya/EB54
205–544–8453

Steve C. Johnson/EB54
205–544–3478

Direct global measurements of tropospheric winds from space are highly desired for many NASA, National Oceanic and Atmospheric Administration (NOAA), Department of Defense (DOD), Department of Energy (DOE), Environmental Protection Agency (EPA), and industrial applications.[1] The two most paramount uses of the data would be for global climate change research and for greatly improved weather forecasting. In 1986, W.D. Bonner, Director of the National Meteorological Center wrote, "The addition of global wind profiles offers the best opportunity for significant improvement in medium- and large-scale forecasts...Wind data will enhance forecasts on all scales." In 1993, R. Errico of the National Center for Atmospheric Research added, "...With no wind observing system planned for EOS [Earth Observing System], process studies will be extremely limited since advection, both horizontally and vertically, is such a dominant mechanism...The usefulness of the EOS data will be greatly enhanced if concurrent wind information is available."

NASA/MSFC responded to this pressing need, and in 1992 completed dual Phase A and B studies, enlisting the support of GE Astro Space (now Martin Marietta Astro Space) and Lockheed Missiles and Space Company, for a full tropospheric profiling instrument, the Laser Atmospheric Wind Sounder (LAWS). Both contractors recommended a pulsed, isotopic, carbon dioxide (CO_2) laser, coherent laser radar (CLR) system with pulse energy near 20 joules (J), pulse repetition frequency (PRF) near 5 hertz (Hz), optical diameter near 1.6 meters (m), and full-time operation (100-percent orbit duty cycle). However, the projected mission costs were deemed unacceptable for this new era of reduced NASA resources, and the projected spacecraft resource requirements exceeded the capabilities of small satellites.

MSFC has therefore conducted an in-house effort to investigate innovative versions of space-based wind profilers that are smaller, lighter, and less expensive; consume less power, require less heat removal, and fit on small spacecraft and launch vehicles; provide valuable engineering data and space heritage; and still deliver a significant scientific product consistent with NASA's Mission To Planet Earth (MTPE). The working acronym for these instruments is the "Autonomous Earth Orbiting Lidar Utility Sensor (AEOLUS)," named after the mythical Greek god of wind.

The project consists of a series of point designs for a small, lightweight, low-cost, low-risk instrument to measure tropospheric winds from space in regions of high aerosol

backscatter.[2] Mission goals have included providing valuable scientific information in support of NASA's Mission to Planet Earth; demonstrating space operation of key technologies required for a full-scale Laser Atmospheric Wind Sounder; and implementing a logical, affordable, evolutionary process leading to full-scale measurement of global tropospheric winds. Basic ground rules have been to use components as close to commercial off-the-shelf (COTS) as possible, utilize scalable technology and measurement techniques, and design a flexible instrument capable of being accommodated on a variety of platforms in space (such as small satellites, the space shuttle, space station, and so forth). Considering the various mission requirements that must be achieved simultaneously from a system perspective, the sensor of choice is a pulsed coherent laser radar consisting of a laser transmitter, an optics subsystem, a receiver, a control computer, a data acquisition subsystem, and a data processing computer.

The MSFC team has completed six instrument point designs. Two candidate laser technologies are being examined: the carbon dioxide laser with a 9.11-micrometer (μm) wavelength; and the thulium, holmium: yttrium lithium fluorine (Tm, Ho: YLF) diode-pumped, solid-state laser at 2.06 micrometers. Each design is examined from the mechanical, electrical, thermal, optical, laser, and coherent laser radar wind measurement performance—as well as spacecraft accommodation—perspectives. The six point designs are presented in figure 76. The aerosol

2 meters

| LAWS Phase B Design | AEOLUS Designs 1 and 3 | AEOLUS Designs 2 and 4 | AEOLUS Designs 5 and 6 |
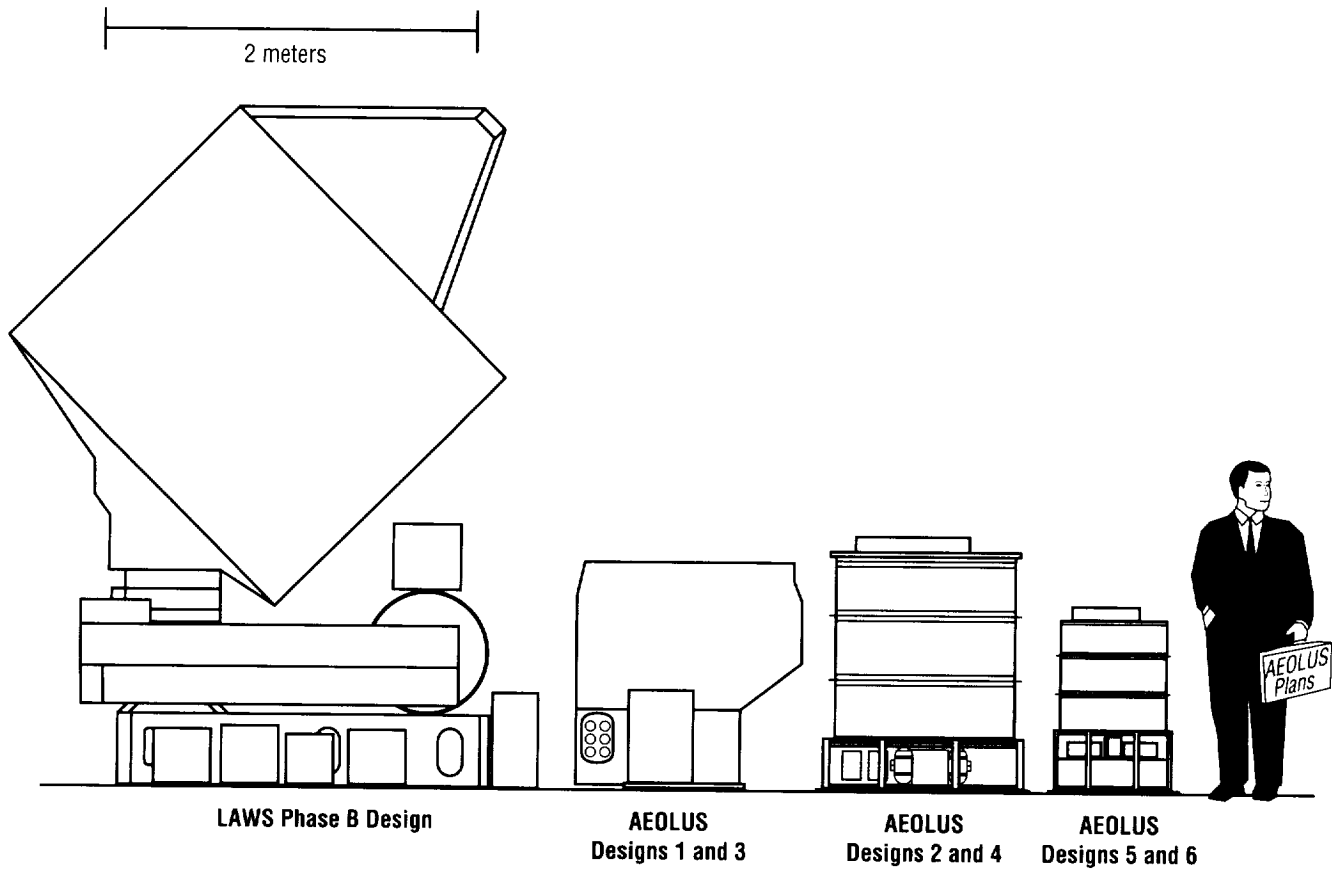
FIGURE 76.—Comparison of Autonomous Earth Orbiting Lidar Utility Sensor point designs and one of the Laser Atmospheric Wind Sounder Phase B designs.

backscatter sensitivity of each design is the lowest level of aerosol backscatter that would yield "good" wind estimates, i.e., estimates tightly grouped around the true wind velocity at least 50 percent of the time. Care must be taken when comparing these values at the two different optical wavelengths, since backscatter varies with wavelength. Features common to all six point designs are a signal-to-noise ratio (SNR) margin of 3 decibels (dB), a budgeted misalignment loss of 3 decibels, a sun-synchronous orbit height of 350 kilometers (km), a

30-degree laser beam nadir angle, a target (atmospheric aerosol particles) altitude of 300 meters, transmit and receive optics efficiencies of 0.9 each, and no polarization mismatch loss.

When comparing the six designs (table 8), one notes that point designs 5 and 6 have a pulse energy-receiver aperture area product (hence, aerosol backscatter sensitivity) a factor of 32 smaller (15 decibels) than designs 3 and 4 due to the desire to be accommodated on a Pegasus rocket. They achieve considerable volume

and mass savings. The orbit average electrical power needed by design 5 is higher than that for designs 3 and 4 due to the increase of orbit duty cycle to 30 percent (versus 5 percent), as well as an increase in laser pulse repetition frequency to 50 hertz (versus 10 hertz). Design 6 requires more power than design 5, even though the number of laser shots per orbit is identical, because the orbit duty cycle is 100 percent (versus 30 percent), and all components of the instrument are always turned on. Designs 2, 4, 5, and 6 use a rotating

131

TABLE 8.— *Autonomous Earth Orbiting Lidar Utility Sensor designs intercomparison*

Parameter	No. 1	No. 2	No. 3	No. 4	No. 5A Thin Clouds	No. 5B Thick Clouds	No. 6A Thin Clouds	No. 6B Thick Clouds
Performance Backscatter (/m-sr) (1-shot) @ P_g = 50%	7.8E–09	1.1E–08	5.1E–08	6.8E–08	2.2E–06	2.4E–05	2.2E–06	2.4E–05
SNR Margin, dB	3	3	3	3	3	3	3	3
Vertical Resolution, m	1000	1000	1000	1000	1000	64	1000	64
Wind Processing Search Space, Horizontal, m/s	±20	±20	±20	±20	±20	±20	±20	±20
Instrument Laser Wavelength, µm	9.11	9.11	2.06	2.06	2.06	2.06	2.06	2.06
Scan Type	dual-look	scan wedge	dual-look	scan wedge	scan wedge	scan wedge	scan wedge	scan wedge
Pulse Energy, mJ	400	400	200	200	25	25	25	25
PRF, Hz	20	20	10	10	50	50	15	15
Telescope Diameter, m	0.5	0.5	0.5	0.5	0.25	0.25	0.25	0.25
Misalignment Loss, dB	3	3	3	3	3	3	3	3
Misalignment Angle, µRAD	13.9	16.1	3.15	3.64	7.28	7.28	7.28	7.28
Size, m	1.22x1.24x1.33	1.22(D)x1.35	1.22x1.24x1.33	1.22(D)x1.35	0.73(D)x0.99	0.73(D)x0.99	0.73(D)x0.99	0.73(D)x0.99
Inches	48.0x48.8x52.4	48.0(D)x53.3	48.0x48.8x52.4	48.0(D)x53.3	28.8(D)x38.9	28.8(D)x38.9	28.8(D)x38.9	28.8(D)x38.9
Volume, m³	2	1.6	2	1.6	0.4	0.4	0.4	0.4
ft³	71	55.8	71	55.8	14.7	14.7	14.7	14.7
Mass, kg	231	266	191	226	130	130	124	124
Pounds	508	585	420	497	286	286	273	273
Power, W (Standby/Warm-up/Oper)	160/332/437	168/378/476	75/182/355	83/226/391	88/227/334	88/227/334	235	235
Orbit Duty Cycle, Percent	5	5	5	5	30	30	100	100
Orbit Average Power, W	203	219	107	122	185	185	235	235

wedge to create a conical scan about the nadir direction, while designs 1 and 3 have two fixed pointing directions, fore and aft, to allow biperspective wind measurements along a line parallel to the ground track, but offset by 144 kilometers. The two views of a single point in the atmosphere would be accomplished by switching the coherent laser radar between two 50-centimeter (cm) telescopes, and would occur about 40 seconds apart. This configuration has less science value than the conical scan. Comparing design 1 with 2 and design 3 with 4 reveals that wedge scanning increases the mass and power and reduces the volume.

No attempt has been made to have equal science value between the point designs at 2.06 and 9.11 micrometers. A MSFC study is underway to quantify the ratio of aerosol backscatter values between the two wavelengths for various candidate atmospheric targets within the sensitivity range of the different point designs. Note that holding the misalignment loss fixed at 3 decibels causes the misalignment angle specification to become stricter at 2.06 micrometers.

Accurate global tropospheric wind measurements are highly desired and will provide many benefits. Atmospheric winds have been successfully measured with coherent laser radar systems since 1967. A full-scale mission that measures the lowest levels of aerosol backscatter is technically feasible but not practical in today's economic climate. However, valuable and exciting scientific products are still possible with a smaller and more affordable

instrument. Significant benefits could be achieved in only a few years by starting a faster, smaller, and cheaper mission now. NASA/MSFC is ready to design and perform such a mission.

[1]Baker, W.E. 1993. Why We Need LAWS. *Storm, The World Weather Magazine* 1(1):26–30.

[2]Kavaya, M.J.; Spiers, G.D.; Lobl, E.S.; Rothermel, J.; and Keller, V.W. April 1994. Direct Global Measurements of Tropospheric Winds Employing a Simplified Coherent Laser Radar Using Fully Scalable Technology and Technique, 2214–31. Society of Photo-optical Instrumentation Engineers' International Symposium on Optical Engineering in Aerospace Sensing; Technical Conference 2214 on Space Instrumentation and Dual-Use Technologies, Session on Faster, Cheaper, Smaller Space Science Optical Instruments, Orlando, Florida.

Sponsor: Office of Mission to Planet Earth

University Involvement: University of Alabama in Huntsville; University of Colorado at Boulder

• • • • •

DIAGNOSTIC AND INSPECTION SYSTEM

New Optically Stimulated Electron Emission Instrument

Billy H. Nerren/EH12
205–544–2636

H. DeWitt Burns/EH12
205–544–2529

Optically stimulated electron emission (OSEE) is currently utilized in surface cleanliness inspection of redesigned solid rocket motor (RSRM) hardware. A joint effort between MSFC, Langley Research Center (LaRC), and Thiokol Corporation's Space Operations has been undertaken to develop a new-generation inspection instrument to improve system reliability, reproducibility, and sensitivity.

Optically stimulated electron emission is a photoelectron emission technique used for surface inspection. The surface of interest is irradiated with ultraviolet (UV) light. Ultraviolet photons bombard the subject area, resulting in electron emission from the surface. If the energy of bombarding photons is greater than the substrate photoelectric work function, electrons are emitted from the surface. Surface contamination attenuates the photons from reaching the surface and, to a lesser extent, the electrons from leaving the surface. Due to these effects, a signal from a contaminated surface is less than a signal from a clean one. This signal decline can be measured, thereby determining the relative contamination.

Optically stimulated electron emission is used in redesigned solid rocket motor manufacturing to verify case-internal surface cleanliness prior to insulation application and nozzle steel housing inspection prior to adhesive bonding of phenolic liners. The first-generation optically stimulated electron emission instrument used for motor case inspection had problems with stability, stemming from electronics design, bulb reliability, and shielding problems.

NASA Headquarters provided funding to Langley Research Center for research leading to the design, development, and fabrication of a next-generation electron emission system. The purpose of the redesign effort was to decrease equipment variability due to electromagnetic interference, electronics design, ultraviolet bulb degradation, and environmental fluctuations. MSFC and Thiokol provided data on the existing technology and identified needed improvements for the new instrument. An optically stimulated electron emission instrument was provided to Langley for their evaluation. Their findings have been documented in a Langley report.[1] As a result, a redesign was initiated in Langley Research Center's Instrument Development Laboratory, employing the talents of Langley personnel, laboratory support contractors, and faculty members from the College of William and Mary.

Improvements that were most feasible and could be accomplished within the allotted budget have been implemented into the fabrication of the new instrument. Electronics improvements have resulted from new shielding and electronics design. The new ultraviolet source, designed with an active feedback loop, maintains constant bulb output. Environmental fluctuations have been alleviated by incorporating an argon purge system into the sensor head. Patents on resulting improvements—including light source stability, a Kelvin probe attachment for surface photoelectric work function measurements, and sensor circuit and technique refinement—have been applied for by the Langley team.

The implementation of the redesigned instrument in redesigned solid rocket motor production could result in minimized hardware rework, as well as reduced production cost, rework time, and scheduling. The instrument has applications in industry where surface cleanliness is critical and must be verified. High instrument sensitivity makes it an excellent process control tool. Langley has worked with an electronics consortium on application of the instrument for inspecting electronic printed circuit board materials.

The new optically stimulated electron emission equipment is currently in MSFC's Materials and Processes Laboratory for characterization testing. An instrument will be shipped to Thiokol for planned future implementation in redesigned motor case hardware processing to reduce rework rates, scheduling changes, and costs.

[1] Yost, William T.; Welch, C.S.; and Abedin, N. OSEE Science Base, Final Report.

• • • • •

MATERIALS AND MANUFACTURING PROCESSES

Space-Stable, Electrically Conductive, Thermal Control Coatings

Ralph Carruth/EH12
205-544-7647

The requirements for electrically conductive thermal control coatings are changing. Some thermal control coatings with limited conductivity have been available for some time, but these have been mostly useful only for controlling spacecraft charging in the geosynchronous environment. Also, such coatings as indium-tin oxide have been used, but these thin films have had problems in application and in sustaining use on a large scale. A definite need exists for conductive thermal control coatings whose electrical and thermo-optical properties are stable in a space environment.

In the past, spacecraft utilized power distribution at 28 volts, direct current (Vdc), with a solar array operating in the 30-volt range. Larger power systems, such as that on the International Space Station *Alpha*, utilize 160-volt solar arrays. The interaction of such systems with space plasma can place a structure at a high voltage relative to the local plasma, thereby producing some very undesirable results. The use of conductive, rather than insulating, thermal control surfaces can aid in preventing such effects. The space station will use an active device, a plasma contactor, to control the potential difference between station structure and the space plasma.

The use of satellites—tethered with other spacecraft by a conducting tether and moving at orbital velocity across the Earth's magnetic field lines—can produce both large voltages and large current collection. The current density to the surface of such satellites is orders of magnitude higher than those necessary for spacecraft charging control. The need for coatings with much higher electrical conductivity, possessing thermo-optical and material properties that will not degrade significantly in the space environment, has become evident.

In January of 1994, a phase I Small Business Innovation Research (SBIR) contract was awarded to AZ Technology located in Huntsville, Alabama. Work is directed at producing space-stable, conductive thermal control coatings. Computer modeling and analysis of the various molecular characteristics that influence electrical conductivity has been initiated. During this period, some of the efforts that have focused on the molecular modeling of compounds of potential interest include determining the feasibility of synthesizing compounds that literature or theory indicate should be good candidates; identifying potential kinetic or steric factors that may inhibit the formation of a compound; and identifying candidate compounds to better understand their spatial configuration, electron cloud formation, and overlap.

Some of the ceramic pigments of interest have been synthesized in the laboratory. The compounds addressed initially have been antimony and indium-doped tin oxide, which have exhibited qualitatively good electrical conductivity. Plans are to continue the synthesis of materials, produce initial coating formulations, and evaluate deposition characteristics.

Sponsor: Office of Advanced Concepts and Technology; Small Business Innovation Research

Industry Involvement: AZ Technology

•••••

135

Improved Facility for Investigating Combined Space Environmental Effects

David L. Edwards/EH15
205–544–4081

James M. Zwiener/EH15
205–544–2528

Development of a world-class facility to simulate combined space environmental effects has long been a goal for MSFC's Materials and Processes Laboratory. The Space Environmental Effects Facility (SEEF) Combined Environmental Effects Test-Cell 3 (CEETC3) system (fig. 77) has been improved to fulfill this goal. Temperature-controlled samples in the system can be exposed to simultaneous multienvironment sources (protons, high-energy electrons, low-energy electrons, vacuum ultraviolet (VUV) radiation, and near-ultraviolet (NUV) radiation). This system also offers an in-situ reflectance measurement capability utilizing a vacuum-integrating sphere methodology. Total integrated specular reflectance from 250 to 2,500 nanometers (nm) is measured using the Gier-Dunkle integrating sphere technique.

The system generates energetic protons over the range of 0.1 to 0.8 million electron volts (MeV) and electrons from 0.2 to 2.5 million electron volts from the two particle accelerators. Electrons over the range of 1 to 50 kiloelectron volts (KeV) are generated from an electron flood gun. Two ultraviolet radiation sources are integral to the system.

A near-ultraviolet source, mercury-xenon (Hg-Xe), is located external to the test chamber and produces photons over the range of 200 to 2,500 nanometers. This source can produce up to 10 near-ultraviolet (200 to 400 nanometers) equivalent suns for accelerated testing.

A vacuum ultraviolet, D, source is located within the system's test chamber and produces photons over the range of 118 to 200 nanometers. This source also provides up to 10 vacuum ultraviolet equivalent suns for accelerated testing.

All of the above defined sources can be tailored to expose a material to the predicted space environment for specific missions.

Sponsor: Office of Space Flight

• • • • •

FIGURE 77.—Combined Environmental Effects Test-Cell 3 system.

The Reaction of Nitrogen With 2195 Aluminum-Lithium Alloy

Arthur C. Nunes/EH23
205-544-2699

While studying the reaction of properties to the structure of the 2195 aluminum-lithium alloy—the main structural material for the new super-lightweight external tank for the space shuttle—a reaction with nitrogen has been noted to occur at temperatures above 360 °C. Even though this temperature is well above service temperatures, the reaction has definite implications for welding and other processing situations.

This reaction manifests itself through weight gain and the formation of a brown surface layer that reacts with platinum when the 2195 alloy is heated in the nitrogen atmosphere of a thermogravimetric analyzer. Exothermic peaks have been observed in the output of a differential thermal analyzer, but only for weld metal and not for wrought parent metal. (The absence of exothermic peaks in the parent metal could result from a slowing of the reaction, perhaps due to a less-penetrable grain bouldary structure, rather than an absence of reaction.) The weld metal, but not the wrought parent metal, also shows signs of an internal nitriding reaction when the alloy is heated above 360 °C for a few minutes in a nitrogen-containing atmosphere (alternating in etching character at the dendrite boundaries and porosity formation).

Nitrogen contamination of the shield gas during welding has been observed to produce porosity as well as a surface film that keeps the molten metal in the weld pool from flowing together properly. Surface films on variable polarity plasma arc (VPPA) welds (the process used to fabricate the space shuttle external tank) result in a sunken, crinkled bead surface, often with a distinct seam where the streams of molten metal from each side of the plasma jet join behind the jet. A dark surface coloration (possibly lithium nitride) has also been exhibited. A laser weld has cracked when heated in nitrogen at 450 °C, but not when heated in vacuum or inert gas. Heated 2195 alloy surfaces exposed to air have exhibited surface porosity. All the above effects do not occur during normal welding procedures where proper shielding is employed (fig. 78).

Talia, J.E., and Nunes, A.C., Jr. May 17–19, 1994. Cracking During Welding of 2195 Aluminum-Lithium Alloy: Experimental Approaches Towards Mechanism. Conference on Advanced Earth-to-Orbit Propulsion Technology. Al-Li Alloys for Aerospace Applications Workshop, MSFC.

Sponsor: Office of Space Flight

• • • • •
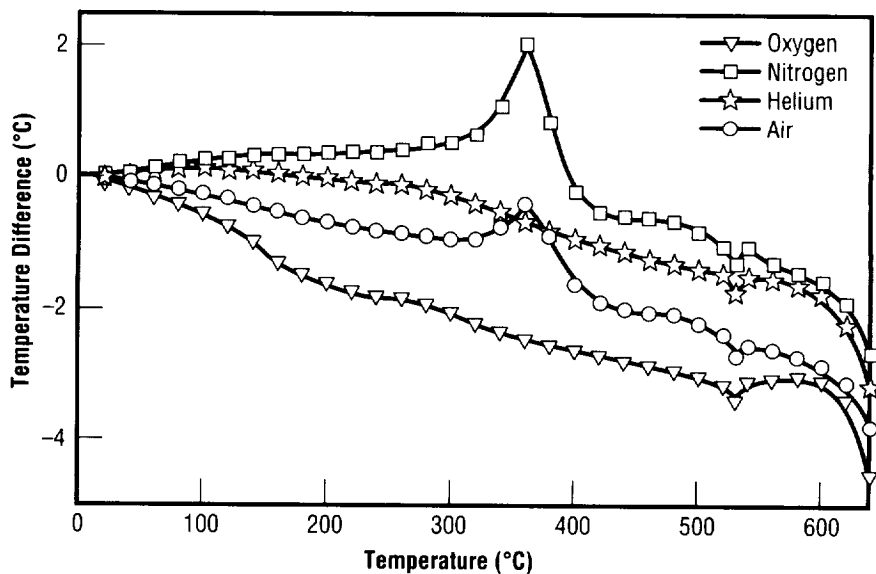
FIGURE 78.—Differential thermal analysis curves for 2195 weld metal.

Relating Weld Strength to Weld-Bead Geometry

Arthur C. Nunes/EH23
205–544–2699

One would expect that the strength of a weld depends upon the configuration of the weld-bead cross-sectional geometry as well as upon microstructural features. Empirical observations[1] bear out this expectation. Yet the nature of the relation of weld strength to weld-bead geometry is not spelled out in welding textbooks, and weld diagnostic practice usually only deals with the effects of bead geometry in a qualitative manner at best. Quantitative precision is desired for meeting the stringent requirements of welding procedures currently under development for the assembly of aerospace hardware. This effort supports the weld development program for the 2195 aluminum-lithium alloy to be used for the space shuttle super-lightweight external tank, while building upon earlier work in support of the current 2219 aluminum external tank. The approach is general and potentially adaptable to a wide range of metals.

The objective of this study has been to synthesize some relatively simple analytic formulas relating weld-bead geometry to ultimate tensile strength, yield strength, and elongation of a butt-weld tested in tension perpendicular to the weld line. The theory entails five elements: a description of the initial weld structure, deformation compatibility, force equilibrium, a stress-strain relation, and a microfracture criterion.

Thus far, these elements have been put together only in the simplest of cases: a parallel-sided weld with no projecting reinforcements. (Even in this case, it became apparent that the microfracture criterion used was inadequate.)

For the sake of computational simplicity, the weld geometry is represented not by discrete boundaries, but by an initial hardness distribution function. The function tentatively chosen has been selected from the "Creation and Destruction Function" family synthesized previously[2] for other weld-modeling applications. Compatibility is built into the analysis by approximating the strain field over the weld section as a result of pure slip occurring on two families of planes at ±45° to the tension axis.

The flow stress distribution along a 45° slip line determined by the initial hardness distribution fixes the weldment tensile load at the point at which flow begins to take place along that particular line. The region of plastic flow in the weld lies between those two pairs of 45° lines in the incipient slip condition.

For a flow stress, σ_p, in the weld parent metal and a flow stress, σ_w, at the center of the weld, the yield strength ,σ_y, of a shaved weldment with a straight-sided weld of thickness, w, in a plate of thickness, t, is estimated as:

$$\sigma_y = \sigma_p - (\sigma_p - \sigma_w) \left(\frac{\arctan\left(\frac{t}{w'}\right)}{\frac{t}{w'}} \right)$$

A local plastic stress-strain hardening curve for the metal allows computations of the strain undergone by each slipping plane to bring its strength into equilibrium with the applied load on the specimen.

Results of preliminary computations indicate that a microfracture criterion needs to be constructed to be in better agreement with local microstructural conditions. Under consideration is a local fracture criterion where particles are considered as lines of weakness rupturing at stresses inversely proportional to the square root of the particle size, as is the case for cracks in the Orowan-Griffith fracture criterion. In this instance, size distribution for critical particles determines the local fracture stress distribution.

[1] Nunes, A.C., Jr.; Novak, H.L.; and McIlwain, M.C. March 1981. Weld Geometry Strength Effect in 2219–T87 Aluminum. NASA Technical Memorandum TM–82404.

[2] Nunes, Arthur C., Jr. 1992. Creation and Destruction Functions for Building Complex Representations of Data. NASA Technical Briefs.

• • • • •

Understanding Weld-Bead Penetration

Arthur C. Nunes/EH23
205-544-2699

Whenever one tries to deal with welding in a quantitative way, the matter of the relation between welding parameters and weld geometry, or "penetration," takes on central importance. The present study has been directed in support of the development of a multivariable control system for variable polarity plasma arc (VPPA) welding, which plays a major role in the assembly of the space shuttle external tank.

The first attempts to deal with penetration modeled the molten weld-pool boundary as the melting temperature isotherm of a moving point heat source, with the weld bead itself being the envelope of successive pools. Strong currents, particularly those due to surface tension gradients in the weld pool, as well as phase transformations on the weld-pool surfaces, upset the computations of the simple point source model. In the past, it was proposed[1] to deal with these factors through the introduction of dipoles and quadrupoles into a moving heat source model.

Characteristic of the variable polarity plasma arc process is the full penetration "keyholing" mode of operation where the plasma jet penetrates through the workpiece and the molten metal flows around the arc to join in a weld pool behind the arc. The arc itself rides up onto the forward surface of the keyhole cavity

to deliver its heat and melt its way forward. At first, attempts were made to model keyhole welding as a moving line source, but it was found (fig. 79) that the efficiency of power transmission to the workpiece went up as the weld speed increased, i.e., the weld width did not drop as fast with speed as it would have had the power to the workpiece been constant.

Changes in the geometry of the keyhole, which occur with speed changes, were found to be responsible for the change in efficiency.[3] As the speed increased, the forward surface of the keyhole sloped backward more and, in doing so, caught more of the power of the plasma jet. If the portion

of the plasma coming in contact with the forward interface is assumed to give up its fraction of power at the point of contact like an electron beam, then a simple computation of efficiency, η, as a function of weld speed yields:

$$\eta = \left(\frac{1 + \dfrac{C(T_m - T_o)}{L} + }{\dfrac{\rho_L C_L (T_s - T_m)}{\rho L}} \right) \frac{\rho L V_w}{p d_c}$$

where:

C = specific heat of solid weld metal
C_L = specific heat of liquid weld metal
L = latent heat of melting
ρ = density of solid weld metal
ρ_L = density of liquid weld metal
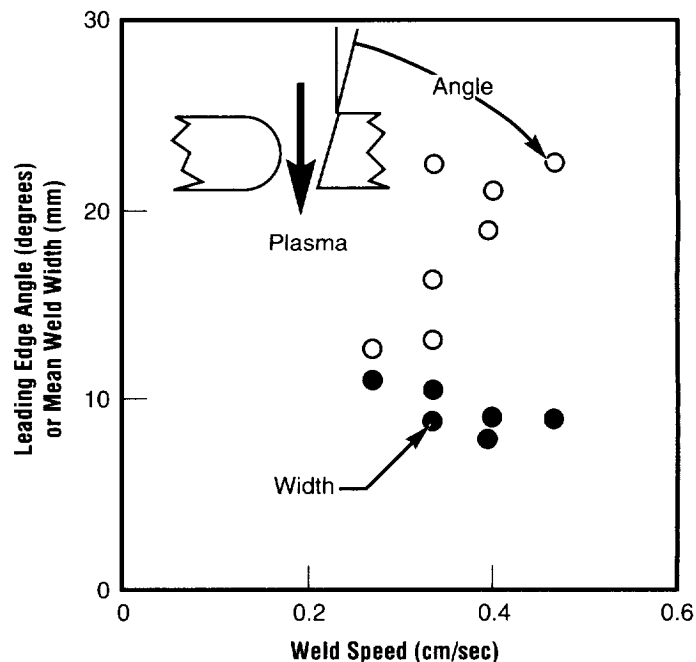
FIGURE 79.—Mean weld width and keyhole leading edge angle for variable polarity plasma arc weld in one-half-inch (12.7-millimeter) 2219 aluminum plate versus weld speed. Power held constant at approximately 8.1 kilowatts.[2]

139

T_o = ambient temperature
T_m = melting temperature of weld metal
T_s = superheat temperature of liquid at forward interface
V_w = weld speed
p = power density of plasma jet
d_r = plasma jet diameter.

The above concept has been the basis of an attempt to increase depth-to-width penetration of a variable polarity plasma arc weld by elongating the electrode in the weld direction and shrinking the lateral dimension proportionately. This attempt has been thwarted by an inability to control the distribution of current emission over the noncircular electrode; however, it is likely other ways can be found to take advantage of the increased understanding of plasma arc penetration.

[1]Nunes, A.C., Jr. 1983. An Extended Rosenthal Weld Model. *Welding Journal* 62(6):165s–170s.

[2]Nunes, A.C., Jr. December 8–10, 1993. A Welding Mini-Model and Some Applications. Presented (by J.C. McClure) at 1993 International Conference on Modeling and Control of Joining Processes, Orlando, Florida.

[3]Gordon, S., 1992. VPPA Weld Model Evaluation. Nichols Research Corporation Final Report: Contract Number NAS8–38812.

Sponsor: Office of Space Flight

• • • • •

Benefits of Eutectic-Free/Bimodal Gamma-Prime Microstructures

Deborah D. Schmidt/EH23
205–544–4943

When components of the space shuttle main engine's (SSME's) turbopumps are exposed to gaseous hydrogen, they undergo a degrading phenomenon known as hydrogen environment embrittlement (HEE). This embrittlement significantly reduces the service life of these components, the space shuttle main engine itself, and potentially futuristic space vehicles as well. A program is currently ongoing to develop an improved, single-crystal, nickel-based superalloy specifically tailored for use in hydrogen-fueled rocket engine turbopumps.

At present, two single-crystal turbine blade alloys, PWA 1482 and PWA 1484, have successfully been processed by super solutionizing and hot isostatic pressing (HIP) to a eutectic-free microstructure (figs. 80, 81, and 82). The alloys have then been heat-treated for the addition of a gamma-prime bimodal microstructure. This microstructure improves the fatigue and crack-growth properties to a highly significant degree (figs. 83, 84, and 85).

Several patent applications have been submitted on this technology, and the technology has been diversified to include equiaxed alloys as well, such as MAR–M247 used in the alternate turbopump development (ATD)

turbopump vane rings. This very versatile technology is also being considered for other alternate turbopump development applications. The vane rings have been tested at Stennis Space Center for over 5,000 seconds (with 10 starts) without any cracking. Increased service life (which equates to a more economical machine) and increased safety margins are major benefits.

General conclusions are:

• PWA 1482 and PWA 1484 can be produced in a hot isostatic-pressing, eutectic-free form with a bimodal gamma-prime microstructure.

• Eutectic-free single crystals offer a significant benefit over conventional single crystals.

• A bimodal gamma-prime precipitant structure provides a significant improvement in fatigue crack growth capability compared to a conventional gamma-prime structure.

• Eutectic-free processing combined with a bimodal gamma-prime morphology has a synergistic effect on fatigue and fracture capability.

• This technology is versatile and benefits equiaxed microstructures in addition to single crystals.

Sponsor: Office of Advanced Concepts and Technology

Industry Involvement: Pratt & Whitney

• • • • •

(a)

(b)

(c)

(d)
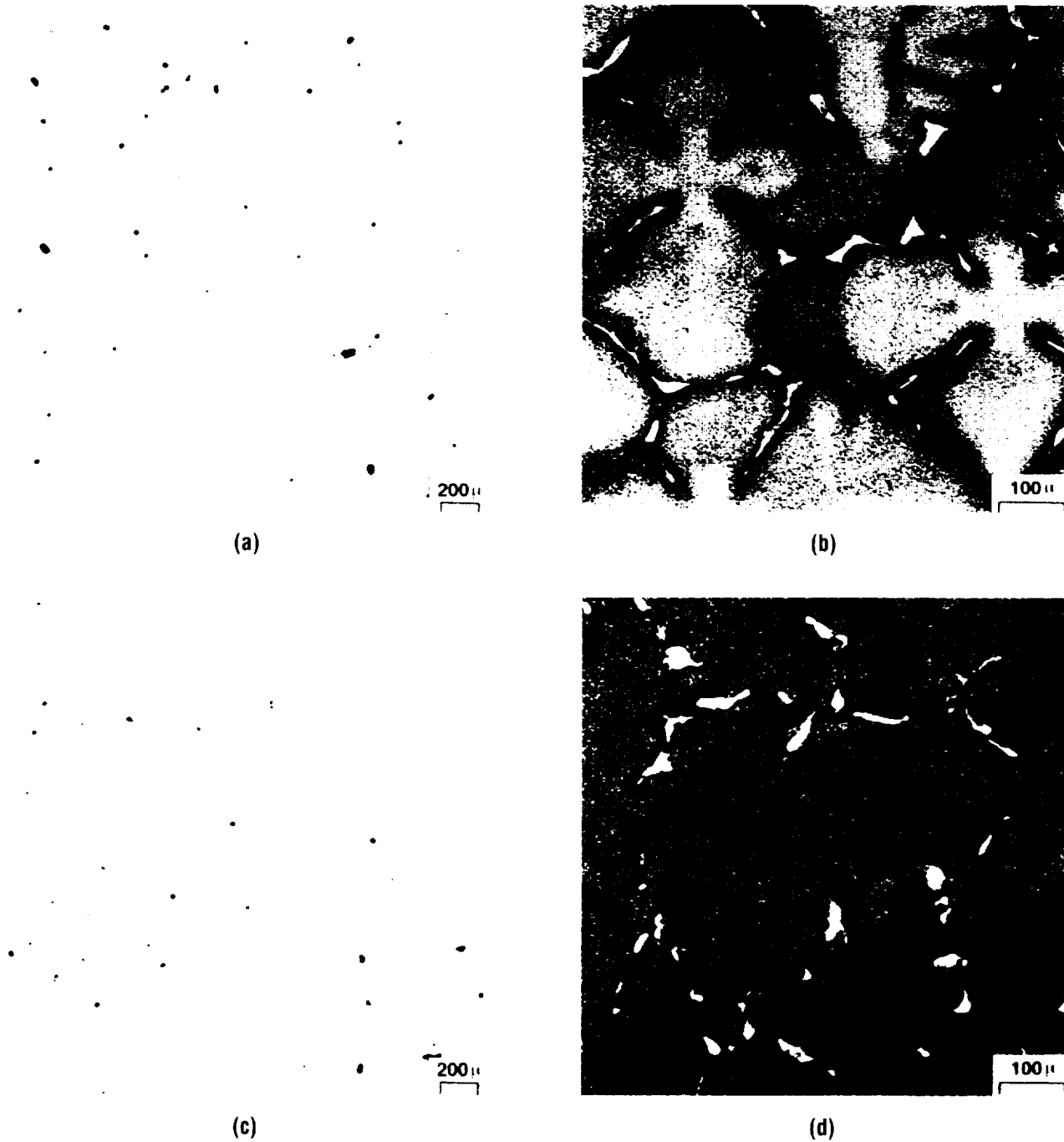
FIGURE 80.—Typical as-cast microstructure for PWA 1482 and PWA 1484: (a) PWA 1482 as-polished, (b) PWA 1482 AG21 etched, (c) PWA 1484 as-polished, and (d) PWA 1484 AG21 etched.

141

(a)

(b)

(c)

(d)
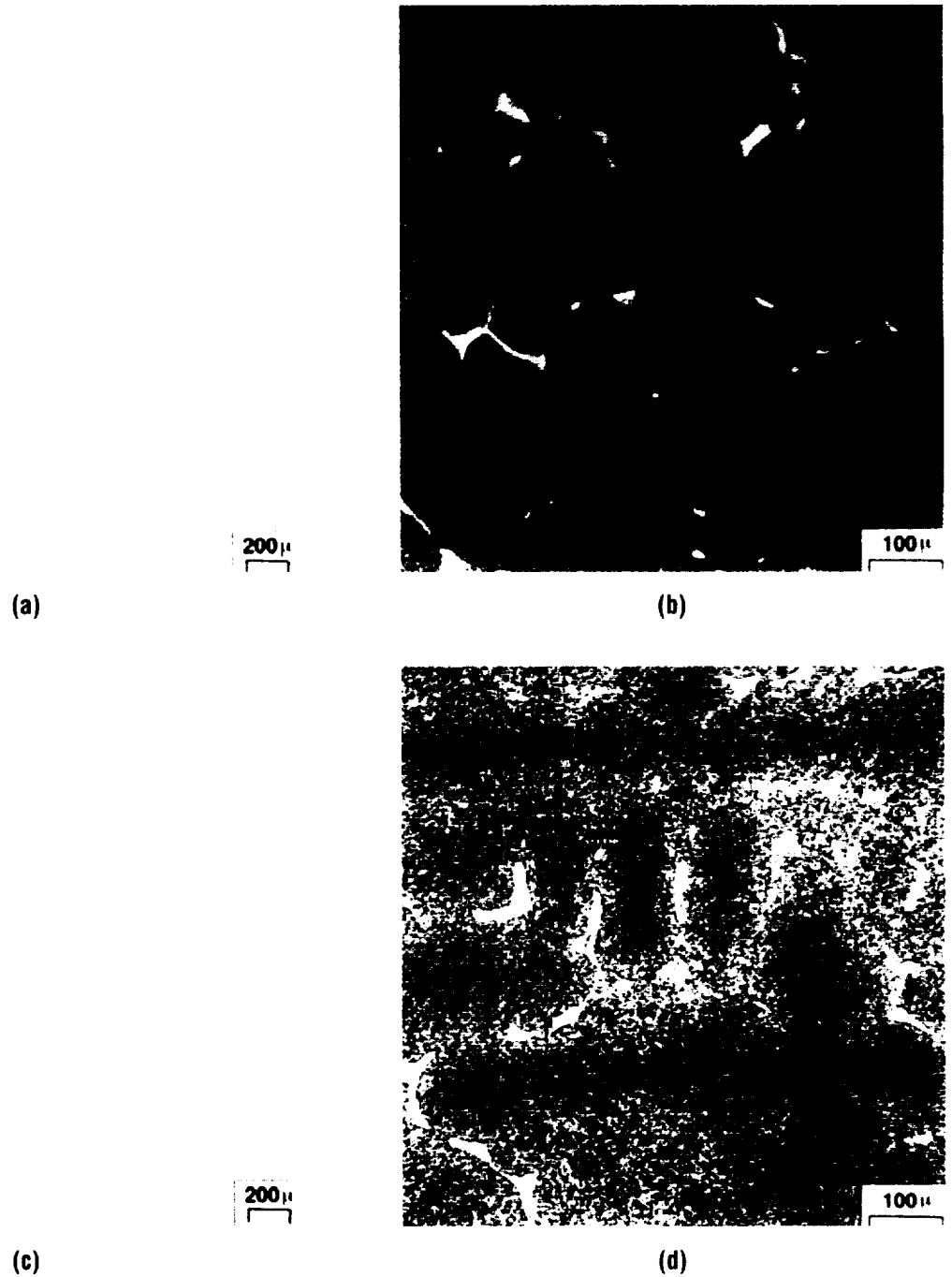
FIGURE 81.—Typical as-HIPed microstructure for PWA 1482 and PWA 1484: (a) PWA 1482 as-polished,(b) PWA 1482 AG21 etched, (c) PWA 1484 as-polished, and (d) PWA 1484 AG21 etched.
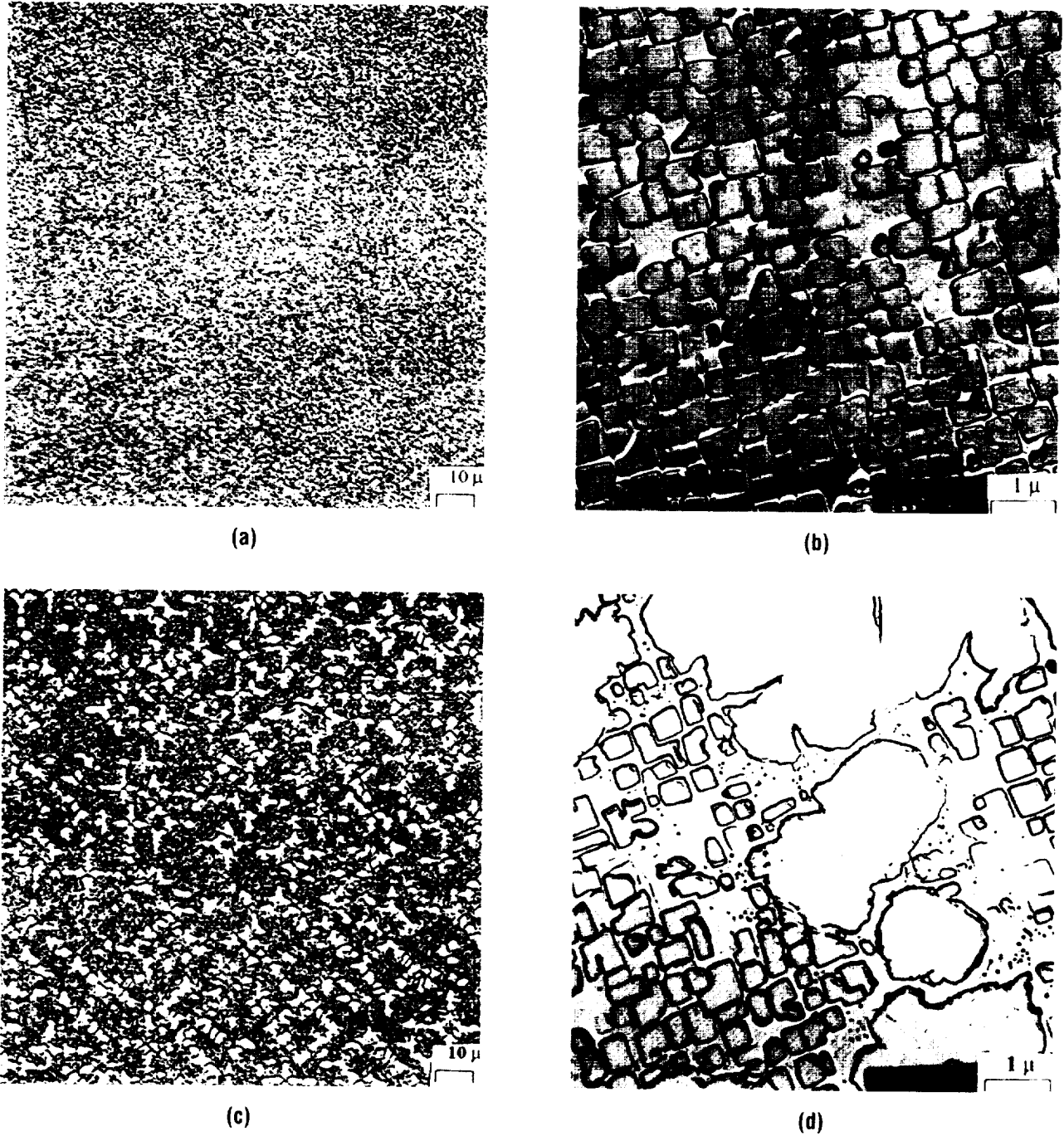
FIGURE 82.—Alternate heat-treat microstructures produced in PWA 1484: (a) pore-free, eutectic-free, fine cuboidal γ'; (b) transition electron microscope (TEM) replica of microstructure in (a); (c) pore-free, eutectic-free, bimodal γ'; (d)TEM replica of microstructures in (c).
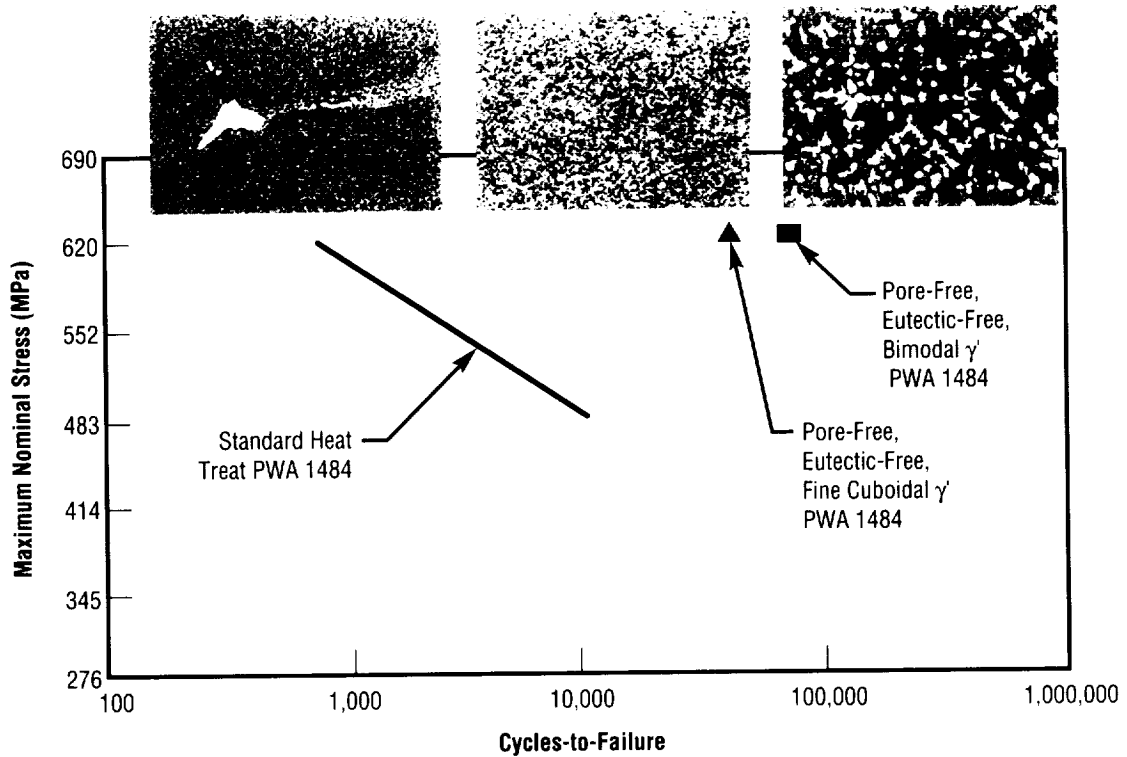
FIGURE 83.—Comparison of microstructures and double-notch, low-cycle fatigue (LCF) data (K_t = 2.18) for various PWA 1484 heat treatments at 26 °C in 34.5-megaPascal hydrogen with R = 0.05.
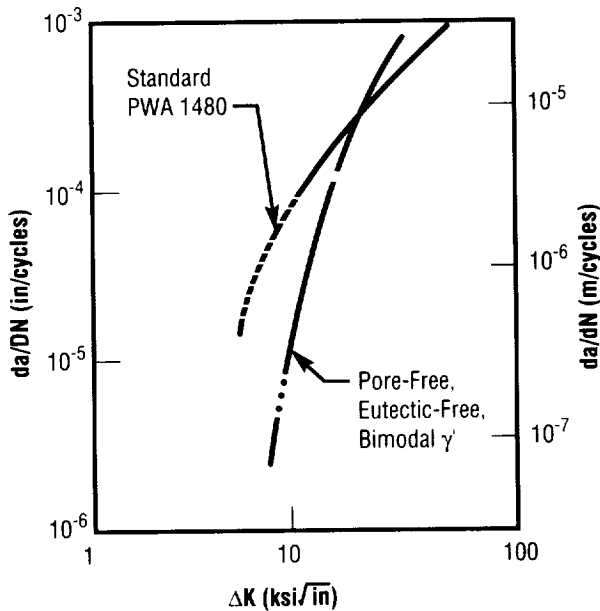
FIGURE 84.—Comparison of crack growth data from PWA 1484 pore-free, eutectic-free, bimodal γ' microstructure (heat-treat no. 6) with baseline PWA 1480 data at 26 °C in 34.5-megaPascal hydrogen with R = 0.1.
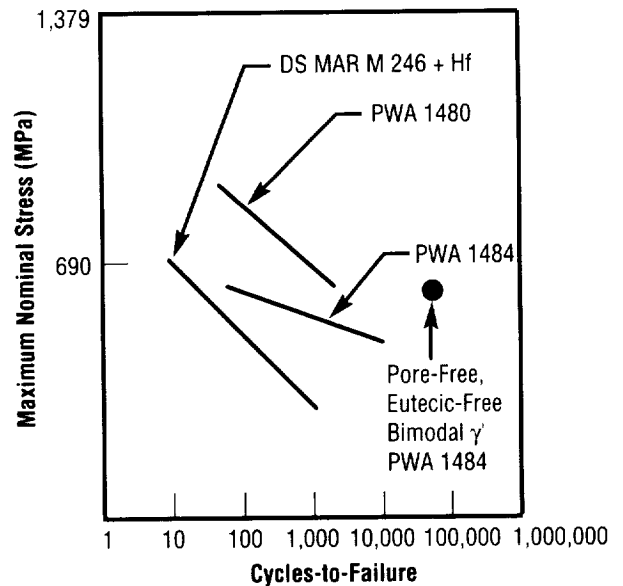
FIGURE 85.—Comparison of double-notch LCF data (K_t = 2.18) for alternate heat-treated PWA 1484 versus standard heat-treated cast, nickel-base superalloys at 26 °C in 34.5-megaPascal hydrogen with R = 0.05.

Off-line Programming of Welding Robot Using Graphical Simulation

Clyde S. Jones/EH25
205-544-2701

An off-line robotic programming system has been developed for space station automatic welding. The system, developed jointly by NASA/ MSFC, Boeing, and Intergraph, supports the implementation of robotic welding for fabrication of common module structural elements.

Robotic welding will be used to complete approximately 25 percent of the common module structural

elements. While most of these weld-joint geometries do not require complex motion, the joining of the node cylindrical skin to a large aluminum forging that supports the radial docking port uses nine separate axes of motion simultaneously to trace the path (fig. 86). Programming robotic motion to complete this task would require several days using the conventional approach. The programming system developed in this effort has reduced the time required for programming this complex geometry, while increasing accuracy and resolution.

The robotic off-line programming system accepts a computer-aided design (CAD) representation of the parts to be welded and incorporates this into a three-dimensional model of

the robot cell. A graphical simulation software package takes these geometric models and simulates the welding operation based on such process factors as weld-torch orientation, speed, and start position. During the simulation, the computer generates a table of robot positions for each programmed point on the weld joint. These tables are sent over a computer network from the simulation computer to the robot work-cell in the production facility, where a second computer converts the positions to machine-readable codes. The second computer then transfers the machine codes to the robot computer for execution (fig. 87).

Procedures have been developed and tested that can adjust the robot programs in the event that conditions have changed since their last successful use. Changes might be caused by maintenance of the robot, slight variations between production parts, or changes in the tooling that holds the parts for joining. In any event, the robot can be manually moved to previously defined key points on the weld joint, and the position of the robot's axes recorded. These recorded positions can then be sent back to the simulation computer using the network and used to adjust the welding motion program to "fine-tune" the path to achieve the accuracy necessary for a successful weld. Tests of this procedure have shown that major adjustments can be made in the robot program in less than 1 hour, where a conventional approach might take more than 1 day.
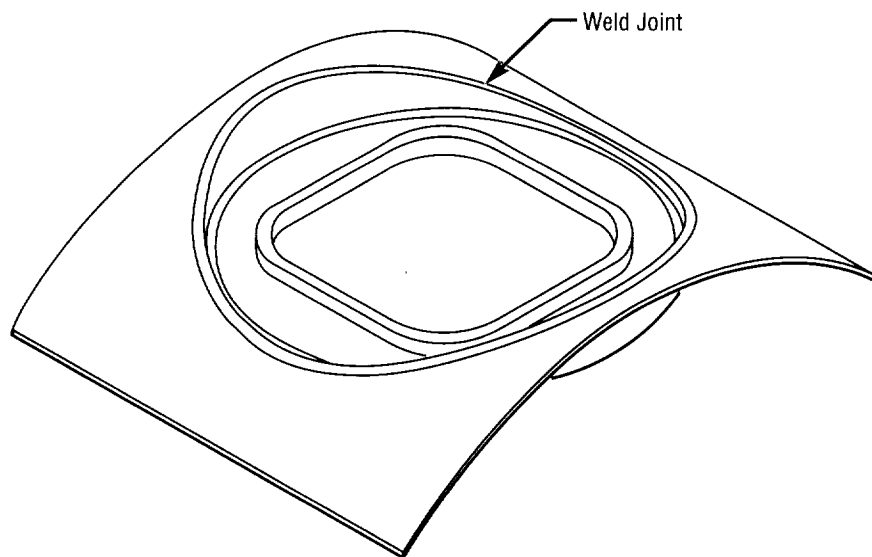
FIGURE 86.—Radial docking port.

145

CAD Design

Simulation

Edit Programs | View Robot Files | View Help Files

Text Files

Computer Network

Calibration Data

Translate Robot Files to Text Files

Program Text Files to Robot Machine Language

Taught Points

Robot Program

Robot Controller

Robotic Welding Work-Cell
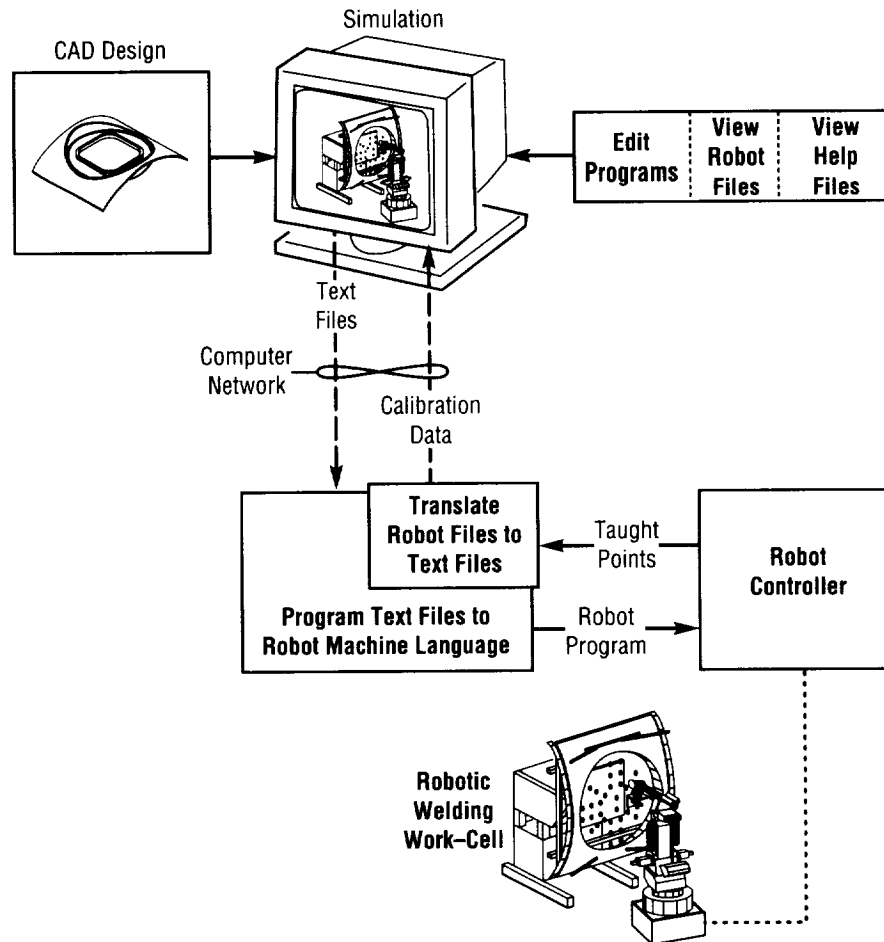
FIGURE 87.—System configuration.

This robotic programming system has been developed for use on the space station in the MSFC Productivity Enhancement Complex. All major features have been tested, and the system was used to program the first production radial docking port weld.

Sponsor: Office of Space Flight

Industry Involvement: Intergraph Corporation; Boeing Aerospace Corporation

• • • • •

Thermal-Sprayed Aluminum for Corrosion Protection in Cryogenic Applications

Frank R. Zimmerman/EH25
205–544–4958

In response to the need for eliminating the release of hexavalent chromium and volatile organic compounds, thermal spray coatings are being developed at MSFC to replace traditional chromate paints and primers now used to prevent pitting and stress corrosion cracking. A wire-arc-sprayed aluminum coating has been developed for corrosion protection of low-pressure, liquid-hydrogen-carrying ducts on the space shuttle main engine (fig. 88). Thermal spray processing, salt-fog corrosion testing, and adhesion and flexibility testing in ambient and cryogenic environments have been completed. Results show the wire-arc-sprayed aluminum coating meets all service requirements and provides the necessary corrosion protection for flight hardware in cryogenic applications.

The wire-arc-spray process includes applying metal coatings that use metal feedstock in wire form. Two wires, serving as the positive and negative electrodes, advance to meet in a stream of atomizing gas. A potential is applied to the wires, forming an arc across them, and the heat of the arc melts the tips of the wires. Atomizing gas then flows across the arc zone, propelling molten metal droplets to the substrate (fig. 89).
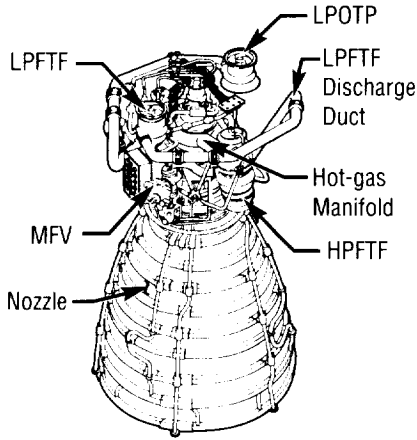
FIGURE 88.—The space shuttle main engine showing the low-pressure fuel turbopump discharge duct.

incomplete, or when the coating is scratched or damaged in service. With the addition of a sealant or a topcoat, a thermal-sprayed coating has long life and is easy to clean and maintain. In addition, the sealant does not affect cathodic protection.

The wire-arc-sprayed aluminum coatings have been proven to be equivalent or superior to the current chromate primer. These aluminum coatings exhibit excellent adhesion, corrosion protection, and room temperature and cryogenic flexibility. Coated samples do not crack or delaminate after being bent around a 0.75-centimeter-diameter mandrel. Bend tests around a 7.1-centimeter-diameter mandrel at liquid nitrogen temperatures (–195 °C) similarly show

no damage, demonstrating the coating's cryogenic flexibility. Wire-arc-sprayed aluminum provides excellent protection of 21–6–9 corrosion-resistant steel (CRES). After 120 days in a 5-percent salt-fog chamber (conforming to American Society for Testing Materials (ASTM) B–117), the coating protected the substrate from the effects of this aggressively corrosive environment. Coatings subjected to multiple thermal cycles, from ambient to cryogenic temperatures of –253 °C, maintained adhesion to substrates without cracking or blistering. This achievement is significant in the fact that no other corrosion protection paints, other than the currently used hazardous chromate primer, have successfully completed such tests.

Although thermal-sprayed corrosion protection coatings have been widely used in industry, none have been previously developed for cryogenic applications. The wire-arc aluminum coating developed at MSFC meets the stringent adhesion and cryogenic flexibility requirements, while also providing corrosion protection for steels and other more corrosion-prone alloys.

The wire-arc-sprayed aluminum coating was selected based on environmental, cost, availability, and performance concerns. These coatings not only act as an effective coating barrier, but also (because they are more anodic than steel) act as a sacrificial anode and give galvanic protection to the substrate. Therefore, corrosion of the substrate is prevented even when coating coverage may be
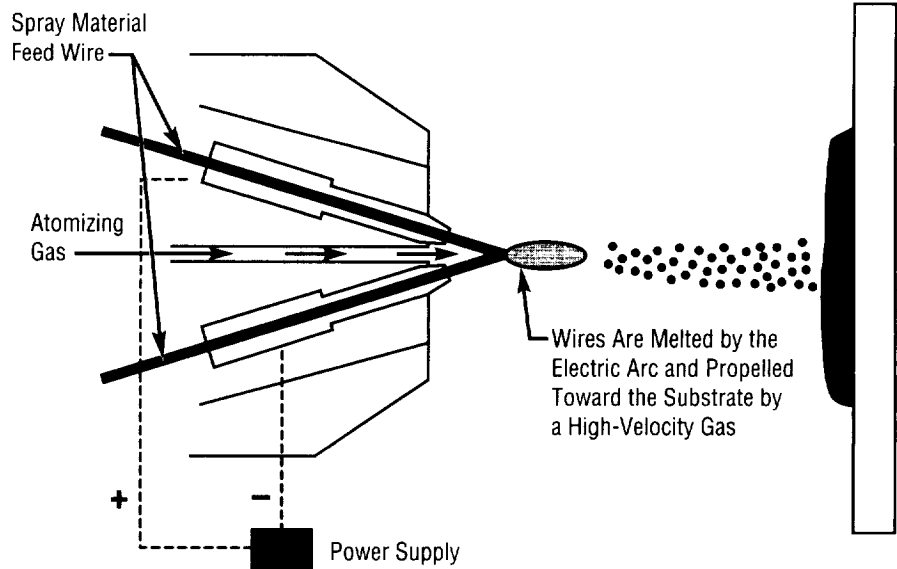
FIGURE 89.—Schematic of the wire-arc spray gun.

147

Although wire-arc-spray coatings have been used in the past for numerous corrosion-prevention applications, its use in a cryogenic environment is new. Requirements to eliminate newly classified hazardous materials on the space shuttle main engine and other rocket engine systems present an excellent opportunity for wire-arc-sprayed aluminum in liquid hydrogen applications. The coating can serve as a viable replacement to the environmentally undesirable chromate paints and primers now used on cryogenic, hydrogen-carrying ducts of the space shuttle main engine.

Sponsor: Office of Space Flight

Industry Involvement: Rocketdyne, A Division of Rockwell International

• • • • •

Near-Infrared Optical Fiber Spectrometry of Critical Surfaces

Billy H. Nerren/EH12
205-544-2636

H. DeWitt Burns/EH12
205-544-2529

Optical fiber spectrometry, in conjunction with multivariate analysis, can be a very powerful tool for identifying and quantifying chemical species in a broad class of environments. Typical applications include process control of chemical flows, environmental streams and wells, and surface chemistry, including both undesirable contamination materials as well as naturally occurring surface oxides and hydroxides. Examples such as principal component regression (PCR) or partial least squares (PLS) are used to extract important variations in the acquired data for identifying and quantifying contaminants.

Clean bonding surfaces are critical to the successful manufacturing of such space-flight hardware as the redesigned solid rocket motor. Critical surfaces must be inspected prior to bonding in order to verify that no contaminants (e.g., silicones, oils, or grease) are present.

This particular study has been performed to develop the capability to identify and quantify contamination levels which might be detrimental to the bonding process and cause in-process failures. Assuring that surfaces are clean prior to bonding

provides significant savings, eliminating costly repair operations when bond failures are found later in the manufacturing process. Although other analytical tools are being considered to assist in the determination of critical surface cleanliness, most techniques do not always provide an unambiguous signal of cleanliness. For example, optical stimulated electron emission (OSEE) can provide a useful measure of contamination on bondline surfaces, but naturally occurring oxidation and hydrolysis processes might also be indicated as contamination.

A potential source of contamination in the manufacturing environment is the use of various masking tapes within the redesigned solid rocket motor case and nozzle areas. Once applied to the surface, residues from the tape are difficult to remove and can be detrimental to critical bonds later on in the assembly phase of the process.

Four tapes used by Thiokol in their solid rocket motor manufacturing process have been studied. Tape adhesives were extracted using 1,1,1 trichloroethane, then applied as contaminants on test panels. Data have been collected on tape residue that sometimes remains on a bonding surface even after tape has been removed and the surface area has been cleaned. The four tapes under analysis included B-mask, a masking used in the grit-blast process; P-mask, a masking tape used in the painting operation; Teflon™ tape, used in conjunction with B-mask in the grit-blast process; and vinyl tape, used as all-purpose tape in the manufacturing area.
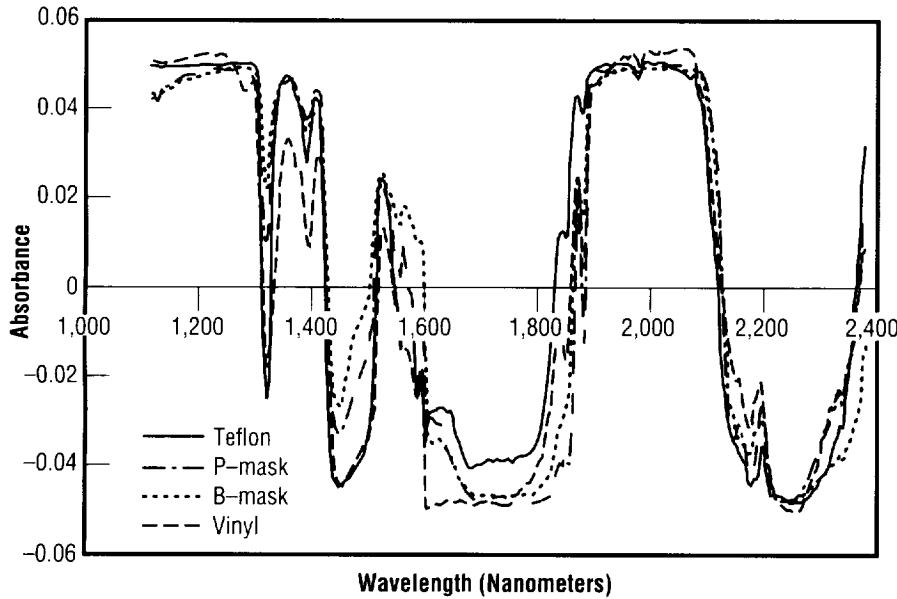
Figure 90.—Plot of first factor for all four residues.

model was then used to predict the individual contamination levels for each different residue as if they were unknown. This information can then be used to predict a single residue signature using the significant factors identified in the PLS2 model. Results of the analysis (figs. 91 to 94) offer predicted versus measured values. The scatter of the data about the regression line is indicative of a good model.

No patents are pending at this time. The techniques developed in this work are currently being applied to many other activities, including environmental sampling, identification of hazardous wastes, discrimination and separation of plastics for recycling, and in-process inspection of chemical processes.

The residue solutions were sprayed on large aluminum plates and a witness foil concurrently. The gravimetric weights were determined for the witness foils, and conclusions about the plates were deduced. Each residue was applied in two distinct levels of contamination, yielding eight contaminated levels, two for each type of contaminant. A blank panel was prepared to provide a zero reference for the study. Spectral data for three different spots over each contaminated level were taken and recorded. Also, three different spots were scanned on the blank panel. Spectral data were collected with a Guided Wave 260™ using an optical-fiber probe to illuminate and receive data after contaminant application. Data were then subtracted from a gold reference scan, smoothed, and the PLS2 analysis performed to determine the predicted contamination levels of each residue using Unscrambler II® software. The

first factor extracted from a principal component analysis for each contaminant is shown in figure 90. There are a number of similar spectral features due to the similar chemistry of the tape residues.

The PLS2 model includes all the data from all the contaminated panels. This

Sponsor: Office of Space Flight

University Involvement: University of Alabama in Huntsville

• • • • •

Figure 91.—Predicted versus measured values for Teflon™ tape.

149

P–Mask Tape Residue
Predicted With 15 Factors
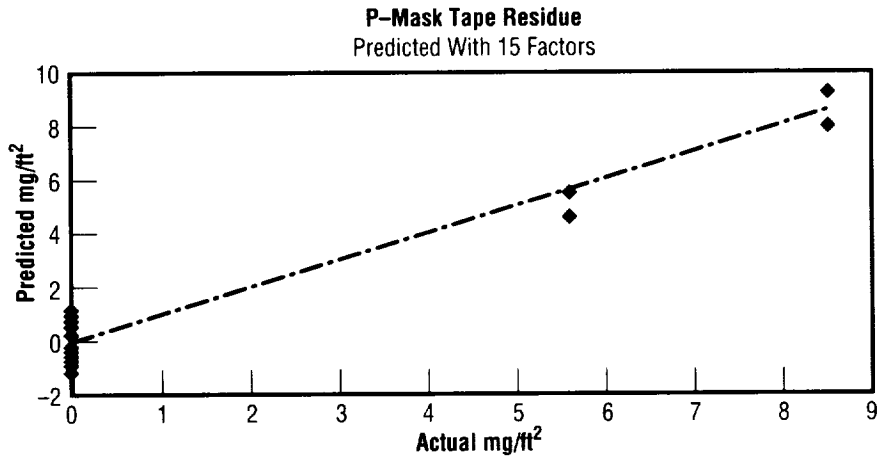
Figure 92.—Predicted versus measured values for P-mask tape.

B–Mask Tape Residue
Predicted With 15 Factors
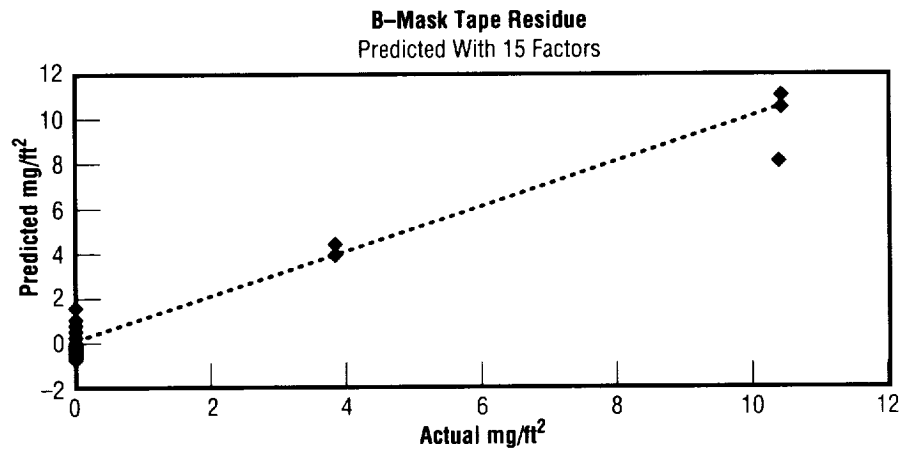
Figure 93.—Predicted versus measured values for B-mask tape.

Vinyl Tape Residue
Predicted With 15 Factors
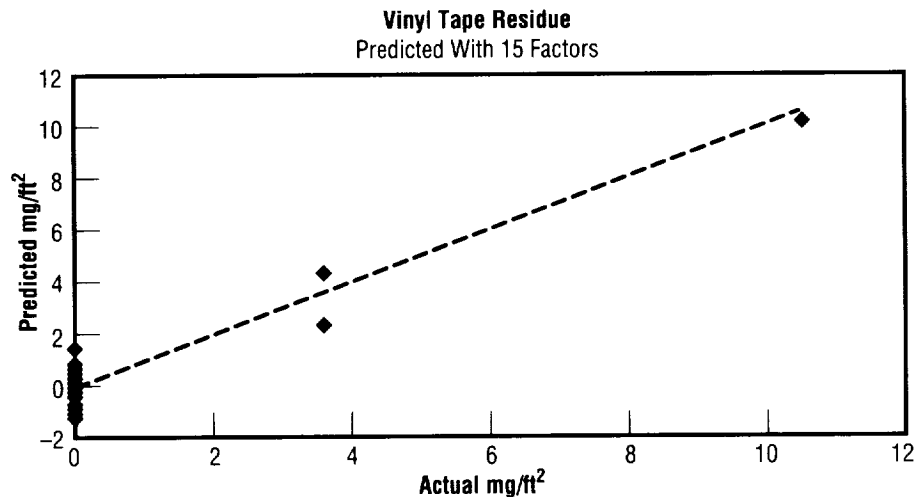
Figure 94.—Predicted versus measured values for vinyl tape.

Development of Low Thermal Conductivity, Polyacrylonitrile-Based Fibers for Solid Rocket Motor Nozzle Applications

Raymond G. Clinton, Jr./EH34
205–544–2682

During the past 5 years, the Materials and Processes Laboratory, in cooperation with the Solid Propulsion Integrity Program (SPIP), has conducted a research effort to develop and evaluate low thermal conductivity (LTC), polyacrylonitrile- (PAN-) based carbon fibers as potential replacements for rayon-based fibers currently used as reinforcement for phenolic matrix composites in solid rocket motor nozzle applications. As part of this program, material performance results have been collected from the static motor firing that occurred in September 1993.

Specific placement of the test materials in the nozzle rings and material descriptions are provided in figure 95. The nozzle was designed with split rings to enable comparison of the two low thermal conductivity polyacrylonitrile candidates to each other and to a baseline rayon-based ablative (FM5055). The FM5939LDC materials tested in the aft end of the aft exit cone addressed two objectives. First, the product served as the baseline rayon-based, low-density carbon phenolic for performance comparison with the polyacrylonitrile-

based, low-density materials, notwithstanding aft exit cone environment variation. Second, two "different" FM5939LDC materials were tested for performance comparison—the difference being the type of carbon microballoons used as filler. The T-type microballoons were a higher purity subset of the industry-standard A-type microballoons produced by Carbospheres.

Performance results are summarized as follows. Both standard-density low thermal conductivity polyacrylonitrile materials in the forward inlet ring exhibited pocketing, which prevented any direct performance comparisons. However, no pocketing occurred in the forward portion of the throat ring. Erosion trends indicated that both polyacrylonitriles tended to erode slightly less than the baseline rayon material, and overall thermal performance was similar. In the aft section of the throat, again both polyacrylonitriles exhibited pocketing that prevented performance comparisons. Downstream wash effects from throat pocketing were evident in the forward portion of the forward exit cone, so meaningful performance comparisons were not possible. In the aft section, erosion- and heat-affected depth tendencies for both polyacrylonitrile materials were similar (within 10 percent) to rayon. The low-density, low thermal conductivity polyacrylonitriles in the aft exit cone exhibited lower char and erosion than the rayon baseline. Further, the baseline materials, both T-type and A-type carbon microballoons, exhibited plylift, whereas the polyacrylonitriles did not.

The occurrence of pocketing was unexpected. A study of causal factors contributing to the anomalous performance included ply-angle considerations, material pedigree, processing, and material properties. Pocketing in the forward inlet and throat rings originated at ply angles to the surface of 65° and 68°, respectively, indicating an increased ply-angle sensitivity range in comparison to the
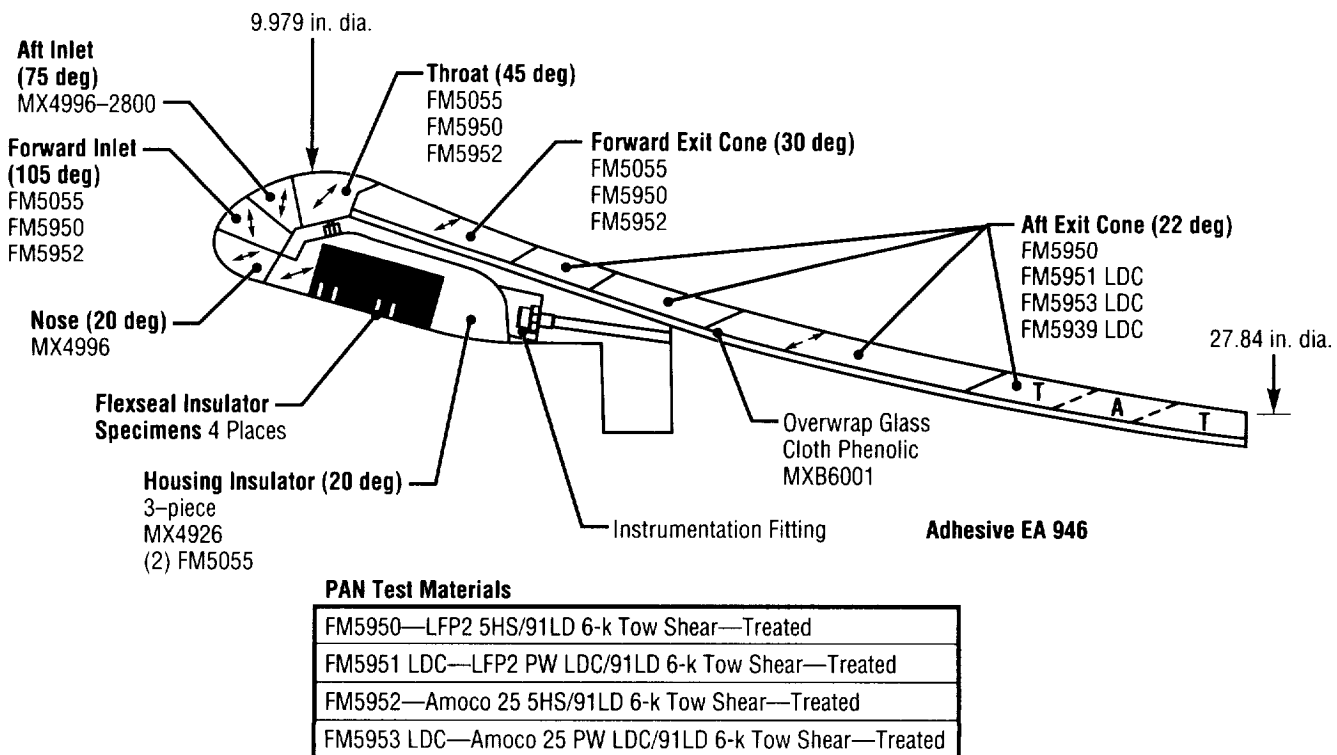
FIGURE 95.—Solid Propulsion Integrity Program (SPIP–3) MNASA nozzle as-built.

PAN Test Materials

FM5950—LFP2 5HS/91LD 6-k Tow Shear—Treated
FM5951 LDC—LFP2 PW LDC/91LD 6-k Tow Shear—Treated
FM5952—Amoco 25 5HS/91LD 6-k Tow Shear—Treated
FM5953 LDC—Amoco 25 PW LDC/91LD 6-k Tow Shear—Treated

rayon-based materials. In assessing material pedigree changes between those product versions tested in Thiokol's 40-pound charge motor and NASA's Solid Propulsion Integrity Program MNASA motor, the Amoco-25 fiber tow size was increased from 3 to 6 K for the Thiokol test. Sizing and surface treatment were reportedly unchanged. The sizing was changed and a surface treatment added to the Hercules LFP-2 fiber for the MNASA test. Resulting across-ply tensile strengths increased between 60 and 100 percent in comparison to earlier versions of the products. In-plane permeability for the FM5950 material was –12.7 log Darcy's constant, due to microcracking, and ranged from –18.5 to greater than –20 log Darcy's constant for the FM5952 material. (For purposes of reference, the mean value of baseline redesigned solid rocket motor North American Rayon Corporation (NARC) rayon-based carbon phenolic is approximately 15.7 log Darcy's constant). No differences were documented in the processing area. The pocketing hypothesis was that changes in surface treatment and sizing which successfully improved interfacial properties decreased room temperature and elevated temperature permeability, resulting in pocketing when the ply angle was sufficiently high.

Additional tests are being conducted by Thiokol and Southern Research Institute to address the above issues and hypothesis. A sister lot of the FM5952 and a post-cured version of the FM5950 material will be tested in the split-ring configuration in the throat of the RSRM–4 MNASA motor in 1994. The results of these tests will be given in the 1995 annual report.

Clinton, R.G., Jr. 1993. Development of Low Thermal Conductivity PAN-Based Fibers for SRM Nozzle Applications. *Research and Technology 1993: Annual Report of the Marshall Space Flight Center,* NASA TM–108420.

Clinton, R.G., Jr.; Pinoli, P.C.; and Canfield, A.R. October 1990. Development of Low Thermal Conductivity PAN-Based Fibers for Solid Rocket Nozzle Applications. Joint Army, Navy, NASA, and Air Force (JANNAF) Rocket Nozzle Technology Subcommittee (RNTS) Meeting, Pasadena, California.

Emery, E.A., and Hill, K.H., December 1992. PAN Material Performance Evaluation. JANNAF RNTS Meeting, Lockheed Missiles and Space Corporation (LMSC), Sunnyvale, California. CPIA Publication 592.

Sponsor: Office of Space Systems Development

Industry Involvement: Thiokol Corporation; Southern Research Institute; Hercules Aerospace Corporation; Amoco; B.P. Chemicals, Fibers and Materials Division

• • • • •

MISSION OPERATIONS

Virtual Reality as a Human Factors Design Analysis Tool for Architectural Spaces: Control Rooms to Space Stations

Joseph P. Hale/EO23
205-544-2193

A virtual reality (VR) applications program has been under development at MSFC since 1989. Its objectives have been to develop, assess, validate, and utilize virtual reality in hardware development, operations development and support, mission operations training, and science training. [1] Human factors issues and considerations in hardware and operations development present a wide range of potential virtual reality applications. Two of the goals of this technology program have been to enable specialized human factors analyses to enter earlier in the hardware and operations development process and to develop more effective training and mission support systems. [2]

One specific application of virtual reality is as a human factors design analysis tool for work areas and other architectural spaces. The use of virtual reality in the macro-ergonomic analyses of work-area topological design enables the consideration of the fields of view (FOV) from a variety of eye reference points and can include operationally driven components, such as translation paths among the various worksites. Examples of "spaces" include control rooms, space stations, and orbiting telescopes. [3] A study has

been conducted to compare subjects' qualitative and quantitative judgments of two "real-world" control rooms at MSFC and their corresponding virtual counterparts. Results indicate a level of filtering occurring in the virtual environments.

The Spacelab payload control room (PCR) and simulation control room (SIM) were selected as experiment sites based on their apparent separation on a variety of continua (e.g., large versus small, spacious versus cramped, aesthetically well-designed versus poorly designed, and so forth). A corresponding virtual payload control room (VPCR) and virtual simulation control room (VSIM) were developed that contain the basic elements (tables, monitors, printers, communication panels, etc.) and spatial layout of their real-world counterparts.

The experimental design used in this study was a 2 × 2 (× 2 × 2), full-factorial design with two within-subjects variables and two blocking variables. Also, two pairs of crossed, two-level within-subjects variables were nested in one of the main within-subjects variables. The overall independent variables (IV's) were *World* (real/virtual) and *Room* (payload control room/simulation control room), with *Gender* and *World Order* (virtual-real/real-virtual) as blocking variables. Nested within *Room* were *Range* and *Relative Range* estimations. Range estimations, where subjects estimated the range to specified items in the room, took place in both the simulation control room and virtual simulation control room and were composed of two independent variables: *Item* (object/surface) and the item's *Range* from the

observer (near versus far). The *Relative Range* estimations, where subjects were required to make a forced choice of which object of a pair of objects was closer, took place in the payload control room and virtual payload control room, and were also composed of two independent variables: *Field of View* (same versus different, i.e., whether or not the subject could see both objects simultaneously in the same field of view) and the objects' *Distance* from the observer (close versus far away). Objects' faces were either green or blue, and colors were counterbalanced across conditions. Range Estimation, Relative-Range Forced Choice, and Elapsed Time to answer range and relative-range questions were collected as dependent variables.

Materials and apparatus used included the MSFC virtual reality systems residing in the Computer Applications and Virtual Environments (CAVE) Laboratory in Building 4610. System components utilized in the study included the VPL Research Eyephones LX™ and software (Swivel 3D™, Body Electric™, and ISAAC™); the Polhemus Fastrak spatial tracking system; a Macintosh™ IIfx computer; and two Silicon Graphics™ computers (4D/310VGX and 4D/320VGXB).

Results from each relative range choice were coded as "correct" or "incorrect." Z tests for proportions were then carried out on each condition. The criterion of significance was set at $p = .05$ for all tests. Regardless of *World* or *Distance*, subjects accurately selected the correct closer object when both objects were in the same field of view ($p < .05$). However, when making judgments about objects in different fields of

view (requiring subjects to turn their heads in order to visually capture each object), those in the real world were unable to discriminate which object of the two close objects was closer ($p > .05$). Subjects were able to make an accurate selection when the object pair was further away from them ($p < .05$). In the virtual world, subjects selected the wrong object of the close objects, reversing the actual relative range when each object appeared in different fields of view ($p < .05$). When object pairs were further away, subjects in the virtual world were unable to discriminate between items ($p > .05$).

Elapsed Time (ET) for each judgment was bounded by verbal acknowledgment from the subjects that they had visually acquired the target items and by their verbal selection of an item. No effects were found for the *Gender* or *World Order* blocking variables ($p > .05$). However, a significant main effect was noted for *World* ($F(1,28) = 5.468$, $p < .05$) and for *World Order*World* ($F(1,28) = 6.469$, $p < .05$). Throughout this analysis and subsequent analyses involving time, subjects took longer to make judgments in the virtual world than in the real world ($M = 43.78$ seconds and 25.67 seconds, respectively). A post-hoc contract on the *World Order*World* interaction was significant ($t(28) = 2.44$, $p < .05$), indicating that subjects who began a task in the virtual world required more time to make judgments when in the virtual reality world than did subjects in the other *World/World Order* combinations. (M for each world by world order combination was 29.41 seconds for the real-virtual order in the real world, 27.81 seconds

for the real-virtual order in the virtual world, 21.94 seconds for the virtual-real order in the real world, and 59.75 seconds for the virtual-real order in the virtual world (table 9)).

TABLE 9.—*Relative Range Elapsed Time as a function of World and World Order*

	VR-Real	Real-VR
VR	59.75 s	27.81 s
Real	21.94 s	29.41 s

In addition, a significant effect was observed for *Field of View* ($F(1,28) = 28.826$, $p < .05$), indicating that subjects took longer to make judgments when each of the objects of the comparison pair was in different fields of view than when both objects were in the same view ($M = 53.85$ seconds and 15.61 seconds, respectively). This is consistent with the difficulties experienced by subjects in accuracy of selection under different field-of-view viewing. (Refer to table 10 for a

summary of Relative Range accuracy and Elapsed Time as a function of *World Field of View* and *Distance*.)

Two measures were obtained for range estimation: actual judgments (expressed in feet) made by subjects regarding their distance from an object or surface and elapsed time measures for all estimates. Range estimates were transformed to provide a measure of the subject's range estimation accuracy. The estimates were subtracted from the actual distances involved in order to acquire a raw deviation, expressing the differences between judgments and actual values. Each deviation was divided by the actual distance, with the goal of minimizing the effects of making different types of distance judgments (closer versus further away). The resulting transformation thus expressed a ratio between the deviation and the actual value. Underestimates of distance are expressed as positive values, and overestimates are expressed as negative values. A perfect estimate (no deviation) would take the value of 0.

TABLE 10.—*Summary findings for Relative Range accuracy and Elapsed Time as a function of World, Field of View, and Distance*

	Real		Virtual		
	Close	**Away**	**Close**	**Away**	**ET**
Same FOV	Correct	Correct	Correct	Correct	15.61 s
Diff. FOV	Random	Correct	Reversed	Random	53.85 s
ET	25.67 s		43.78 s		

A 2 (*Gender*) × 2 (*World Order*) × 2 (*World*) × 2 (*Range*) × 2 (*Item: Object/Surface*) mixed ANOVA was carried out on the range judgments, with *Gender* and *World Order* as blocking variables and *World, Range*, and *Object/Surface* as within-subject variables. No effects were found for blocking variables. A significant main effect was obtained for *Range*, indicating that subjects were more accurate in their judgments of far items ($F(1,28) = 7.49$ $p < .05$). A significant main effect was also obtained for *Item*, indicating that a subject's estimates were more accurate for objects than for surfaces ($F(1,28) = 4.93$, $p < .05$). A significant interaction was obtained for *World*Gender* ($F(1,28) = 4.58$, $p < .05$). Post-hoc comparisons revealed that women underestimated distance more in the real, as compared with the virtual reality, worlds ($t(15) = 3.1$, $p < .05$), while men underestimated distance more in the virtual reality worlds as compared with the real worlds ($t(15) = -2.79$, $p < .05$). No other sources of variation in this analysis were significant.

A mixed ANOVA with the configuration described above was utilized to analyze the elapsed time associated with range estimation judgments. No significant effects were obtained for blocking variables. A significant main effect was obtained for *World* ($F(1,28) = 7.42$, $p < .05$). As in the relative range judgments, subjects took longer to make judgments in virtual reality than in the real world (M VR = 46.56 seconds, M Real = 22.62 seconds).

The primary objective of this experiment was to start the process of validating and calibrating the use of

virtual reality as a human factors analytical tool. Overall, there appears little difference between real and virtual worlds in one's ability to differentiate and estimate distances at approximately 3 and 6 feet. This is also true for discrimination of 2-inch differentials at those distances with objects within the same field of view. For different fields of view, this discrimination ability starts to deteriorate in the real world and is lost in the virtual world. Thus, analyses using this technology that depend upon gross range estimations seem permissible, but those relying upon fine range perceptions should be approached with caution. The very clear main effect of *World* (increased time to make judgments in the virtual world) provides guidance as to when and when not to use this technology as an analytical tool. If task times, for example, are a critical component of the analysis, the use of this technology should be carefully considered.

However, these cautions will naturally be relaxed as the technology evolves. Texture mapping, a feature now generally available but not a part of this study's virtual reality system, is an example of a technological advance that should modify these cautions and enlarge the set of virtual reality application classes.

In summary, based on the results of this study, the use of virtual reality as a human factors analytical tool has its limitations. The different perceptions and the longer response times point to a level of filtering occurring in the virtual environment. This is not particularly surprising. As more cues are enabled (e.g., texture mapping, point sources of illumination, shadow, and sound), we would expect more

"realistic" perceptions and thus expanded utility. The goal now should be to better quantify this filtering effect and determine where and when it has an effect on virtual reality applications. As the technology continues to evolve, these issues will need to be readdressed and the technology recalibrated and further considered for expanded applications.

[1] Hale, J.P. 1993. MSFC's Virtual Reality Applications Program. In Proceedings of the Contributed Sessions 1993 Conference on Intelligent Computer-Aided Training and Virtual Environment Technology. NASA/Johnson Space Center, Houston, Texas.

[2] Hale, J.P. 1993. Virtual Reality as a Human Factors Design Analysis Tool. In Proceedings of the Southeastern Simulation Conference. Society for Computer Simulation, San Diego, California.

[3] Null, C.H., and Jenkins, J.P. (eds.). 1993. NASA Virtual Environment Research, Applications, and Technology.

• • • • •

Ground-to-Air Television

David W. Scott/EO62
205-544-3226

Ground-to-air-television (GATV) is a proposed mission kit that will provide a system and methodology for uplinking real-time, full-screen, color television signals from MSFC and/or Johnson Space Center (JSC) to the space shuttle and Spacelab, and for simultaneously downlinking low-bandwidth television. The system requires minimum crew attention and maximizes use of the extensive onboard and ground-based video and audio systems already in place. The system is small (flight unit weighs 12 pounds and fills 0.3 cubic feet) and fairly inexpensive (with the total cost of flight and ground units plus spares under 300,000 dollars).

Uplink video is of particular interest relative to extended-duration orbiter (EDO) or contingency extravehicular activity (EVA) missions where unforeseen problems are more likely to occur. Long-term implications for space station operations (e.g., in-flight maintenance (IFM) and onboard training) are also significant.

Multimedia research conducted at MSFC from the 1991–1993 Center Director's Discretionary Fund (CDDF), Project 91–16, identified the potential for low-bandwidth television transmission with space shuttle uplink communications bandwidths. Following discussions with engineering and management personnel at MSFC and Johnson, preliminary system development was accomplished via sustaining engineering efforts on an as-available basis.

To date, a working flight unit prototype has been built at Johnson's Electronic Systems Test Laboratory, EE2. MSFC has developed and tested a ground systems architecture that will enable MSFC or Johnson to originate video signals using industry-standard video-conferencing equipment. Originally proposed as a demonstration test objective (DTO), ground-to-air television viability, based on progress to date, was such that reviewers recommended escalation to the mission kit approach.

A National Television Standards Committee (NTSC) television signal is digitized, compressed, and uplinked in real-time via the 128 kilobits per second (kbps), Ku-band (15.250 to 17.250 gigahertz) uplink via a video encoder/decoder (codec) located in the control center. (This is the same bandwidth used for Thermal Input Printing System (TIPS) transmissions, the shuttle's equivalent of a FAX system.) Any signal available on the sending center's video matrix can be selected. A variety of audio signals can similarly be chosen. The signal is decoded and interfaced to orbiter/Spacelab closed-circuit television and audio distribution systems via an onboard, locker-stowed video processor unit.

Downlink source signals are selected via existing onboard video and audio systems, with the resulting digital data stream transmitted on Ku-band Channel 2 at 128 kilobits per second, the same rate as uplink. MSFC and/or Johnson codecs convert the downlink to National Television Standards Committee format and distribute to their video and audio matrices.

The onboard codec unit consists of a 28-volt, direct-current (Vdc) power supply, a 486 motherboard, hard disk, PictureTel PCS1000 video/audio codec (two cards), an RS–449 communications card, and a VGA-to-NTSC conversion card. Support software is auto-loaded on startup, so that the operator is only required to connect the codec unit and turn on the power.

The quality of video received at either end is similar to a consumer-grade video cassette recorder except for reduction in motion rendition (15 frames per second (fps) versus the standard 30 frames per second). The output of the onboard video decoder is in standard National Television Standards Committee composite format, compatible for color monitoring and recording by the orbiter/Spacelab television systems. Current plans are to evaluate a variety of preplanned uplink scenarios under mission conditions and to provide video-assisted support for actual mission situations. Future improvements may include near-broadcast quality downlink at data rates between 384 and 1,200 kilobits per second (Ku-band Channel 2 can process up to 2,000 kilobits per second), though this would preclude simultaneous uplink.

Significant operational benefits for space shuttle/Spacelab in-flight maintenance procedures, payload/science operations, medical, and/or extravehicular activity operations can be derived by sending color television

with embedded audio from a control center to a manned orbiting spacecraft:

- Transmission time required to convey information is reduced compared to existing operational communications methods, or significantly greater content is communicated in the same amount of time. "One picture is worth a thousand words…a moving picture is worth a million."

- Benefits range from productivity enhancement (quality or quantity increase) to loss prevention or recovery.

- Existing bandwidths can support this type of video and audio transmission without obstructing core voice communications circuits.

- Ground-to-air television (fig. 96) can support extended conversations, keeping core circuits clear.

- Audio quality is better than current air-to-ground circuits and is full-duplex.

- Ground-to-air downlink does not interfere with high-rate data downlink. (Standard orbiter TV downlink precludes high-rate data.)

- "Virtual presence" of ground equipment and personnel clarifies communications with the onboard crew.

This type of technology is directly applicable to other operations environments. An effort is currently underway to establish a two-way voice, video, and data (VVD) capability for NASA's KC–135 zero-gravity aircraft and to identify other NASA activities with needs for low-cost airborne voice, video, and data capabilities.

Sponsor: Office of Life and Microgravity Sciences and Applications

• • • • •
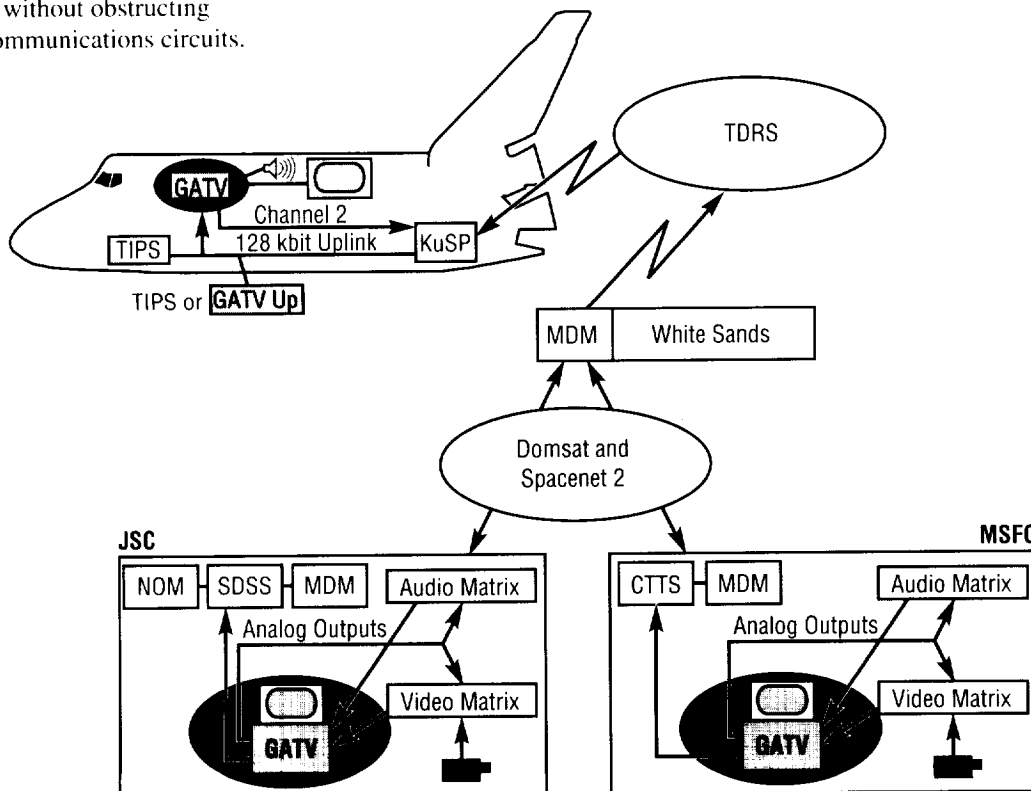
FIGURE 96.—Ground-to-air television system architecture.

High-Packed Digital Television— Multichannel Downlink From Spacelab

David W. Scott/EO62
205-544-3226

High-packed digital television (HI-PAC DTV, or simply HI-PAC) will demonstrate multichannel television downlink capabilities by interfacing commercially available video compressor-decompressors (codecs) with Spacelab's high-rate multiplexer (HRM) (fig. 97). Up to six television signals will be simultaneously transmitted during the U.S. Microgravity Laboratory 2 (USML–2) mission in 1995, alleviating a potentially massive scheduling conflict and drastically reducing turnaround time for science teams to obtain their data.

Multimedia research conducted at MSFC from 1991 to 1993 (under the Center Director's Discretionary Fund, Project 91–16) identified a potential for digital compression and transmission of television signals. During a discussion of low-bandwidth uplink possibilities, it was discovered that multiple downlink signals would be extremely useful if sufficient quality could be maintained. Researchers were able to identify several technologies yielding high-quality results in the 6-megabits-per-second (MB/s) range. Since Spacelab provides data paths up to 48 megabits per second, a solution seemed possible.
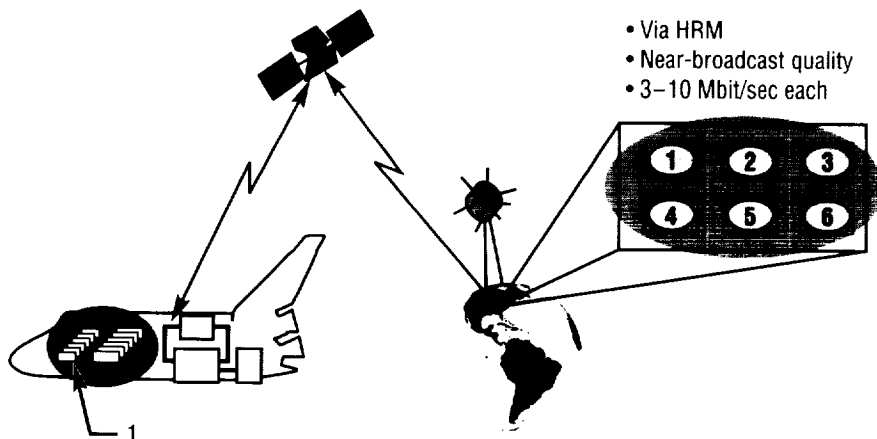
Figure 97.—High-packed digital television.

Several mission managers were consulted as to their video downlink requirements, revealing that U.S. Microgravity Laboratory 2 had 16 signals that would compete for the use of a single television downlink if current shuttle capabilities were used. Further discussion with consultants and vendors identified a very small, lightweight unit used for downlinking video from fighter aircraft during missile tests that could be adapted directly for Spacelab use.

The core components of high-packed digital television include video encoder assemblies (VEA's), one for each downlink channel (six for U.S. Microgravity Laboratory 2, plus one spare). These units have dimensions of 7 inches by 3 inches by 4.5 inches and weigh 4 pounds. They operate at 28 volts, direct current (Vdc) at less than 10 watts (W), each with passive cooling. Each provides four software-selectable inputs (one at any given time), digital serial output, a programmable data rate of 1 to

13 megabits per second; nominal rates for missions 3.3, 5.0, and 10.0; and Joint Photographic Experts Group (JPEG) compression format.

Also included are video decoder assemblies (VDA's), one for each channel (six downlink and two playback for U.S. Microgravity Laboratory 2). These are 19-inch, rack-mounted, and operate at 115 volts, alternating current (Vac).

Onboard interface and power control units have been added to provide compatible connections to standard closed-circuit television, Spacelab power, experiment computer and high-rate data systems, and to an enclosure support structure for mounting the video encoder assemblies in the Spacelab module. All features are ground-controllable, while limited in-flight maintenance (IFM) can be performed (and certain subsets controlled) by the flight crew as a backup.

A ground-based high-packed digital television workstation houses video decoder assemblies and interfaces with the Huntsville Operations Support Center's (HOSC) high-rate demultiplexer (HRDM) and video distribution systems. Principal investigators (PI's) and/or operations cadre members provide their own analog video recorders for taping directly from the support center's video matrix. High-rate digital recorders provide backup playback capability.

High-packed digital television will improve science payload operations on U.S. Microgravity Laboratory 2 by:

- Enabling principal investigator teams to receive and record most of their video during the course of the mission, much of it in real time

- Making more data available in real-time or near real-time. (Observations about payload behavior can be made in time to change operational parameters or techniques before a mission ends, which could save the expense of re-flight or allow reflown experiments to examine other facets of the area under study.)

- Lessening scheduling conflicts for video since more channels will be available.

- Ensuring that a troubleshooting downlink can occur without interfering with nominal payloads.

- Minimizing post-mission video data reduction efforts.

For future missions or platforms (e.g., space station), high-packed digital television or its derivatives will multiply telescience possibilities. Motion Picture Experts Group (MPEG) compression formats could be adapted to improve motion resolution. Flight units can be configured to embed a voice channel, so that crew commentary or payload-generated audio may be downlinked without affecting core voice communication channels.

Sponsor: Office of Life and Microgravity Sciences and Applications

• • • • •

159

PROPULSION AND FLUID MANAGEMENT

Advanced Main Combustion Chamber Development

Henry J. Dennis/EP33
205-544-4670

Sandra K. Elam/EP33
205-544-8902

The advanced main combustion chamber (AMCC) effort was initiated to enhance the state-of-the-art in design and fabrication of hydrogen-cooled combustion chambers for large liquid rocket engines. Using the current space shuttle main engine (SSME) main combustion chamber (MCC) as a baseline, design goals are to increase hardware reliability, reduce critical failure modes, and reduce fabrication time at a fraction of the cost of the current combustion chamber. The advanced chamber incorporates a formed platelet coolant liner and a single-piece cast structural jacket, both of which greatly reduce the number of fabrication processes.

The advanced main combustion chamber program began in 1989 with the purpose of developing technology for an improved, low-cost combustion chamber. The fabrication methodology for the existing main engine chamber was studied to see where improvements could be made. Researchers found that most of the fabrication problems occur during the assembly of the structural jacket and coolant manifolds, which is a forged and welded assembly. Findings indicated that one way to reduce these

fabrication problems was to use investment casting technology to fabricate the structural jacket and coolant manifolds with as few parts as possible. The resulting casting, although complex in shape, is not susceptible to the inherent part-to-part variability of a forged and welded design.

The investment cast structure is being developed by Precision Castparts Corporation (PCC) of Portland, Oregon, under contract NAS8-39027.

A single-piece casting incorporating both forward and aft coolant manifolds, gimbal actuator lugs, instrumentation bosses, and an engine-controller forward mounting bracket, the structure is made of the hydrogen-environment-resistant, nickel-based superalloy JBK-75. To date, Precision has produced 17 of 24 planned castings in the development of the part.

Another area of the existing chamber studied for improvements was the
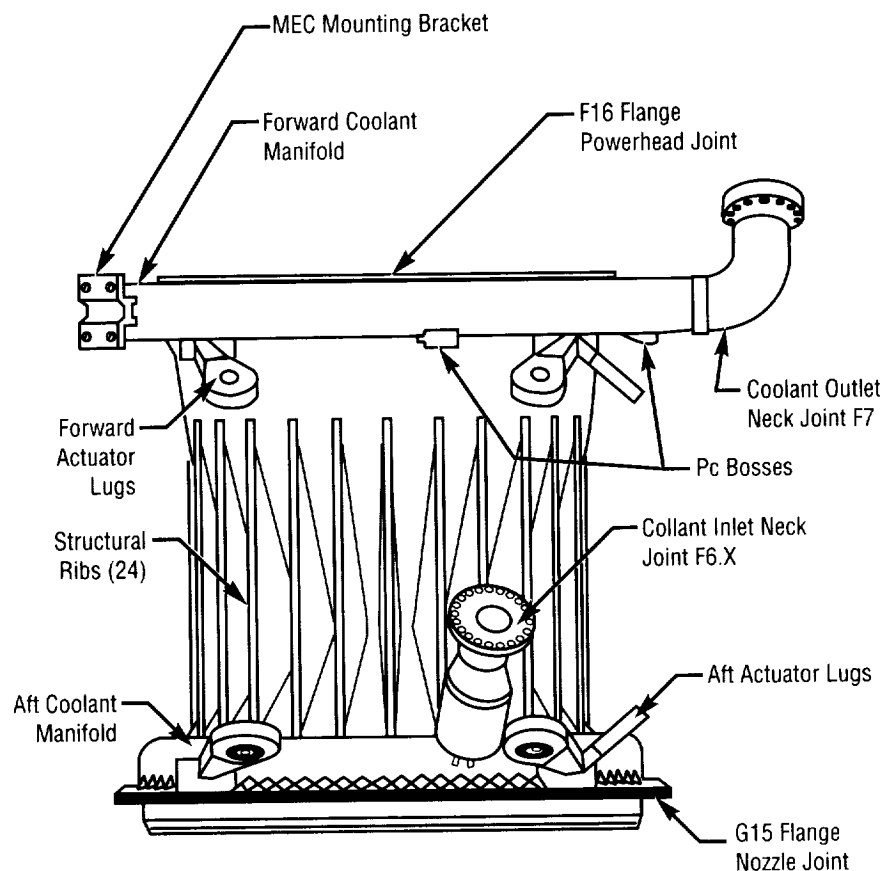
FIGURE 98.—Production advanced main combustion chamber configuration.

160

coolant liner. The current liner design, in some cases, has degraded over a wide variation of engine cycles to a point at which those chambers had to be retired from service before their designed cycle life had been reached. Locally high wall-mixture ratios and lower coolant flow rates, along with other engine variabilities, are strong drivers for premature liner degradation. Researchers decided that a more robust liner was needed that would not be as easily affected by engine operating variabilities.

A formed platelet liner is the baseline for the new liner design. The technology is being developed with Aerojet of Sacramento, California, under contract NAS8–37456. The platelet forming process allows the liner to be made with a larger number of internal flow coolant channels that have a higher aspect ratio (height-to-width) than those in the current liner. It also incorporates a thinner hot gas wall, enabling the wall to operate at a significantly lower temperature and thereby increasing the life and durability of the liner.

These newer methods of fabrication have an added benefit in that they allow production of a combustion chamber in 12 months, as compared to 40 to 60 months for the conventional chamber. The cost for producing an advanced combustion chamber (fig. 98) is projected to be less than 1 million dollars, compared to over 3 million dollars for the existing design.

An aggressive schedule is in progress to demonstrate the lower fabrication time and costs by building two
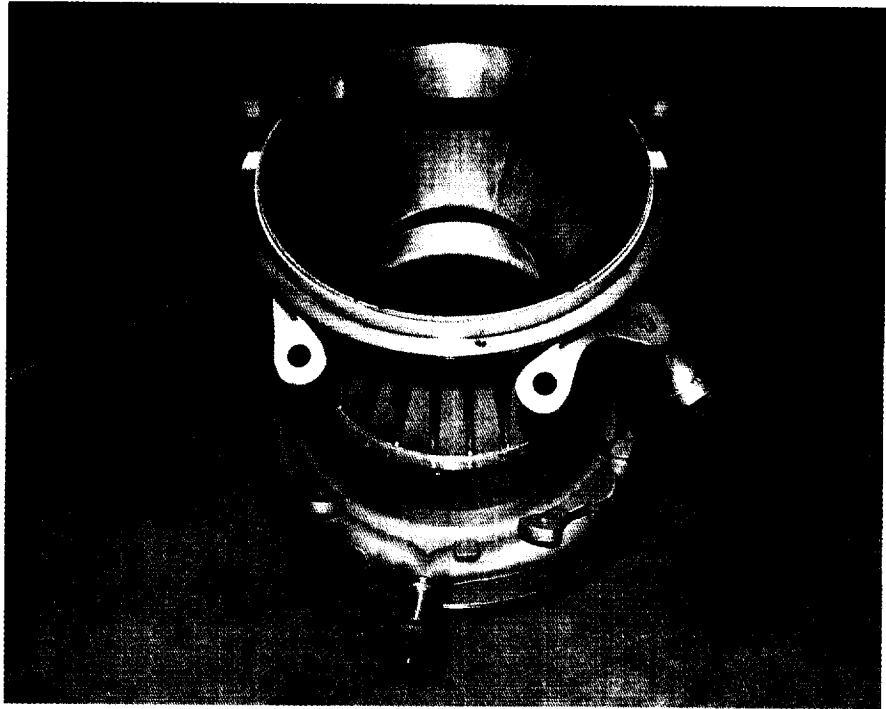
FIGURE 99.—Advanced main combustion chamber demonstrator.

demonstrator units and two hot-fire prototypes. The demonstrator units have been successfully completed (fig. 99), and fabrication of the first hot-fire prototype is on schedule for full-scale testing at MSFC's Technology Test-Bed Engine Facility.

Sponsor: Office of Advanced Concepts and Technology

Industry Involvement: Gencorp Aerojet, Sacramento, California.; Precision Castparts Corporation, Portland, Oregon.; Sverdrup Technology, Inc., Huntsville, Alabama.

University Involvement: University of Alabama

• • • • •

Ablative Combustion Chamber Liner Feasibility Study

David L. Sparks/EP33
205-544-7111

The Propulsion Laboratory's Component Development Division has an ongoing commitment to produce low-cost, reliable liquid propulsion subsystems. Use of ablative combustion chambers or chamber liners in liquid rocket engines is one way of accomplishing this objective. The Orbital Science Corporation, for example, is interested in using these types of chambers in the next-generation engine for air-launched orbital systems because of the potential reductions in manufacturing and operational costs. MSFC will, therefore, conduct a series of tests to determine if ablative materials are suitable for this application.

The chamber liners are fabricated by wrapping silica-phenolic tape around a combustion chamber form (called a mandrel) with outer diameters that match the desired inner contour of the combustion chamber. Next the wrapped mandrel is baked at high temperature until an equilibrium condition is reached. The liner is then removed from the mandrel, final machined, and installed in a structural jacket. The liner is now ready for testing. Key process variables such as tape-wrap thickness and angle will be assessed during the design and manufacture of the liners.

Utilizing in-house capabilities, Marshall personnel will design and fabricate the new combustion chamber
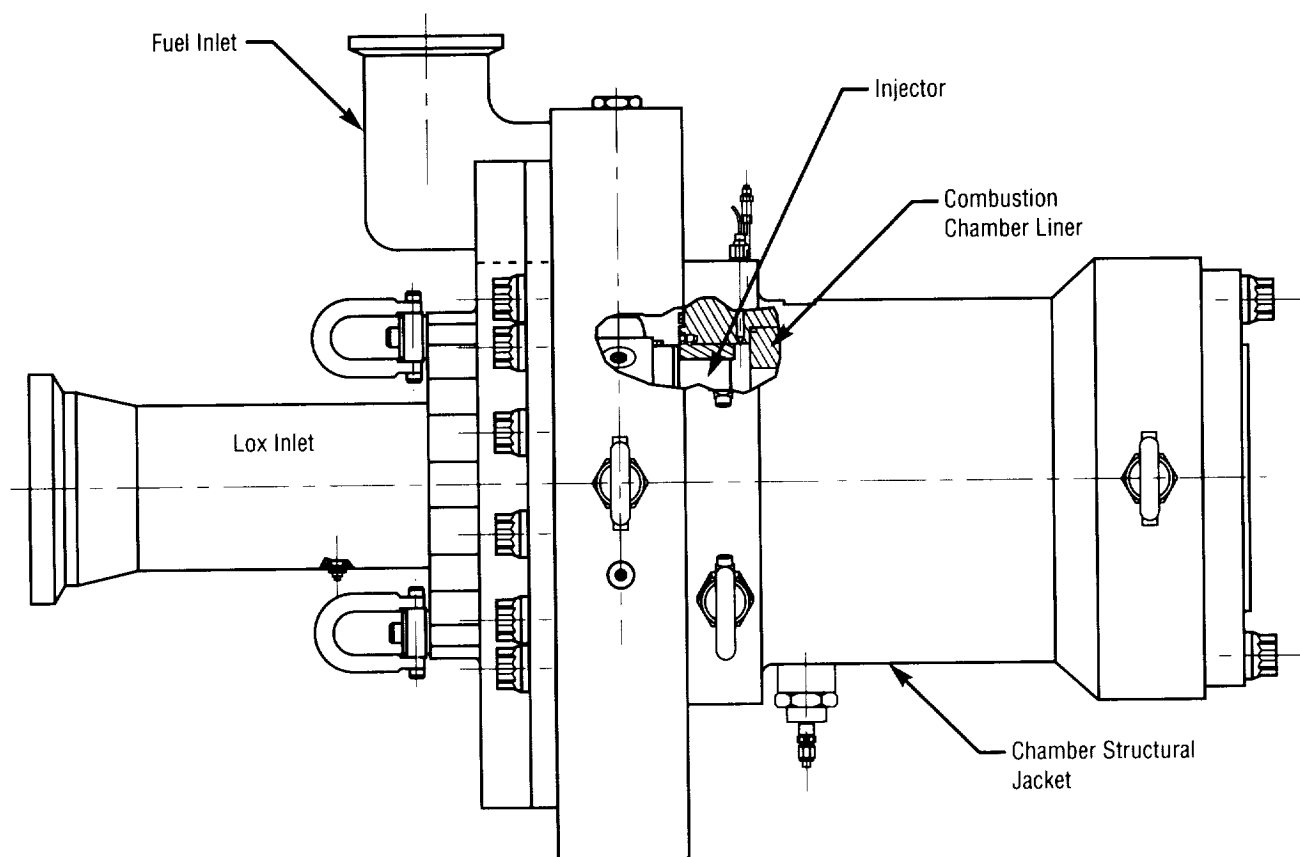
FIGURE 100.—"Fastrak" engine assembly.

ablative liners for use in hardware modified specifically for this application (dubbed the "Fastrak" engine), as illustrated in figure 100. The objective of Fastrak testing is to evaluate the performance of ablative materials in a liquid-engine-like combustion environment. Once installed in the thrust chamber assembly (TCA), the liners will be tested at MSFC Facility 116, which will be modified for testing with liquid oxygen (lox) and RP–1 (kerosene), and utilized in breadboard fashion to demonstrate the erosion characteristics of the ablative liner materials as a function of percent film coolant, chamber pressure, and injector design. A secondary objective of the hot-fire testing is to demonstrate acceptable combustion efficiency of a low-cost, like-on-like (L-O-L) quadlet injector designed specifically for this program. The tests will be conducted at chamber pressures ranging from 300 to 500 pounds per square inch absolute (psia) and film-cooling flow rates up to 10 percent. Pressures and propellant flow rates will be recorded to assess engine performance during the test. Post-test hardware inspections will also be performed to evaluate liner surface regression as a function of time and other parameters. Test data and post-test hardware inspections will be used concurrently to weigh the feasibility of using low-cost ablatives in the construction of future liquid rocket engine combustion chambers.

Sponsor: Office of Space Flight

• • • • •

Prediction of Performance and Wall Erosion Rate of a Liquid Rocket Ablative Wall Thrust Chamber

Huu P. Trinh/EP13
205–544–2260

A demonstrative rocket thrust chamber, called a "Fastrak" chamber, using a silica-phenolic material as an ablative wall, has been designed and fabricated at MSFC. To support this activity, predictions of thrust chamber wall temperature and ablation erosion rates have been performed using the REactive FLow EQuation Solver (REFLEQS) computational fluid dynamics program. The analysis is intended to assess the amount of fuel necessary for film cooling so that the erosion rate of the chamber ablation does not exceed its allowable limit. In addition, thrust chamber performance loss due to an increase in film cooling has been examined.

In the study, the thrust chamber flow field is assumed to be axisymmetric, and the chamber inlet is divided into two regions. The outer region represents the film-cooling inlet, and the inner one has a uniform fuel/oxidizer mixture ratio. The propellants injected into the chamber are considered to be gaseous and react according to equilibrium chemistry.

The estimation of the ablative silica-phenolic material erosion rate is based on limited test data reported in 1969 by Aerojet-General Corporation[1]—results of a test series conducted for a large hydrogen/oxygen thrust chamber. The only reported data suitable for the present analysis are the erosion rates of silica-phenolic at the chamber throat. In the current analysis, the erosion rate is considered to be applicable for every point along the chamber wall.

Calculations have been conducted for various operating film-cooling flow rates. A summary of the thrust chamber geometry (fig. 101) and
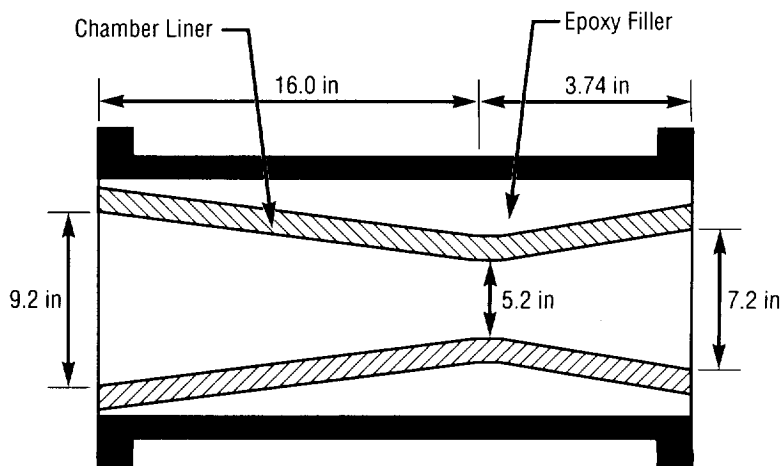
FIGURE 101.—"Fastrak" thrust chamber geometry.

operating conditions used in the
analysis is as follows:

Chamber pressure
(pounds per square
inch absolute (psia)) 300.00

Overall mixture ratio 2.34

Fuel (RP–1) flow rate
(pound mass per second
(lbm/sec)) 14.19

Oxidizer (lox) flow rate
(pound mass per second) 33.19

Fuel for film cooling (percent
in mass) 0, 4, 6, 8, 10, 12, 14

Combustion chamber
length (inches) 16.00

Contraction area ratio 2.45

Due to the prescribed assumptions, the
results of the present analysis should
not be interpreted as representative of
the actual thrust chamber
characteristics. The results do, rather,
provide the trend of the thrust
chamber behavior and tend to portray
the upper bound on the estimated
erosion rate. On the other hand, the
solutions seem to provide the lower
bound on the performance loss.

Thrust chamber wall erosion rates at
various film-cooling percentages are
presented in figure 102, and the
corresponding maximum erosion rates
are plotted in figure 103. Findings
indicate that when the percentage of
fuel to be used for film cooling is
greater than 10 percent, the chamber
wall conditions no longer respond
strongly to an increase in film cooling.
The additional fuel to be used for the
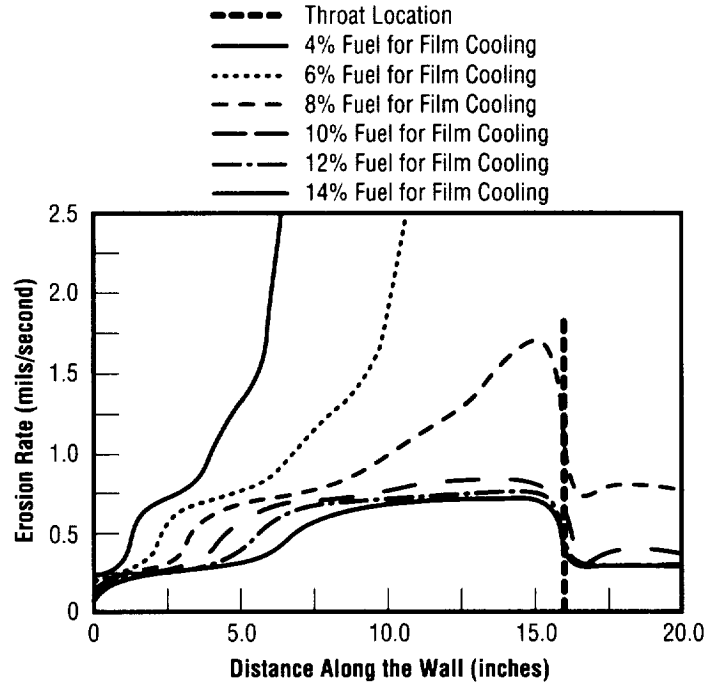
FIGURE 102.—Erosion rate profiles at various film-cooling flow rates.
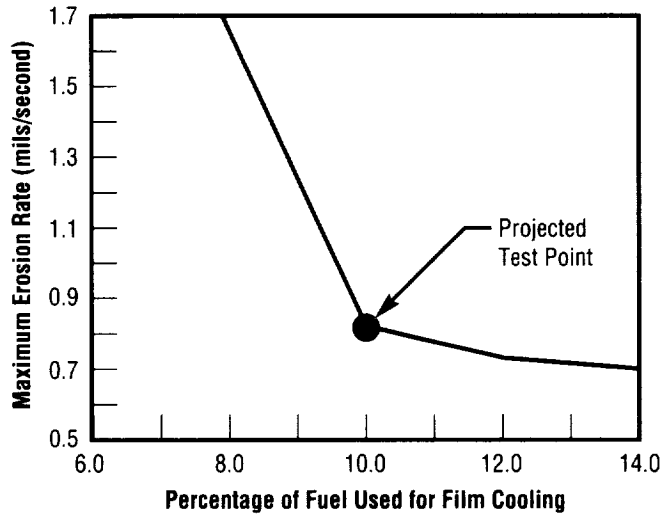
FIGURE 103.—Change in maximum erosion rate due to film-cooling increase.
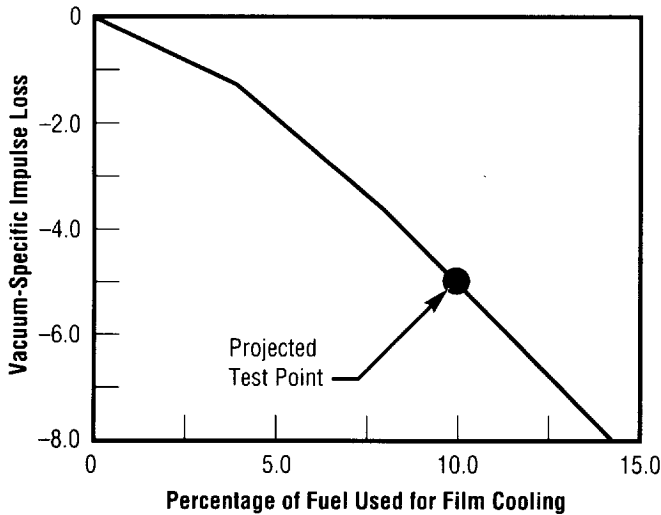
FIGURE 104.—Performance loss due to film-cooling increase.

film cooling results in a higher hot core mixture ratio (MR). Consequently, the hot core flow has a higher temperature, so adding more film cooling no longer has a strong effect on the wall erosion rate reduction. On the other hand, the thrust chamber performance loss, as shown in figure 104, decreases linearly with the film cooling. Approximately 10 percent of fuel to be used for film cooling, as projected for the hot-fire test, seems to be reasonable based on the analysis.

[1]Moise, J.C., and Kovach, R.J. June 1969. Performance of Various Ablative Materials in a Large Hydrogen/Oxygen Thrust Chamber, 69–442. American Institute of Aeronautics and Astronautics (AIAA).

Sponsor: Office of Advanced Concepts and Technology

● ● ● ● ●

Post-Test Diagnostics of the Space Shuttle Main Engine

Catherine D. McLeod/EP14
205–544–6227

Dave C. Seymour/EP14
205–544–7116

An assessment of engine and component health is made following each ground test and flight of the space shuttle main engine (SSME). Currently, this assessment is done manually by engine and component experts looking at large amounts of data in an effort to make decisions regarding engine health and judge the preparedness of each engine for future tests and flights.

The objective of the Post-Test Diagnostic System (PTDS) effort is to develop a software tool to automate many aspects of the data analysis process. The tool will not replace analysts, but will relieve many of the mundane and time-consuming aspects of the process. The system is composed of several types of software packages, including a relational data base for storing all data, features, and hypotheses as they flow through the system; statistical pattern recognition for feature extraction; an expert system for diagnostics; and a case-based reasoner for anomaly resolution.

The Post-Test Diagnostic System activity actually began in 1989 at the Lewis Research Center with the definition of a system architecture to do nonreal-time health monitoring of a generic rocket engine. Since that time, a tool has evolved to detect the health

of the space shuttle main engine specifically. Researchers recognized that data analysis on the space shuttle main engine was so labor-intensive that it would provide the ideal test-bed in terms of available data to test such a system, and the reduction in manpower would justify system development costs. The components of this architecture are depicted in figure 105.

Since that initial architecture study, a system-level performance module has been developed that looks at data recorded on the entire engine. (The data flow through the system is depicted in fig. 106). The data are loaded into the system, at which time specific features of the current test are extracted. The feature-extraction

Component Analysis					
Performance Systems	Combustion Devices	HPOTP	HPFTP/ LPOTP/ LPFTP	Valves and Actuators	Dynamics
Analysis Software	Feature Extractor	Sensor Validation	Graphical User Interface	Transient Analysis	

Support Applications	SunPlot	Relational DB • Anomalies • Test Data

Platform	• Sun Workstations • GUI—Motif • CAE—PV-Wave/Metrica	• DB—Metrica • Expert Systems—CLIPS • Procedural Language—C

FIGURE 105.—Post-Test Diagnostic System architecture.
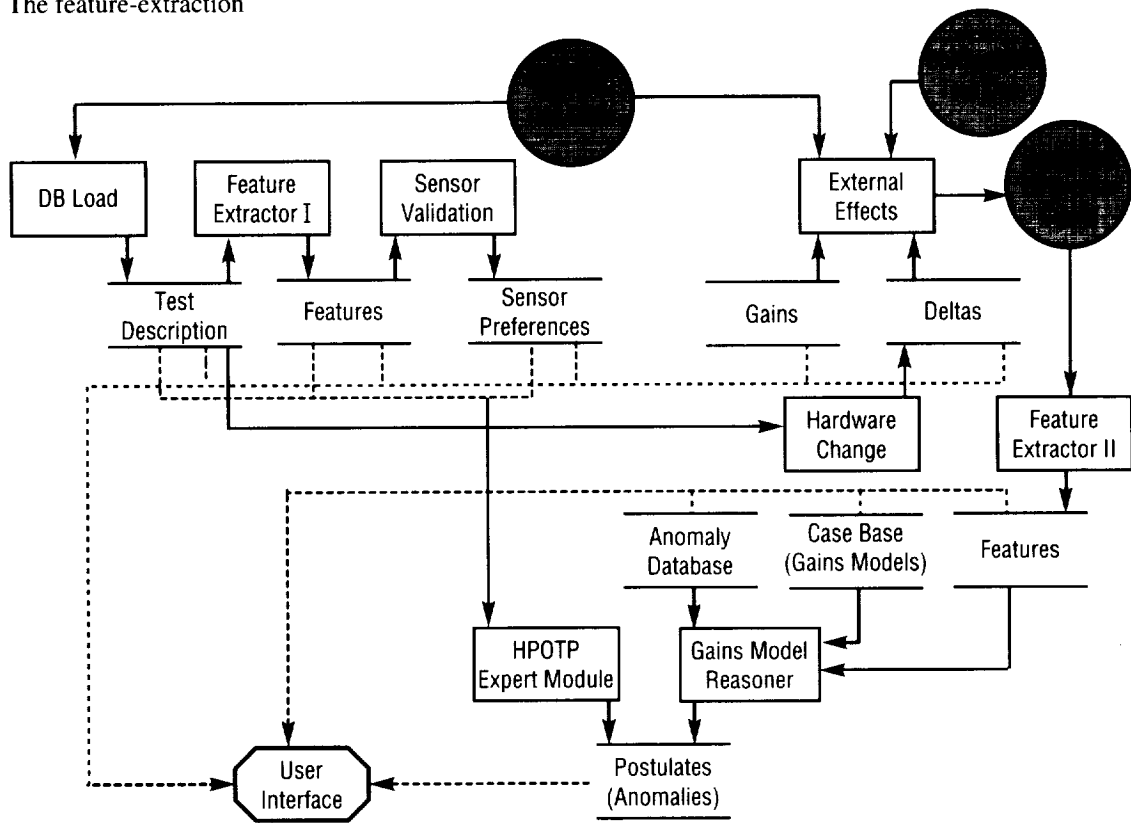
FIGURE 106.—Post-Test Diagnostic System data flow.

software, a set of statistical software routines, feeds the sensor information to an expert system, which, in turn, looks for abnormal features within each parameter and reports on the validity of each sensor based on these abnormal features.

A comparison test that has no known anomalies and best matches the current test hardware configuration and inlet conditions is then chosen. This test is baselined as "nominal" behavior for the current test's engine. The external effects and hardware change reporter is run to normalize the difference between the data of the current and comparison tests. The external effects code is procedural in nature, while the hardware change reporter is a rule-based system.

For a nominal test situation, this normalized difference curve will be a flat line at zero, indicating that all differences between current and comparison tests are completely explainable. To ensure this, a second feature extraction algorithm is run on these normalized difference curves. Any features detected at this point are hypothesized as anomalies. An attempt is made—by using the Gains Model Reasoner, a case-based reasoner tool—to map the current anomaly to one that has been seen in the past. If an exact match cannot be found, a list of those with common characteristics is provided for the analysts to use in anomaly resolution. (Also, attempts have been made to develop a constraint-based model for classifying these unknown anomalies).

In addition to a system-level module, the high-pressure oxidizer turbopump (HPOTP) module has been developed, which combines the feature extraction

and sensor validation of the performance module with a rule base of turbopump-specific knowledge to assess the health of the high-pressure oxidizer turbopump on the current test. The two modules are currently capable of reasoning independently and are not yet integrated. System integration should be complete and the Post-Test Diagnostic System in production by the end of 1994. Modules to reason the remaining components of the main engine are expected within 2 years.

As the space shuttle main engine moves to a production mode of operation, the diagnostic system will become an even more useful tool. One special benefit of the system is its ability to become smarter about what is detected in the data. As the system gains knowledge, it will aid NASA in retaining an historical memory of space shuttle main engine diagnostics.

Sponsor: Office of Advanced Concepts and Technology

Industry Involvement: Gencorp Aerojet, Sacramento, California; Martin Marietta Manned Space Systems, Huntsville, Alabama; SAIC, San Diego, California

University Involvement: University of Alabama in Huntsville

● ● ● ● ●

Advanced Liquid Oxygen Propellant Conditioning Concept Testing

Gretchen L.E. Perry/EP23
205-544-4646

The concept of propellant conditioning refers to the proper propellant temperatures required for engine ignition while preventing geysering in the propellant feedlines. In recent years, evaluations have been conducted to reveal promising propellant conditioning options for increasing reliability and operability while, at the same time, reducing costs of future advanced launch vehicles.

The current shuttle system uses high-propellant bleed through the engine to maintain cold oxidizer temperatures at the engine interface. The high bleed rate is actively controlled. The hardware associated with the high bleed can be manpower-intensive, requiring preflight maintenance and checkout, thereby increasing on-pad operations, failure hazards, and alterations to flight schedules. Consequently, increased manpower and hardware requirements increase costs. Therefore, reducing or eliminating bleed requirements will help in improving the reliability, operability, and cost-effectiveness of future launch vehicles.

A joint independent research and development (JIRAD) project between MSFC and General Dynamics Space Systems (GDSS) was undertaken to perform full-scale testing and evaluation of several liquid oxygen (LO$_2$) propellant conditioning options

167

with emphasis on the no-propellant bleed concept. The project was conducted between October 1992 and January 1994. Other concepts studied included low-bleed helium (He) injection and use of a recirculation line. These options were evaluated for feasibility in the event that the no-bleed concept could not adequately condition the propellant.

While the design of the test article was intended to simulate the National Launch System (NLS), the layout was actually very similar to many generic heavy-lift-type vehicle feed ducts that have been discussed in recent years. Testing was conducted in the Hydrogen Cold Flow (HCF) Facility of the West Test Area (WTA) at MSFC. Two full-scale feedline test articles were provided by General Dynamics for testing. The articles, which simulated propellant engine feed ducts, had slopes of 25 and 15 degrees, respectively. At the bottom of each article was a simulator that emulated heat input from a liquid oxygen turbopump. Figure 107 is a detailed drawing of the type of test articles used for the project. (For safety and operational concerns, liquid nitrogen (LN$_2$)—which shows very similar fluid properties, heat fluxes, and flow velocities to that of liquid oxygen—was used for actual testing.)

The no-bleed concept relies on convection to induce fluid flow in the feed ducts. Natural recirculation flow within a heavy-lift vehicle removes heat from the main propellant feedlines, provides low cryogenic temperatures for satisfactory engine ignition, and conditions propellant in engine feed ducts by inducing a series of circulation cells within each feed duct. These cells are believed to
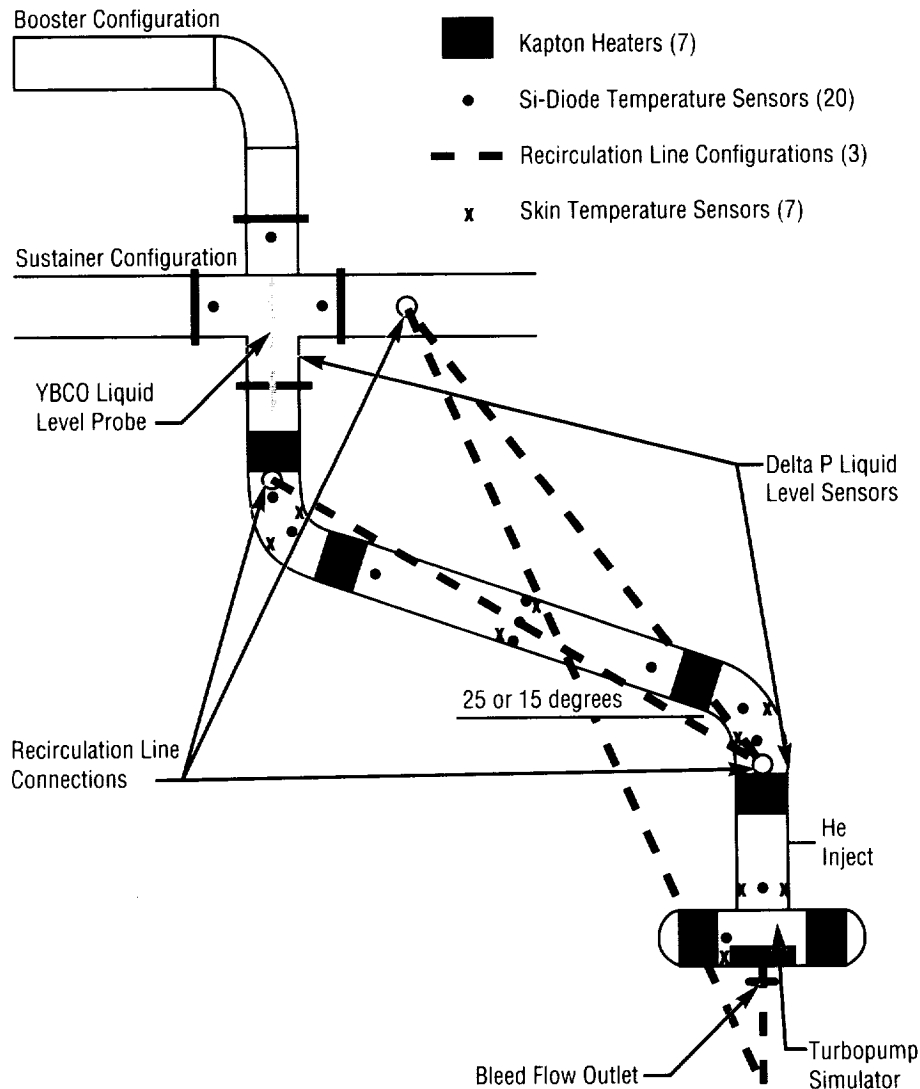
FIGURE 107.—Detailed drawing of the type of test article used in the liquid oxygen propellant conditioning test project. Each article constructed of 6061 12-inch-inner-diameter (ID) aluminum.

enhance the transfer of heat up through the duct by forced convection. However, proven analytical models were not available to accurately predict conditions at the ending interface.

The objectives of this project were to validate and anchor analytical feedline models and to demonstrate the feasibility of no-bleed. While earlier trade studies showed that the no-bleed conditioning concept was the best

option, there were conflicting model predictions of turbopump inlet temperature and pressure conditions. The test data would be used to anchor analytical models and develop design guidelines for the development of a main propulsion feed system.

The MSFC/General Dynamics joint testing was conducted in two phases. The first full-scale tests conducted included a feasibility check that involved the 25-degree, sloped test article in the sustainer mode. All four concepts of no-bleed, low-bleed, helium injection, and use of a recirculation line were tested. The parameters gauged at this time were baseline values of pressure, temperature, velocity, the intended range of bleed flows, and all recirculation line configurations.

The next phase of testing involved studying the impact of important design parameters, including—but not limited to—testing the 25-degree article in the booster configuration and the 15-degree article in the sustainer mode. Table 11 displays a layout of parameters tested during this phase.

A test matrix of over 100 tests was developed to evaluate all four propellant conditioning concepts. All four concepts were tested with the 25-degree, sloped article in the sustainer mode. The 25-degree article was also tested in the booster configuration, while the 15-degree article was tested solely in the sustainer configuration. Tests such as recirculation and/or booster applications were not repeated in the 25-degree booster or 15-degree

sustainer configurations. Analysis revealed that the data from these tests would not provide any additional information to the data already obtained from the 25-degree sustainer configuration.

Based on the analysis to date, the no-bleed propellant conditioning concept may be applied to such future heavy-lift-type launch vehicles as the Atlas IIB and single-stage-to-orbit (SSTO).[1,2] Other propellant conditioning projects are currently being pursued to elaborate on the work started in this joint effort. Additionally, work is underway to complete the data base on liquid oxygen propellant conditioning at the Hydrogen Cold Flow Facility. Also planned is the construction of a facility to accommodate actual liquid oxygen testing at the West Test Area within the next few years.

[1]Cleary, N., et al. NASA TM to be published.

[2]Innovative LO$_2$ Propellant Conditioning Systems Test Report, GDSS–94–H–R–002.

Sponsor: Office of Space Flight

Industry Involvement: General Dynamics Space Systems Division

• • • • •

TABLE 11.—*Parameters and levels tested for the liquid oxygen propellant conditioning test project (bold level values tested during the feasibility check phase)*

Parameters	Level	
Slope	**25-degree**	15-degree
Configuration	**Sustainer**	Booster
Side Heating	**2,500 Btu/hr**	4,500 Btu
Bottom Heating	**3,000 Btu/hr**	5,500 Btu/hr
Velocity	**1.5 ft/s**	1 ft/s
Pressure	**100 psia**	60 psia
Helium Bubbling	**0 lb/s**	0.005 lb/s
Bleed Rates	**0, 0.3, 0.5, and 1.0 lb/s**	
Recirculation Line		
Before Pump	**2 in**	
After Pump	**2 in**	
Before Pump–Alternate	**2 in**	

Space Shuttle Main Engine Bearing Assessment Program

Barbara S. Breithaupt/EP44
205-544-5401

Leslie Alexander, Jr./EP44
205-544-6228

The space shuttle main engine (SSME) was the first reusable large liquid rocket engine in the world. With a design life of 55 starts before disassembly, it promised to be the most cost-effective and optimum engine for space travel. However, since its inception, it has had bearing problems that limit its reusability. Bearings within the engine's four high-speed turbopumps must withstand a very harsh environment and operate at peak performance to avoid catastrophic engine failure. As a safety precaution, bearings within one of the main engine turbopumps are replaced after every three flights—a time-consuming and costly process that frequently appears to be unnecessary.

Of the four turbopumps on an engine, the high-pressure oxidizer turbopump (HPOTP) bearings have the most wear problems and currently have no reliable inspection method or diagnostic tool. Consequently, a conservative 2,000-second limit is placed on these bearings to ensure mission safety, amounting to a maximum of three flights before pump disassembly. If this limit could be expanded by a reliable inspection method, then the engine could possibly fly for a total of nine flights

before it would have to be torn down. At an expense of 1.5 million dollars per tear-down, this amounts to a cost savings of 3 million dollars per engine.

In response to this critical need for an inspection system, the bearing assessment program was created. The program's purpose is to develop a nondestructive evaluation system to detect anomalies in bearings on assembled main engines without component disassembly. The plan is to develop a data base of various types of signatures obtained from slowly turning the turbopump shafts before and after every engine firing. These signatures would, in turn, be analyzed and compared to the original signatures to predict bearing wear more accurately.

To begin, a spare high-pressure oxidizer turbopump was obtained to determine concept feasibility quickly and concisely. Hardware was then developed to dry-spin the pump's shaft a maximum of 8 revolutions per minute. Three areas of research were investigated: acoustic emission, vibration, and torque. Acoustic emission and vibration have demonstrated very little success. At such slow speeds, there is not enough energy in the system to trigger the sensors. Testing will continue, but at higher speeds such as 50 revolutions per minute.

A new approach, dynamic torque analysis, was also investigated. Little, if any, work had ever been done investigating space shuttle main engine torque signatures for bearing
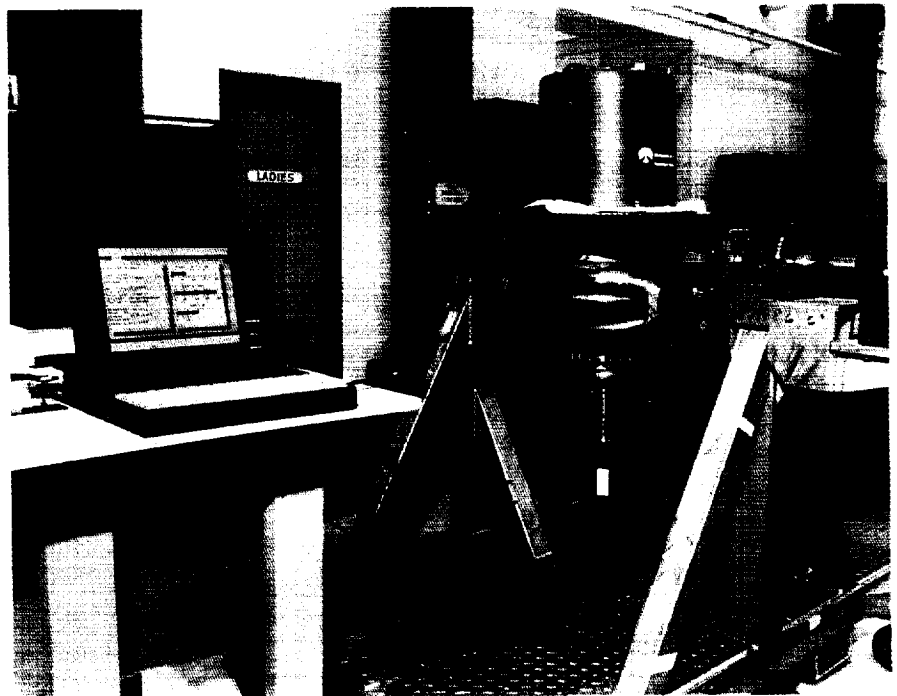
FIGURE 108.—Automated torque sensor.

signature content. Since manual torque tests had to be routinely performed on turbopumps during checkout to determine breakaway and running torque, it seemed reasonable to design an automated tool to measure the torque and store the data for later analysis and review. Moreover, the dynamic content of the available torque signature might prove useful in determining bearing health.

A prototype device, an automated torque sensor (ATS), was developed (fig. 108). The battery-powered, computer-controlled, and easy-to-use tool was designed to be portable and durable for operation on test stands. The complete system is composed of two parts, a torque test head and a data acquisition system. The entire unit fits in two cases that have a combined

weight of less than 40 pounds. A software program, written especially for the automated torque sensor, controls its entire operation.

The unit has been in use for some time, and the resulting high-frequency torque data looks promising, since the signature content has been repeatable from test to test with different transducers. There is definite frequency content in the torque signal that merits further investigation. A pump with good bearings has been baselined. What is needed now is a high-pressure oxidizer turbopump with heavily damaged bearings to unequivocally prove feasibility (fig. 109).

The automated torque system itself will be optimized by making the unit

lighter and shorter for ease of handling and installation. The software package will be enhanced to accommodate more user-defined parameters to enable the operator to manipulate the data immediately following the test. This nondestructive evaluation system may one day be adapted for industrial use to perform quick and reliable bearing checks, thus providing another level of quality assurance.

Sponsor: Office of Space Flight

Industry Involvement: Global-Tron, Inc.

• • • • •
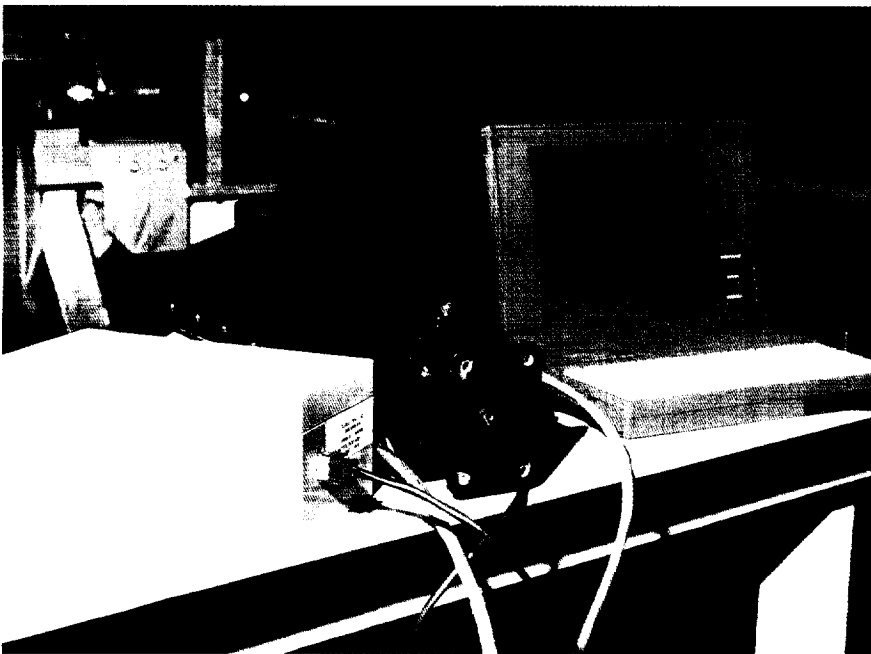
FIGURE 109.—High-pressure oxidizer turbopump undergoing actual torque test.

Low-Temperature Testing of Static Seals

R. Lance Moore/EP42
205-544-7155

The objective of this test program is to create a data base of static seal performance at low temperatures. One of the primary objectives is to determine the actual performance of Viton® elastomer Gask-O-Seals when exposed to temperature conditions from ambient to –101.1 °C. Additional testing is being conducted on static O-ring seals of several materials, including ethylene propylene (EO692), Viton® (VO835–75), and silicone (SO383). The O-rings conform to Parker size no. 2–022 (2.51 ± 0.025 centimeters O.D., 0.178 ± 0.007 centimeter cross-sectional diameter).

The Viton® elastomer Gask-O-Seals used to seal the flanges of the space shuttle main engine's (SSME's) helium system are designed to operate in the temperature range of –40 to 371 °C. This fluorocarbon seal maintains satisfactory performance during normal space shuttle flight conditions. Sometimes, however, during reentry or during a return-to-launch-site (RTLS) abort, seal temperature falls well below –40 °C. At these low temperatures, the Viton® Gask-O-Seal can lose much of its ability to stop leakage. Currently, this condition is covered for the space shuttle main engine by a change to interface control document (ICD) #13M15000, which increases the allowable seal leakage rate. Static seal manufacturer data provides little information on seal material characteristics when exposed to low temperatures.

For this effort, the test configuration consists of a sealed fixture that contains two bolted flanges sealed with either a Gask-O-Seal or an O-ring. The inside surface of the seal is pressurized to 5.86 megaPascals with gaseous helium (GHe). The outside of the test seal is held in a vacuum, and the fixture is placed inside an open dewar containing liquid nitrogen (LN₂). Kapton™ heaters are mounted inside the fixture to maintain the temperature of the test article between ambient and –101.1 °C. Leakage is measured using a helium mass spectrometer.

The test cycle begins at ambient temperature, as the temperature is reduced at a rate of approximately 1 °C per minute until the article reaches –101.1°. Test article temperature is then increased to ambient conditions. The helium leakage rate is measured continuously throughout the cycle.

The flange compression of the O-ring seals is varied (10 to 40 percent) to determine if increased compression improves the ability to maintain a seal at low temperatures. Shims are installed between the flanges to vary seal compression. Four O-rings are being tested for each material and each compression level. Some of the O-rings are being exposed to several temperature cycles to determine if repeated exposure to low temperatures has any effect on the O-ring's ability to seal.

To date, seal testing has provided some informative results. The Gask-O-Seals began leaking at the recommended manufacturer's minimum temperature (–40 °C), and the leakage rate reached a maximum of approximately 1,000 standard cubic inches per minute (SCIM) almost immediately. The leak rate remained at this level while the temperature was decreased to –101.1°. As the temperature was increased to ambient conditions, the seal leak rate began to decrease at approximately –40° to a point well below the design
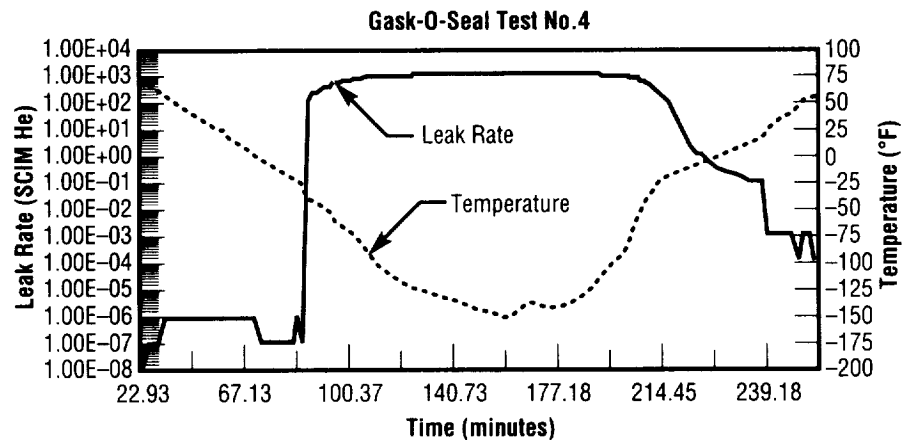
FIGURE 110.—Typical plot of Gask-O-Seal leak rate versus temperature.

O-Ring Test No. VO835–75–14 (40% Squeeze)
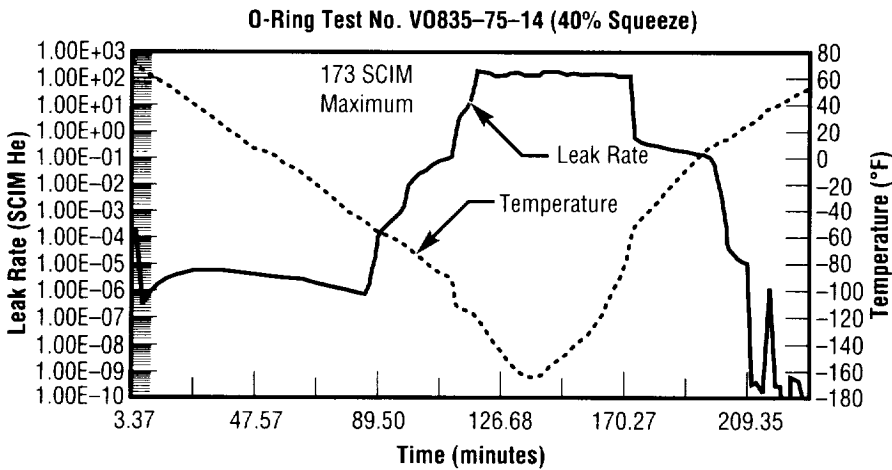
FIGURE 111.—Typical plot of Viton® O-ring leak rate versus temperature.

O-Ring Test No. EO692–16 (40% Squeeze)
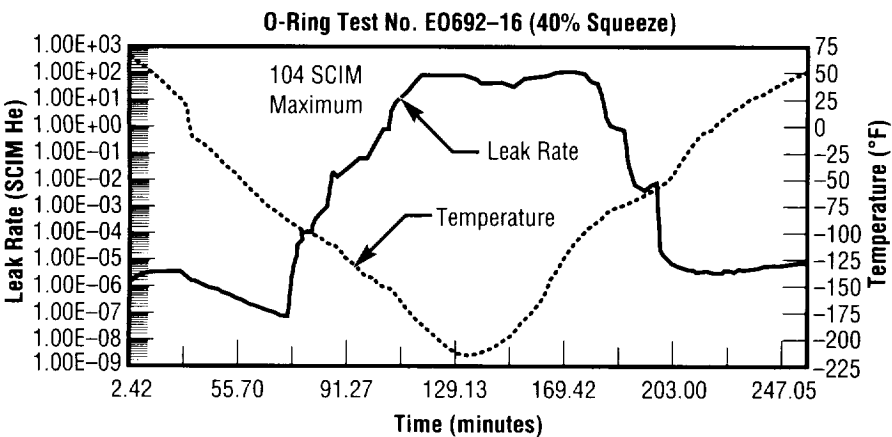
FIGURE 112.—Typical plot of ethylene propylene O-ring leak rate versus temperature.

O-Ring Test No. SO383–16B (40% Squeeze, Third Cycle)
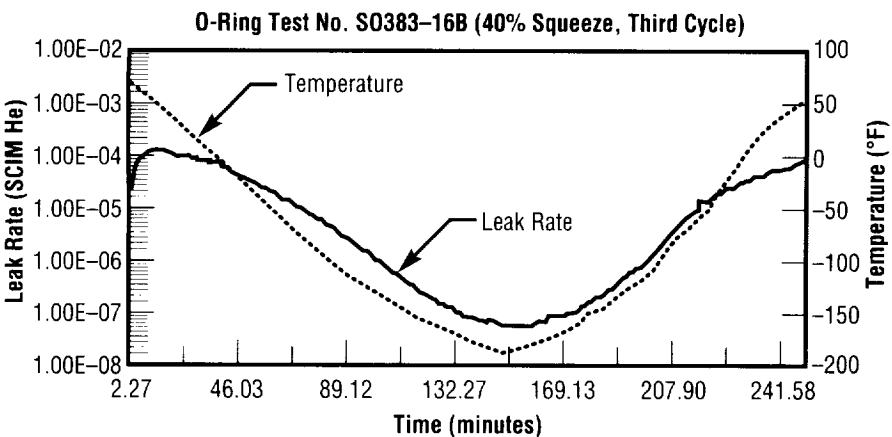
FIGURE 113.—Typical plot of silicone O-ring leak rate versus temperature.

verification specification definition of "zero" leakage (4.2 standard cubic inches per minute helium). A typical plot of leak rate versus temperature is illustrated in figure 110 for the Gask-O-Seal tests.

All O-ring tests at 40 percent compression have been completed, and the results indicate a direct correlation between increased compression or squeeze, compression time, and leakage. Plots of leak rates versus temperature for all three materials are provided in figures 111 through 113. After performing several O-ring tests, the testing team realized the need to compress the O-ring for some time period (to be determined) to simulate aging. The test team is considering the possibility of artificially aging the O-rings in a compressed state and then performing leak tests.

Data collected from these tests are being compiled to provide a data base of static seal material properties when exposed to low temperatures. The data base will contain information useful for determining candidate materials in future low-temperature seal applications. Results obtained thus far indicate a potential for substituting metallic seals with O-rings in certain applications.

Sponsor: Office of Space Flight

• • • • •

173

A Model of Critical and Supercritical Evaporation of Drops in Clusters

Klaus W. Gross/EP13
205-544-2262

A model has been developed from first principles that take into account the supercritical fluid phenomena for a liquid oxygen-liquid hydrogen (LO_2-LH_2) system in which drops of liquid oxygen exchange heat and mass with fluid hydrogen. Eventually, the liquid drops become spherical entities of fluid, so that it is the interaction between portions of space containing different supercritical fluids that is actually modeled. To depict these situations (drops-fluid and fluid-fluid), the model does not follow the traditional approach of assuming there is a surface whose surface tension vanishes eventually. Quite the contrary, in the present model it is only assumed that there is an interface between the fluids—so the same equations can be solved for all portions of space, with boundary conditions at the interfaces. The solution for the density from the state equation indicates if a liquid, a fluid, or a gas is found at a particular location. A liquid and gas combination exists if there are multiple roots for the molar volume in the state equation; a supercritical fluid exists if there is a single root. Far from the critical point, if the density is of order 0.001 grams per cubic centimeter (g/cm^3), there is a gas at that location; if the density at a location is of order 1 gram per cubic centimeter, then there is a liquid at that location. This novel approach

bypasses the conceptual difficulty of the surface tension vanishing instantaneously.

In the drop-fluid situation, the drops evaporate and oxygen enters the surrounding hydrogen. Boundary conditions at the interface take into account nonequilibrium effects. In the fluid-fluid situation, hydrogen enters the location occupied by the oxygen through solubility effects, causing a change in the composition of the fluid in the space formerly occupied by the liquid, with the critical point varying according to the mixture composition.

The model is based upon general conservation equations for a fluid and the rigorous description of transport processes through "fluctuation theory." In this theory, both heat and mass transport are related to a transport matrix and to gradients of chemical potentials. Fick's diffusion for species, thermal mass diffusion (the Soret effect), Fourier diffusion of heat associated with thermal conductivity, and the Dufour effect (resulting from unequal species diffusion velocities producing concentration gradients that induce heat transport) are all taken into account. The constituent relationships are calculated from classical thermodynamic expressions for binary mixtures combined with either expressions for the chemical potentials or the equations of state.

Equations of state calculations are based upon the concept of the departure function. Thus, for a pure component, a state function is equal to the sum of the departure function from an ideal gas and the state function calculated at conditions close to ideal.

The departure function can be calculated using the Peng-Robinson equation of state, whereas the state function for the near-ideal conditions can be curve-fitted to agree with high-order, semiempirical equations of state based upon experimental data. The advantages of this approach over the National Institute for Standards and Technology (NIST) or Peng-Robinson equations of state are the following:

- The National Institute for Standards and Technology equations of state do not cover the high temperature range needed here.

- No mixing rules have been developed for the many-term, semiempirical equations of state.

- The Peng-Robinson equation of state has been developed for hydrocarbons and does not necessarily agree with exact equations of state for hydrogen-oxygen.

From the equations of state calculated as described above, other important quantities can be derived, including the chemical potentials, fugacity coefficients, heat capacity at constant pressure, expansivity, and the isothermal compressibility. Also calculable are the viscosity, the thermal conductivity, and the mixture diffusivity (values valid for the liquid phase, for the gas phase, and for the fluid). Mixing rules are used to calculate the values for mixtures of hydrogen and oxygen. The expressions obtained for all properties have been cross-checked to ensure the consistency of the thermodynamic approach. The formulation also takes into account that all equations of state

are poor near the saturation conditions and near the critical point; therefore, exact saturation curves have been used to correct the fugacity coefficient near saturation in order to yield correct values.

Work in progress is focused on the coding of the conservation equations and the coupling with the subroutines, calculating the state functions and the thermodynamic properties of the mixture. These efforts are being conducted at the Jet Propulsion Laboratory (JPL) in Pasadena, California, by Dr. K. Harstad and Dr. J. Bellan.

Sponsor: Office of Advanced Concepts and Technology

• • • • •

High-Mixture Ratio Core Gas Generator

Huu P. Trinh/EP13
205-544-2260

An advanced gas generator with a high-mixture ratio core, which has a potential use for future liquid engines, has been studied numerically. Because of the high-mixture ratio core, such a generator can be ignited reliably during startup. The generator can also be applicable for nonbleed start operation, which has an initially low-mixture ratio. As a negative, the high-mixture ratio core generates a hot temperature streak (hot core) in the gas generator. Since the turbine has definite temperature limitations, the stratification of hot gases needs to be diffused with reasonable internal pressure drop.

Several mixing-enhancement devices of various sizes, shapes, and positions were previously studied.[1] Figure 114 demonstrates the bulk temperature at the gas generator exit and the pressure drop across the gas generator for various cases of geometry performed from that study. Under this investigation, the geometry of case 23 (fig. 114) was found to offer reasonably low-pressure drop across the gas generator and fairly uniform gas temperature at the gas generator exit, and it was selected for further study. Figure 115 illustrates the selected geometry and qualitative mixture ratio distributions along the injector.

Since the splash plate is located near the high-mixture ratio core region that produces the high temperature, the splash plate and its supporting shaft have to be protected from the hot
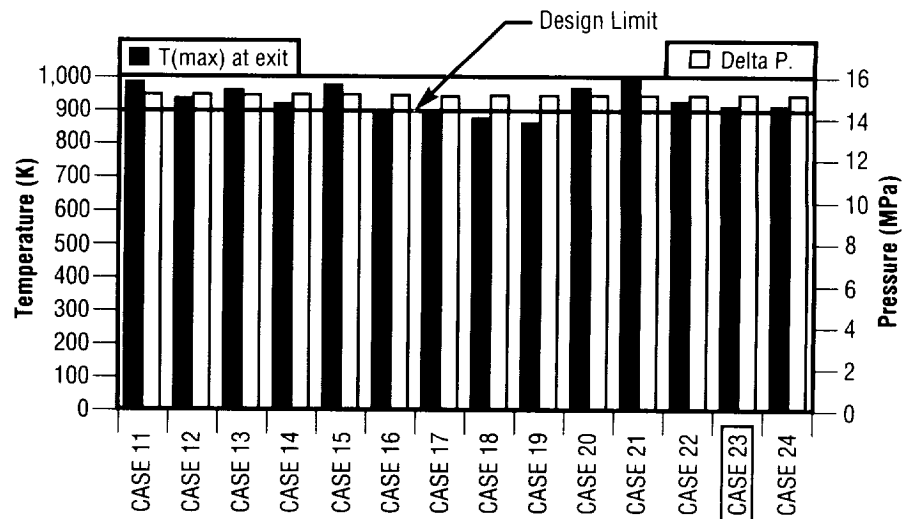
FIGURE 114.—Temperature at generator exit and pressure loss within the generator.
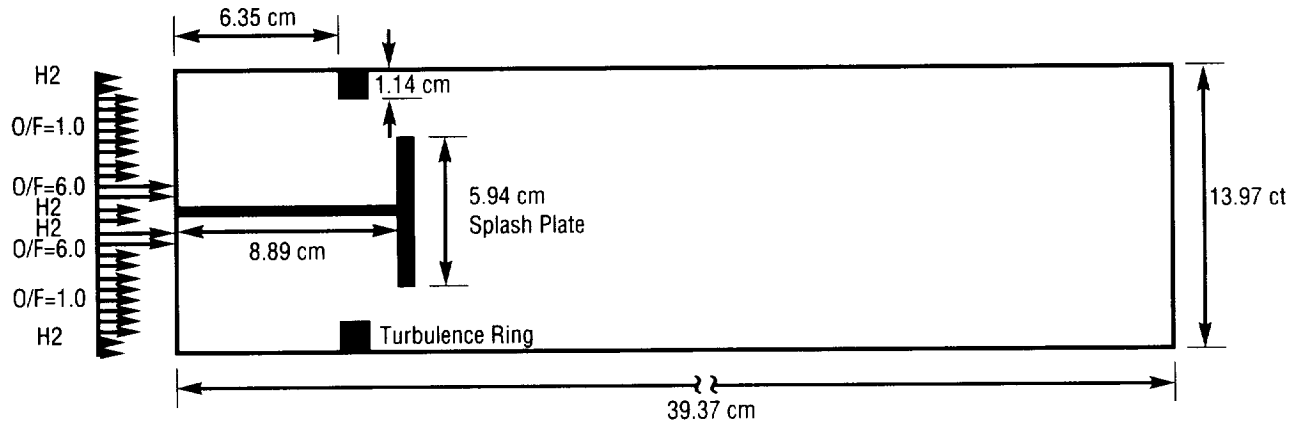
FIGURE 115.—Geometry of an advanced gas generator.

temperature. With this in mind, researchers have looked for an effective method of injecting hydrogen coolant into the combustion chamber and have studied its impact on the exit gas temperature. The maximum allowable gas temperature at the generator exit is limited to 890 Kelvin (K), and the downstream pressure is fixed at 15 megaPascals (MPa)

because gas leaving the generator has to run the gas turbine.

Two methods of introducing the coolant to the splash plate were compared. One involves cold hydrogen being injected at high speed parallel to the splash-plate supporting shaft, which is assumed to be an adiabatic wall that protects the splash

plate (case 1). In the other, cold hydrogen is fed into the hollow supporting shaft and is bled out through the supporting shaft and splash-plate surfaces (case 2). This study investigates the optimum design condition that meets both temperature and pressure conditions.

Figure 116 shows the results of the comparison. The maximum exit gas temperature for case 2 is 796 Kelvin, which is below the design limits of 890, while that for case 1 is 905 Kelvin. Case 2 effectively lowers the maximum gas temperature by 109 degrees. Pressure drop across the gas generator for both cases is approximately 2.1 megaPascals.

[1]Kim, S., and Trinh, H.P. 1993. Design Study of an Advanced Gas Generator, 93–2158. American Institute of Aeronautics and Astronautics (AIAA).

Sponsor: Office of Advanced Concepts and Technology

• • • • •

FIGURE 116.—Temperature distribution at generator exit.

Laser-Level System for Liquid Hydrogen Run Tank

Sidney W. Garrett/EP85
205–544–1228

The measurement of a continuous liquid level in a cryogenic tank, such as a liquid hydrogen (LH_2) run tank, has historically been very difficult to achieve. At MSFC's Advanced Engine Test Facility (AETF), the existing cryogenic-level systems have consisted only of several capacitance probes that provided discrete-level indications at 10-percent intervals within the tank. In 1991 and 1992, the Space Systems Division of General Dynamics designed and installed an experimental laser-level system on the liquid hydrogen run tank, while MSFC's Combustion Physics Branch developed a signal processor to convert laser sensor output into a signal compatible with existing data acquisition systems. Data from the laser system was compared with the data from the discrete system during actual test firings of the Advanced Engine Test Facility's Technology Test-Bed (TTB) engine. The laser system produced some useful data, but resulting noise levels and insufficient laser range measurements suggested improvement was needed. In 1994, Innova Laboratories of San Diego, California, was contracted to design, build, test, and calibrate an improved laser-level system.

The goal is to increase range usefulness and the accuracy of the experimental laser-level system by installing a new laser-level sensor to interface with existing tank hardware and signal processing equipment. All integration will be conducted by MSFC personnel. Data from Technology Test-Bed hot-firings will once again be compared with the old discrete-level system to assess the accuracy, reliability, and range of the laser technology.

This laser-level system will be completely nonintrusive to the cryogenic tank, requiring no costly cryogenic feed-through connectors to carry electrical signals from within the tank, nor any costly or time-consuming internal repairs to the cryogenic tank itself. If a laser sensor can be developed that will produce reliable, noise-free, continuous-level indications over the entire range of the cryogenic tank, test operations efficiency will be markedly improved and maintenance costs significantly reduced.

This technology is not limited to liquid hydrogen tanks, but could also be utilized on liquid oxygen (lox), liquid nitrogen (LN_2), and other cryogenic tanks. Other possible applications uses include high-resolution displacement measurements such as those required in structural testing of space vehicles and tanks. Commercial application benefits could occur anywhere that liquid levels within large cryogenic tank volumes must be determined.
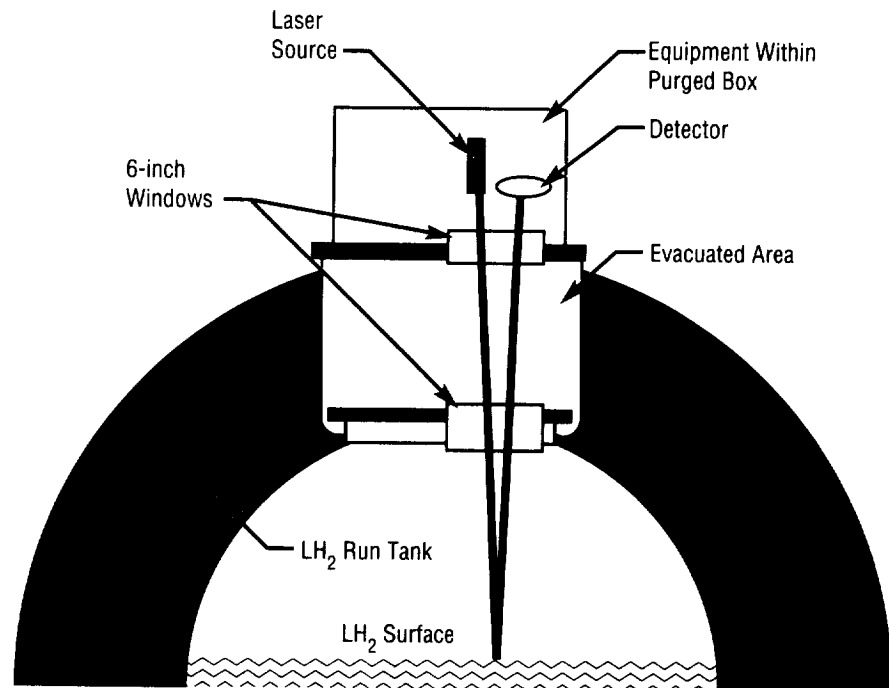
FIGURE 117.—Hydrogen run tank laser-level detector.

The initial demonstration of the laser-level technology at Marshall's Advanced Engine Test Facility has demonstrated the feasibility of the concept. With additional development, the technology may be improved enough to provide a practical, nonintrusive way to measure liquid levels within a cryogenic tank, where continuous measurement, accuracy, repeatability, and measurement range are of great importance (fig. 117).

Sponsor: Office of Advanced Concepts and Technology

Industry Involvement: Innova Laboratories, San Diego, California

• • • • •

Influence of Two-Phase Thermocapillary Flow on Liquid Acquisition Device Retention

George R. Schmidt/EP25
205–544–6055

In microgravity, liquid tends to assume an indeterminate orientation, and spacecraft tanks often incorporate devices that exploit surface tension to position, control, and maintain access to gas-free liquid. The outside surfaces of these liquid acquisition devices (LAD's) usually consist of a fine mesh screen or porous barrier that segregates liquid from pressurant gas in the tank. Although such systems are used extensively with nonvolatile fluids, their performance with cryogens, particularly liquid hydrogen, is rather unpredictable. Prior tests have indicated that pressurization with heated vapor (i.e., autogenous vaporization) can reduce or even eliminate the ability of liquid acquisition devices to retain gas-free liquid.

The objective of this project was to investigate the possible causes for this mode of retention loss and determine whether convection processes arising in liquid acquisition device pores are responsible for such failures. Rather than assessing performance of a particular device, the project focused on effects at the screen-pore level and involved computational modeling and experimental observations of two-phase fluid behavior near liquid/vapor interfaces.

The approach consisted of :
(1) formulating a pore physical model;

(2) deriving the governing equations and parameters characterizing fluid flow with thermocapillary stress, evaporation, and condensation;
(3) developing a finite element model that calculates the steady-state velocity, pressure, and temperature distributions in the pore, while accounting for deformation of the free surface; and (4) computationally examining two-phase flow and free surface behavior in a pore containing a volatile low-contact angle fluid. A series of experiments were also conducted with specialized equipment (the apparatus shown in fig. 118). The hardware consisted of a windowed cylindrical test chamber containing a 120-micron-wide slot representative of a small liquid acquisition device pore. During tests, conditions about the pore (i.e., liquid flow rate and vapor/gas temperature) were varied, while the liquid/vapor interface was recorded with a combined videotape/microscope.

The analytical portion of the project, which was successfully completed in November 1993, is described in NASA Technical Paper 3463, entitled "Thermocapillary Flow With Evaporation and Condensation and Its Effect on Liquid Retention in Low-G [gravity] Fluid Acquisition Devices." Because the project successfully identified an heretofore unknown cause of retention failure, it received an MSFC Research and Technology Award in June 1994. The project also served as a dissertation topic for the principal investigator who earned his doctorate in Mechanical Engineering from the University of Alabama in Huntsville (UAH) in December 1993. In addition to the NASA report and dissertation, three papers have been written and submitted to the *Journal*
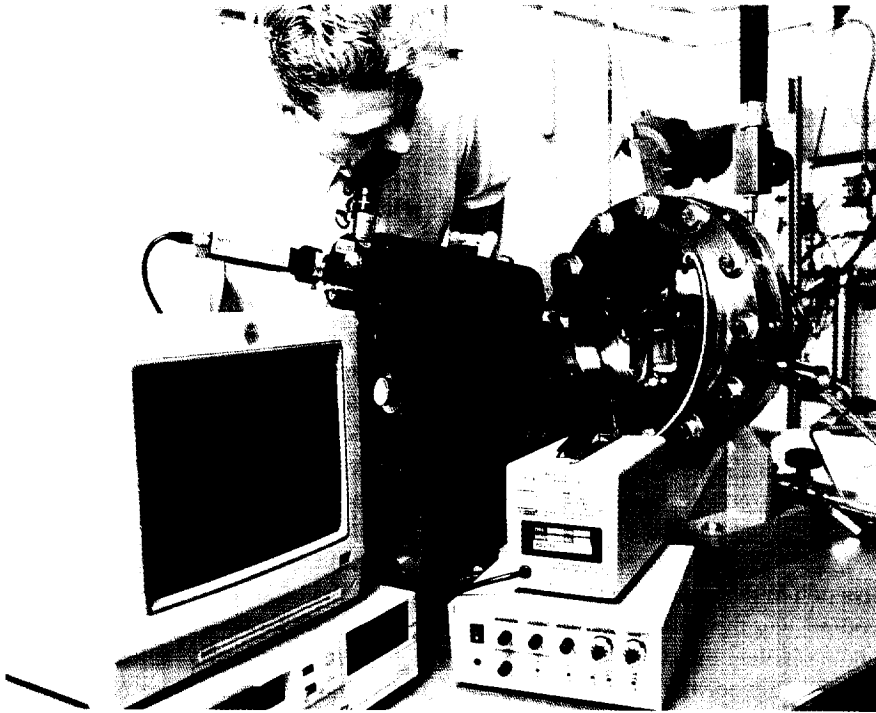
Figure 118.—Experimental setup for two-phase thermocapillary flow tests.

of Fluid Mechanics and *Journal of Thermophysics and Heat Transfer.*

The results confirmed the original hypothesis of retention loss being caused by convection within the pores of acquisition device screens. The retention loss encountered with liquid hydrogen and heated hydrogen vapor is caused by the thermocapillary flow arising from condensation-induced temperature gradients along the liquid surface of each pore. This flow, which is shown in the subcooling/condensation streamline and isotherm profiles of figure 119, establishes an interfacial pressure variation that deforms the surface into the liquid. The situation is physically unstable, since the deformation serves to increase the net thermocapillary stress force and pressure gradient even further. The end result is an expansion of the meniscus into the liquid and
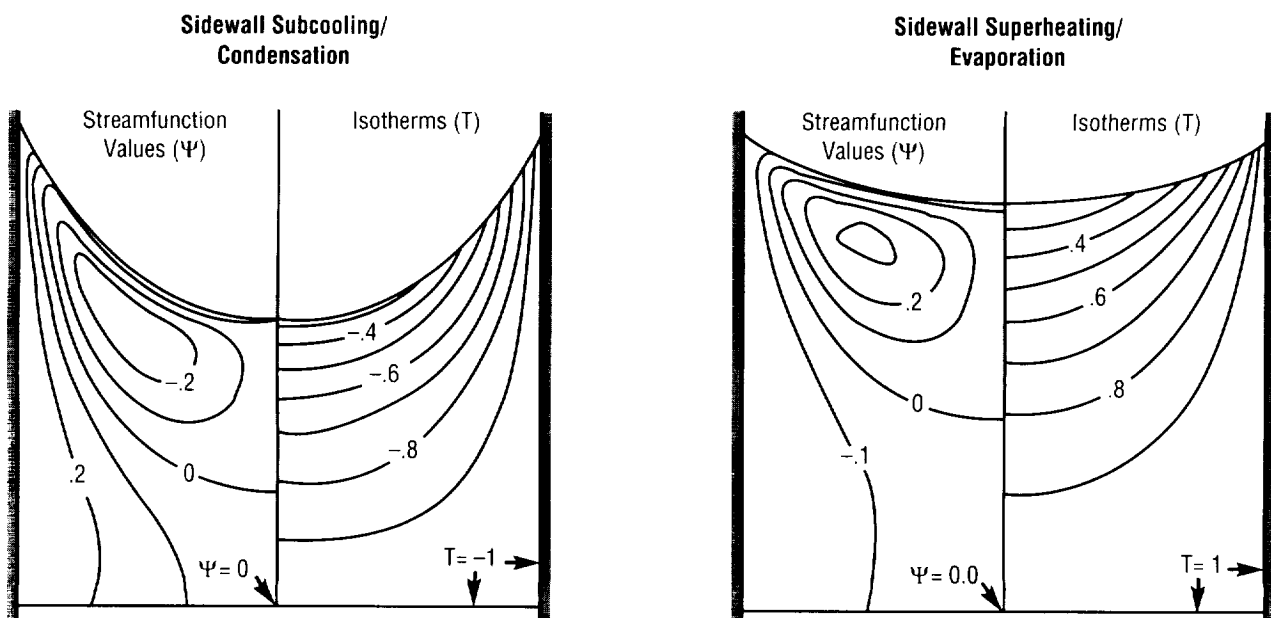
Figure 119.—Steady-state flow field, temperature, and meniscus with equivalent magnitudes of subcooling and superheating.

eventual detachment from the screen wires. Alternatively, the resistance to retention loss observed with heated helium pressurant is due to the change in direction of heat and mass transfer at the surface. As shown in the superheating/evaporation profiles of figure 119, an evaporating surface establishes a flow structure opposite to the subcooling/condensation case. Instead of depressing the meniscus, the pressure gradient tends to raise the surface in the center of the pore. This situation is inherently stable because deformation in this direction serves to reduce the thermocapillary stress force, circulation, and interfacial pressure gradient. As long as the wicking rate of the screen can accommodate evaporative losses, pressurization with heated helium promotes mechanical equilibrium and mitigates retention loss.

Sponsor: Center Director's Discretionary Fund

● ● ● ● ●

Low-Gravity Propellant Control Via Magnetic Fields

George R. Schmidt/EP25
205–544–6055

Jim J. Martin/EP25
205–544–6054

Acquisition and control of vapor-free propellant in low gravity is not as straightforward as similar operations on the ground or during vehicle acceleration. The indeterminate location of the liquid/ullage interface complicates the design of engine feed and propellant transfer systems, which depend on predictable liquid orientation and control. The traditional methods used to alleviate these problems, such as screen-channel propellant management devices (PMD's), vaned propellant management devices, and thruster settling burns, work well in some applications, but can detract from vehicle performance. (For example, propellant management devices are rather massive and bulky, and their reliability with cryogenics is questionable. Settling burns, on the other hand, complicate flight operations and require additional propellant.)

Another alternative which could minimize and possibly eliminate these mass and operational impacts is to exploit the inherent paramagnetism of liquid oxygen (lox) and diamagnetism of liquid hydrogen as a means of control. With the advent of lightweight, high-temperature superconductors and high-flux density,

rare-Earth magnets, the use of magnetic fields to control large fluid quantities in microgravity appears feasible and could enable low-gravity settling, venting, fill, and acquisition without the need for capillary retention systems or propulsive firings. Some of these potential applications are illustrated in figure 120.

The goal of this project is to evaluate the practicality of magnetic propellant control for spacecraft applications. The scope has been restricted to liquid oxygen, primarily because it offers the nearest-term application of magnetic control technology, the magnetic properties of liquid oxygen are well known, and liquid oxygen behavior has been tested before in low gravity on a laboratory scale. One of the primary objectives is to determine the range of magnetic field strengths required to perform reorientation and maintain liquid orientation during tank fill and expulsion. This range will provide a basis for evaluating whether these magnetic field requirements fall within the capabilities of current or anticipated superconducting magnet technology.

The project involves experiments aboard the KC–135 low-gravity aircraft. All experiments employ subscale hardware and a noncryogenic ferrofluid that simulates the paramagnetic behavior of liquid oxygen. The ferrofluid is a commercially available, water-based solution containing a suspension of extremely fine ferrous particles. Several properties of this fluid (i.e., particle density, viscosity, and surface tension), along with tank diameter, flow rates, and magnetic field intensities, are being scaled to model

Paramagnetic Fluid (lox)

Ullage

Ring Magnet

Liquid

Magnet

Coiled Standpipe

Diamagnetic Fluid (LH₂)

Tank-Encircling Coil

Reorientation and Explusion

Tank Fill

Long-Term In-Space Storage
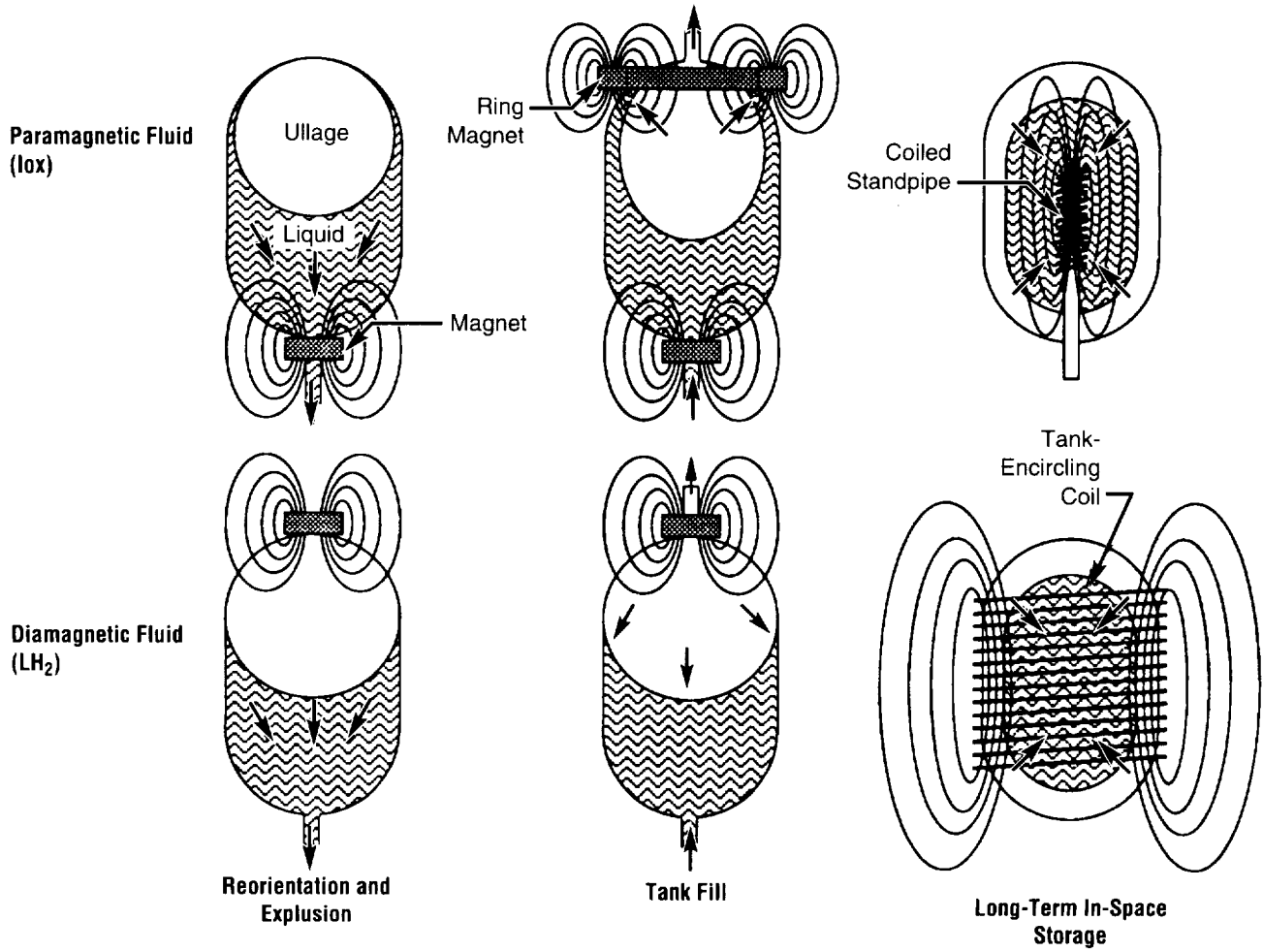
Figure 120.—Potential applications of magnetic propellant control for spacecraft.

liquid oxygen behavior in a spacecraft-type application.

Scaling analyses have shown that magnets in the size range of 1 to 10 Tesla should be adequate for propellant reorientation in a full-scale liquid oxygen application. These results, however, are rather limited since the fields can typically assume very complicated geometries, which are difficult to characterize in terms of dimensionless groupings.

Consequently, another aspect of this activity is focused on modifying an existing computational fluid dynamics (CFD) model to include the body and surface forces arising from interactions between the fluid and magnetic field. This will provide a more rigorous means of assessing fluid behavior and will enable the modeling of more complicated field geometries and advanced concepts, such as liquid hydrogen. Videotaped recordings of fluid motions taken from

the low-gravity tests will be used to validate the revised computational fluid dynamics model.

Support: Center Director's Discretionary Fund

● ● ● ● ●

STRUCTURES AND DYNAMICS

Phased-Array Mirror, Extendible Large Aperture

Henry B. Waites/ED11
205-544-1441

The Phased-Array Mirror, Extendible Large Aperture (PAMELA) prototype telescope is the first to have a fully adaptive primary mirror, which consists of 36 hexagonal, injection-molded Pyrex™ segments seven centimeters flat to flat. Segments are mounted on three long-throw, voice-coil actuators for tip, tilt, and piston

motion. Tip and tilt angles are measured with a Hartmann-Shack wave-front sensor, and piston errors between adjacent segments are measured via inductive edge sensors. Requirements are: to demonstrate closed-loop, edge-matching control to $\lambda/20$, where $\lambda = 0.6328$ micrometers (μm), using the 36 individual active mirror segments; to show that the edge control can be maintained on edges of the hexagonal segments while simultaneously controlling the tip/tilt of segments to the required precision; and to demonstrate that the instrument can produce diffraction-limited target images despite various internal and external disturbances up to 100 hertz.

The integration and testing of the Phased-Array Mirror, Extendible Large Aperture prototype telescope is underway. The primary focus of this activity consists of developing and/or performing control algorithm tests for the system. Ancillary tasks include conducting modal tests on the bench setup (fig. 121), sensor and effector calibrations, optical system alignment, open-loop testing, closed-loop testing, and dynamics verification. The telescope is now fully assembled, and modal testing is complete. In the modal test, 29 triaxial measurement points and the wave-front sensors yielded 245 modes below 200 hertz (Hz). To effect a control synthesis of
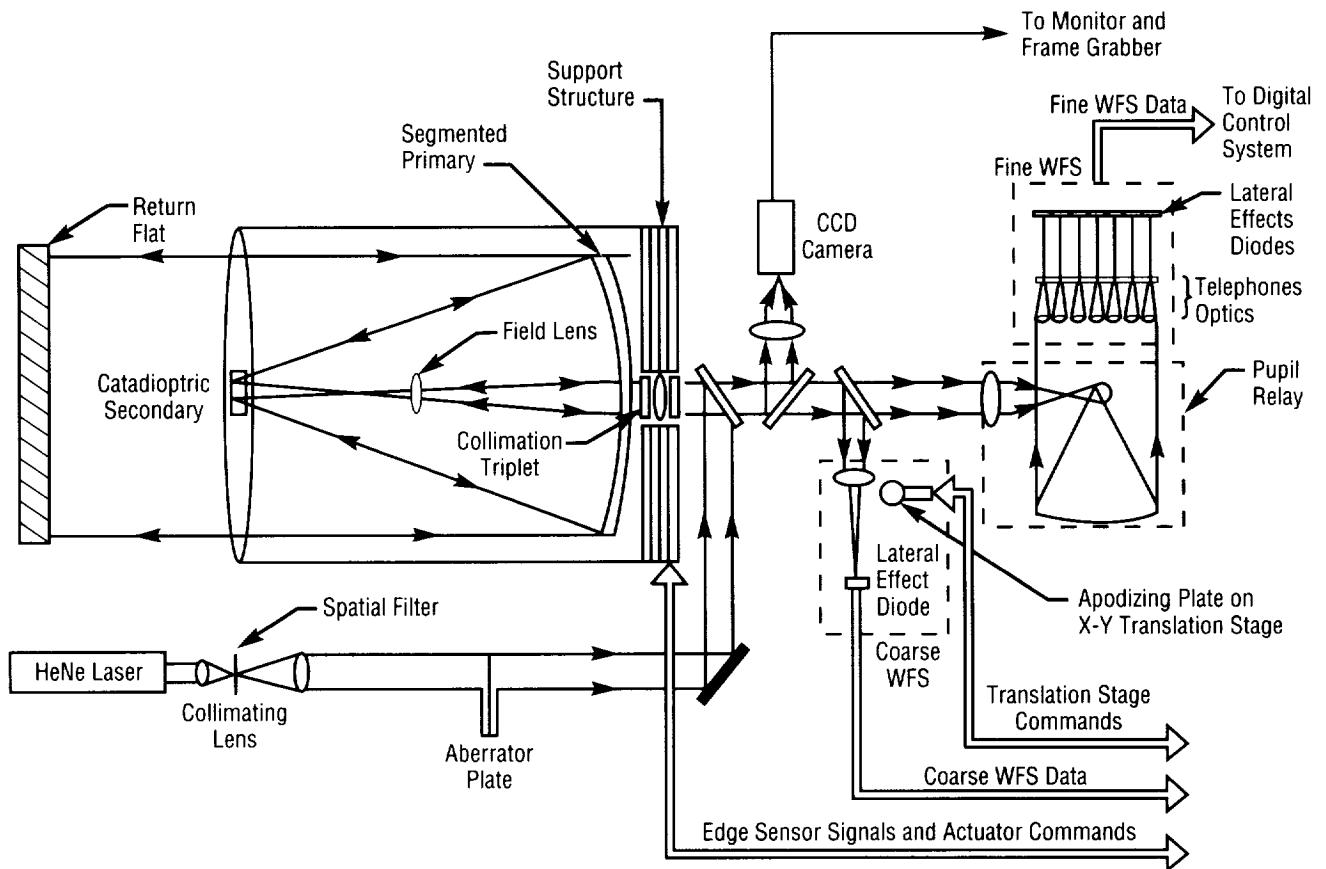
FIGURE 121.—Phased-Array Mirror, Extendible Large Aperture optical path and block diagram.

adequate bandwidth (> 100 hertz), the controller must add damping and accommodate all modes. Work is currently ongoing to evaluate control methodologies.

The overall activity is an excellent extension to MSFC's control technology in that active optics experiments are conducted at MSFC and the experience gained through these experiments can be applied to multidiscipline systems that involve controls, optics, structures, and thermal (COST) interactions. Because the project does encompass these effects, a methodology is required to assuage multidiscipline interactions. The telescope consists of 36 moveable segments—each segment having three modes—on a flexible backplane and a secondary mirror assembly on a flexible truss support, resulting in a flexible multibody problem. The control system sensor and effectors consist of 72 wave-front gradients, 108 edge sensors, and 108 effectors. The control system configuration includes 180 inputs and 108 outputs, with control bandwidths in the hundreds of hertz. A computational control problem exists—the resolution of which is another task of the control technology program.

Once the Phased-Array Mirror, Extendible Large Aperture/controls, optics, structures, and thermal interactions technology is developed and tested, the adaptive-optics primary mirror will be capable of removing monochromatic atmospheric turbulence. Presently, some modifications are required so that prototype telescopes can be used for the removal of chromatic atmospheric turbulence. Once the wave-front sensor is modified and curvature

radius adjustment is made on some of the segments, the instrument could be integrated into large astronomical telescopes' Coude paths so that either interferometric experiments could be effected or image motion compensation could remove atmospheric turbulence. Either way, the Phased-Array Mirror, Large Extendible Aperture telescope could be used to enhance the capability of large astronomical instruments.

Glecker, A.D.; Ames, G.; Markason, D.; Radau, S.; and Waites, H. March 13–18, 1994. PAMELA: Progress Report on a 0.5-Meter-Diameter Telescope With a 36-Segment Adaptive Primary Mirror, #2201–95. Society of Photo-optical Instrumentation Engineers (SPIE): Astronautical Telescopes and Instruments for the 21st Century, Kona, Hawaii.

Review of Proposed SELENE Position Algorithms. January 19, 1993. ED12–92–163.

Implementation of a Tip/Tilt and Piston Control Strategy for the Phased-Array Mirror, Extendible Large Aperture (PAMELA). April 13, 1994. ED12–94–13

Sponsor: Center Director's Discretionary Fund; Office of Advanced Concepts and Technology; commercial involvement; universities; and astronomical facilities

Industry Involvement: Science Research Laboratories

• • • • •

Flexible Structure Control Ground Test Facilities

Mark S. Whorton/ED12
205–544–1435

The Controls/Structures Interaction Ground Test Facility (CSI/GTF) (fig. 122) has been developed for experimental verification and demonstration of state-of-the-art techniques in flexible space structure control. The facility is capable of supporting research in a broad range of areas, including multiobjective controller design, system identification, and sensor/actuator failure analysis. In addition, practical implementation issues—such as real-time computer software and hardware evaluation and electronics, power, and optical measurement systems—may be addressed.

The facility employs a large, flexible space system with numerous low-frequency, coupled, tightly spaced, lightly damped modes. The test article consists of a 32-meter (105-foot) boom that supports a simulated occulting plate at the boom tip. A state-of-the-art control computer is capable of implementing a hundredth-order controller with 64 inputs and 64 outputs at a 250-hertz sample rate. The control objective of the experiment is to maintain alignment of the tip plate with an optical detector at the base of the boom, which would simulate the pointing of the occulting plate toward a star to perform an x-ray experiment. Control authority is provided by angular momentum exchange devices (AMED's) and bidirectional linear thrusters. Research
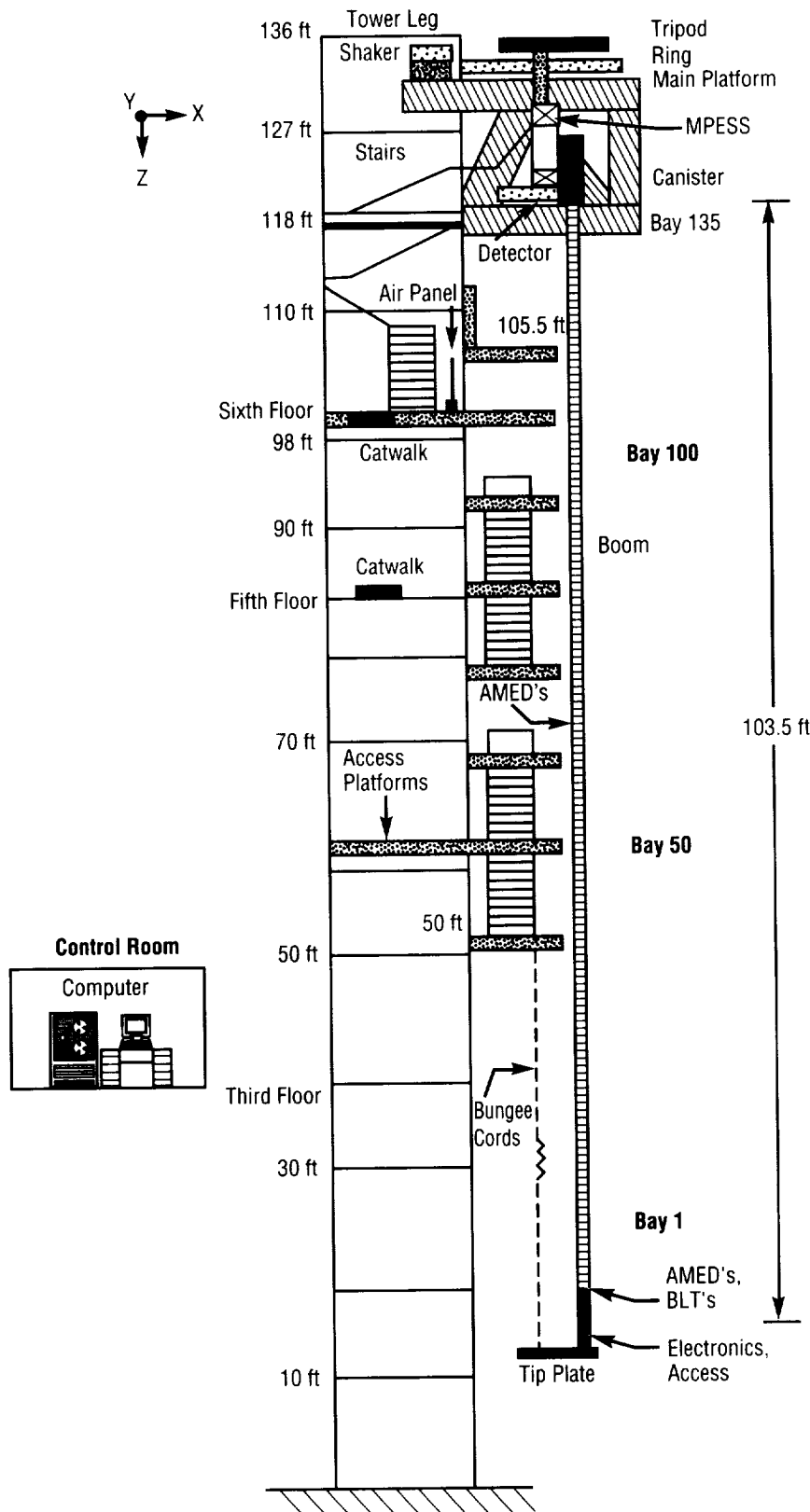
FIGURE 122.—Controls/Structures Interaction Ground Test Facility (CSI/GTF).

is currently under way using internal funding to develop state-of-the-art modern control techniques that simultaneously optimize performance and robustness and may be tuned on orbit. A cooperative research effort is also ongoing with Sandia National Laboratory to investigate system identification and control theory.

A second test facility, the Advanced Control Evaluation for Structures (ACES) Facility (fig. 123), is a variable-configuration evolutionary test site for control technology. Available equipment consists of a 30-meter flexible boom that is representative of a Cassegrain telescope on a flexible optical bench. Numerous universities and private companies have utilized the facility for technology development, including development of the control architecture used for the Hubble Space Telescope (HST) pointing control system redesign. Under funding provided by the Tennessee Space Grant Consortium, the Vanderbilt University Mechanical Engineering Department has been developing actuation hardware and control techniques for tendon control using the facility.

Sponsor: Office of Advanced Concepts and Technology

University Involvement: Vanderbilt University

1. Base Excitation Table
2. 3-Axis Base Accelerometers
3. 3-Axis Gimbal System
4. 3-Axis Base Rate Gyros and Counterweight
5. 3-Axis Tip Accelerometers
6. 3-Axis Tip Rate Gyros
7. Optical Detector
8. Mirrors
9. Laser
10. 2-Axis Pointing Gimbal System
11. LMED System
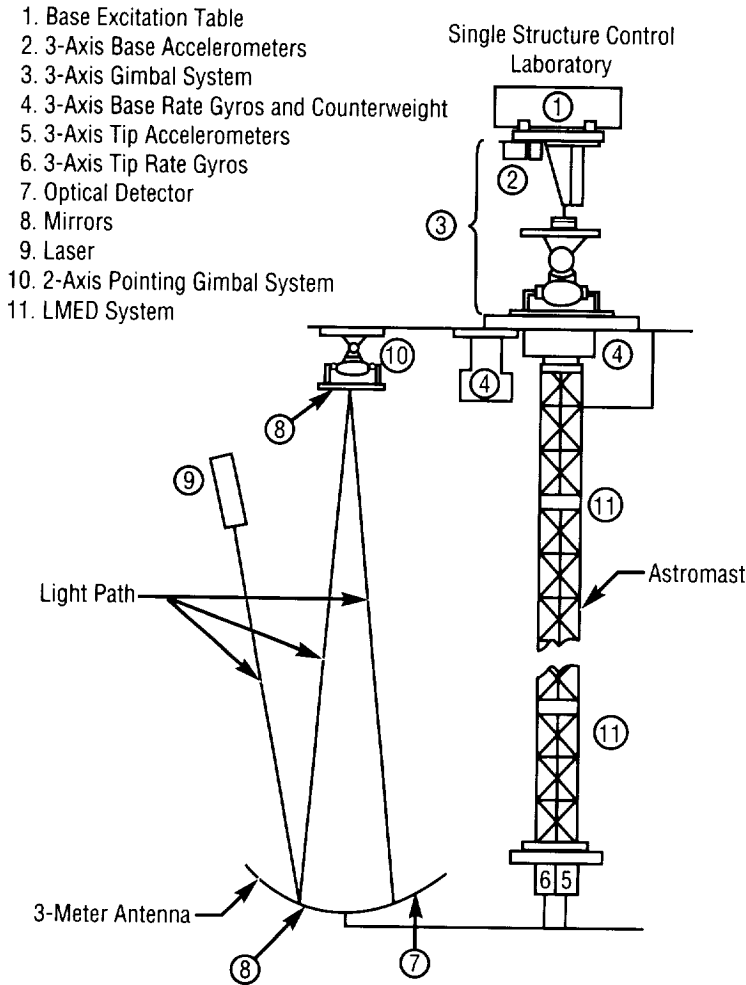
FIGURE 123.—Advanced Control Evaluation for Structures (ACES) Facility.

Automated Rendezvous and Capture

Richard W. Dabney/ED13
205-544-1473

The goal of the automated rendezvous and capture (AR&C) program is the development of a flight-ready hardware and software package readily adaptable to any spacecraft that must rendezvous, dock, or station-keep with another vehicle without the participation of a human pilot. This endeavor includes all elements of the system—sensors; guidance, navigation, and control (GN&C) algorithms; and computer hardware and software. The program heavily leverages past research technology in each of these areas with the objective of performing a technology-validating flight demonstration at minimal cost by flying the system on an existing vehicle. Near-term development, testing, and verification is being accomplished at MSFC's Flight Robotics Laboratory (FRL), which has been recently upgraded to provide full-fidelity hardware-in-the-loop simulation throughout the mission profile.

Interest in automated rendezvous and capture capabilities, first developed during the early 1980's, focused at that time on enabling the servicing of tumbling satellites and the link-up of lander and interplanetary vehicles for exploration programs. During this period, studies of docking systems based on several different means of sensing the target's relative alignment were performed, resulting in the

selection of optical imaging methods as being most mission suited and cost effective. Guidance, navigation, and control algorithms were developed to reliably dock with tumbling spacecraft at low-contact velocities. Work began on the current sensor (the video guidance sensor) and, in 1987,

resulted in the award of patents for its design and that of its target. The reference mission shifted to automated transfer of cargo to the space station by expendable launch vehicle, so the guidance, navigation, and control capabilities were expanded to include Global Positioning System- (GPS-)

guided ascent, orbit transfer, and rendezvous. Consistent docking alignment requirements of better than one degree and two centimeters were established to assure meeting projected worst-case mechanism requirements.
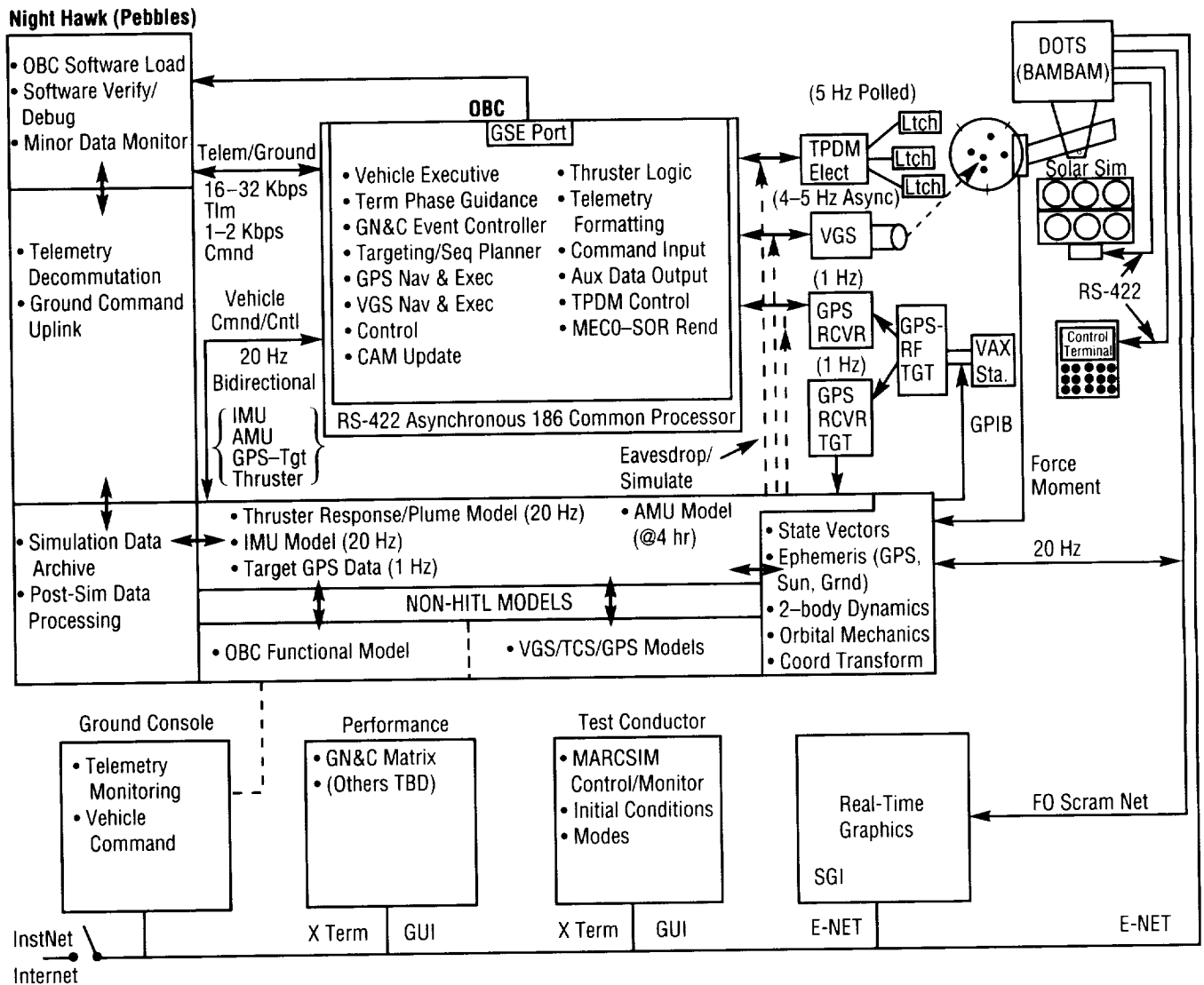
FIGURE 124.—MSFC automated rendezvous and capture simulation (MARCSIM).

The current developmental effort emphasizes integration of these products into a largely self-contained package suitable for installation on any space vehicle with minimal impact. A complete, flight-qualifiable prototype is being designed and built in-house, including the onboard computer and video guidance sensor. Software is being developed to flight standards using computer-aided software engineering (CASE) tools with autocoding and autodocumentation capabilities, designed for ease of reconfigurability and upgradability. The interfaces between the automated rendezvous and capture package and laboratory simulation facilities are shown in figure 124, which concisely depicts the functionality of the complete ground demonstration setup. The facility incorporates world-class simulation devices including a solar simulator; Earth-background simulator; full-range, 20-channel Global Positioning System radio frequency simulator; and an eight-degree-of-freedom dynamic overhead motion simulator with contact load measurement capability for testing the positioning system receivers, the video sensor, and their respective software under realistic conditions. Open-loop testing will be conducted to refine and validate the sensor and flight dynamics models, followed by closed-loop testing to verify and optimize the guidance, navigation, and control algorithms. Complete system testing will then be performed with all hardware-in-the-loop, from orbital injection to hard dock with full fidelity dynamics.

The program received funding of 800,000 dollars in FY93 and 1.2 million dollars in FY94 to upgrade all aspects of the automated rendezvous and capture package and Flight Robotic Laboratory facilities to the level needed to produce a flight-qualifiable system. Validation of the system is scheduled for completion in FY96, at which time it will be ready for an actual flight whenever an opportunity arises. The package has the potential of substantially reducing operational costs and risks associated with both manned and teleoperated rendezvous and docking operations, since pilot training is eliminated and no long-range communications links are involved. The completely deterministic nature of the system assures close adherence to a specified trajectory, increasing the accuracy with which fuel consumption can be forecast and enabling the reduction of propellant reserve requirements. If redundancy is desired, the modular nature of the system makes it possible to add multiple units whose output may be compared and voted by the host vehicle computer. Intrinsic reliability is expected to be very high, since the system is fully solid state and contains no moving parts. Being constructed almost entirely from readily available, low-cost, off-the-shelf components, it is ideal for expendable vehicles. The system is more compact, lighter weight, and uses less electrical power than all other rendezvous and capture technologies known, making it straightforward to integrate into existing vehicles' avionics systems and structural capabilities. Compatibility with vehicles equipped with the European optical target makes it attractive for use in international programs. Potential commercial, nonspace applications include automated precision helicopter landings, guidance of ships and heavy trucks approaching loading docks, and control of mobile robots in factory and medical environments.

The automated rendezvous and capture program is very close to achieving its goal of a dependable, versatile, and affordable system with virtually unlimited applications. In the next two years, ground and potentially flight testing will result in the system being fully validated and ready for use.

Sponsor: Office of Space Flight

• • • • •

System for Anomaly and Failure Detection

Thomas H. Fox/ED14
205-544-1462

Since ground testing of the space shuttle main engine (SSME) began in 1975 there have been 28 major incidents. These failures—most of which were during the early phases of testing when significant design changes were still taking place— occurred despite an extensive internal system of self-checking and measurement redlines. This number almost seems insignificant when compared to the more than 1,500 other tests without major incidents. However, these failures have costs— engine damage, stand damage, analysis costs, engine component loss, loss of failure evidence, and schedule impacts—associated with them that belie their small numbers.

A program was initiated in 1985 to catalogue all of the space shuttle main engine failures and determine which engine measurements or suites of measurements would indicate an incipient engine failure. A thorough analysis revealed that most failures could have been detected earlier even with the present engine sensors. The study also defined a small list of generic failure types and determined the necessary instrument suite to provide engine observability for the detection of these failures (table 12).

An effort was initiated to develop an algorithm for the detection of incipient engine failure during the steady-state engine operation based on the results

TABLE 12.—*System for Anomaly and Failure Detection parameter suite*

1. High-Pressure Fuel Turbopump (HPFTP) Radial Accel
2. HPFTP Balance Cavity Press
3. High-Pressure Oxidizer Turbopump (HPOTP) Discharge Press
4. HPOTP Intermediate Seal Purge Press
5. HPOTP Secondary Seal Drain Press
6. HPOTP Boost Pump Discharge Press
7. HPOTP Boost Pump Radial Accel
8. HPOTP Boost Pump Bearing Coolant Discharge Temp
9. Main Combustion Chamber (MCC) Press
10. MMC Coolant Discharge Press
11. HPFTP Shaft Speed
12. HPFTP Turbine Discharge Temp (CH A)
13. HPFTP Turbine Discharge Temp (CH B)
14. HPOTP Turbine Discharge Temp (CH A)
15. HPOTP Turbine Discharge Temp (CH B)
16. Low-Pressure Fuel Turbopump (LPFTP) Shaft Speed
17. Low-Pressure Oxidizer Turbopump (LPOTP) Pump Discharge Press
18. HPFTP Discharge Press
19. HPFTP Coolant Liner Press
20. Heat Exchanger (Hex) Bypass Mix (Interface) Temp
21. Hex Venturi Delta Press
22. Oxidizer Preburner Oxidizer Valve (OPOV) Actuator Position
23. Fuel Preburner Oxidizer Valve (FPOV) Actuator Position
24. Fuel Flow Rate

of the earlier study. During its development, the algorithm was tested using data from a mixture of hot-fire tests (ranging from "good tests" to those that contained failures and anomalies) and simulations using the digital transient model (DTM) program for failure modes for which no hot-fire data could be found. The system has also successfully monitored more than 20 hot-fire tests on the Technology Test-Bed (TTB) stand.

In all cases where failure has occurred, the System for Anomaly and Failure Detection (SAFD) algorithm has shown an improvement over redline methodology by issuing significantly earlier shutdown commands (table 13). In part, due to the instrumentation-selection process, all past engine failures would have been detected

earlier, barring the few catastrophic failures that failed in a matter of milliseconds. The algorithm has also demonstrated that no inadvertent shutdown commands would have been issued.

Work on the steady-state algorithm has been put on hold in favor of testing a new version of the System for Anomaly and Failure Detection algorithm. This new algorithm has been expanded to cover the transient and nonlinear portions of engine operation as well as the steady-state operation. It has also erased concerns about the large amount of critical input data that was necessary with the previous steady-state version. It also has the capability to disqualify some bad sensors, thereby making it more robust.

TABLE 13.—*Space shuttle main engine simulated actual and hypothetical failures—Technology Test-Bed tests*

TTB Tests

No.	Test No.	Cut SAFD	Request RESID	Comments
1	TTB–26	No	–	First monitored test
2	TTB–27	No	–	Full duration test
3	TTB–28	Yes	–	Lack of compensation for mixture ratio (MR) shift
4	TTB–29	No	–	Full duration test
5	TTB–30	No	–	Redline cut made at 5.3 sec. (good test)
6	TTB–31	No	No	Full duration. RESID start alg. added
7	TTB–32	No	No	Full duration. RESID mainstage alg. added
8	TTB–33	No	No	Full duration. Hydrostatic bearing test
9	TTB–34	No	No	Full duration. Hydrostatic bearing test
10	TTB–35	No	No	Full duration. Hydrostatic bearing test
11	TTB–36	No	Yes	Pratt and Whitney (P&W) HPFTP
12	TTB–37	No	Yes	P&W HPFTP
13	TTB–38	No	Yes	P&W HPFTP
14	TTB–39	Yes	No	Large throat MCC. First instance check error Parameter sigma bandwidth adjusted too narrow
15	TTB–40	Yes	No	Large throat MCC. First instance check error Parameter sigma bandwidth adjusted too narrow
16	TTB–41	No	–	Large throat MCC, P&W HPOTP RESID removed
17	TTB–42	No	–	Large throat MCC, P&W HPOTP & HPFTP
18	TTB–43	No	–	Large throat MCC, P&W HPOTP & HPFTP
19	TTB–44	No	–	Large throat MCC, P&W HPOTP & HPFTP
20	TTB–45	Yes	–	Large throat MCC, RKDN pumps, input data typo and bad 1st instance check on two other values
21	TTB–46	Yes	–	Large throat MCC, RKDN pumps. Stand had power profile error for throttle shift (1 sec early)
22	TTB–47	Yes	–	Large throat MCC, facility measurements drift
23	TTB–48	No	–	Large throat MCC, RKDN HPOP & HPFP
24	TTB–49	No	–	Large throat MCC, RKDN HPOP & HPFP

HST Tests

No.	Test No.	R/L	SAFD	Comments
1	901–173	201.17	201	Main injector, also run at Canoga Park
2	901–558	–	–	United Technology Research Center (UTRC) algorithms only, full duration
3	901–577	–	–	UTRC algorithms only, high-pressure oxidizer turbine discharge temperature redline
4	902–249	450.57	350.32	HPFTP, also run at Canoga Park
5	902–461	–	–	Run to develop a statistical base
6	902–462	–	–	Run to develop a statistical base
7	902–463	–	–	Run to develop a statistical base
8	903–149	109.86	109.78	Facility accel redline on HPOTP

TABLE 13.—*Space shuttle main engine simulated actual and hypothetical failures—Technology Test-Bed tests (continued)*

Canoga Park Tests

No.	Test No.	R/L	SAFD	Comments
1	750–175	116.06	116.06	High-pressure oxidizer duct
2	750–285	223.50	212.48	Feed-line
3	901–173	201.17	201.02	Main injector, also run at Canoga Park
4	901–183	51.	50.35	Main injector
5	901–225	255.63	255.61	Main oxidizer valve
6	901–284	9.88	7.14	Controller
7	901–340	405.50	295.42	HPFTP
8	901–364	392.16	386.	HPFTP, venting/repressurization
9	901–511	–	–	Nominal
10	901–551	–	–	Nominal
11	901–558	–	–	Run for UTRC algorithms only, full duration
12	901–577	–	–	Run for UTRC algorithms only, high-pressure oxidizer turbine total discharge temp redline
13	901–683	–	–	Nominal
14	902–249	450.57	350.32	HPFTP, venting/repressurization, Canoga Park, HSL
15	902–398	–	–	Nominal
16	902–428	204.12	190.	Oxidizer preburner injector, venting/repressurization
17	902–461	–	–	Run to develop a statistical base
18	902–462	–	–	Run to develop a statistical base
19	902–471	147.68	146.76	Duct, flex joint
20	902–463	–	–	Run to develop a statistical base
21	902–519	–	–	Nominal
22	902–532	–	–	Nominal
23	903–149	109.86	109.78	Facility accel redline on HPOTP
24	DTM	–	–	Hypothetical preburner pump Discharge Duct
25	DTM	–	–	Discharge Flow Block

NOTE: A simulation of engine 0215 in test 901–666 showed that a shutdown command issued only 0.38 seconds earlier than the redline shutdown would have avoided significant engine damage.

The System for Anomaly and Failure Detection has been installed on two identical computer systems, one in the Huntsville Simulation Laboratory (HSL) and the other on the Technology Test-Bed (TTB). The system at the test-bed has successfully monitored a variety of engines tests, including a complete Rocketdyne engine, a wide-throat engine, and a wide-throat engine with a mix of Rocketdyne and Pratt & Whitney high-pressure pumps. The Technology Test-Bed system is expected to be moved to Stennis Space Center in 1995. This move will increase the number of hot-fire tests that the system has available for monitoring.

Recent developments have allowed the new algorithm to be tested in the Huntsville Simulation Laboratory against hot-fire data for 33 major failure cases for which no fixes have been identified. This testing has also included 120 other cases that are more or less nominal. Before its release to Stennis, the number of hot-fire tests is expected to exceed 250. Preliminary results indicate that the new algorithm is performing satisfactorily, needing only some minor adjustments.

Sponsor: Office of Advanced Concepts and Technology

• • • • •

Nonintrusive Damping for Integrally Bladed Turbine Disks

Katherine K. Mims/ED22
205-544-1506

Cost studies have shown the potential for significant savings, particularly in production phases, if components can be fabricated integrally (e.g., single-piece castings). However, structural response of these single-piece structures to high-vibration environments must be considered. While vibration due to sinusoidal excitation can be accounted for to a limited degree through careful design practices, random vibration response of the structure to mechanical operation is not readily anticipated, particularly for extended (reusable), high-cycle fatigue requirements. This article describes one such single-piece component, the integrally bladed turbine disk (blisk), now under consideration for next-generation or future liquid rocket engine turbines, and addresses damping of its structural response under operating dynamic loads through acquisition of an empirical data base for damping concepts which would provide maximum benefit to the single-piece cast blisk.

The integrally bladed turbine is the design of choice when optimized turbine efficiency is desired. However, the unshrouded metallic blisk provides little or no damping with the blades integral with the disk, and the blades are preferred unshrouded because it is difficult and more costly to achieve the quality required in the blading region if a shroud is included as part

of the finishing process during fabrication. Without damping, there is an impact on high-cycle fatigue (HCF) life and the blisk can become a life-limiting component. Thus, alternate techniques of providing damping to an unshrouded blisk are required to extend high-cycle fatigue life. Passive or nonintrusive damping is best suited for blisks to maintain turbine efficiency and will improve high-cycle fatigue life of the turbine blisk. It is a goal of this task to empirically demonstrate the level of nonintrusive damping for the integrally bladed turbine similar to that exhibited by current inserted-blade rocket engine turbine systems.

MSFC is in the process of examining the effects of various types of dampers to random vibration excitation by placing the dampers into cavities

within the bladed regions of a blisk and characterizing response under selected input-forcing functions during spin tests. Initial damper concepts include viscoelastic materials, internal mechanical friction dampers, and particle damping. During the initial phase of the program, limited subscale testing was performed for several internal damping concepts; using finite element methods (FEM), a mathematical representation of a fuel pump space transportation main engine (STME) blisk was analyzed to characterize blisk modes. In addition, data were examined for several rocket engines in an attempt to qualitatively assess random vibration effect. In phase II, it is intended to characterize damping of various damping concepts through spin tests of strain-gaged full-scale blisks in which the damping treatment has been implemented. The
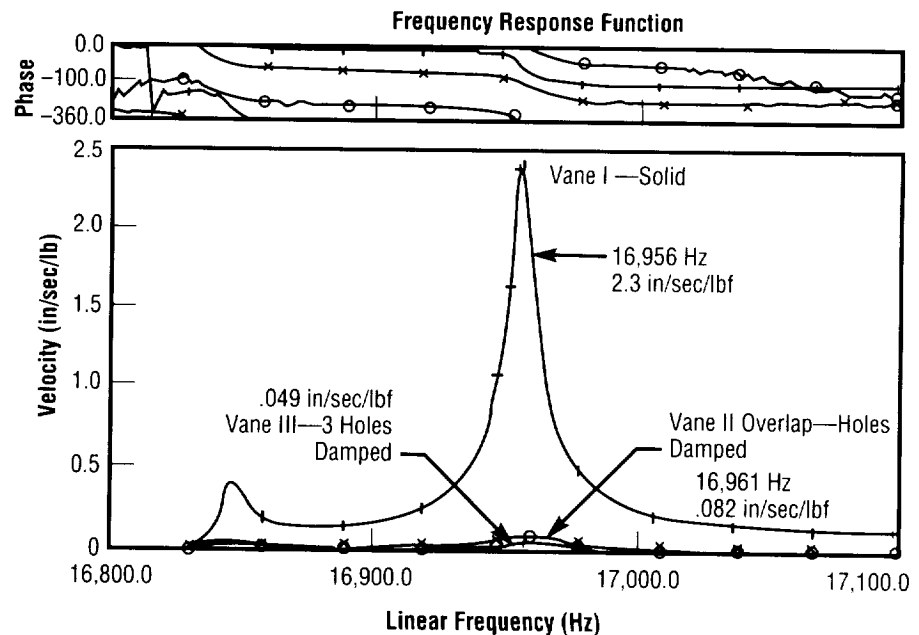
Figure 125.—Response amplitude comparisons of blade-tip velocity under damped and undamped conditions.

acquired data base would then be available for design optimization of future turbopump designs.

Selected damper concepts were used in subscale turbine blade tests. Results indicate a general improvement over values for current configurations that require external dampers. Figure 125 is an example of the reduction in amplitude exhibited by single blades, solid versus damped. Damped blade data were obtained using particle damping inserted into the airfoil region of the subscale blade for the two-hole cavity and overlapped three-hole cavity configurations under sinusoidal excitation. Similar results were obtained for other concepts. Frequency dependence on concept parameters remain to be determined.

Examination of the liquid rocket engine turbine data indicates that blade modes are typically much higher in frequency than for the inserted-blade design, usually above 10 kilohertz (KHz)—while, for the latter, blade modes are in the 4- to 8-kilohertz range. All inserted blade designs in successful operation use external dampers. Only one data point of experience exists for a current, operational, unshrouded, and undamped rocket engine blisk; it is for an expendable configuration and has been shown to develop cracks under extended limit life testing.

The following were observed from the structural dynamics normal modes analysis using the blisk finite element method model. Blisk system modes possess high modal density and appear to vary with diametral number (fig. 126). There is a significant interaction between the disk and blades. Displacement plots of the

modes suggest that as frequency increases and as internal energy is exchanged between the system and blades in alternating fashion, characteristic modes will vary with diametral number rather than remain true to the original harmonic number. Complexity of the disk-blade interaction emphasizes the need for

careful turbine design and consideration of engine operation parameters.

Results from the initial phase of this program indicate an improvement can be achieved. The next phase is to test a full-scale blisk with the implemented damping concept. Fabrication of a
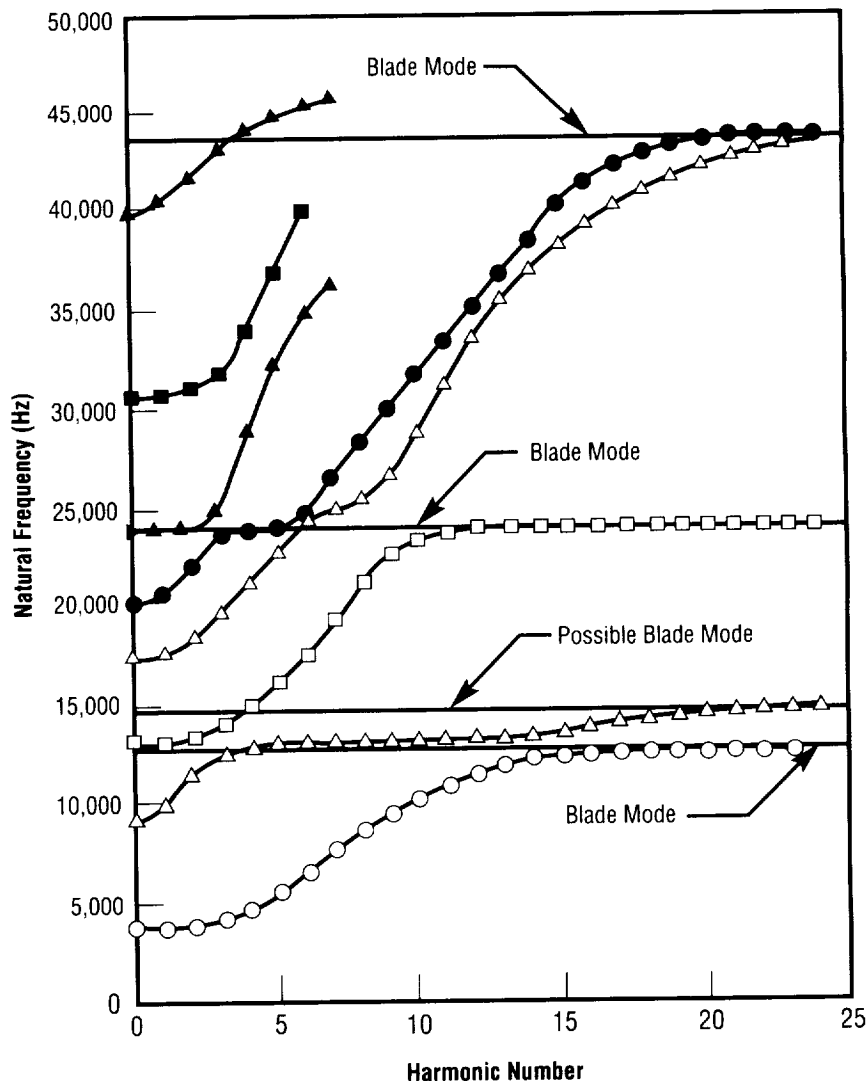
Figure 126.—Advanced blisk natural frequencies.

blisk model is complete. The current immediate goal is to obtain a data base of empirically obtained damping values for use in future turbopump designs. Use of these data could be extended to the industrial sector wherever severe turbomachinery (space or nonspace) vibration environments are experienced. Other alternative concepts include possible use of constrained layers or composites for damping. MSFC is continuing, as part of its proactive initiative, to examine mechanisms for improved damping for the upcoming designs that promote use of single-piece castings or composites.

Greenhill, L./Aerojet Propulsion Systems; Shi, J./Rocketdyne, Canoga Park, California; Moore, D./ Pratt & Whitney Government Systems; Kiefling, L. and Mims, K./ NASA-MSFC. April 1993. STME Structural dynamics Working Group—Tabulated Turbine Dynamic Parameter for Liquid Rocket Engines, ED22-93-22.

McDonough, C.F. 1992–93. Advanced Integrally Bladed Disk (Blisk) Damping Technology. 1992–93 Final Report, Pratt & Whitney.

Panossian, H.V.; Kwok, L.C.; and Davis, G.A. 1994. Blade-to-Blade Interactions and Vibration Damping in a Simulated Integrally Bladed Turbine Disk. 1994 Conference, Advanced Earth-to-Orbit Propulsion Technology, Huntsville, Alabama.

• • • • •

Phase-Synchronized Enhancement Method for Machinery Diagnostics

Tony R. Fiorucci/ED23
205-544-1551

A new diagnostic signal analysis technique, the phase-synchronized enhancement method (PSEM) has been developed for space shuttle main engine (SSME) diagnostics at MSFC's Structures and Dynamics Laboratory. Previous diagnostic studies using generalized hyper-coherence (GHC) have demonstrated that the frequency of the main engine turbomachinery shaft rotational component (synchronous) fluctuates around a center frequency during steady-state operation, while its power spectral density (PSD) exhibits a discrete peak indicative of a constant frequency. This micro-frequency variation phenomenon broadens other synchronous-related components and smears the spectral information within the power spectral density. The basic principle of the phase-synchronized enhancement method is to force the frequency of the quasi-periodic synchronous response into a constant frequency (a pure-tone periodic component). This generates a highly desirable enhancement effect over the entire signal, whereby all other synchronous-related components (synchronous harmonics, ball-bearing ball train, ball spin, outer-race ball pass, and inner-race ball pass) automatically become discrete. The resulting discrete signal provides better power spectral density resolution, improving overall engine diagnostic evaluation.

Under NASA's Technology Transfer program, data from a Seagate computer disc drive spindle motor test have been used to demonstrate the phased-synchronized enhancement technique. During steady-state operation of the spindle motor, the synchronous frequency of the motor appears very constant. Generalized hyper-coherence analysis, however, indicates that the synchronous frequency component is moving slightly around its center frequency. This micro-frequency variation phenomenon smears the detailed spectral information in the high-frequency region (fig. 127a). By utilizing the phased-synchronous algorithm, the synchronous frequency of the spindle motor is forced into a constant frequency from the micro-frequency variation, and the desired enhancement effect is generated on the entire signal (fig. 127b). The signal frequency resolution becomes much sharper as all synchronous-related components are enhanced (such as 16, 18, 20, and 22 times the ball-spin frequency component, as well as many other components that are synchronous-related). These important signatures are totally obscured in the original power spectral density.

Machinery failure detection has always been a significant technical challenge in MSFC's propulsion technology development. A reliable health-monitoring system can prevent catastrophic failures and costly downtime due to false alarms. The phased-synchronized method could prove invaluable in the areas of engine health monitoring and diagnostics.

Especially useful for machinery diagnostics, the phased-synchronized enhancement method technique has
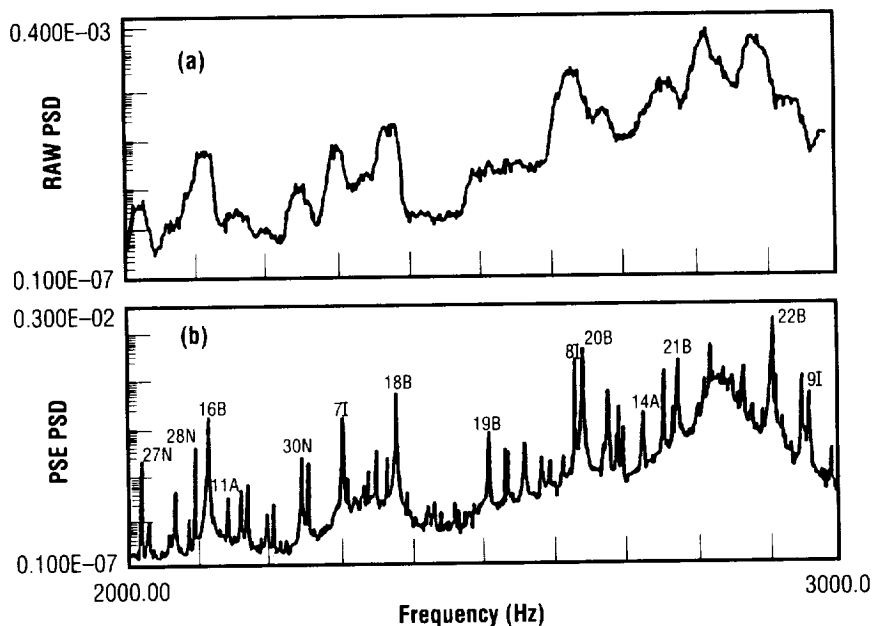
FIGURE 127.—Power spectral density of (a) raw signal and (b) phase-synchronized enhancement method signal from 2,000 to 3,000 hertz.

considerable commercial applications potential outside the space shuttle main engine arena, as demonstrated with the Seagate spindle motor test data. This method can greatly increase spectral density resolution when performing quality control on the production line, as well as enhance system reliability and reduce system monitoring manpower requirements.

Jong, J.; Jones, J.; McBride, J.; Jones, P.; Fiorucci, T.; Zoladz, T.; and Nesman, T. 1994. Phase-Synchronized Enhancement Method for Space Shuttle Main Engine Diagnostics. NASA Conference on Advanced Earth-to-Orbit Propulsion Technology.

Sponsor: Office of Space Flight

Development of Improved Cryogenic Tanks for Upper Stages

Rafiq Ahmed/ED24
205-544-2217

In view of the increasing competition the United States faces in the worldwide commercial space arena, the need to improve and redesign the current fleet of launch vehicles (some of which are based on 30-year-old designs) has become more and more apparent. One component of these vehicles receiving particular attention is the upper stage. Any weight reduction in the upper stage results in an almost corresponding increase in payload, so the payoff for improvement is particularly advantageous. To help accomplish the goal of optimizing payload-carrying stages, MSFC and General Dynamics Space Systems Division (now Martin Marietta, Huntsville) have teamed up in a joint industrial research and development (IRAD) program, the Cryogenic Tank Technology Program (CTTP).

The program's primary objective is to design a "flight-like" liquid hydrogen tank using advanced materials (e.g., aluminum-lithium), construction methods (e.g., low-profile domes; near-net forged and extruded stiffeners/panels; and advanced welding techniques), and analysis (e.g., design optimization programs and finite element analysis). (A flight-like article is one that is designed to flight loads, and is therefore representative of one that would be flown, but has not yet been designed

to fit a particular launch vehicle.) Optimization began with the baseline Atlas Centaur upper stage built by General Dynamics (now Martin Marietta).

The program initially began with the test of a low-profile, spin-formed, ring-stiffened, 2219 subscale aluminum dome. This accomplished three main goals: feasibility demonstration of using low-profile domes; verification of advanced analytical tools; and demonstration of advanced, nondestructive evaluation (NDE) techniques (such as laser shearography, digital image correlation, and acoustic emission). The test has been very successful, and accurate predictions have been made of the circumferential buckling expected with low-profile domes, as well as with the ultimate failure load.

Currently, a low-profile, subscale, aluminum-lithium dome test is being planned as the next logical step for the effort. Afterward, the full-scale, flight-like test article (a 14-foot-diameter tank with low-profile domes) will be constructed—using advanced manufacturing techniques—and tested under various loading conditions indicative of a flight environment. The data from this activity can then be used by the industry in the design of future upper-stage vehicles.

Sponsor: Research and Technology Office

Industry Involvement: Martin Marietta

• • • • •

Development of State-of-the-Art Proof Test Methodology

Charles L. Denniston/ED25
205-544-7248

The current NASA document that serves as the proof test guideline is *Fracture Control of Metallic Pressure Vessels* (NASA SP–8040), written late in the 1960's and considered state-of-the-art for that era. A document currently used to supplement SP–8040 is a U.S. Air Force standard, MIL–STD–1522A, most recently updated in 1984. Whereas 1522A reflects a more current fracture mechanics technology than 8040, it still has two shortcomings as a guidelines document. First of all, 1522A is based on technology that is more than 10 years old and, as such, predates many of the developments now incorporated into current nonlinear fracture mechanics methodology. Furthermore, 1522A is a requirements document, and thereby offers little guidance to its reader as to how to implement the requirements it defines. Neither document supplies an engineer with guidance reflecting the current state-of-the-art in fracture mechanics practice.

One of the expected outcomes from the Proof Test Philosophy to State-of-the-Art contract is a guidelines document describing how an engineer can deal with two types of fracture mechanics problems not dealt with in SP–8040 or 1522A—predicting crack growth not related to traditional fatigue mechanisms and predicting crack behavior in the elastic-plastic

regime. Both of these topics are very important issues to be considered when designing a proof test.

One of the purposes for conducting a proof test is to screen out unacceptably large cracks by inducing them to fail as a result of a proof loading. To bring about this failure in a ductile material, the crack is usually grown by both fatigue and tearing mechanisms, under the influence of an elastic-plastic loading condition. If the engineer does not consider these factors when estimating the required proof load, the proof test may not screen out all the pertinent cracks.

The most common approach to predicting crack growth utilizes the da/dN curve. This curve is a plot of total crack growth per unit cycle versus the loading amplitude and can be divided into three parts: the threshold region, the Paris region, and a high-growth-rate region. The Paris region of the da/dN curve has a linear relationship on a log-log plot of da/dN versus loading amplitude that can be taken to indicate crack growth due to pure fatigue loading. Once the high growth rate is entered, however, the da/dN curve starts curving sharply upward, indicating there is now some mechanism besides pure fatigue contributing to crack growth. This new mechanism is crack tearing. The high-growth-rate region of the da/dN curve can, to a limited extent, be used to predict total crack propagation under extreme loading. However, a better approach has come to the forefront over the past 10 years.

Resistance curves (or R-curves), such as the one shown in figure 128, plot the strain energy release rate against the change in crack length due to
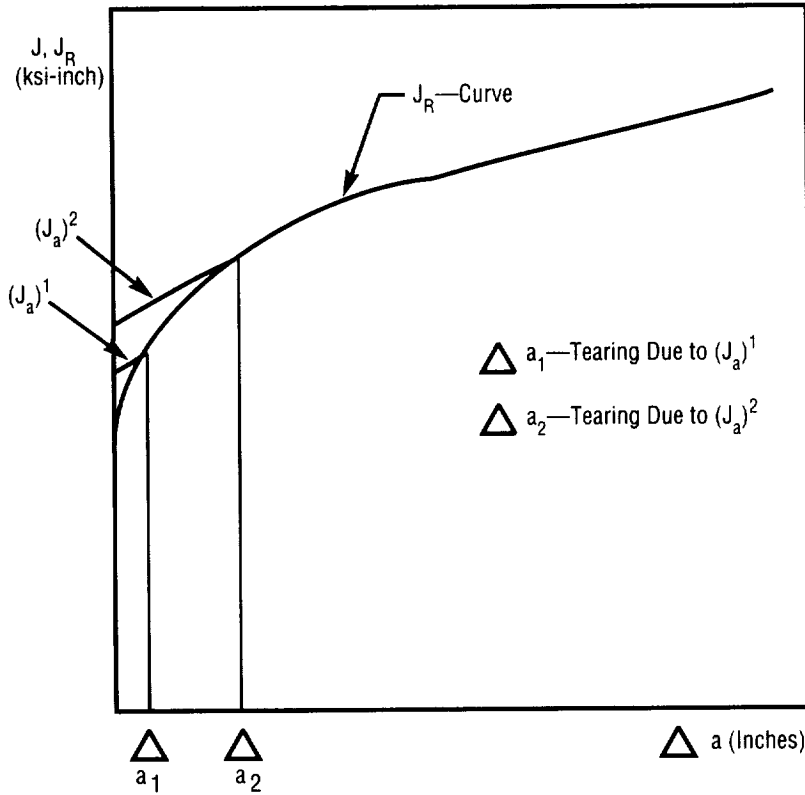
FIGURE 128.—Sample resistance curves.

mechanics analysis necessary for designing proof tests. Often times, not only is the loading at the crack tip important, but so too is the state of stress in the component containing the crack. When the crack-tip loading and the component stress influence each other, then an elastic-plastic fracture condition can be said to exist. One way to deal with this loading condition is to use a failure assessment diagram (FAD) as shown in figure 129. The K_r and L_r terms are defined below:

(3)

$$K_r = \left(\frac{J_{app}}{J_C} \right)^{\frac{1}{2}}$$

(4)

$$L_r = \frac{P_{app}}{P_0^*}$$

where:

J_{app} = J–Integral due to applied load
J_C = Critical "J" value
P_{app} = Applied loading
P_0^* = Optimum yield load.

tearing. No crack growth due to fatigue mechanisms is represented in this figure. For a loading of the crack (sufficient to induce tearing), a $(J_a)^1$ curve can be plotted, as shown in figure 128, and the intersection with the J_R resistance curve (or J_R curve) determined. The load responsible for $(J_a)^1$ (applied remotely) can then be removed and then reapplied. The resulting loading curve for the reapplied remote load is represented in figure 128 as the $(J_a)^2$ curve. As also illustrated in figure 128, it is predicted that some additional crack tearing will occur as a result of $(J_a)^2$. When one continues the aforementioned process, failure due to tearing is predicted to

occur when the following two criteria are met:

(1)

$$J_a \geq J_R, \text{ and}$$

(2)

$$\frac{dJ_a}{d(\Delta a)} \geq \frac{dJ_R}{d(\Delta a)}$$

It should be noted that where the failure criteria given in equation 1 can be anticipated from a da/dN curve, the failure criteria implied by equation 2 cannot be so easily deduced.

There is another complicating factor that occurs with the type of fracture

Failure is determined using a failure diagram simply by calculating K_r and L_r, plotting their location on a figure (like that shown in fig. 129) and seeing if the point (called an assessment point) is inside or outside the enclosed region. If the assessment point falls outside the enclosed area, failure is predicted to occur. The failure assessment diagram is projected to be the primary approach recommended for use in the guideline to be developed for the proof test philosophy contract. The reason for this decision is based on three factors: the need to have an elastic-plastic capability in the guideline, the failure
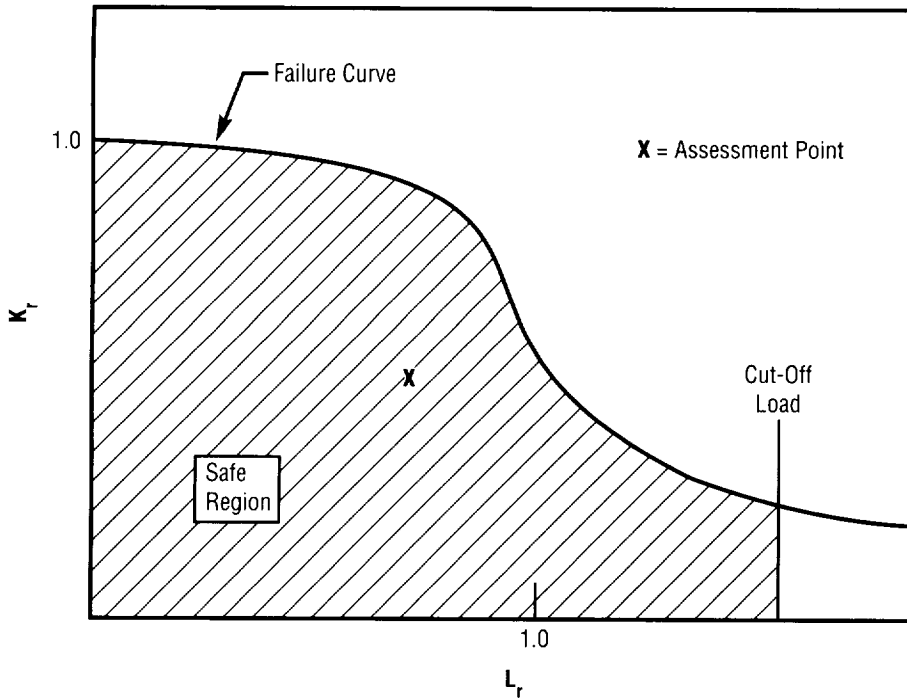
FIGURE 129.—Failure assessment diagram.

assessment diagram's ease of use, and the versatility of the approach.

There is an effort being initiated on the contract to verify the accuracy of the failure assessment approach for a couple of materials typically used with the space shuttle main engine. The results of this verification will form the initial basis for placing bounds on the applicability of the failure assessment diagram.

The development of an updated proof test methodology should bring a greatly enhanced proof testing design capability to NASA. However, the development of such a document should have implications beyond proof testing. Such analytical tools as R-curves and failure assessment diagrams can also be applied to

hardware analysis, where high loads and/or large cracks are of concern.

Sponsor: Office of Advanced Concepts and Technology

• • • • •

Verification of Analytical Methods—Single-Cycle Versus Multiple-Cycle Proof Testing

Henry M. Lee/ED25
205–544–7245

The overall objective of this effort is to assess the relative advantages and disadvantages of single-cycle versus multiple-cycle proof testing.

A computer program has been developed for the probabilistic analysis of the multicycle proof test (MCPT) problem. The program involves an integration of NESSUS™ and MCPT tear-fatigue software. The code will use advanced probabilistic methods in addition to Monte Carlo simulations to compute the distribution of final crack sizes after proof testing. The benefits of the advanced methods are that a typical probability solution can be obtained in much less time, and probabilistic sensitivity factors can be computed as a by-product. The distribution of crack size after proof testing can be calculated using the conditional probability equation:

$$P(B/A) = P(A \cap B) / P(A)$$

where $P(B)$ is the probability of having a crack less than or equal to a given size, and $P(A)$ is the probability of not failing after a given number of cycles.

This problem can be solved analytically for the single random variable problem under consideration and used to verify the correctness of the computer code. The probability of not failing after proof cycles (N_j) and

the probability of having a final crack size (a_f) can be mapped in terms of the crack-size random variable and then solved analytically.

Some success has been obtained using the advanced multicycle proof test application. The NESSUS/MCPT code will be enhanced to automate some calculations, such as the final crack size distribution as a function of a user-defined number of proof cycles. This enhancement will provide a convenient method to explore various proof-testing scenarios, including the effects of different material properties or initial crack-size distributions.

Sponsor: Office of Advanced Concepts and Technology

Verification and Validation of Quarter Elliptical Solutions in NASCRAC

Roderick Stallworth/ED25
205-544-7189

NASCRAC—a state-of-the-art computer code for performing fracture mechanics analysis—is currently going through the final stages of a comprehensive verification and validation effort. The quarter-elliptical crack configuration code results have been compared against various literature, the finite element code, NASA/FLAGRO code, and other tests results. Because NASCRAC may be employed as an integral part of MSFC's total fracture control program, an assessment of the code's accuracy and limits of its applicability must be established. Quarter-elliptical configurations are frequently used by analysts to predict the safe-life of space-flight hardware. The three quarter elliptical shapes are: corner-crack-in-a-hole-in-a-plate, corner-crack-from-a-hole-in-a-lug, and quarter-elliptical-crack-in-a-plate.

Both the corner-crack-in-a-hole and corner-crack-from-a-hole-in-a-lug models have been derived from the NASA/FLAGRO fracture mechanics code. Neither of the models incorporates a weight function; therefore, only simple loads, uniform tension, and/or pin-load cases could be analyzed. The NASCRAC results for
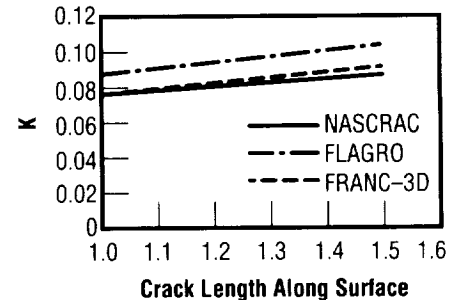
FIGURE 130.—Pin load ($a/c = 0.5$, $r = 4$).
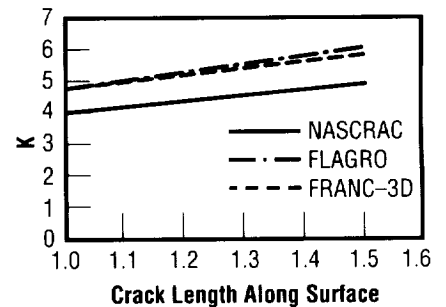
FIGURE 131.—Uniform tension ($a/c = 0.5$, $r = 4$).

the corner-crack-from-a-hole-in-a-plate were compared with the NASA/FLAGRO and FRANC–3D results (figs. 130 and 131). As figure 131 indicates, NASCRAC does not agree with FLAGRO or FRANC–3D when the applied load consists of a uniform stress. When the load is a pin load and the hole diameter is large compared to the crack length, NASCRAC is in agreement for small crack lengths. In general, crack model comparisons between NASCRAC and other references resulted in varying degrees of agreement, but none of the NASCRAC solutions have been

deemed incorrect due to an improper implementation of a model or major coding error.

Extensive effort has been undertaken—comparisons for all 28 geometry model configurations—to verify the accuracy of the NASCRAC code. The end results will enable researchers to predict the life of space-flight hardware components with greater reliability.

Sponsor: Office of Advanced Concepts and Technology

• • • • •

Measurement of Plastic Stress and Strain for Analytical Method Verification

Gregory R. Swanson/ED25
205-544-7191

Brian E. Steeve/ED25
205-544-7174

John M. Price/ED27
205-544-4645

Flight structure analysis requires the calculation and prediction of plastic strains, residual stresses, and their resulting effects on life—conditions that can arise from welding, bolt-torquing dimensional mismatches causing assembly stresses, anomalous loading, thermal loading, and engine hot-firing. The validity of analytical solutions to these problems is often in question, particularly finite element models (FEM) and the material property models used in them. Approximations and assumptions made regarding the plastic behavior of materials often lead to widely varying results, particularly when calculating the useful life of a part. The goal of this research project is to conduct a series of tests in order to directly verify the methods used by finite element models to calculate plastic stress and strain.

The first step in the verification procedure is to develop an accurate material model (Inconel 718, in this case) to be used by the finite element

programs. A series of tensile tests have been performed to develop a stress-strain curve describing the material's behavior into the plastic regime.

The verification process then involves inputting the stress-strain model into the finite element program and analyzing the next series of tests. Four-point bend specimens machined from the same material stock will be loaded beyond the elastic limit and then released, leaving a residual stress field along the surface. Hole-drilling will be used to measure the strength of the residual strains. Results can then be directly compared with the finite element analysis, providing a real-life verification of the methods generally employed by finite element codes to determine plastic stress and strain.

Sponsor: Center Director's Discretionary Fund

• • • • •

Grid Optimization Tools for Complex Models

Gregory R. Swanson/ED25
205–544–7191

John M. Price/ED27
205–544–4645

Today, cost plays a decisive role in the design of aerospace structures. New computational tools are available but are not being used routinely because of implementation costs. Probabilistic methods, large-scale design optimization of aerospace vehicle structures, structural sensitivity, and inverse design problems require repeated analysis. The practical implementation of these computational technologies depends on the cost of a single analysis. The goal is to seek the most cost-effective analysis.

An analysis can be divided into preprocessing, solution, and postprocessing tasks. In the past, much attention has been directed toward reducing the time required to obtain a solution. Today, most of the analysis time is spent in preprocessing and postprocessing activities. One of the most costly and time-consuming preprocessing tasks is the construction of the finite element model representing the physical problem. Grid quality directly affects the quality of the solution, but grid quality depends strongly upon the specific problem to be solved. Hence, a good grid for a specific load case becomes a poor grid for another load case. Current practice is to generate a grid for a specific problem. A more efficient approach would be to generate a generic grid and then optimize it for a specific problem. The cost of preprocessing can be reduced through the development of software tools that allow the rapid modification and conditioning of finite element grids.

A Small Business Innovation Research (SBIR) phase II contract, NAS8–40164, entitled "Grid Optimization Tools for Complex Structural Models," with Alabama Research, Inc., of Huntsville, Alabama, is developing a grid optimization tool for complex structural models. The principle investigators are Mr. Lawrence Spradley, Dr. Rainald Lohner, and Mr. Jean Cabello. The phase II project has accomplished some major milestones during the first quarter: three-dimensional finite element model data transfer between the grid optimization tool and commercial finite element software packages (ANSYS44a and Intergraph I/FEM™) has been implemented; the spring smoother works with three-dimensional solid elements; algorithms to allow surface and interface mesh optimization have been developed and coded; and the variational method grid optimization has been implemented for three dimensions. In addition to these major milestones, the capability to handle "gap" elements between two surfaces is undergoing debugging.

Cabello, J.; Lohner, R.; and Jacquotte, O.P. June 3–6, 1991. A Variational Method for the Optimization of Directionally Stretched Elements Generated by the Advancing Front Method (AFM). Third International Conference on Numerical Grid Generation in Computational Fluid Dynamics and Related Fields, Barcelona, Spain.

Lohner, R., and Parikh, P. 1989. Three-Dimensional Grid Generation by the Advancing Front Method. *International Journal of Numerical Methods in Fluids* 8:1135–49.

Spradley, L.W.; Lohner, R.; and Cabello, J. 1993. Grid Optimization Tools for Complex Structural Models, NASA AR–93–01.

Elastic-Plastic and Fully Plastic Fatigue Crack Growth

Wayne Gregg/ED27
205-544-5501

Life prediction of fatigue cracks in the elastic-plastic and fully plastic regime has generally been a difficult task. Currently, engineers are limited to using existing solutions from independent research or from more collected efforts such as the *Electric Power Research Institute (EPRI) Handbook*. More expensive and time-consuming methods (e.g., finite element method or laboratory testing) are required to develop these solutions and any other solutions for new geometries or boundary conditions. Practical analytical models that apply to several geometric configurations and boundary conditions are needed to simplify elastic-plastic fatigue crack growth (EPFCG) predictions.

The Southwest Research Institute (SWRI) has been working to develop such analytical solutions and has progressed considerably in several areas. A summary of their latest advancements includes:

- Further development of reference stress J–integral estimates and new finite element model (FEM) J solutions

- J estimation for combined loading

- Crack closure

- Creep-fatigue algorithms

- Evaluation of alternative governing parameters.

The reference stress methodology for a semi-elliptical surface flaw in a flat plate was investigated last year to determine the J solution at the depth of the flaw. A closed form equation for the J solution has been developed, and predictions have agreed well with the literature solutions. Recently, Southwest Research Institute and Rocketdyne have developed a parametric finite element model for a surface flaw, an embedded flaw, and a corner crack in a flat plate. The J solution at the surface for the semi-elliptical surface flaw in a flat plate (the most widely used flaw configuration for space shuttle main engine (SSME) fracture analysis) and for a corner crack has been estimated with promising results.

Combined loading occurs frequently in space shuttle main engine applications, but is not easily resolved for elastic-plastic fatigue crack growth. Because the available simple approaches do not have a sound theoretical basis, Southwest Research Institute is developing a new scheme based on reference stress concepts. The approach is to derive the optimum yield load for independently acting loads via a finite element model, determine the optimum yield load for the combined loads based on limit-load theory, and then match independent solutions. This approach has been validated by comparison with the limited available finite element model solutions for combined mechanical loads. To date, solutions for single-edge cracked plates and circumferential through-wall defects in hollow cylinders have been

investigated. Early estimation of the J–integral for multiaxial stress states has been approximated by replacing the stress and strain in the fully plastic solution by the effective values for stress and strain. Southwest Research Institute has formulated an estimation scheme by incorporating changes in h_1 for plane stress and plane strain. Validation of this approach has been limited to two-dimensional mode I cracks.

Many of the issues being investigated for crack closure are based on the normalized stress intensity ratio developed last year. Elastic-plastic fatigue crack growth is being addressed with a simple, closed-form equation derived from the modified Dugdale model (Newman equation), which has been validated against other analytical models, finite element models, and various experiments. The Newman equation is based on an infinite center cracked panel (CCP). Although its applicability to other geometries is not clear, the Newman equation gives a conservative lower bound for estimating crack-tip opening stresses for the center cracked panel, even with appreciable ligament plasticity.

Investigations into the area of creep fatigue have led to different treatments for the different creep regimes, including transient and steady-state. Instead of the usual crack growth versus stress intensity factor approach, a parameter calculated from creep deformation data and time-dependent fracture parameters is used to characterize creep crack growth. This parameter, C_t, has also been calculated with the reference stress method. The creep fatigue algorithm developed by

Southwest Research Institute is used to predict growth with considerations for constraint effect and crack closure. The final value of growth is simply a linear summation of fatigue crack growth and creep crack growth.

Although the J–integral is the primary area of investigation for the elastic-plastic fatigue crack growth, Southwest Research Institute is aware that ΔJ has several suggested theoretical limitations, including unloading, closure, loss of path independence for thermal gradients, and loss of J dominance for large-scale yielding. With this in mind, other parameters are also being investigated. Along with some simple parameters (e.g., the strain intensity factor and crack-tip opening displacement (CTOD)), more advanced path-area integrals such as ΔT^* and ΔJ^* are also being examined.

Once completed, this overall effort will contain the most comprehensive and practical list of collected J solutions for elastic-plastic fatigue crack growth. Ideas for incorporating these solutions into NASA/FLAGRO are currently being discussed.

Sponsor: Office of Advanced Concepts and Technology

Industry Involvement: Southwest Research Institute; Rocketdyne Division of Rockwell International

● ● ● ● ●

Fracture Control/Damage Tolerance Methods for Composite/Anisotropic Materials

Rene Ortega/ED27
205–544–5448

The objective of this effort is to compile and consolidate damage tolerance methods for composite/anisotropic materials. Increasingly, these materials are being considered for primary structures of space systems because of their strength capabilities, thermal properties, and reduced weight. Over the past 20 years, characterizations of composite/anisotropic materials' ability to withstand damage and sustain a load thereafter have been extensively researched. This particular effort provides a means of organizing that research into a set of guidelines for using composite and anisotropic materials.

The focus of activities under this program has involved the residual strength and crack propagation aspects of composite/anisotropic material damage tolerance. Residual strength is the maximum damage the structure can resist under fail-safe loads, while crack propagation defines the time period in which a crack grows from a defined, detectable length to the allowable length determined by the residual strength requirement. The program's ultimate goal is to develop a handbook for damage tolerance testing of composite/anisotropic materials that includes test-verified algorithms for calculating flaw growth.

To date, literature reviews have been conducted on single-crystal, laminated-metal, and laminated-fiber composites. Initial reviews will be conducted on particulate composites including nonmetallic and metallic matrix composites. Application of this technology includes the space shuttle main engine (SSME) main combustion chamber using laminated metals; laminated fiber-composite optical benches; single-crystal, high-pressure turbopump turbine blades; and lightweight propellant tank systems using metal matrix composites.

Engineering algorithms for calculating fatigue crack growth life of composite/anisotropic materials will be developed. A wide range of crack-type geometry and loading cases will be considered. Laboratory test data, when available, will be used to verify the accuracy of the developed algorithms.

Sponsor: Office of Advanced Concepts and Technology

● ● ● ● ●

Constitutive Law Development Procedures Applied to Redesigned Solid Rocket Motor Solid Propellant

Joe Chamlee/ED28
205-544-7247

In order to improve margin-of-safety computations for solid propellant rocket motors, better representations of the propellant's stress-strain response, or constitutive law, as well as its failure properties, are required. Failure properties are determined from test data that must be interpreted by structural analysis. To compute margins of safety, failure properties are compared to induced quantities in the loaded motor, and these, likewise, must be obtained from structural analyses. A necessary ingredient to the accuracy of structural analyses is a suitable constitutive law. For steel, aluminum, and many other materials, linear elastic constitutive laws are quite adequate, but for viscoelastic materials such as solid propellant, which may undergo strains in excess of 10 to 20 percent, a nonlinear, viscoelastic constitutive law is required to properly represent material behavior. Unlike the case for linear elastic constitutive laws, procedures for determining nonlinear viscoelastic constitutive laws are not well defined. Researchers in the solid propellant community have worked to establish such procedures for several decades.

Among the goals of the Solid Propulsion Integrity Program (SPIP) are the further development of

procedures for the determination of constitutive laws for solid propellants, as well as the development of a law for the redesigned solid rocket motor (RSRM) propellant; implementation of this law into a finite element code; and demonstration of its capabilities through structural analyses of verification tests.

Earlier in the program, Dr. Steven Peng of the Jet Propulsion Laboratory, who performed most of the propellant structural testing, established some important assumptions regarding the form that a constitutive law for a redesigned solid rocket motor propellant should take, and he utilized a particular data interpretation procedure to develop a first-draft constitutive law for the propellant. This law was implemented by

Sverdrup Technology, Inc., into the ABAQUS finite element code and tested on sample problems. Findings have indicated that while this law appeared to fit the test data well, it violated certain stability requirements essential for finite element analysis. In this past year, Sverdrup personnel have established an alternative, and improved, means of interpreting the test data and have used this to develop a new constitutive law. This law, based on the assumptions established by Dr. Peng, matches the test data very well and displays markedly improved stability. Predictions for uniaxial, equibiaxial, and restrained biaxial stress conditions are shown in figure 132, along with actual test data from uniaxial and equibiaxial test data. Having been implemented in the ABAQUS code, the new constitutive
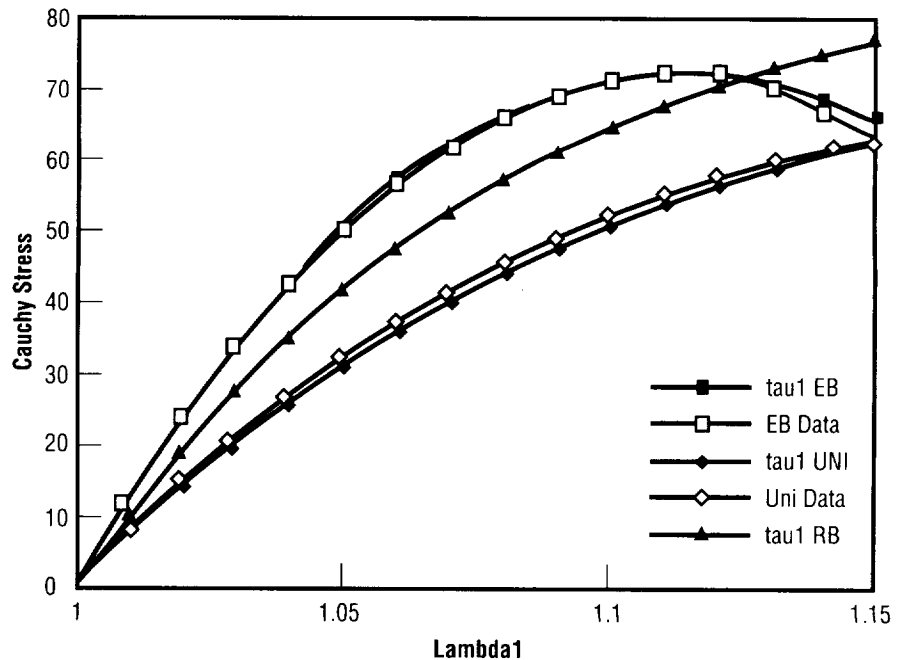
FIGURE 132.—Principal stress versus principal stretch.

law is currently being tested on sample analyses. Later this year, it will be used to predict results of verification tests currently being done by Thiokol of Huntsville.

Researchers anticipate that these procedures can be used for other solid propellants, as well as for rubber materials (such as that used in the redesigned solid rocket motor flex bearing) and hybrid propellants. These procedures can also be applied in other industries, e.g., the automobile tire industry, where the structural behavior of rubbery materials is of great importance.

Peng, S.T.J., May 1992. Constitutive Equations of Solid Propellants With Volume Dilation Under Multiaxial Loading. Proceedings of the 1992 Joint Army, Navy, NASA, and Air Force (JANNAF) Propulsion Meeting.

Springfield, C.W.; McLeod, M.P.; Jackson, B.; and Berry, D.M. October 1993. A Large Strain Constitutive law for Finite Element Analysis of RSRM Propellant. Proceedings of the 1993 JANNAF Structures and Mechanical Behavior Subcommittee Meeting.

Sponsor: Office of Space Flight

Industry Involvement: Sverdrup Technology, Inc.

Advanced Multiphase Flow Analysis for a Solid Rocket Motor

Eric T. Stewart/ED32
205-544-7099

The simulation of solid rocket motor (SRM) internal flow fields with aluminum-based propellants requires a complex multiphase turbulent flow model. For example, particle size distributions and particle combustion inside the motor are important factors for an accurate description of the flow field and prediction of the motor's performance. The objective of this effort have been to enhance an existing computational fluid dynamics (CFD) code, Finite-Difference, Navier-Stokes (FDNS) solver in general coordinates to account for these complicated physical phenomena. During the enhancement process, available experimental data have used to both direct and validate the included physical models. Thus far, the current version of the Finite-Difference, Navier-Stokes solver has been applied to the advanced solid rocket motor (ASRM), the redesigned solid rocket motor (RSRM), and Thiokol's five-inch, subscale test motor.

The overall effort began in 1993, funded by the Office of Space Flight at NASA Headquarters, with the purpose of improving predictions of solid rocket motor performance by enhancing NASA/MSFC's ability to accurately analyze the internal flow within a given motor. Obviously, this

enhanced capability should significantly impact future solid rocket motors by streamlining the design process; however, the potential impact on current motor designs should not be understated. For example, the appearance of pressure spikes in the redesigned solid rocket motor is currently being investigated. Even though the magnitude of the spikes is within acceptable limits, it is still desirable to eliminate, or at least minimize, their existence. The first step toward this goal is to gain an understanding of their origin, which is where the computational fluid dynamics analysis proves beneficial.

Basically, the effort involves the addition of a particle-tracking methodology, the addition of relevant physical models, the proper treatment of boundary conditions, and the validation of the resultant version of the Finite-Difference, Navier-Stokes solver. A Eulerian/Lagrangian multiphase solution method for multizone meshes constitutes the particle-tracking framework. The physical models that have been added thus far include evaporation, combustion, breakup, turbulent dispersion, and agglomeration models. Each directly affects the particle distribution and its evolution throughout the interior of a given solid rocket motor. Currently, Thiokol's subscale test is being analyzed to provide a validation of the solver's enhancement.

In conclusion, work has been initiated at NASA/MSFC to enhance the Finite-Difference, Navier-Stokes solver so that it more closely reflects the complicated physics occurring within a given solid rocket motor. Necessary

Velocity Magnitude

0.00e+00   3.67e+03   7.35e+03   1.10e+04   1.47e+04
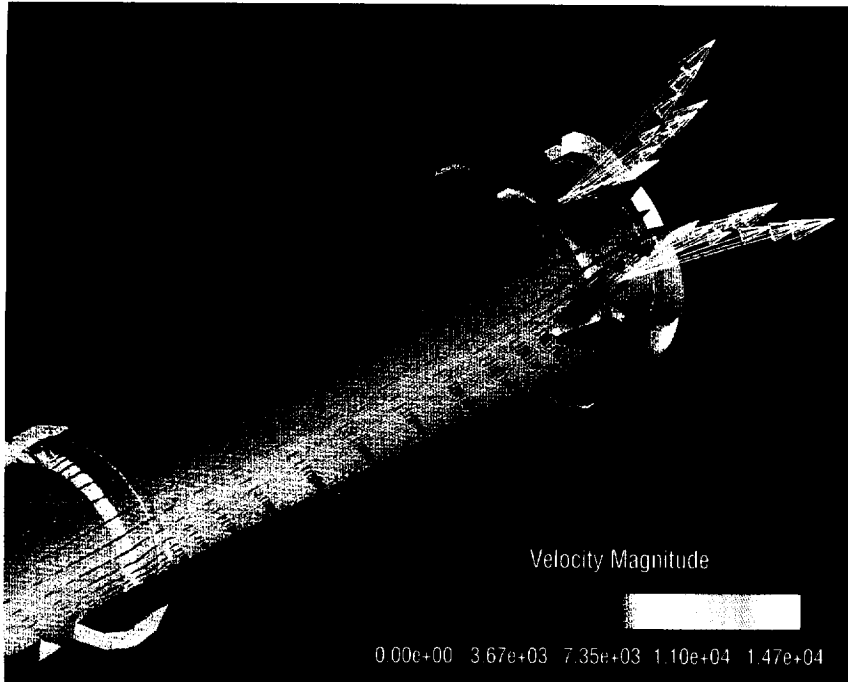
FIGURE 133.—Redesigned solid rocket motor slag accumulation analysis at 67-second burn time.

Quick-Turnaround Flow Analysis of Turbomachinery Subcomponents

Robert W. Williams/ED32
205-544-3998

Computational fluid dynamics (CFD) has been successfully applied to the design process of a rocket engine turbopump. An in-house team was formed at NASA/MSFC to develop a liquid oxygen turbopump that would provide high-pressure liquid oxygen to a 24-inch hybrid rocket motor. Design goals were to deliver a turbopump with a low part count, minimum testing requirements, and an 18-month design and development schedule. To meet these requirements, the turbopump was first designed using conventional one-dimensional empirical methods. Then, most major pump and turbine subcomponent primary flow paths were analyzed with a computational fluid dynamics code. If potential problem areas were discovered in the analysis, a modification could be made to the geometry and more analysis performed to verify the modifications.

The turbine is a single-stage, axial, partial admission, supersonic impulse design. Computational fluid dynamics analysis was performed on the inlet nozzles, rotor, and disk cavity; results indicated that modifications should be made to the nozzle and bearing coolant circuit. The pump, also single-stage, with an inducer and centrifugal shrouded impeller, underwent analysis on its inducer retaining nut, inducer,

code modifications have been identified based on previous research. Once identified, modifications were implemented into the solver's existing framework. Validation of the current version of Finite-Difference, Navier-Stokes is in progress (i.e., Thiokol's subscale test). In addition, the solver has been applied to problems of practical importance (e.g., advanced and redesigned solid rocket motors). An example of these results is shown in figure 133.

Sponsor: Office of Space Flight

Industry Involvement: Engineering Sciences, Inc. (ESI)

● ● ● ● ●

impeller, diffuser, and volute subcomponents; results indicated that modifications needed to be made to the inducer retaining nut, inducer, and diffuser.

Applying quick-turnaround computational fluid dynamics in the design process helped meet project design goals and demonstrated its importance in design verification (figs. 134 to 140).

Sponsor: Office of Advanced Concepts and Technology
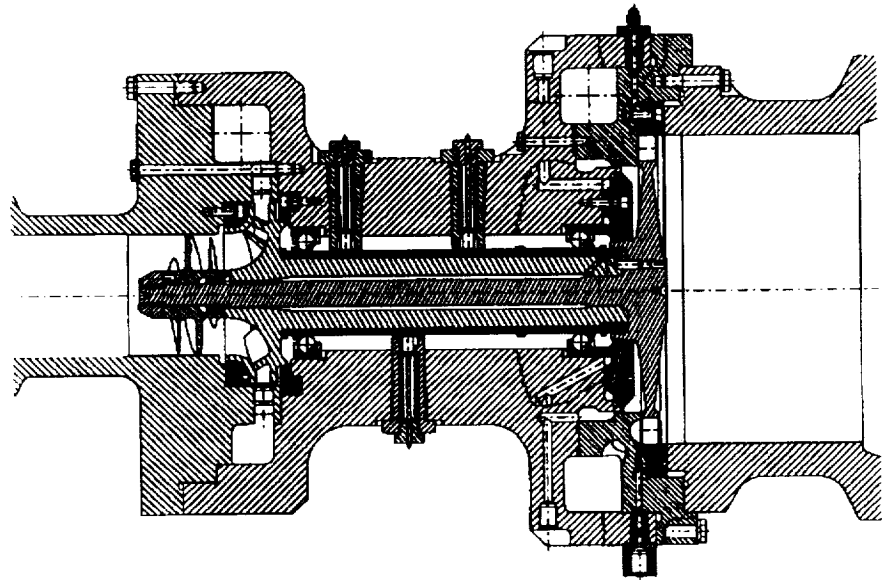
FIGURE 134.—Cross section of the Simplex turbopump.
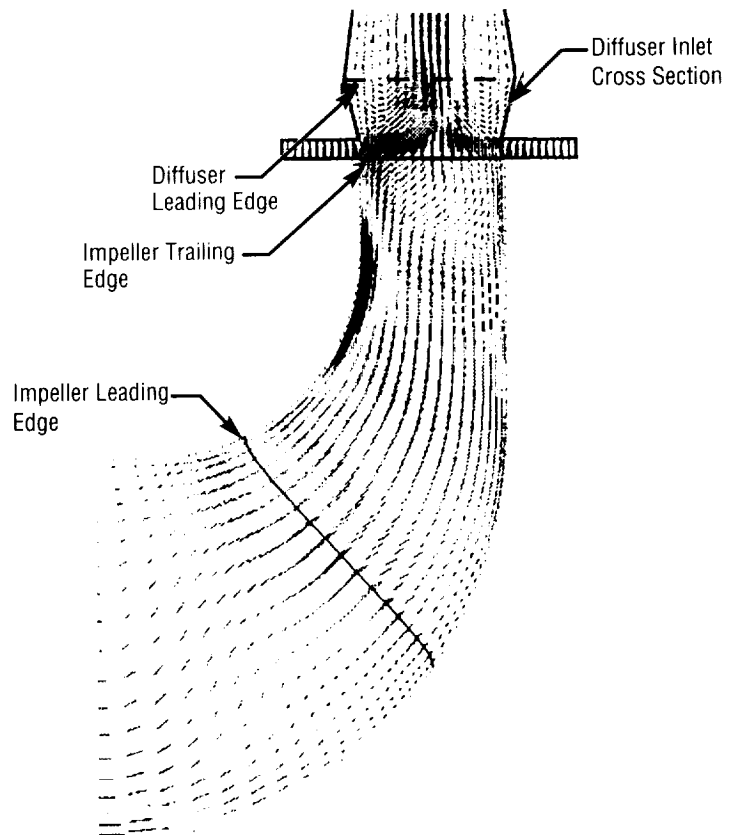
FIGURE 135.—Impeller velocity vectors near mid-span, axial radial projection.
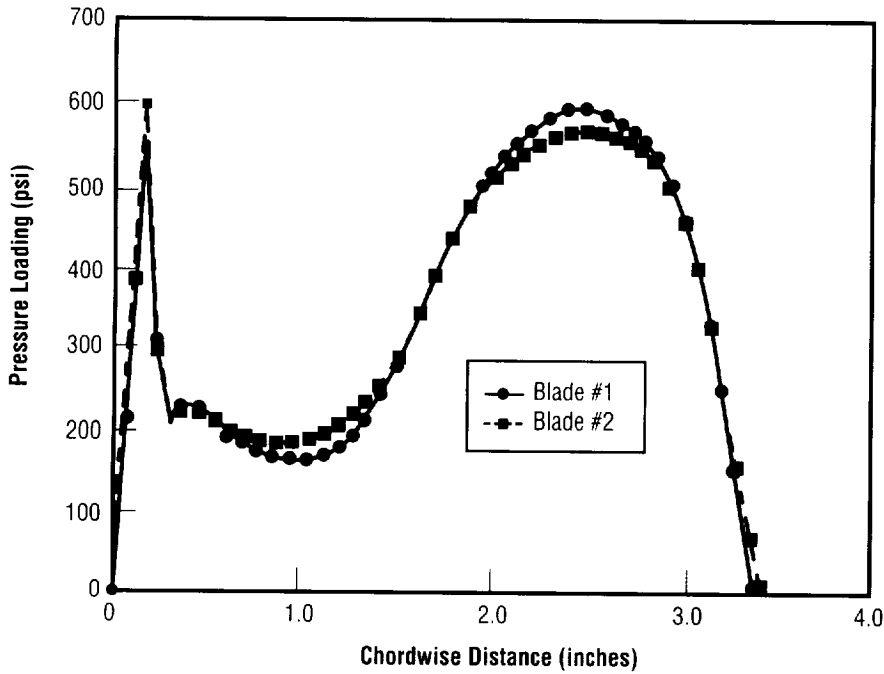
FIGURE 136.—Blade loading for adjacent blades in the two-channel impeller solution.

FIGURE 138.—Stream-wise pressure contours in Simplex turbine nozzle (pressure in pounds per square inch).

FIGURE 137.—Impeller exit hub-to-shroud circumferentially average velocity profile.
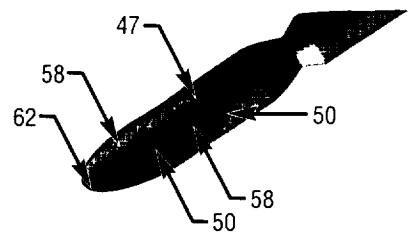
FIGURE 139.—Pressures (in pounds per square inch) at the Simplex nozzle exit plane.
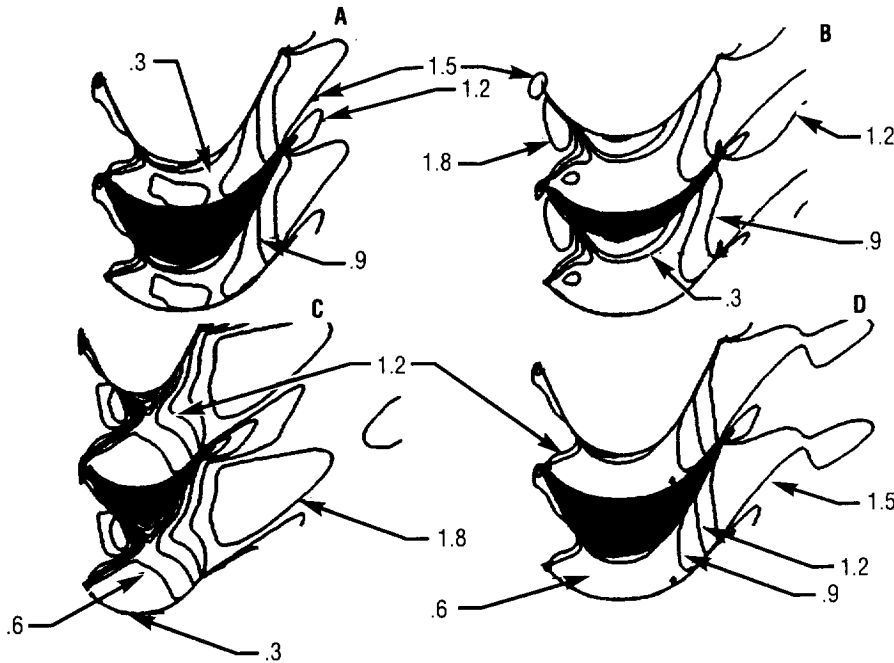
FIGURE 140.—Two-dimensional rotor parametrics showing Mach number contours.

Direct Simulation Monte Carlo Analysis of Microthruster Rarefied Flow Characteristics

Alan R. Droege/ED32
205-544-7911

Once the Gravity Probe B spacecraft is in orbit, microthrusters will be the main mode of attitude control for the satellite, which will use the boil-off from its liquid helium dewar as the microthruster working fluid (propellant). In view of this, a precise modeling of microthruster characteristics is necessary to assure an adequate and efficient attitude control system for the satellite, since the Gravity Probe B will carry a finite amount of liquid helium and the dewar must have an operating life of over 1 year. In order to determine the thrust characteristics of microthrusters operating in the rarefied flow regime, MSFC's Computational Fluid Dynamics (CFD) Branch has used direct simulation Monte Carlo (DSMC) analysis to model the internal flow fields of two prototype and one flight microthruster nozzles.

To incorporate the microthrusters into the attitude control system, their thrust characteristics must be known over the entire expected operating range, which, for Gravity Probe B, is entirely in the transitional and free molecular flow regimes. Therefore, traditional methods of continuum computational fluid dynamics cannot accurately predict microthruster flow characteristics. Instead, direct

simulation Monte Carlo analysis (specifically the method of Dr. G. Bird with a variable hard-sphere model for the helium molecules) has been used. Flow has been characterized for the plenum upstream of the microthruster nozzle throat to the exit plane of the microthruster.

Monte Carlo results have been used to interpret and verify the experimental data gained from Gravity Probe B microthruster experiments conducted at MSFC and at Stanford University. Statistics compared favorably with the experimental data (fig. 141) and also compared well with theoretical approximations. The analysis also demonstrated the truly transitional nature of the flow. In addition, the analysis was able to illustrate trends that the experimental data did not reveal due to inaccuracies inherent in the test equipment. For example, the Monte Carlo analysis was able to disclose that specific impulse was a function of the throat Reynolds number (fig. 142), whereas the experimental data did not have the resolution capability to provide such correlations.

Researchers can now use direct simulation Monte Carlo analysis to characterize entire flow regimes largely due to the size and speed of today's computers. Simulations are now able to be run that only a few years ago would have been impossible. As long as the current trend of increasing the speed and memory of computers continues, larger and higher density flow fields can be calculated using the Monte Carlo technique.

Future work will include analysis to investigate temperature and external
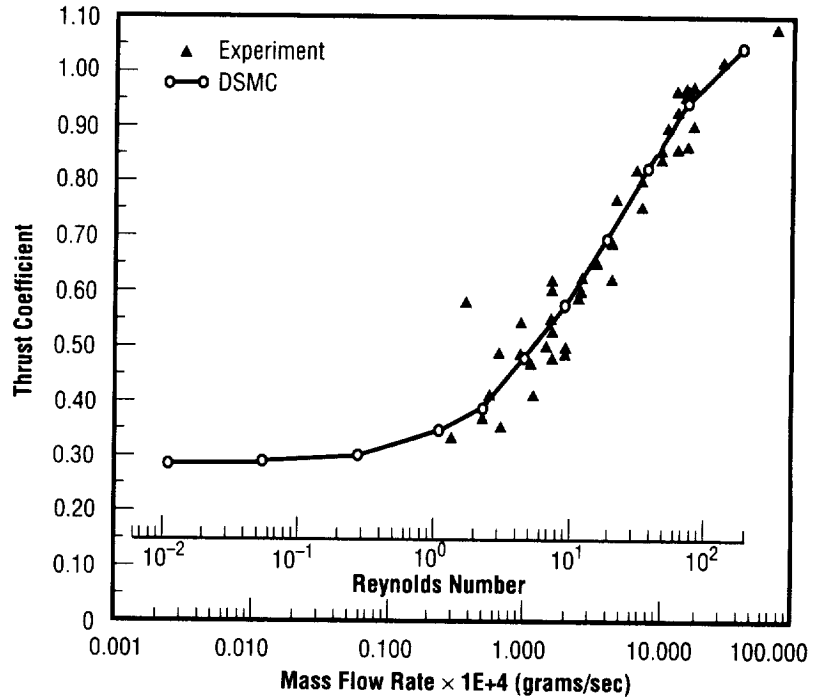
Figure 141.—Direct simulation Monte Carlo data compared to experimental data.
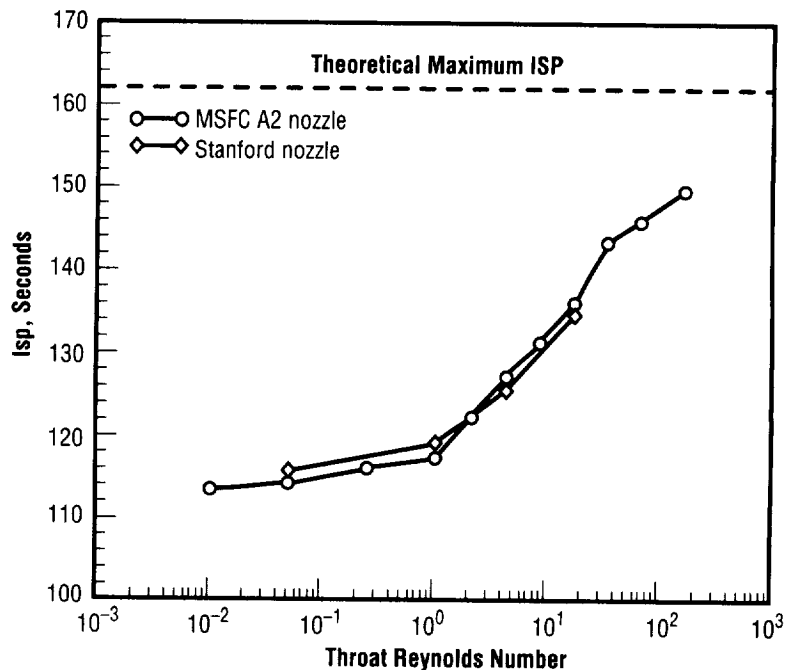
Figure 142.—Specific impulse as a function of the throat Reynolds number.

209

(back pressure) effects on the thrust characteristics. Previous experimental data has shown a variation in thrust at higher back pressures as the external geometry of the microthruster is varied, suggesting that the external flow-field influences the thrust generated by the microthruster. Direct simulation Monte Carlo analysis seems like the only viable alternative for shedding light on this issue.

Sponsor: Office of Space Science

University Involvement: Stanford University

• • • • •

GENIE++ — General Grid Generation System

Theodore G. Benjamin/ED32
205–544–9402

NASA, always striving to advance and optimize present and future liquid-fueled rocket engines, maintains an applications-oriented computational fluid dynamics (CFD) effort complementary to, and in support of, aerodynamic propulsion design and test activities. Numerical grid generation plays a significant role in a fluid-flow simulation utilizing fluid dynamics, and the first step in such a simulation is the generation of an appropriate grid. The geometry of interest must be accurately modeled and the points distributed in an efficient and smooth manner. These constraints often cause this step to be one of the most time consuming.

Over the years, several grid generation codes of increasing capability have been developed. During 1983 to 1985, SVTGD2D–3D was developed and operated in batch mode. As graphics workstations progressed in power and capability, INGRID2D–3D was developed during 1985 to 1988 to use available interactive techniques to speed the process. As an outgrowth of these programs and other research activities, GENIE (the general grid generation system) was developed during 1988 to 1991 as a semi-interactive grid generation package. From 1992 to the present, GENIE++ has demonstrated the capability to generate grids about very complex configurations of interest to MSFC with complete geometric fidelity.

Thus, current development efforts deal with techniques to decrease the time required—and to enhance the fidelity of—the geometry representation. The transfer of information directly from the computer-aided design (CAD) system to the grid generation system has the potential to facilitate the fulfillment of these goals; therefore, a computer-aided grid interface (CAGI) has been developed, and the Initial Graphics Exchange Specification (IGES) has been implemented. This translator is fully compatible with the NASA-Initial Graphics Exchange Specification standard and allows direct transfer of information from a computer-aided design system. The development of the computer-aided grid interface has been supported by NASA/MSFC, and complex configurations of current NASA interest have been used as test cases to validate the grid generation system.

The GENIE++ computer code is a continuously evolving grid system containing a multitude of proven geometry/grid techniques. The GENIE++ generation process follows that employed in earlier versions, using several techniques, either separately or in combination, to generate sculptured/analytical geometry descriptions and grids for arbitrary geometries quickly and economically. The computational mesh is formed by using an appropriate algebraic method. Grid clustering is accomplished with either exponential or hyperbolic tangent routines that allow the user to specify a desired point distribution. Grid smoothing can be accomplished by using an elliptic solver with proper forcing functions. B-spline and nonuniform rational B-spline (NURBS) algorithms are used for
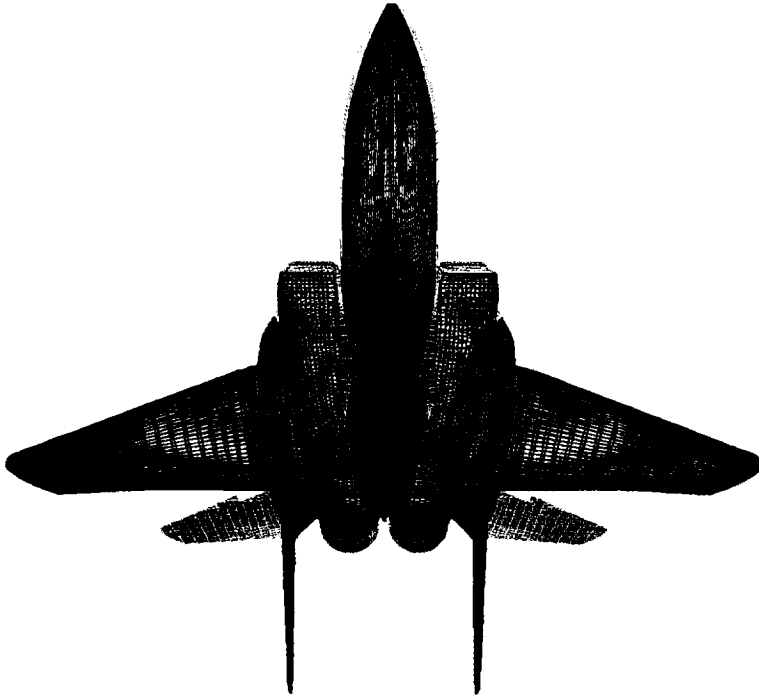
Figure 143.—F15 E volume grid.

intersection is performed. Once this intersection curve is determined, the job is still not complete. The intersection curve must conform to a series of I, J, or K constant lines in the computational space. Experience has indicated that the typical practice of breaking a surface into a larger number of patches to surround the intersection curve can lead to slope discontinuities on the surface. These points not lying on the surface can substantially affect a subsequent flow solution. The procedure developed to eliminate this problem involves the use of nonuniform rational B-spline algorithms. The surface containing the smaller surface, called the mother, is fitted by one of the algorithms, as is the contained, or baby, surface. An example of this would be the intersection of a wing root and a fuselage (figs. 143 and 144) or a vane in a fuel-feed line (figs. 145 and 146). In this procedure, all manipulations to blend the baby into the mother are performed in a parametric space and mapped back into physical space. This ensures that all points lie smoothly on the surface, while also greatly accelerating the grid generation process.

surface definition and redistribution. Salient features of this system, resulting in a significant time savings for a given geometry/grid application, are as follows: the built-in sculptured/analytical geometry definition with desired distribution of points; automatic Bezier curve/surface generation for interior boundaries/surfaces; surface redistribution or remapping based on NURBS-weighted, Lagrange/Hermite transfinite interpolation methods; interactive geometry/grid manipulation modules; and on-line

graphical visualization of the generation process.

Even when geometry data are obtained directly from a computer-aided design system, they are not generally in a form suitable for generation. Often patches defining portions of a surface do not match with their background surface. Also, surface/surface intersections are not defined and sometimes do not fully intersect. In this case, an extrapolation must be performed, which is done automatically when a surface/surface

In short, the enhancements made available with the computer-aided grid interface have significantly decreased the labor required to generate grids for complex configurations. The fidelity of the geometry has also been increased, allowing for more complex

Figure 144.—Fuselage patch before and after blending.

211

Figure 145.—Original Initial Graphics
Exchange Specification
data for vanes.
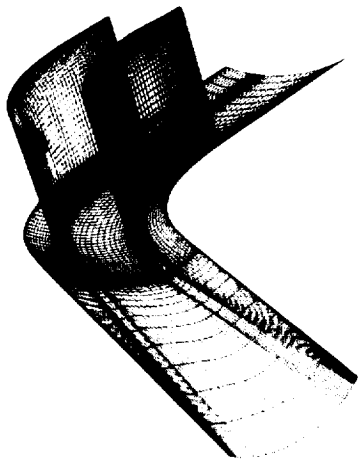
Figure 146.—Selected surfaces of
vaned-elbow volume
grid.

configurations to be analyzed, as well
as allowing a larger number of
concepts to be evaluated with a given
level of effort. The goal is, as always,
a better and more economical design.

Sponsor: Office of Advanced
Concepts and Technology

University Involvement: Mississippi
State University

• • • • •

Computational Fluid Dynamics Analysis of the Bonding-Agent-Induced Flow of Hip Prostheses Implantation

Francisco Canabal III/ED32
205–544–3053

For many years, the medical
community has been surgically
implanting prosthetic devices that take
on functions previously performed by
lost organs or parts of the human body.
Among the many prostheses available,
the hip implant is distinguished by a
high strength-to-volume ratio—a
consequence of having to carry most
of the body weight while fitting into
the limited hip area—as one of its
design considerations. This strength
requirement is satisfied by a well-
designed hip implant and by a strong
bond between the implant and the
femur bone.

Studies reveal that the majority of
unsuccessful hip implants are due to
failure on the bond; therefore,
extensive research has been done to
assess the effects of several aspects of
the implantation procedure (i.e.,
preparation and application of the
bonding agent) on the strength of the
bonding. Research indicates that the
induced flow of the bonding agent
during implantation is responsible for
introducing voids and flaws, leading
to deterioration of bonding structure
strength and triggering the early loss
of the implant. Figure 147 shows a hip
prosthesis superimposed on a cross-
sectional view of the femur bone.

To characterize the induced flow of
the bonding agent during implantation,
computational fluid dynamics (CFD)
analysis numerically solves the
differential equations governing flow
dynamics. Simulation results
demonstrate that the induced flow is in
continuous swirling motion during the
implantation process and that the shear
stress developed in the flow is highly
dependent upon the insertion rate of
the prosthesis. (Figure 148 shows the
velocity distribution at the instant in
which the prostheses has reached its
assembly position.) Both of these flow
characteristics have detrimental effects
on the bonding strength. Fortunately,

Hip Prosthesis

Femur
Bone
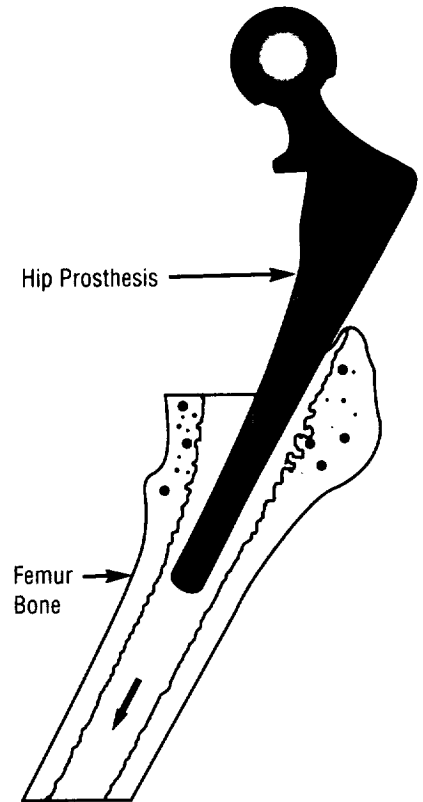
FIGURE 147.—Sample hip prosthesis.

14.7   16.8   18.9
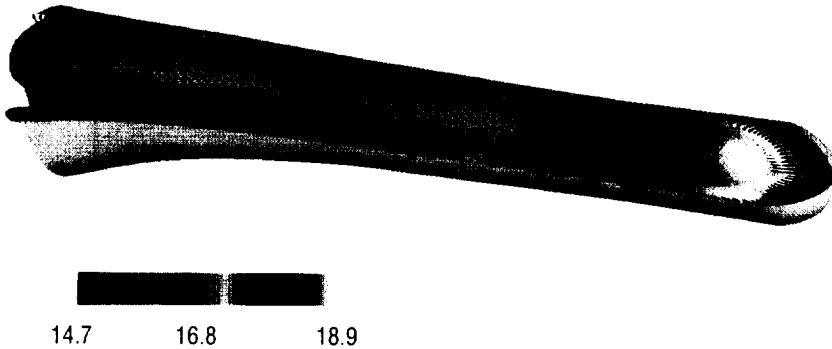
FIGURE 148.—Velocity distribution colored by pressure.

shear stress can be controlled or minimized by regulating the insertion rate of the device. The swirling motion, on the other hand, is an inherent effect of implanting prosthetic hips.

This observation led NASA engineers to produce a modified hip prosthesis design that minimizes the detrimental swirling motion of the bonding agent during implantation and reduces shear stress for a given insertion rate. A U.S. patent is pending. This product could provide all hip prosthesis manufacturers the means through which to produce a better, more long-lasting product.

Sponsor: Office of Advanced Concepts and Technology

• • • • •

External Flow Computations of Launch Vehicle Configurations

Bruce T. Vu/ED32
205–544–8384

The primary objective of this work is to establish confidence in computational fluid dynamics (CFD) simulation capabilities for external flows over launch vehicle configurations. Numerical results from the General Aerodynamic Simulation Program (GASP) have been compared to OVERFLOW results in order to validate each code's capability in predicting surface pressures and aerodynamic coefficients of flight vehicles. Also, comparisons between the measured and computed data have been performed in order to ensure the accuracy of the numerical predictions.

The General Aerodynamic Simulation Program uses a finite volume, cell-centered approach for solving the integral form of the time-dependent, three-dimensional, Reynolds-averaged Navier-Stokes equations. The solution is recorded on multizone, structured grids. The OVERFLOW code—developed at NASA/Ames Research Center (ARC) and capable of solving problems with overlapped grids—is a combination of ARC3D and F3D, both of which had been widely used for external flow computations of the orbiter.

These solvers have been used to calculate the flow past several launch vehicle configurations flying at different angles of attacks under free-

213

stream conditions, covering subsonic
to hypersonic speed regimes.
Computed surface pressures and
aerodynamic coefficients have been
used for comparison with available
wind tunnel test data. The results have
illustrated a general agreement
between simulations and
measurements.

Both the General Aerodynamic
Simulation Program and OVERFLOW
codes are robust and efficient. The
exercise has proven that converged
solutions with acceptable accuracies
can be obtained in a timely response
(figs. 149 to 152).

Sponsor: Office of Advanced
Concepts and Technology

Industry Involvement: Sverdrup
Technology, Inc.

• • • • •
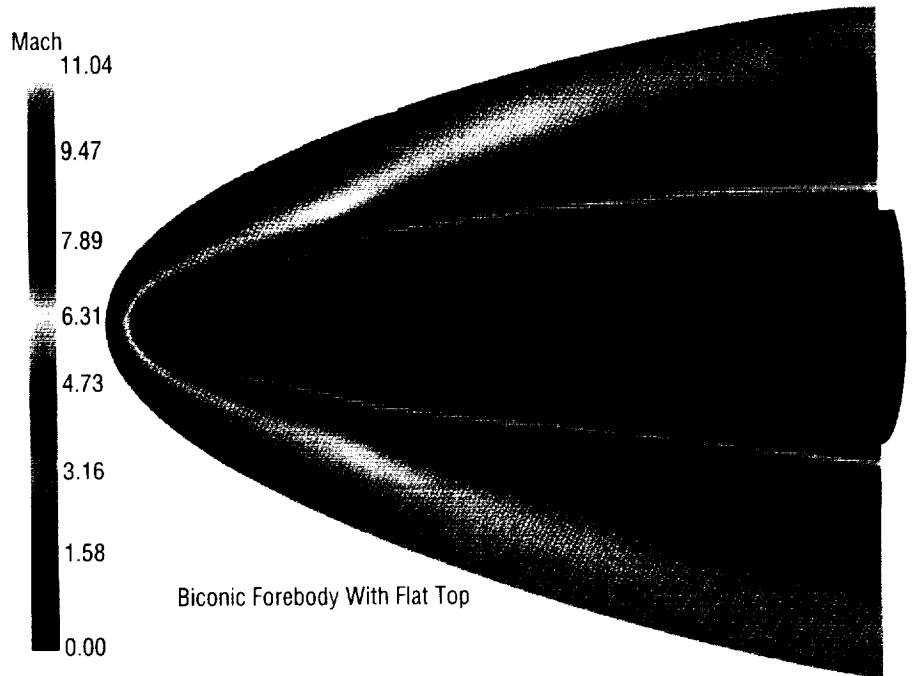
FIGURE 149.—Mach contours at the symmetry plane ($M\infty=10$, $\alpha=2°$)
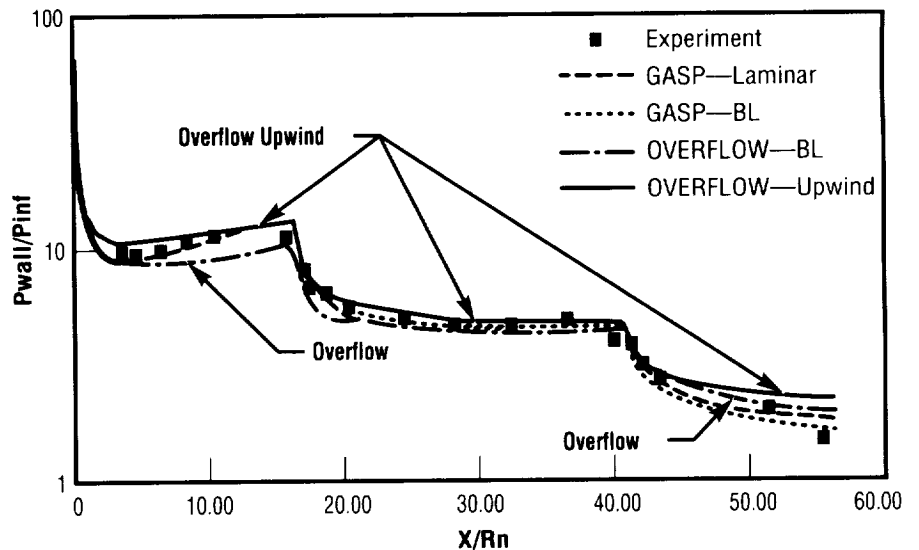
FIGURE 150.—Hypersonic case: biconic with flat.

214

Trajectory Points (by Flight Mechanics Branch):
- M=1.09, α= 2.77, 6, 7.25 deg.
- M=5.72, α=6.86 deg.

Flow Solver:
- OVERFLOW Navier–Stokes code on overlapped grids, developed at NASA–Ames

Progress:
- Complete inviscid analysis of transonic cases
- Results are given to MSFC Structure group for wing–loading analysis

MACH=1.09
A.O.A=6 deg.

Pressure

0.10   0.24   0.38   0.52   0.66   0.80   0.94   1.08   1.22
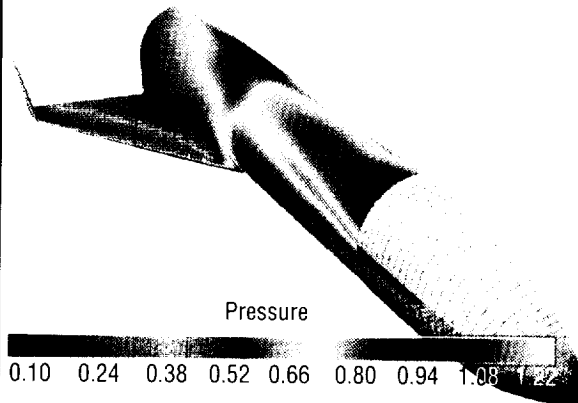
MACH=1.09
A.O.A=6 deg.

MACH=1.09
A.O.A=6 deg.

Pressure
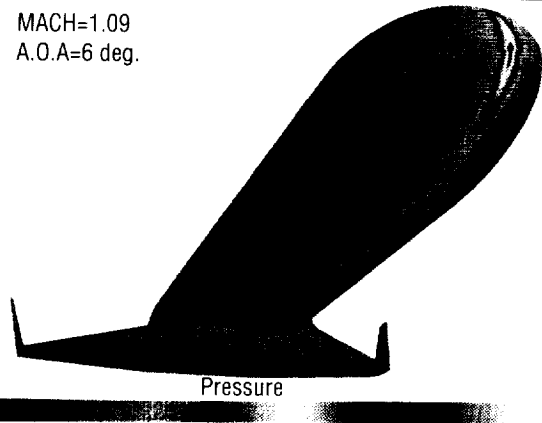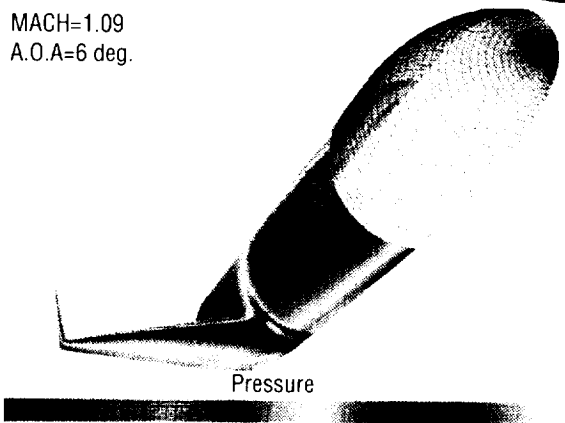
0.10 0.49 0.88 1.27 1.66 2.05 2.44 2.83 3.22 3.61 3.99 4.38

Pressure

0.10   0.24   0.38   0.52   0.66   0.80   0.94   1.08   1.22

FIGURE 151.—SSV001 transonic simulation by OVERFLOW.

M=5.72, AOA=6

0.0405   0.7939   1.5474   2.3008   3.0542   3.8077   4.5611   5.3146   6.0680

FIGURE 152.—SSV001 supersonic simulation by OVERFLOW.

A Solution-Adaptive Grid Analysis of Base Flow Field for a Four-Engine Clustered Nozzle Configuration

Ten See Wang/ED32
205–544–0503

Excessive base heating has been a problem for many launch vehicles. For certain designs such as the direct dump of turbine exhaust inside and at the lip of the nozzle, the potential burning of the turbine exhaust in the base region can be of great concern. Accurate prediction of the base environment at altitudes is, therefore, extremely important during the vehicle design phase. Otherwise, the consequences could be disastrous.

A computational methodology—based on a three-dimensional, viscous-flow, pressure-based computational fluid dynamics (CFD) formulation—has been developed to effectively anchor the base flow field of a four-engine clustered nozzle configuration. For an efficient computational fluid dynamics calculation, a Prandtl-Meyer solution treatment is applied to the algebraic grid lines for initial plume expansion resolution. As the solution evolves, the computational grid is solution-adapted to the pertinent flow gradients. The computational fluid dynamics model employs an upwind scheme using second- and fourth-order central differencing schemes with artificial dissipation. The predicted physical flow features (e.g., the reverse jet,

wall jet, recompression shocks due to plume-plume and reverse jet-base impingement, total plume enclosure, and vent area choking) are in excellent agreement with those described in the experiment. The predicted quantitative results—such as the radial base flow distribution, static pressure, Mach number and impact pressure variations along model centerline, and the base pressure characteristic curve—also agreed well with those of the measurement. This methodology not only provides insight into the multiple engine base flow physics, but also will be useful in the design and analysis of thermal protection systems for launch vehicles (figs. 153 and 154).
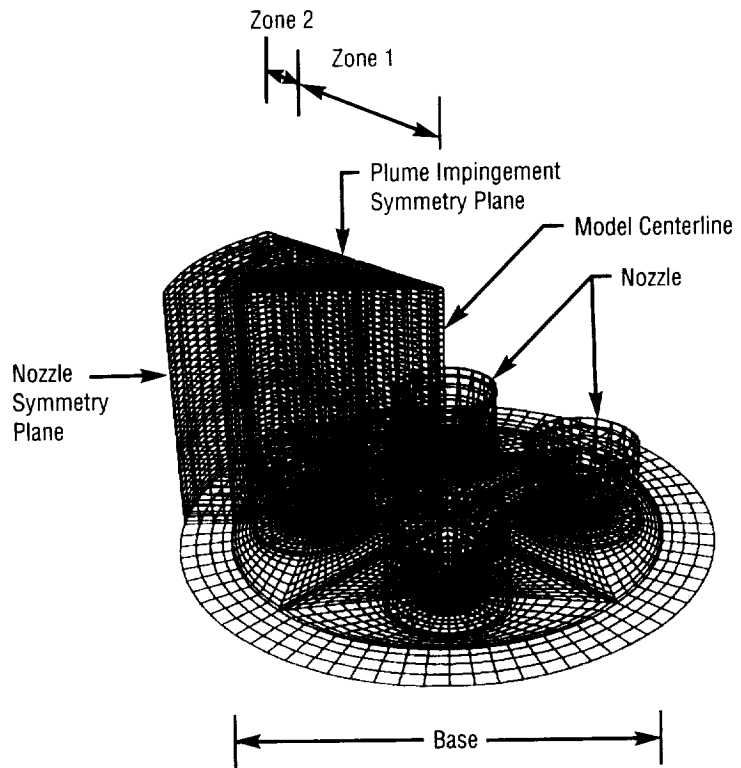
FIGURE 153.—Layout of a typical algebraic grid.

Sponsor: Office of Advanced Concepts and Technology
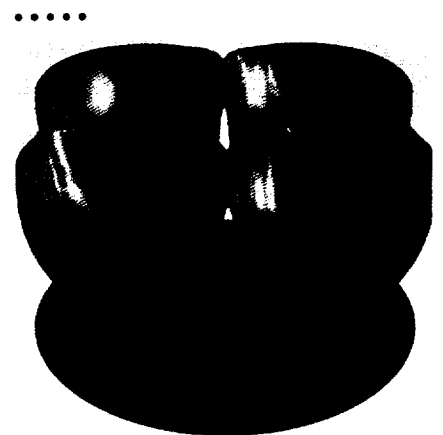
FIGURE 154.—Computed interaction of sonic plume surfaces.

216

Pollutant Environment From RD–170 Propulsion System Testing

Ten See Wang/ED32
205–544–0503

Computational fluid dynamics (CFD) technology has been used to assess the exhaust plume pollutant environment of the RD–170 engine hot-firing on the F1 test stand at MSFC. Researchers know that rocket engine hot-firing has the potential for forming thermal nitric oxides (NOx), as well as producing carbon monoxide (CO) when hydrocarbon fuels are used. The release of these pollutants into the atmosphere not only contributes to acid rain and ozone depletion, but also poses a potential threat to living organisms. Because of the complicated physics involved, however, little attempt has been made to predict pollutant emissions from ground-based engine testing, except for one-dimensional and/or two-dimensional modeling from the combustion chamber down to the exit plane of the nozzle, which can grossly underpredict and/or overpredict pollutant formations in a test environment.

The objective of this effort, therefore, has been to develop a technology using computational fluid dynamics to describe the underlying pollutant emission physics from ground-based rocket engine testing, including three-dimensional air entrainment; three-dimensional multiple-nozzle clustered engine plume interaction and air

Temperature Contour Levels

5,000.0
4,120.0
3,240.0
2,360.0
1,480.0
600.0
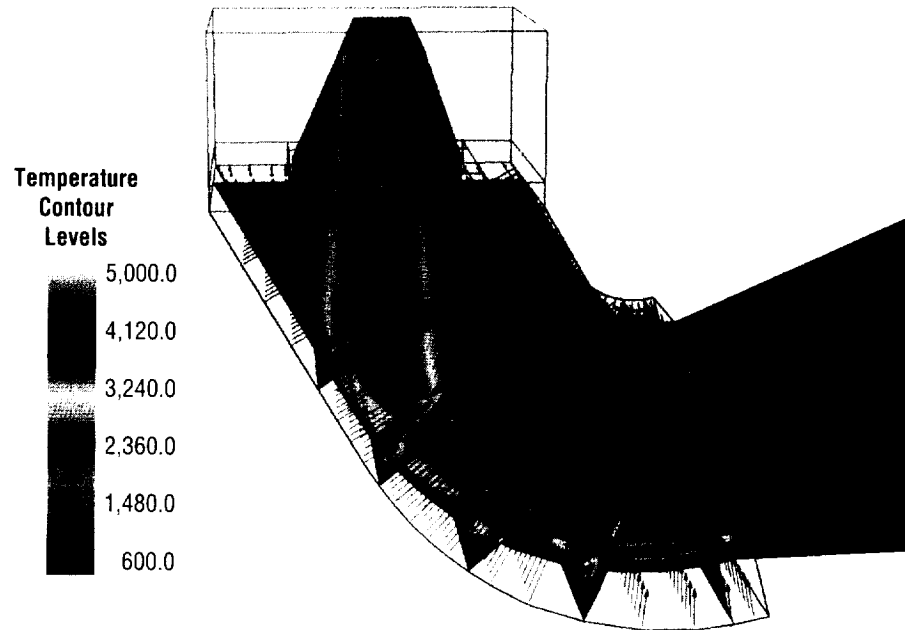
FIGURE 155.—Computational fluid dynamics simulation of kerosene engine test at MSFC (water-quenching in flame deflector).

mixing; finite-rate chemical reaction and after-burning; plume impingement with flame bucket and plume quenching through water deluging; and three-dimensional, restricted multiple plume expansion (fig. 155). A pressure-based computational fluid dynamics method heavily benchmarked for nozzle, plume, and combustion-driven flows has been used for this development. For the purpose of this study, an 11-species, 18-reaction, finite-rate chemistry set describes the after-burning. A nominal hot-firing with water-quenching has been computed, along with two cases including the frozen chemistry and finite-rate chemistry (both without water-quenching) for comparison. The emission rates of the pollutants and the exhaust plume properties have

been computed, and the effects of after-burning and water-quenching on the pollutant formation have been compared. This resultant technology has potential applications in actual rocket launches and in the development of air-breathing engines.

Sponsor: Office of Advanced Concepts and Technology

• • • • •

217

Computational Fluid Dynamics Methods for Rocket Propulsion System Applications

Ten See Wang/ED32
205-544-0503

Under this effort, a series of computational modules that describe real-fluid thermodynamic and physical properties—designed to be easily incorporated into computational fluid dynamics (CFD) codes for the purpose of analyzing propulsion systems—is being developed. Currently, the standard source of propulsion thermodynamics is the NASA Lewis Chemical Equilibrium Computer (CEC) code, which only describes ideal gases in the temperature range of 300 to 5,000 Kelvin (K). Given that many important propulsion problems lie well outside this range and require nonthermodynamic properties, researchers have recognized a need to produce a more realistic representation of combustion gas properties in preburners and main combustion chambers of rocket motors. Computational modules for the following phenomena are being developed by SECA, Inc., under contract NAS8–40139:

Module 1—ideal gas equilibrium module. An ideal gas equilibrium submodel should approach theoretical $C_p(0)$ and $C_p(\infty)$ values, but since essentially all of the species of interest are already described with the Chemical Equilibrium Computer code, and since this code does not necessarily approach the theoretical

$C_p(0)$ limit, a compromise will be used for providing these extreme values—namely, the chemical equilibrium computer data will be used (except at temperatures below 300 Kelvin, in which case interpolation to the $C_p(0)$ value will be used).

Module 2—real gas equilibrium module. A real fluid equilibrium submodel is being developed which is the analog of the submodel in Module 1. Several cubic equations of state will be evaluated, but the Hirschfelder-Buehler-McGee-Sutton (HBMS) equations will probably be used. This equation of state generalizes the Van der Waals equation by replacing "a" with "a(T)+a'(T)/V" and "b" with "b–b' /V." Approximate analyses are being used for radicals, since they are not expected to be present in the liquid state.

Module 3—spray/solid rocket motor combustion module. A stream-tube, two-phase, real-fluid equilibrium spray submodel is being developed, which will be an implemented version of Wieber's vaporization model, as found in the coaxial injection combustion model (CICM) code.

Module 4—hybrid/solid rocket motor burning surface module. An equilibrium burning surface/combustion gas interaction has been formulated. Methods for predicting effective heat of pyrolysis and pyrolysis gas composition, including soot, have been developed by using a constrained equilibrium analysis to eliminate the formation of species which are believed to be kinetically limited.

Module 5—combustion kinetics module. The PARASOL code is being updated to provide a stream-tube combustion kinetics model to treat hydrogen and hydrocarbon combustion and solid propellant combustion. Currently, Finite-Difference, Navier-Stokes (FDNS) with PARASOL can be used to analyze one-dimensional problems with many species and reactions.

Module 6—turbulent mixing analysis. A single-phase, constant-pressure mixing analysis is being made with the Finite Difference, Navier-Stokes code to evaluate turbulence models. This analysis will not be a submodel, but rather an evaluation of turbulent, combustion-mixing models which will, in turn, be used in computational fluid dynamics codes.

Sponsor: Office of Advanced Concepts and Technology; Small Business Innovation Research

Industry Involvement: SECA, Inc.

218

Cold Air-Flow Turbine Testing of the Oxidizer Technology Turbine Rig

Susan T. Hudson/ED34
205-544-1582

The Oxidizer Technology Turbine Rig (OTTR) has been designed to support the development of advanced turbines for future liquid rocket engines. This rig is a scaled model of the Gas Generator Oxidizer Turbine (GGOT) developed by the Turbine Technology Team within the Consortium for Computational Fluid Dynamics Applications in Propulsion Technology. The aerodynamic design of the Gas Generator Oxidizer Turbine—a highly loaded, single-stage oxidizer turbine that uses inlet and exit volutes to provide optimum performance in a compact configuration—has been incorporated into the Oxidizer Technology Turbine Rig, which is to be tested with MSFC's cold air-flow turbine test equipment (TTE). The rig was heavily instrumented to obtain a benchmark quality data set. The data set will be used to evaluate the aerodynamic performance of the turbine and the volutes and to validate various computational fluid dynamics (CFD) codes used in the turbine design phase.

MSFC's turbine test equipment is a blow-down facility that operates by expanding high-pressure air from 2,756-kiloPascals (400-pounds-per-square-inch-gauge) storage to atmospheric conditions. Power absorption is provided by a

447-kilowatt (600-horsepower) drive train consisting of a torquemeter, gear box, and a dynamometer. Turbines are tested at scaled shaft speeds, mass flows, pressures, and temperatures. The ability to test up to full-scale turbopump turbines and accurately control the pressure, temperature, shaft speed, and pressure ratio make MSFC's facility unique among both the government and industry.

The Oxidizer Technology Turbine Rig (fig. 156) is a single-stage, 50-percent-scale, air-flow model with volutes at

the turbine inlet and exit. Extremely high-turning blades are being used to meet the power requirements with a single turbine stage. The blade turning angle is 157 degrees, compared with a 113-degree turning angle for the space shuttle main engine (SSME) alternate turbopump development (ATD) high-pressure fuel turbine (HPFT) blade, which is the blade typical of turbine blades currently being used in liquid rocket engine turbines. Both the volutes and the turbine are highly instrumented with detailed pressure, temperature, and flow-angle
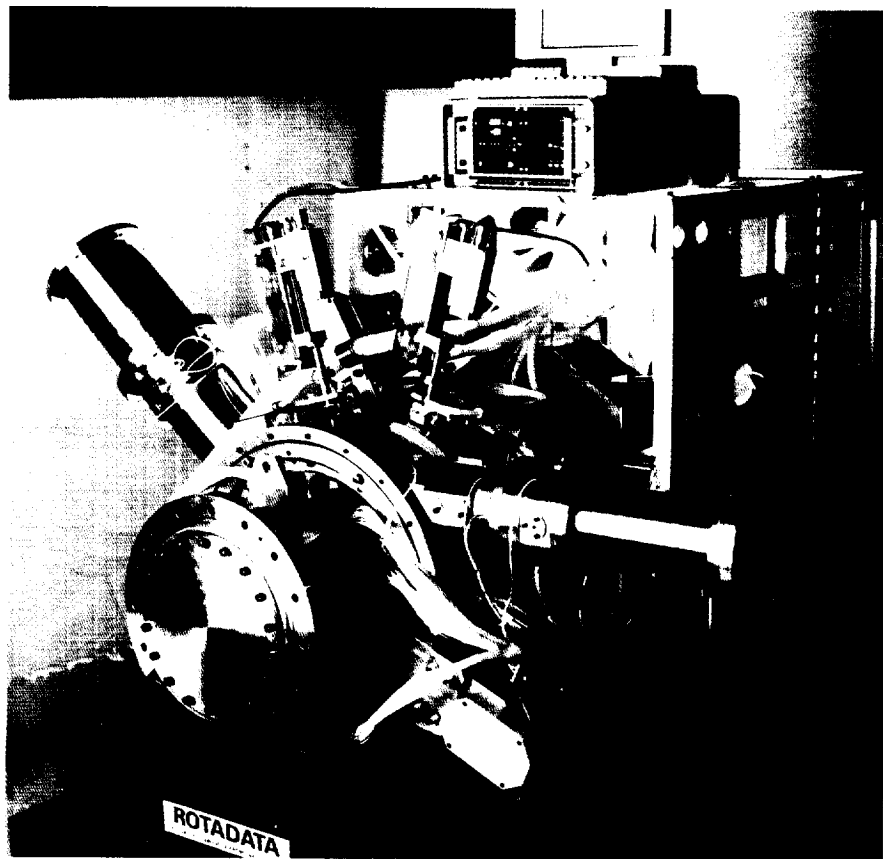
FIGURE 156.— Oxidizer Technology Turbine Rig.

measurements to accurately define the operating environment and performance. Unsteady pressures will be measured on the rotor blade surfaces, and extensive laser Doppler velocimeter (LDV) measurements will be taken in the inlet and exit volutes. Several geometric variables—axial gap spacing; blade radial tip clearance; and variations in blade number, shape, and tip treatment—have been incorporated into the design to make the rig as flexible as possible.

The Oxidizer Technology Turbine Rig has already been designed and fabricated. The rig has been run over its operating range to verify its mechanical design, has met its design requirements, and has been accepted by NASA. Baseline performance testing is now underway. Efforts are expected to advance liquid rocket engine turbine design technology, as well as demonstrate the benefits of computational fluid dynamics application to component design.

Hydson, S.T.; Johnson, P.D.; and Wooler, A. May 1994. Baseline Design of the Oxidizer Technology Turbine Rig. Conference on Advanced Earth-to-Orbit Propulsion Technology, MSFC, Alabama.

Sponsor: Office of Advanced Concepts and Technology

• • • • •

Investigation of Inducer Cavitation and Blade Loads

Wayne J. Bordelon, Jr./ED34
205–544–1579

Stephen W. Gaddis/ED34
205–544–1612

In working with the alternate turbopump development (ATD) liquid oxygen (lox) turbopump, two issues related to the pump's inducer surfaced: synchronous rotor vibration and inducer blade load. Currently, at MSFC's Inducer Test Loop (ITL), a full-scale, water-flow inducer test article (fig. 157) is being used to investigate inducer cavitation characteristics and blade loads at reduced shaft speeds and ambient water temperature. Past testing has focused on investigating cavitation characteristics of the four-bladed inducer using shroud-mounted, dynamic pressure measurements and flow visualization. This work revealed that the inducer exhibits three distinct cavitation modes—tip vortex cavitation, alternate blade cavitation, and asymmetric cavitation—with the latter believed to be a contributor to the rotor synchronous vibration issue. As a result of this work, the inducer tip clearance was increased in an effort to reduce the inducer cavitation excitation force.
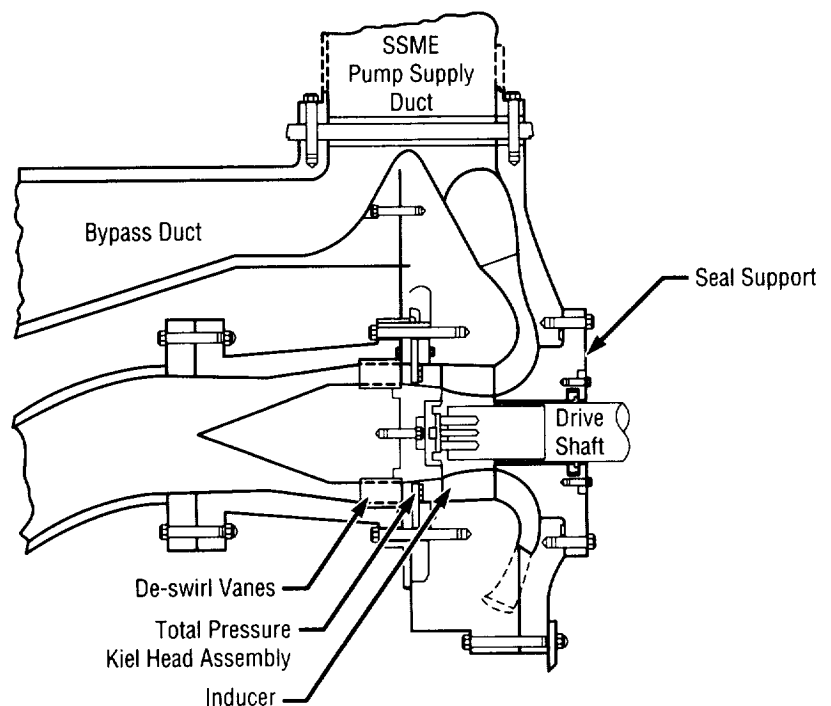
FIGURE 157.—MSFC water-flow inducer test article cross section.
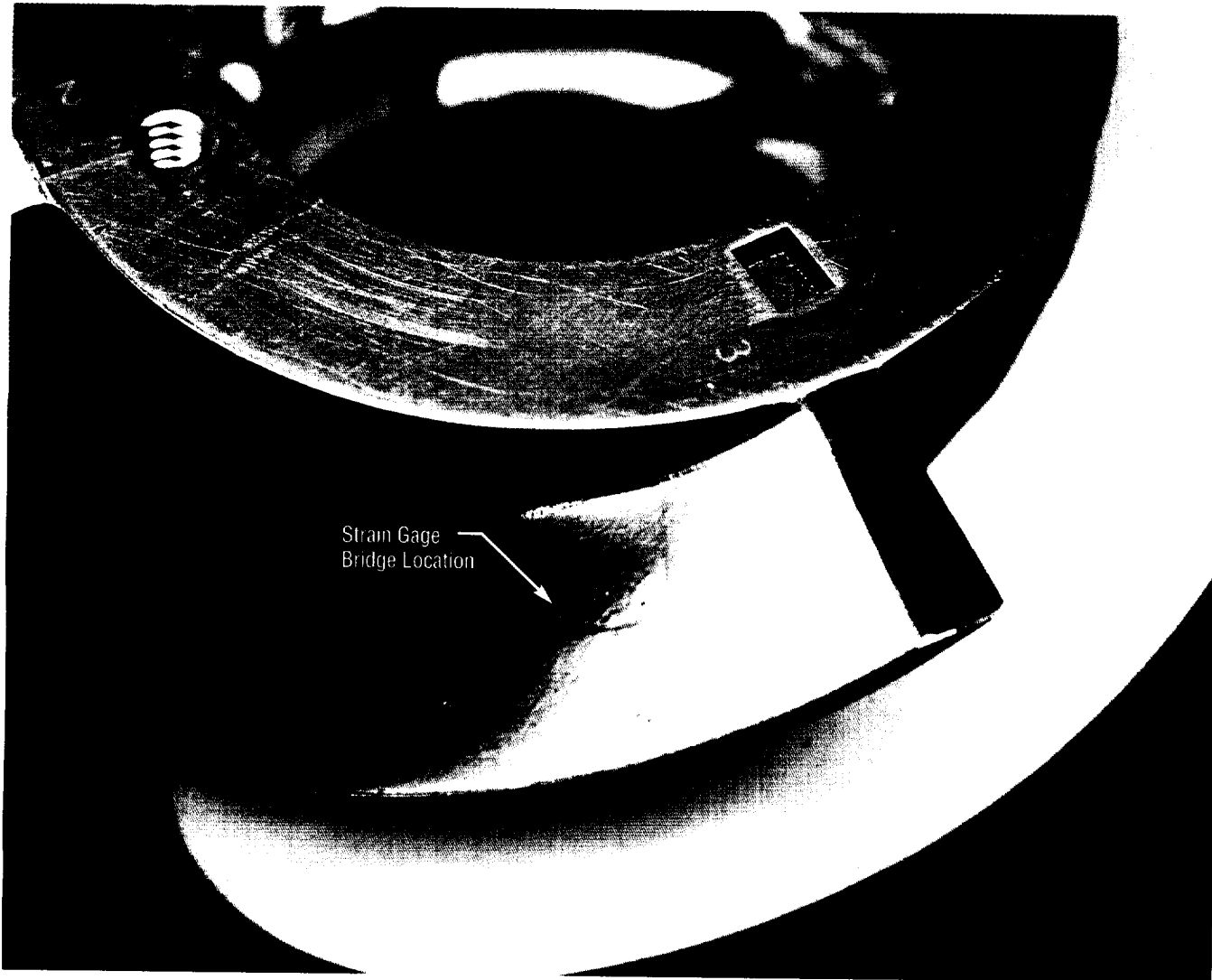
Figure 158.—Typical inducer strain gage bridge installation.

Current work is directed at measuring the steady and alternating inducer blade loads at noncavitated and cavitated conditions. Each of the four blades has been instrumented with four strain gage bridges (fig. 158). Using a slip ring to transmit the strain gage signal off the rotating inducer, the strain measurements will be used to determine the steady and alternating blade stresses. This information will, in turn, be used to verify the inducer blade high-cycle fatigue life. With identical strain measurements on all four blades, additional information regarding the inducer cavitation characteristics will also be obtained, providing insight into cavitation-induced excitation forces and inducer blade stresses not previously available for advanced turbopump inducer designs.

Sponsor: Office of Advanced Concepts and Technology

• • • • •

221

Cold Air-Flow Turbine Testing Incorporating Rapid Prototyping Techniques

Stephen W. Gaddis/ED34
205–544–1612

The space shuttle main engine (SSME) alternate turbopump development (ATD) high-pressure fuel turbine test article (TTA) was configured with state-of-the-art aerodynamic design concepts and tested with MSFC's cold air-flow turbine test equipment (TTE). A cooperative endeavor between MSFC and Pratt & Whitney's Government Engine Division, testing evaluated the feasibility of using rapid prototyping techniques in experimental cold-flow, turbine air-testing research and development.

MSFC's turbine testing equipment is a cold air-flow blowdown facility that operates by expanding high-pressure air from 2.9 megaPascals (420 pounds per square inch) to atmospheric conditions, delivering air run times from 30 seconds to over 30 minutes depending on test conditions. The equipment can accurately control and measure pressures, temperatures, shaft speed, torque, and horsepower. Full-scale test articles can be tested at scaled performance conditions, accurately measuring pressures, temperatures, gas path flow angles, blade tip clearances, dynamic pressures, and gas path velocities by hot-wire or laser Doppler velocimetry.

Researchers, always striving to find faster and cheaper ways of conducting cold air-flow testing, chose
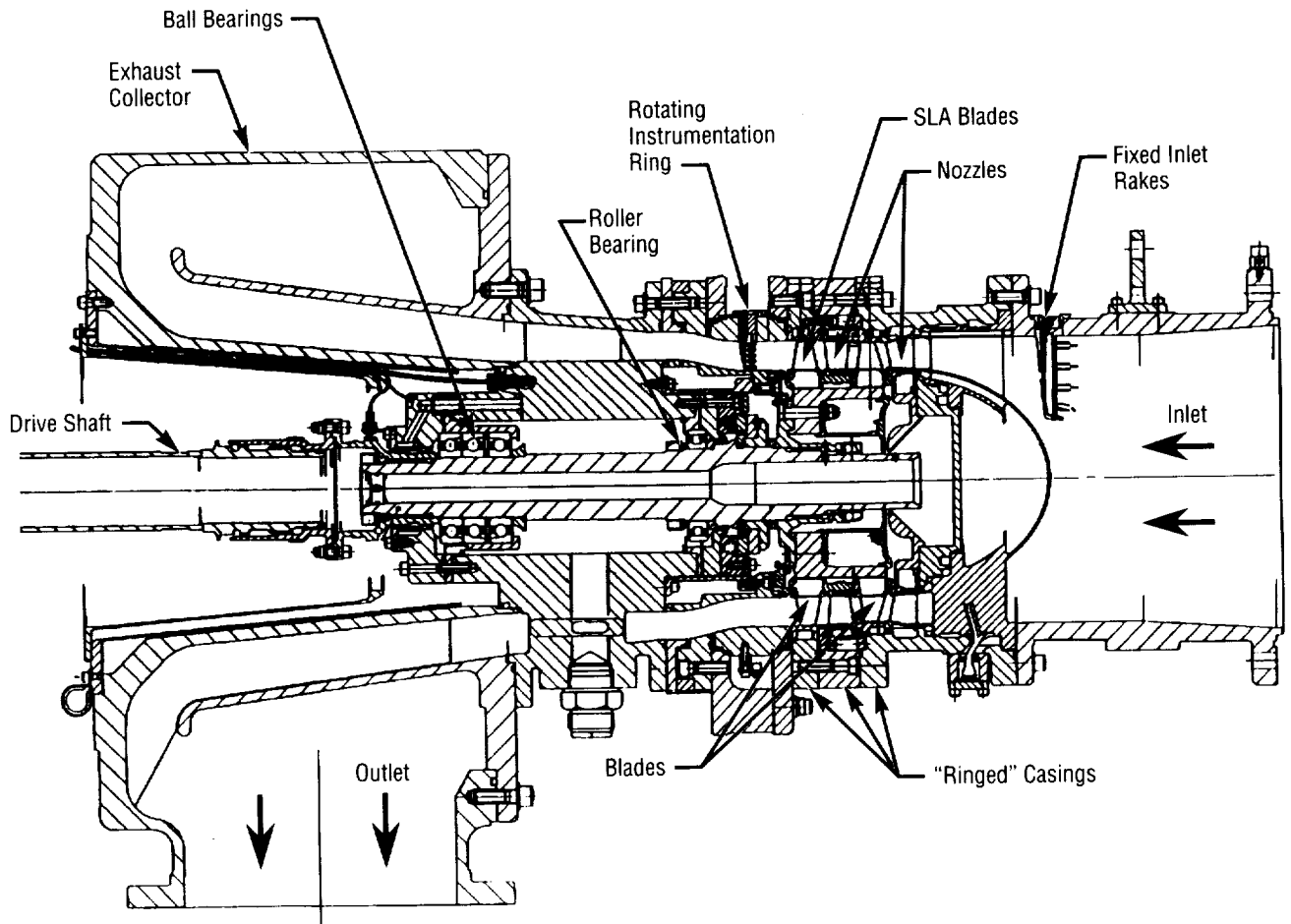
FIGURE 159.—Cross section of turbine test article.

Stereolithographic Vaned-Elbow Flow Test

David M. McDaniels/ED34
205-544-1578

General Dynamics Space Systems, now Martin Marietta Astronautics, and MSFC's Fluid Dynamics Division have collaborated on a test using the ED31 Water-Flow Facility to evaluate a propellant feed system elbow with integral turning vanes. The model tested was produced using stereolithography, a process that uses a laser-catalyzed plastic resin and a laser guided by a computer-aided design (CAD) file to produce a solid plastic model. In the past, these types of models have been used for design visualization and for fit and assembly checks. This particular test will evaluate the suitability of such a model for flow visualization and laser velocimetry, as well as produce data describing the flow field of this particular feed system elbow configuration.

Test objectives include:

• Obtaining total pressure profiles upstream and downstream of the elbow model

• Obtaining velocity profiles upstream and downstream of the elbow model

• Visually observing and recording internal flow characteristics of the model and the fore and aft acrylic sections.

The model is a full-scale propellant feed system 80-degree elbow with
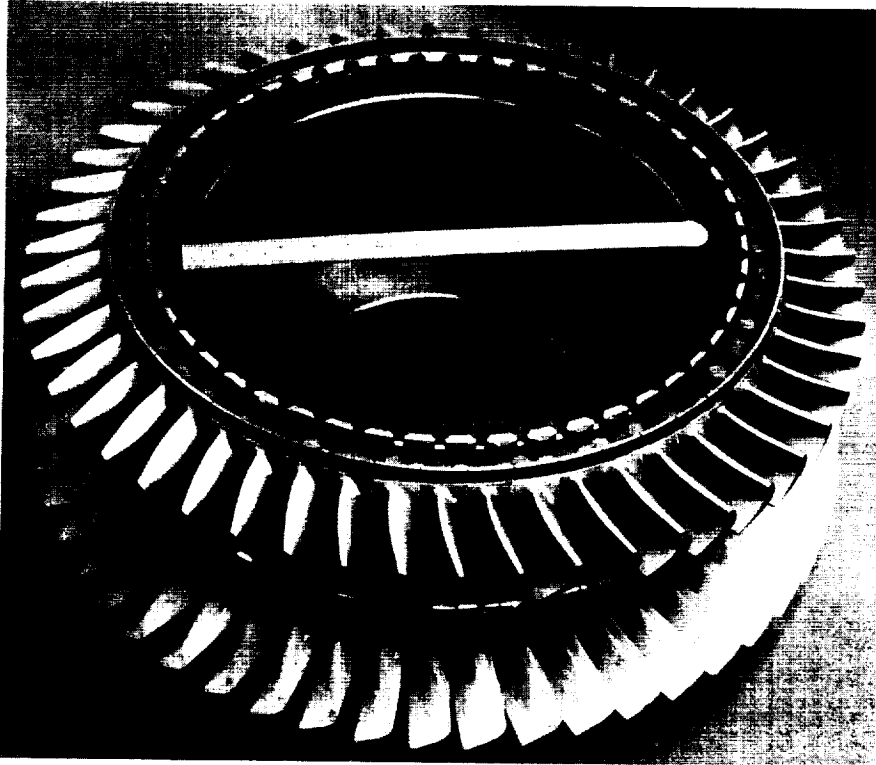
FIGURE 160.—Second-stage stereolithography blades.

stereolithography (SLA) as the particular rapid prototyping technique to be employed because of the potential quick fabrication of test model turbine blades. Testing incorporated the original two-stage, axial-flow advanced turbopump development high-pressure fuel turbine test article (fig. 159), with the second-stage metal blades replaced with stereolithography blades (fig. 160). Pratt & Whitney provided the blades using already available computer-aided design (CAD) files in a matter of weeks.

All tests were successful, and all stereolithography blades remained intact during the entire test program. Performance results indicated

reasonable efficiency trends and values. The potential of using rapid prototyping hardware for this application is promising. Stronger resins and other rapid prototyping techniques are continually being made available so the study is still ongoing. The special features incorporated in this test program are beneficial to aircraft engine-, liquid rocket engine-, and land-based turbomachinery component testing.

Sponsor: Office of Space Flight

Industry Involvement: Pratt & Whitney Government Engine Division

• • • • •

integral turning vanes (fig. 161). The resin in its final cured state is semitransparent, while the exterior surfaces of the model have been left as flat planes rather than contoured surfaces to facilitate flow visualization. Some surfaces have been polished or recured to facilitate flow visualization.

The test will be a continuous-flow, water-flow test with a one-piece plastic model to evaluate the flow through the elbow. Several flow rates will be used, with the maximum being 780 gallons per minute or the flow rate at the maximum pressure of the acrylic pipe, whichever comes first.

The first portion of the test involves the recording of flow visualization. During a typical flow visualization run, dye or bubbles will be introduced either through a wall tap or through a probe extending into the flow. The flow marker will be illuminated with either a laser sheet or a series of bright theatrical lights and recorded on videotape.

The second portion of the test will focus on data acquisition. A typical run will involve setting the proper facility flow rate, keying in the appropriate test parameters into the computer, positioning the probes or laser, and starting the data acquisition computer.

Data acquired during the test will include total pressure loss across the elbow, total pressure profiles upstream and downstream of the elbow, laser-velocimeter-acquired velocity profiles up- and downstream of the elbow (fig. 162), and flow visualization. Velocity profiles will be used by the
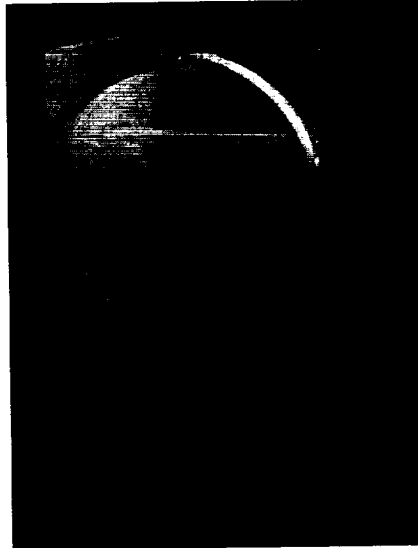
FIGURE 161.—Stereolithography elbow model.

FIGURE 162.—Laser velocimeter being applied at model exit.

Computational Fluid Dynamics Branch to benchmark computational models of this type of integral-vaned elbow.

Test results will provide the requisite knowledge to allow cheaper and much quicker production of flow-test models to evaluate internal flow components. The rapid production of such models would allow for near-real-time optimization of component contours during cold-flow performance testing, saving significant amounts of hot-fire test time and, in turn, saving significant amounts of money.

Sponsor: Office of Advanced Concepts and Technology

• • • • •

224

Spacecraft Meteoroid/ Orbital Debris Penetration Hazards Testing

Joel E. Williamsen/ED52
205-544-7007

The hazards associated with meteoroid or orbital debris penetration of spacecraft interior volumes can be quantified and minimized through efficient spacecraft internal design and crew operations practices. To do this, researchers must perform the requisite tests to determine the magnitude of such penetration hazards as fragments, overpressure, light, heat, and depressurization rates.

MSFC has begun a test series at the University of Alabama in Huntsville's Aerophysics Research Center (UAH-ARC) using a light gas gun to simulate penetration of manned spacecraft cabins by orbital debris. Acoustic, light, and temperature sensors register the magnitude of penetration-induced hazards in a large chamber that emulates the interior of a manned spacecraft. Hardware is then added to the walls of the chamber to represent the hazard-reducing attributes of internal equipment (fig. 163).

MSFC is also investigating the expected depressurization rates associated with penetration-induced holes in manned module pressure walls. In this test series, a steady stream of air is pumped through a pressure wall section sample with a penetration-induced hole to determine the discharge coefficient associated with the choked-flow condition. The
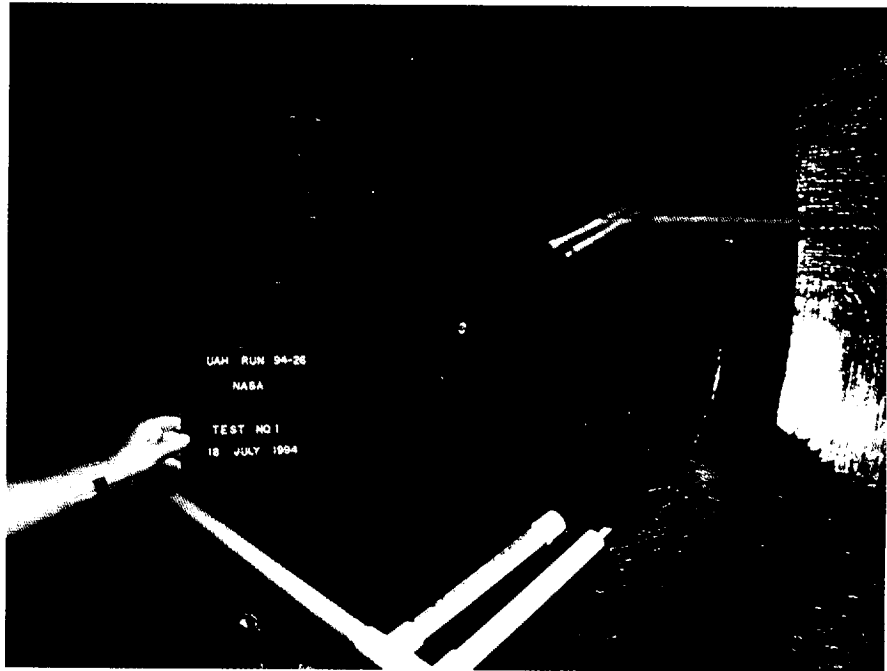
View Towards Shield
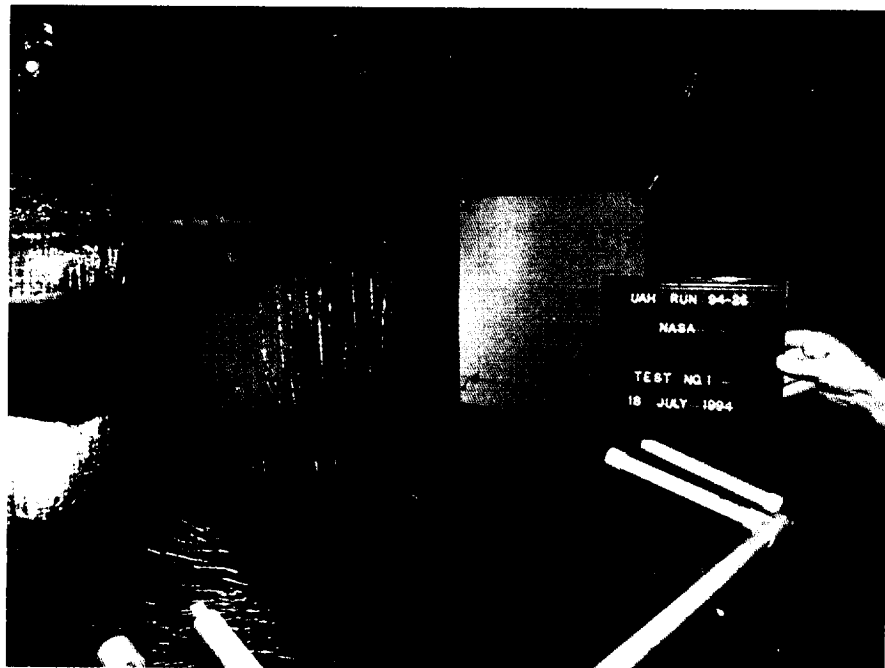
View Away From Shield

NASA Test No. 1-7/18/94
Velocity = 6.7 km/sec
Diameter = 0.52 inch

U.S. Lab Whipple Shield
No Internal Equipment

Figure 163.—Orbital debris penetration effects chamber.

225

general effects of many impact-induced hole geometries on depressurization are then modeled and applied to other penetration conditions.

Test data, when input into the Manned Spacecraft Crew Survivability (MSCSurv) computer simulation tool, allows the designer to identify interior spacecraft designs, crew work and sleep schedules, and other factors that affect crew safety following the remote possibility of spacecraft penetration by orbital debris. The hazard analysis and quantitative output from this safety study is invaluable to crewed spacecraft designers. The development of this unique NASA technology will provide the scientific community with a new design tool for spacecraft orbital debris protection systems and support structures.

Sponsor: Office of Space Flight

• • • • •

Enhanced Orbital Debris Shielding for Space Station Manned Modules

Joel E. Williamsen/ED52
205–544–7007

With the growing threat of orbital debris penetration, spacecraft in low-Earth orbit (LEO) require enhanced shield designs that maximize spacecraft protection-to-weight ratios while still meeting volumetric, thermal, and repairability criteria. Toward this goal, engineers at MSFC and Johnson Space Center (JSC) have created a prototype-enhanced orbital debris shield compatible with existing space station module design constraints (fig. 164).

This shield design employs Nextel AF62 and Kevlar 49 cloth over a graphite support structure suspended between a preexisting aluminum outer bumper and pressure wall. The half-scale mock-up shows the options available for replacing the enhanced shield should it become damaged by orbital debris.

Shield concepts from this study are broadly applicable to other government or industry spacecraft designs. This new technology in the design of orbital debris shields is a bold departure from the traditional all-metallic shields used across the aerospace industry. Further, this development provides substantial weight savings while offering equal or better protection than the traditional shields.

Sponsor: Office of Space Flight

• • • • •
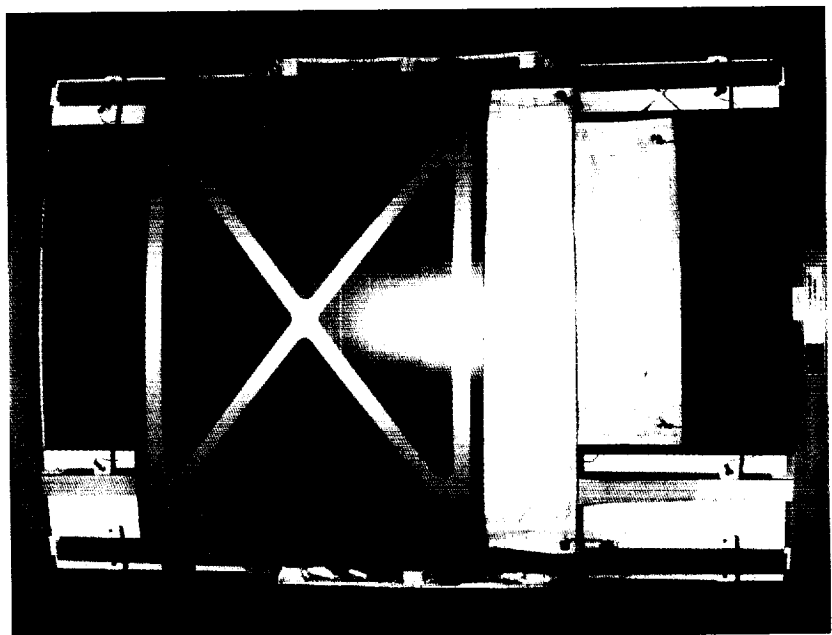
FIGURE 164.—Enhanced orbital debris shield space station manned module.

Non-Autoclave Curing of Composite Flight Structures

Jeffrey L. Finckenor/ED52
205–544–77041

William M. McMahon/EH35
205–544–2802

Ward M. Overton, Jr./ED72
205–544–6862

Chuck E. Wilkerson/EH13
205–544–8834

The unique strength and stiffness of fiber composites make them an excellent choice of material for use in flight structures. Since many of these components are quite large, materials are often formed and then cured under high temperature and pressure in very expensive autoclaves. If composites could be cured in a standard oven while maintaining their strength, significant tooling and processing costs would be saved. Some preliminary panel tests have been done that show promise for non-autoclave curing.

The technology under investigation pushes the state-of-the-art in the use of fiber composite materials and offers the potential for large cost savings in aeronautics and access to space applications. Production expenses could be significantly reduced for both aircraft (such as for the Boeing 777) and spacecraft (such as the shuttle's external tank, intertank, or expendable launch vehicle shrouds). Small business owners who cannot afford to buy (or operate) an autoclave could easily afford an oven.

Four objectives are to be obtained through this study:

- Quantify the effects of cure, lay-up, and ply thickness

- Ensure that the behavior of composite honeycomb structures can be predicted whether they are oven- or autoclave-cured

- Evaluate the strength and reliability of bonded structural joints in composite structures

- Evaluate embedded fiber-optic health monitoring.

Bonded joint tests will include composite-composite and composite-aluminum joints. A fiber-optic sensor, embedded into composite splice plates, will be incorporated into the panel splice tests.

Research will identify how significant the penalty, if any, of using different manufacturing methods. Knowing this penalty and the difference in costs between the manufacturing methods will allow the best part to be made at the lowest cost. This study will indicate the feasibility of bonded joints in aerospace applications and the predictability of honeycomb composites with different cures. The reliability of fiber-optic sensors in comparison with traditional strain measurement methods will also be evaluated for potential application to vehicle health monitoring.

Sponsor: Center Director's Discretionary Fund

• • • • •

Cylinder Optimization of Rings, Skin, and Stringers With Tolerance Sensitivity

Jeffrey L. Finckenor/ED52
205–544–7041

Mat Bevill/EP12
205–544–6941

Cylinder Optimization of Rings, Skin, and Stringers With Tolerance (CORSSTol) is a design program for examining the sensitivity of optimum design dimensions with respect to design tolerances—giving the design engineer a tool to determine which dimensions are the most critical to weight and failure.

The program (1) begins by optimizing cylinder dimensions without including tolerances (Limiting constraints include skin buckling, shell buckling, allowable stress, stringer crippling, and local stringer buckling.); and (2) then uses the same analysis call and optimization routine to find the optimum weight for the worst combination of tolerances. This worst-case scenario is coupled with the maximum material condition for weight, and the constraints are calculated with the least conservative value allowed, either the upper-bound or the lower-bound tolerance.

Table 14 shows a nontoleranced optimization, while table 15 provides the solution from the Cylinder Optimization of Rings, Skin, and Stringers With Tolerance program. The "Optimum" and the "Opt+Tol" columns indicate dimension bounds.

Table 14.—*Nontoleranced optimized solution*

```
Cylinder Weight = 603.8
(Skin: 377.5, Stringers: 226.3, Rings: 0.0, Flanges: 0.0)

h    =   1.2992,      Stringer height
12   =   0.0676,      I top flange thickness
tst  =   0.0400,      I stringer web thickness
Nst  = 231.8100,      Number of stringers, b = 4.3669
t    =   0.0756,      Skin thickness
W    =   2.1993,      I stringer width


Stringer: I = 0.021898, J = 0.000251, Z = 1.141558, A = 0.197992
End ring I should be at least 13.6819
End ring area should be at least 0.000296251* (r+Z)

                                                             G[ ] value
Skin: (shear ratio)**2 + stress ratio       = 0.99516 < 1   –0.00484

Applied column stress (SF = 1.40)           = 17135.0
   Critical coupled buckling stress (m = 1) = 17220.0        –0.00493
   Critical flange elastic buckling stress  = 17189.8        –0.03189
   Critical column stress                   = 17219.5        –0.00491

Applied Von Mises stress (SF = 1.40)        = 17003.3
   Yield compressive stress                 = 53000.0        –0.67918

General cylinder buckling controlled by critical column buckling
```

Table 15.—*Cylinder Optimization of Rings, Skin, and Stringers With Tolerance solution and weight sensitivity*

	Optimum	Maximum	Delta	
Cylinder Weight	614.87	876.20	261.32	
Design Variable Solutions				
DV =	Optimum	Opt+Tol	dWt/dDV	dWt
h =	1.31268	1.34268	41.5324	1.2460
12 =	0.06734	0.09734	2222.1721	66.6652
tst =	0.04003	0.07003	1291.9617	38.7589
(b =	4.81125	4.78125)		
Nst =	216.13228	217.48840	0.9446	1.2810
t =	0.08230	0.11230	4988.4277	149.6825
W =	2.18202	2.21202	69.8608	2.0958

Number of stringers, Nst = 2*pr*r/b, b = stringer spacing

The difference between these columns is a user input of .03 inches for all the dimensions in the example. The "dWt/dDV" column offers the sensitivity of the weight to each dimension, illustrating that skin thickness greatly affects weight, while the stringer height, stringer width, and stringer spacing have a much smaller impact. The "dWt" column reveals the weight that can be attributed to each tolerance. The skin tolerance of 0.03 inches can add up to 150 pounds to the optimum weight. The engineer can use this table to identify which tolerances need to be kept the tightest.

Table 16 shows the sensitivity of the constraints to each design variable. "SkB" is skin buckling; "ShB," shell buckling; "Str," stress; "LBF," local buckling of the stringer flange; and "ICB" is the coupled buckling of an I stringer. A negative number indicates that the margin of safety on the failure mode increases as the dimension increases, and a larger stringer width improves the safety of all failure modes except local buckling of the flange. Engineers could use this table to determine if a part made out of tolerance is still safe.

Table 17 displays the widest possible tolerance range without allowing a failure. In some cases, there will not be a limit based on failure. The skin could get very thick and there would be no structural failures, but the weight would quickly become unreasonable. The "Lower Limit" column illustrates how small the dimension can get before there is a failure mode with zero margin; "Weight Savings" shows the effect the additional tolerance could have on the weight; "Added Toler" is the difference between the smallest

Table 16.—*Failure mode sensitivity*

DV	dSkB/dDV	dShB/dDV	dStr/dDV	dLBF/dDV	dICB/dDV
h	-0.0697	-1.5112	-0.0261	-0.0801	0.0200
12	-3.6022	-7.4098	-1.3515	-32.7170	-5.4748
tst	-2.0910	-0.8052	-0.7853	-2.4117	-1.8436
b	0.4742	0.1121	0.0411	0.1262	0.1291
t	-31.1784	-5.0338	-3.7721	-11.6666	-11.9349
W	-0.1131	-0.2536	-0.0424	0.7675	-11.0453
G [i]	0.00225*	-0.00076*	-0.67862	-0.00174*	-0.00107*

Table 17.—*Increased tolerance range*

	Below Optimum ———			Above Maximum ———			
DV	Lower Limit	Weight Savings	Added Toler.	Upper Limit	Weight Penalty	Added Toler.	New Tol. Band
h	1.31218	0.0209	0.00050	1.34491	0.09261	0.00223	0.03273
12	0.06729	0.1184	0.00005	No constraint limits the upper bound			
tst	0.03945	0.7511	0.00058	No constraint limits the upper bound			
Nst	215.82778	0.2876		No constraint limits the upper bound			
(b	No limit on the lower bound			4.81804		0.00679	4.81804)
t	0.08222	0.4480	0.00009	No constraint limits the upper bound			
W	2.18100	0.0716	0.00103	2.21429	0.1587	0.00227	0.03330

possible dimension and the optimum dimension from table 17; and "Upper Limit," "Weight Penalty," and "Added Toler" relate to the allowable difference from the "Opt+Tol" dimension of table 15. The design program will always accommodate the input tolerance band.

The Cylinder Optimization of Rings, Skin, and Stringers With Tolerance Sensitivity program gives the design engineer a tool to derive tolerances based on a specific need, rather than choosing them arbitrarily. Given the choice between manufacturing methods that can provide different tolerances at different costs, this is the definitive way to choose the best possible design.

During the design and development of advanced launch vehicles, design/analysis tools that provide product-oriented results are of critical significance. The development of this design technology will provide designers with a cost-effective and weight-savings design tool for the next generation of space vehicles.

Sponsor: Office of Advanced Concepts and Technology

• • • • •

SYSTEMS ANALYSIS AND INTEGRATION

Automated Rendezvous Guidance and Targeting

John M. Hanson/EL58
205-544-2239

An automated spacecraft rendezvous and docking system would reduce the cost of ground operations for a space station resupply mission or a rendezvous with other space vehicles. The actual phrase "automated rendezvous and docking" refers to an onboard system that steps through a sequence of events, including orbit transfers, to achieve chaser/target vehicle rendezvous and docking with no assistance from a ground support team. The system could be applied to NASA vehicles as well as to commercial microgravity and servicing missions. Guidance and targeting schemes to control the phasing of the two spacecraft, from arrival in orbit through rendezvous, are necessary for such an automated system to be successful. Also required are guidance schemes for terminal rendezvous through docking.

Ongoing work at MSFC includes the testing of an expert rule-based targeting system that determines the phasing orbits and orbit transfer times necessary for rendezvous. Efforts also involve the implementation of the targeting system and a guidance scheme—an optimal scheme based on the calculus of variations—in simulation. Missions to the space station at various altitudes and relative phasing angles are currently being simulated.

The phasing of two spacecraft can be quantified by the relative phase angle (the difference in the angular positions of the chaser vehicle and the target vehicle). The phase angle is gradually reduced as the two vehicles travel at different angular rates dictated by the difference in the size of the two orbits. The targeting scheme controls this phasing rate by controlling the intermediate orbits of the chaser vehicle and by supplying the guidance scheme with orbital targets and ignition times for each of the on-orbit burns.

The targeting system uses a rapid-phasing orbit after main engine cutoff (MECO) to achieve most of the phasing quickly (fig. 165). Two adjustable intermediate phasing orbits follow. The perigees of these intermediate orbits are chosen to give the proper total phasing for rendezvous.

Since the orbital energy is always increased, the rendezvous is achieved in a fuel-optimal manner. At the end of the rendezvous sequence, perigee and apogee burns place the chaser in the proper orbit relative to the target (usually behind the target and either in the same orbit or below the orbit by some specified distance). After arrival near the target, guidance and navigation procedures maneuver the vehicle in for docking or capture. The targeting scheme produces output that enables the launch window and orbital targets for launch vehicle ascent to be set automatically.

A second set of algorithms operates once the chaser and target vehicles are within some predetermined proximity and takes the chaser in to the capture or docking point. MSFC project efforts include the development and simulation of guidance schemes for
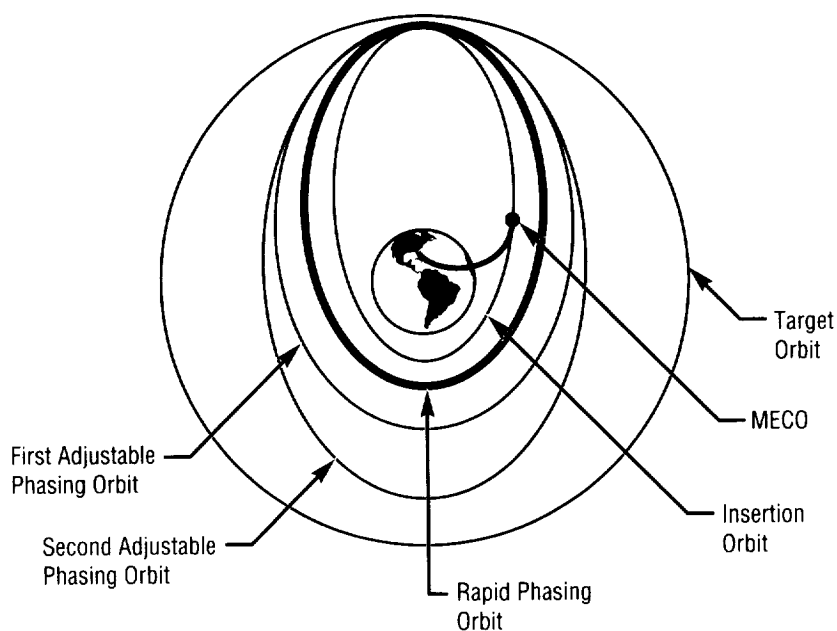
FIGURE 165.—Orbit phase adjustment.

moving in to the docking position. The chaser is assumed to use a passive proximity sensor for proximity navigation, and the chaser and target are both assumed to have Global Positioning System (GPS) receivers and to use a relative navigation filter for operation further apart. The guidance schemes are not necessarily optimal, but appear to work well. The primary difference between these and previously used methods is that they are intended to perform their tasks completely automatically, with relatively large velocity errors. An example of the simulated motion is shown in figure 166.

Deaton, A.W.; Lomas, J.J.; and Mullins, L.D. October 1992. A Plan for Spacecraft Automated Rendezvous, NASA TM–108385.

Hanson, J.M., and Deaton, A.W. Guidance Schemes for Automated Terminal Rendezvous, AAS–163. Presented at the 1994 American Institute of Aeronautics and Astronautics/American Astronautical Society (AIAA/AAS) Space Flight Mechanics Meeting.

Lomas, J.J.; Hanson, J.M.; and Shrader, M.W. Guidance and Targeting Simulation for Automated Rendezvous, AAS–162. Presented at the 1994 American Institute of Aeronautics and Astronautics/ American Astronautical Society (AIAA/AAS) Space Flight Mechanics Meeting.

Sponsor: Office of Space Flight

• • • • •
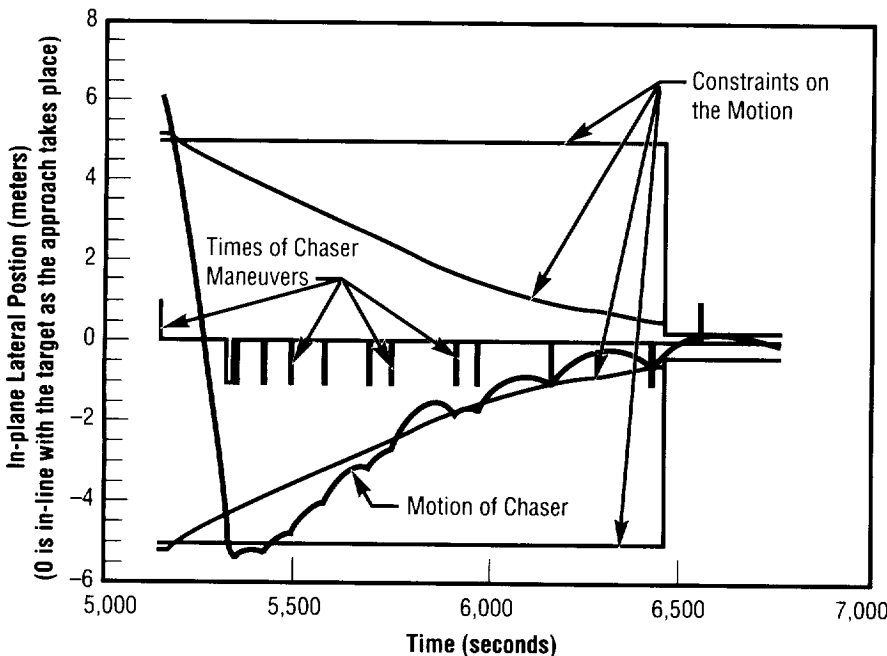
FIGURE 166.—Transfer between 100 meters and 10 meters from target.

Ascent Guidance Research

John M. Hanson/EL58
205–544–2239

Ongoing MSFC research is addressing issues in ascent guidance for launch vehicles. Studies include investigation of different open-loop (preset) and closed-loop (feedback) guidance schemes for a variety of potential launch vehicles. The proper ascent guidance reduces operations costs, reduces load indicator stresses on vehicles, and increases performance (mass to orbit).

According to a 1988 study on the space shuttle, about 20 percent of each mission's cost can be traced back to mission design—not primarily the design of the trajectories themselves, but rather the extensive effort expended to develop mission plans and timelines to ensure that the trajectories will be successful when flown and to ensure that the trajectories will satisfy vehicle constraints. While a change in philosophy towards mission design is crucial for cost reductions, the proper guidance scheme, if vehicle envelopes are defined, will enable ground programs to automatically verify that the trajectory will be successful. This eliminates the need to spend significant resources for each flight just to guarantee an acceptable ascent mission plan.

Ground efforts associated with engine-out situations, aborts (such as the return-to-launch-site aborts of the

shuttle), and verification of the trajectories could be significantly reduced through automated design or by closed-loop design onboard the vehicle. Improved ascent procedures could be coupled with automated mission design for orbital operations (e.g., automated mission design for rendezvous missions currently under development at MSFC).

Improved ascent guidance could also help control load indicators by adapting to actual in-flight conditions. A combination of day-of-launch wind design for loads reduction and an adaptive guidance would yield maximum launch availability by giving the best possible control over load indicator dispersions, possibly eliminating the need for load-relief control.

Improved guidance or trajectory design can also lead to increased performance (payload in orbit) by flying a more optimal trajectory, either through atmospheric open-loop or closed-loop optimization. During closed-loop operation, performance can be improved by adapting to actual in-flight dispersions, rather than relying only on those estimated preflight on the ground. Appropriate guidance schemes might also be flexible enough to be used for orbital transfers as well as for ascent guidance and may be adaptable to a variety of launch vehicles.

Presently, MSFC is comparing guidance schemes for four launch vehicle concepts that span a range of possible launch vehicle types. Results to date indicate that open-loop guidance designs that are functions of altitude or velocity are preferable to designs that are functions of time. Optimized open-loop trajectories can increase performance while maintaining load indicators within limits. Closed-loop atmospheric schemes that involve linear tangent steering or those that involve feedback of velocity terms for trajectory modification do not yield any improvement.

Early release of vacuum closed-loop guidance, including use during solid rocket booster operation, also yields improvements. In MSFC's research to investigate dispersions for several potential guidance schemes and launch vehicles, a closed-loop optimization scheme for flying through the atmosphere shows promise. Future work will complete the development of this closed-loop scheme and may include modification of a vacuum closed-loop optimization guidance to include atmospheric terms.

Bordano, A.J.; McSwain, G.G.; and Fernandes, S.T. February 1991. Autonomous Guidance, Navigation, and Control, AAS 91–022. Presented at the 14th Annual American Astronautical Society (AAS) Guidance and Control Conference, Keystone, Colorado.

Hanson, J.M.; Shrader, M.W.; Chang, H.P.; and Freeman, S.E. Guidance and Dispersion Studies of National Launch System Ascent Trajectories, AIAA 92–4306. Proceedings of the 1992 American Institute of Aeronautics and Astronautics (AIAA) Guidance and Control Conference.

Hanson, J.M.; Shrader, M.W.; and Cruzen, C.A. August 1994. Ascent Guidance Comparisons, AIAA 94–3568. Proceedings of the 1994 AIAA Guidance and Control Conference, Scottsdale, Arizona.

NITROX Use in Class III Extravehicular Mobility Unit (Space Suit)

Gene A. Hartsfield, Jr./EL67
205-544-6965

The Neutral Buoyancy Simulator (NBS) was chosen as the chief training facility for the STS–61 crew (Hubble Space Telescope (HST) first service mission). This particular simulator was selected primarily because it was large enough to accommodate a standard-size orbiter cargo bay equipped with two pallets of hardware and a full-size telescope mock-up. Both the cargo bay and telescope hardware were configured as if in flight.

Five extravehicular activities (EVA's) would be necessary to accomplish all of the required tasks involved in the Hubble Space Telescope complex service mission. Each activity was projected to be 6 hours in duration. In order for all hardware to be held in the tank at the same time, the entire depth—40 feet—of the simulator would be utilized. In the past, diving in the Neutral Buoyancy Simulator had always been governed by the standard U.S. Navy air-dive tables, which limited dive times to 200 minutes at this water depth. The depth- and length-of-time requirements posed a definite problem: crew members could become "bent" (which occurs when nitrogen bubbles form in body tissue).

Options to prevent such a problem were to reduce either the depth, time, or the amount of nitrogen the crew members were to breathe. Since the 40-feet depth was mandatory to accommodate all telescope hardware, and the 6-hour extravehicular activity times were minimums, the only viable alternative was to reduce the nitrogen in the breathing mixture. Even though the private sector had been using a NITROX (increased oxygen/reduced nitrogen) mix for scuba divers for some time, never before had the mix been used in a closed system. For these particular depth and time constraints, plus an additional 40 minutes for safety (400 minutes total), the mix would require 46 percent oxygen, with the balance nitrogen. The highest oxygen mix that had been used commercially for scuba diving was 36 percent to date.

Because the mixture contained a higher percentage of oxygen and was being supplied to a Space Suit Assembly (SSA), the risk for fire in the suit or the supply system was greatly increased. If a fire were to occur, the person in the suit would be seriously, if not fatally, injured.

Since oxygen and a combustible material (two of the three required components necessary for a fire to occur) were inherent in the Space Suit Assembly, the third item, the ignition source, must be totally eliminated. The most likely ignition sources stemmed from a suit's electrical systems (the communication system), particle impingement in the gas system supplying the suit, and system hydrocarbons. The electrical concern was reduced by limiting the electrical current to the suit assembly to only a few milliamperes. The particle impingement was satisfied by proper sizing of the piping to reduce velocities and by adding filters to the piping system. The hydrocarbons were removed by cleaning all system components and keeping all components clean during manned testing.

The NITROX system was placed in service and tested before the final dress rehearsal of STS–61 at the Neutral Buoyancy Simulator in October 1993. The NITROX system was deemed a complete success. The crew of the STS–61 acknowledged that the addition of the system greatly enhanced the fidelity of training for their mission. The system is currently in service and can be used for crew extravehicular activity training in the future, such as for the space station.

Sponsor: Office of Space Flight

· · · · ·

ENVIRONMENTS

A New Vector Wind Profile Model for Launch Vehicle Design

Charles K. Hill/EL02
205-544-1664

A new vector wind profile model has been developed for application in the initial phase of launch vehicle design to establish baseline dispersions for critical aerodynamic load indicators and to establish propellant reserve to protect for flight performance dispersions attributable in part to wind profile dispersions. This new model is an improvement of the original vector wind model developed for the shuttle program. The basic statistical concept of the new model is that wind components at any two selected altitudes are quadravariate normal (QN) distributed, defined by 14 statistical parameters. Given the wind components at a reference altitude, the distribution of the wind components at any other altitude is conditional bivariate normal.

Wind profile construction is a straightforward application of the statistical model. The configuration of the computer code for implementation of the model produces 12 vector wind profiles for each of 28 reference altitudes from 0 to 27 kilometers (km). Profile construction using this model is for monthly reference periods; as few as 2 months (February and July at Kennedy Space Center (KSC)) are representative of the annual wind profile dispersion. Alternatively, the annual dispersion can be derived by specification of the given wind vector

from an ellipse that envelopes the monthly ellipses at the selected reference height. Model statistical parameters are calculated from the Kennedy Center's 19-year, serially complete Rawinsonde (1956 to 1974) wind profile data base.

The new vector wind model has been used in design studies for the National Launch System (NLS). Aerodynamic load indicators were calculated with a six-degree-of-freedom trajectory simulation for a 90-degree flight azimuth using 1,800 (150 per month) Jimsphere-measured wind profiles and 336 wind profiles from the new vector

wind model configured to envelop the annual dispersion. Vehicle steering established prior to trajectory simulation was biased with respect to a nominal wind profile. Trajectory simulation included vehicle control system response to correct for flight wind profile deviation from the nominal wind profile, an important contributor to aerodynamic loads because of the relationship between vehicle control and vehicle attitude. Model wind profiles produced dispersion in aerodynamic load indicators that covered the dispersion range calculated from an extensive sample of Jimsphere wind profiles
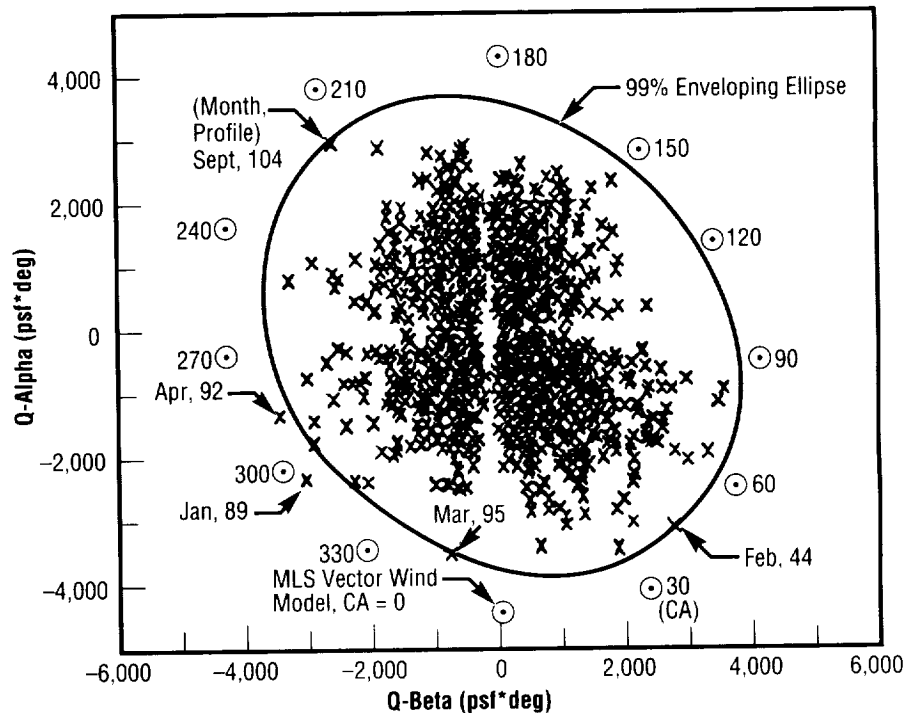
FIGURE 167.—Aerodynamic load indicators, Q*ALPHA and Q*BETA, at 12 kilometers obtained from trajectory simulations using 1,800 Kennedy Space Center Jimsphere profiles (150/month) and the 12 enveloping vector wind model profiles for H1 = 12 kilometers.
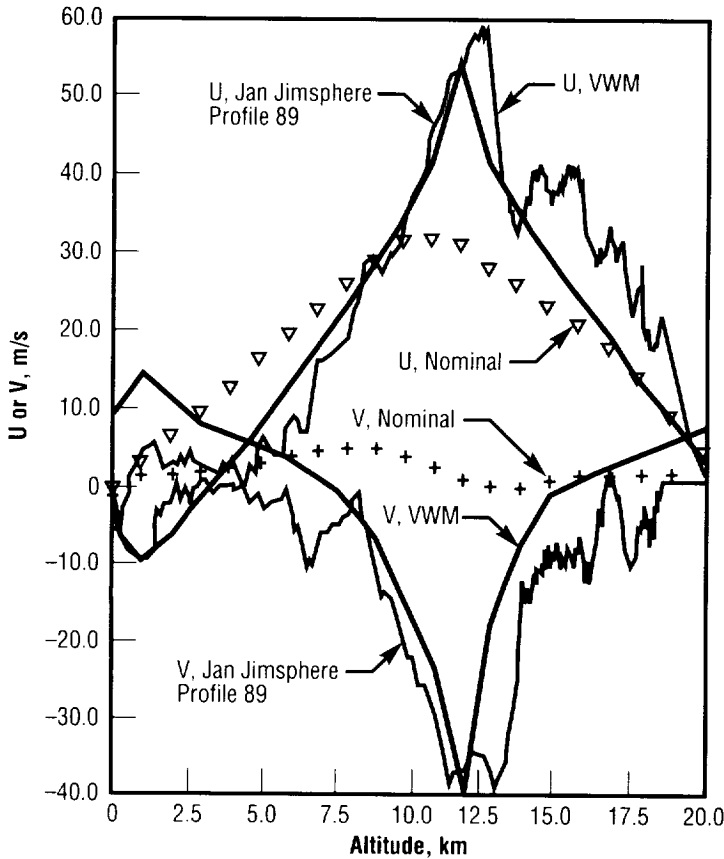
Figure 168.—Enveloping vector wind model (VWM) profile for 300-degree clocking angle (CA) and 12-kilometer reference altitude, January 1989 Kennedy Space Center Jimsphere profile, and nominal wind profile used to bias ascent vehicle steering.

Smith, O.E., and Austin, L.D. September-October 1983. Space Shuttle Response to Ascent Wind Profiles. *Journal of Guidance Control and Dynamics*, AIAA 6:5:355–360.

Smith, O.E.; Adelfang, S.I.; and Brown, R.P. January 1988. Ascent Structural Wind Loads for the National Space Transportation System (NSTS), 88:0293. Proceedings of the AIAA 26th Aerospace Sciences Meeting.

Smith, O.E.; Adelfang, S.I.; Batts, G.W.; and Hill, C.K. August 1989. Wind Models for the NSTS Ascent Trajectory Biasing for Wind Load Alleviation. NASA TM–100375.

Sponsor: Office of Space Flight

Industry Involvement: New Technology, Inc. (Stanley I. Adelfang, Orvel E. Smith, and Glen W. Batts)

(1,800 Jimsphere profiles for a selected reference altitude compared to 12 model wind profiles). Findings indicate that this wind model should be used in the initial design phase for future NASA launch vehicles (figs. 167 and 168).

Adelfang, S.I.; Smith, O.E.; and Batts, G.W. May–June 1994. Ascent Wind Model for Launch Vehicle Design. *Journal of Spacecraft and Rockets* 31:3:502–8.

Smith, O.E., July 1976. Vector Wind and Vector Wind Shear Models 0–27 Kilometer Altitude for Cape Kennedy, Florida, and Vandenburg Air Force Base, California. NASA TMX–73319.

Smith, O.E., and Austin, L.D. March 1982. Sensitivity Analysis of the Space Shuttle to Ascent Wind Profiles. NASA TP 1988.

Space Shuttle Launch Probabilities for Assigned Weather Constraints to Support Space Station Requirements

Charles K. Hill/EL02
205-544-1664

Space shuttle launch operations to support space station assembly are constrained by weather conditions. A study—motivated by a meteorology team (one of four teams) tasked to investigate methods for improving space shuttle capabilities to meet space station assembly requirements—has established probabilities for shuttle launch and emergency return-to-launch-site (RTLS), given certain weather constraints. The goal of the study has been to ensure that a launch could occur with a 95-percent probability, given 11 opportunities within a 16-day period. Launch probabilities for assigned weather constraints were calculated for specific operational timeline characteristics:

- A launch opportunity occurs at approximately the same hour of the day for the 16-day period.

- The launch window is 5 minutes.

- There are two consecutive launch opportunities (one per day) followed by a stand-down day, with repetition thereafter until a launch is made.

- There are at most 11 launch opportunities in a 16-day period.

The study team proposed the addition of three revisionary weather constraints—cloud ceiling, crosswind, and the southerly wind components—to the existing eight baseline operational weather constraints. An analysis of 35 years of weather data at Kennedy Space Center (KSC) suggested that improvement in shuttle launch availability could be achieved with the incorporation of the team's proposed revisions to current operational weather constraints, and would result in a decrease in the number of launch opportunities necessary to achieve a 95-percent launch probability. Of course, this increased success percentage must counterbalance the costs of implementing these findings, which

TABLE 18.—*Minimum number of launch opportunities needed to achieve at least a 98.3-percent launch probability for weather constraints alone, Kennedy Space Center*

Minimum Number of Opportunities													
		Month											
TIME /		1	2	3	4	5	6	7	8	9	10	11	12
EST	GMT/	BN	BN	BN	BN	BN	BN	BN	BN	BN	BN	BN	BN
0	5	55	43	43	33	33	32	22	33	54	43	54	65
1	6	54	43	44	33	33	32	22	33	43	54	54	54
2	7	55	44	33	33	33	32	22	33	44	44	54	54
3	8	55	44	43	33	33	33	22	33	43	44	54	54
4	9	55	44	43	33	33	32	22	33	33	44	55	66
5	10	55	44	43	32	33	32	32	33	43	44	55	66
6	11	55	54	53	33	33	33	33	33	44	54	66	66
7	12	66	55	54	33	43	33	32	33	44	54	66	86
8	13	65	55	65	43	43	33	22	43	44	54	65	65
9	14	65	64	54	43	43	33	32	43	54	55	64	55
10	15	65	65	54	53	43	43	33	44	54	55	65	64
11	16	75	65	74	53	43	43	43	43	64	65	65	66
12	17	65	64	64	64	44	43	43	53	64	65	65	64
13	18	64	75	75	53	54	44	43	43	64	55	55	65
14	19	74	75	64	53	54	55	44	44	84	55	54	64
15	20	64	65	74	54	64	65	54	54	64	55	54	54
16	21	54	55	64	54	64	65	44	43	64	55	54	64
17	22	54	54	54	53	64	64	54	54	44	54	44	55
18	23	55	54	54	43	54	44	44	44	44	44	54	54
19	0	55	54	44	43	44	43	43	33	43	54	54	54
20	1	55	54	44	33	43	33	33	53	54	64	54	55
21	2	55	54	44	33	33	33	33	33	44	54	55	54
22	3	55	64	44	33	33	33	33	33	54	44	54	54
23	4	55	43	43	33	33	33	33	33	44	54	55	55

Column B: 8 Baseline Constraints
Column N: 5 Baseline +3 Recommended Constraints

TABLE 19.—*Improvement in launch probability for the revised weather constraints indicated by the listed distribution of the reduction in the number of launch opportunities needed to achieve a 98.3-percent launch probability*

Reduction of Opportunities	Month												All Months	
	1	2	3	4	5	6	7	8	9	10	11	12	Total	%
	Number of Hours (Out Of 24)													
0	13	7	6	11	12	12	15	15	9	12	8	8	128	44.44
1	7	12	11	7	9	11	9	7	9	11	15	11	119	41.32
2	3	5	5	6	3	1	0	2	5	1	1	5	37	12.85
3	1	0	2	0	0	0	0	0	0	0	0	0	3	1.04
4	0	0	0	0	0	0	0	0	1	0	0	0	1	0.35

will be evaluated by other study teams. At the same time, if the revised weather constraints are not implemented, a 95-percent launch probability for weather constraints will be achieved for, at most, five launch opportunities.

If other factors that influence launch probability (ascent structural loads constraints, transatlantic landing (TAL) site weather constraints, or malfunctions of flight systems or any one of several critical ground support systems) are taken into consideration, the probability level for weather constraints needs to be greater than 95 percent. To illustrate the statistical methodology for combining launch probabilities for weather constraints and other factors, the study team made some basic statistical assumptions:

• Launch delays attributable to other factors are independent of weather constraint delays.

• Launch delays attributable to other factors are modeled as independent Bernoulli trials.

• The launch probability for other factors for a single launch attempt is 57.2 percent.

• Four launch attempts are required to achieve a 96.6-percent launch probability for other factors.

• A 98.3-percent launch probability for weather constraints is required to achieve a combined launch probability of 95 percent $(.966 \times .983 = .95)$.

The hypothetical number of launch opportunities required to achieve a 95-percent combined launch probability varies from six (four for other factors plus two for weather) to twelve (four plus eight) for baseline, and from six (four plus two) to ten (four plus six) for the revised constraints. Hence, from this scenario the desired objective of 95-percent launch probability within 16 days can be achieved (tables 18 and 19).

NASA/ME Summary of Launch Probability Study Team Meeting. March 15, 1994.

Smith, O.E.; Adelfang, S.I.; and Batts, G.W. April 1,1994. Space Shuttle Launch Probabilities for Assigned Weather Constraints to Support Space Station Requirements, New Technology, Inc., Technical Note.

Smith, O.E., and Batts, G.W. January 1993. Atmospheric Statistics for Aerospace Vehicle Operations, 93–0756. 31st Aerospace Sciences Meeting, Reno, Nevada.

Smith, O.E.; Adelfang, S.I.; and Batts, G.W. May 25, 1994. Space Shuttle Launch Probabilities for Assigned Weather Constraints to Support Space Station Requirements. New Technology, Inc.

Space Shuttle Launch Probability to Support Space Station Assembly. Briefing Prepared By NASA/OSF.

Sponsor: Office of Space Flight

Industry Involvement: New Technology, Inc. (Orvel E. Smith, Stanley I. Adelfang, Glen W. Batts)

• • • • •

237

Sensitivity of Wind Loads Uncertainties to Wind Profile Smoothing

Charles K. Hill/EL02
205-544-1664

This study demonstrates how a wind profile measurement system with an altitude resolution less than the currently used Jimsphere system could be used for the shuttle prelaunch wind profile and ascent loads assessments for the commit-to-launch decision. The analysis to support this conclusion, however, requires high-resolution Jimsphere wind profile pairs to derive the appropriate load allowances for the combined effects of temporal- and reduced-wind profile resolution. These combined effects are included in a 99-percentile wind-load increment derived from a filtered (smoothed) first of each 3.5-hour Jimsphere wind profile pair and unfiltered second of each pair.

When the appropriate wind-load increment is used, the joint number of occurrences of wind profile go/no-go's for the low-pass, 1,500-meter (m) filtered first of each Jimsphere pair and unfiltered second of each pair is essentially the same as the number of go/no-go's for the unfiltered winds for both of the pairs.

The NASA 50-megahertz (MHz) Doppler wind profiler yields a wind profile with a resolution of roughly 750 meters. Therefore, the analysis for the 1,500-meter filtered first of each Jimsphere pair overestimates the wind-load increments when compared

to that which would be derived from a pair with resolution equivalent to the wind profiler.

This study establishes loads increments (allowances) for the resolution deficiency in prelaunch wind monitoring systems relative to the high-resolution Jimsphere system. This resolution deficiency is attributable to either the measurement system itself, such as the Doppler wind profiler and updated Rawinsonde, or the intentional low-pass filtering of the Jimsphere profile to remove spurious, transient small-wavelength perturbations. The derivation of an appropriate load allowance will be required to establish the viability of the NASA Doppler wind profiler for shuttle prelaunch wind profile and loads assessments for the commit-to-launch decision.

Adelfang, S.I.; Smith, O.E.; and Batts, G.W. January 1994. Sensitivity of Wind Loads Uncertainties to Wind Profile Smoothing, 94:0478. American Institute of Aeronautics and Astronautics (AIAA) 32nd Aerospace Sciences Meeting, Reno, Nevada.

Smith, O.E.; Adelfang, S.I.; and Brown, R.P. January 1988. Ascent Structural Wind Loads for the National Space Transportation System, 88:0293. AIAA 26th Aerospace Sciences Meeting, Reno, Nevada.

Smith, O.E., and Adelfang, S.I. January 1992. STS Ascent Structural Loads Statistics, 92:0720. AIAA 30th Aerospace Sciences Meeting, Reno, Nevada.

Wilfong, T.L.; Smith, S.A.; and Creasey, R.L. May–June 1993. High Temporal Resolution Velocity Estimates From a Wind Profiler. *Journal of Spacecraft and Rockets* vol. 30:3:348–354.

Space Transportation System Ascent Structural Loads Statistics

Charles K. Hill/EL02
205–544–1664

This study describes the application of extreme value (Gumbel) analytical-statistical probability functions in space transportation system (STS) loads assessments for the day-of-launch, commit-to-launch decision. This decision is based on trajectory and loads simulations using a wind profile 3.5 hours prior to launch. Load increments that protect for 99 percent of the load change during the 3.5-hour period are calculated for all wind-profile-sensitive load indicators.

Following the *Challenger* accident in January 1986, the shuttle Ascent Flight Systems Integration Group (AFSIG) explored new methods to account for the ascent wind-load change with respect to time—now called the wind-load persistence increment. Researchers established the concept of load minimum margin (LMM, fig. 169) and the statistical methodology to derive the wind-load persistence increment. The load minimum margin, an extreme value statistic, is obtained from simulations using 3.5-hour Jimsphere wind pairs for Kennedy Space Center (KSC). The univariate Gumbel probability distribution function (PDF) is used (fig. 170) to compute the probability for load excedences for each of the 41 most wind-sensitive load indicators. This yields the probability for launch without the wind-load
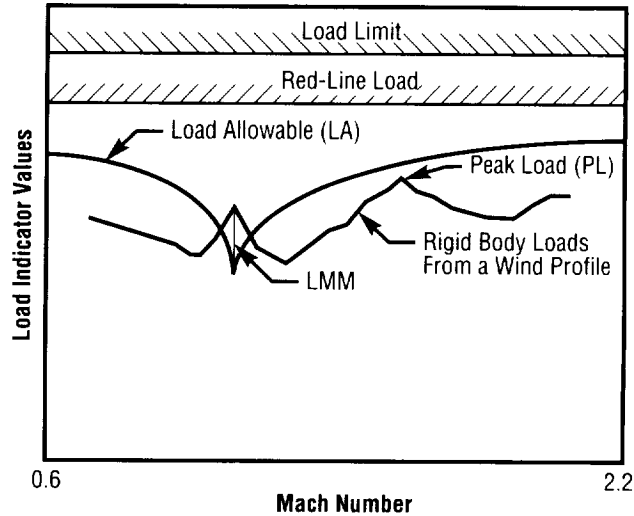
FIGURE 169.—Schematic for load minimum margin (LMM) and peak load (PL) from a wind profile loads simulation.
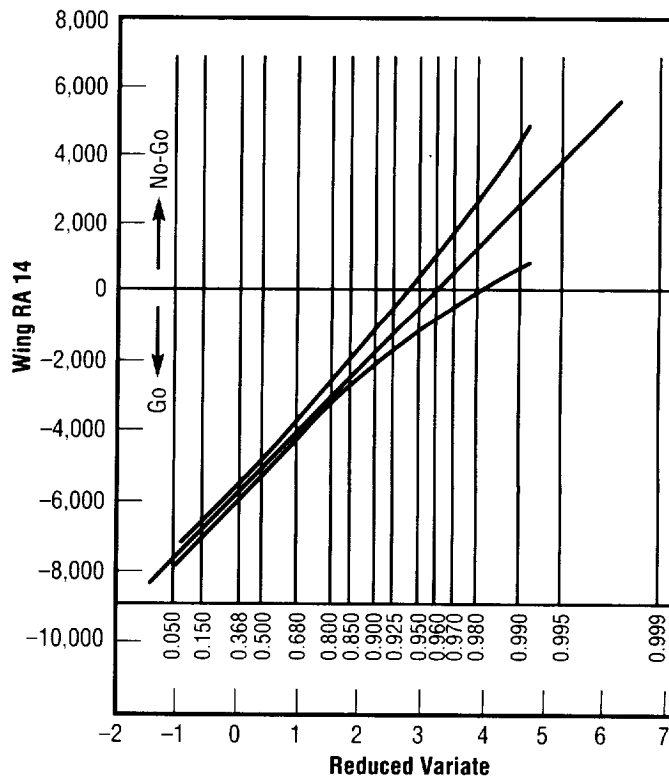
FIGURE 170.—Gumbel extreme value probability distribution for load minimum margin baseline I-Load for Wing RA 14 from the first of 114-winter, 3.5-hour wind pairs, Kennedy Space Center.

239

persistence increment. The conditional probability distribution function is derived from the Gumbel bivariate extreme value probability distribution function. The 99th-percentile time-conditional wind-load value is called the wind-load persistence increment. The differences between two Gumbel variates has the form of a logistic probability distribution function.

The results of the statistical analysis for two wing-load and two vertical tail-load indicators are presented in table 20 for three wind-load alleviation techniques. They include the baseline, which is a wind bias trajectory to the profile of monthly vector mean wind; the DIBS, which is a trajectory bias to the smoothed q-alpha and q-beta profile for the first of the 3.5-hour wind profiles (performed on the day of launch using the wind profile 3.5 hours prior to lift-off); and the FIBS, the same as DIBS but based on the filtered (smoothed) wind profile. In table 20, columns 2 and 3 are the Gumbel-reduced variates. Column 4 illustrates the load-allowable load minimum margin (LALMM), which is the 99th-percentile value based on the time-conditional probability distribution function or wind-load persistence increment. Column 5 is the launch probability after accounting for the wind-load persistence increment; column 6 is the 99-percent change in loads; and column 7 denotes the probability for launch using the logistic probability distribution function. The load-allowable load minimum margin is less than the baseline for DIBS and FIBS, and the probability for launch is greater for DIBS and FIBS than for baseline.

TABLE 20.—*The conditional 99th-percentile values (load allowable load minimum margin) and the 99th-percentile load change ($\Delta L_{.99}$) for load minimum margin from 3.5-hour wind pairs*

I-Load	X*	$Y_{.99}$	LALMM*	P (LALMM)	$\Delta L_{.99}$	$P(\Delta L_{.99})$
Col. 1	Col. 2	Col. 3	Col. 4	Col. 5	Col. 6	Col. 7
(a) Baseline						
Wing RA 14 (−)	3.210	1.062	−3743	.7066	4182	.6410
Wing LA 14 (−)	3.109	0.986	−3891	.6886	3964	.6775
VTL II (+)	5.372	3.422	−0.21	.9679	0.205	.9669
VTL II (−)	5.607	3.752	−0.10	.9768	0.1136	.9777
(b) DIBS						
Wing RA 14 (−)	4.443	2.103	−2850	.8850	3773	.7841
Wing LA 14 (−)	3.909	1.387	−3530	.7790	3762	.7412
VTL II (+)	9.135	6.776	−0.14	.9989	0.187	.9977
VTL II (−)	9.385	7.006	−0.13	.9991	0.098	.9998
(c) FIBS						
Wing RA 14 (−)	4.718	2.507	−2567	.9217	3963	.8128
Wing LA 14 (−)	3.822	1.460	−3457	.7928	3788	.7448
VTL II (+)	8.400	6.002	−0.12	.9975	0.200	.9906
VTL II (−)	10.583	8.188	−0.13	.9997	0.106	.9999

*This is the 99% wind loads persistence increment.

TABLE 21.—*Number of no-go wind profiles and empirical go probabilities for load minimum margin for 41 space transportation system load indicator variables from 114-winter, 3.5-hour Kennedy Space Center wind pairs*

I-Load	Without Wind-Load Resistance		With 99% Conditional Wind-Load Persistence #	
	# No-Go Winds	% of Go* Winds	# No-Go Winds	% of Go Winds
(a) Baseline				
1st of Pair	10	90	70	38
2nd of Pair	12	89	73	36
(b) DIBS				
1st of Pair	1	98	42	63
2nd of Pair	2	97	47	58
(c) FIBS				
1st of Pair	4	96	40	64
2nd of Pair	2	97	43	61

* Percent Go winds = (114 − # No-Go Winds/115) 100
# Wind-load persistence increment applied to both the 1st and 2nd of pairs

Table 21 presents the probability for launch (go versus no-go) for the occurrence of any one of the 41 load indicators with and without the wind-load persistence increment for Baseline, DIBS, and FIBS. The significance of the wind-load persistence increment is illustrated by the large reduction in the launch probability (percent go). The percent of go-wind profiles increases for DIBS and FIBS over that of the Baseline. The FIBS and DIBS launch probabilities are basically the same.

These ascent structural load statistical techniques have been implemented to determine the space transportation system launch probability and are used for the day-of-launch decisions. The fundamental principles described for the day-of-launch wind bias trajectory could be adapted for the design and operations of future NASA launch vehicle development programs.

Gumbel, E.J., 1958. *Statistics of Extremes*. New York: Columbia University Press, 57:10160.

Gumbel, E.J., and Mustafi, C.K. June 1967. Some Analytical Properties of the Bivariate Extreme Distributions. *American Statistical Association Journal* 569–588.

Smith, O.E., and Adelfang, S.I. January 1992. STS Ascent Structural Loads Statistics, 92:0720. Proceedings of the American Institute of Aeronautics and Astronautics (AIAA) 30th Aerospace Sciences Meeting and Exhibit, Reno, Nevada.

Smith, O.E.; Adelfang, S.I.; and Brown, R.P. January 1988. Ascent Structural Wind Loads for the National Space Transportation System, 88:0293. Proceedings of the AIAA 26th Aerospace Sciences Meeting, Reno, Nevada.

Sponsor: Office of Space Flight

Industry Involvement: New Technology, Inc. (Orvel E. Smith and Stanley I. Adelfang)

• • • • •

Global Reference Atmospheric Model

Dale L. Johnson/EL54
205–544–1665

One of MSFC's goals is to provide realistic atmospheric models that can be easily accessed by computers for valid design analyses. The NASA Global Reference Atmospheric Model (GRAM), instituted more than 20 years ago, aids in achieving this goal and has been continuously updated to meet everchanging requirements and capitalizes upon the advent of technologically advancing data bases. The global model has been used both in the design as well as in the operational planning phases of various NASA programs and projects, including the current Space Transportation System, Shuttle–II, Shuttle–C, the Orbital Transfer Vehicle, the Aeroassist Flight Experiment, the Advanced Launch System, the National Aerospace Plane, Single-Stage-To-Orbit, and others.

Being a three-dimensional, worldwide atmospheric model, the Global Reference Atmospheric Model currently provides monthly mean values, along with the variability (including large- and small-scale effects) of pressure, temperature, density, and winds from the Earth's surface up to 2,500 kilometers (1,553 miles) in altitude (table 22). These parameters can be output from any latitude/longitude/altitude location in the form of vertical profiles as well as trajectories. Monte Carlo simulations of the parameters, representing random realizations of the atmosphere along any path, are also possible.

TABLE 22.—*Global Refrence Atmospheric Model–90 tabular output example*

Page
1

Page
2

In its latest version, Global Reference Atmospheric Model–90 (GRAM–90), the model is currently undergoing revision by a team from Computer Science Corporation (CSC) under the direction of the Electromagnetics and Environments Branch (EL54) of the MSFC's Systems Analysis and Integration Laboratory. Project goals include incorporating an improved, low-level (surface to 25-kilometer altitude), global data base to provide better values of the standard output parameters within that layer. (Figure 171 depicts a graphical zonal wind comparison of one candidate data base with the Global Reference Atmospheric Model–90 and the Kennedy Range Reference Atmosphere.) In addition, the code is being streamlined for faster computational operation and will include various atmospheric constituent values, including moisture, from the surface to orbital altitudes. This new version, tentatively identified as the Global Reference Atmospheric Model–95 (GRAM–95) (for planned release in 1995), will provide the flight community with a more accurate, cohesive reference atmosphere, valid from the surface to Earth orbit, for use in both engineering and scientific analyses.

Sponsor: Office of Space Flight

Industry Involvement: Computer Science Corporation (Jere Justus and William Jeffries)
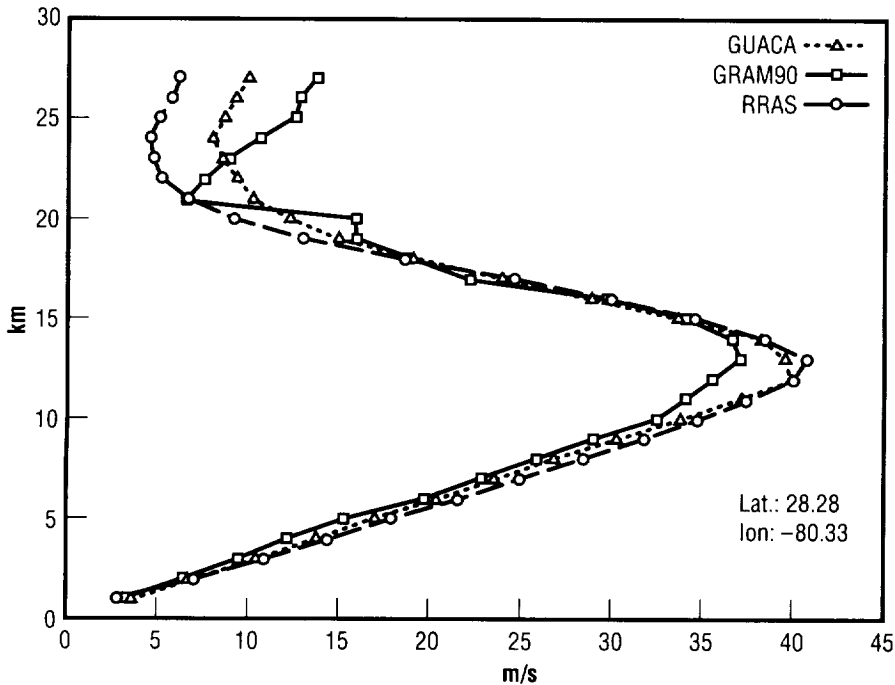
FIGURE 171.—Graphical wind comparison of Global Reference Atmospheric Model-90 and the Kennedy Range Reference Atmosphere.

Terrestrial and Space Environment Reference Documents

Dale L. Johnson/EL54
205-544-1665

B. Jeffrey Anderson/EL54
205-544-1661

Two key documents describing the natural environment—both used extensively in spacecraft design, mission planning, and analyses—have been completely updated by the Electromagnetics and Environments Branch of the Systems Analysis and Integration Laboratory. One of these documents, *Terrestrial Environment (Climatic) Criteria Guidelines for Use in Aerospace Vehicle Development, 1983 Revision* (NASA TM-82473), has been updated to NASA TM-4511, 1993 revision (keeping the same title). The other, *Space and Planetary Environment Criteria Guidelines for Use in Space Vehicle Development, 1982 Revision, Volume 1* (NASA TM 82478), has been updated to *Natural Orbital Environment Guidelines for Use in Aerospace Vehicle Development*, NASA TM-4527 (1994). In this case, all of the lunar and planetary data were excluded in the new document and were replaced with a greatly expanded description of the near-Earth space environment experienced by low-Earth orbiting spacecraft. These two documents present comprehensive Earth and near-Earth natural environment information in a concise statistical format ideal for the aerospace engineering community. These data may be tailored to meet specific space system design and

Scales VII to XI shown are the modified
Mercalli intensity scale of 1931.

0   100   200 miles

0   100   200 kilometers

Index map showing approximate
region (shading) where epicenters
might occur.
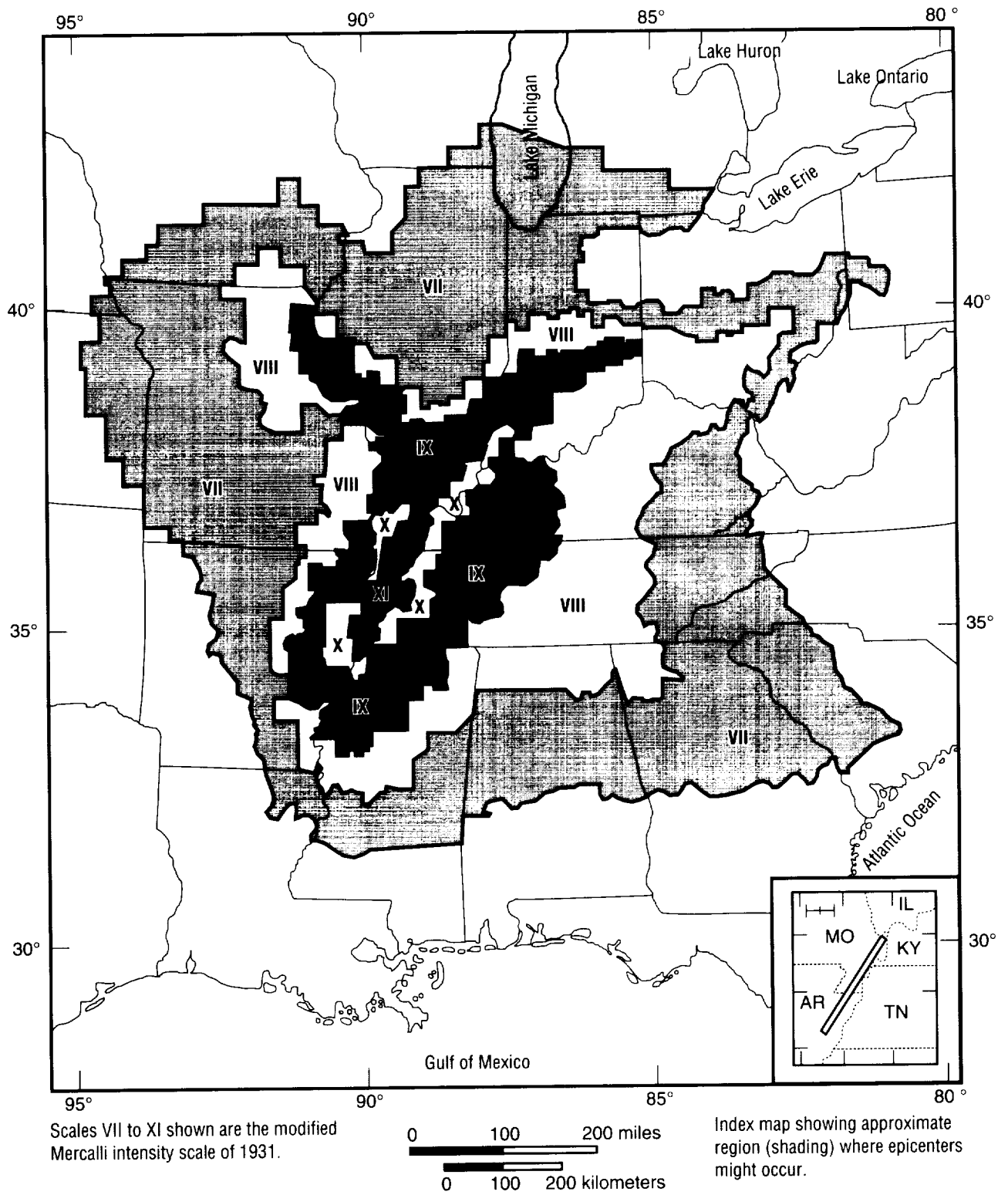
FIGURE 172.—Estimated maximum regional seismic intensities associated with great earthquakes that could occur along
the New Madrid seismic zone.

development needs where advanced environmental information is required.

The terrestrial environment document (NASA TM–4511) provides environments information for the 0- to 90-kilometer (km) altitude range. Perhaps the most important update is presented in section II, "Winds/ Ground and Aloft." Here, the wind modeling information provides a greatly improved capability for the estimation of wind loads and their effects on the design and development of launch vehicles and for use in mission planning studies in general. Other improvements were made in the descriptions of atmospheric electricity and atmospheric constituents, as well as in vehicle exhaust, atmospheric moisture aloft, and earthquake and sea-state statistics. This reference document also provides the user with information concerning atmospheric models, radiation, precipitation, fog and icing, cloud cover, and tornado/ hurricane statistics. Figures 172 and 173 present examples of expected seismic intensities and raindrop sizes that can be used in design study analyses.

The material used to update the document describing the orbital environment (NASA TM–4527) was developed primarily because of the technical challenges presented by space station and other NASA programs over recent years. In particular, the necessity for developing a guidance, navigation, and control system capable of providing long-duration microgravity environments and difficulties related to the design of various thermal control systems led to detailed analysis of atmospheric density and environmental thermal parameter variations experienced at
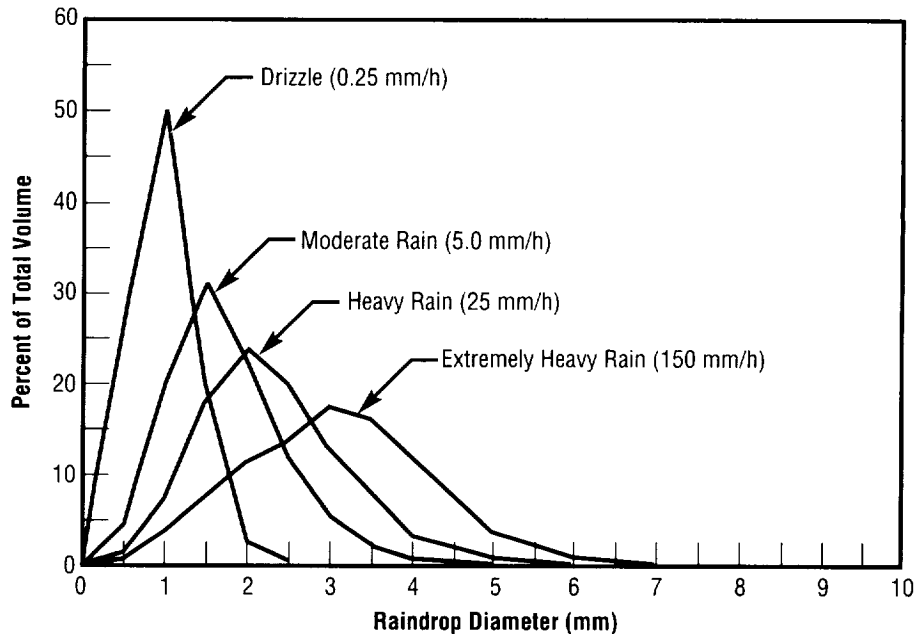
FIGURE 173.—Distribution of raindrop sizes.
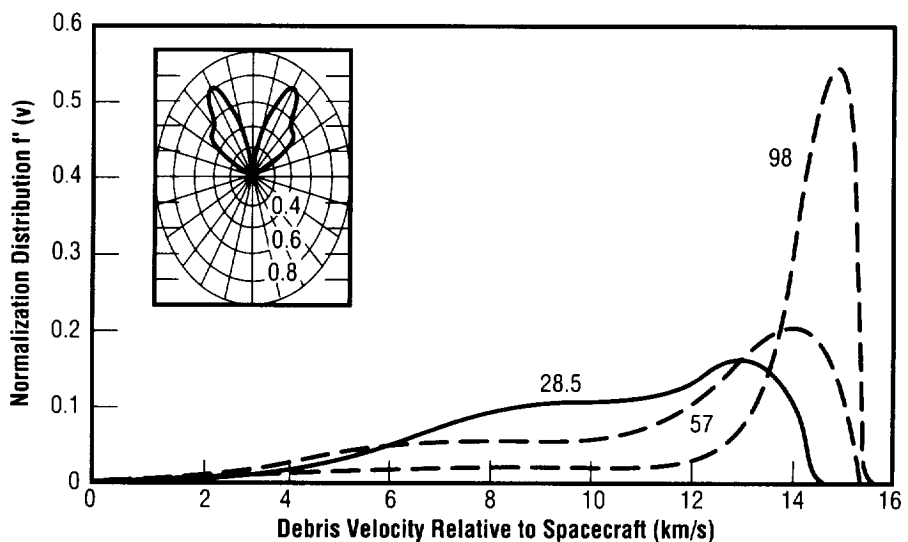
FIGURE 174.—Normalized collision velocity distribution as a function of the debris velocity for a spacecraft with orbital inclinations of 28.5°, 57°, and 98°.

245
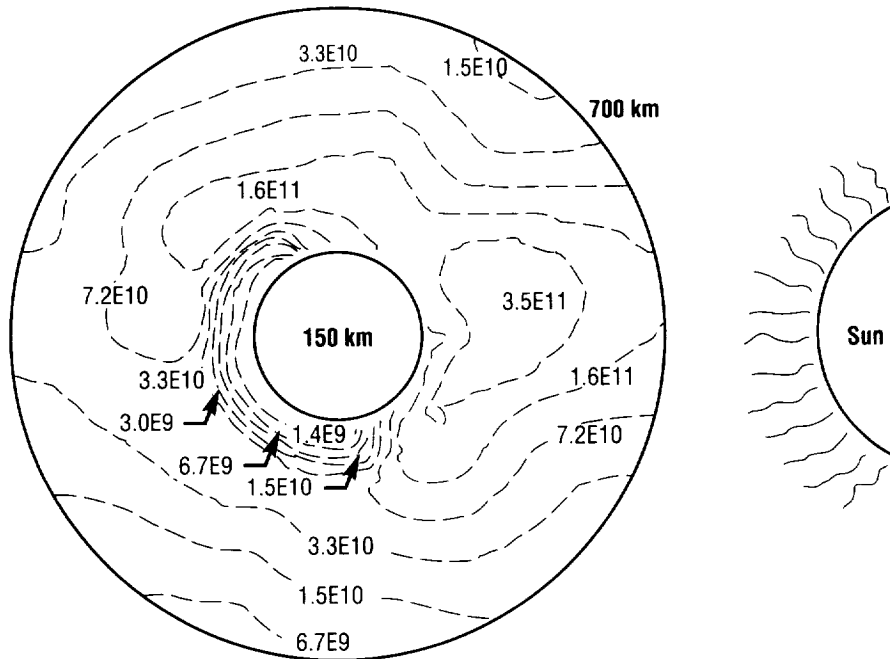
FIGURE 175.—Noon-midnight cross-section view of plasma density (m^{-3}) as a function of altitude from 150 to 700 kilometers for June 21; solar minimum conditions ($F_{10.7}$=70.1, contours in the 0° and 180° longitude plane; IRI90 results with default options selected).

Spacecraft/Environmental Interaction: Spacecraft Charging Overview

Matthew B. McCollum/EL54
205–544–2351

Above an altitude of approximately 90 kilometers, a portion of the molecules comprising the Earth's atmosphere is ionized by solar radiation, producing positively charged ions and free electrons. This collection of electrically charged particles—known as the natural space plasma—occurs in all spacecraft orbits. The energy of the charged particles causes them to move continuously, which creates an electric current. When a spacecraft orbits the Earth, some of this current flows to the spacecraft, causing charge to accumulate on its exposed surfaces. The charge accumulation—a phenomenon known as "spacecraft charging"—can cause such unwanted effects as arc discharging, increased surface contamination, and sputtering.

Natural space plasma is a source of both negative and positive current to spacecraft surfaces. Plasma electron incidence on spacecraft surfaces creates a negative current, while plasma ion incidence creates a positive current. The natural space plasma is not, however, the only source of electric current to spacecraft surfaces. Others include photo and secondary electron currents (which are positive currents) composed of electrons liberated from spacecraft surface materials when given sufficient energy by solar radiation or impinging plasma particles.

orbital altitudes. This document presents the results of this work in a handy statistical format. The orbital debris and micrometeoroid environment descriptions were also developed, at least partially, out of work motivated by the space station (fig. 174). Work on other programs expected to fly in polar orbits led, similarly, to an expanded description of the ionospheric plasma (low-energy charged particle) environment (fig. 175). This document also includes descriptions of ionizing radiation, electromagnetic radiation,

solar cycles, and magnetic and gravitational fields, so that all areas of the low-Earth orbit natural environment are described.

Sponsor: Office of Space Flight

• • • • •

The relative magnitudes of the different sources of positive and negative current depend on the properties of the natural space plasma, sunlight conditions, and the electrical properties of spacecraft surface materials. If the sum of the positive and negative currents are not equal, spacecraft charging occurs and a net charge will accumulate on spacecraft surfaces. As one type of charge accumulates (negative or positive), it generates an electric force field that decelerates like-charged particles (decreasing their current, positively or negatively) and accelerates oppositely charged particles (increasing their current, positively or negatively). The process continues until the accelerated particles can be collected rapidly enough to balance the currents. At this point, the spacecraft has reached its equilibrium charging level, or
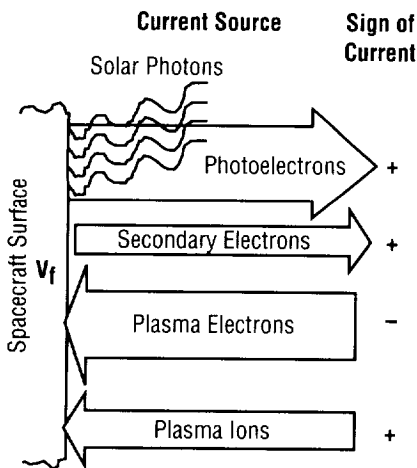
FIGURE 176.—Sources of electric current to a spacecraft surface. (Arrows show the direction of the current flow; the width of the arrows is proportional to the flux of each charged particle species.)

"floating potential," V_f, and no more charges accumulate (fig. 176).

If the spacecraft is all metal (i.e., conductive), the entire spacecraft will be charged to the same equilibrium or floating potential. If, however, dielectric exterior surface materials have been used and the electric current varies, different surfaces may charge to different floating potentials, a process called "differential charging." (Dielectrics are poor distributors of accumulated charge because they maintain a portion of the charge deposited on them.) A variation in the charged particle flux causes surfaces to reach different floating potentials. The largest levels of differential charging typically develop between sunlit and shaded surfaces since the photoelectron current (which in some cases can be the largest source of positive current to a surface) maintains the floating potential of sunlit surfaces positive relative to shaded surfaces (fig. 177). A difference in floating potentials produces an electric force field—causing stress in surface materials and possibly leading to arc discharging—between two surfaces.

Spacecraft charging occurs in all orbits, although the highest levels of charging, with typically the worst effects, occur when spacecraft encounter high-energy plasma. At high inclination, low-altitude, Earth-orbit spacecraft can be charged to large negative values by energetic electrons precipitating from the magnetosphere during auroral events. This is similar to the situation in geosynchronous orbit (GEO), where spacecraft frequently encounter high-energy plasma associated with geomagnetic substorms. The low inclination, low-Earth orbit (LEO) plasma has a
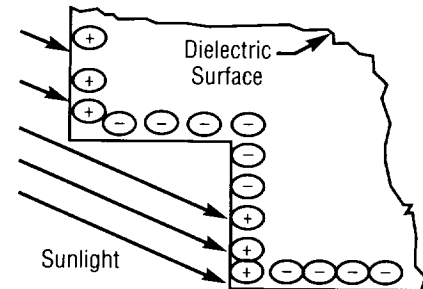
FIGURE 177.—Differential charging.

relatively low energy and typically does not charge spacecraft surfaces to high levels independently. However, interaction between the plasma and exposed, electrically biased surfaces (e.g., solar arrays) can cause high levels of charging that lead to arc discharging, increased surface contamination, and sputtering.

The fact that spacecraft charging occurs in all orbits makes it an important issue in the design of any spacecraft. As in response to other natural environmental effects, such as those from the thermal or ionizing radiation environments, a spacecraft can be designed to minimize the detrimental effects attributed to spacecraft charging. This requires both an understanding of the natural space environment and a knowledge of how the interaction between that environment and a spacecraft leads to spacecraft charging.

Sponsor: Office of Space Flight

Industry Involvement: Sverdrup Technology, Inc. (Joel L. Herr)

• • • • •

Spacecraft Thermal Environment Modeling

Bonnie F. James/EL54
205-544-6985

Correct definition of the orbital thermal environment—which varies significantly over orbit and over a mission's lifetime—is an integral part of an effective spacecraft thermal design. Because temperature control requirements for spacecraft components should normally fall within a predetermined range, temperature fluctuations need to be minimized to prevent system fatigue. One of the most frequently encountered concerns is the ability to provide adequate heat rejection to cold-sensitive systems. Fluctuations in temperature can fatigue different system components and lead to system failures. Another major concern is the possibility of excessive freeze-thaw cycling of thermal control fluids caused by abrupt changes in the thermal environment which may require oversizing of radiators or permanent radiator freezing.

Spacecraft receive radiant thermal energy from three sources—incoming solar radiation (from which the solar constant is derived); reflected solar energy (albedo); and outgoing longwave radiation (OLR), which is emitted by the Earth and its atmosphere—and radiate or reflect it to the cold sink of space. When one considers the Earth and its atmosphere as a whole and averages long periods
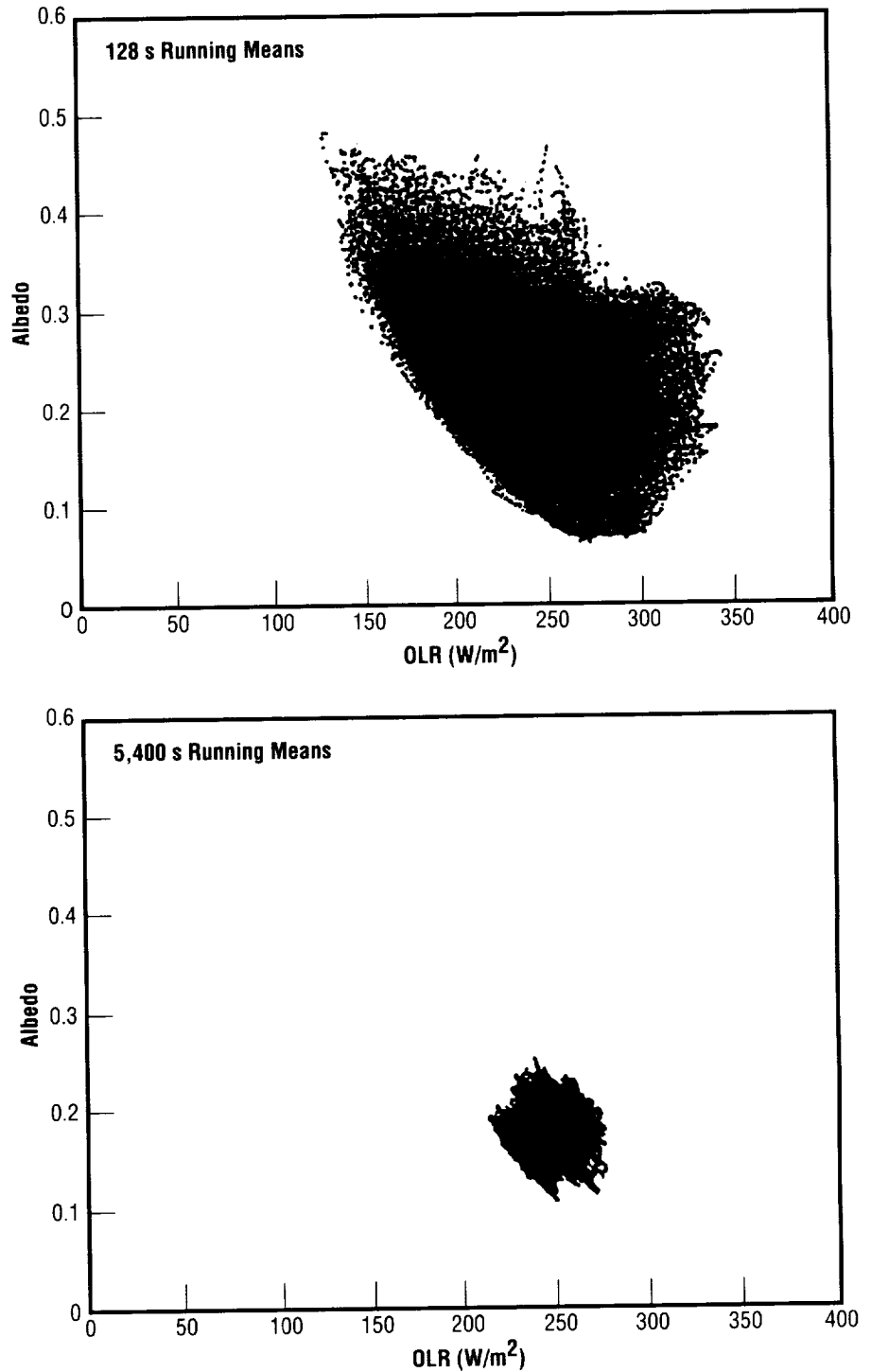
FIGURE 178.—Altitude/outgoing longwave radiation correlated pairs for 30° inclination orbits.

of time, the incoming solar energy and outgoing longwave radiation energy are essentially in balance. However, they are not in balance everywhere on the globe, and there are variations with respect to local time, geography, and atmospheric conditions. A spacecraft's motion with respect to the Earth results in its sensing only a particular swath across the full global thermal profile.

The Electromagnetics and Environments Branch of the Systems Analysis and Integration Laboratory is conducting a study of the variations of the albedo and outgoing longwave radiation to improve initial environments inputs into spacecraft thermal design models. The study uses data from the Earth Radiation Budget Experiment (ERBE, which began in the 1980's and is still ongoing), a comprehensive, multisatellite experiment that has as its primary objective global data collection of such Earth radiation budget parameters as incident sunlight (solar constant), reflected sunlight (albedo), and outgoing longwave radiation. This experiment was selected because of its thorough coverage and its up-to-date information.

The results of this study provide the design engineer with a description of how albedo and outgoing longwave radiation vary and correlate for differing orbital characteristics (fig.178). Final study results should provide the thermal design community with a much more accurate and comprehensive representation of the thermal environment for use in spacecraft thermal design, development, and operations.

Sponsor: Office of Space Flight

Industry Involvement: New Technology, Inc. (G. Wade Batts)

• • • • •

Protecting Against the Effects of Spacecraft Charging

Matthew B. McCollum/EL54
205-544-2351

Spacecraft charging is the process by which all orbiting spacecraft accumulate electric charge from natural space plasma. A thorough understanding of this process is necessary because the effects attributed to spacecraft charging—arc discharging and surface material degradation by increased contamination and sputtering—have proven to be of serious engineering concern. One method to protect against these detrimental effects is to implement a spacecraft charging effects protection plan, which includes adopting design guidelines that limit spacecraft-charging-related effects and performing computer analyses to assess the risks of design choices that are less than ideal from a spacecraft-charging standpoint.

The accumulation of charge on exposed surfaces of a spacecraft is caused by unequal negative and positive electric currents to spacecraft surfaces. Sources of electric current include positive ion and negative electron currents from natural space plasma, as well as photo and secondary electron currents composed of electrons liberated from spacecraft surface materials when given sufficient energy by solar radiation and impinging plasma particles. Spacecraft surfaces accumulate charge until the generated electric field can

equilibrate the positive and negative currents, which results in no net current being collected. At this point, the spacecraft has reached its equilibrium charging level or "floating potential," with a value depending on the relative magnitudes of the different sources of current.

Spacecraft charging occurs in all orbits, although the highest levels of charging, with typically the worst effects, occur when spacecraft encounter high-energy plasma. At high inclination, low-altitude, Earth-orbit spacecraft can be charged to large negative values by energetic electrons precipitating from the magnetosphere during auroral events. This is similar to the situation in geosynchronous orbit (GEO), where spacecraft frequently encounter high-energy plasma associated with geomagnetic substorms. The low-inclination, low-Earth orbit (LEO) plasma has a relatively low energy and typically does not charge spacecraft surfaces to high levels independently. However, interaction between the plasma and exposed, electrically biased surfaces (e.g., solar arrays) *can* cause high levels of charging.

The primary mechanism by which spacecraft charging disturbs mission activities is through arc discharging— when generated electric fields from spacecraft charging exceed breakdown thresholds. The arc-discharge process rapidly releases large amounts of electric charge that gives rise to currents flowing in the spacecraft's structural elements. The arcing produces a broadband electromagnetic field which can couple into spacecraft electronics and cause operational anomalies ranging from minor irritations (i.e., telemetry glitches,

logic upsets, component failure) to the fatally catastrophic. An example of a spacecraft charging event leading to arc discharging is shown in figure 179.[1] The upper panels are spectrograms of electron and ion fluxes showing the encounter of the P78-2 spacecraft with a high-energy geomagnetic substorm. The bottom panel illustrates the charging level of a dielectric Kapton surface relative to the underlying structure and the occurrence of two discharges detected by the pulse analyzer.

Besides generating electromagnetic interference, arc discharging produces localized heating and ejection of surface material from the arc-discharge site. The loss of material degrades spacecraft structural integrity and alters the properties of spacecraft surface materials. Other spacecraft-charging-related effects of concern include degradation of spacecraft surface material properties due to increased surface contamination and

ion sputtering. In the case of sputtering, large negative floating potentials of spacecraft surfaces accelerate positively charged ions to high energies, leading to the physical removal of surface atoms (i.e., sputtering) by the impacting ions. Contamination occurs when organic molecules, outgassed from spacecraft surfaces and ionized while still near the spacecraft, are attracted to negatively charged surfaces. The more negative the floating potential of a surface, the greater the probability of its contamination.

A spacecraft charging effects protection plan protects against the detrimental effects of spacecraft charging. Such a plan includes defining the natural space plasma to which the spacecraft will be exposed and developing design guidelines with the purpose of reducing or eliminating the harmful effects attributed to spacecraft charging. An important step in implementing a protection plan is
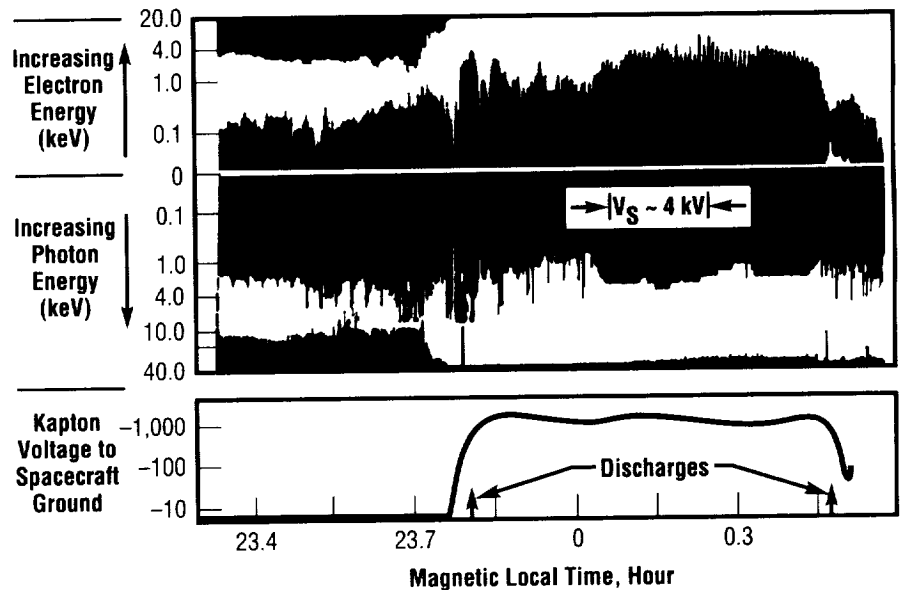
Figure 179.—Spacecraft charging event on P78-2 spacecraft in eclipse.
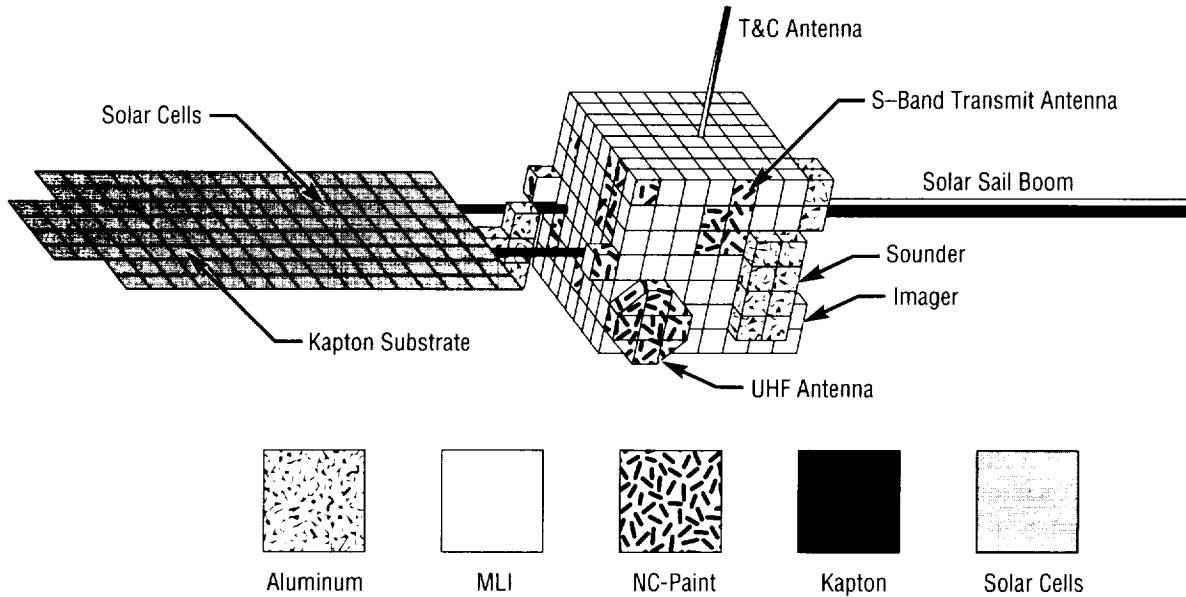
FIGURE 180.—NASA Charging Analyzer Program for Geosynchronous Orbit (NASCAP/GEO) model of a geosynchronous communications satellite.

the application of computer modeling to estimate the extent and likelihood of electric charge buildup on spacecraft surfaces. Three-dimensional computer programs specifically designed for this purpose include the NASA Charging Analyzer Program for Low-Earth Orbit (NASCAP/LEO), used to simulate spacecraft charging of low-inclination, low-altitude, Earth-orbit spacecraft; Potentials of Large spacecraft in Auroral Regions (POLAR), used to model spacecraft charging in low-altitude, POLAR orbit; and the NASA Charging Analyzer Program for Geosynchronous Orbit (NASCAP/GEO), used to model spacecraft charging by a geomagnetic substorm.

A NASCAP or POLAR model of a spacecraft is formed by combining various geometric shapes in an attempt to simulate the spacecraft structure,

and then assigning materials to the outer surfaces of the structure (fig. 180). Areas on the model of the spacecraft where large levels of charging develop are identified as possible arc-discharge sites. Using computer analysis, trade studies are conducted on alternative spacecraft designs in an effort to balance the risks associated with charging effects (primarily the probability and severity of discharges) against other design considerations. As a result of the computer analyses, design recommendations are made to address specific spacecraft charging issues that arise.

The fact that the effects attributed to spacecraft charging can be of serious engineering concern makes spacecraft charging an important issue in the design of any spacecraft. One method to guard against charging effects is to

implement a spacecraft charging effects protection plan. The desired outcome of such a protection plan is a resulting spacecraft design that both limits the causes and effects of spacecraft charging and incorporates immunity to those effects.

[1]Vampola, A.L., 1980. P78-2 Engineering Overview. Spacecraft-Charging Technology, 1980 Conference, NASA CP-2182:439-60.

Sponsor: Office of Space Flight

Industry Involvement: Sverdrup Technology, Inc.

• • • • •

251

Abbreviations and Acronyms

AADSF	Advanced Automated Directional Solidification Furnace	BTOS	Beam Transmission Optical System
AAS	American Astronautical Society	CA	clocking angle
ACES	advanced control evaluation for structures	CAD	computer-aided design
ACTIS	Advanced Computed Tomography Inspection System	CAGI	computer-aided grid interface
		CAMEX	Convection and Moisture Experiment
AEOLUS	Autonomous Earth Orbiting Lidar Utility Sensor	CaPE	Convection and Precipitation/ Electrification
AETF	Advanced Engine Test Facility	CAR	critical area response
AFM	advancing front method	CASE	computer-aided software engineering
AFSIG	Ascent Flight System Integration Group	CAVE	Computer Applications and Virtual Environments Laboratory
Ag-MH	silver-metal hydride	CBL	convective boundary layer
Ag-Zn	silver-zinc	CCD	charge-coupled device
AGU	American Geophysical Union	CCP	center cracked panel
AI	artificial intelligence	CCT	cognitive computing techniques
AIAA	American Institute of Aeronautics and Astronautics	Cd	cadmium
		CDDF	Center Director's Discretionary Fund
AITP	Aerospace Industry Technology Program	CEC	Chemical Equilibrium Computer
albedo	reflected solar energy	CEETC3	Combined Environmental Effects Test-Cell 3 system
AMCC	advanced main combustion chamber		
AMPR	Advanced Microwave Precipitation Radiometer	CFC	chlorofluorocarbon
		CFD	computational fluid dynamics
ANOVA	analysis of variance	CFE	continuous-flow electrophoresis
AOPL	Aerosol Optical Properties Laboratory	CGRO	Compton Gamma-Ray Observatory
AR&C	automated rendezvous and capture	CHymP	CaPE Hydrometeorology Project
ARC	Ames Research Center	CICM	coaxial injection combustion model
ARCS	Argon Release for Controlled Studies sounding rocket	CIRS	composite infrared spectrometer
		CLR	coherent laser radar
ASCA	Advanced Satellite for Cosmology and Astrophysics	cm	centimeter
		CO	carbon monoxide
ASRM	advanced solid rocket motor	CO_2	carbon dioxide
ASTEX	Atlantic Stratocumulus Transition Experiment	codecs	compressor-decompressors
		COHMEX	Cooperative Huntsville Meteorological Experiment
ASTM	American Society for Testing Materials		
ATD	alternate turbopump development	CORSSTol	Cylinder Optimization of Rings, Skin, and Stringers with Tolerance sensitivity
ATLAS-3	Third Atmospheric Laboratory for Applications and Science Mission	COST	controls, optics, structures, and thermal interactions
ATMOS	Atmospheric Trace Molecules Observed By Spectroscopy		
		COTS	commercial off-the-shelf
ATS	automated torque sensor	CRES	corrosion-resistant steel
AXAF-I	Advanced X-Ray Astrophysics Facility—Imaging	CSC	Computer Science Corporation
		CSI	controls/structures interaction
BATSE	Burst and Transient Source Experiment	CSI/GTF	Controls/Structures Interaction Ground Test Facility
blisk	integrally bladed turbine disk		
BOL	beginning-of-life	CTOD	crack-tip opening displacement

CTTP	Cryogenic Tank Technology Program	g/cm^3	grams per cubic centimeter
Cu	copper	Ga	gallium
CW	continuous wave	GASP	General Aerodynamic Simulation Program
DAAC	Distributed Active Archive Center		
dc	direct current	GATV	ground-to-air television
DC-X	Delta Clipper Experimental vehicle	GC	generic card
dc/dc	direct current/direct current	GCIP	GEWEX Continental Scale International Project
DCE	DC electric field instrument		
DMSP SSM/I	Defense Meteorological Satellite Program Special Sensor Microwave/Imager	GCM	general circulation model
		GDSS	General Dynamics Space Systems
DOD	Department of Defense	Ge	germanium
DOE	Department of Energy	GENIE	general grid generation system
DSMC	direct simulation Monte Carlo analysis	GEO	geosynchronous orbit
DTM	digital transient model	GEOSIM	GEOphysical fluid-flow SIMulator
DTO	demonstration test objective	GEOWARN	Global Emergency Observation Warning and Relief Network
ECMWF	European Center for Medium-range Weather Forecasting		
		GEWEX	Global Energy and Water Cycle Experiment
EDO	extended-duration orbiter		
ELV	expendable launch vehicles	GGOT	Gas Generator Oxidizer Turbine
EOL	end-of-life	GGS	Global Geospace Study
EOS	Earth Observation System	GHC	generalized hyper-coherence
EPA	Environmental Protection Agency	GHe	gaseous helium
EPFCG	elastic-plastic fatigue crack growth	GIS	geographic information system
EPRI	Electric Power Research Institute	GLOBE	GLObal Backscatter Experiment
EPS	electrical power system	GN&C	guidance, navigation, and control
ERBE	Earth Radiation Budget Experiment	GOES	Geostationary Operational Environmental Satellite
ESA	European Space Agency		
ET	elapsed time	GONG	Global Oscillations Network Group
ETO	Earth-to-Orbit	GPC	Gravity Probe B
EUV	extreme ultraviolet	GPS	Global Positioning System
eV	electron volts	GRAM	Global Reference Atmospheric Model
EVA	extravehicular activity	GSFC	Goddard Space Flight Center
EVM	Experimental Vector Magnetograph (also EXVM)	GST	glutathione S-transferase
		GTF	ground test facility
f#	focal ratio	GVaP	Global Energy and Water Cycle Experiment Water Vapor Project
FACE	Florida Area Cumulus Experiment		
FAD	failure assessment diagram	H^+	hydrogen ion
FDIR	fault detection, isolation, and recovery	HBMS	Hirshfelder-Buehler-McGee-Sutton
FDNS	Finite-Difference, Navier-Stokes	HCF	high-cycle fatigue
FEM	finite element model	HCF	hydrogen cold flow
FOV	field of view	HDOS	Hughes Danbury Optical Systems
fps	frames per second	He	helium
FRL	Flight Robotics Laboratory	He^+	helium ion
FSSP	Forward-Scattering Spectrometer Probe	He-Cd	helium-cadmium
ftp	file transfer protocol	He-Ne	helium-neon
FUV	far ultraviolet	HEE	hydrogen environmental embrittlement
G	units of gravitational force	HESI	High-Energy Solar Imager

Hex	heat exchanger	ITCZ	InterTropical Convergence Zone
Hg	mercury	ITL	Inducer Test Loop
Hg-Xe	mercury-xenon	IV	independent variable
HH-PCAM	hand-held protein crystallization in microgravity hardware	IWC	integrated water content
		J	joule
HI-PAC DTV	high-packed digital television (also HI-PAC)	JANNAF	Joint Army, Navy, NASA, and Air Force
		JIRAD	joint independent research and development
HIP	hot isostatic pressing		
HIV	human immunodeficiency virus	JPEG	Joint Photographic Experts Group
Ho, Tm:YAG	holmium, thulium: yttrium aluminum garnet	JPL	Jet Propulsion Laboratory
		JSC	Johnson Space Center
HOMO–LUMO	highest occupied molecular orbital-lowest unoccupied molecular orbital	K	Kelvin
		KAO	Kuiper Airborne Observatory
HOSC	Huntsville Operations Support Center	KATE	Knowledge-based Autonomous Test Engineer
HPFT	high-pressure fuel turbine		
HPFTP	high-pressure fuel turbopump	kbps	kilobits per second
HPOTP	high-pressure oxygen turbopump	keV	kiloelectron volts
HPOTP	high-pressure oxidizer turbopump	kHz	kilohertz
HRDM	high-rate demultiplexer	km	kilometer
HRM	high-rate multiplexer	km/s	kilometers per second
HRV	highly reusable vehicles	KSC	Kennedy Space Center
HSL	Huntsville Simulation Laboratory	Ku-band	15.250 to 17.250 gigahertz
HST	Hubble Space Telescope	kWh	kilowatt hours
Hz	hertz	L-O-L	like-on-like
IAU	International Astronomical Union	LAD	liquid acquisition device
ICD	interface control document	LALMM	load-allowable load minimum margin
IDNDR	International Decade for National Disaster Reduction	LaRC	Langley Research Center
		LAWS	Laser Atmospheric Wind Sounder
IECEC	Intersociety Energy Conversion and Engineering Conference	lbm/sec	pound mass per second
		LCF	low-cycle fatigue
IFM	in-flight maintenance	LDV	laser Doppler velocimeter
IGES	Initial Graphics Exchange Specification	LEIF	Low-Energy Ion Facility
ILC	intelligent load controller	LEO	low-Earth orbit
IMF	interplanetary magnetic field	LIS	Lightning Imaging Sensor
IML–2	International Microgravity Laboratory 2	LLPC	liquid-liquid partition chromotography
INS	inertial navigation system	LMM	load minimum margin
InSb	indium antimonide	LMSC	Lockheed Missiles and Space Corporation
IPC	intelligent power controller	LN_2	liquid nitrogen
IR	infrared	LO_2	liquid oxygen (also lox)
IRAD	industrial research and development	LO_2-LH_2	liquid oxygen-liquid hydrogen
IRAS	Infrared Astronomy Satellite	LOLC	Laser Optical Particle Counter
IRTF	Infrared Telescope Facility	lox	liquid oxygen (also LO_2)
ISCCP	International Satellite Cloud Climatology Project	LPFTP	low-pressure fuel turbopump
		LTC	low thermal conductivity
ISO	Infrared Space Observatory	LUTE	Lunar Ultraviolet Telescope Experiment
ISOPHOT	Infrared Space Observatory spectrophotometer	m	meter

MACAWS	Multicenter Airborne Coherent Atmospheric Wind Sensor	NiH_2	nickel-hydrogen
maglev	magnetically levitated	NIR	near-infrared
MARCSIM	MSFC automated rendezvous and capture simulation	NIST	National Institute for Standards and Technology
MB/s	megabits per second	NITROX	increased oxygen/reduced nitrogen
MCC	main combustion chamber	NLO	nonlinear optical
MCP	microchannel plates	NLS	National Launch System
MCPT	multicycle proof test	nm	nanometer
MECO	main engine cutoff	NOAA	National Oceanic and Atmospheric Administration
MeV	million electron volts	NOx	nitric oxide
MHD	magnetohydrodynamic	NS	neutron star
MHz	megahertz	NSTS	National Space Transportation System
MI	Magnetosphere Imager	NTSC	National Television Standards Committee
MIMR	Multifrequency Imaging Microwave Radiometer	NURBS	non-uniform rational B-splines
		NUV	near-ultraviolet
MIXE	Marshall Imaging X-Ray Experiment	O^+	oxygen ion
MLT	magnetic local time	OACT	Office of Advanced Concepts and Technology
MNA	2-methyl-4-nitroniline		
MOSFET	metal oxide semiconductor field-effect transistor	OLR	outgoing longwave radiation
		OMV	orbital maneuvering vehicle
MPa	megaPascal	OSEE	optically simulated electron emission
MPEG	Motion Picture Experts Group	OSHA	Occupational Safety and Health Administration
MR	mixture ratio		
MSCSurv	Manned Spacecraft Crew Survivability	OTD	Optical Transient Detector
MSU	microwave sounding unit	OTTR	Oxidizer Technology Turbine Rig
MTPE	Mission to Planet Earth	P&W	Pratt and Whitney
mV/m	millivolts per meter	P-T	pressure-temperature
v	frequency	PAM	portable automated mesonet
NAOMI	National Adaptive Optics Mission Initiative	PAMELA	Phased-Array Mirror, Extendible Large Aperture
NARC	North American Rayon Corporation	PAN	polyacrylonitrile
NASCAP/GEO	NASA Charging Analyzer Program for Geosynchronous Orbit	PBL	planetary boundary layer
		PCC	Precision Castparts Corporation
NASCAP/LEO	NASA Charging Analyzer Program for Low-Earth Orbit	PCR	payload control room
		PCR	principal component regression
NASP	National Aerospace Plane	PDF	probability distribution function
NAVC	Northeast Alternative Vehicle Consortium	PEG	polyethylene glycol
NBS	Neutral Buoyancy Simulator	PI	principal investigator
NCAR	National Center for Atmospheric Research	PL	peak load
NDE	nondestructive evaluation	PLS	partial least squares
Ne	neon	PMD	propellant management device
NESDIS	National Environmental Satellite Data Information Service	PMM	probability matching method
		POLAR	Potentials of Large Spacecraft in Auroral Regions
Ni	nickel		
Ni-Cd	nickel-cadmium	PRF	pulse repetition frequency
Ni-MH	nickel-metal hydride		

PRISM	Passively Cooled Reconnaissance of the Interstellar Medium	*Sj*GST	Schistosoma japonicum
PSD	power spectral density	SLA	stereolithography
PSEM	phase-synchronized enhancement method	SNR	signal-to-noise ratio
PSI	phase-shifting interferometry	SNTP	space nuclear thermal propulsion
PSI	plasma source instrument	SOF	scintillating optical fibers
psia	pounds per square inch absolute	SOFIC	Scintillating Optical Fiber Ionization Calorimeter
PSW	physical split-window	SOHO	Solar and Heliospheric Observatory
PTDS	Post-Test Diagnostic System	SPIE	Society of Photo-optical Instrumentation Engineers
QE	quantum efficiency		
QN	quadravariate normal	SPIP	Solid Propulsion Integrity Program
R-curves	resistance curves	SPSR	space-portable spectroreflectometer
R/S	range over standard	SRM	solid rocket motor
REFLEQS	REactive FLow EQuation Solver	SSA	Space Suit Assembly
RGB	red, green, blue	SSM/I	Special Sensor Microwave/Imager
RIMS	retarding ion mass spectrometer	SSM/PMAD	Space Station Module Power Management and Distribution
RLV	reusable launch vehicle		
RMS	remote manipulator system	SSME	space shuttle main engine
rms	root-mean-square	SSTO	single-stage-to-orbit
RNTS	Rocket Nozzle Technology Subcommittee	STICS	super thermal ion composition spectrometer
ROSETA	range over standard deviation experimental trend analysis	STME	space transportation main engine
RPC	remote power controller	STS	space transportation system
RSRM	redesigned solid rocket motor	STV	space transfer vehicle
RTG	radioisotope thermoelectric generator	SWRI	Southwest Research Institute
RTLS	return-to-launch-site	SXI	Solar X-Ray Imager
SAFD	System for Anomaly and Failure Detection	TAL	time after launch
		TAL	trans-Atlantic landing
SAO	Smithsonian Astrophysical Observatory	TAL	transoceanic abort landing
SBIR	Small Business Innovation Research	TAPP	Twin Auroral Plasma Probes
SBTD	space booster technology demonstrator	TCA	thrust chamber assembly
SCIFER	Sounding of the Cleft Ion Fountain Energization Region	τ_{decay}	time constant
		Te	tellurium
SCIM	standard cubic inches per minute	TEM	transition electron microscope
SCN/H$_2$0	succinonitrile/water	THM	traveling heater method
SDIO	Strategic Defense Initiative Organization	TIDE	Thermal Ion Dynamics Experiment
SDT	science definition team	TIPS	Thermal Input Printing System
SEDS	Students for the Exploration and Development of Space	Tm, Ho: YLF	thulium, holmium: yttrium lithium fluorine
SEDSAT	Students for the Exploration and Development of Space Satellite	TMI	Tropical Rainfall Measuring Mission Microwave Imager
SEEF	Space Environments Effects Facility	TOA	top-of-atmosphere
SHEELS	Simulator for Hydrology and Energy Exchange at Land Surface	TOGA COARE	Tropical Ocean Global Atmosphere Coupled Ocean Atmosphere Response Experiment
SHG	second harmonic generation		
Si	silicon	TPS	thermal protection system
SIM	simulation control room	τ_{rise}	rise time

TRMM	Tropical Rainfall Measuring Mission
TRP	Technology Reinvestment Project
TTA	turbine test article
TTB	Technology Test-Bed
TTE	turbine test equipment
UAH	University of Alabama in Huntsville
UAH-ARC	University of Alabama in Huntsville Aerophysics Research Center
ULE	ultra-low expansion
UPS	uninterruptible power supply
USML–2	U.S. Microgravity Laboratory 2
USMP–2	Second United States Microgravity Payload
USNAWC	U.S. Navy Air-Warfare Center
UTC	universal time coordinated
UV	ultraviolet
UVI	Ultraviolet Imager
V	volt
Vac	volts, alternating current
VAS	Visible Infrared Spin-Scan Radiometer Atmospheric Sounder
VDA	video decoder assembly
Vdc	volts, direct current
VEA	video encoder assembly
VETA–I	Verification Engineering Test Article I
VGS	video guidance sensor
VI	virtual instrument
VISSR	Visible Infrared Spin-Scan Radiometer
VPCR	virtual payload control room
VPPA	variable polarity plasma arc
VR	virtual reality
VSIM	virtual simulation control room
VUV	vacuum ultraviolet
VWM	vector wind model
WTA	West Test Area
XUV	x-ray ultraviolet
Z-R	reflectivity-rain rate
Zn	zinc
°C	degrees Celsius
μm	micrometer

Index of Contacts

263

Index of Key Words

About Key Words

To broaden the availability of this report, the text is placed on-line on the FEDIX Technology Information System computer, which can be easily accessed by phone and terminal. This enhances the opportunities for technology transfer to the private sector.

For further information about FEDIX, contact:

Office of the Associate Director for Science
Mail Stop DS01
Marshall Space Flight Center, AL 35812
205–544–3033